

Advances in Volcanology

Christoph Breitkreuz
Sergio Rocchi *Editors*

Physical Geology of Shallow Magmatic Systems

Dykes, Sills and Laccoliths



 Springer

The Springer logo, which consists of a white chess knight piece on a pedestal, followed by the word "Springer" in a white, serif font.

Advances in Volcanology

An Official Book Series of the International
Association of Volcanology and Chemistry
of the Earth's Interior

Series editor

Karoly Nemeth, Palmerston North, New Zealand

More information about this series at <http://www.springer.com/series/11157>

Christoph Breitkreuz · Sergio Rocchi
Editors

Physical Geology of Shallow Magmatic Systems

Dykes, Sills and Laccoliths

 Springer

Editors

Christoph Breitzkreuz
Freiberg University of Mining and
Technology
Freiberg
Germany

Sergio Rocchi
Università di Pisa
Pisa
Italy

ISSN 2364-3277

ISSN 2364-3285 (electronic)

Advances in Volcanology

An Official Book Series of the International Association of Volcanology and
Chemistry of the Earth's Interior

ISBN 978-3-319-14083-4

ISBN 978-3-319-14084-1 (eBook)

<https://doi.org/10.1007/978-3-319-14084-1>

Library of Congress Control Number: 2017963549

© Springer International Publishing AG, part of Springer Nature 2018, corrected publication 2018
This work is subject to copyright. All rights are reserved by the Publisher, whether the whole or
part of the material is concerned, specifically the rights of translation, reprinting, reuse of
illustrations, recitation, broadcasting, reproduction on microfilms or in any other physical way, and
transmission or information storage and retrieval, electronic adaptation, computer software, or by
similar or dissimilar methodology now known or hereafter developed.

The use of general descriptive names, registered names, trademarks, service marks, etc. in this
publication does not imply, even in the absence of a specific statement, that such names are exempt
from the relevant protective laws and regulations and therefore free for general use.

The publisher, the authors and the editors are safe to assume that the advice and information in this
book are believed to be true and accurate at the date of publication. Neither the publisher nor the
authors or the editors give a warranty, express or implied, with respect to the material contained
herein or for any errors or omissions that may have been made. The publisher remains neutral with
regard to jurisdictional claims in published maps and institutional affiliations.

Printed on acid-free paper

This Springer imprint is published by Springer Nature

The registered company is Springer International Publishing AG

The registered company address is: Gewerbestrasse 11, 6330 Cham, Switzerland

Foreword

The intersection between surface volcanic rocks and their feeder systems has a fascinating history. What is the volcanic-plutonic interface telling us about the spatial, temporal and thermal evolution of sub-volcanic magmatic systems? Do they preserve information of use in forecasting future volcanic hazards? What is the link to deeper-level magmatism and the geochemical evolution of Earth's continental crust? Are there extra-terrestrial counterparts?

Mostly these questions are not new. Some of the greatest names in the development of igneous geology including Bowen, Cloos, Daly, Geikie, Harker, Holmes, Iddings, Mercalli, Sapper and Tyrrell embraced this topic. Between them they agreed the defining feature of high-level igneous intrusions (injected bodies) is that they are visibly enclosed by surrounding country rock with the exception of the magma feeding channel. However, the position regarding plutons and batholiths was far less clear. Were these subjacent rocks, apparently downwardly enlarging, magma intrusions at all, given the lack of observational evidence for a floor or base? If not, how did plutons relate to chemically associated volcanic rocks, often found in conjunction? And should large mafic intrusions be treated the same way?

Looking back through geological literature on the forms and structures of igneous rocks in the first 50 years of the 20th century makes fascinating reading. The conclusion by many of his contemporaries that batholiths were indeed injected bodies is rejected by R. A. Daly in the 1933 edition *Igneous Rocks and the Depths of the Earth* as “premature”. This comes despite the relaxed acceptance that in places including Dartmoor, England, “extensive granites, formally called batholiths, have been shown to be of sheet-like, laccolithic, phacolithic or lopolithic nature”. To those familiar with contemporary views of batholith formation, the freshness of this statement is striking—confirmation that there really is nothing new under the sun. Yet the ease by which two opposing points of view on the origin of batholiths can be accommodated seems odd—surely there should be one consistent truth? It seems these great minds could slip easily between rival interpretations of how intrusive rocks came to be.

One reason could be that early debate on high level intrusions revolved mostly around definitions to describe and classify their shape and geometry as opposed seeking a coherent view on underlying processes. Descriptive terms abound. Some of them, including Bysmaliths, Entmoliths, Sphenoliths,

Akmaliths and Harpoliths, sound like monsters from a Harry Potter novel! The overriding sense is that of a community deliberately seeking out small differences which become amplified into conflicting theories about origins and meaning. From small beginnings these debates unchecked proliferate into so-called controversies, which, as happened with granites, are a sure sign of a subject area becoming moribund.

Luckily, understanding how magmas move about in the near sub-surface has improved significantly in the last 50 years. The realisation that shape and form are largely viscosity-related means that magmatic systems can be seen from a physical perspective as a continuum between differing compositions. In this system-wide view, arguments about intrusion geometry are understood to be manifestations of a deeper, dissipative and self-similar process.

That is why the integrated, systems-level approach put forward in this book is the right one. The science of shallow-level magmatic systems has entered a new and exciting mature phase. The editors both have long and distinguished track records in researching the origins and emplacement of shallow igneous intrusions, most notably sills and laccoliths. They have published research papers and edited special volumes on this topic for several decades now and the knowledge gained from multidisciplinary studies by international teams of geologists, geophysicists and petrologists has been distilled cleverly into this welcome and timely book.

Northampton, UK
November 2017

Nick Petford

Preface



History, Design and Aims of This Book

The origins of intrusive rocks have been widely discussed for a couple of centuries, and the ways volcanoes work have attracted scientists and laymen since the dawn of mankind. However, shallow igneous intrusions, representing the obvious link between the hidden plutonic kingdom and the fiery volcanic realm, have not received the attention they deserve, leading to some shortcomings in the communication between “plutonic” and “volcanic” researchers. This book is an effort devoted to heal this breach and should also serve as a reference in the field of subvolcanic systems for master- and Ph.D. students, geo-scientists and professionals. At the same time, we hope that future research in the field will be sparked by its publication.

The present book is directly related to, and a result of, a series of five field workshops that occurred from 2002 to 2012 in various countries. The series of LASI¹ field workshops started in October 2002 in Freiberg (Saxony,

¹LASI stands for Laccoliths, sills and dykes—Physical geology of shallow-level magmatic systems

Germany), where one of us (C.B.) and Alex Mock hosted 40 participants coming from 10 countries. A one-day field trip was undertaken to examine Late Paleozoic sill and laccolith complexes in eastern Germany (abstract and field guide volumes of LASI can be found on the LASI web site).²

LASI II followed in April 2006 on the Isle of Skye in NW Scotland, organized by Ken Thomson, Nick Petford and Donny Hutton, gathering 53 scientists from 16 countries. Of course, the mafic Cenozoic sill complex of that island was the topic of the field trip.

Weather conditions improved somewhat with the field workshops that followed. LASI III was held on Elba Island (Tuscany, Italy) in September 2008, where 44 participants from 17 countries gathered and examined the classical Christmas-tree laccolith complex and surrounding waters of the Tyrrhenian island.

LASI IV led to the mother of laccolith systems, the Henry Mountains in Utah (USA). There, in 1877 following two weeks of field work, Karl Groove Gilbert defined what a laccolith looks like. In September 2010, the team led by Sven Morgan made sure that 33 participants from 10 countries deeply enjoyed both seminars and outcrops. Connected to this, in a one-day field trip, David Hacker introduced the spectacular subvolcanic bodies and related landslides of the Iron Axis Mountains in SW Utah (Chapter “[Catastrophic Collapse Features in Volcanic Terrains: Styles and Links to Subvolcanic Magma Systems](#)”).

In November 2012, LASI V was held in South Africa with 44 participants from 11 countries. A warm-hearted welcome, a smooth organisation and an interdisciplinary data set were the ingredients applied by the people around Sverre Planke and Henrik Svensen for a successful introduction to the magnificent saucer-shaped sill complex in the Karoo Basin (Chapter “[Subvolcanic Intrusions in the Karoo Basin, South Africa](#)” and parts of Chapter “[Geochemical Fingerprinting and Magmatic Plumbing Systems](#)”).

A total of 350 geoscientists from 32 countries co-authored papers that were presented during the five LASI field workshops. The most prominent methods applied to subvolcanic systems were geometric and textural studies, geophysics (mostly 3D seismic and paleomagnetism), and analog and numeric modelling, as well as petrological/geochemical investigations. Silica-rich and —poor complexes, and deep-seated as well as shallow systems have been examined. Within plate tectonic settings, intra-continental rift and plume-related systems dominated.

During all five LASI events, Europe was the most prominent host of subvolcanic complexes described; LASI V boasted examples from the venue country, South Africa. Clearly, Mesozoic and Cenozoic subvolcanic complexes, being less altered and deformed, prevailed over Paleozoic and Precambrian examples.

A large number of papers authored by LASI participants have been published in the last 15 years, and have been widely cited in the present book. As a direct outcome of LASI conferences, two Special Publications

²https://people.unipi.it/sergio_rocchi/lasi/

of the Geological Society of London (Breitkreuz and Petford 2004; Thomson and Petford 2008), as well as a special issue of *Geosphere* (Rocchi et al. 2010), can be noted.

The series of LASI field workshops displayed the enormous range in size, emplacement depth and composition of subvolcanic systems. Fossil volcanic centres often have been eroded down to the subvolcanic level, exposing coherent weathering-resistant subvolcanic rocks (volcanic necks, paleo-magmatic arc successions). As a consequence, subvolcanic rocks are overrepresented in the geological record and their preservation potential is high compared to many volcanic rocks such as fallout or non-welded pyroclastic flow deposits. Understanding the geometry of subvolcanic complexes and “reading” the internal and external textures of these rocks enable geologists and geophysicists to distinguish subvolcanic complexes from volcanic counterparts. This distinction obviously bears importance for the lithostratigraphic and magmatic evolution of a particular lithospheric block.

This book, presented by experts in their respective fields, intends to summarize the wealth of knowledge about subvolcanic systems. The first part of the book (Chapters “[Physical Geology of Shallow-Level Magmatic Systems—An Introduction](#)”–“[Sills in Sedimentary Basins and Petroleum Systems](#)”) collects comprehensive reviews on various aspects of subvolcanic systems. In the second part (Chapters “[The Subvolcanic Units of the Late Paleozoic Halle Volcanic Complex, Germany: Geometry, Internal Textures and Emplacement Mode](#)”–“[Laccolithic Emplacement of the Northern Arran Granite, Scotland, Based on Magnetic Fabric Data](#)”), case studies of important subvolcanic complexes are being presented.

Acknowledgements

In times of demanding publication efforts in high-impact journals, preparedness of authors to contribute to such a book is supremely acknowledged. We thoroughly enjoyed working closely with high-level scientists to finally produce this hopefully useful piece of work.

At the same time, we really have to thank the reviewers for their outstanding effort to improve the scientific quality of every chapter. We acknowledge reviews by Valerio Acocella, Olivier Bachmann, Eric H. Christiansen, Alexander Cruden, Christopher Henry, John P. Hogan, Eric Horsman, Nina Kukowski, William P. Leeman, Craig Magee, Julian Marsh, Nick Petford, Nick Schofield, Lee Siebert, David S. Westerman, and Paul Wignall.

Thanks go to the series editor, Karoly Nemeth, for including this book into the IAVCEI series *Advances in Volcanology*. We also highly appreciate the professional editorial assistance by the team of Annett Büttner from Springer Nature.

Freiberg, Germany
Pisa, Italy
September 2017

Christoph Breitkreuz
Sergio Rocchi

References

- Breitkreuz C, Petford N (2004) Physical Geology of High-Level Magmatic Systems. In: Geological Society, London, Special Publication, 234, p 253
- Rocchi S, Dini A, Mazzarini F, Westerman DS (2010) Themed Issue: LASI III—Magma pulses and sheets in tabular intrusions. *Geosphere*
- Thomson K, Petford N (2008) Structure and Emplacement of High-Level Magmatic Systems. In: Geological Society, London, Special Publication, 302, p 227

The original version of the book was revised: Incorrect chapter DOIs and Copyright Year information for all chapters have been updated and the series subtitle has been included. The erratum to the book is available at https://doi.org/10.1007/11157_2018_2005

Contents

Physical Geology of Shallow-Level Magmatic Systems—An Introduction	1
Sergio Rocchi and Christoph Breitkreuz	
Geometric Scaling of Tabular Igneous Intrusions: Implications for Emplacement and Growth	11
A.R. Cruden, K.J.W. McCaffrey and A. P. Bungler	
Plumbing Systems of Shallow Level Intrusive Complexes	39
Dougal A. Jerram and Scott E. Bryan	
The Volcanic-Plutonic Connection	61
Allen F. Glazner, Drew S. Coleman and Ryan D. Mills	
Structures Related to the Emplacement of Shallow-Level Intrusions	83
David Westerman, Sergio Rocchi, Christoph Breitkreuz, Carl Stevenson and Penelope Wilson	
Geochemical Fingerprinting and Magmatic Plumbing Systems	119
Christophe Y. Galerne and Else-Ragnhild Neumann	
Geophysics and Remote Sensing	131
Sverre Planke, Henrik Svensen, Reidun Myklebust, Stephen Bannister, Ben Manton and Lars Lorenz	
Laboratory Modelling of Volcano Plumbing Systems: A Review	147
Olivier Galland, Eoghan Holohan, Benjamin van Wyk de Vries and Steffi Burchardt	
Catastrophic Collapse Features in Volcanic Terrains: Styles and Links to Subvolcanic Magma Systems	215
David B. Hacker, Peter D. Rowley and Robert F. Biek	
Sub-Volcanic Intrusions and the Link to Global Climatic and Environmental Changes	249

Henrik H. Svensen, Sverre Planke, Else-Ragnhild Neumann, Ingrid Aarnes, Julian S. Marsh, Stéphane Polteau, Camilla H. Harstad and Luc Chevallier	
Sills in Sedimentary Basins and Petroleum Systems	273
Nick Schofield, Dougal A. Jerram, Simon Holford, Stuart Archer, Niall Mark, Adrian Hartley, John Howell, David Muirhead, Paul Green, Donny Hutton and Carl Stevenson	
The Subvolcanic Units of the Late Paleozoic Halle Volcanic Complex, Germany: Geometry, Internal Textures and Emplacement Mode	295
Christoph Breitzkreuz, Bodo-Carlo Ehling and Nicole Pastrik	
Rise and Fall of a Multi-sheet Intrusive Complex, Elba Island, Italy	309
D.S. Westerman, S. Rocchi, A. Dini, F. Farina and E. Roni	
Progressive Construction of Laccolithic Intrusive Centers: Henry Mountains, Utah, U.S.A	327
Eric Horsman, Robert J. Broda, Nathan Z. Gwyn, Elizabeth A. Maurer, Erik D. Thornton and Mitchell T. Ward	
Sub-volcanic Intrusions in the Karoo Basin, South Africa	349
Henrik H. Svensen, Stéphane Polteau, Grant Cawthorn and Sverre Planke	
Dykes, Sills, Laccoliths, and Inclined Sheets in Iceland	363
Agust Gudmundsson, Federico A. Pasquarè and Alessandro Tibaldi	
Laccolithic Emplacement of the Northern Arran Granite, Scotland, Based on Magnetic Fabric Data	377
C.T.E. Stevenson and C. Grove	
Erratum to: Sub-volcanic Intrusions in the Karoo Basin, South Africa	E1
Henrik H. Svensen, Stéphane Polteau, Grant Cawthorn and Sverre Planke	
Erratum to: Physical Geology of Shallow Magmatic Systems	E3
Christoph Breitzkreuz and Sergio Rocchi	
Index	403

About the Editors



Chris (right) and Sergio (left) enjoying the overview of the Golden Valley saucer-shaped sill in Karoo during LASI V

Christoph Breitkreuz

Born 1955 in Berlin, Christoph Breitkreuz studied geology at TU Berlin. At the same university he completed PhD in 1982 with a topic on Mesozoic plutons in the Coastal Cordillera in northern Chile. Also at TU Berlin, 1986 he obtained habilitation with a revision of Paleozoic volcanosedimentary successions in northern Chile.

After a research stay at University of Kansas (1992-1994), Christoph Breitkreuz received a Heisenberg Fellowship (1995-2000) which he spent at GFZ Potsdam. This was also the start for research on Late Paleozoic volcanic and subvolcanic systems in central Europe – a topic that forms focus of his activity until today. Since 2000 Christoph Breitkreuz is full professor at the TU Bergakademie Freiberg. There, he established a Centre for Volcanic Textures with more than 3000 samples.

<http://tu-freiberg.de/geo/sedi/team/cbreitkreuz>

Sergio Rocchi

Full professor at University of Pisa, head of the Dipartimento di Scienze della Terra.

Research activities: Magma emplacement in tabular igneous intrusions and link to ore deposits, Tuscany. Intrusive and shallow-level magmatism in post-collisional settings, Paleozoic in Antarctica, and Neogene in Tuscany. Rift/post-rift/mantle plume magmatism, Antarctica, Senegal and Sicily. Glacial volcanology and drill cores for paleo-environmental evolution, Antarctica. Sediment geochemistry and detrital zircon geochronology, northern Apennines.

Author of over 100 publications in peer-reviewed scientific journals.

http://people.unipi.it/sergio_rocchi/

List of Acronyms (only non-geographical)

AFC	Assimilation fractionation crystallisation process
AFTA	Apatite fission track analysis
AMS	Anisotropy of magnetic susceptibility
AVO	Amplitude versus offset
CFBP	Continental flood basalt province
CSD	Crystal size distribution
CSEM	Controlled-source electromagnetic survey
DIC	Digital image correlation
DSI	Discrete smooth interpolation
EC-RAFC	Effects of concurrent eruption, recharge, variable assimilation and fractional crystallization (EC-E'RA χ FC)
FS-DFA	Forward stepwise-discriminant function analysis
GEOROC	Geochemistry of rocks of the oceans and continents (database)
GPS	Geopositioning system
ICP-AES	Inductively coupled plasma atomic emission spectrometry
ICP-MS	Inductively coupled plasma mass spectrometry
InSAR	Interferometric synthetic aperture radar
LASI	Laccoliths, sills and dykes—Physical geology of shallow-level magmatic systems (series of field workshop)
LEFM	Linear elastic fracture mechanics
LIP	Large igneous province
LNB	Level of neutral buoyancy
LOI	Loss on ignition
MME	Mafic microgranular enclave
MPS	Maximum particle size
NAIP	North Atlantic Igneous Province
NAVDAT	North American volcanic and intrusive rock database
PAST	Paleontological statistics software package
PCA	Principal component analysis
PDMS	Polydimethylsiloxane
PETM	Paleocene-Eocene thermal maximum
PM	Primitive mantle
REE	Rare earth element
RMA	Reduced major axis regression
RTV	Room temperature vulcanization silicone
SDP	Spatial distribution pattern
SLI	Shallow-level intrusions
SPO	Shape-preferred orientation

TAS	Total alkali silica (plot)
TIMS	Thermal ionisation mass spectrometry
TOC	Total organic carbon
VPDB	Vienna Peedee Belemnite standard
VR	Vitrinite reflectance

Physical Geology of Shallow-Level Magmatic Systems—An Introduction

Sergio Rocchi and Christoph Breitzkreuz

The fate of magma is commonly seen as either eruption from volcanic vents or emplacement at depth into the crust. However, magmas often solidify in the very shallow crust (i.e. less than ca. 3 km deep), as either subhorizontal intrusions such as sills and laccoliths, or as frozen vertical conduits, i.e. dykes. Which of these processes will prevail is controlled by intrinsic parameters like magma density, viscosity, volume and ascent rate. Among external parameters, far field stress, as well as variations of density and strength in the host rock, are significant.

1 What Is a Subvolcanic Body?

A subvolcanic intrusion is a cooled magma body emplaced at shallow depth into the upper crust, between a few tens of m and approximately

3 km.¹ In the absence of stratigraphic and/or geobarometric evidence, it can be recognized by having emplaced below the Earth's surface (e.g. displaying no scoria carapace, in case of a SiO₂-poor body) and nevertheless showing an aphanitic groundmass (Fig. 1A.1).

Among subvolcanic intrusions, those with tabular shapes and attitudes crosscutting pre-existing rock structures (i.e. most commonly a subvertical attitude) are called dykes (Fig. 1A.2). For shallow-level intrusions with attitudes more or less concordant with preexisting rocks (i.e. most commonly a subhorizontal attitude; Fig. 1A.2), a large variety of names were proposed in the 19th and early 20th century (Corry 1988), among which the terms laccolith, sill, bysmalith, and lopolith are still in use (Jerram and Bryan this volume—Chap. “[Plumbing Systems of Shallow Level Intrusive Complexes](#)”). Sills have

S. Rocchi (✉)
Università di Pisa, Pisa, Italy
e-mail: sergio.rocchi@unipi.it

C. Breitzkreuz
TU Bergakademie, Freiberg, Germany
e-mail: cbreit@geo.tu-freiberg.de

¹3 km depth has been quoted as maximum emplacement depth for the laccolith complex in the Henry Mtns. (Horsman et al. this volume—Chap. “[Progressive Construction of Laccolithic Intrusive Centers: Henry Mountains, Utah, U.S.A.](#)”), and it is the maximum value for a subvolcanic complex published so far. However, many dyke systems may have emplaced even deeper in the crust.

A - What is a SUBVOLCANIC igneous body?

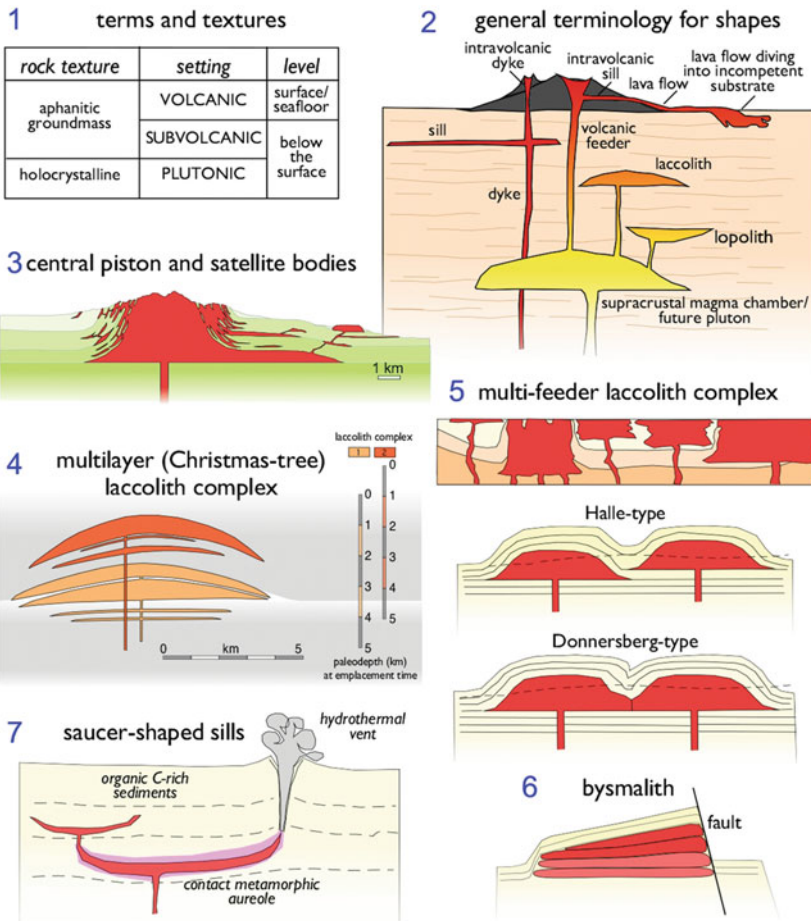


Fig. 1 Schematic representations of shallow-level intrusive systems. Scaling parameters for sill and laccoliths are most commonly in the range of diameter of 1–10 km and 10–1000 m thickness, and dykes can have thickness from a few cm to tens of m and lengths up to thousand of km. A.1. Definitions of terms defining the three main realms of igneous rocks based on the combination of rock texture and emplacement level. A.2. Overview of the terminology describing igneous bodies related to their emplacement level. A.3. Example of the common occurrence of laccoliths as groups of intrusions composed of a central piston-like intrusion below strongly arched host rocks (Horsman et al. 2009; Hunt 1953; Saint-Blanquat et al. 2006). A.4. Schematic drawing of an example of the occurrence of laccoliths as multiple separate sheets, fed by a single major dyke, and building up a Christmas tree-like complex (Rocchi et al. 2002, 2010; Westerman et al. this volume—Chap. “Rise and Fall of a Multi-Sheet Intrusive

Complex, Elba Island, Italy”). A.5. Example of a cluster of laccoliths emplaced more or less at the same level (Lorenz and Haneke 2004; Bretkreuz et al. this volume—Chap. “The Subvolcanic Units of the Late Paleozoic Halle Volcanic Complex, Germany: Geometry, Internal Textures And Emplacement Mode”) and fed by multiple dykes. A.6. Typical shape of a fault-bound bysmalith. A.7. Example of a sill characterized by a saucer shape, with upward pointing limbs (Malthe-Sørenssen et al. 2004; Planke et al. this volume—Chap. “Geophysics and Remote Sensing”), with hydrothermal vent systems originating from the fringes of the sill (Jamtveit et al. 2004; Rocchi et al. 2007; Svensen et al. 2006, 2009; Planke et al. this volume—Chap. “Geophysics and Remote Sensing”; Svensen et al. this volume—Chap. “Sub-Volcanic Intrusions and the Link to Global Climatic and Environmental Changes”)

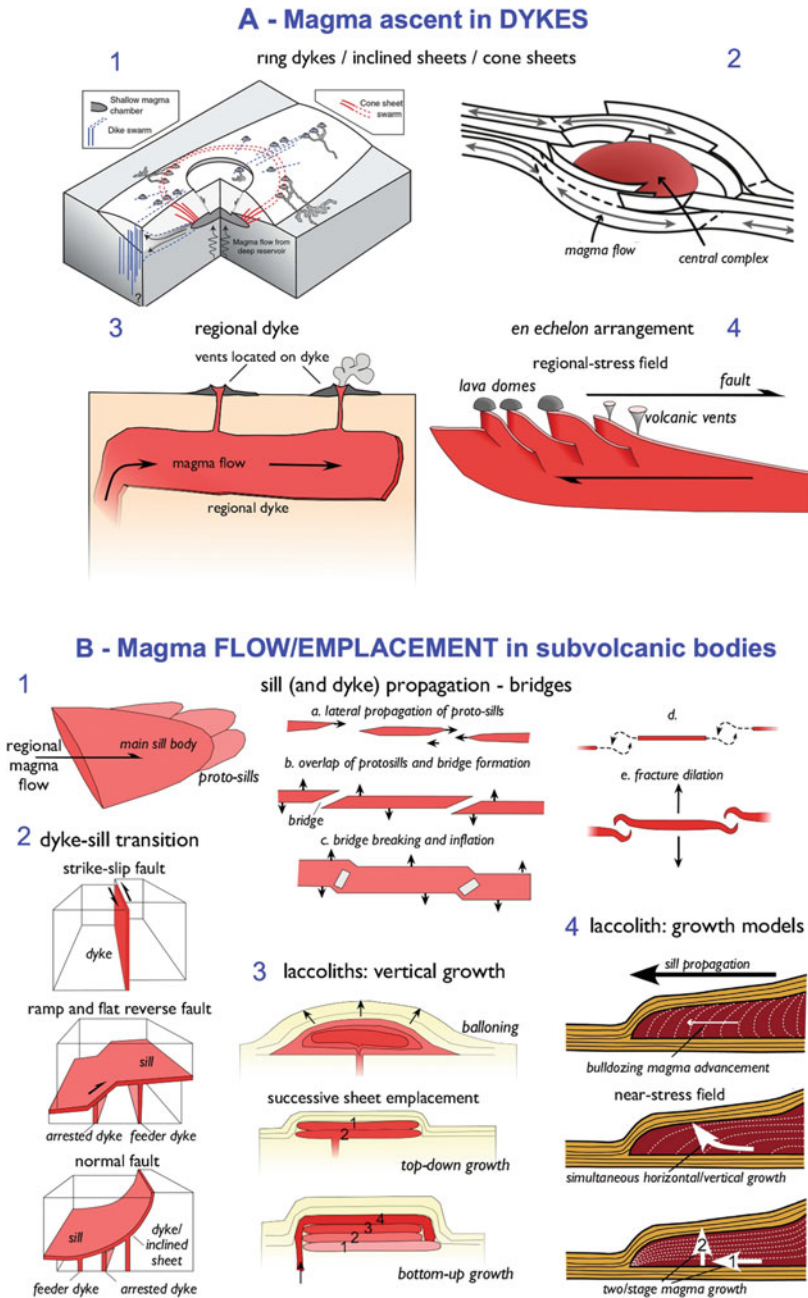


Fig. 2 A.1. Confocally dipping intrusions originating from an unexposed central magma chamber (Galland et al. 2014). A.2. Block diagram showing cone sheets originated from lateral flow of a magma around a central intrusive complex (Magee et al. 2012). A.3. Alignment of volcanic vents fed by a regional dyke transporting magma long distance laterally. A.4. Regional arrangement of a group of *en echelon* dykes. B.1. Initial sill/laccolith formation with lateral expansion of a subhorizontally oriented magma disk or ellipse. Upon magmatic inflation,

the protolobes merge and the intervening sediment become “bridges”. When neighbouring lobes come close, near-field stress generates curved cracks. B.2. Shape of dyke-to-sill transition in strike-slip, compressional and extensional settings. B.3. Vertical inflation of a laccolith by ballooning or stacking of magma sheets through under- and over-accretion. B.4. Growth models for laccolith intrusions (Corry 1988; Hunt 1953; Wilson et al. 2016): bulldozing (radial growth only), simultaneous vertical and horizontal growth, two-stage growth

tabular shapes with parallel roof and floor contacts, while a sub-concordant intrusion with a flat bottom and an upward convex roof is called a laccolith (Gilbert 1877) (Fig. 1A.2). Laccoliths commonly occur as groups of intrusions, and they can be composed of (i) a central piston-like intrusion below strongly arched host rocks (Fig. 1A.3), (ii) multiple separate sheets, building up a complex with a Christmas tree-like geometry (Fig. 1A.4; Rocchi et al. 2010; Westerman et al. this volume—Chap. “[Rise and Fall of a Multi-Sheet Intrusive Complex, Elba Island, Italy](#)”), (iii) a cluster of laccoliths emplaced more or less at the same level (Fig. 1A.5; Lorenz and Haneke 2004; Breitzkreuz et al. this volume—Chap. “[The Subvolcanic Units of the Late Paleozoic Halle Volcanic Complex, Germany: Geometry, Internal Textures And Emplacement Mode](#)”). A sub-concordant intrusion with a flat top and a downward convex floor is called a lopolith (Fig. 1A.2), whereas a discordant, cylindrical intrusion with part of their contacts roughly sub-vertical (fault-bound) is called a bysmalith (Fig. 1A.6).

In recent years, growing evidence has accumulated both from outcrops and from 2D/3D seismic data for sills characterized by saucer shapes, with upward pointing limbs (Fig. 1A.7; Malthe-Sørensen et al. 2004; Planke et al. this volume—Chap. “[Geophysics and Remote Sensing](#)”). Often, spectacular hydrothermal vent systems originate from the fringes of these sills (Jamtveit et al. 2004; Rocchi et al. 2007; Svensen et al. 2006, 2009; Planke et al. this volume—Chap. “[Geophysics and Remote Sensing](#)”; Svensen et al. this volume—Chap. “[Sub-Volcanic Intrusions and the Link to Global Climatic and Environmental Changes](#)”).

Sill and laccolith complexes are characterised by various types of feeder systems. Magma ascent may take place along a central conduit (Horsman et al. 2009; Roni et al. 2014; Westerman et al. this volume—Chap. “[Rise and Fall of a Multi-Sheet Intrusive Complex, Elba Island, Italy](#)”) or synchronously, in terms of geological time, along a number of neighbouring conduits (Breitzkreuz and Mock 2004; Breitzkreuz et al. this volume—Chap. “[The Subvolcanic Units of the](#)

[Late Paleozoic Halle Volcanic Complex, Germany: Geometry, Internal Textures And Emplacement Mode](#)”). A vertical feeding conduit may also be located laterally to a growing magmatic body, e.g. on a master fault of a tectonically controlled basin (Awdankiewicz et al. 2004; Francis 1982; Saint-Blanquat et al. 2006). Oblique to subhorizontal feeding channels have been mapped, e.g. in the Henry Mtns., along which melt has been transported laterally away from the central body to a number of satellite intrusions (Horsman et al. 2009; Horsman et al. this volume—Chap. “[Progressive Construction of Laccolithic Intrusive Centers: Henry Mountains, Utah, U.S.A](#)”).

2 Magma Ascent

The formation of shallow-level intrusions implies a previous transport of magma from deeper sources that are located either in the mantle or in the middle or deep crust. When magma solidifies in such a tabular pathway, a dyke forms. In vertical dykes, magma flow is commonly assumed as vertical, from the deep magma source towards the emplacement level, however, within such pathways, magma can flow in either vertical, oblique or horizontal directions (Marsh 2000). Magma flow direction can be directly monitored by seismology (e.g. in Iceland) or it can be reconstructed by measurement of the orientation of phenocrysts or vesicles and by determining the anisotropy of the magnetic susceptibility (AMS; Westerman et al. this volume—Chap. “[Structures Related to the Emplacement of Shallow-Level Intrusions](#)”).

Inclined dykes are usually part of ring dykes that have actual three-dimensional shapes of cone or funnel sheets. They are associated with volcanic centres or subvolcanic intrusions, and the commonly accepted cone sheet model is that these confocally-dipping intrusions originate from an unexposed central magma chamber through dip-parallel magma flow, owing to overpressure within the magma chamber that imparts a local stress field, favouring formation of new inverted conical fractures (Anderson 1936;

Galland et al. 2014; Schirmick et al. 1999; Gudmundsson et al. this volume—Chap. “Dykes, Sills, Laccoliths, and Inclined Sheets on Iceland”) (Fig. 2A.1). An alternative emplacement model for cone sheets invokes lateral flow of magma supplied via regional dykes originating from a laterally adjacent igneous system (Magee et al. 2012; Fig. 2A.2).

Famous examples of extended horizontal (i.e. lateral) flow along vertically oriented pathways are the Proterozoic Giant Dyke swarms, such as the MacKenzie swarm in northwestern Canada, that can be followed over 3000 km crossing cratonic continental crust (LeCheminant and Heaman 1989). Long-distance (>3000 km) transport of magmas from a single reservoir through dyke swarms at middle to upper crustal levels has also been invoked for the Jurassic Ferrar Large Igneous Province, Antarctica (Elliot et al. 1999). Evidence for regionally extensive dykes transporting magma laterally are also represented by alignment of volcanic vents at the surface (Fig. 2A.3).

Formation of dykes is commonly favored by an extensional tectonic setting, resulting in a simple tabular geometry. Nevertheless, where a strike-slip component is active, the regional stress field leads to their arrangement in groups of *en echelon* dykes (Fig. 2A.4).

The far-field stress and the orientation of pre-existing joints and faults in the country rock influence the orientation and geometry of dykes. Similar to the case for sills, straight segments are generated when there is a strong fabric/bedding anisotropy in the rock (Fig. 2B.1a–c). When neighbouring disk-shaped melt domains expand laterally, their tips may come close and near-field stress then controls dyke geometry, resulting in curved cracks (Fig. 2B.1d,e) owing to the mechanical interaction between the adjacent crack tips, especially if the rock properties and ambient stress field are isotropic (Nicholson and Pollard 1985).

Where dykes serve as conduits for explosive volcanic eruptions, pyroclastic dykes may form above the fragmentation level by the conduit walls or as vent fall-back breccias (Winter et al. 2008).

3 Magma Flow/Emplacement

3.1 From Dyke to Sill—The Flip in Flow Direction

Sills or laccoliths form when the orientation of magma flow changes from vertical to horizontal along a subhorizontally oriented plane. This change in orientation depends, among others things, on geometric parameters and the strength ratio between melt and host (Galland et al. 2014). Neutral buoyancy, i.e. the crustal level where the magma density equals the integrated density of the overburden (Corry 1988), may play a role, in particular with SiO₂-poor, high density magma. However, several other parameters are important, such as the magma driving pressure (Baer and Reches 1991; Hogan and Gilbert 1995; Hogan et al. 1998; Malone et al. 2014; Reches and Fink 1988). Otherwise multi-level sill/laccolith complexes, e.g. like the Christmas tree laccolith complex on Elba (Westerman et al. this volume—Chap. “Rise and Fall of a Multi-Sheet Intrusive Complex, Elba Island, Italy”); Rocchi et al. 2002, 2010; Westerman et al. 2004), could not have formed. Also important are the ascent rate and viscosity of the ascending magma, and the variation in density and strength of the host rock. Numerous studies reveal that sills form at the level of abrupt changes of strength of the host rock (Awdankiewicz et al. 2004; Hogan et al. 1998). Magma viscosity and volume, and the difference in strength between the emplacing melt and the host are fundamental parameters in shaping the type, geometry and size of subvolcanic bodies (Galland et al. 2014). Geochemical composition (especially volatile content) and temperature, along with abundance of phenocrysts, microliths and vesicles, in turn affect the viscosity of laminarily flowing melt.

The geometric shape of the transition zone is affected by the regional/local tectonic setting (Fig. 2B.2). In strike-slip settings, the magma will tend to keep ascending in a dyke rather than changing its movement to horizontal. In the case of compressional settings, magma can start to move sub-horizontally if its driving pressure is sufficient, generating sills with ramp-and-flat

geometry. In extensional settings, normal faulting usually helps magma emplacement; in low-angle segments of the fault zone, the transition from dyke to sill is generally clear, while such transitions in high-angle segments are generally less so.

3.2 Filling up a Subvolcanic Body

Sill/laccolith formation initiates with the lateral expansion of a subhorizontally oriented magma disk or ellipse (a thin sill, Fig. 2B.1), driven by magma pressure. The giant Ferrar sill complex in Antarctica and other examples of basaltic sill systems reveal spectacular features of horizontal lobes fingering into sedimentary successions at different levels (Hutton 2009; Muirhead et al. 2011). Upon magmatic inflation, the protolobes may merge and the intervening sediment packages become “bridges” (Fig. 2B.1; Hutton 2009). The orientation of the lobe fringes and bridge edges indicates the orientation of melt flow. When neighbouring disk-shaped lobes expand laterally, their tips may come close and near-field stress starts to determine their geometries, generating curved cracks (Fig. 2B.1; Nicholson and Pollard 1985).

Whether horizontally spreading magma forms a sill with a low aspect ratio (height to diameter, commonly called length) or a laccolith with a high aspect ratio depends on magma viscosity, density, and volume. Reaching a certain sill diameter, high-viscosity magma is rather able to lift up the overburden than to further propagate sill extension at the sill tips. However, with large laccoliths and sills, the mass of the emplaced melt becomes the driving force for continued lateral enlargement (Bunger and Cruden 2011; Galland et al. this volume—Chap. “Laboratory Modelling of Volcano Plumbing Systems: A Review”).

Emplacement models for growing laccoliths evolved through time. Early studies emphasized ballooning as a typical modality of growth (Cloos 1927) leading in the simplest case to an onion skin-shaped flow foliation geometry (Fig. 2B.3). Detailed field studies in the Henry Mountains led to the suggestion of three general

emplacement models for shallow level intrusions (Hunt 1953; Fig. 2B.4): (i) radial growth only, with magma emplaced at a constant thickness, and country rocks displaced both vertically and laterally (“bulldozing” mechanism); (ii) simultaneous vertical and horizontal growth, (iii) radial growth of a thin sill, followed by dominantly vertical growth and associated vertical uplift of the overlying host rocks (“two-stage growth” mechanism). Evidence suggests that shallow-level crustal intrusions are emplaced and grow through the incremental addition of small volumes of magma, with the amalgamation and stacking of sill-like sheets (Glazner et al. 2004; Mahan et al. 2003; Menand 2008; Morgan et al. 2008). Therefore, the two stage growth model (Hunt 1953) appears most applicable for many larger shallow-level intrusions, i.e. vertical inflation by stacking of sill sheets through under- and over-accretion (Fig. 2B.3; Annen et al. 2008; Menand et al. 2008, 2011). Nevertheless, for the emplacement of individual sills, all three of Hunt’s models may still be viable.

Recent studies accumulated evidence for a successive emplacement of sheets, sill-like units, whereby two modes have been observed: overplating and underplating (Westerman et al. this volume—Chap. “Structures Related to the Emplacement of Shallow-Level Intrusions”). The latter also resembles recent growth models for plutons and batholiths (Grocott et al. 2009).

The host of emplacing sills or laccoliths, be it crystalline rock, consolidated sediment or loose sediment, does not stay unaffected. Fracturing and folding, thermal overprint, shearing and deformation, fluidization and mingling with the melt (peperite) are common textures, which form at the melt/host contact visible in outcrop, drill core, hand specimen or thin section (Westerman et al. this volume—Chap. “Structures Related to the Emplacement of Shallow-Level Intrusions”). Subvolcanic systems are notorious for the small contact metamorphic halos they produce in the host. This is presumably due to the effective advective heat transport away from the intrusive margin, e.g. in wet unconsolidated sediments, compared to the slow conductive heat flow inside the cooling magmatic body.

4 Timing for the Emplacement

Estimates of magma ascent rate from recent dome eruptions and swarm earthquake data suggests emplacement of individual dykes, sills or laccoliths may take minutes to a few thousands of years (Mock et al. 2005; Mock and Jerram 2005; Saint-Blanquat et al. 2011). This and the fact that these processes take place in the subsurface impede direct observation. At least, remote sensing methods like interferometric modeling of satellite data allows monitoring dome uplift indicative of a growing laccolith (Planke et al. this volume—Chap. “[Geophysics and Remote Sensing](#)”). As a consequence, analog and numeric modeling is essential to better understand textures and geometry of subvolcanic systems (Galland et al. this volume—Chap. “[Laboratory Modelling of Volcano Plumbing Systems: A Review](#)”).

Textural studies and emplacement models of subvolcanic sill and laccolith complexes upgrade also the understanding for the evolution of plutons and batholiths. With plutonic rocks, initial emplacement textures are typically overprinted or eliminated by late recrystallization (Glazner et al. this volume—Chap. “[The Volcanic-Plutonic Connection](#)”; Westerman et al. this volume—Chap. “[Structures Related to the Emplacement of Shallow-Level Intrusions](#)”).

5 Environmental and Societal Impact

Emplacement of shallow-level intrusion can directly or indirectly generate threats to the living beings and their environment, as well as be the trigger of the generation of earth natural resources such as geothermal heat, mineral deposits, building materials. Over the last fifteen years, evidence accumulated that giant sill complexes typically associated with flood basalt provinces may have strong impact on climate change and on bio-evolution. Sill emplacement into organic carbon-rich sediments triggers release of large volumes of gases with high environmental impact such as methane and carbon dioxide

(Svensen et al. 2007; 2009; Svensen et al. this volume—Chap. “[Sub-Volcanic Intrusions and the Link to Global Climatic and Environmental Changes](#)”).

Laccoliths may evolve into intrusive/extrusive complexes (Stark 1912) when large volumes of high-viscosity melt emplace. The rising melt pierces the sedimentary cover, and the sediments along the sides of the growing magmatic body are folded, faulted and overturned. Landslides transport cover sediments down from the growing dome and, finally, lava flows and lava dome collapse generate block-and-ash-flows testifying to the subaerial appearance of the rhyolitic melt (Lorenz and Haneke 2004). Recently, case studies of emplacement of cryptodomes and laccoliths causing large slope failures have been reported. Thus, the emplacement of subvolcanic bodies can generate a threat in the form of catastrophic landslides of oversteepened slopes, sometimes leading also to explosive eruptions (Hacker et al. 2014; Malone et al. 2014; Hacker this volume—Chap. “[Catastrophic Collapse Features in Volcanic Terrains: Styles and Links to Subvolcanic Magma Systems](#)”).

Recent literature indicates that subvolcanic systems can also have significance for hydrocarbon plays. They influence hydrocarbon maturation, control its pathways and, in some cases, can serve as unconventional hydrocarbon reservoirs (Monreal et al. 2009; Schofield et al. this volume—Chap. “[Sills in Sedimentary Basins and Petroleum Systems](#)”).

Another aspect of economic relevance is that ore deposits form in many instances in association with subvolcanic complexes. Indeed, shallow level intrusions are commonly involved in at least one, if not all, of the four agents leading to the genesis of hydrothermal ore deposits, i.e. source of metals, source of fluids, heating of fluids triggering hydrothermal circulation, and mineral precipitation in a structural trap. Shallow-level intrusions are the common source for heating fluids in the world-class porphyry copper deposits, as well as in skarn-type base-metal sulphide deposits (Dill 2010; Vezzoni et al. 2016; Zentilli et al. 1995). Sources of metals and fluids are still debated for most hydrothermal ore

deposits, while for the fluid deposition it has been recently reported how the lateral displacement of the overburden of a shallow felsic intrusion can generate structural traps that draw in hydrothermal fluids from which sulphide ores precipitate (Vezzoni et al. 2017).

Finally, subvolcanic rocks, which are typically more homogeneous and coarser grained compared to their volcanic counterparts, are being quarried all over the world for split and gravel, and in some cases they are also utilized as dimension stone (e.g. in the Halle Volcanic Complex; Breitzkreuz et al. this volume—Chap. “[The Subvolcanic Units of the Late Paleozoic Halle Volcanic Complex, Germany: Geometry, Internal Textures And Emplacement Mode](#)”).

References

- Anderson EM (1936) Dynamics of formation of cone-sheets, ring-dykes, and cauldron subsidence. *Proc Royal Soc Edinb* 56:128–157
- Annen C, Pichavant M, Bachmann O, Burgisser A (2008) Conditions for the growth of a long-lived shallow crustal magma chamber below Mount Pelée volcano (Martinique, Lesser Antilles Arc). *J Geophys Res* 113: B07209
- Awdankiewicz M, Breitzkreuz C, Ehling B-C (2004) Emplacement textures in Late Palaeozoic andesite sills of the Flechtingen-Roßlau Block, north of Magdeburg (Germany). In: Breitzkreuz C, Petford N (eds) *Physical geology of high-level magmatic systems*. Geological Society, London, Special Publication, 234, pp 51–66
- Baer G, Reches Z (1991) Mechanics of emplacement and tectonic implications of the Ramon dike systems, Israel. *J Geophys Res* 96:11, 895–811, 910
- Breitzkreuz C, Mock A (2004) Are laccolith complexes characteristic of transtensional basin systems?—Examples from Permocarboneous Central Europe. In: Breitzkreuz C, Petford N (eds) *Physical geology of high-level magmatic systems*. Geological Society, London, Special Publication, 234, pp 13–32
- Bunger AP, Cruden AR (2011) Modeling the growth of laccoliths and large mafic sills: role of magma body forces. *J Geophys Res* 116(B2):B02203
- Cloos H (1927) Die Quellsuppe des Drachenfels am Rhein. Ihre Tektonik und Bildungsweise: *Zeitschr. Vulkanologie* 11:33–40
- Corry CE (1988) Laccoliths—mechanics of emplacement and growth. *Geol Soc Am Spec Pap* 220:110
- Dill HG (2010) The “chessboard” classification scheme of mineral deposits: mineralogy and geology from aluminum to zirconium. *Earth Sci Rev* 100(1–4):1–420
- Elliot DH, Fleming TH, Kyle PR, Foland KA (1999) Long-distance transport of magmas in the Jurassic Ferrar Large Igneous Province, Antarctica. *Earth Planet Sci Lett* 167:89–104
- Francis EH (1982) Magma and sediment-I. Emplacement mechanism of late Carboniferous tholeiite sills in northern Britain. *J Geol Soc London* 139:1–20
- Galland O, Burchardt S, Hallot E, Mourgues R, Bulois C (2014) Dynamics of dikes versus cone sheets in volcanic systems. *J Geophys Res Solid Earth* 119 (8):6178–6192
- Gilbert GK (1877) Report on the geology of Henry Mountains. In: Department of the Interior, U.S. Geographical and Geological Survey of the Rocky Mountain Region. Washington D.C. Government Printing Office, p 160
- Glazner AF, Bartley JM, Coleman DS, Gray W, Taylor RZ (2004) Are plutons assembled over millions of years by amalgamation from small magma chambers? *GSA Today* 14(4/5):4–11
- Grocott J, Arevalo C, Welkner D, Cruden A (2009) Fault-assisted vertical pluton growth: Coastal Cordillera, north Chilean Andes. *J Geol Soc London* 166:295–301
- Hacker DB, Biek RF, Rowley PD (2014) Catastrophic emplacement of the gigantic Markagunt gravity slide, southwest Utah (USA): implications for hazards associated with sector collapse of volcanic fields. *Geology* 42(11):943–946
- Hogan JP, Gilbert MC (1995) The A-type Mount Scott Granite sheet: importance of crustal magma traps. *J Geophys Res* B8:15, 779–715, 792
- Hogan JP, Price JD, Gilbert MC (1998) Magma traps and driving pressure: consequences for pluton shape and emplacement in an extensional regime. *J Struct Geol* 20(9/10):1155–1168
- Horsman E, Morgan S, Saint-Blanquat Md, Habert G, Hunter R, Nugent A, Tikoff B (2009) Emplacement and assembly of shallow plutons through multiple magma pulses, Henry Mountains, Utah. *Earth Environm Sci Trans Royal Soc Edinb* 100:1–16
- Hunt CB (1953) Geology and geography of the Henry Mountains region. Utah, U S Geol Survey Prof Paper, p 228
- Hutton D (2009) Insights into magmatism in volcanic margins: bridge structures and a new mechanism of basic sill emplacement—Theron Mountains, Antarctica. *Petrol Geosci* 15:269–278
- Jamtveit B, Svensen H, Podladchikov YY, Planke S (2004) Hydrothermal vent complexes associated with sill intrusions in sedimentary basins. In: Breitzkreuz C, Petford N (eds) *Physical geology of high-level magmatic systems*. Geological Society, London, Special Publication 234, pp 229–232

- LeCheminant AN, Heaman LM (1989) Mackenzie igneous events, Canada: middle Proterozoic hotspot magmatism associated with ocean opening. *Earth Planet Sci Lett* 96:38–48
- Lorenz V, Haneke J (2004) Relationship between diatremes, dykes, sills, laccoliths, intrusive-extrusive domes, lava flows, and tephra deposits with unconsolidated water-saturated sediments in the late Variscan intermontane Saar-Nahe basin, SW Germany. In: Breitkreuz C, Petford N (eds) *Physical geology of high-level magmatic systems*. Geological Society, Special Publication 234, pp 75–124
- Magee C, Stevenson C, O'Driscoll B, Schofield N, McDermott K (2012) An alternative emplacement model for the classic Ardnamurchan cone sheet swarm, NW Scotland, involving lateral magma supply via regional dykes. *J Struct Geol* 43:73–91
- Mahan KH, Bartley JM, Coleman DS, Glazner AF, Carl BS (2003) Sheeted intrusion of the synkinematic McDoogie pluton, Sierra Nevada, California. *Geol Soc Am Bull* 115(12):1570–1582
- Malone DH, Craddock JP, Anders MH, Wulff A (2014) Constraints on the emplacement age of the heart mountain slide, Northwestern Wyoming. *J Geol* 122(6):671–685
- Malthe-Sørenssen A, Planke S, Svensen H, Jamtveit B (2004) Formation of saucer-shaped sills. In: Breitkreuz C, Petford N (eds) *Physical geology of high-level magmatic systems*. Geological Society, London, Special Publication 234, pp 215–227
- Marsh BD (2000) Magma chambers. In: *Encyclopedia of Volcanoes*. Academic Press, pp 191–206
- Menand T (2008) The mechanics and dynamics of sills in layered elastic rocks and their implications for the growth of laccoliths and other igneous complexes. *Earth Planet Sci Lett* 267(1–2):93–99
- Menand T, de Saint-Blanquat M, Annen C (2011) Emplacement of magma pulses and growth of magma bodies. *Tectonophysics* 500:1–2
- Menand T, Phillips J, Sparks R (2008) Circulation of bubbly magma and gas segregation within tunnels of the potential Yucca Mountain repository. *Bull Volc* 70(8):947–960
- Mock A, Ehling B-C, Breitkreuz C (2005) Anatomy of a laccolith complex—geometry and texture of porphyritic rhyolites in the Permian carboniferous Halle Volcanic Complex (Germany). *N Jahrb Geol Pal Abh* 237:211–271
- Mock A, Jerram DA (2005) Crystal size distributions (CSD) in three dimensions: insights from the 3D reconstruction of a highly porphyritic rhyolite. *J Petrol* 46:1525–1541
- Monreal FR, Villar HJ, Baudino R, Zencich S (2009) Modeling an atypical petroleum system: a case study of hydrocarbon generation, migration and accumulation related to igneous intrusions in the Neuquen Basin, Argentina. *Mar Pet Geol* 26:590–605
- Morgan S, Stanik A, Horsman E, Tikoff B, de Saint-Blanquat M, Habert G (2008) Emplacement of multiple magma sheets and wall rock deformation: Trachyte Mesa intrusion, Henry Mountains, Utah. *J Struct Geol* 30(4):491–512
- Muirhead JD, Airoidi G, Rowland JV, White JDL (2011) Interconnected sills and inclined sheet intrusions control shallow magma transport in the Ferrar large igneous province. Antarctica. *Geol Soc Am Bull* 124:162–180
- Nicholson R, Pollard DD (1985) Dilation and linkage of echelon cracks. *J Struct Geol* 7:583–590
- Reches Z, Fink J (1988) The mechanism of intrusion of the Inyo Dike, Long Valley Caldera, California. *J Geophys Res* 93:4321–4334
- Rocchi S, Mazzotti A, Marroni M, Pandolfi L, Costantini P, Bertozzi G, di Biase D, Federici F, Lô PG (2007) Detection of Miocene saucer-shaped sills (offshore Senegal) via integrated interpretation of seismic, magnetic and gravity data. *Terra Nova* 19:232–239
- Rocchi S, Westerman DS, Dini A, Farina F (2010) Intrusive sheets and sheeted intrusions at Elba Island (Italy). *Geosphere* 6(3):225–236
- Rocchi S, Westerman DS, Dini A, Innocenti F, Tonarini S (2002) Two-stage laccolith growth at Elba Island (Italy). *Geology* 30(11):983–986
- Roni E, Westerman DS, Dini A, Stevenson C, Rocchi S (2014) Feeding and growth of a dyke–laccolith system (Elba Island, Italy) from AMS and mineral fabric data. *J Geol Soc* 171:413–424
- Saint-Blanquat M, Habert G, Horsman E, Morgan SS, Tikoff B, Launeau P, Gleizes G (2006) Mechanisms and duration of non-tectonically assisted magma emplacement in the upper crust: the Black Mesa pluton, Henry Mountains, Utah. *Tectonophysics* 428:1–31
- Saint-Blanquat M, Horsman E, Habert G, Morgan S, Vanderhaeghe O, Law R, Tikoff B (2011) Multiscale magmatic cyclicality, duration of pluton construction, and the paradoxical relationship between tectonism and plutonism in continental arcs. *Tectonophysics* 500:20–33
- Schirmick C, van den Bogaard P, Schmincke H-U (1999) Cone sheet formation and intrusive growth of an oceanic island—the Miocene Tejada complex on Gran Canaria (Canary Islands). *Geology* 27(3):207–210
- Stark M (1912) Beiträge zum geologisch-petrographischen Aufbau der Euganeen und zur Lakkolithenfrage. *Mineralog Petrogr Mitteil* 31:1–80
- Svensen H, Jamtveit B, Planke S, Chevallier L (2006) Structure and evolution of hydrothermal vent complexes in the Karoo Basin, South Africa. *J Geol Soc London* 163:671–682
- Svensen H, Planke S, Chevallier L, Malthe-Sørenssen A, Corfu F, Jamtveit B (2007) Hydrothermal venting of greenhouse gases triggering Early Jurassic global warming. *Earth Planet Sci Lett* 256(3–4):554–566
- Svensen H, Planke S, Polozov AG, Schmidbauer N, Corfu F, Podladchikov YY, Jamtveit B (2009) Siberian gas venting and the end-Permian environmental crisis. *Earth Planet Sci Lett* 277(3–4):490–500

- Vezzoni S, Dini A, Rocchi S (2016) Reverse telescoping in a distal skarn system (Campiglia Marittima, Italy). *Ore Geol Rev* 77:176–193
- Vezzoni S, Rocchi S, Dini A (2017) Lateral extrusion of a thermally weakened pluton overburden (Campiglia Marittima, Tuscany). *Int J Earth Sci.* doi:<https://doi.org/10.1007/s00531-017-1539-9>
- Westerman DS, Dini A, Innocenti F, Rocchi S (2004) Rise and fall of a nested Christmas-tree laccolith complex, Elba Island, Italy. In: Bretkreuz C, Petford N (eds) *Physical geology of high-level magmatic systems*. Special publication, Geological Society, London, 234:195–213
- Wilson PIR, McCaffrey KJW, Wilson RW, Jarvis I, Holdsworth RE (2016) Deformation structures associated with the Trachyte Mesa intrusion, Henry Mountains, Utah: implications for sill and laccolith emplacement mechanisms. *J Struct Geol* 87:30–46
- Winter C, Bretkreuz C, Lapp M (2008) Textural analysis of a Late Palaeozoic coherent to pyroclastic rhyolitic dyke system near Burkersdorf (Erzgebirge, Saxony, Germany). In: Thomson K, Petford N (eds) *Structure and emplacement of high-level magmatic systems*. Special publication, Geological Society, London, 302:197–219
- Zentilli M, Graves MC, Lindsay G, Ossandon G, Camus F (1995) Recurrent mineralization in the Chuquicamata porphyry copper system: restrictions on genesis from mineralogical, geochronological and isotopic studies. *Proceedings Second Giant Ore Deposits Workshop, Ontario*, pp 90–113

Geometric Scaling of Tabular Igneous Intrusions: Implications for Emplacement and Growth

A.R. Cruden, K.J.W. McCaffrey and A.P. Bunger

Abstract

The horizontal (L) and vertical (T) dimensions of broadly tabular, sub-horizontal intrusions of mafic to felsic composition emplaced into shallow to mid-crustal levels of continental crust reveal two well-defined and continuous curves in $\log L$ vs. $\log T$ space. The data set spans six and five orders of magnitude in L (1 m to 1000 km) and T (10 cm to 10 km), respectively. Small tabular sheets and sills (mafic and felsic) define a straight line with a slope ~ 0.5 at all horizontal length scales, similar to the known geometric scaling of mafic dikes, indicating that the L/T ratio of these intrusions to increases with increasing L (horizontal lengthening dominates over vertical thickening). Laccoliths, plutons, layered mafic intrusions and batholiths define an open, continuous S-shaped curve that bifurcates from the tabular sheets and sills curve at $L \sim 500$ m towards higher T values. For $L \sim 0.5$ to 10 km the slope of this curve is ~ 1.5 , corresponding to laccoliths that are characterized by a decrease in L/T ratio with increasing L (vertical thickening dominates over horizontal lengthening). Between $L \sim 10$ and 100 km the slope has a mean value ~ 0.8 , indicating that plutons and layered mafic intrusions have a tendency for horizontal lengthening over vertical thickening as L increases. Batholiths

A.R. Cruden (✉)
School of Earth, Atmosphere and Environment,
Monash University, Melbourne, VIC 3800, Australia
e-mail: sandy.cruden@monash.edu

K.J.W. McCaffrey
Department of Earth Sciences, University of
Durham, Durham DH1 3LE, UK

A.P. Bunger
Department of Civil and Environmental Engineering,
University of Pittsburgh, Pittsburgh, PA 15261, USA

A.P. Bunger
Department of Chemical and Petroleum Engineering,
University of Pittsburgh, Pittsburgh, PA 15261, USA

Adv in Volcanology (2018) 11–38
DOI 10.1007/11157_2017_1000
© Springer International Publishing AG 2017
Published Online: 06 May 2017

and very large layered mafic intrusions with $L > 100$ km lie on a slope ~ 0 with a threshold thickness ~ 10 km. The continuous nature of the dimensional data over such a wide range of length scales reflects a spectrum of igneous emplacement processes repeated in space and time. We discuss how thresholds and transitions in this spectrum, defined by bifurcations between the curves (e.g., between sill and laccolith emplacement) and changes in slope, largely reflect depth- and time-dependent changes in emplacement mechanisms rather than factors such as magma viscosity, composition and temperature.

1 Introduction

Dimensional scaling data of tabular igneous intrusions has been employed in several contexts to progress understanding of emplacement mechanisms. For example, the dimensional scaling of plutons and laccoliths has been used qualitatively to contrast their emplacement mechanisms, namely the relative roles of horizontal lengthening versus vertical thickening, the relative contributions of roof lifting in the shallow crust (laccoliths) versus floor subsidence in the middle to lower crust (plutons) and to discuss whether they grow by a single or multiple step process (McCaffrey and Petford 1997; Cruden and McCaffrey 2001). Dimensional scaling data from mafic dikes has been employed to determine dike initiation conditions and magma driving pressures (Babiker and Gudmundsson 2004; Gudmundsson 2011a, b) and to differentiate between propagation regimes predicted by Linear Elastic Fracture Mechanics (LEFM) (Delaney and Pollard 1981; Olson 2003; Schultz et al. 2008a; see review of Rivalta et al. 2015). Similarly, Bunger and Cruden (2011a) developed a combined LEFM-fluid mechanics model for the emplacement of sills and laccoliths that attempts to explain the different power-law scaling relationships of both types of intrusion as well as several leading-order geometric features, such as the flat tops and steep sides of laccoliths. Abdelmalak et al. (2012) and Galland and Scheibert (2013) have shown experimentally and theoretically that interpretation and prediction of

surface deformation related to shallow magma emplacement is critically dependent on understanding natural intrusion shapes and morphologies.

In this chapter we present the most recent compilation of available dimensional data from tabular igneous intrusions. The data set spans six orders of magnitude in the horizontal dimension and five orders of magnitude in the vertical dimension. We focus on the implications of the data for understanding emplacement and growth mechanisms of dykes, sills and laccoliths, and highlight gaps in understanding igneous intrusion processes as avenues for future research.

2 Geometric Scaling Analysis

It has been shown previously that there is a power-law scaling relationship between the vertical thickness, T , and horizontal length, L , of laccoliths and plutons described by

$$T = bL^a, \quad (1)$$

where a is the power-law exponent and b is a constant (McCaffrey and Petford 1997; Cruden and McCaffrey 2001; Cruden 2006). Dimensional measurements of both mafic dikes, in which case T is the horizontal width, and sills are also consistent with power-law scaling relationships (Olson 2003; Babiker and Gudmundsson 2004; Schultz et al. 2008a; Klimczak et al. 2010; Bunger and Cruden 2011a). Alternatively, if sufficient three-dimensional information is

available a power-law relationship between T and intrusion volume, V , can also be proposed:

$$T = dV^c \quad (2)$$

where c is the power-law exponent and d is a constant.

For the purpose of this analysis, for approximately horizontal intrusions we define L as the equivalent diameter of a circle given by measurements of either the major and minor axes of elliptical bodies or their areas, and T as the mean vertical thickness value where data are sufficient.

For dykes, L is the horizontal trace and T is the horizontal width, both in map view. To estimate V , we assume that horizontal tabular intrusions are disk shaped such that $V = \pi T(L/2)^2$. This is a reasonable first-order assumption for sills, minor sheets, meso-scale intrusions and laccoliths. However, it is known that plutons and layered intrusions are characterised by end-member wedge- and disk-shaped morphologies (Vigneresse 1995; Cruden 2006) so V will be overestimated for the former type. We do not attempt to estimate V for dykes as the vertical height is rarely constrained. However, we note that recent

Table 1 Dimensional data and power law scaling parameters of tabular intrusions

	N	L (km)	T (km)	L/T	a	b (m)	References
Batholiths	4	95–600	3–15	20–90	–	–	Cruden (2006)
Plutons	61	3.5–86	1–10	1.5–17	0.81 ± 0.12^a	1.08 ± 1.38^a	Cruden (2006), McCaffrey and Petford (1997), Cruden and McCaffrey (2001)
Layered Mafic intrusions	8	8–550	3–13	2.3–68.7	–	–	
Laccoliths	131	0.3–80	0.03–3	2–50	0.92 ± 0.11	0.12 ± 0.02	McCaffrey and Petford (1997), Corry (1988)
Henry Mtns	38	0.8–7.2	0.03–2.5	1.8–25.8	1.77 ± 0.36	0.07 ± 0.02	Corry (1988)
La Sal Mtns	10	0.8–5.6	0.2–1.0	3.8–12.3	1.52 ± 0.39	0.12 ± 0.04	Corry (1988)
Sleeping Ute Mtns	14	0.8–3.6	0.06–0.76	2.6–17.8	1.83 ± 0.77	0.09 ± 0.03	Corry (1988)
Abajo Mtns	32	0.3–6.4	0.1–0.78	1.9–13.3	1.06 ± 0.20	0.21 ± 0.02	Corry (1988)
Elba Island	9	1.6–10	0.05–0.7	11.8–33.3	1.41 ± 0.17	0.03 ± 0.01	Rocchi et al. (2002)
Average for groups					1.52 ± 0.31^b	0.02 ± 0.07^b	
Horizontal Sheet Intrusions	68	0.001–450	0.0001–0.6	1.9–2400	0.57 ± 0.02	0.4 ± 0.22	
Mafic sills ($L > 1$ km)	31	1–450	0.01–0.6	10–2400	0.85 ± 0.1	0.01 ± 0.02	Bunger and Cruden (2011a)
Mesoscale intrusions	13	0.14–1.6	0.0005–0.025	37–290	0.49 ± 0.13	0.47 ± 0.33	Corazzato and Gropelli (2004)
Minor Intrusions (Skye)	17	0.001–0.004	0.0001–0.0005	1.9–9.2	0.91 ± 0.25	0.27 ± 0.04	Walker (1993)

^aRMA regression for plutons and layered mafic intrusions, excluding the Bushveld complex

^bAverage of a or b values; error is given as 1 standard deviation

analytical work suggests that for swarms of blade-shaped dykes their height scales approximately to their horizontal spacing (Bunger et al. 2013).

Because T and L (and V) are dependant variables, analysis of individual sets of intrusion data, subdivided by intrusion type and geographical location were carried out by Reduced Major Axis regression (RMA) (McCaffrey and Petford 1997; Smith 2009). This method is preferred over the Ordinary Least Squares method because there is no a priori reason why the measurement errors in L (and V) and T should be asymmetrically distributed. Mean values of the power-law exponent, a , and ranges of values of the intercept, b , for groups and sub groups of intrusions are summarized in Table 1.

3 General Characteristics and Scaling of Tabular Intrusion

Log thickness, T , and log length, L , data from >320 sub-horizontal tabular intrusions and ~ 90 sub-vertical mafic dikes are plotted in Fig. 1a. For comparison, log T is plotted against log V in Fig. 1b. More than 99% of the data are derived from peer-reviewed literature sources and comprise measurements based on field observations (maps, cross sections, exposures in high relief areas, boreholes) and geophysical surveys (forward modelling of 2D and 3D gravity data and interpretation and analysis of seismic reflection data). As noted in previous work (e.g., Cruden 2006), no obvious difference is found between intrusion dimensions determined by field and geophysical methods, except for very large intrusions with $L > 50$ km, which are too large to provide field-based means for thickness estimation.

All classes of intrusion analysed here display well-defined power law scaling relationships between T and L (Fig. 1a; Table 1). In general, the exponent, a , differentiates between growth behaviour in which the aspect ratio L/T is increasing ($a < 1$, “lateral spreading”) and decreasing ($a > 1$, “uplifting”). This is well illustrated in the log L/T versus log L de-correlation plot (Fig. 2). For laccoliths, the

growth regime favours uplifting with $a > 1$. Indeed, when applied to individual provinces, a has been observed to be as large as 1.5 (Rocchi et al. 2002). In contrast, plutons, large mafic sills, mafic dykes and minor and mesoscale sheets favour lateral spreading with $a < 1$.

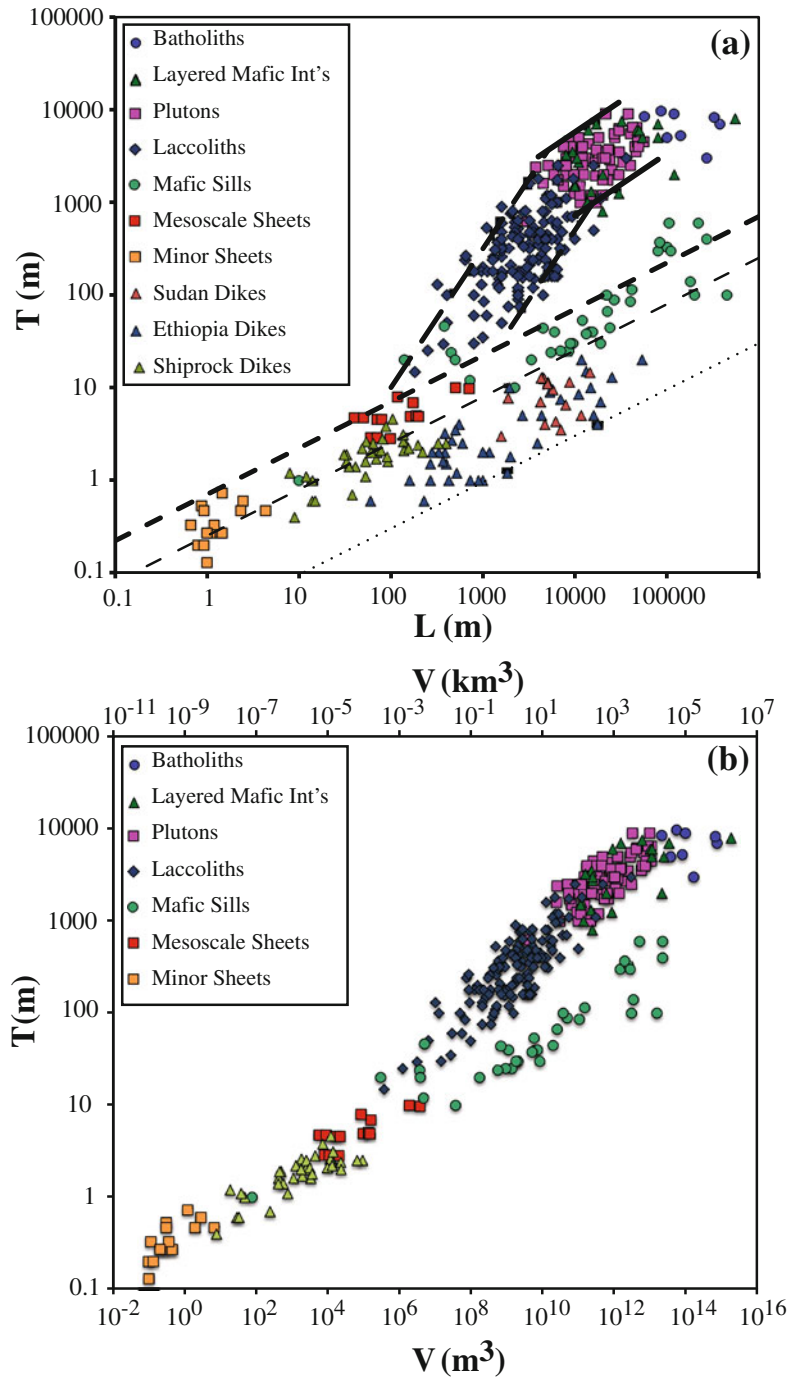
A pronounced feature of the log T versus log L data plot is a bifurcation between the array for minor sheets, mesoscale sheets, sills and dykes, which fall along a fit line with $a \sim 0.5$, and the array for laccoliths ($a \sim 1.5$), plutons ($a \sim 0.8$), layered mafic intrusions and batholiths (a approaches 0) (Fig. 1a). The bifurcation occurs where $L \sim 500$ –1000 m and $T \sim 10$ –30 m. The log T versus log V plot also shows a similar bifurcation between the data arrays, occurring where $V \sim 1 \times 10^7$ – 1×10^8 m³ (0.01–0.1 km³) and between slopes of $c \sim 0.3$ for sills and $c \sim 0.4$ for laccoliths (Fig. 1b). Both plots also highlight several important differences between intrusion types. For example, sills and laccoliths share a similar range of thickness but sills have approximately one order of magnitude greater length and two orders of magnitude greater volume. Similarly, although there is overlap between the lengths of the largest mafic sills and those of batholiths and very large layered mafic intrusions (Fig. 1a), the latter two classes of intrusion are ~ 1.5 orders of magnitude thicker and have volumes one to two orders of magnitude greater than the largest sills (Fig. 1b). The change in slope between the laccolith array and the plutons and layered mafic intrusions array is also much less pronounced, if not absent, in the log T versus log V plot, with all three classes of intrusions sharing an RMA slope of $c \sim 0.38$.

The first-order geometric characteristics and scaling relationships for individual classes of intrusion are discussed in more detail below.

3.1 Mafic Dykes

Mafic dykes are vertical to sub-vertical tabular intrusions that transport mafic magma both vertically and laterally in the crust. They occur over a wide range of scales from crustal-scale giant

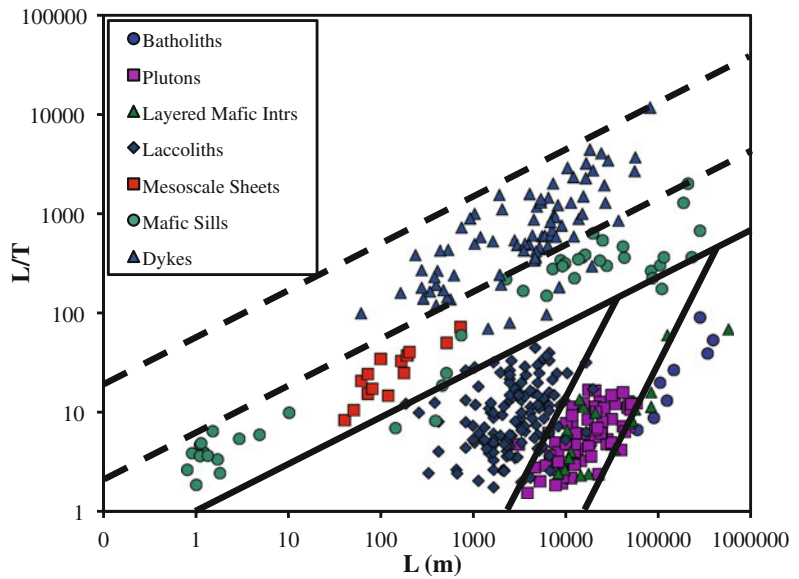
Fig. 1 **a** log Thickness (T) versus log Length (L), and **b** log Thickness versus log Volume (V) plots for tabular intrusions. *Solid and dashed lines* are bounding curves for different classes of intrusion, as discussed in the text



radiating and linear swarms that transport enormous volumes of mantle-derived magma associated with Large Igneous Province events (e.g., Ernst et al. 2005) to kilometer to decameter-scale individual dykes and dyke swarms associated

with moving magma from mid-crustal to shallow magma chambers toward the surface to feed volcanic eruptions (e.g., Geshi et al. 2010). Dykes are also integral components of crustal-scale magma transport networks,

Fig. 2 Log L/T versus log L plot for the same intrusion data plotted in Fig. 1. *Solid* and *dashed* lines delineate different classes of intrusion, as discussed in the text



connecting mantle reservoirs to sills and layered intrusions and eventually the surface (Marsh 2004; Barnes et al. 2016). Although the first-order tabular or blade-shaped geometry of dykes is simple, individual dykes and dyke swarms can show considerable structural complexity owing to their mode of propagation and interactions with country rock structure and other dykes. Examples of such complexity include the propagation of en echelon dykes and their eventual bridging and linkage (broken bridges) (Nicholson and Pollard 1985; Schofield et al. 2012), bifurcation, deviation and arrest due to intersection with pre-existing fractures and mechanical barriers (Gudmundsson 2011a, b; Rivalta et al. 2015). Such complexity is not captured by the scaling data.

The mafic dyke data sets used here come from observations and measurements in the USA (Ship Rock; Delaney and Pollard 1981), Ethiopia (Schultz et al. 2008b) and Sudan (Babiker and Gudmundsson 2004). The data span a horizontal length range from $L \sim 10$ m to 50 km and thicknesses $T \sim 0.5$ –20 m. Clearly, this data set is limited in that it misses out measurements from giant radiating and linear dyke swarms in which individual dykes can be traced for 100–1000 s of kilometers with widths in the 10 s of meters (e.g., Halls and Fahrig 1987). Unfortunately, reliable

measurements from such settings are hard to come by as the true lateral extent of very long dykes is hampered by poor geological preservation and thickness data is limited, often relying on poorly constrained estimates from aeromagnetic data.

Although the focus here is on sub-horizontal tabular intrusions, mafic dikes are included for comparison and because LEFM is also proposed to control their emplacement (Olson 2003; Gudmundsson 2011a). Consistent with previous analyses (Schultz et al. 2008a, b), the mafic dikes analysed here are characterized by power-law slopes with $a \sim 0.5$ and the combined dataset can be bounded by lines with $b = 0.03$ –0.25 (Fig. 1a). Mafic dikes share a common power-law slope with mafic sills and mesoscale and minor sheets but they are systematically thinner, with a greater L/T ratio for any given length (Fig. 2).

3.2 Sills and Sub-horizontal Sheets

Sills and sub-horizontal sheets are generally thought to have simple disk or penny shapes with uniform thickness and parallel upper and lower contacts that are concordant to the enveloping strata over most of their area, and tapered margins (Fig. 3). Unlike laccoliths (see below), sills

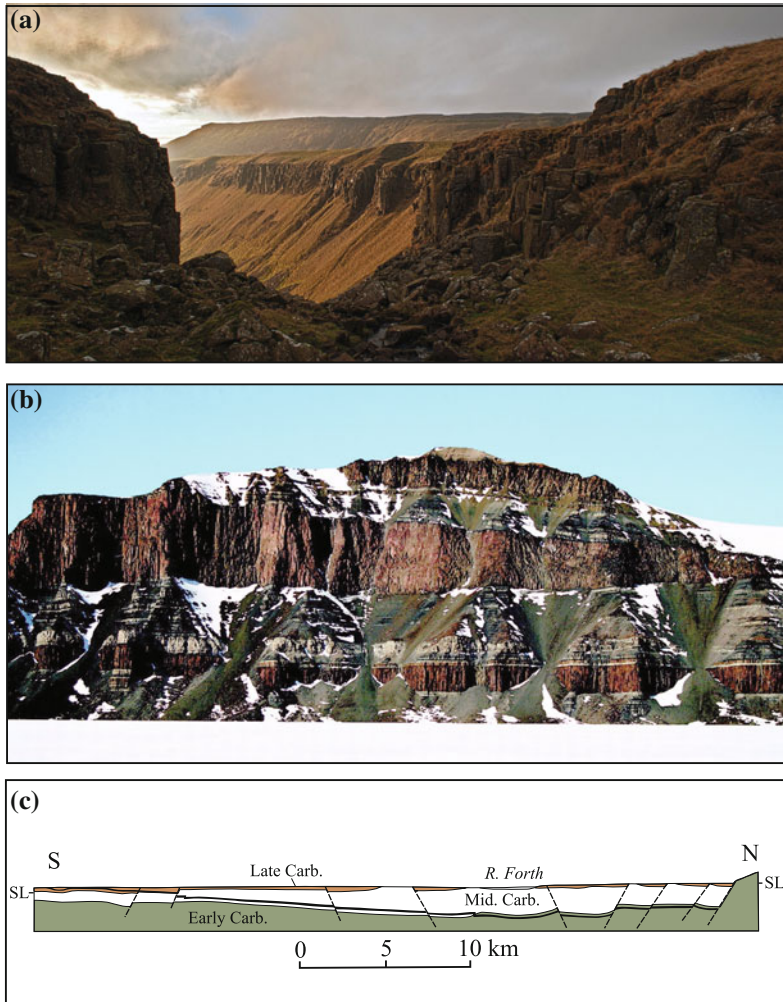


Fig. 3 **a** Valley exposure of the Cretaceous Whin Sill showing uniform thickness and parallelism with country rock strata, High Cup Nick, Cumbria UK (photograph courtesy of M. Lishman). Sill is ~ 30 m thick. **b** Vertical exposure of Jurassic sills at Coalseam Cliff, Theron Mountains, Antarctica [courtesy of Hutton (2009), Fig. 14]. The Scarp Capping Sill is observed in the center of the cliff, where it clearly tapers to the south (*right*) from a regional thickness of 200 to <70 m. Cliff is

700 m high. **c** North-south cross section of the Permian Midland Valley sill, Scotland (after Francis 1982). The sill (*black*) intrudes early Carboniferous volcanics in the north and transgresses upward to the south through middle and upper Carboniferous sediments, respectively. The sill has a maximum thickness of 150 m at its deepest point below the River Forth, decreasing to <10 m to the south

display little or no evidence for up bending of overlying strata. However, like dykes their simple first-order geometry is often more complex in detail. For example, some sills exhibit concave-up, saucer-shaped geometries, which in cross sections with no vertical exaggeration have dihedral angles of $>160^\circ$ (Fig. 3c) (e.g., Malthé-Sørensen et al. 2004; Galland et al.

2009; Planke et al. this volume). Some sills exhibit stair-stepping geometries in cross section that are regionally transgressive to stratigraphy (Fig. 3) (e.g., Bradley 1965; Thomson and Schofield 2008; Bédard et al. 2012; Muirhead et al. 2012; Magee et al. 2016; Walker 2016). Three-dimensional seismic surveys of sedimentary basins have revealed sills with complex

lobate and elongate morphologies (e.g., Thomson 2007; Thomson and Hutton 2004) that are similar to the margins of lava flows and to lava channels, respectively. As with dykes, this complexity is not reflected in the scaling data, nor do most analytical and numerical models of emplacement explain it. However, it should be noted that three-dimensional analogue experiments have successfully simulated saucer-shaped geometries and complex lobate margin structure (Hansen and Cartwright 2006; Miles and Cartwright 2010; Galland et al. this volume).

The sills and sheets data array comprises sub-horizontal, meter-scale minor mafic sheets (Skye; Walker 1993), mesoscale ($L \sim 40\text{--}700$ m) intermediate sheets (Montecampione; Corazzato and Gropelli 2004) and mafic sills ranging from $L \sim 10$ m to 450 km. The minor/mesoscale sheets and mafic sills data array is represented predominantly by fine grained igneous rocks with low silica contents (i.e., basaltic \gg trachytic and phonolitic compositions). The intrusions analysed here were mostly emplaced into layered sedimentary host rocks at shallow depths (<100 to 3000 m) (e.g., Bradley 1965; Mudge 1968; Francis 1982; Leaman 1975). However, it is known from seismic reflection profiles and tilted crustal sections that sills and sheets occur at deeper levels in the crust, including the crust-mantle boundary (Quick et al. 1994; McQuarrie and Rogers 1998). Unfortunately, lack of outcrop continuity and insufficient spatial resolution of seismic reflection data make it difficult to acquire scaling data for this class of intrusion at depths more than a few kilometres.

Although there is a reasonable amount of data (36) from mafic sills with $L > 1000$ m in the literature, there is limited geometrical information for smaller intermediate and mafic sheets. Nevertheless, the individual mafic sills and mesoscale/minor sheets data are characterized by power-law slopes with $a \sim 0.5$ and the combined dataset can be bounded by lines with $b = 0.25\text{--}0.7$ (Fig. 1a). Several very large mafic sills with $L > 80$ km lie above these bounds and may represent multi-pulse, stacked intrusions (see below). A subset of the smaller mafic sills also lies above this line, suggesting that they

would be better classified as laccoliths. The power-law scaling for the complete data set indicates that the L/T ratio of sills and sub-horizontal sheets increases systematically from as low as ~ 2 for $L \sim 1$ m to as high as ~ 2000 for $L \sim 20,000$ m (Fig. 2).

3.3 Laccoliths

Laccoliths usually have flat floors, steep sides and slightly arched roofs (Fig. 4) and are generally considered to be emplaced at depths that rarely exceed 3000 m (e.g., Pollard and Johnson 1973; Corry 1988). They are typically made up of fine-grained to hypabyssal-textured rocks with basaltic to rhyolitic compositions (Corry 1988), occur in all tectonic environments throughout the geological record, and are commonly, but not always, associated with volcanism. Deeper (e.g., de Saint Blanquat et al. 2001) and/or larger (e.g., Michel et al. 2008) gabbroic to granitic laccoliths are characterized by coarse-grained plutonic textures, and some of these are also emplaced into crystalline country rocks (Fig. 4c) (e.g., Cruden 2008; Friese et al. 2012).

The type region for laccoliths are the Tertiary igneous provinces of the western interior United States (Corry 1988), including the Henry Mountains where the laccolith concept was first formulated by Gilbert (1877) and carefully documented by Hunt et al. (1953), Johnson and Pollard (1972), and Jackson and Pollard (1988), among others. The majority, but not all (e.g., Friese et al. 2012), of the laccoliths intrude layered sedimentary rocks, and based on the bell-jar profile of deflected strata from the sides over the roof (e.g., Fig. 4a; Gudmundsson et al. this volume), they are inferred to grow by upward bending of their wall rocks during vertical inflation of magma after initial emplacement of a bedding parallel sill (Pollard and Johnson 1973). Field and geochronological studies indicate that laccolith growth commonly occurs by multiple injections of sheets over time-scales ranging from 100 years to 100 ka (Jackson and Pollard 1988; de Saint Blanquat et al. 2006, 2011; Leuthold et al. 2012).

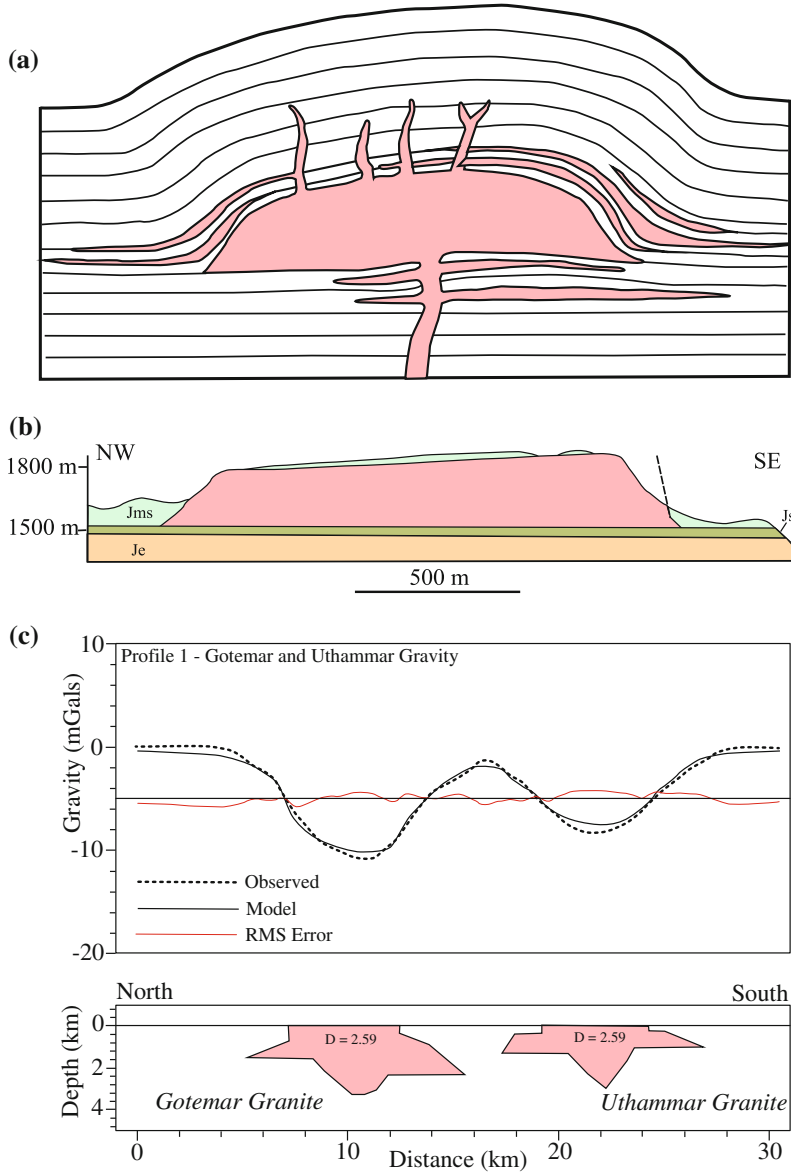


Fig. 4 a G.K. Gilbert’s conceptual cross section of laccoliths in the Henry Mountains, Utah (after Gilbert 1877; Corry 1988). Laccolith is pink, and curved lines represent traces of bedding in wall rock strata. b Cross section of the Oligocene Black Mesa laccolith (or bysmalith; Corry 1988), Henry Mountains, Utah (after de Saint Blanquat et al. 2006). Pink is diorite; Jms is Jurassic Morrison formation (sandstone); Js is Jurassic Summerville formation (shale); Je is Jurassic Entrada formation (sandstone). Note flat-topped profile of

laccolith and faulted southeast margin. c Residual gravity anomaly profiles (above) over the Mesoproterozoic Götemar and Uthammar granites in south east Sweden and corresponding 2.5 D forward gravity models (below), constrained by borehole data. Both granites intrude crystalline rocks but have laccolithic forms. Dotted curve = gravity data, solid black curve = forward gravity model, red curve = RMS error, granite bodies in forward model are pink. After Cruden (2008; see also Friese et al. 2012)

Like dykes and sills, laccoliths are known to deviate from their ideal circular, bell-jar shape, forming intrusions with a variety of complexities

that are not captured in the geometric scaling data. For example, some laccoliths are distinctly asymmetric in cross section bounded by a steep

fault on one margin and a tapered contact on the other (a.k.a., bysmalith; Fig. 4b) (e.g., de Saint Blanquat et al. 2006). Other laccoliths, such as the Maiden Creek and Trachyte Mesa, Utah, have tube and finger like morphologies and some laccolith margins have been shown to have lobe-shaped contact relationships in detail (Johnson and Pollard 1973; Horsman et al. 2010). However, recent work indicates that these examples may form as stacked saucer-shaped sheets rather than lobate fingers (Wilson et al. 2016). Stacked systems of tabular intrusions (e.g., Rocchi et al. 2002; Westerman et al. this volume) have also been referred to as Christmas-tree laccoliths (Corry 1988).

Most of the laccolith data analysed here are derived from a global database compiled by Corry (1988), updated, checked and censored to remove spurious and incorrect information. RMA analysis of the original laccolith dataset found a poorly determined power-law with $a \sim 0.88$ (McCaffrey and Petford 1997). Rocchi et al. (2002) subsequently analyzed laccoliths from the Island of Elba, Italy and found a robust power-law scaling relationship with $a \sim 1.5$. We have determined similar slopes for the individual major laccolith groups in the western USA (Corry 1988) and reassessment of the complete data set, including a handful of intrusions classified earlier as mafic sills (Fig. 1a), indicates that it can be bounded by lines with slopes of $a \sim 1.5$ and $b = 0.0005\text{--}0.01$ (Table 1). A key feature of the scaling data is that laccoliths are characterized by $a > 1$ so that they thicken faster than they lengthen; this leads to a general decrease in L/T ratios from ~ 30 to ~ 3 between $L \sim 500$ and ~ 8000 m (Fig. 2), which is opposite to the trend displayed by sills and sub-horizontal sheets.

3.4 Plutons, Layered Intrusions and Batholiths

For the purpose of this analysis, plutons are coarse-grained felsic to intermediate intrusive bodies with circular, elliptical to irregular outer

margins in map view that are emplaced in the upper to lower crust. Layered mafic intrusions have a similar geometry and range of emplacement depths but are made up of coarse-grained mafic and ultramafic rocks that often display distinct compositional layering at a variety of scales. Both plutons and layered mafic intrusions typically comprise more than one compositional phase or pulse and they can show simple (i.e., zoned) or complex internal structure. Batholiths are large composite intrusive masses that are made up of multiple plutons and, in some cases, layered mafic intrusions. Determination of the vertical dimensions of plutons, layered intrusions and batholiths relies on the use of geophysical techniques (gravity, magnetic, seismic reflection/refraction surveys), direct measurement in tilted crustal sections or regions with deep erosional dissection, or analysis of structural patterns (see Cruden 2006 and references therein). The floor and roof of the intrusion are commonly observed in cases where direct measurement can be made, whereas geophysical data typically only provides information on thickness from a sub-roof erosion level to the intrusion floor. Recent field and geochronological studies of plutons indicate that the majority are constructed by multiple pulses over timeframes ranging from ca. 0.1 to 6 Ma (Coleman et al. 2004; Miller et al. 2007; Michel et al. 2008; Schaltegger et al. 2009; de Saint Blanquat et al. 2011; Leuthold et al. 2012). Due to their composite nature, batholiths are constructed over 10 s of Ma.

The pluton data array ranges from 1000 to 9000 m in thickness and 3.7 to 54 km in length (Fig. 1a, Table 1). There is some overlap between the laccolith and pluton fields, which reflects some ambiguity in classifying intrusions in the $L = 4\text{--}10$ km size range. Layered mafic intrusions with $L < 80$ km are not distinguishable from plutons in terms of dimensions. We therefore treat both classes of intrusion together in the following analysis and discussion. Plutons and layered mafic intrusions are characterised by a power law scaling with $a = 0.81$ and the combined data set can be bounded by curves

with $b = 0.37$ and 3.13 (Fig. 1a). The $a < 1$ power law for these intrusions indicates a return to a geometric scaling in which lengthening dominates over thickening and a general increase in L/T ratio from ~ 5 for smaller plutons to ~ 10 for the largest (Fig. 2). The transition from laccoliths to plutons can be described as a gradual change in scaling from $a > 1$ to $a < 1$ and therefore from a thickening- to a lengthening-dominated growth regime.

Batholiths and layered mafic intrusions with $L > 80$ km plot at the top right of the scaling diagram (Fig. 1a), ranging in thickness from $T = 2000\text{--}9700$ m and length from $L = 57\text{--}550$ km. Unlike the smaller classes of intrusion, there is no obvious dependence between thickness and length for batholiths and large layered mafic intrusions. Instead there appears to be a thickness threshold of ~ 10 km, corresponding to one third to one quarter the thickness of continental crust. The transition from plutons and small layered intrusions to batholiths and large layered mafic intrusions can be described as a change from a lengthening dominated growth regime with a < 1 to a constant thickness regime.

4 Relationships Between Emplacement Mechanisms, Depth and Scaling Relationships

Although the dimensional data clearly separate different classes of intrusions in terms of size, shape (Fig. 1a), volume (Fig. 1b), aspect ratios and empirical L - T scaling relationships (Fig. 2; Table 1), they do not capture information on depths of emplacement, H , compositions and timescales.

Following the material reviewed above, there is a general tendency for intrusions in the laccolith-plutons-layered mafic intrusions array to become deeper as L , T and V increase, although there is currently insufficient information that couples geometric data with emplacement depth to assess this rigorously. There is also a general tendency for larger intrusions to take longer to grow, which is a consequence of their greater volume and a limited range of likely magma

fluxes (e.g., Petford et al. 2000; Cruden 2006; de Saint Blanquat et al. 2011; Menand et al. 2015). Within the same data array there does not appear to be a major compositional control on geometry and scaling. Hence laccoliths are emplaced at shallower depths over shorter timescales than plutons and layered mafic intrusions but composition is not a differentiating factor.

Intrusions in the minor/mesoscale sheets and sills array vary in composition from basalt to trachyte and they are all emplaced at depths shallower than ~ 3 km. Hence, neither emplacement depth nor magma composition are likely to be differentiating factors controlling the power law scaling of these data. However, as sub-horizontal sheets and sills increase in size and volume the ratio between L and the emplacement depth, H , will increase. This implies that small sheets with $L \ll H$ will propagate in a regime under which the dynamics of emplacement does not involve interaction with Earth's free surface (known in mechanics as the thick sheet approximation). Conversely, large sheets and sills with $L \gg H$ will be emplaced under conditions where intrusion growth is strongly coupled to the deformable free surface (known in mechanics as the thin sheet approximation). The transition between these two regimes will occur when $L \sim H$, which for our data set roughly corresponds to the bifurcation between the sheets and sills array and the laccoliths array at $L \sim 1000$ m. However, since laccoliths and sills share similar ranges of T and are emplaced at comparable depths, the bifurcation cannot be related to the L - H transition alone, as discussed below.

Whether the growth of tabular intrusions involves interaction with Earth's free surface ($L \gg H$) or not ($L \ll H$) defines two first-order emplacement regimes that will be used as the framework for the discussion below. However, it should be noted that this framework cannot apply to deeper plutons and layered mafic intrusions, which generally satisfy the condition $L > H$ but rarely show evidence for emplacement involving roof uplift and interaction with Earth's surface (e.g., Cruden 2006 and references therein). Vertical movement of country rocks is likely

involved in making space for these types of intrusions (e.g., Clough et al. 1909; Myers 1975; Paterson et al. 1996) but this process most likely involves displacements of interfaces below the level of emplacement (Brown and McClelland; Cruden 1998; Grocott et al. 2009).

4.1 Intrusions that Do not Interact with Earth's Surface

The minor/mesoscale sheets and smaller sills in the data array are generally emplaced under conditions where $L \ll H$, and therefore they are unlikely to interact with the surface during emplacement. Dykes can also be considered as intrusions that do not interact with the surface during their propagation and growth; hence they are included in the analysis below (Fig. 5). Under conditions where the magma pressure is spatially uniform and the growth of the intrusion is implied by $K_I = K_{Ic}$, where K_I is the mode I stress intensity factor and K_{Ic} is the mode I fracture toughness of the rock, LEFM predicts (e.g. Olson 2003):

$$T = \frac{K_{Ic}(1 - \nu^2)\sqrt{8}}{E\sqrt{\pi}}\sqrt{L}, \quad (3)$$

where E is Young's modulus and ν is Poisson's ratio. The $a \sim 0.5$ exponent of the L - T scaling for mafic dykes (Delaney and Pollard 1981; Olson 2003; Schultz et al. 2008a, b) and minor/mesoscale sheets and smaller sills (Fig. 5) is therefore consistent with this LEFM prediction. However, as noted in previous studies, K_{Ic} values 10–1000 times laboratory values are required to fit the different data sets (Delaney and Pollard 1981; Olson 2003; Schultz et al. 2008a; Cruden et al. 2009). For example, best fit curves that bracket the dyke, sheet and sill data in Fig. 5 are computed for values $E = 100$ GPa, $\nu = 0.3$ and $K_{Ic} = 300$ – 3000 MPa m^{1/2} whereas typical laboratory rock toughness values range from 0.5 to 2 MPa m^{1/2}. The relationship between these bounding curves and the individual data sets also indicate that dykes require systematically lower effective fracture toughness values than sheets and sills, which as noted above tend to be also systematically thicker than dykes for any given

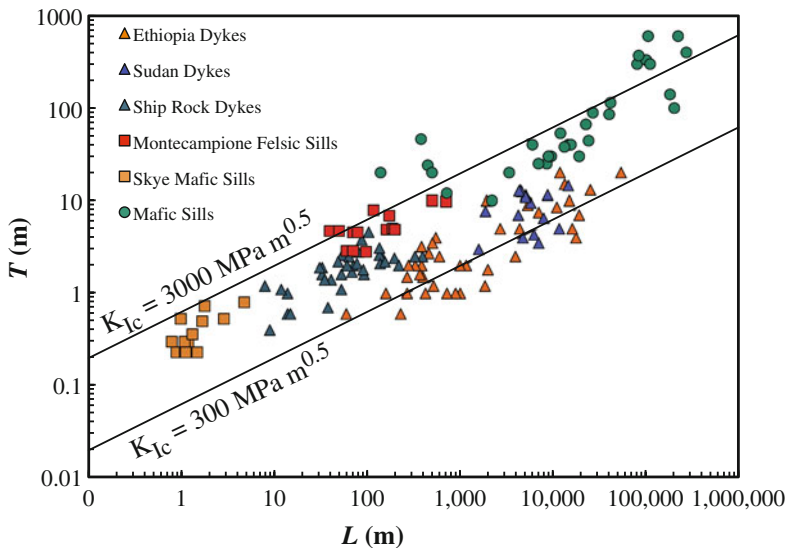


Fig. 5 Dimensional data for large mafic sills (multiple sources), felsic-intermediate sills (Montecampione—Corazzato and Groppelli 2004; Skye—Walker 1993) and mafic dykes (Ship Rock—Delaney and Pollard

1981; Ethiopia—Schultz et al. 2008b). *Black curves* are fit lines for LEFM conditions dominated by fracture toughness (Eq. 3) and for fracture toughness values K_{Ic} —3000 and 300 MPa m^{0.5}. See text for further discussion

length (Fig. 5). Therefore, LEFM accounts satisfactorily for the scaling of these intrusion types if large effective K_{Ic} values can be accounted for by scale effects (e.g., Olson 2003), fracture network branching (e.g., Gudmundsson 2011a) or cooling/solidification at fracture tips (viz., tip screen out; Smith et al. 1987). Furthermore, this model is favoured relative to the LEFM model under conditions of uniform magma pressure, which is at odds with the data because it predicts $a \sim 1$ (Olson 2003). A toughness-dominated model is also favoured relative to models that consider viscous flow to be predominant because the magma viscosity range required to bracket the data is implausibly high (Cruden et al. 2009).

For completeness, large mafic sills have been included in Fig. 5 and contribute to a well-defined RMA slope for the sheets and sills data array with $a = 0.57 \pm 0.02$ (Table 1). However, RMA analysis of mafic sills with $L > 1000$ m alone gives a slope $a = 0.85 \pm 0.1$, which is influenced by the presence of thick sills with $L > 100$ km that lie above the bounding curve plotted in Fig. 1a. As discussed above, mafic sills with $L \gg 1$ km likely interact with the surface and their emplacement is discussed together with laccoliths below.

4.2 Intrusions that Do Interact with Earth's Surface

The growth of intrusions with $L \gg H$ involves vertical displacement of overlying strata and ultimately the creation of positive surface topography (Hamilton 1965; Corry 1988; Cruden 1998; Galland and Scheibert 2013). Because their growth does not normally require deflection of rock units below the level of emplacement, intrusions with $L \gg H$ are characterised by asymmetric geometries in cross section (i.e., flat floors, curved roofs), which contrasts with the symmetric deflection of strata above and below intrusions with $L \ll H$ (Fig. 6; Koch et al. 1981). In addition to uplift of overlying strata, a further manifestation of interaction with the surface is the tendency for some sill tips to curve upwards during sill growth, resulting in the formation of

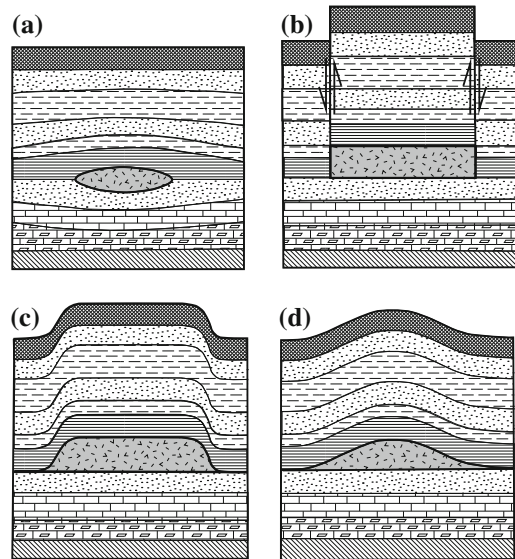


Fig. 6 Conceptual models for host rock deformation associated with emplacement of sills and laccoliths (after Koch et al. 1981). **a** Emplacement of an initial sill with $H \gg L$ and no interaction with Earth's surface. **b** Vertical growth of a laccolith by plastic failure on ring faults and roof uplift (a.k.a. punched laccolith). **c** Vertical and horizontal growth of a laccolith by the rolling hinge mechanisms, which requires intra layer slip in the roof rocks. **d** Classical model of laccolith growth by elastic displacement of roof rocks under a thin, clamped, circular elastic plate mechanical regime. See text for further discussion

saucer-shaped intrusions in shallow sedimentary basins (Malthe-Sørenssen et al. 2004; Thomson and Hutton 2004; Polteau et al. 2008; Magee et al. 2016; Planke et al. this volume).

Several end-member mechanisms for the growth of laccoliths have been proposed (e.g., Hunt et al. 1953; Sneddon and Lowengrub 1969; Pollard and Johnson 1973; Koch et al. 1981; Corry 1988; Price and Cosgrove 1990; Zenzri and Kerr 2001; Horsman et al. 2010). Most analytical models start with the emplacement of an initial sill (Fig. 6a), followed by vertical inflation (Fig. 6b–d). Such models can also be employed to estimate the critical conditions (L , H , driving pressure, etc.) required to initiate the so-called sill-to-laccolith transition. Gilbert's (1877) original concept for laccolith emplacement envisaged that uplift of overlying rigid strata was facilitated by a ring fracture (Fig. 6b) and that the final

thickness of the flat-topped intrusion was a consequence of the balance between magma overpressure, the weight of the overlying rocks and friction on the fault. Corry (1988) has termed these intrusions punched laccoliths. Also based on fieldwork in the Henry Mountains, Hunt et al. (1953) introduced the rolling monoclinial flexure (hinge) model for laccolith emplacement, subsequently modelled by Koch et al. (1981) to incorporate interlayer sliding, which again predicts a flat topped geometry and also the upwarping of strata adjacent to the intrusion margin (Fig. 6c). Building on elastic plate theory (e.g., Sneddon and Lowengrub 1969), the third end-member model type for laccolith growth (Fig. 6d) is based on vertical deflection of a circular, thin elastic plate (e.g., Perkins and Kern 1961; Pollard and Johnson 1973; Zenzri and Kerr 2001). For example, Pollard and Johnson (1973) adopted a solution for a thin, clamped, circular elastic plate to model laccolith growth and the sill-to-laccolith transition. This model, which has been used extensively to estimate driving pressures and intrusion thicknesses (e.g., Price and Cosgrove 1990; McCaffrey and Petford 1997), predicts the bell-jar shape that has come to be synonymous with laccoliths in textbooks (Fig. 6d).

Common to these analytical solutions for laccolith growth is that L must be assumed prior to calculation of the final intrusion thickness. Hence, in these models the sill-to-laccolith transition does not emerge spontaneously from the dynamics because the solution lacks a moving propagation condition at the sill (then laccolith) tip. Furthermore, although the punched laccolith and rolling hinge models predict laccoliths with flat tops, the elastic plate model predicts bell jar-shaped cross sections, which are generally not supported by field observations.

Analogue and numerical studies of sill and laccolith emplacement and growth overcome some of the limitations of analytical solutions (e.g., Dixon and Simpson 1987; Roman-Berdiel et al. 1995; Mathieu et al. 2008; Polteau et al. 2008; Galland et al. 2006; Kavanagh et al. 2006, 2015; Menand 2008; Galland and Scheibert 2013). While such experimental studies provide

considerable insight into the dynamics and structural evolution of sills and laccoliths (see Galland et al. this volume, for a comprehensive review), like the analytical models, they are still not able to predict the observed L - T (and V) scaling of intrusions.

5 Modelling the Growth of Sills and Laccoliths

In order to further explore the mechanical significance of the L - T scaling of sills and laccoliths, as well as their leading-order geometrical attributes, Bunger and Cruden (2011a) developed an elastic, thin plate model that also takes into account a moving fracture propagation condition at the sill/laccolith tip, fluid flow within the intrusion and the influence of the magma weight on intrusion growth and shape. Key features of the model are summarised in Fig. 7a. A circular crack at depth, H is fed by a central conduit at a volumetric flow rate, Q_0 , which depends implicitly on magma overpressure. The problem is then to determine the fluid pressure, crack opening w , and radius R as a function of time. The resulting mathematical model comprises a continuity equation for fluid flow, and equations for fluid flow rate, an elastic plate and crack tip propagation, and suitable initial and boundary conditions. The combined solutions to these coupled equations, including details of the required numerical routine are detailed in Bunger and Cruden (2011a, b).

The model results are presented using scaling factors that relate the dimensional intrusion opening, w , radius, R , net pressure, p , and radial fluid flux, q , to equivalent dimensionless values Ω , γ , π , and Ψ , respectively. The equations are simplified by using the alternative host rock and magma parameters:

$$E' = \frac{E}{1 - \nu^2}, \quad \mu' = 12\mu, \quad K' = 4 \left(\frac{2}{\pi} \right)^{\frac{1}{2}} K_{Ic}, \quad (4)$$

where μ is magma dynamic viscosity. Two dimensionless groups, or evolution parameters,

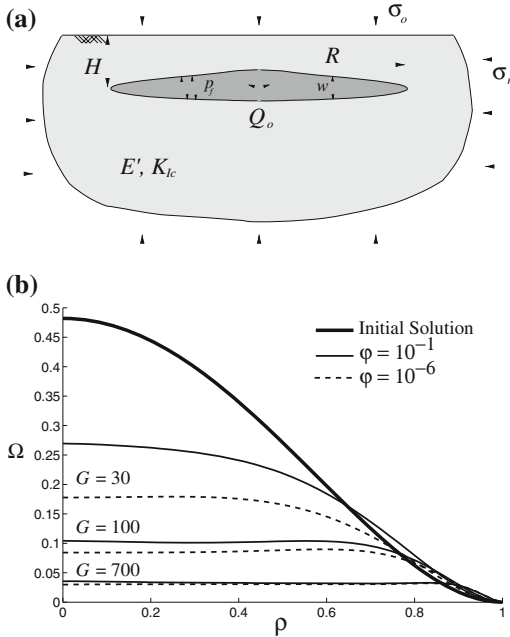


Fig. 7 **a** Sketch of the sill and laccolith growth model introduced by Bungler and Cruden (2011a). See text for explanation of symbols. **b** Profiles of the dimensionless opening, Ω , across a dimensionless half width of the intrusion as a function of dimensionless time, expressed by the evolution parameter, G . The upper dark curve is the initial solution, which corresponds to the elastic plate solution illustrated in Fig. 6d. With increasing time and G the outwardly growing intrusion develops a flat top and uniform thickness

and two characteristic times describe the behaviour of the model:

$$G_m = \frac{E'^2 H^3 \mu'}{K'^2 t}, \quad G = \frac{\rho_m g Q_0 t}{H^3/2 K}, \quad (5)$$

$$t_m = \frac{E'^2 H^3/2 \mu'}{K'^3}, \quad t_p = \frac{H^3/2 K'}{\rho_m g Q_0}, \quad (6)$$

where G_m describes the behaviour when magma viscosity dominates the dynamics and G describes the dynamics when magma weight, $\rho_m g$ dominates, and t_m and t_p are the corresponding characteristic times.

When t_m is large in comparison to time, t , G_m is also expected to be large, indicating that fluid pressure gradients will be large and the system will be “viscosity dominated.” When $t \gg t_m$, G_m

becomes vanishingly small and the system is referred to as “toughness dominated” (e.g., Savitsky and Detournay 2002; Detournay 2004). The system therefore evolves from viscosity to toughness dominated as time increases relative to t_m . Simultaneously t will increase relative to t_p , which is the characteristic time for the transition from an early regime when the influence of magma weight is negligible to a later time when its influence is significant, as implied by the evolution parameter G . A “trajectory” parameter $\varphi = t_m/t_p$ can be defined, which plays the role of a dimensionless viscosity. φ indicates the time required for viscous effects to vanish and for magma weight to become dominant, which is predicted to occur very early on in the evolution of real intrusions (Bungler and Cruden 2011a).

The effects of G (and time) and φ on the dimensionless opening profile of the model intrusion are illustrated in Fig. 7b, where $\rho = r/R$ is the dimensionless horizontal distance from the centre. Model intrusion growth can be characterised by a transition from a bell jar shaped, uniformly pressurised solution when $G \ll 1$, to a solution for $G \gg 1$ in which the thickness is uniform over most of the extent of the intrusion. The bell jar shape when $G \ll 1$ essentially corresponds to the well-known solution of Pollard and Johnson (1973). When $G \gg 1$ the intrusion becomes increasingly flat topped over time as G increases, becoming a thin disk by $G = 1000$. The role of φ is to slow down the transition from the bell jar shaped plate solution to the flat-topped solution. Corrected numerical solutions for Ω and G are tabulated in Bungler and Cruden (2011b) for values of $\varphi = 10^{-1}$ and $\varphi = 10^{-6}$.

The tabulated values for Ω and G , together with emplacement depth and host rock and magma parameters (Eq. 4) can be used to determine the dimensional intrusion radius and opening from:

$$w = \left(\frac{G K'^2}{E' g \rho_m} \right)^{\frac{1}{2}} \Omega, \quad R = \left(\frac{G E' H^3}{g \rho_m} \right)^{\frac{1}{4}} \gamma. \quad (7)$$

By equating $T = w$ and $L = 2R$, results from Eq. 7 can be used to model the growth of laccoliths and sills over time (expressed as

increasing G) in $\log T$ versus $\log L$ space and to explore the roles of emplacement depth and host rock fracture toughness and rigidity on intrusion shape and aspect ratio. Because the equation for G contains the expression $Q_o t = V$, intrusion growth times can be estimated for different volumetric flow rates and host rock properties and emplacement depths; conversely, if t is known independently (e.g., from geochronology) then volumetric flow rate can be estimated for different conditions. Usually both Q_o and t are unknown, in which case the outcome of increasing V can be explored while varying host rock properties and emplacement depths.

Growth curves for laccoliths and sills predicted by the model follow paths with a common shape in $\log T$ versus $\log L$ space (Fig. 8).

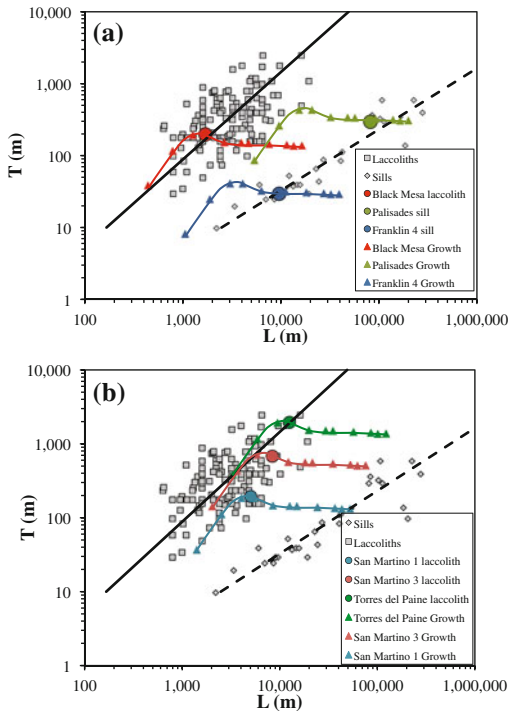


Fig. 8 Geometric growth curves of some natural laccoliths modelled using the model of Bungler and Cruden (2011a) and plotted in $\log T$ versus $\log L$ space. Dimensional data for laccoliths and sills, and scaling lines from Fig. 1 are included for reference. **a** Growth scenarios for the Black Mesa laccolith, Palisades sill and Franklin 4 sill. **b** Growth scenarios for the San Martino 1 and 2 laccoliths and Torres del Paine pluton. See Table 2 and text for model parameters and further discussion

Starting at $G = 0.1$, initial growth follows a trajectory with a similar slope to the power law scaling curve for laccoliths, meaning that during this phase it thickens faster than it lengthens. The intrusion reaches a maximum thickness between $G = 5$ and 10, at which point it has the typical flat-topped and steep sided morphology of laccoliths. After this stage, as the intrusion continues to lengthen, T decreases as G approaches 30. For $G = 70$ –1500 the thickness remains essentially constant as it approaches an asymptotic value. For $G > 100$ the intrusion has the high aspect ratio, uniform thickness and tapered margin characteristic of sills.

Here we explore the effects of varying H , K_{IC} , and E' on the evolution of T , L and V over time. We also attempt to constrain the growth histories and conditions for selected laccoliths and sills in nature.

5.1 Influence of Emplacement Depth and Bulk Country Rock Mechanical Properties

When H , K_{IC} , or E' are varied, the intrusion growth trajectory will be shifted up down or sideways on a $\log T$ versus $\log L$ plot but its shape remains unchanged. This is illustrated in Fig. 8 for different case studies of natural intrusions, detailed below.

The effect of increasing the emplacement depth is to move the growth trajectory curves from left to right in the $\log L$ direction, as expected from the dimensional radius, R , predicted by Eq. 7. Hence, keeping G and the country rock properties equal, deeper sills and laccoliths will have greater widths and larger aspect ratios, which is consistent with the findings of analogue experiments on sills and laccoliths (Dixon and Simpson 1987; Roman-Berdiel et al. 1995) and some geophysical and numerical modelling constraints (Polteau et al. 2008). Not accounted for in the Bungler and Cruden (2011a) model is the concept of the effective overburden thickness, T_e . Pollard and Johnson (1973) introduced T_e in order to account for the mechanical behaviour of multilayered rocks overlying a growing sill or laccolith. If each layer boundary is able to slide freely they found that $T_e \sim 1/7H$ to

$2/3H$ for examples studied in the Henry Mountains, Utah. Evidence for layer parallel sliding and detachments has since been documented in the roof rocks of laccoliths in the Henry Mountains (Wilson et al. 2016). Hence sills and laccoliths emplaced into thick sequences of mechanically layered host rocks can exhibit growth histories and aspect ratios characteristic of shallower depths.

When K_{Ic} is increased, growth trajectory curves are shifted vertically towards higher T values, consistent with the prediction for the dimensional opening, w , in Eq. 7. Hence when all else is equal, high fracture toughness country rocks will favour thicker, lower aspect ratio intrusions.

The country rock stiffness parameter has a counteracting effect on both H and K_{Ic} , such that an increase in E' will move the growth trajectory curve from top left to bottom right, owing to the fact that E' appears in the denominator and numerator of the equations for w and R , respectively (Eq. 7). Hence when all else is equal, high stiffness country rocks will favour thinner, wider, higher aspect ratio intrusions. The magma density, ρ_m , is also a factor in Eq. 7 and higher values will shift growth curves downwards. However, the effect of ρ_m is minor compared to that of K_{Ic} and E' .

5.2 Selected Case Studies of Sills and Laccoliths

Using the growth trajectories described above it is possible to match growth curves for specific examples in nature. However, any solution for a given sill or laccolith will not be unique because three parameters (four including density) can be varied to achieve the desired outcome. The approach we have taken here is to vary E' and K_{Ic} such that the known T and L dimensions are achieved for the appropriate H (if known) and G -value. We have taken $G \sim 10$ to be representative of laccoliths and $G \sim 100\text{--}300$ to be likely end points for sills. The most favoured growth curve will be one that satisfies these constraints while keeping K_{Ic} and E' as close as possible to accepted values (Fig. 8, Table 2). For reference, the typical range of laboratory-derived values of

K_{Ic} and E' are $0.5\text{--}2$ MPam^{0.5} and $1.04 \times 10^3\text{--}8.3 \times 10^4$ MPa, respectively (Olson 2003). Delaney and Pollard (1981) and Olson (2003) report values estimated from the Ship Rock dyke, Colorado Plateau, of $K_{Ic} = 40\text{--}4000$ MPam^{0.5} and $E' = 2.5 \times 10^3\text{--}2.5 \times 10^4$ MPa, which highlight the current uncertainty in field-scale versus laboratory-scale rock property characterisation.

5.2.1 Black Mesa Laccolith, Henry Mountains, Utah

We start with modelling possible growth histories for the Tertiary age Black Mesa laccolith (Johnson and Pollard 1973; de Saint Blanquat et al. 2006). The first three scenarios presented in Table 2 result in identical growth trajectories, arriving at the same L - T dimensions when $G = 10$ (Fig. 8a). The first scenario starts with an emplacement depth $H = 2500$ m derived from stratigraphic constraints (Johnson and Pollard 1973) and is optimised to keep K_{Ic} within the range of laboratory values. In this case the desired dimensions are reached when $K_{Ic} = 1.2$ MPam^{0.5} and $E' = 0.01$ MPa, so the country rocks must have anomalously low elastic stiffness to achieve sufficient vertical growth at the known emplacement depth. In the second scenario, following Johnson and Pollard (1973), we adopt an effective elastic thickness $T_e = 0.15$ $H = 375$ m and find that the correct dimensions can be achieved when $K_{Ic} = 20$ MPam^{0.5} and $E' = 2.5$ MPa, which again requires a very low country rock elastic stiffness. Finally, we explore a scenario that is optimised for E' and find that Black Mesa growth could have occurred for acceptable field-scale values $K_{Ic} = 400$ MPam^{0.5} and $E' = 1000$ MPa but the required emplacement depth, $H = 50$ m is 2450 m short of the known value. Modelling the final dimensions of the Black Mesa laccolith therefore requires emplacement into country rocks that are extremely compliant ($E' \sim 1000$ times lower than normal values) or with a very low effective overburden thickness, in this case $T_e \sim 0.02H$.

One limitation of the present modelling approach is that it does not consider plastic yielding of the country rocks. The Black Mesa

Table 2 Sill and laccolith growth scenarios

Intrusion (scenario)	Type	L (m)	T (m)	G	H (m)	K_{ic} MPam ^{0.5}	E' MPa	V (m ³)	Q_0 m ³ /s	t (year)	References	Comments
Black Mesa (1)	Laccolith	1700	200	10	2500	1.2	0.01	2.0×10^8	0.1	66	Johnson and Pollard (1973), Blanquat et al. (2006)	Estimated emplacement depth
Black Mesa (2)	Laccolith	1700	200	10	375	20	2.5	2.0×10^8	0.1	66	Johnson and Pollard (1973), de Saint Blanquat et al. (2006)	Effective thickness $T_e = 0.15H$
Black Mesa (3)	Laccolith	1700	200	10	50	400	1000	2.0×10^8	0.1	66	Johnson and Pollard (1973), de Saint Blanquat et al. (2006)	Optimised for E' , $T_e = 0.02H$
Black Mesa (4)	Laccolith	1700	10	10	55	20	1000	2.3×10^7	0.1	3.3	Johnson and Pollard (1973), de Saint Blanquat et al. (2006)	Single pulse, $T_e = 0.022H$
San Martino 1 (1)	Laccolith	5000	200	10	2200	15	1.5	2.0×10^9	0.1	648	Rocchi et al. (2002)	Estimated emplacement depth
San Martino 1 (2)	Laccolith	5000	200	10	250	400	1000	2.0×10^9	0.1	648	Rocchi et al. (2002)	Optimised for E' , $T_e = 0.11H$
San Martino 3	Laccolith	8300	700	10	1900	150	10	1.6×10^{10}	0.1	5200	Rocchi et al. (2002)	Estimated emplacement depth
Torres del Paine (1)	Laccolith	12400	2000	10	2500	700	30	2.5×10^{11}	0.04	91500	Michel et al. (2008), Leuthold et al. (2012)	Estimated emplacement depth
Torres del Paine (2)	Laccolith	12400	100	10	600	300	2000	5.7×10^9	0.04	4600	Michel et al. (2008), Leuthold et al. (2012)	Single pulse, $T_e = 0.24H$
Palisades	Sill	80000	300	300	4000	200	50	2.0×10^{12}	10	6350	Walker (1969)	Estimated emplacement depth
Franklin 4	Sill	9500	30	100	1000	6	5	2.5×10^9	10	7.9	Robertson and Baragar (1972), Bédard et al. (2012)	Minimum emplacement depth

laccolith is partially bounded by a steep fault on its southeast side (Fig. 4b), indicating failure of overburden rocks during vertical inflation (de Saint Blanquat et al. 2006). We suggest that plastic failure of overburden rocks during laccolith emplacement could result in significant reduction in T_e or E' as a consequence of reducing the amount of elastic bending required to accommodate vertical inflation. Punched laccoliths (Fig. 6b; Gilbert 1877) and bysmaliths (Daly 1905) are examples of intrusion types that form by this process.

Another limitation of our modelling approach is that it does not allow for the emplacement of pulses and stacking of sheets, which are thought to have played a role in the growth of the Black Mesa laccolith (de Saint Blanquat et al. 2006) and many other intrusions. In order to attempt to take this into account for the Black Mesa laccolith, we have explored a fourth scenario for the conditions required for the emplacement of a 10 m thick sheet with a width, $L \sim 1700$ m equal to the final intrusion (Table 2). This corresponds to modelling one of 20 arbitrary pulses of equal thickness that will eventually be stacked to form the final laccolith. The result presented here has been optimised for a large $E' = 1000$ MPa and relatively small $K_{Ic} = 20$ MPam^{0.5}. For these parameters we find that the effective depth must be 55 m or $T_e = 0.022H$. A general conclusion we can draw for the Black Mesa laccolith is that either the effective overburden thickness or the elastic stiffness of the overburden must have been very low, even if it grew by injection of multiple thin pulses. This points to host rock plasticity as an important factor for its emplacement and growth.

5.2.2 San Martino Laccoliths, Elba Island

The San Martino 1 and 3 intrusions are part of a stack of Miocene age (Tortonian-Messinian) laccoliths that are well exposed on central Elba Island, Italy (Rocchi et al. 2002, 2010). They are emplaced into a layered and thrust stacked sequence of Cretaceous to Eocene flysch. The vertical and horizontal dimensions of the laccoliths are well constrained by field mapping and

their depths of emplacement have been estimated from their stratigraphic position (Table 2). Growth trajectories for both laccoliths (Fig. 8b) can be matched to their dimensions without making adjustments for depth and for reasonable field-scale values of $K_{Ic} = 15\text{--}150$ MPam^{0.5} but require low values of $E' = 1.5\text{--}10$ MPa. Higher values of E' could be offset by $T_e < H$ and larger K_{Ic} as in scenario 2 for San Martino 1 (Table 2). In this case $T_e = 0.11H$, which approaches the range of effective thicknesses proposed by Pollard and Johnson (1973). Hence the model accounts for the scaling for the Elba laccoliths reasonably well given the known mechanical layering of the overburden rocks. However, the role of plastic yielding cannot be ruled out and is supported by local evidence for intrusion-related faulting in the country rocks (Westerman et al. this volume).

5.2.3 Torres Del Paine Pluton, Patagonia

In order to assess the emplacement of a very large laccolith, we have modelled the growth of the Miocene age (Tortonian) Torres del Paine granite, Patagonia, Chile (Skarmeta and Castelli, 1997). The tabular Torres del Paine pluton comprises three compositionally distinct, 400–800 m thick sheets of the Paine granite, which are underlain by the >500 m thick Paine Mafic Complex (Michel et al. 2008). Both the granite units and the mafic complex are themselves made up of multiple pulses of variable thickness. Emplacement occurred into layered and folded Cretaceous flysch at a depth estimated from geobarometry of 2–3 km (Michel et al. 2008). The estimated 88 km³ of the entire plutonic complex is thought to have grown from the top down (underplating) over a period of 162 ± 11 ka (Leuthold et al. 2012) and the granitic units were emplaced over 90 ± 40 ka (Michel et al. 2008).

Assuming continuous emplacement, we first model the growth trajectory for the granitic part of the Torres del Paine pluton without making any adjustment for depth and for a reasonable field-scale value of $K_{Ic} = 700$ MPam^{0.5} (Fig. 8b; Table 2). As in the other laccolith examples

above, growth to the correct dimensions at the known emplacement depth cannot be achieved without adopting a relatively low host rock stiffness, here $E' = 30$ MPa. In the case of Torres del Paine, this could partly be explained by thermal softening of the host rocks, which is supported by the presence of a well-developed contact metamorphic aureole (Putlitz et al. 2001). In a second scenario we consider injection of a 100 m thick pulse with L spanning the entire width of the pluton (Table 2). In this case we find that emplacement and growth can occur for geologically reasonable values of both K_{Ic} and E' if $H = 600$ m. The latter corresponds to $T_e = 0.24H$, which is well within the range estimated by Pollard and Johnson (1973). These findings strongly support the field-based interpretation that the Torres del Paine pluton grew by vertical stacking of multiple sheet-like pulses (Michel et al. 2008; Leuthold et al. 2012).

5.2.4 Palisades Sill, Eastern USA and Franklin Sills, Nunavut, Canada

Finally, we consider two mafic sills in order to assess growth up to larger values of G and L (Fig. 8a; Table 2). The Jurassic age Palisades sill intruded layered sedimentary and volcanic rocks of the Mesozoic Newark Basin, eastern USA (Walker 1969; Puffer et al. 2009). Stratigraphic arguments and thermal modelling suggest an estimated emplacement depth of 3–4 km (Walker 1969; Shirley 1987). We also examine one of the mafic sills that make up part of the Neoproterozoic Franklin large igneous province, Victoria Island, Canada (Robertson and Baragar 1972; Bédard et al. 2012). The sills intruded gently folded layered sedimentary rocks and basalt flows of the Neoproterozoic Shaler supergroup at emplacement depths ranging between ~ 1 and 4 km (Bédard et al. 2012). We focus on Franklin Sill 4 (see Fig. 2 in Robertson and Baragar 1972 for location), which we assume to have been emplaced at a minimum depth of 1000 m.

Growth trajectories for both sills show that their final dimensions can be modelled for $G = 300$ (Palisades) and 100 (Franklin 4) using their

estimated or minimum emplacement depths and for reasonable field-scale values of K_{Ic} (Fig. 8a; Table 2). In both cases we find that the country rocks must have low values of elastic stiffness. For the Palisades sill, this could be offset by replacing H with a lower T_e , given the strongly layered nature of the host rocks, and by considering emplacement by several pulses, for which there is debated field and petrological evidence (Walker 1969). In the case of Franklin 4, low values of E' would be compatible with host-rock plasticity and failure, which is consistent with detailed mapping by Bédard et al. (2012) who documented significant interaction between pre-existing faults and sills during their emplacement and propagation through the crustal section.

5.3 Timescales of Laccolith and Sill Growth

Given that the final intrusion volume can be estimated from T and L we also can assess likely emplacement times by assuming typical magma volumetric flow rate values (Q_o). These times can be compared to independent estimates of emplacement duration from geochronology or thermochronology and cooling calculations. The value of $Q_o = 0.1$ m³/s (~ 0.003 km³/yr) adopted for the Black Mesa and San Martino laccoliths is based on representative and conservative magma volumetric flow rate values estimated for felsic-intermediate intrusions and eruptions (Petford et al. 2000; White et al. 2006; de Saint Blanquat et al. 2011; Menand et al. 2015). This gives an emplacement time of 66 years for the Black Mesa laccolith, which is close to the maximum value of 100 years estimated by de Saint Blanquat et al. (2006) based on thermal modelling. Using the volumetric flow rate value above San Martino 1 and 3 laccoliths could have been emplaced over ~ 600 to ~ 5000 years, respectively. However, Rocchi et al. (2002) estimated a filling time for the combined San Martino laccoliths of ~ 100 years based on an estimated dyke-fed magma ascent rate of 3×10^{-3} m/s. Increasing Q_o to 5 m³/s would result in a combined emplacement time for both

laccoliths of ~ 100 years, consistent with this previous estimate, although the required volumetric flow rate ($\sim 0.1 \text{ km}^3/\text{year}$) is very high compared to known eruption and emplacement rates of felsic magmas (White et al. 2006; de Saint Blanquat et al. 2011).

Precise geochronology indicates that the granitic part of the Torres del Paine pluton was emplaced over $90 \pm 40 \text{ Ka}$ (Michel et al. 2008). Using this as a constraint, continuous growth of the pluton requires a magma flux $Q_o \sim 0.04 \text{ m}^3/\text{s}$ ($\sim 0.001 \text{ km}^3/\text{year}$), which is also consistent with previous estimates from other intrusions and eruptions (White et al. 2006; de Saint Blanquat et al. 2011). Note that this does not take into consideration the possibility of a time lag or repose period between magma pulses (e.g., Cruden 2006; White et al. 2006). In such cases and when the time lag is relatively long compared to the pulse emplacement time, Q_o could be much larger.

There are no geochronological constraints for the emplacement duration of the Palisade and Franklin 4 sills. Thermal modelling of the Palisades sills indicates magma solidification over ~ 1000 years (Shirley 1976), which provides a minimum estimate of the emplacement time. Since both mafic sills were emplaced during high magma flux mantle melting events, we assume a conservative value of $Q_o \sim 10 \text{ m}^3/\text{s}$ ($\sim 0.3 \text{ km}^3/\text{year}$), corresponding to the upper end of mafic magma eruption rates (White et al. 2006; de Saint Blanquat et al. 2011). This gives continuous emplacement times for the Palisades and Franklin 4 sills of ~ 6000 and ~ 8 years, respectively.

6 Discussion

6.1 Bifurcation Between Laccolith and Sill Growth Histories

Current models do not predict the observed bifurcation between mafic sills and laccoliths at $L \sim 500 \text{ m}$. Neither emplacement depth nor composition provides an explanation because laccoliths and large mafic sills are similar in this

regard. However, it is clear that both intrusion types follow different evolutionary pathways with laccoliths forming in a thickening (roof lifting, $a > 1$) dominated regime and large mafic sills forming in a lengthening (horizontal propagation, $a < 1$) dominated regime. Below $L \sim 500 \text{ m}$ and $T \sim 10 \text{ m}$ tabular intrusion types are indistinguishable.

The modelling discussed in the previous sections shows that laccoliths and large mafic sills share a common evolutionary path at early growth stages, initially thickening faster than they lengthen (Bunger and Cruden 2011a). However, laccoliths appear to stop growing at low G , which may occur due to cessation in magma supply and/or freezing, resulting in a low aspect ratio intrusion ($LT < 10$). If more magma is available, the additional magma weight is capable of driving the intrusion outwards with constant thickness to large aspect ratios, stopping at large G when magma supply ends or solidification occurs. Hence, large mafic sill formation is favoured in tectonic settings that generate large volumes of hot melt, such as during continental breakup and Large Igneous Province development (e.g., Ernst et al. 2005). Conversely, laccoliths tend to form in settings where magma supply is restricted, such as intraplate settings. We therefore suggest that the main control on the observed bifurcation in scaling behaviour is related to tectonic setting and available magma supply, rather than depth, composition or viscosity.

An alternative or complementary cause of the data bifurcation is that laccoliths and plutons tend to grow incrementally by stacking of sheets (e.g., Cruden and McCaffrey 2001; Coleman et al. 2004; Horsman et al. 2010; Rocchi et al. 2010; Annen 2011; Menand 2011), consistent with growth dominated by vertical inflation. By contrast, most sills are thought to represent one or a small number of intrusion events (e.g., Hergt and Brauns 2001; Marsh 2004), consistent with growth dominated by horizontal elongation. Formation of a laccolith or pluton by sheet stacking would result in a vertical growth trajectory on a $\log T$ versus $\log L$ plot with $a \gg 1$ (see Fig. 7 in Cruden and McCaffrey 2001 and Fig. 8 in Rocchi et al. 2010). However, it is

currently unclear why such a two-stage growth history would result in the observed power-law scaling of laccoliths and plutons, or the bifurcation in the scaling data at $L \sim 500$ m.

6.2 Intrusions Too Deep to Interact with Earth's Surface

Polyphase granitic to dioritic plutons and layered mafic intrusions are typically emplaced at upper to mid-crustal depths (2–15 km) into both layered and crystalline host rocks. Multiple processes likely operate during their emplacement, including brittle and ductile wall-rock deformation, stoping and assimilation (Paterson et al. 1996; Cruden 2006). However, space for most plutons and layered mafic intrusions is thought to be created by vertical displacement of wall rocks, which at the shallowest depths can occur by roof lifting but below ~ 3 km is likely dominated by floor depression (e.g., Myers 1975; Cruden 1998; Wiebe and Collins 1998; Brown and McClelland 2000). The process of floor depression is driven by a periodic exchange of material (melt) from a partially molten source region in the lower crust

to the growing pluton in the mid- to upper crust (Cruden and McCaffrey 2001; Cruden 2006) or between an upper and a lower chamber (Clough et al. 1909; Myers 1975). The cumulative downward displacement of the intervening crustal column requires large-scale brittle or ductile deformation depending on emplacement depth. Although many plutons and layered mafic intrusions are constructed by multiple pulses (Glazner et al. 2004; de Saint Blanquat et al. 2011; Annen 2011), which could be treated as individual sill emplacement events (Menand 2011), the requirement of large-scale plasticity to make space indicates that a single LEFM-based model cannot be used to predict their observed $a < 1$ power-law scaling. Acknowledging the roles of local and far-field deformation, the underlying control on the dimensions and scaling of plutons and layered mafic intrusions likely originates in the lateral extent and melt productivity of underlying magma source region, which will determine both the length and thickness of the resulting intrusion, respectively (Cruden 2006; Scaillet and Searle 2006). The transition from laccoliths with $a > 1$ to plutons and layered mafic intrusions with $a < 1$ therefore reflects an

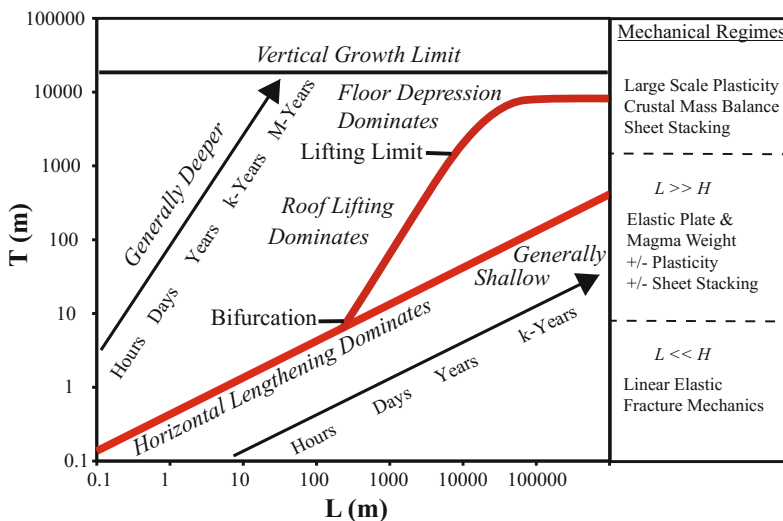


Fig. 9 Regime diagram for tabular intrusion scaling and growth mechanisms in $\log T$ versus $\log L$ space. Red curves summarize the dimensional scaling relationships (Fig. 1) for different classes of intrusion. Arrows indicate

tendencies for increasing emplacement depth and time. Dominant mechanical regimes for emplacement are indicated at right with approximate boundaries or thresholds based on intrusion thickness and depth

increase in the depth of emplacement and a transition from an intrusion regime where interaction with the surface is important to one where interaction with the underlying source region controls the leading order behaviour (Fig. 9).

Batholiths and large layered mafic intrusions are composite bodies built over long time periods. The building blocks of batholiths are plutons whereas large layered mafic intrusions comprise multiple sheet-like bodies enclosed within a single envelope (Cawthorn 1996; Saumur and Cruden 2016). Batholiths and large layered mafic intrusion are therefore emplaced by multiple processes and grow by a combination of vertical stacking and lateral accretion. The final size and shape of these structures is likely controlled by the underlying tectonic regime. The upper bound on $T \sim 10$ km corresponds to $1/3$ – $1/4$ of the thickness of normal or over-thickened continental crust and likely reflects a growth limit related to long-term magma supply in arc, extensional and plume settings.

7 Towards a General Framework for Tabular Intrusion Emplacement and Growth

The geometric scaling of tabular intrusions provides a useful framework for defining and understanding three first-order magma emplacement regimes in the crust (Fig. 9). Small, horizontal tabular intrusions with $L \sim 5$ – 1000 m are characterised by a power law scaling with $a \sim 0.5$. These intrusions satisfy the condition $L < H$ and their emplacement can be explained by LEFM if field-scale fracture toughness values are allowed to exceed laboratory values.

When $L \sim 500$ – 1000 m there is a pronounced bifurcation in the scaling data with shallow, large mafic sills defining one branch with $a < 1$, and laccoliths defining second branch with $a > 1$ (Fig. 9). The emplacement of both laccoliths and large mafic sills occurs in a regime where $L > H$, whereby space is made predominantly by roof lifting. The geometry and scaling of laccoliths and large mafic sills can be adequately explained by elastic plate models that take

into account a propagation condition at the crack tip and the role of magma weight (Bunger and Cruden 2011a). As with small sheets with $L < H$ modelled by LEFM, these models require country rocks to have large field-scale fracture toughness values compared to laboratory values. More importantly, when attempting to match the dimensions of specific examples in nature we also find that the host rocks must have anomalously low elastic stiffness and/or the effective emplacement depth must be much lower than the known depth. The latter can be partly explained by the mechanical behaviour of well-layered overburden rocks (Pollard and Johnson 1973). In some cases (e.g., Torres del Paine pluton) the low stiffness of the country rocks might also be accounted for by thermal softening. However, in general we suggest that this requirement and that of low elastic stiffness are best explained by plastic failure of the country rocks during intrusion growth, in agreement with field observations.

A final consideration in modelling the emplacement of laccoliths and sills is the likelihood that they grow by vertical stacking of multiple pulses. For the intrusions assessed here we find that intrusion of thin pulses alleviates the requirement for low stiffness country rocks as well as bringing down the fracture toughness to more acceptable values. However, in all cases an effective emplacement depth that is lower than the true depth is required. Nevertheless, construction of laccoliths and sills by multiple pulses together with plastic failure of host rocks during emplacement appears to reconcile the mismatch between observations and theory. It should be noted that both of these effects have yet to be implemented in numerical models, and that although growth of laccoliths by multiple pulses is widely accepted, the incremental emplacement of sills is still debated.

The origin of the bifurcation in the data set between laccoliths and large mafic sills (Fig. 9) is an outstanding problem for future research. However, since laccoliths and large mafic sills share common evolutionary pathways, we argue that the bifurcation is not related to differences in emplacement depth or composition, density or viscosity. Instead, we suggest that whether an

intrusion ends up in the laccolith or large mafic sill field depends largely on a combination of magma productivity and the rates of magma supply and solidification. Hence, low melt production regimes will be only capable of delivering a sufficient volume of magma to form a laccolith at low G . By comparison high melt productivity regimes will ensure enough magma supply to allow lengthening to large G , aided by the additional effect of the magma weight. Magma supply rate will also be a contributing factor in both scenarios, as this will influence how long flow in the growing intrusion can continue before solidification occurs. This latter effect might also provide an alternative explanation for the $a < 0.5$ scaling of large mafic sills, although this requires further development of both numerical and laboratory modelling of sill emplacement incorporating the effects of solidification (e.g., using the approach of Lister 1995 and Bolchover and Lister 1999).

When $L \sim 8\text{--}12$ km there is a transition between laccoliths and plutons and layered mafic intrusions, which are characterised by a scaling regime with $a < 1$. This transition corresponds to a change in emplacement mechanism from one dominated by roof lifting to one dominated by floor depression. As such, it represents a “lifting limit” (Fig. 9), which is likely controlled by the tendency for plutons and layered intrusions to be emplaced at deeper crustal levels than laccoliths. The origin of the $a < 1$ scaling for plutons and layered mafic intrusions, as well as the tendency for a to decrease with L remain poorly understood. We note that growth of these types of intrusions, together with composite batholiths, is likely governed by the mass balance of magma transfer from the source to the emplacement site, and how this transfer and space for growth is accommodated by large-scale deformation of the crust. Growth of plutons and layered intrusions by vertical stacking of pulses is expected to be an important contributing factor in both of these processes. A significant challenge for future research will be to couple these constraints, as well as heat transfer and solidification within a self-consistent model of intrusion growth in the mid- to lower crust.

Lastly, we have given some consideration to timescales of emplacement, which in general will increase with increasing intrusion size and volume (Fig. 9). Assuming reasonable estimates for magma volumetric flow rate, laccoliths and sills can be emplaced in 10's of years to k-years, while single pulses can potentially be injected over months to a few years. These results are consistent with thermal modelling studies and rare, direct observation of shallow intrusion growth from surface deformation. Timescales for larger laccoliths, plutons and layered mafic intrusions are likely to be strongly influenced by the time lag between rapidly emplaced pulses, which in turn relates to the productivity and magma supply rate in the source. Hence plutons and layered mafic intrusions grow over ka to Ma timescales, in agreement with constraints from precise geochronology.

Acknowledgements We are grateful to Sergio Rocchi and Christoph Breitkeuz for their forbearance and editorial input, and two anonymous reviewers for positive comments and suggestions. Michael Lishman is thanked for introducing ARC to the Whin Sill at High Cup Nick and for Fig. 3a.

References

- Abdelmalak MM, Mourgues R, Galland O, Bureau D (2012) Fracture mode analysis and related surface deformation during dyke intrusion Results from 2D experimental modelling. *Earth Planet Sci Lett* 359–360:93–105
- Annen C (2011) Implications of incremental emplacement of magma bodies for magma differentiation, thermal aureole dimensions and plutonism–volcanism relationships. *Tectonophysics* 500:3–10
- Babiker M, Gudmundsson A (2004) Geometry, structure and emplacement of mafic dykes in the Red Sea Hills, Sudan. *J Afr Earth Sc* 38:279–292
- Barnes SJ, Cruden A, Arnt N, Saumur B (2016) The mineral system approach applied to magmatic Ni-Cu-PGE sulfide deposits. *Ore Geol Rev* 76:296–316
- Bédard JH, Naslund HR, Nabelek P, Winpenny A, Hryciuk M, Hayes B, Steigerwaldt K, Hadlari T, Rainbird R, Dewing K, Girard E (2012) Fault-mediated melt ascent in a Neoproterozoic continental flood basalt province, the Franklin sills, Victoria Island, Canada. *Geol Soc Am Bull* 124:723–736

- Bolchover P, Lister JR (1999) The effect of solidification on fluid-driven fracture, with application to bladed dykes. *Proc R Soc A* 455:2389–2409
- Bunger AP, Cruden AR (2011a) Modeling the growth of laccoliths and large mafic sills: the role of magma body forces. *J Geophys Res* 116:B02203. doi:10.1029/2010JB007648
- Bunger A, Cruden A (2011b) Correction to “Modelling the growth of laccoliths and large mafic sills: the role of magma body forces”. *J Geophys Res* 116:B08211. doi:10.1029/2011JB008618
- Bunger A, Menand T, Cruden A, Zhang X, Halls H (2013) Analytical predictions for a natural spacing within dyke swarms. *Earth Planet Sci Lett* 375:270–279
- Bradley J (1965) Intrusion of major dolerite sills. *Trans R Soc* 3:27–55
- Brown EH, McClelland WC (2000) Pluton emplacement by sheeting and vertical ballooning in part of the southeast Coast Plutonic Complex, British Columbia. *Geol Soc Am Bull* 112:708–719
- Cawthorn RG (ed) (1996) Layered intrusions. Elsevier Science, Amsterdam, p 531
- Clough CT, Maufe HB, Bailey EB (1909) The cauldron-subsidence of Glen Coe, and the associated igneous phenomena. *J Geol Soc London* 65:611–678
- Coleman D, Gray W, Glazner AF (2004) Rethinking the emplacement and evolution of zoned plutons: geochronologic evidence for incremental assembly of the Tuolumne Intrusive Suite, California. *Geology* 32:433–436
- Corazzato C, Groppelli G (2004) Depth, geometry and emplacement of sills to laccoliths and their host-rock relationships: Montecampione group, Southern Alps, Italy. *Geol Soc London Spec Publ* 234:175–200
- Corry CE (1988) Laccoliths: mechanics of emplacement and growth. *Geol Soc Am* 220:110 (Special Publication)
- Cruden AR (1998) On the emplacement of tabular granites. *J Geol Soc London* 155:853–862
- Cruden AR (2006) Emplacement and growth of plutons: implications for rates of melting and mass transfer in continental crust. In: Brown M, Rushmer T (eds) *Evolution and differentiation of the continental crust*. Cambridge University Press, Cambridge, pp 455–519
- Cruden AR (2008) Oskarshamn site investigation: emplacement mechanisms and structural influence of a younger granite intrusion into older wall rocks—a principal study with application to the Götömar and Uthammar granites. SKB. Swedish Nuclear Fuel and Waste Management Co., R-Report R-08-138, 48 p
- Cruden AR, McCaffrey KJW (2001) Growth of plutons by floor subsidence: implications for rates of emplacement, intrusion spacing and melt-extraction mechanisms. *Phys Chem Earth Part A* 26:303–315
- Cruden AR, Mazzarini F, Bunger A, Musermeci G (2009) Geometry, scaling relationships and emplacement dynamics of a ca. 6 Ma shallow felsic sill complex, Calamita Peninsula, Elba Island, Italy. *Eos Trans AGU*, 90(52), Fall Meeting Supplement, Abstract T13A-1843
- Daly RA (1905) The classification of igneous intrusive bodies. *J Geol* 13:485–508
- Delaney PT, Pollard DD (1981) Deformation of host rocks and flow of magma during growth of minette dikes and breccia-bearing intrusions near Ship Rock, New Mexico. US Geological Survey Professional Paper 1201
- Detournay E (2004) Propagation regimes of fluid-driven fractures in impermeable rocks. *Int J Geomech* 4:35–45. doi:10.1061/(ASCE)1532-3641(2004)4:1(35)
- Dixon JM, Simpson DG (1987) Centrifuge modelling of laccolith intrusion. *J Struct Geol* 9(87–103):1987
- Ernst RE, Buchan KL, Campbell IH (2005) Frontiers in large igneous province research. *Lithos* 79:271–297
- Francis EH (1982) Magma and sediment—I. Emplacement mechanism of late Carboniferous tholeiite sills in northern Britain. *J Geol Soc London* 139:1–20
- Friese N, Vollbrecht A, Tanner DC, Fahlbusch W, Weidemann M (2012) Multi-stage emplacement of the Götömar Pluton, SE Sweden: new evidence inferred from field observations and microfabric analysis, including cathodoluminescence microscopy. *Int J Earth Sci* 101:1149–1167
- Galland this volume
- Galland O, Scheibert J (2013) Analytical model of surface uplift above axisymmetric flat-lying magma intrusions: implications for sill emplacement and geodesy. *J Volcanol Geoth Res* 253:114–130
- Galland O, Cobbold PR, Hallot E, de Bremond d’Ars, Delavaud G (2006) Use of vegetable oil and silica powder for scale modeling of magmatic intrusion in a deforming brittle crust. *Earth Planet Sci Lett* 243:786–804
- Galland O, Planke S, Neumann E-R, Malthe-Sørenssen A (2009) Experimental modelling of shallow magma emplacement: application to saucer-shaped intrusions. *Earth Planet Sci Lett* 277:373–383
- Geshi N, Kusumoto S, Gudmundsson A (2010) Geometric difference between non-feeder and feeder dikes. *Geology* 38:195–198
- Gilbert GK (1877) Report on the Geology of the Henry Mountains. U.S. Geographical and Geological Survey of the Rocky Mountain Region, Government Printing Office, Washington, 160 p
- Glazner AF, Bartley JM, Coleman DS, Gray W, Taylor RZ (2004) Are plutons assembled over millions of years by amalgamation from small magma chambers? *GSA Today* 14:4–11
- Gudmundsson A (2011a) Rock fractures in geological processes. Cambridge University Press, Cambridge, 592 p
- Gudmundsson this volume
- Gudmundsson A (2011b) Deflection of dykes into sills at discontinuities and magma-chamber formation. *Tectonophysics* 500:50–64
- Grocott J, Arevalo C, Welkner D, Cruden AR (2009) Fault-assisted vertical pluton growth: Coastal Cordillera, northern Chilean Andes. *J Geol Soc London* 166:295–301

- Halls HC, Fahrigr WF (eds) (1987) Mafic Dyke swarms. Geological Association of Canada, Special Paper 34
- Hamilton WB (1965) Diabase sheets of the Taylor Glacier Region, Victoria Land, Antarctica. US Geological Survey, Professional Papers 456-B, 77 p
- Hansen DM, Cartwright J (2006) The three-dimensional geometry and growth of forced folds above saucer-shaped igneous sills. *J Struct Geol* 28:1520–1535
- Hergt JM, Brauns CM (2001) On the origin of Tasmanian dolerites. *Aust J Earth Sci* 48:543–549
- Horsman E, Morgan S, de Saint Blanquat M, Habert G, Nugent A, Hunter RA, Tikoff B (2010) Emplacement and assembly of shallow intrusions from multiple magma pulses, Henry Mountains, Utah. *Earth Environ Sci Trans R Soc Edinburgh* 100:1–16
- Hunt CB, Averitt P, Miller RL (1953) Geology and geography of the Henry Mountains region, Utah. U.S. Geological survey professional paper 228, 234 p
- Hutton DHW (2009) Insights into magmatism in volcanic margins: bridge structures and a new mechanism of basic sill emplacement—Theron Mountains, Antarctica. *Petrol Geosci* 15:269–278
- Jackson MD, Pollard DD (1988) The laccolith-stock controversy: new results from the southern Henry Mountains, Utah. *Geol Soc Am Bull* 100:117–139
- Johnson AM, Pollard DD (1973) Mechanics of growth of some laccolithic intrusions in the Henry Mountains, Utah. I. Field observations, Gilbert's model, physical properties and flow of the magma. *Tectonophysics* 18:261–309
- Kavanagh JL, Menand T, Sparks RSJ (2006) An experimental investigation of sill formation and propagation in layered elastic media. *Earth Planet Sci Lett* 245:799–813
- Kavanagh J, Boutelier D, Cruden A (2015) The mechanics of sill inception, propagation and growth: experimental evidence for rapid reduction in magmatic overpressure. *Earth Planet Sci Lett* 421:117–128
- Klimczak C, Schultz RA, Parashar R, Reeves DM (2010) Cubic law with aperture-length correlation: implications for network scale fluid flow. *Hydrogeol J* 18:851–862
- Koch F, Johnson A, Pollard DD (1981) Monoclinical bending of strata over laccolithic intrusions. *Tectonophysics* 74:T21–T31
- Leaman DE (1975) Form, mechanism, and control of dolerite intrusion near Hobart, Tasmania. *Aust J Earth Sci* 22:175–186
- Lister JR (1995) Fluid mechanical models of the interaction between solidification and flow in dykes. In: *Physics and chemistry of Dykes*, Balkema, pp 115–124
- Leuthold J, Muntener O, Baumgartner LP, Putlitz B, Ovtcharova M, Schaltegger U (2012) Time resolved construction of a bimodal laccolith (Torres del Paine, Patagonia). *Earth Planet Sci Lett* 325–326:85–92
- Magee C, Muirhead JD, Karvelas A, Holford SP, Jackson CAL, Bastow ID, Schofield N, Stevenson CTE, McLean C, McCarthy W, Shtukert O (2016) Lateral magma flow in mafic sill complexes. *Geosphere* 12:809. doi:[10.1130/GES01256.1](https://doi.org/10.1130/GES01256.1)
- Malthe-Sørenssen A, Planke S, Svensen H, Jamtveit B (2004) Formation of saucer-shaped sills. In: *Physical geology of high-level magmatic systems*, vol 234. Geological Society, London, Special Publications, pp 215–227
- Marsh BD (2004) A magmatic mush column Rosetta Stone: the McMurdo Dry Valleys of Antarctica. *EOS, Trans Am Geophys Union* 85:497–508
- Mathieu L, van Wyk de Vries B, Holohan EP, Troll VR (2008) Dykes, cups, saucers and sills: analogue experiments on magma intrusion into brittle rocks. *Earth Planet Sci Lett* 271:1–13
- McCaffrey K, Petford N (1997) Are granitic plutons scale invariant? *J Geol Soc London* 154:1–14
- McQuarrie N, Rogers DW (1998) Subsidence of a volcanic basin by flexure and lower crustal flow: the eastern Snake River Plain, Idaho. *Tectonics* 17:203–220
- Miles AJ, Cartwright JA (2010) Hybrid flow sills: a new mode of igneous sheet intrusion. *Geology* 38:343–346
- Miller JS, Matzel JEP, Miller CF, Burgess SD, Miller RB (2007) Zircon growth and recycling during the assembly of large, composite arc plutons. *J Volcanol Geotherm Res* 167:282–299
- Menand T (2008) The mechanics and dynamics of sills in layered elastic rocks and their implications for the growth of laccoliths and other igneous complexes. *Earth Planet Sci Lett* 267:93–99. doi:[10.1016/j.epsl.2007.11.043](https://doi.org/10.1016/j.epsl.2007.11.043)
- Menand T (2011) Physical controls and depth of emplacement of igneous bodies: a review. *Tectonophysics* 500:11–19
- Menand T, de Saint Blanquat M, Annen C (2011) Emplacement of magma pulses and growth of magma bodies. *Tectonophysics* 500:1–2
- Menand T, Annen C, de Saint Blanquat M (2015) Rates of magma transfer in the crust: Insights into magma reservoir recharge and pluton growth. *Geology* 43:199–202
- Michel J, Baumgartner L, Putlitz B, Schaltegger U, Ovtcharova M (2008) Incremental growth of the Patagonian Torres del Paine laccolith over 90 ky. *Geology* 36:459–465
- Mudge MR (1968) Depth control of some concordant intrusions. *Geol Soc Am Bull* 79:315–332
- Muirhead JD, Airoldi G, Rowland JV, White JDL (2012) Interconnected sills and inclined sheet intrusions control shallow magma transport in the Ferrar large igneous province, Antarctica. *Geol Soc Am Bull* 124:162–180
- Myers JS (1975) Cauldron subsidence and fluidization: mechanisms of intrusion of the Coastal Batholith of Peru into its own volcanic ejecta. *Geol Soc Am Bull* 86:1209–1220
- Nicholson R, Pollard D (1985) Dilation and linkage of echelon cracks. *J Struct Geol* 7:583–590
- Olson JE (2003) Sublinear scaling of fracture aperture versus length: An exception or the rule? *J Geophys Res* 108:2413. doi:[10.1029/2001JB000419](https://doi.org/10.1029/2001JB000419), B9

- Paterson SR, Fowler TK Jr, Miller RB (1996) Pluton emplacement in arcs: a crustal-scale exchange process. *Trans R Soc Edinburgh: Earth Sci* 87:115–123
- Perkins TK, Kern LR (1961) Widths of hydraulic fractures. *J Petrol Technol* 13:937–950
- Petford N, Cruden AR, McCaffrey KJW, Vigneresse J-L (2000) Dynamics of granitic magma formation, transport and emplacement in the Earth's crust. *Nature* 408:669–673
- Planke et al. this volume
- Pollard DD, Johnson AM (1973) Mechanisms of some laccolithic intrusions in the Henry Mountains, Utah, Part II: bending and failure of overburden and sill formation. *Tectonophysics* 18:311–354
- Polteau S, Mazzini A, Galland O, Planke S, Malthe-Sørenssen A (2008) Saucer-shaped intrusions: Occurrences, emplacement and implications. *Earth Planet Sci Lett* 266:195–204. doi:10.1016/j.epsl.2007.11.015
- Price NJ, Cosgrove JW (1990) Analysis of geological structures. Cambridge University Press, Cambridge, p 507
- Puffer JH, Block KA, Steiner JC (2009) Transmission of flood basalts through a shallow crustal sill and the correlation of sill layers with extrusive flows: the Palisades intrusive system and the basalts of the Newark basin, New Jersey, U.S.A. *J Geol* 117:139–155
- Putlitz B, Baumgartner LP, Oberhaensli R, Diamond L, Altenberger U (2001) The Torres del Paine Laccolith (Chile); intrusion and metamorphism. In: XI Goldschmidt Conference, Abstract No. 3534. Hot Springs, United States
- Quick JE, Sinigoi S, Mayer A (1994) Emplacement dynamics of a large mafic intrusion in the lower crust, Ivrea-Verbano Zone, northern Italy. *J Geophys Res* 99:21559–21573
- Rivalta E, Taisne B, Bungler AP, Katz RF (2015) A review of mechanical models of dike propagation: Schools of thought, results and future directions. *Tectonophysics* 638:1–42
- Rocchi S, Westerman DS, Dini A, Innocenti F, Tonarini S (2002) Two-stage growth of laccoliths at Elba Island, Italy. *Geology* 30:983–986
- Rocchi S, Westerman DS, Dini A, Farina F (2010) Intrusive sheets and sheeted intrusions at Elba Island (Italy). *Geosphere* 6:225–236
- Robertson WA, Baragar WRA (1972) The petrology and paleomagnetism of the Coronation Sills. *Can J Earth Sci* 9:123–140
- Roman-Berdiel T, Gapais D, Brun JP (1995) Analogue models of laccolith formation. *J Struct Geol* 17:1337–1346
- de Saint Blanquat M, Law RD, Bouchez J-L, Morgan SS (2001) Internal structure and emplacement of the Papoose Flat pluton: an integrated structural, petrographic, and magnetic susceptibility study. *Geol Soc Am Bull* 113:976–995
- de Saint Blanquat M, Habert G, Horsman E, Morgan S, Tikoff B, Launeau P, Gleizes G (2006) Mechanisms and duration of non-tectonically assisted magma emplacement in the upper crust: The Black Mesa pluton, Henry Mountains, Utah. *Tectonophysics* 428:1–31
- de Saint Blanquat M, Horsman E, Habert G, Morgan S, Vanderhaeghe O, Law R, Tikoff B (2011) Multiscale magmatic cyclicality, duration of pluton construction, and the paradoxical relationship between tectonism and plutonism in continental arcs. *Tectonophysics* 500:20–33
- Saumur BM, Cruden AR (2016) On the emplacement of the Voisey's Bay intrusion (Labrador, Canada). *Geol Soc Am Bull* 128:147–168
- Savitski AA, Detournay E (2002) Propagation of a penny-shaped fluid-driven fracture in an impermeable rock: asymptotic solutions. *Int J Solids Struct* 39:6311–6337
- Scaillet B, Searle MP (2006) Mechanisms and timescales of felsic magma segregation, ascent and emplacement in the Himalaya. *Geol Soc London Spec Publ* 268:293–308
- Schaltegger U, Brack P, Ovtcharova M, Peytcheva I, Schoene B, Stracke A, Marocchi M, Bargossi GM (2009) Zircon and titanite recording 1.5 million years of magma accretion, crystallization and initial cooling in a composite pluton (southern Adamello batholith, northern Italy). *Earth Planet Sci Lett* 286:208–218
- Schultz RA, Soliva R, Fossen H, Okubo CH (2008a) Dependence of displacement-length scaling relations for fractures and deformation bands on the volumetric changes across them. *J Struct Geol* 30:1405–1411
- Schultz RA, Mege D, Diot H (2008b) Emplacement conditions of igneous dikes in Ethiopian Traps. *J Volcanol Geotherm Res* 178:683–692
- Schofield NJ, Brown DJ, Magee C, Stevenson CT (2012) Sill morphology and comparison of brittle and non-brittle emplacement mechanisms. *J Geol Soc London* 169:127–141
- Shirley DN (1987) Differentiation and compaction in the Palisades Sill, New Jersey. *J Petrol* 28:835–865
- Skarmeta JJ, Castelli JC (1997) Intrusion sintectónica del granito de las Torres del Paine, Andes Patagónicos de Chile. *Rev Geol Chile* 24:55–74
- Smith RJ (2009) Use and misuse of the reduced major axis for line-fitting. *Am J Phys Anthropol* 140:476–486
- Sneddon IN, Lowengrub M (1969) Crack problems in the classical theory of elasticity. Wiley, New York, p 230
- Thomson K (2007) Determining magma flow in sills, dykes and laccoliths and their implications for sill emplacement mechanisms. *Bull Volc* 70:183–201
- Thomson K, Hutton D (2004) Geometry and growth of sill complexes: insights using 3D seismic from the North Rockall Trough. *Bull Volc* 66:364–375
- Thomson K, Schofield N (2008) Lithological and structural controls on the emplacement and morphology of sills in sedimentary basins. *Geol Soc London Spec Publ* 302:31–44
- Vigneresse JL (1995) Control of granite emplacement by regional deformation. *Tectonophysics* 249:173–186

- Walker GPL (1993) Re-evaluation of inclined intrusive sheets and dykes in the Cuillins volcano, Isle of Skye. *Geol Soc London Spec Publ* 76:489–497
- Walker KR (1969) The Palisades sill, New Jersey: a reinvestigation. *Geological Society of America Special Paper* 111, 155 p
- Walker RJ (2016) Controls on transgressive sill growth. *Geology* 44:99–102
- White SM, Crisp JA, Spera FJ (2006) Long-term volumetric eruption rates and magma budgets. *Geochem Geophys Geosyst* 7:Q03010. doi:[10.1029/2005GC001002](https://doi.org/10.1029/2005GC001002)
- Westerman et al. this volume
- Wiebe RA, Collins WJ (1998) Depositional features and stratigraphic sections in granitic plutons: Implications for the emplacement and crystallization of granitic magma. *J Struct Geol* 20:1273–1289
- Wilson PIR, McCaffrey KJW, Wilson R, Jarvis I, Holdsworth RE (2016) Deformation structures associated with the Trachyte Mesa intrusion, Henry Mountains, Utah: implications for sill and laccolith emplacement mechanisms. *J Struct Geol* 87:30–46
- Zenzri H, Kerr LM (2001) Mechanical analyses of the emplacement of laccoliths and lopoliths. *J Geophys Res* 106:13781–13792

Plumbing Systems of Shallow Level Intrusive Complexes

Dougal A. Jerram and Scott E. Bryan

Abstract

We have come a long way from simple straw and balloon models of magma plumbing systems to a more detailed picture of shallow level intrusive complexes. In this chapter, the sub-volcanic plumbing system is considered in terms of how we can define the types and styles of magma networks from the deep to the shallow subsurface. We look at the plumbing system from large igneous provinces, through rifted systems to polygenetic volcanoes, with a view to characterising some of the key conceptual models. There is a focus on how ancient magmatic centres can help us better understand magmatic plumbing. New innovative ways to consider and quantify magma plumbing are also highlighted including 3D seismic, and using the crystal cargo to help fingerprint key magma plumbing events. Conclusions are drawn to our understanding of the 3D plumbing system and how these recent advances can be helpful when exploring the other chapters of this contribution.

1 Introduction

Traditionally, shallow magma systems have been conceived as relatively simple, direct pathways allowing magma to rise from a holding chamber to the surface (cf. magma conduit). The plumbing system at this shallow level (<5 km) is often simply depicted as a vertical cylindrical conduit leading from a simple magma chamber where magma passes through (the straw and balloon model; Fig. 1) but does not really reside or stagnate (except as indicated by solidified plugs, volcanic necks etc). Deeper plumbing systems that feed the shallow level chambers, are

D.A. Jerram (✉)
Centre for Earth Evolution and Dynamics (CEED),
University of Oslo, Oslo, Norway
e-mail: dougal@dougalearth.com

D.A. Jerram
DougalEARTH Ltd., Solihull, UK

D.A. Jerram · S.E. Bryan
School of Earth, Environmental and Biological
Sciences, Queensland University of Technology,
GPO Box 2434, Brisbane, QLD 4001, Australia
e-mail: scott.bryan@qut.edu.au

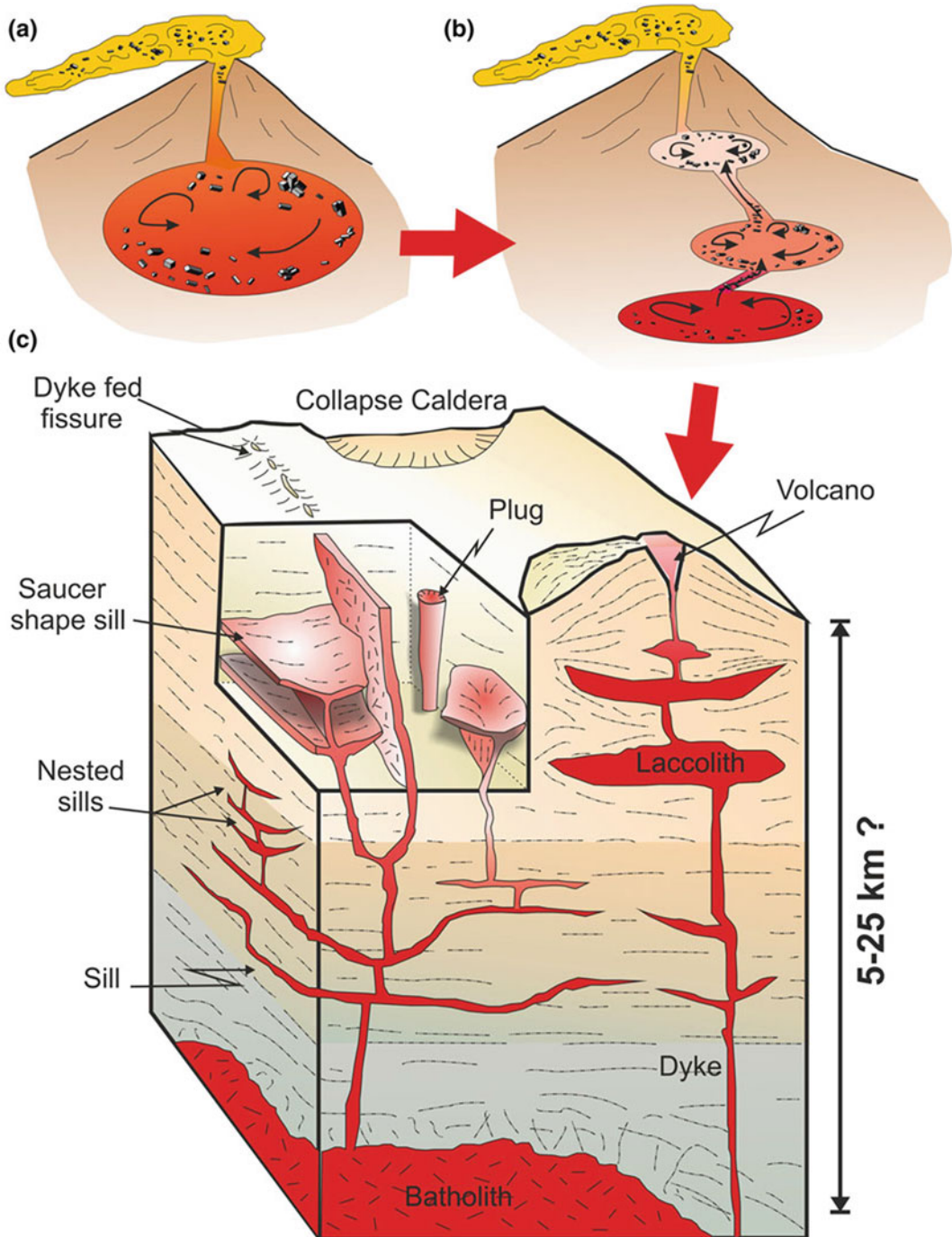


Fig. 1 Conceptual evolution of our understanding of the complexities of the subvolcanic plumbing system. **a** The classic 'Balloon and Straw' model, with a balloon-like magma chamber feeding a volcano; **b** realisation of

multiple magma storage zones and a complex plumbing system; **c** 3D distribution network of magma plumbing from deep to shallow levels in the crust feeding a variety of volcanoes

somewhat more enigmatic, with often little physical linkage made from the sources of melting, to the volcanic system near the surface, and particularly confused for granitic magma ascent that was viewed early on as slow-rising, hot Stokes diapirs from their source (see Petford 1996). Recent studies (some of which will be touched on here) have illustrated the variability in dimensions and geometry of shallow systems and the possible way in which they are linked at depth. Fissures are increasingly recognised as important pathways and vents for many mafic and even silicic eruptions. Magma may pond at shallow depths (<1–5 km) before eruption in sill complexes of variable size and complexity, or as more circular central complexes. Sill intrusion can be observed to be at shallow depths within the volcanic sequences themselves and the disaggregation and direction of flow of the magma plumbing system is strongly affected by the nature of lithologies the magma passes through e.g., syn-sedimentary (stratified and sometimes poorly lithified) versus old metamorphosed or igneous basement hosts. Volcanic centres can appear, when exposed at the surface or imaged in gravity data, as relatively discrete sub-circular bodies, or as a more complex amalgam of multiple centres with linked feeding systems, replenished and reused several times in their evolution. Once melt has been segregated and extracted from source rocks, many processes can then operate within the plumbing network, the magma chamber(s) and on eruption at the surface that combine to define the final chemistry, crystallinity, eruptive style and even aerosol injections into the atmosphere.

In this short overview, the sub-volcanic plumbing system is considered in terms of how we can define the types and styles of magma networks from the deep to the shallow, their common settings, innovative ways in which we can image and capture the complexities of magma systems, and new techniques using volcanic eruptive products as a proxy for recording information from depth. The closing remarks point to our current knowledge, and a way forward to better understand shallow level intrusions. The aim here is not to provide an

exhaustive review, but to touch on some of the key points that will be emphasised by the other studies within this book.

2 What is the Magma Plumbing System?

How we define the shallow-level magma system and how it relates to the overall journey that magma makes from deep within the lithosphere, or even the asthenosphere, to the sub-volcanic domain, is a non-trivial task. One person's shallow magma chamber is another person's deep magma storage zone, and the scales and depths involved can range from a few meter thick dykes to km³ sized magma batches, and from a few 100s of meters to a few to several 10s of km, respectively. We have advanced significantly from the classic text book views of simple balloon and stick-type magma chambers depicted in the introduction (e.g., Fig. 1a) to a realisation of much more complexity in the subvolcanic system linking several subvolcanic chambers (Fig. 1b), and finally to a conceptual 3D model linking the sub-surface system to volcanoes at the surface (Fig. 1c) (e.g., Jerram and Davidson 2007; Jerram and Martin 2008; Thomson and Schofield 2008; Cashman and Sparks 2013). This progression of understanding has resulted from numerous research programs and published bodies of work, but how do we build a detailed picture of the types and variation that we may find in the subvolcanic system?

Generally speaking, the way in which magma can journey through the crust is through dykes, sills and variably shaped magma chambers, the latter being also areas where magma may reside for some time. Dykes mainly represent the vertical transport component of the system with typical widths of meters to a few 10s of meters with commonly observed continuous strike extents of 100s of meters to 10s of km's; discontinuous dyke swarms can laterally extend for >1000 km on Earth (e.g., 1270 Ma Mackenzie dyke swarm; LeCheminant and Heaman 1989; Ernst and Baragar 1992). All magma

compositions can form dykes, but by far the most common and volumetrically significant dykes are basaltic in composition. Dykes are observed to form over a wide range of depths from deep crustal examples such as the Scourie Dykes (at mid to lower crust e.g., O'Hara 1961; Tarney 1973), through sedimentary basins (e.g., NAIP dyke swarms, Macdonald et al. 2010) to very shallow systems feeding lavas (e.g., fissure fed lava systems, as evidenced by chains of scoria cones; e.g., Iceland, Thordarson and Self 1993).

Sills provide potential storage zones of some significant magma volumes particularly when found in nested sill complexes (e.g., Marsh 2004) or in large igneous provinces (e.g., Bryan et al. 2010 and references therein). Sill thicknesses vary in a similar manner to dykes, but tend to have a larger average thickness, 10s of meters is common with sills over 100 m in thickness commonly found in continental flood basalt provinces (e.g., Penepplain Sill, Jerram et al. 2010). This thickness requires inflation and accommodation space, and often the overburden can be faulted and folded (White et al. 2009). The potential for contemporaneous eruption and sill intrusion may be particularly important to help feed large lava sequences in flood basalts.

In both sills and dykes, evidence for lateral flow as well as vertical (upwards flow) in the system can be observed. Magma can flow significant distances laterally in sub-volcanic plumbing systems (>1000 km) such as the Mackenzie dyke swarm (e.g., Ernst and Baragar 1992), and the Dry Valleys sill complex, Antarctica (e.g., the Penepplain sill and Basement sill; e.g., Marsh 2004) both showing major along strike extent, and significant lateral injection and flow. Magmatic centres represent sites where a magma pathway persists for a relatively long period of time (100,000 years to millions of years), which also include the potential for contemporaneous tapping and eruption of spatially separate chambers within the same complex (e.g., Brown et al. 1998; Smith et al. 2005; Martin et al. 2010).

In terms of tectonic setting, we can broadly consider three major magma generating systems:

those at rifted settings (e.g., continental rifts, mid-ocean ridges), those at subduction zones, and those associated with plumes/hot spots, which can occur through both oceanic and continental crust. While tectonic stresses can have important controls on magma pathways at regional scales, it has also been recognised that at the volcano-scale, magma chamber stresses and volcanic evolution that can generate load stresses or new magma pathways to the surface through collapse are also important. It is not so clear then that considering magma plumbing at these separate tectonic settings truly reflect the systems in detail, as often similar volcanic systems can develop irrespective of tectonic setting. It may also be possible to consider the magmatic plumbing system in terms of long-lived versus short lived systems, or by dominant magma composition types. Again, problems arise here in the fact that is difficult to define what maybe meant by short vs long lived, particularly in pulsed systems. Although one magma type might dominate, a compositional diversity can exist with different magma types utilising the plumbing system either during one eruption or over time, blurring such a definition.

To help simplify the approach of considering magma plumbing systems, in this contribution we will consider the magma plumbing in terms of three types of scenarios (which are partly determined by scale, tectonic setting and by time/longevity) which are not mutually exclusive: Large Igneous provinces, predominantly rifted settings, and polygenetic volcanoes where magma plumbing systems can persist for long periods. Within this broad sub-division, a number of the key features of the magma systems are introduced, and we look at how these are manifest in terms of the volcano plumbing that can be observed at the surface, or inferred through innovative ways of imaging or remotely sampling the magma plumbing. More specific case studies and examples showing the plumbing styles from a number of settings will appear throughout the rest of the contributions in this series, and will hopefully build on what we introduce here.

3 Large Igneous Provinces

Here we briefly consider the intrusive component associated with continental flood basalt provinces (CFBPs), as an example of large igneous provinces (LIPs). LIPs are sites of the most frequently recurring, largest volume basaltic and silicic eruptions in Earth history (e.g., Bryan et al. 2010 and references therein), and as such, require the flux of huge amounts of magma from the upper mantle and deep to shallow crust, through multiple pathways to the surface. How is that recorded in the geological record and what can it tell us about what is beneath modern volcanoes?

There are many locations where CFBPs are preserved on the planet at differing degrees of erosion which partly exposes the plumbing system, and from which we can gain insight into the nature and evolution of the system (e.g., Jerram and Widdowson 2005). Examples such as the Siberian Traps, Paranã-Etendeka province, North Atlantic igneous province, Antarctic Ferrar-South African Karoo provinces, Columbia River and Deccan

Traps, are some of the more well-known and studied examples. Due to differing levels of erosion and combined with geochemical variations that occur, we are able to construct a general idea of the regional plumbing systems for CFBPs. These systems are vast and in practice, any investigation of them starts to identify almost all possible types of intrusion, from complex forms in volcanic centres, plugs, laccoliths/lopoliths, through dyke swarms, to nested sill complexes (e.g., Ernst and Baragar 1992; Marsh 2004; Jerram and Widdowson 2005; Macdonald et al. 2010; amongst many examples). By looking at the resultant ways in which mantle-derived melts make it from depth to surface, it is possible to produce a schematic picture of the styles of magma plumbing. Bryan et al. (2010), considered the largest known eruptions that have occurred on Earth, and constructed a simplified end-member diagram to highlight the relative journey that magmas of all volumes can have from the mantle to the surface (Fig. 2). The general plumbing under CFBPs is normally characterised by that depicted in Fig. 2a, b. Here, sometimes magma plumbing

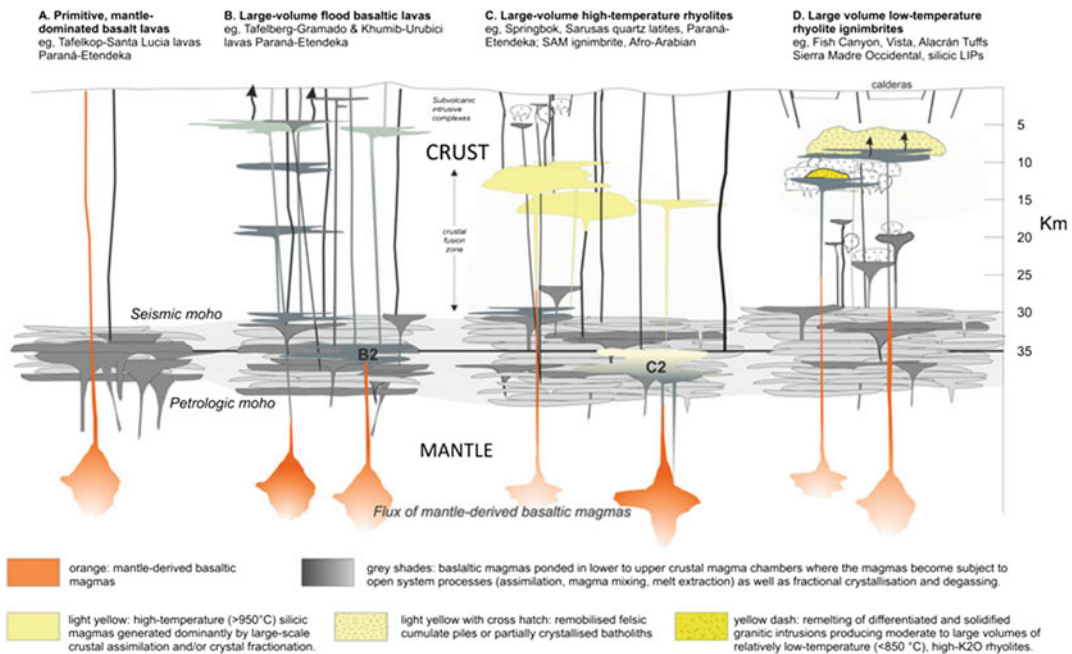


Fig. 2 Types of plumbing and magma pathways present at Large Igneous Provinces (modified from Bryan et al 2010). The figure text highlights the main styles of pathway from simple eruption of primitive melt at the

surface to more complex batches of magma with varying degrees of complexity in terms of composition, volumes, and crystal loads

can be simple and deep, leading to very primitive ‘mantle-like’ melts making it to the surface (Fig. 2a). More commonly, magma stalls in chambers and intrusive complexes that occur in the middle to upper crust, producing sill complexes (Fig. 2b). These complexes can be vast and very complex internally (see below). New constraints on eruption rates, particularly for the largest eruptions known, require 10^3 – 10^4 km³ of magma available for eruption over decadal (flood basalts) or days to weeks (flood rhyolite) timescales, and thus the existence of substantial magma reservoirs most likely residing within the upper crust, but also a highly efficient transport network allowing magma to readily evacuate from holding chamber (s). This includes the existence of large volume sills as un-erupted examples (see Bryan et al. 2010).

4 Predominantly Rifted Settings

In areas where the Earth’s crust is spreading apart, both the generation of melt through decompression as well as the accommodation space for the resultant magma are found in close proximity. One of the most common magma generating systems to consider is that which occurs at mid-ocean ridges. These are very important given their distribution around the globe and that they are responsible for creating the constant conveyor belt of present-day oceanic crust and where ophiolite complexes preserve examples of this process throughout Earth’s history. It can also be shown that the latter stages of continental break-up require a transition from continental to oceanic rifting. Recent work on Iceland and in the Afar desert has looked at the shallow plumbing system as measured using shallow geophysics (e.g., Wright et al. 2012a, b). Fig. (3a, b) highlights the generalised model of dynamic spreading at the Dabbahu rift in Ethiopia, along with a picture showing the manifestation of part of this rifting at the Earth’s surface, the Dabbahu Fissure (Fig. 3c, d, e). The stresses that build up along the rift are released during rifting episodes, when bursts of magmatic activity lead to the injection of vertical

sheets of magma (dykes) into the crust. The magma is supplied to the crust periodically, and is stored at multiple positions and depths. It then laterally intrudes in dykes within the brittle upper crust during the rifting episodes (Wright et al. 2012a, b). This represents the current picture at thinned crust at the stages of continent separation. The dyke swarms that can be found through continental crust in ancient flood basalt settings likely represent the onset of this rifting phase (e.g., Macdonald et al. 2010 and references therein). These rift systems and large fissure type eruptions are present in many of the larger flood basalt settings as discussed above, and in some cases the fissure systems can be linked directly to flood basalt flows such as the Roza flow in the Columbia River (e.g., Thordarson and Self 1998). Where oceanic rifting is concomitant with a plume setting such as in the Iceland example, complex fissure, rift and shallow magma chamber systems develop, as recently imaged during the 2010 Eyjafjallajökull eruption (Sigmundsson et al. 2010).

5 Plumbing at Polygenetic Volcanoes—Persistent Magma Pathways

Some of the more complex plumbing systems we encounter are those where persistent magma pathways exist, which can occur in a variety of different settings. Polygenetic volcanoes, principally lava shields, stratovolcanoes and calderas, characterise many present-day tectonic settings such as subduction zones (both extending and non-extending), continental rifts and ‘hotspots’ (both continental and oceanic). Despite this variability in tectonic and crustal setting, the construction of polygenetic volcanoes reflect not only persistent magma supply but also the ‘centralised’ venting of magma over time scales of 10^3 – 10^7 years. Lava shield volcanoes typically reflect the frequent venting of mafic magmas only, whereas at stratovolcanoes and calderas, a much broader compositional range of magmas are supplied and vented. A fundamental implication then is that a

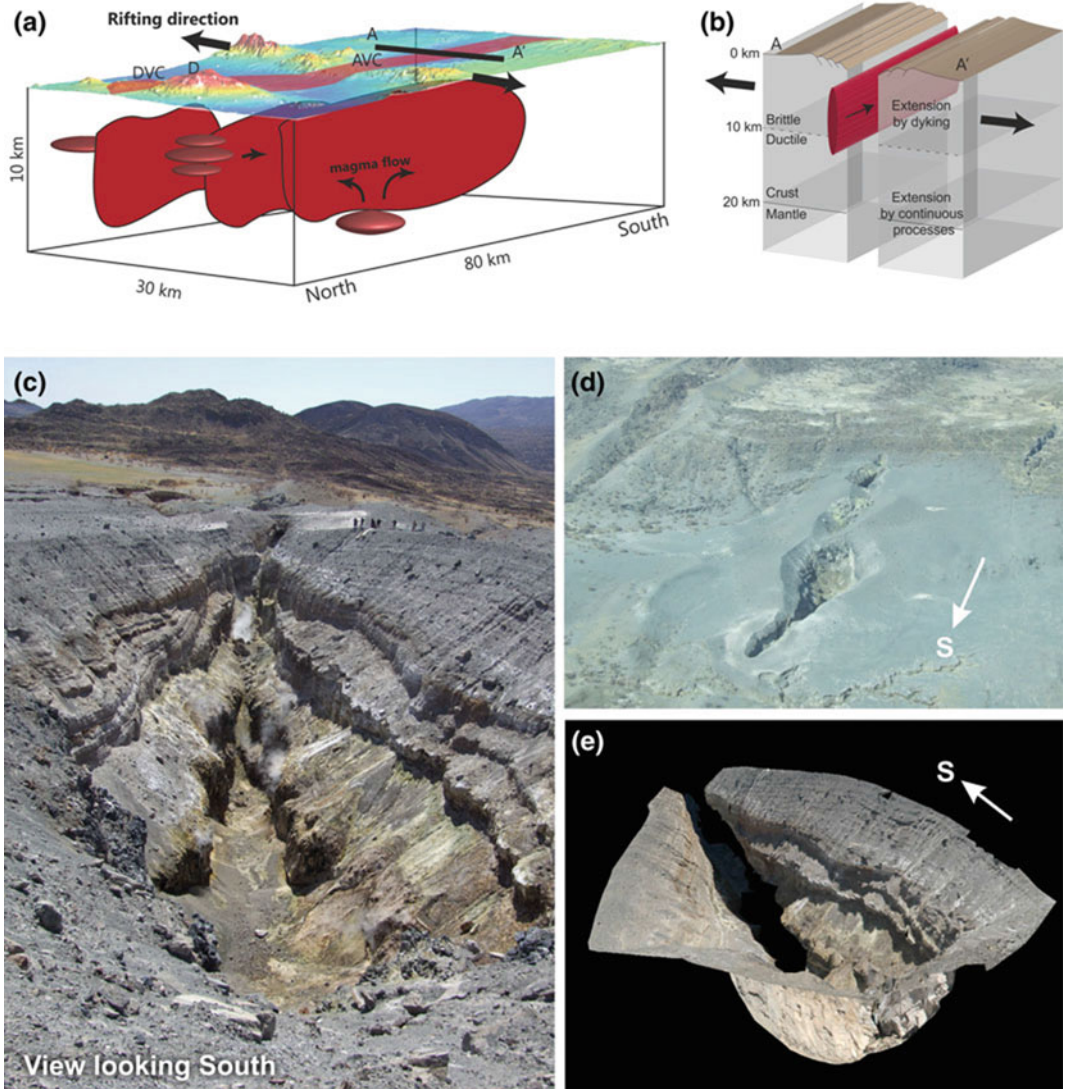


Fig. 3 Magma plumbing in predominantly rifted settings, example from the Afar rift, Ethiopia. **a** schematic model of magma plumbing at Dabahu rift showing schematic locations of magma chambers (*red ellipsoids*). Also labelled are Dabbahu (D), Dabbahu Volcanic Centre (DVC), Ado ‘Ale Volcanic Centre (AVC), and location of cross section in **b**. Coloured map shows topography

and also the zone of fissuring and faulting (highlighted in *light red* on map surface); **b** generalised cross-section of a typical slice of crust away from a magmatic centre (**a** and **b** courtesy of T. Wright, see also Wright et al. 2012a, b for details); **c** view of Dadahu fissure; **d** Dadahu fissure from the air; **e** 3D surface map of Dabahu fissure from laser scanning (from Jerram and Smith 2010)

plumbing system, once established from the magma source regions, remains in existence and can essentially be re-used by new magma batches that may be separated by as much as 100,000s years and have no connection to the previous magmatic batch or episode. This is evident for

example from the growth history of the andesitic Ngauruhoe cone (New Zealand), which reflects an open magma and plumbing system that supplies small (<0.1 km³) and short-lived (100–10³ years) magma batches but which have no simple time–composition relationships between

successive batches even when separated by only a few tens of years (Hobden et al. 2002). Another fundamental implication is that it increases the possibility and likelihood of cannibalisation of previous magmatic material transported and stored along that plumbing system as succeeding magma batches attempt to successfully arrive at the surface for eruption. Consequently, magmas erupted from stratovolcanoes and calderas are likely to exhibit “contamination” effects arising simply from prior use of the magma plumbing system. This has been widely recognised in many recent studies of andesites and their crystal cargoes from arc settings (e.g., Dungan and Davidson 2004; Streck et al. 2007; Reubi and Blundy 2009; Kent et al. 2010; Zellmer et al. 2003, 2014). For caldera systems, “contamination” can also be generated by the involvement of spatially separate but contemporaneous magma bodies that are tapped during catastrophic caldera collapse and/or by tectonic faults that become active during eruption (e.g., Brown et al. 1998; Gravelly et al. 2007).

Current views then of sub-volcanic magmatic systems is that magma storage can occur at multiple levels in the crust. As principally driven by studies on the origin of crystal-rich magmas, the main magma reservoir may be best represented as a crystal mush zone that can quickly be replenished and rejuvenated through new (mafic) magma injections (e.g., Bachmann and Bergantz 2003, 2004, 2008a, b; Glazner et al. 2004; Bachmann et al. 2007) (see example in Fig. 4a). This is analogous to the view of magmatic systems as “mush columns” (e.g., Marsh 1996, see Fig. 4b) where:

1. a sufficient magnitude and frequency of magma supply exists to sustain supersolidus and permissive zones for magma transport upwards;
2. the local mush state of the plumbing system is important as a source of crystal cargo for new magmas;
3. the tectonic immobility of the magmatic centre allows a sustained supply of magma to promote development of an intrusive, partly mushy underpinning that can be reprocessed through reheating by later magmas; and
4. the magmatic ‘strength’ of the system affects petrologic and chemical variability of erupted magmas.

The timescales involved in the storage of crystal mushes and their remobilisation are quite variable and somewhat difficult to constrain. In many crystal-rich systems the magma chamber or storage zones in the ‘mush column’ can reside in the crust for long times (e.g., Gelman et al. 2013; Cooper and Kent 2014). This suggests that the timescales of magma storage can be large, up to hundreds of thousands of years. Yet for the eruption of volcanoes responding to new magma influx in the system, it can be shown to happen quite quickly. Indeed, short residence times have been calculated for some crystal-poor, caldera-forming eruptions (e.g., Santorini) where the erupting magma may only reside for a few thousand years before a caldera forming eruption (e.g., Fabbro et al. 2013). With a complex magmatic plumbing system we can expect elements of the system to have a long-lived nature in terms of some crystal mushes and residence times, with events (particularly eruptive cycles, and largely crystal-free magmas) being short-lived (e.g., Cooper and Kent 2014). The eruptive, short-lived parts of the cycle may be triggered relatively quickly, i.e. rapid responses to new magma batch injections, but there may also be only a limited window in which to get magma through the system to erupt before it becomes locked up in the mush zone of the plumbing system (e.g., Barboni and Schoene 2014).

Shallow level pathways can also develop as a result of magma chamber/volcano growth and evolution. The stresses around magma chambers will change with magma flux, and can act as a vehicle to focus magma-feeding dykes, known as ‘magmatic lensing’ (e.g., Karlstrom et al. 2009). Key controls on the pathway that magmas take from their holding chambers to reach the surface are any superimposed regional-scale tectonic stresses, and more localised stresses generated by the subvolcanic magma chamber (e.g., Bistacchi et al. 2012) and/or gravitational loading by the edifice (e.g., Muller et al. 2001). Recent numerical

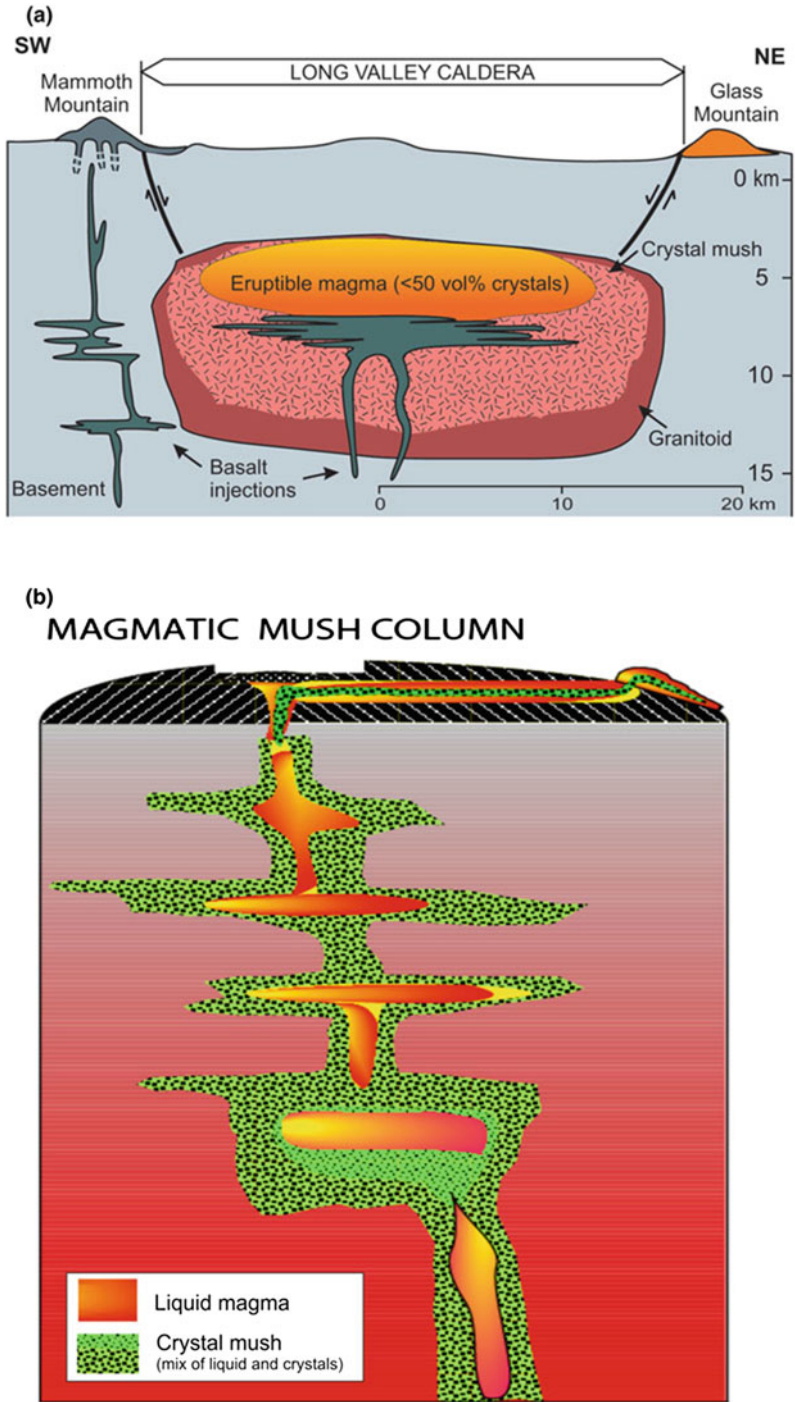


Fig. 4 Examples of magma plumbing in polygenetic systems; **a** schematic plumbing beneath Long Valley Caldera, USA (after Bachmann and Bergantz 2008a, b). In systems like Long Valley, large pools of silicic magma are produced by extracting interstitial liquid from long-lived “crystal mushes” (magmatic sponges containing >50 vol% of crystals) and collecting it in unstable,

eruptible liquid-dominated lenses. **b** The magma mush column (after Marsh 2004), where liquid rich lenses and linked plumbing bodies are intricately associated with crystal mushes around the walls and in the chambers within the column. Shallow sills and eruptions from such systems can contain a variety of crystal cargos from crystal-poor to crystal-rich batches (see also Fig. 7)

modelling-based studies indicate the shape of the magma chamber can significantly affect the stress field distribution around the chamber and thus the resulting geometry of the magma plumbing system (Martí and Geyer 2009).

Surrounding polygenetic volcanic centres are three main types of intrusion geometries that are related to shallow magma chambers: (i) radial subvertical intrusions, (ii) vertical to outward-dipping, concentric intrusions or ring dykes, and (iii) inward-dipping concentric swarms (inclined or cone sheets). Magma chamber inflation has been shown experimentally to generate radial fractures that can act as magma pathways and produce radial dyke systems (e.g., Martí et al. 1994), and cone sheets can also develop above the inflating magma system (Bistacchi et al. 2012). Ring dykes, characteristic of many calderas and cauldrons, have classically been interpreted to have formed during piston-like roof subsidence (e.g., the classic study of Smith and Bailey 1968). Recent work has interpreted some classic ring dykes as inflated sheets (e.g., Stevenson et al. 2008) sparking debate about the origin of some of the classic ring-like features surrounding polygenetic volcanic centres (Emeleus et al. 2012). Given these ring fractures are now filled by igneous rock, they must have acted as major magma pathways in initial inflation, and during and after caldera collapse.

Studies of many caldera-forming eruptions have demonstrated that vents, either central or fissure, initially existed within the ensuing area of collapse (e.g., Smith and Houghton 1995; Bryan et al. 2000), and that the eruptions evolved to having multiple vents located along the ring fault system or other collapse-controlling faults (e.g., Bacon 1983; Druitt and Sparks 1984; Hildreth and Mahood 1986; Suzuki-Kamata et al. 1993). The arcuate train of post-collapse rhyolite domes within the Valles Caldera are an example of continued utilisation of the collapse ring fault as these rhyolites were erupted over an ~ 1 Myr interval from immediately following caldera formation until ~ 200 ka (Spell and Harrison 1993). The very presence of calderas reflect the prior existence of a relatively large holding chamber at shallow depth (<10 km) of sufficient

magma vol (>5 km³) which, after eruption, allowed roof failure and collapse.

6 Exposed Shallow Volcanic Centres and Complexes

In many instances, sub-volcanic centres and complexes are exposed due to exhumation. These provide a wonderful opportunity to explore the relationships within the intrusive system and in some cases, how they link to surface volcanism. The classic centres from the British and Irish Paleogene province (known by many as the British Tertiary Igneous Province) in Scotland and Ireland, are one such case where the rocks provide a window into ‘fossil’ volcanoes (e.g., Emeleus and Bell 2005; Jerram et al. 2009a). Two classic centres, Rum and Skye, provide excellent insights into magma dynamics and evolution, as well as the form and complexities of volcanic centres that once fed volcanoes at the surface. Figure 5 highlights some of the features preserved in the Rum intrusion, with a dynamic interpretation of the magma chamber at the time of formation (from Goodenough et al. 2008). Everything from pyroclastic rocks, igneous layering with repeated geochemical cycles, and jumbled up intrusive breccias that remobilise existing rigid as well as ductile layered sequences are testament to a dynamic and open magma chamber (see Emeleus and Troll 2009, and references therein). The Skye volcanic centre (Fig. 6) has a similar level of complexity and is interpreted to be a cone-shaped structure, which was repeatedly in-filled with new batches of magma, forming complex layering and compositional types from peridotites to granites. The intrusion is dissected in such a way that it is possible to view the side contact of the magma chamber (Fig. 6c), which helps to further constrain the lower parts of the chamber structure. Such exposures of the internal structure of these volcanic centres are thus vital to be able to picture how they act as plumbing systems to volcanoes. In more simple closed systems such as the Skaergaard intrusion (e.g., Nielsen 2004), the overall geometry of the preserved intrusion more closely

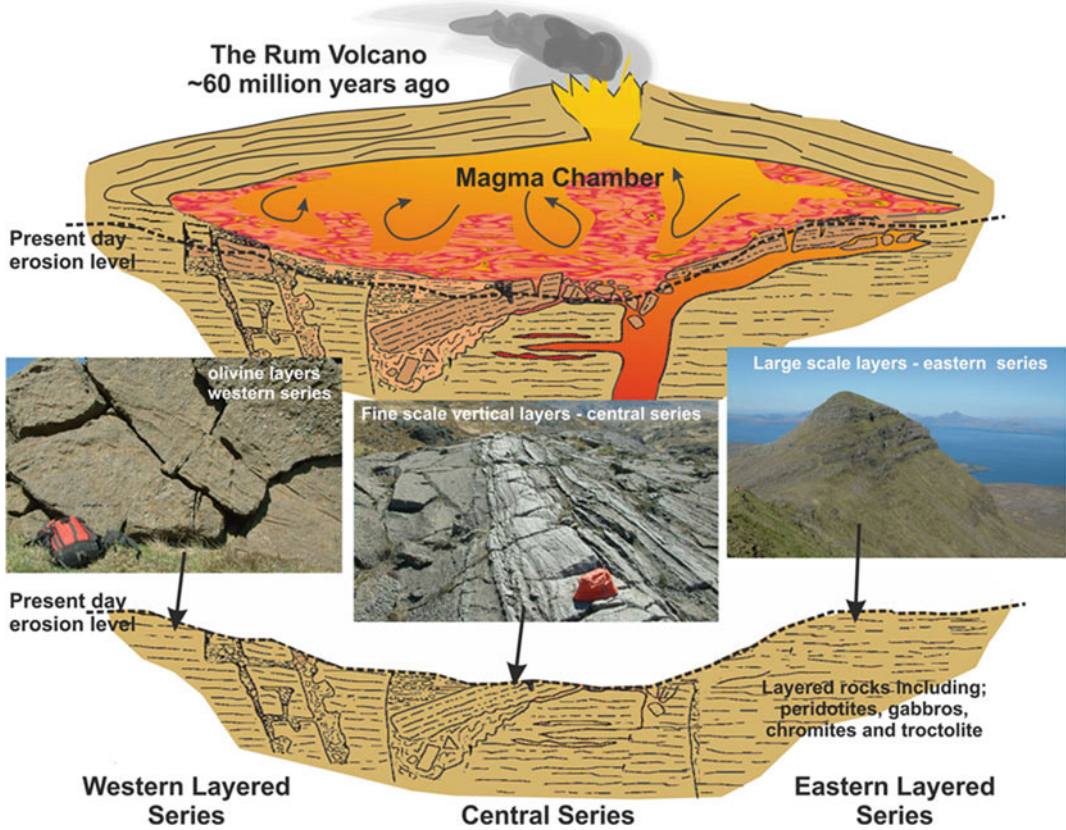


Fig. 5 Internal structures and reconstruction of the Rum volcanic centre (after Goodenough et al. 2008). Evidence for the open-system nature of the Rum Centre is preserved in the complex layering structures seen in the Western, Eastern and Central Layered Series. Repeated

injections of new magma have resulted in repetitive cycles of peridotites, gabbros and troctolites, as well as complex slumps, breccias and cross cutting relationships in the now exposed core of the magma chamber

represents that of the original body at depth, and may provide some idea of the extent of systems that do not make it to the surface to erupt. In these cases where the volcanic centres or shallow, closed magma chambers are very well-constrained, the feeding pathways to these ‘igneous centres’ are somewhat poorly constrained and in some cases hypothetical.

In other examples, extensive sill complexes exist such as those found offshore in the North Atlantic; (e.g., Hansen and Cartwright 2006; Schofield et al. 2012), the Karoo basin (see Svensen et al., this book), offshore West Africa (Rocchi et al. 2007) and Antarctica (Jerram et al. 2010). Many of the sills form classic saucer shapes (see Polteau et al. 2008), and these saucer shapes have

been used to help explain their emplacement with layered sedimentary and volcanic sequences (e.g., Gouly and Schofield 2008; Hansen et al. 2011), and many can be traced for several km’s laterally. These sill complexes are commonly interlinked and are sometimes nested directly one on top of another, with the magma feeding zone being used repeatedly. Although examples exist where the sills are intruded before the eruption of the lava flows, in most of the examples of flood basalt provinces, significant sill complexes develop after a thick ‘lid’ of lava material has developed. This can be evidenced by the cross cutting relationships and absolute dating of the emplacement events. In some instances saucer-shaped sill complexes can even be found intruding into the thick flood basalt

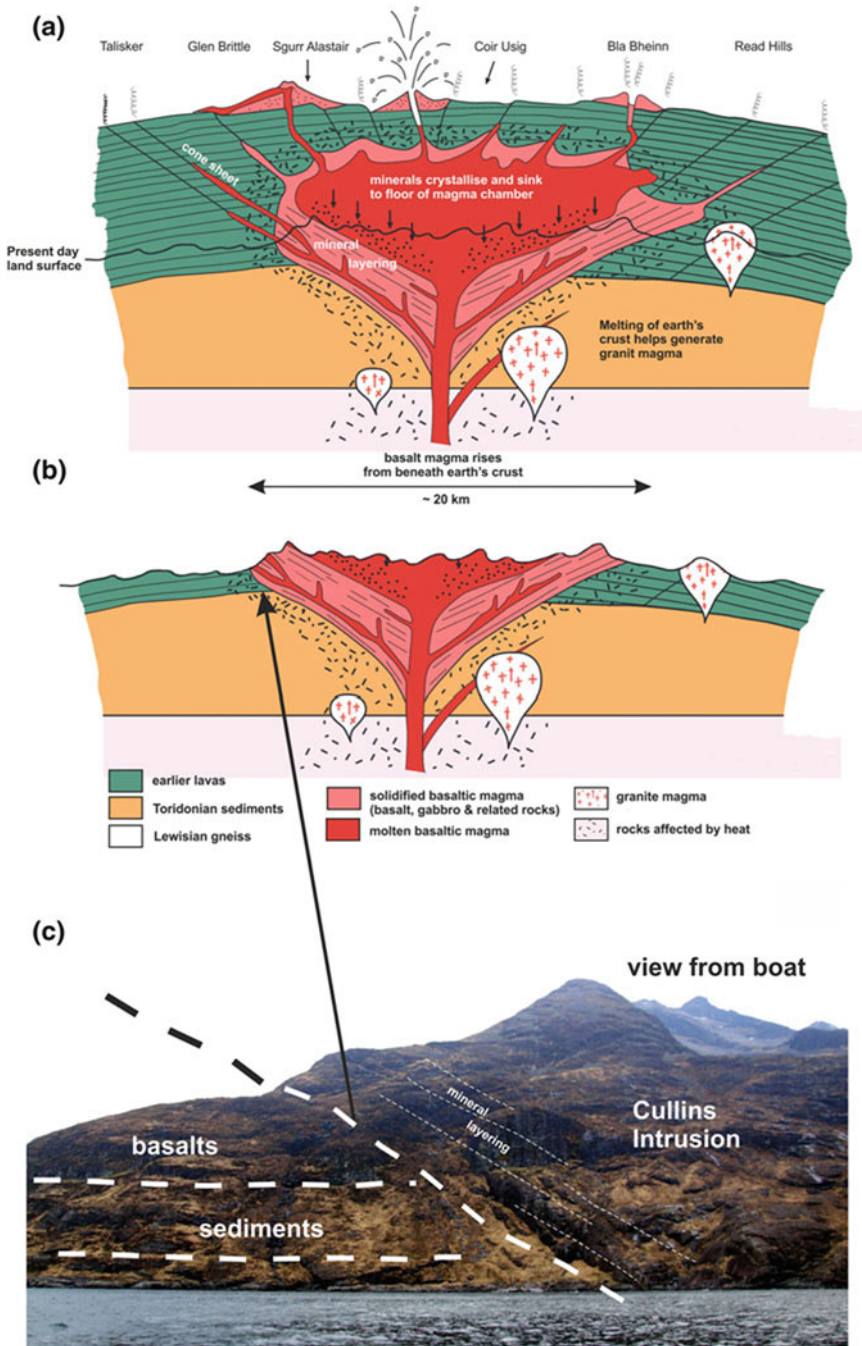


Fig. 6 Internal plumbing of the Skye volcanic centre; **a** artistic impression of the plumbing at the time of eruption, (Reproduced and based on Stephenson and Merritt 2006, with the permission of the British Geological

Survey © NERC. All rights reserved' and Scottish Natural Heritage © Scottish Natural Heritage 2006), **b** present-day erosion level removed, **c** edge of the volcanic edifice as seen from the boat trip into the Cullins for Elgol

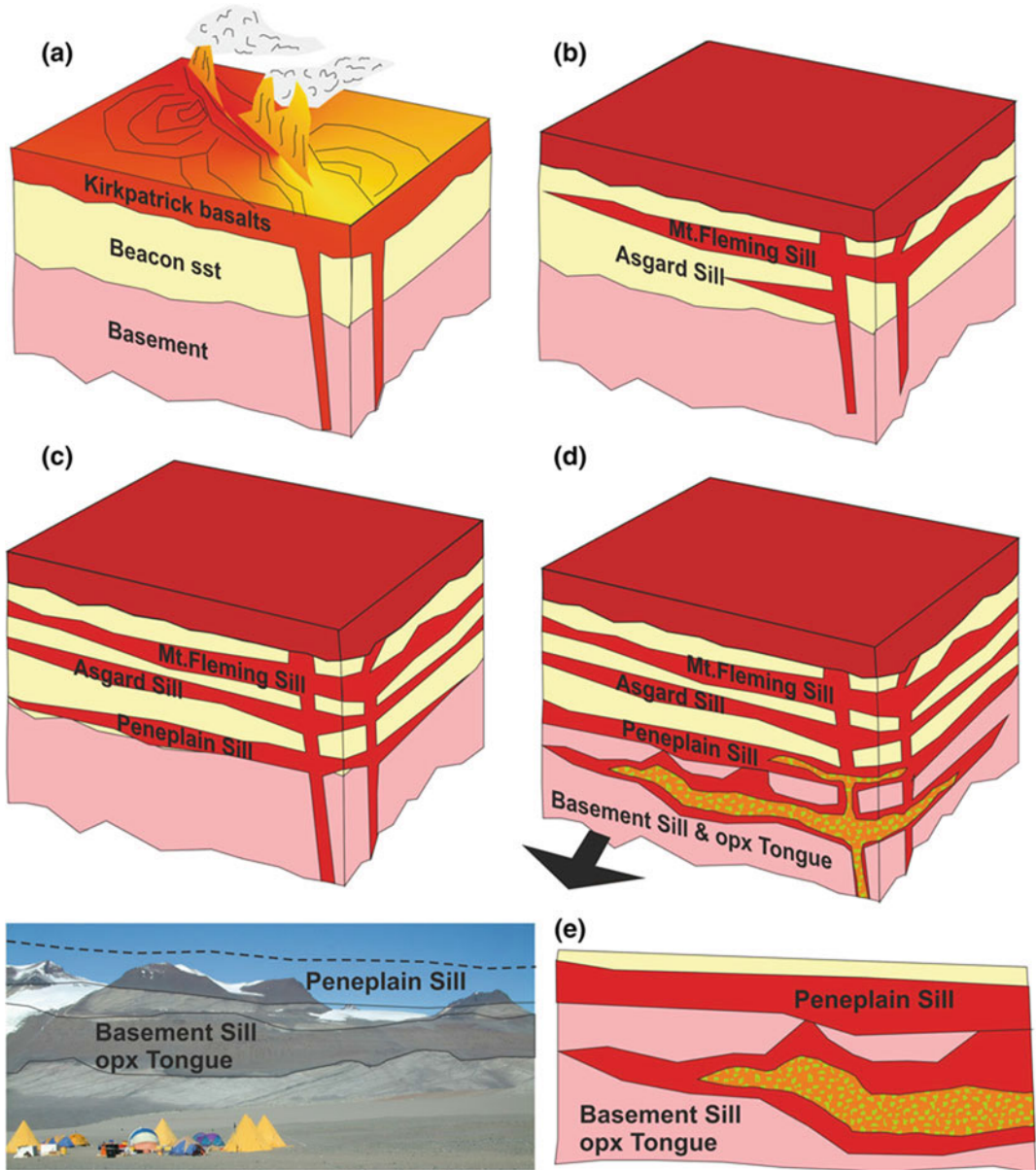


Fig. 7 Schematic representation of how the magma plumbing system developed in the Dry Valleys, Antarctica, ~ 180 Ma (after Jerram et al. 2005). **a** Onset of flood volcanism with the outpouring of the Kirkpatrick Basalts. **b** Initial sills start to form close to the sediment lava contact, first with the Fleming Sill then with the Asgard Sill. **c** The Penneplain Sill follows and intrudes along the Kukri Penneplain between the basement and the Beacon

Supergroup. **d** Finally, the Basement Sill is intruded into the basement granites with an irregular contact. During emplacement of the Basement sill, a magma laced with orthopyroxene (opx) crystals, from the magma mush column, invades the base of the plumbing system producing the opx tongue. **e** Present-day erosion levels expose the Basement Sill and Penneplain sill in the Wright Valley

lava sequences themselves (e.g., the Faroe Islands in the North Atlantic Igneous Province, Hansen et al. 2011).

The example given in Fig. 7 highlights the evolution of the nested sill complex from the Dry Valleys, Antarctica (see Jerram et al. 2010, and

references therein). Here, the sill complex was part of the plumbing system that fed flood basalts above, and resulted in a series of large-volume sill bodies that stepped down through the Karoo sedimentary sequence and into basement rocks (Fig. 7). Seismic imaging has been instrumental in helping to map out the extent of these sill complexes in offshore settings like the North Atlantic (e.g., Thomson and Schofield 2008; Schofield et al. 2012), and is discussed further below.

7 Innovative Ways to Image and Understand Magma Plumbing

It has long been a goal to attempt to image and map out active and ancient magma systems. Remote sensing techniques have been applied to monitor active volcanoes and volcanic settings, to image where possible, what is happening to magma in shallow systems in the sub surface. With modern volcanoes and active volcanic settings, geophysical methods have long been used to help image the shallow volcanic subsurface (e.g., Miller and Smith 1999). The magma pathway can be mapped out by epicentres of shallow magmatically-induced earthquakes highlighting the route the magma is taking from depth to the surface. Very detailed mapping of ground deformation at active volcanic centres is now possible with very high resolution GPS and ground surveying from satellites that when combined with subsurface imaging, can be used in turn to build an understanding of the subsurface structure, magma pathways and movement (e.g., Sigmundsson et al. 2010; Wright et al. 2012a, b).

Physical models are another method to test 3D geometries and subsurface plumbing structure (e.g., Galland et al., this book). Additionally, where good outcrop and erosion permit (e.g., Figs. 6 and 7), it is possible to map out and interrogate the intrusions directly. These data are vital as it provides case studies to build our understanding on (e.g., Westerman et al., this book; Svensen et al., this book; Gudmundsson

et al., this book). Magma flow directions can be inferred from the sill structures (e.g., Schofield et al. 2012) and by using magnetic fabric data (e.g., Stevenson and Grove, this book). Geochemical fingerprinting can also be used to determine the relative emplacement of sill-dyke complexes in eroded sub-volcanic systems (e.g., Galerne et al. 2008; Galerne and Neumann, this book). However, developing a robust 3D picture of ancient plumbing systems can be more difficult as when exposed on the surface and are partly eroded. Examples in the subsurface that can be remotely imaged can provide a window into the geometrical relationships and linkages of the magma pathways to the surface. Additionally, we may be able to use the products from modern eruptions to interrogate the subsurface, where they contain information about the magma migration and evolution through time. These two areas will be briefly elaborated on below.

7.1 Geophysical Imaging of Ancient Magma Plumbing Systems in 3D

One recent innovative way to image and map out the 3D distribution of sub-surface intrusions has actually come from data-sets that have been generated by offshore exploration for oil and gas. 2D and 3D seismic surveys in volcanic rifted margins are providing increasingly complex data sets that image the volcanic and intrusive facies across large areas offshore (e.g., Planke et al. 2000; Cartwright and Hansen, 2006; Jerram et al. 2009a, b; Wright et al. 2012a, b). Where 3D data are available, volume rendering of the high amplitude parts of the surveys can often reveal much detail within the sub-volcanic system at a scale, which is difficult to appreciate at the outcrop level. Saucers, lobes/fingers of magma intrusion can be mapped out invading shallow sedimentary basins (e.g., Thomson and Schofield 2008; Schofield et al. 2012). The examples in Fig. 8 highlights high amplitude reflectors in seismic and how their morphology can be picked out in 3D (Thomson 2005; Gouly and Schofield

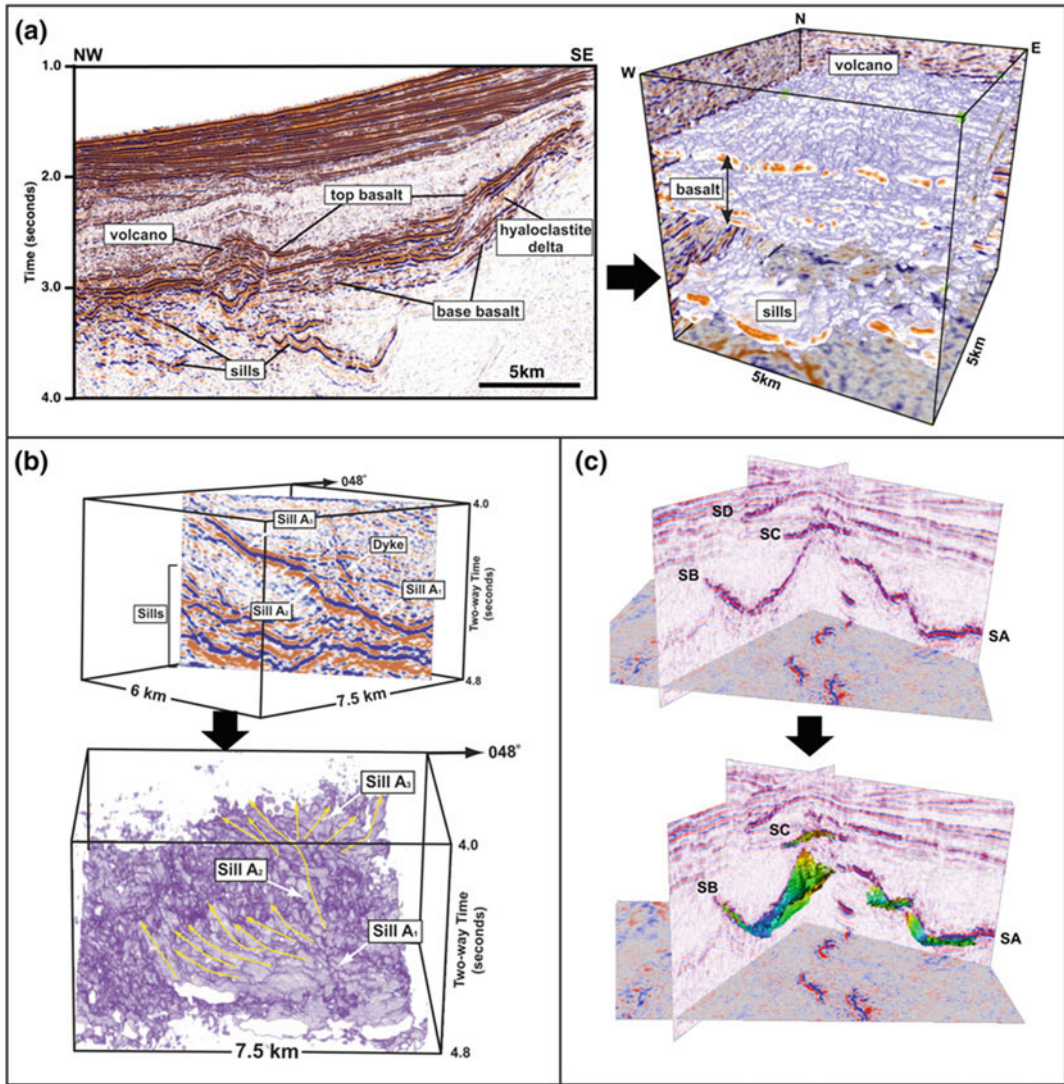


Fig. 8 Intrusions imaged from seismic images in 3D. **a** Volcanic features from seismic highlighted on a 2D seismic line and on a 3D volume rendering of high amplitudes (images courtesy of K. Thomson, see also Thomson 2005). **b** 2D seismic image and 3D rendered image, from a 3D data set, highlighting sill and dyke intrusions in offshore sedimentary units (igneous rocks

show up as bright reflectors). The volume-rendered image of the intrusion network that can be used to show magma pathways (image courtesy of Schofield, see Gouly and Schofield 2008). **c** Three cross-cutting seismic lines showing high amplitude saucer shaped sills, the surface of the sills is highlighted in the lower image (see Planke et al. this book)

2008; Planke et al., this volume). In these cases, it is intrusion of material into sedimentary basins that enable their imaging due to the large contrast between the igneous and sedimentary rocks. Further examples of the geophysical imaging of the sub-surface are provided by Planke et al., this volume.

7.2 Using Volcanic Products to Investigate the Sub-volcanic System

When volcanoes erupt with a crystal payload/cargo, it is possible to use the crystal population to help unravel the magma system at depth (e.g.,

Jerram and Davidson 2007; Cashman and Sparks 2013). As crystals grow, they record the magma around them, and if residency in magma is long-lived, periods of growth and recycling of crystals through different parts of the magma system can occur, and the resultant crystal population records those changes (e.g., Jerram and Davidson 2007; Jerram and Martin 2008). The crystal population can be characterised by examining the crystal size distribution (CSD) (e.g., Jerram and Higgins 2007), and variations that the crystal may have experienced during growth can be characterized by the geochemistry and textures in the growth zones. In some instances, the combination of CSD and geochemical analysis can be used in combination to find out about magma dynamics (e.g., Turner et al. 2003; Morgan et al. 2007). In a sense, the crystals are used as a fingerprint of the magmatic history and residency in the shallow sub-volcanic realm. The final crystal population that is found within the erupted rock may consist of phenocrysts and microlites (autocrysts) that are directly linked to the erupting magma, antecrysts which represent recycled crystals from the plumbing system, and xenocrysts which are alien to the magmatic system incorporated from country rock (Jerram and Martin 2008 and references therein).

The most recent eruptive cycles in Santorini, for example, can be used as a simple case study to highlight the value of interrogating the crystal population to understand the magma plumbing system. The post-caldera islands of Palaea and Nea Kameni, which have been the focus of historic volcanism on Santorini, lie in the centre of the flooded caldera and represent magmatic activity that resumed soon after the Minoan eruption (most recent caldera-forming eruption). The Nea Kameni edifice broke the surface in 197 BC and subsequently, at least nine subaerial episodes of volcanic activity have occurred, the last of which was in AD 1950. The Kameni islands are formed from dacite lava flows, which contain abundant magmatic enclaves, interpreted to be the quenched fragments of replenishing magmas that periodically triggered eruptive events (Martin et al. 2006). Each eruptive triggering event occurred only a few weeks to

months before the eruptions themselves (Martin et al. 2008). The disequilibrium phenocryst assemblages found in the lavas and the phenocryst-bearing enclaves provide evidence for the entrainment and recycling of older crystal populations into the lavas and enclave magmas. Martin et al. (2006) showed that by combining the phenocryst portion of the crystal size distribution CSD (a measure of the crystal population) with reasonable plagioclase growth rates, the calculated residence times suggested that recycling from a Minoan, or pre-Minoan source was feasible.

This crystal recycling was further investigated using isotopic geochemical fingerprinting of the crystals within the main volcanic cycles looking at different magma batches (Martin et al. 2010). Figure 9 shows the Sr isotopic ratios recorded from crystal separates and from the background glass for several of the eruptive events on Santorini. This highlights a number of different mixing and mingling episodes occurring between the different eruptions as recorded in the resultant eruptive products (Martin et al. 2010), suggesting a very complex model of mixing and recycling of crystals throughout the evolution of the Santorini volcano. Even focusing on a single eruption, e.g., the Minoan cycle (Fig. 10a), identifies a complex picture of magma mixing and mingling with several identifiable magmatic components residing within the subvolcanic plumbing system (Martin et al. 2010).

A similar pattern of crystal recycling exists at other volcanoes with multiple magma inputs and complex plumbing systems with depth. Shiveluch volcano in Kamchatka, provides another case study where the magma plumbing system can be revealed through its crystal cargo at eruption (Cashman and Sparks 2013). Carefully piecing together the different magma inputs, core and rim differences preserved within antecrysts, and the different mixtures of crystal species, it is possible not only to gain insight into the different contributing components but also some semblance of the depth relationships of these processes within the volcano (e.g., Fig. 10b). Detailed investigations of important minor mineral components such as zircons, also display

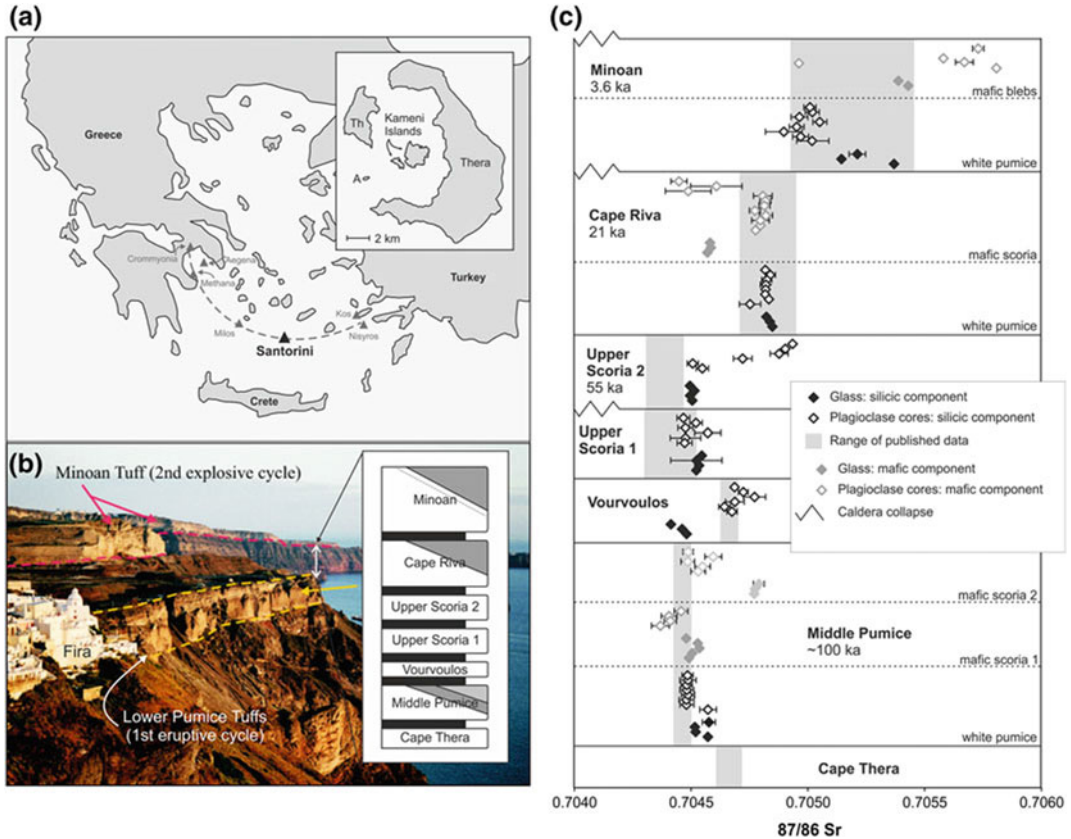


Fig. 9 Detail of volcanic cycles on Santorini (adapted from Martin et al. 2010). **a** Location map of Santorini, **b** Stratigraphy of Minoan cycle (terminology and ages from Druitt et al. 1999), **c** $^{87}\text{Sr}/^{86}\text{Sr}$ values for the different volcanic events showing whole rock vs separate

analysis (crystals + glass). It is clear from these data that the crystal populations and separate melt compositions record far more detail about the isotope variations in the system than by using whole rock data alone (see also Fig. 10a)

crystal population complexities, which highlights the importance of recognising this type of process (e.g., Charlier et al. 2005), particularly as these crystals are often used to provide age constraints on eruptions.

Where volcanic sequences can be very well-constrained in terms of their spatial and temporal relationships, then their crystal populations can potentially provide a valuable link into an understanding of the subsurface complexity and evolution. In some examples such as the Santorini case study presented above, an increase in crystal recycling and complexity is observed at a single volcano, as well as examples which show results

where crystal recycling appears to increase over time at a regional scale (e.g., Bryan et al. 2008; Ferrari et al. 2013). In other examples, volcanoes can show a distinct lack of connectivity between eruptive events, with new influxes of magma and absence of any large, active reservoirs that would promote homogenisation (e.g., Hobden et al. 2002). Although the shallow sub-volcanic system cannot be fully realised in its true extent for many volcanic centres, such examples of textural and geochemical analysis of the volcanic products provide valuable insight on the complexities that can exist in subvolcanic plumbing systems (Jerram and Martin 2008).

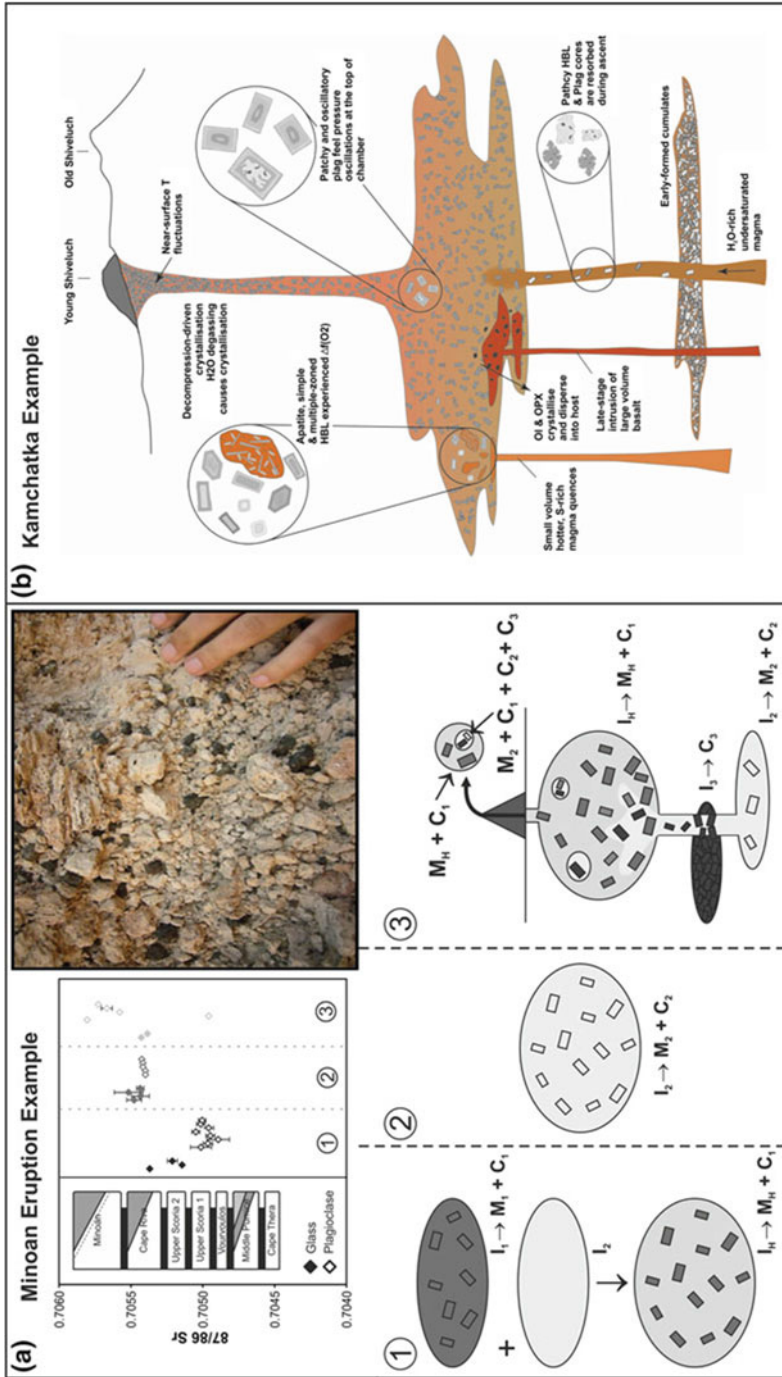


Fig. 10 Examples of complexity locked up within crystal populations as tracers of magma plumbing systems. **a** Highlight of the Minoan eruption showing complex relationships of different magma components that help provide detail of the complex plumbing and recycling of crystals at depth beneath the volcano.

b Kamchatka example where differing crystal types (phenocrysts/antecrysts) and mixed crystal populations help reveal the complexities of the magma plumbing system (adapted from Cashman and Sparks 2013, image courtesy of Kathy Cashman)

8 Closing Remarks

Clearly the styles and types of sub-volcanic plumbing systems are as wide and varied as the volcanism that occurs on the planet today and that which has occurred in the past. It is important as you start to explore the following chapters in this book that complexities exist between different parts of the sub-volcanic system, some of which reflect the historical evolution of the subject, the details available from certain well-constrained studies (or limitations of information where subjects are less well-known), and an ongoing development of types of analysis and imaging that push further our understanding of the subject. In this short contribution, we have touched on some of the key points to consider when looking at shallow intrusive systems with the following main points/conclusions:

1. Although major magma systems on Earth at the first order reflect different styles of magma generation (subduction zones/complex continental, rifting zones and plume/hotspot), regional to local-scale complexities lead to a mixed plumbing system that is not dependent specifically to these volcano-tectonic variants. Types and styles of volcano (e.g., stratovolcano, calderas, shield volcanoes, fissures) can be found in varied contexts and can be driven by the subsurface complexities, tectonic stresses and magma flux.
2. It may not be exactly clear how to define shallow versus deep magma systems, depending on how complex and linked they may be. As an example, it is wise to consider a fairly deep seated system for kimberlite volcanoes but a very shallow system in rifted zones. In other examples, very large-volume single eruption events, such as the high-Ti silicic eruptions in the Parana-Etendeka, are thought to be deep as there are a lack of collapse calderas for these suggesting holding chambers may have been deeper.
3. Large igneous provinces display many volcanic types and plumbing architectures encompassing almost all possible types of intrusion, from complex forms in volcanic centres, plugs, laccoliths/lopoliths, through dyke swarms, to nested sill complexes.
4. In predominantly rifted settings, the magma flux through the system has a marked effect on how complex the plumbing system is.
5. Polygenetic volcanoes represent centralised venting of magma over time scales of 10^3 – 10^7 years, and can develop complex crystal mush pathways to the surface from significant depths in the crust. At shallow levels, intrusion geometries and plumbing are dictated by more localised stresses, and reflect inflation, migration and collapse features close to the volcano surface.
6. The complexities associated with modern volcanic systems and many eroded examples, allow an investigation of magmatism in the upper few 10s of km of the system, but to fully unravel this complexity also requires knowledge and appreciation of the deeper settings and primary magma source regions that can often be lacking.
7. Large-scale magma plumbing networks have been imaged using seismic along volcanic rifted margins as demonstrated by recent 3D seismic exploration data sets, and provide an exciting new methodology in constraining internal complexity and linkages within large-scale plumbing systems.
8. A number of remote sensing techniques are being deployed on active volcanoes to shed light on the very shallow components of the magma system, and revealing magma movement and storage by seismic, GPS and using satellite interferometry.
9. Where well-constrained volcanic products are found on the surface, and particularly where they contain crystal populations, it is becoming increasingly clear that the crystals themselves can be interrogated as a proxy for the magma system at depth. Crystal zoning profiles record changes in the magma system as the crystals grew and this can be a powerful way of fingerprinting key isotopic changes related to contamination, magma mixing and crystal recycling, storage depths and rates of transfer within the shallow magma system.

Acknowledgments We thank Olivier Bachmann and Sergio Rocchi for constructive reviews of the manuscript. This work was partly supported by the Research Council of Norway through its Centres of Excellence funding scheme, project number 223272. We would also like to thank authors of other contributions to this book for early access to their papers and discussions on aspects of this manuscript. The countless discussions with many colleagues and the LASI conferences and trips over the years that have fuelled our interest in magmatic plumbing, have gone some way to help shape our thoughts and indeed drive our conceptual ideas presented in this contribution.

References

- Bachmann O, Bergantz GW (2003) Rejuvenation of the Fish Canyon magma body: a window into the evolution of large-volume silicic magma systems. *Geology* 31(9):789–792
- Bachmann O, Bergantz GW (2004) On the origin of crystal-poor rhyolites: extracted from batholithic crystal mushes. *J Petrol* 45(8):1565–1582
- Bachmann O, Bergantz GW (2008a) Rhyolites and their source mushes across tectonic settings. *J Petrol* 49(12):2277–2285
- Bachmann O, Bergantz GW (2008b) The magma reservoirs that feed supereruptions. *Elements* 4(1):17–21
- Bachmann O, Miller CF, de Silva S (2007) The volcanic–plutonic connection as a stage for understanding crustal magmatism. *J Volcanol Geoth Res* 167:1–23
- Bacon CR (1983) Eruptive history of Mount Mazama and Crater Lake caldera, Cascade Range, USA. *J Volcanol Geoth Res* 18(1):57–115
- Barboni M, Schoene B (2014) Short eruption window revealed by absolute crystal growth rates in a granitic magma. *Nat Geosci* 7:524–528
- Bistacchi A, Tibaldi A, Pasquarè FA, Rust D (2012) The association of cone–sheets and radial dykes: data from the Isle of Skye (UK), numerical modelling, and implications for shallow magma chambers. *Earth Planet Sci Lett* 339:46–56
- Brown SJA, Cole JW, Wilson CJN, Wooden J (1998) The Whakamaru group ignimbrites, Taupo Volcanic Zone, New Zealand: evidence for reverse tapping of a zoned silicic magmatic system. *J Volcanol Geoth Res* 84:1–37
- Bryan SE, Cas RAF, Martí J (2000) The 0.57 Ma plinian eruption of the Granadilla Member, Tenerife (Canary Islands): an example of complexity in eruption dynamics and evolution. *J Volcanol Geoth Res* 103(1):209–238
- Bryan SE, Ferrari L, Reiners PW, Allen CM, Petrone CM, Ramos-Rosique A, Campbell IH (2008) New insights into crustal contributions to large-volume rhyolite generation in the mid-tertiary Sierra Madre occidental province, Mexico, revealed by U–Pb geochronology. *J Petrol* 49:47–77
- Bryan SE, Ukstins Peate I, Peate DW, Self S, Jerram DA, Mawby MR, Marsh JS, Miller JA (2010) The largest volcanic eruptions on Earth. *Earthscience Rev* 102(3):207–229
- Cartwright J, Hansen DM (2006) Magma transport through the crust via interconnected sill complexes. *Geology* 34:929–932
- Cashman KV, Sparks RSJ (2013) How volcanoes work: a 25 year perspective. *Geol Soc Amer Bull* 125:664–690
- Charlier BLA, Wilson CJN, Lowenstern JB, Blake S, Van Calsteren PW, Davidson JP (2005) Magma generation at a large, hyperactive silicic volcano (Taupo, New Zealand) revealed by U–Th and U–Pb systematics in zircons. *J Petrol* 46:3–32
- Cooper KM, Kent AJR (2014) Rapid remobilization of magmatic crystals kept in cold storage. *Nature* 506(7489):480–483
- Druitt TH, Edwards L, Mellors RM, Pyle DM, Sparks RSJ, Lanphere M, Davies M, Barreiro B (1999) Santorini Volcano. Geological Society, London, Memoirs, 19
- Druitt TH, Sparks RSJ (1984) On the formation of calderas during ignimbrite eruptions. *Nature* 310(5979):679–681
- Dungan MA, Davidson JP (2004) Partial assimilative recycling of the mafic plutonic roots of arc volcanoes: an example from the Chilean Andes. *Geology* 32:773–776
- Emeleus CH, Bell BR (2005) British regional geology: the Palaeogene Volcanic districts of Scotland, 4th edn. British Geological Survey. 214 p. doi:10.1017/S0016756806213050
- Emeleus CH, Troll VR (2009) A geological excursion guide to Rum. The Palaeocene Igneous Rocks of the Isle of Rum, Inner Hebrides. NMSE-Publishing Ltd. The Geological Society of Edinburgh (78 colour plates), 152 p. ISBN: 9781-905267224
- Emeleus CH, Troll VR, Chew DM, Meade FC (2012) Lateral versus vertical emplacement in shallow-level intrusions? The Slieve Gullion ring-complex revisited. *J Geol Soc London* 169:157–171
- Ernst RE, Baragar WRA (1992) Evidence from magnetic fabric for the flow pattern of magma in the Mackenzie giant radiating dyke swarm. *Nature* 356:511–513
- Fabbro GN, Druitt TH, Scaillet S (2013) Evolution of the crustal magma plumbing system during the build-up to the 22-ka caldera-forming eruption of Santorini (Greece). *Bull Volcanol* 75(12):1–22
- Ferrari L, López-Martínez M, Orozco-Esquivel T, Bryan SE, Duque-Trujillo J, Lonsdale P, Solari L (2013) Late Oligocene to Middle Miocene rifting and synextensional magmatism in the southwestern Sierra Madre occidental, Mexico: the beginning of the Gulf of California rift. *Geosphere* 9(5):1161–1200
- Galerne CY, Neumann ER, Planke S (2008) Emplacement mechanisms of sill complexes: information from the geochemical architecture of the Golden Valley Sill Complex, South Africa. *J Volcanol Geoth Res* 177:425–440
- Gelman SE, Gutierrez FJ, Bachmann O (2013) The longevity of large upper crustal silicic magma reservoirs. *Geology* 41:759–762

- Glazner AF, Bartley JM, Coleman DS, Gray W, Taylor RZ (2004) Are plutons assembled over millions of years by amalgamation from small magma chambers? *GSA today* 14(4/5):4–12
- Goodenough K, Emeleus CH, Jerram DA, Troll VR (2008) Golden rum: understanding the forbidden isle. *Geoscientist* 18(3):22–24
- Gouly NR, Schofield N (2008) Implications of simple flexure theory for the formation of saucer-shaped sills. *J Struct Geol* 30:812–817
- Gravley DM, Wilson CJN, Leonard GS, Cole JW (2007) Double trouble: paired ignimbrite eruptions and collateral subsidence in the Taupo Volcanic Zone, New Zealand. *Geol Soc Amer Bull* 119(1–2):18–30
- Hansen DM, Cartwright J (2006) Saucer-shaped sill with lobate morphology revealed by 3D seismic data: implications for resolving a shallow-level sill emplacement mechanism. *J Geol Soc London* 163:509–523
- Hansen J, Jerram DA, McCaffrey K, Passey SR (2011) Early cenozoic saucer-shaped sills of the Faroe islands: an example of intrusive styles in basaltic lava piles. *J Geol Soc* 168(1):159–178
- Hildreth W, Mahood GA (1986) Ring-fracture eruption of the Bishop Tuff. *Geol Soc Amer Bull* 97(4):396–403
- Hobden BJN, Houghton BF, Nairn IA (2002) Growth of a young, frequently active composite cone: Ngauruhoe Volcano, New Zealand. *Bull Volcanol* 64:392–409
- Jerram DA, Davidson JP (2007) Frontiers in textural and microgeochemical analysis. *Elements* 3:235–238
- Jerram DA, Higgins DM (2007) 3D analysis of rock textures: quantifying igneous microstructures. *Elements* 3:239–245
- Jerram DA, Martin VM (2008) Understanding crystal populations and their significance through the magma plumbing system. In: Annen C, Zellmer GF (eds) *Dynamics of crustal magma transfer, storage and differentiation*, vol 304. Geological Society, London, Special Publications, pp 133–148
- Jerram DA, Smith S (2010) Earth's hottest place: how to build a 3D volcano. *Geoscientist* 20(2):12–13
- Jerram DA, Widdowson M (2005) The anatomy of continental Flood Basalt provinces: geological constraints on the processes and products of flood volcanism. *Lithos* 79:385–405
- Jerram DA, Davidson JP, Petford N (2005) Hot and cold in the dry valleys. *Geoscientist* 15(9):4–5, 14–15
- Jerram DA, Goodenough K, Troll VR (2009a) From British tertiary into the future: modern perspectives on the British Palaeogene and North Atlantic Igneous provinces. *Geol Mag* 146:305–308 (North Atlantic Special Issue)
- Jerram DA, Single RT, Hobbs RW, Nelson CE (2009b) Understanding the offshore flood basalt sequence using onshore volcanic facies analogues: an example from the Faroe-Shetland basin. *Geol Mag* 146(3):353–367
- Jerram DA, Davis GR, Mock A, Charrier A, Marsh BD (2010) Quantifying 3D crystal populations, packing and layering in shallow intrusions: a case study from the basement sill, dry valleys, Antarctica. *Geosphere* 6:537–548
- Karlstrom L, Dufek J, Manga M (2009) Magma chamber stability in arc and continental crust. *J Volcanol Geoth Res* 190(3–4):249–270
- Kent AJR, Darr C, Koleszar AM, Salisbury MJ, Cooper KM (2010) Preferential eruption of andesitic magmas through recharge filtering. *Nat Geosci* 3(9):631–636
- LeCheminant AN, Heaman LM (1989) Mackenzie igneous events, Canada: Middle Proterozoic hotspot magmatism associated with ocean opening. *Earth Planet Sci Lett* 96(1–2):38–48
- Macdonald R, Bagiński B, Upton BGJ, Pinkerton H, MacInnes DA, MacGillivray JC (2010) The Mull Palaeogene dyke swarm: insights into the evolution of the Mull igneous centre and dyke-emplacement mechanisms. *Mineral Mag* 74:601–622
- Marsh BD (1996) Solidification fronts and magmatic evolution. *Mineral Mag* 60:5–40
- Marsh BD (2004) A magmatic mush column Rosetta Stone: the McMurdo dry valleys of Antarctica. *EOS Trans Am Geophys Union* 85:497
- Marti J, Ablay GJ, Redshaw LT, Sparks RSJ (1994) Experimental studies of collapse calderas. *J Geol Soc* 151:919–929
- Marti J, Geyer A (2009) Central vs flank eruptions at Teide-Pico Viejo twin stratovolcanoes (Tenerife, Canary Islands). *J Volcanol Geoth Res* 181(1):47–60
- Martin VM, Holness MB, Pyle DM (2006) Textural analysis of magmatic enclaves from the Kameni Islands, Santorini, Greece. *J Volcanol Geoth Res* 154:89–102
- Martin VM, Morgan DJ, Jerram DA, Caddick MJ, Prior DJ, Davidson JP (2008) Bang! month scale eruption triggering at Santorini volcano. *Science* 321:1178
- Martin VM, Davidson JP, Morgan DJ, Jerram DA (2010) Using the Sr isotope compositions of feldspars and glass to distinguish magma system components and dynamics. *Geology* 38:539–542
- Miller DS, Smith RB (1999) P and S velocity structure of the yellowstone volcanic field from local earthquake and controlled source tomography. *J Geophys Res* 104 (B7):15105–15121
- Morgan DJ, Jerram DA, Chertkoff DG, Davidson JP, Pearson DG, Kronz A, Nowell GM (2007) Combining CSD and isotopic microanalysis: magma supply and mixing processes at Stromboli volcano, Aeolian islands, Italy. *Earth Planet Sci Lett* 260:419–431
- Muller JR, Ito G, Martel SJ (2001) Effects of volcano loading on dike propagation in an elastic half-space. *J Geophys Res Solid Earth* 106(B6):11101–11113
- Nielsen TFD (2004) The shape and volume of the skaergaard intrusion, Greenland: implications for mass balance and bulk composition. *J Petrol* 45(3):507–530
- O'Hara MJ (1961) Petrology of the Scourie dyke, Sutherlandshire. *Mineral Mag* 32:848–865
- Petford N (1996) Dykes or diapirs? *Trans Roy Soc Ed Earth Sci* 87:104–114
- Planke S, Symonds PA, Alvestad E, Skogseid J (2000) Seismic volcanostratigraphy of large-volume basaltic extrusive complexes on rifted margins. *J Geophys Res [Solid Earth]* 105:19335–19351

- Polteau S, Mazzini A, Galland O, Planke S, Malthe-Sorensen A (2008) Saucer-shaped intrusions: occurrences, emplacement and implications. *Earth Planet Sci Lett* 266(1–2):195–204
- Rubi O, Blundy JD (2009) A dearth of intermediate melts at subduction zone volcanoes and petrogenesis of arc andesites. *Nature* 461:1269–1273
- Rocchi S, Mazzotti A, Marroni M, Pandolfi L, Costantini P, Bertozzi G, di Biase D, Federici F, Lô PG (2007) Detection of Miocene saucer-shaped sills (offshore Senegal) via integrated interpretation of seismic, magnetic and gravity data. *Terra Nova* 19:232–239
- Schofield N, Heaton L, Holford S, Archer S, Jackson C, Jolley DW (2012) Seismic imaging of ‘Broken-Bridges’: linking seismic to outcrop scale investigations of intrusive magma lobes. *J Geol Soc* 169:421–426
- Sigmundsson F, Hreinsdóttir S, Hooper A, Árnadóttir Th, Pedersen R, Roberts MJ, Óskarsson N, Auriac A, Decriem J, Einarsson P, Geirsson H, Hensch M, Ófeigsson BG, Sturkell E, Sveinbjörnsson H, Feigl KL (2010) Intrusion triggering of the 2010 Eyjafjallajökull explosive eruption. *Nature* 468:426–430
- Smith RL, Bailey RA (1968) Resurgent cauldrons. *Geol Soc Am Mem* 116:613–662
- Smith RT, Houghton B (1995) Vent migration and changing eruptive style during the 1800a Taupo eruption: new evidence from the Hatepe and Rongai phreatoplinian ashes. *Bull Volcanol* 57:432–439
- Smith VC, Shane P, Nairn IA (2005) Trends in rhyolite geochemistry, mineralogy, and magma storage during the last 50 kyr at Okataina and Taupo volcanic centres, Taupo Volcanic Zone, New Zealand. *J Volcanol Geoth Res* 148(3):372–406
- Spell TL, Harrison TM (1993) 40Ar/39Ar geochronology of post-Valles Caldera rhyolites, Jemez volcanic field, New Mexico. *J Geophys Res* 98:0148–0227
- Stephenson D, Merritt J (2006) *Skye; a landscape fashioned by geology*. Scottish National Heritage publication, p 22
- Stevenson CTE, O’Driscoll B, Holohan EP, Couchman R, Reavy RJ, Andrews GMD (2008) The structure, fabrics and AMS of the Slieve Gullion ring-complex, N. Ireland: testing the ring-dyke emplacement model. In: Thompson K, Petford N (eds) *Structure and emplacement of high-level magmatic systems: geological society of London special publications*, vol 302. Geological Society of London, London, pp 159–184
- Streck MJ, Leeman WP, Chesley J (2007) High-magnesian andesite from Mount Shasta: a product of magma mixing and contamination, not a primitive mantle melt. *Geology* 35:351–354
- Suzuki-Kamata K, Kamata H, Bacon CR (1993) Evolution of the caldera-forming eruption at Crater Lake, Oregon, indicated by component analysis of lithic fragments. *J Geophys Res* 98:0148–0227
- Tarney J (1973) The Scourie dyke suite and the nature of the Inverian event in Assynt. In: Park RG, Tarney J (eds) *The early precambrian of Scotland and related rocks of Greenland*. University of Keele, Keele, pp 105–118
- Thomson K (2005) Extrusive and intrusive magmatism in the North Rockall Trough. In: Doré AG, Vining BA (eds) *Petroleum geology: north-west Europe and Global Perspectives—proceedings of the 6th Petroleum Geology Conference*, pp 1621–1630
- Thomson K, Schofield N (2008) Lithological and structural controls on the emplacement and morphology of sills in sedimentary basins, structure and emplacement of high-level magmatic systems. *Geol Soc London Spec Publ* 302:31–44
- Thordarson T, Self S (1993) The Laki (Skaftár Fires) and Grímsvötn eruptions in 1783–1785. *Bull Volcanol* 55:233–263
- Thordarson T, Self S (1998) The Roza member, Columbia River Basalt group: a gigantic pahoehoe lava flow field formed by endogenous processes? *J Geophys Res* 103:27411–27445
- Turner S, George R, Jerram D, Carpenter N, Hawkesworth C (2003) Case studies of plagioclase growth and residence times in island arc lavas from Tonga and the Lesser Antilles, and a model to reconcile discordant age information. *Earth Planet Sci Lett* 214:279–294
- White JDL, Bryan SE, Ross PS, Self S, Thordarson T (2009) Physical volcanology of continental large igneous provinces: update and review. In: Thordarson T, Self S, Larsen G, Rowland SK, Hoskuldsson A (eds) *Studies in volcanology: the legacy of George Walker*. Special Publications of IAVCEI 2, Geological Society of London, pp 291–321
- Wright KA, Davies RJ, Jerram DA, Morris J, Fletcher R (2012a) Application of seismic and sequence stratigraphic concepts to a lava-fed delta system in the Faroe-Shetland Basin, UK and Faroes. *Basin Res* 24:91–106
- Wright TJ, Sigmundsson F, Pagli C, Belachew M, Hamling IJ, Brandsdóttir B, Keir D, Pedersen R, Ayele A, Ebinger C, Einarsson P, Lewi E, Calais E (2012b) Geophysical constraints on the dynamics of spreading centres from rifting episodes on land. *Nat Geosci* 5(4):242–250
- Zellmer GF, Sakamoto N, Iizuka Y, Miyoshi M, Tamura Y, Hsieh H-H, Yurimoto H (2014) Crystal uptake into aphyric arc melts; insights from two-pyroxene pseudodecompression paths, plagioclase hygrometry, and measurement of hydrogen in olivines from mafic volcanics of SW Japan. In: Gómez-Tuena A, Straub SM, Zellmer GF (eds) *Orogenic andesites and crustal growth*. Special Publication - Geological Society of London 385(1):161–184
- Zellmer GF, Sparks RSJ, Hawkesworth CJ, Wiedenbeck M (2003) Magma emplacement and remobilization timescales beneath Montserrat: insights from Sr and Ba zonation in plagioclase phenocrysts. *J Petrol* 44(8):1413–1431

The Volcanic-Plutonic Connection

Allen F. Glazner, Drew S. Coleman and Ryan D. Mills

Abstract

One way to frame the debate about the relationships between volcanic and plutonic rocks is this: are plutons samples of magma that passed through the crust, or residues left behind by extraction of erupted liquids? In the former case plutons are compositionally equivalent to cogenetic volcanic rocks, barring biases introduced by passing through the crustal filter; in the latter they are cumulates, having lost liquid to eruption. These hypotheses make specific predictions about trace-element variations, which we test using global geochemical databases for circum-Pacific convergent margins and western North America. Volcanic rocks are far more abundant in these datasets than plutonic rocks and are biased to more mafic compositions. After subsampling the volcanic dataset to match the plutonic dataset, we find little evidence for significant loss of liquid from plutons. Rather, plutonic and volcanic trace-element patterns are generally indistinguishable. Where distinctions do occur, they are backwards; for example, a higher proportion of plutonic rocks has low Eu, Zr, and Ba, features of fractionated liquids, than volcanic rocks. These observations support the hypothesis that liquids fractionated from crystal-rich magmas are of small volume and are relatively immobile (e.g., aplites). These conclusions, derived from bulk-rock geochemistry, are supported by U-Pb zircon geochronology and field and textural observation. These data support the view that plutonic rocks are texturally modified samples of the same magmas that erupt. Partial melting provides an alternative to crystal fractionation for the origin of high-silica volcanic rocks.

Keywords

Pluton · Geochemistry · Geochronology · Geochemical database

A.F. Glazner (✉) · D.S. Coleman · R.D. Mills
Department of Geological Sciences, University of
North Carolina, Chapel Hill, USA
e-mail: afg@unc.edu

1 Introduction

1.1 The Uncertain Relationships Between Volcanic and Plutonic Rocks

A connection between volcanic and plutonic rocks has been implicit since the plutonic origin of granite was established in the 1700s by James Hutton and others. Lyell (1838) showed dikes from a composite batholith feeding a volcano in the frontispiece of his groundbreaking *Elements of Geology* (Fig. 1). Although he finessed the compositional relationship between the erupted rocks and those left behind, this concept has guided thought in the intervening time, having been reproduced in one form or another in myriad textbooks and papers.

The classic balloon-and-soda straw view of magma chambers and volcanoes (e.g., Daly 1933, p. 361) implies a direct connection between km-scale magma bodies and the surface. This appealingly simple concept has been

criticized on numerous grounds (Yoder 1976), yet persists (Paterson and Vernon 1995; Tarbuck and Lutgens 2008). There are multiple reasons (Glazner et al. 2004) to question the widespread existence of voluminous, largely molten magma chambers such as those envisaged in textbooks. These include:

- lack of geophysical evidence for large liquid-dominated magma bodies
- mechanical problems with rapid assembly of such bodies
- short thermal lifetimes of such systems
- field evidence for incremental emplacement
- geochronological evidence for long pluton lifetimes

Of these, zircon geochronological data are probably the most compelling. Diverse datasets indicate assembly of many superficially homogeneous plutons over timescales measured in millions of years (Coleman et al. 2004; Matzel et al. 2006; Davis et al. 2012; Lackey et al. 2012;

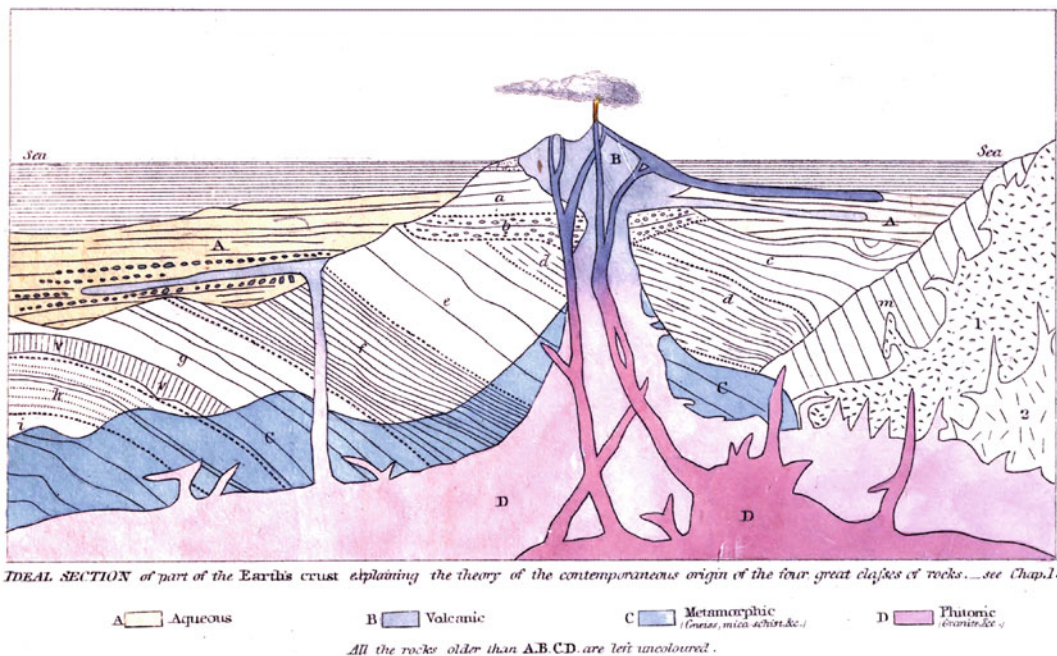


Fig. 1 Cross-section from Lyell (1838) showing “Ideal section of part of the Earth’s crust explaining the theory of the contemporaneous origin of the four great classes of

rocks.” Crosscutting plutons in a batholith (*D*, shades of red) are shown feeding an erupting volcano and associated volcanic rocks (*B*, shades of blue)

Mills and Coleman 2013; Frazer et al. 2014). The geochronologic data require that the plutons were assembled incrementally; but more significantly, they provide input for thermal models of sub-volcanic magma reservoirs. These models consistently show that the flux of magmas into plutonic environments should result in accumulation of melt-poor magma chambers (Annen 2009; Schöpa and Annen 2013) as are imaged under active volcanic regions (Farrell et al. 2014). Multi-millions of years timescales match the lifetimes of many volcanic systems in regions where erosion is slow enough that volcanic products are not rapidly erased (Kay et al. 2008; Klemetti and Grunder 2008).

Volcanic rocks are erupted onto the Earth's surface where their eruptive processes can be observed, their behavior quantified, their products measured and analyzed, and their surface expression duplicated by experiments (Hall 1805; Lofgren 1980; Kouchi and Sunagawa 1983; Alidibirov and Dingwell 1996; Edwards et al. 2013). Timescales of most volcanic processes are measured on human timescales of seconds to decades. For these reasons, the processes that produce lavas, pyroclastic rocks, and volcanic gases are reasonably well understood.

Plutonic rocks, in contrast, are emplaced far from direct observation. Although the temperatures and pressures inferred for plutonic processes in the crust are easily accessible to experimental petrologists, the timescales are not. Geochronologic data indicate that plutonic rocks may cool from emplacement temperatures to biotite Ar closure (± 300 °C) over millions of years, spending lengthy intervals at conditions corresponding to greenschist and amphibolite-facies metamorphism (Evernden and Kistler 1970; Renne et al. 1993; Ortega-Rivera et al. 1997; Bartley et al. 2008; Davis et al. 2012). For these reasons, the processes that produce plutonic rocks are much less well understood.

Part of this uncertainty arises from a lack of clarity about what constitutes a "pluton." Plutons are mostly defined based on field criteria, as mappable bodies of phaneritic, medium- to coarse-grained rock around which one can draw a contact. Although most geologists would

probably echo Justice Potter Stewart of the U.S. Supreme Court, who in 1964 famously said, "I know it when I see it,"¹ a pluton can be just about anything the mapper wants it to be, as long as it contains plutonic rocks and forms a mappable unit. The remarkable diversity of plutons in classic localities such as Donegal (Pitcher and Berger 1972) and California (Larsen 1948; Ross 1969; Bateman 1992) demonstrates how flexible the concept of "pluton" is.

1.2 What Is a Pluton?

A fundamental question about the volcanic-plutonic connection can be stated as: are plutons samples of magma that passed through the crust, or cumulate material left behind after extraction of liquid? Smith (1960) laid out many important questions in a prescient review of pyroclastic flow deposits. He inferred that voluminous pyroclastic rocks are probably underlain by greater volumes of unerupted magma that froze as large plutons, and asked whether rhyolites are erupted from magma of the same composition or from the liquid part of granodiorite magma—presumably leaving behind a crystal mush that would crystallize as a pluton.

The pluton-as-sample viewpoint holds that plutons are magmas that froze in place during passage through the crust rather than erupting, and thus that there are no significant differences in bulk chemical evolution between volcanic and plutonic rocks. The pluton-as-cumulate viewpoint holds that many plutons are chemical remainders left behind as liquid-rich fractions escaped and erupted; this implies fundamentally different chemical evolution between volcanic and plutonic rocks in systems that have undergone such differentiation.

¹Justice Stewart was referring to obscenity, not plutons.

1.3 Historical Views of the Volcanic-Plutonic Connection

Following Lyell, Darwin (1844, pp. 117–124) proposed that settling of denser minerals could produce trachyte from basalt and thus explain volcanic successions seen in places such as Tenerife. Darwin is generally credited with popularizing crystal fractionation as a petrogenetic process. His views on the volcanic-plutonic connection, however, have not weathered as well; he proposed that granitic plutons have been bled of basaltic liquid that drained into “unseen abysses”, later to reinject the granites and erupt (Darwin 1844, p. 124). This proposal is at odds with his hypothesis of mafic mineral fractionation.

Advances in experimental petrology and physical chemistry led Bowen (1915) to propose that differentiation from a basaltic parent to granite and rhyolite is the dominant process producing the diversity of igneous rocks. Studies in the system albite-orthoclase-SiO₂-H₂O by Tuttle and Bowen (1958) led to the general acceptance of an igneous origin for granite and rhyolite controlled by mineral-melt equilibrium.

Field studies in the first half of the last century clearly implied strong connections between volcanic and plutonic rocks for shallowly emplaced plutons. Buddington (1959) inferred that magma bodies, some quite large, probably underlie active silicic systems such as Taupo and Toba. Daly (1917, 1928) suggested that granite sheets in mafic sills form via separation of residual liquid. With analogy, Hamilton (1959) proposed that extensive rhyolites of the Yellowstone region may be the extrusive upper crust of a lopolith that is roofed by its own differentiates—an extrusive lopolith. Hamilton’s proposal explicitly tied high-silica rhyolite to plutonic remains.

It has long been known that at the Earth’s surface, mafic rocks predominate among volcanic rocks and silicic among plutonic rocks (Daly 1914, pp. 44–45). Kennedy and Anderson (1938) and Read (1948) used such observations to argue that volcanic and plutonic rock associations are of fundamentally different origin. In

contrast, Harris et al. (1970) contended that this difference owes its origin to the tendency of water-saturated high-silica magmas to intersect the solidus upon ascent.

Hamilton and Myers (1967) noted that Mesozoic strata of the western North American continental interior apparently contain >1 million km³ of altered volcanic ash. Given prevailing winds, this ash was likely provided by the Cordilleran magmatism to the west. They inferred that the magma bodies that produced these copious ashes are now exposed as Cordilleran plutons.

At the Pleistocene Long Valley caldera in California, Bailey et al. (1976) proposed that the decrease in silica seen in silicic rocks erupted over the ~2 Ma lifetime of the system resulted from progressively deeper tapping of a large magma body that was zoned from 77 wt% SiO₂ at the top to 64 wt% SiO₂ at depth. They proposed that ongoing cooling of this system is producing a pluton zoned from granite at the top to granodiorite at depth. In their hypothesis compositional diversity in the erupted rocks mimics that in the magma, rather than being produced by separation of liquid from a plutonic residue.

Hildreth (1981) reviewed the many processes that can produce compositional diversity in silicic magmatic systems. He argued that eruption of magma bodies that eventually crystallize as plutons is common, but that the erupted products are, in many environments, rapidly removed by erosion or carried far distances as ash, leading to severe underestimation of their relative volume. He noted that although compositional gradients are evident in both volcanic and plutonic systems, they may be produced by different mechanisms. Lipman (1984, 2007) reiterated the strong field connection between roughly coeval plutonic and volcanic rocks in caldera complexes.

Most recently, the recognition that plutonic magma systems have thermal lifetimes spanning millions of years led Lundstrom (2009) to propose formation of granites and chemical gradients in magma systems via thermal migration zone refining of parental andesitic magma. Experimental work demonstrates that maintaining a

thermal gradient across a hydrous andesite charge can produce a solid of granitic composition at the cold end of the charge (Huang et al. 2009). Furthermore, this mechanism predicts stable isotope correlations with bulk rock chemistry that are now recognized in both plutonic and volcanic rocks (Lundstrom et al. 2013; Zambardi et al. 2014).

In the past decade however, most studies invoke the dominant paradigm, appealing to separation of liquids from crystalline remainders (the mush model) to produce rhyolite (Bachmann and Bergantz 2004; Hildreth 2004; Eichelberger et al. 2006), a mechanism that goes back a century or more to those cited above. This hypothesis specifically links rhyolite to coeval granodiorite plutons, consistent with the field-based studies summarized by Lipman (1984), and makes specific predictions about the geochemical and geochronological connections between related volcanic and plutonic rocks.

1.4 Relevant Data

The strong field basis of geology means that observation is commonly given precedence over geochemical data, modeling, and other forms of analysis. Although this is generally a good idea, field data can be highly misleading; whereas rapidly quenched volcanic rocks provide unambiguous evidence about what crystals were present in a magma just before eruption, plutonic rocks provide a murkier history due to recrystallization and coarsening that occurs during prolonged cooling (Bartley et al. 2008).

For example, interpretation of crystal size in rapidly cooled volcanic rocks is unambiguous but can be problematic in plutonic rocks. Crystal size has long been correlated to cooling rate; Pirsson (1909, p. 151) stated that large crystals are favored by slow cooling, which produces few nuclei, allowing the crystals that do form to grow to larger size, and slow annealing also coarsens crystals by redistributing mass from smaller crystals to larger ones, eventually destroying the smaller ones (Marsh 1988; Boudreau 2011). Coarsening processes that occur during the

potentially million-year cooling times of plutonic rocks can greatly complicate interpretation of, for example, K-feldspar megacrysts in granites (Higgins 1999; Johnson and Glazner 2010).

In this paper we give an overview of the volcanic-plutonic connection, using field, geochemical, and geochronological data, and make specific tests of the mush model. This analysis is primarily concerned with subduction-related, I-type rocks; silicic magmas produced by partial melting of metasedimentary rocks are not discussed.

2 Methods

Datasets discussed below were extracted from NAVDAT (www.navdat.org) and GEOROC (www.georoc.mpch-mainz.gwdg.de/georoc); both are available through EarthChem (www.earthchem.org). NAVDAT data are from predominantly Cenozoic and Mesozoic rocks from western North America and thus encompass samples influenced by a number of tectonic settings, including subduction, post-subduction extension, and hot-spot. GEOROC data are from precompiled datasets for circum-Pacific continental arcs (Aleutian, Andean, Cascades, Central American, Honshu, Kamchatka, Mexican, and New Zealand). Datasets, extracted in January 2015, were cleaned by rejecting samples with $\text{SiO}_2 < 40$ or > 80 wt% or listed as having moderate or severe alteration. For trace element comparisons the convergent margin dataset was further screened by eliminating any samples that lack any major elements or Rb, Sr, or Ba. REE data were further screened by rejecting any chondrite-normalized patterns that pointed to troubled analyses, such as spiky patterns or patterns with large gaps from lack of data.

The large numbers of samples available for comparison make standard scatterplots difficult to interpret because a large number of points overlap (e.g., Gelman et al. 2014), thus emphasizing outliers and masking concentrations of data. To ameliorate this we constructed 2-dimensional histograms, using the procedure of Eilers and Goeman (2004) as implemented by

Perkins (2006). As with more conventional histograms, binning involves a certain amount of subjectivity; we used 700 bins in each dimension. The histogram surfaces are constructed such that the volume under them is unity, and colors give the relative height of the surface.

3 The Sampling Problem

Compositional and age patterns in geochemical databases reveal differences between plutonic and volcanic rocks, but these are confounded by sampling issues. For example, volcanic rocks predominate among younger rocks and plutonic among older, and geochemical databases are generally heavily weighted toward volcanic rocks (Fig. 2). The age bias is clearly because plutons are emplaced at depth and only exposed

once overlying rocks (including cogenetic volcanic rocks) have been largely stripped away by erosion or tectonic unroofing. Thus, in many regions one must compare volcanic rocks of a given age with older plutonic rocks; alternatively, differing depths of erosion might leave volcanic rocks preserved along strike of coeval plutons. In a small number of areas, volcanic and plutonic rocks from the same or closely related systems are exposed due to faulting and erosion (see below).

A similar bias is evident in silica contents; exposed plutonic rocks on the continents are on average more silicic than volcanic rocks. Figure 3 shows silica histograms for the NAVDAT and convergent margin datasets. Plutonic rocks from both datasets show unimodal distributions that are skewed toward high-silica compositions, with a dominant mode around 70 wt% SiO₂ and a

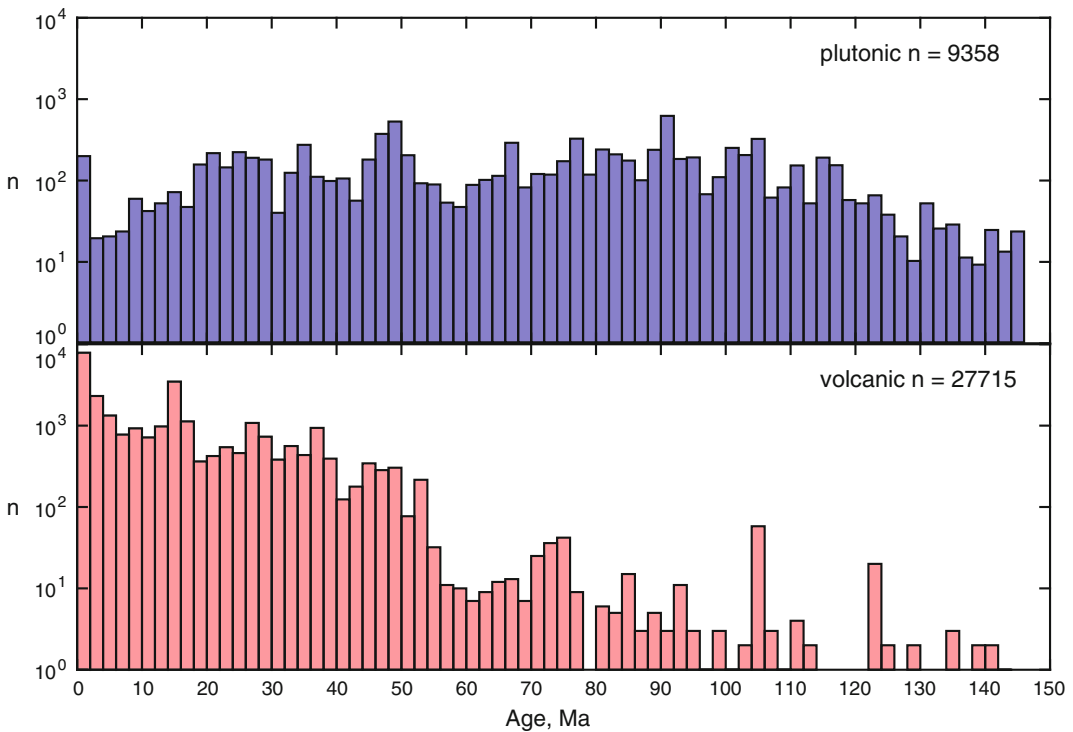


Fig. 2 Age distributions for plutonic and volcanic rocks in western North America for the past 150 million years, taken from NAVDAT. Volcanic rocks predominate among younger rocks and are rare among older (Mesozoic) rocks. Many of the listed ages are estimated based

on correlation rather than geochronologic age determinations. Note logarithmic scale on ordinate. Volcanic subpeak near 15 millions of years is caused by the Columbia River basalt event, which is well represented in the dataset

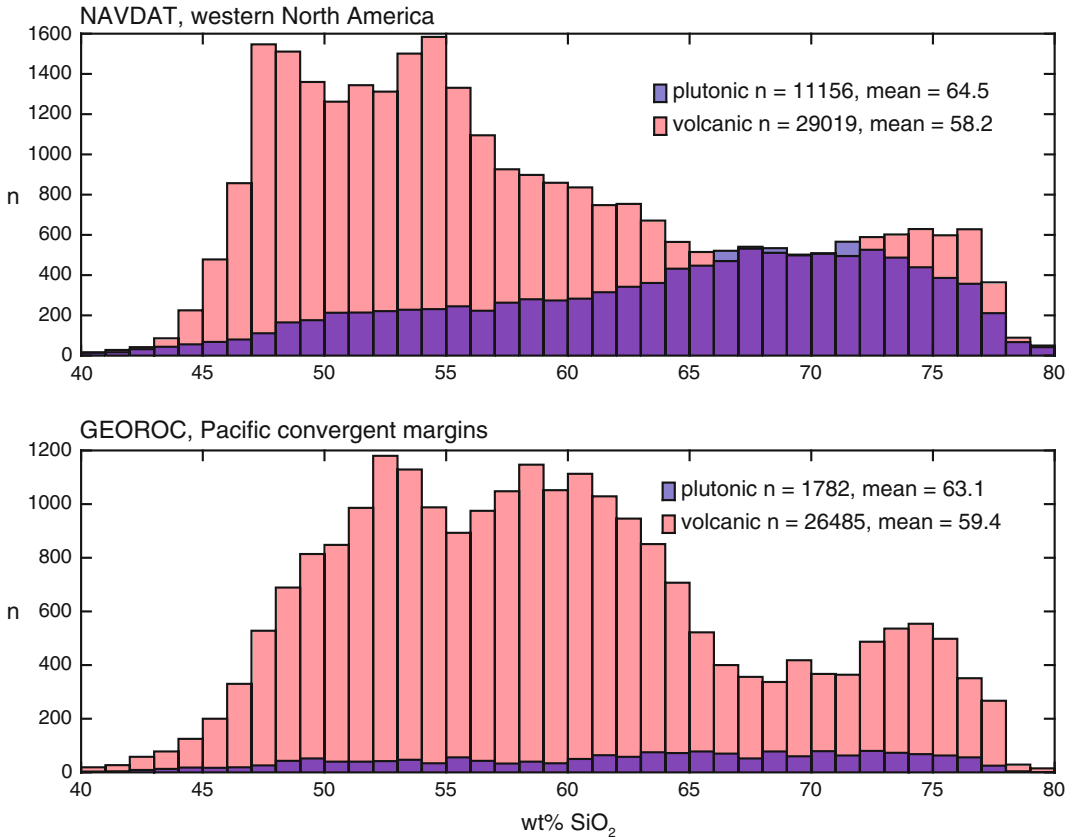


Fig. 3 Histograms comparing SiO₂ distributions of volcanic and plutonic rocks from western North America and from circum-Pacific subduction zones. NAVDAT

data are for all samples for which SiO₂ is reported. NAVDAT volcanic peak at 54 wt% is from the Columbia River basalts

secondary shoulder at 50–55 wt% SiO₂. Volcanic rocks from both datasets are more bimodal, with a primary mode at 50–55 wt% SiO₂ and a secondary mode at 70–75 wt% SiO₂. For both datasets the silica distribution of volcanic and plutonic rocks is roughly a mirror image of the other. This compositional difference has been attributed to the tendency of water-saturated silicic magmas to freeze upon ascent (Harris et al. 1970).

The much greater abundance of volcanic rocks in databases complicates analysis of compositional patterns because element-element plots and compositional statistics are dominated by volcanic rocks. In order to lessen this effect we have subsampled the volcanic convergent-margin dataset in SiO₂ bins. For each 5 wt% bracket in SiO₂ (e.g., 50–55), a random sample

of volcanic rocks equal to the number of plutonic rocks in that bracket was chosen. This procedure yields volcanic subsets with a silica distribution like that of the plutonic dataset. For most elements the patterns are highly consistent across repetitive resamplings.

4 Compositional Comparison of Volcanic and Plutonic Rocks

4.1 Introduction

Compositional similarities between volcanic and plutonic rocks have long been used as evidence for derivation from a common magma (e.g., Buddington 1959; Branch 1967). For example, in

a steeply tilted Miocene magmatic section in Arizona, [Faulds et al. \(1995\)](#) used similarities in trace-element composition to argue for derivation of volcanic and plutonic rocks from the same source. In the following sections we examine global, regional, and local geochemical comparisons.

4.2 Global Comparison for Convergent Margins

If typical granodiorite plutons are material left behind by extraction of rhyolite liquid ([Smith 1960](#); [Lipman 1984](#); [Bachmann and Bergantz 2004](#)), then the extracted rhyolites and residual plutons should show complementary geochemical relationships ([Buma et al. 1971](#); [Hanson 1978](#)). We compare volcanic and plutonic rocks from the convergent margin datasets described above to test the hypothesis of [Bachmann and Bergantz \(2004\)](#) that many rhyolites are derived from intermediate magmas when the fraction of liquid (F) is ~ 0.5 , leaving behind batholith-scale granodioritic plutons. In the discussion below we assume that the parent magma for this process is a dacite with ~ 65 wt% SiO_2 .

The extensive geochemical datasets for the Fish Canyon Tuff of Colorado provide a natural example against which this hypothesis can be tested. The Pagosa Peak Dacite phase of the Fish Canyon eruptive sequence ([Bachmann et al. 2000](#)) contains ~ 45 vol.% crystals dominated by plagioclase (60 vol.% of the crystals), sanidine (14 %), hornblende (9 %), biotite (8 %), quartz (7 %), and minor titanite (1.6 %) and opaque minerals (1 %). The composition and mineral assemblage of the tuff provide a good match for typical granodiorites of the Sierra Nevada of California, including the Half Dome and Cathedral Peak Granodiorites ([Bateman and Chappell 1979](#)), and the tuff provides a model for what those magmas might have looked like at 50 % crystallization.

Analyses of whole-rock samples and individual phases for major and trace elements ([Bachmann et al. 2002, 2005](#)) allow the composition of the

bulk crystalline assemblage to be determined by mass balance. In the discussion that follows, this composition was calculated assuming that the crystalline assemblage made up 50 wt% of the magma. Thus, the crystalline assemblage (black diamonds on [Fig. 4](#)) was calculated such that a 50:50 weight mixture of it and the analyzed glass (white diamonds) produces the whole-rock composition.

[Figure 4](#) compares the convergent-margin plutonic dataset with subsamples of the corresponding volcanic dataset for selected elements. These plots demonstrate that: (1) the patterns for plutonic and volcanic rocks are quite similar, including for those elements not displayed, after the first-order bias in silica is removed; (2) where the patterns differ, the differences are commonly opposite those expected from crystal-liquid separation—for example, the tail toward extremely low Ba concentrations that should be present in high-silica volcanic rocks is absent, but it is obvious in the data for plutonic rocks; and (3) predicted elemental enrichments in purported cumulates are effectively absent.

Plagioclase is a liquidus or near-liquidus phase at crustal pressures for water-saturated dacitic magmas even though water suppresses the appearance of plagioclase relative to ferromagnesian minerals (e.g., [Piwinski 1968](#); [Rutherford et al. 1985](#); [Whitney 1988](#); [Scaillet and Evans 1999](#); [Holtz et al. 2005](#)). Although plagioclase comes in at temperatures well below the liquidus in the Fish Canyon Tuff ([Johnson and Rutherford 1989](#)), mass balance and its abundance in the tuff indicates that it is still a dominant phase. Therefore, liquids separated from a plagioclase-rich mush should have Eu and Sr depletions relative to the starting magma. If significant K-feldspar or biotite is in the crystallizing assemblage, then liquids will be depleted in Ba as well. These depletions are indeed seen in Fish Canyon glass ([Fig. 4](#)). Complementary plutons will be enriched in these elements and in elements found in minor phases such as titanite or apatite that sequester minor and trace elements, as shown by the calculated Fish Canyon crystalline assemblage.

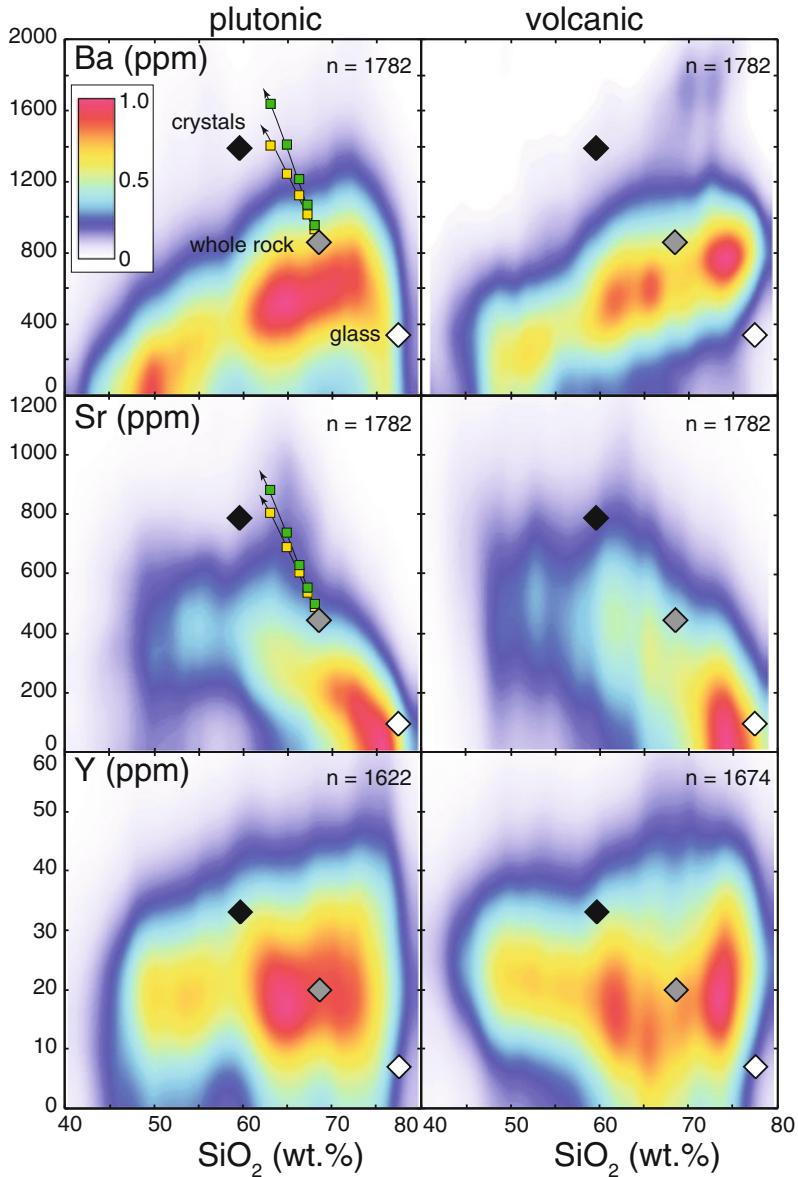


Fig. 4 Comparisons of plutonic and volcanic rock compositions from convergent margins, showing strong similarities after differences in silica distribution are removed. Each pair compares the full plutonic dataset with a subsample of the volcanic dataset (see Sect. 3 for subsampling procedure). For Sr and Ba, calculated cumulate compositions are shown for extraction of 0–50 wt% rhyolite (74 wt% SiO₂) from Pagosa Peak Dacite, using crystal proportions from the dacite and distribution coefficients as specified in Glazner et al.

(2008); bulk distribution coefficients so calculated are 10.4 (Sr) and 4.6 (Ba). Both fractional (*green*) and batch (*yellow*) models are shown. Color bar gives relative height of histogram surface (see Methods); volume under each surface is unity. Eu^* is defined as $Eu_n / \sqrt{Sm_n \cdot Gd_n}$, where subscripts define chondrite normalization (McDonough and Sun 1995). Diamonds show whole-rock (*gray*), glass (*white*), and calculated bulk crystal (*black*) composition for the Fish Canyon Tuff; see Sect. 4.2 for data sources and calculation procedure

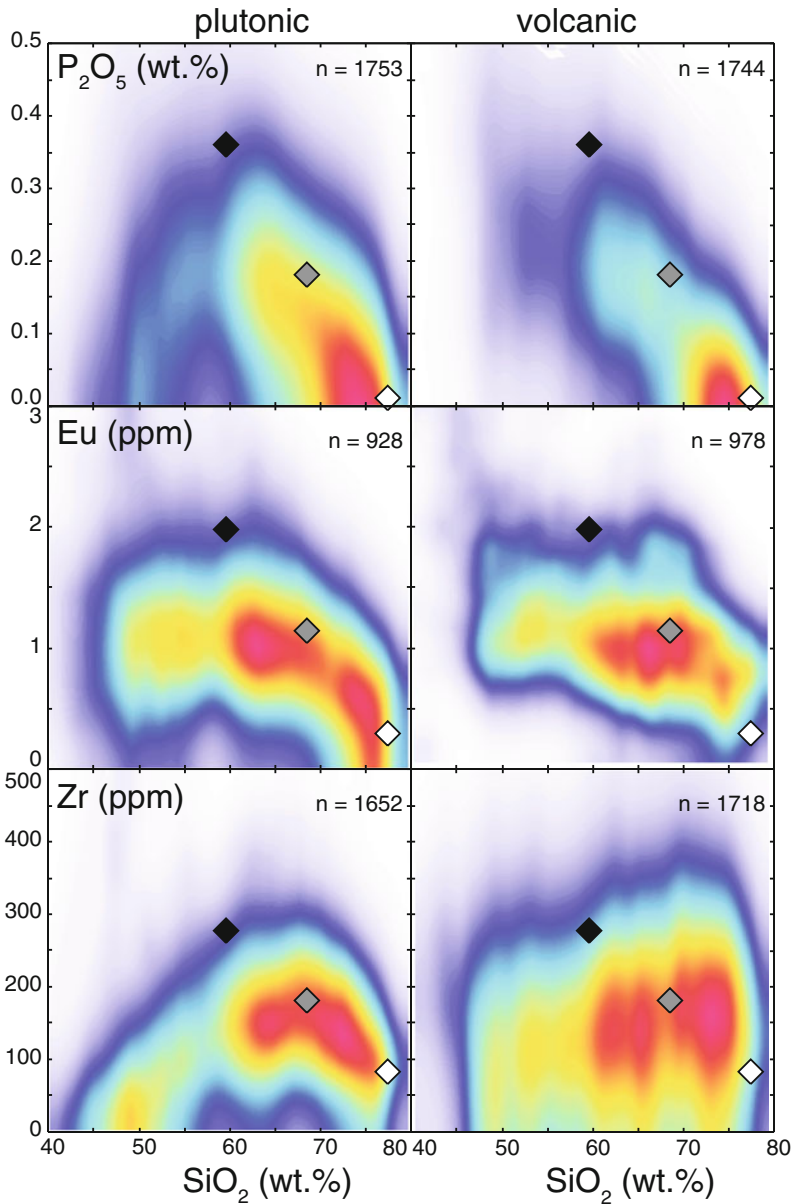


Fig. 4 (continued)

Distribution coefficients for Sr in rhyolite liquid are >10 for plagioclase and 5–10 for K-feldspar (Mahood and Hildreth 1983; Nash and Crecraft 1985; Streck and Grunder 1997; Bachmann et al. 2005), and thus for $F = 0.5$ the concentration of Sr in the bulk crystals should be roughly twice that in the starting magma for either fractional or batch fractionation. The Fish

Canyon Tuff crystalline assemblage is enriched over whole-rock concentrations by 80 and 60 %, respectively (Fig. 4).

Patterns showing the predicted Sr and Ba enrichment are lacking in the convergent-margin plutonic dataset. The cumulate hypothesis predicts that plutonic rocks should be enriched in Sr and Ba along a path extending to lower SiO_2 from the

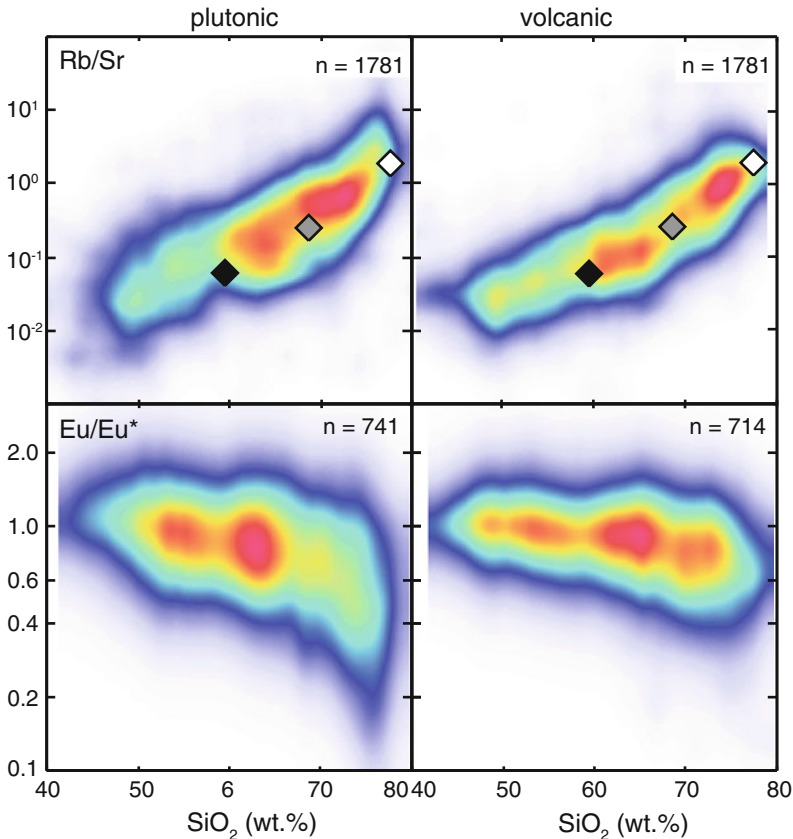


Fig. 4 (continued)

starting composition; Fig. 4 shows calculated enrichments for extraction of 0–50 wt% rhyolite (74 wt% SiO₂) from Pagosa Peak Dacite.

A curious feature of the plots in Fig. 4 is that some elements show trends in the plutonic dataset that are predicted for the mush extraction model, but do not show those trends in the corresponding volcanic dataset. For example, Zr and P₂O₅ display boomerang-shaped patterns that could be interpreted as a liquid line of descent showing saturation in zircon and apatite at ~60 wt% SiO₂ (e.g., Evans and Hanson 1993). However, corresponding volcanic rocks do not show these patterns. In plutonic rocks, Ba and Eu show tails that drop to near zero at high-SiO₂, but volcanic rocks do not; similarly, rocks with deep negative Eu anomalies and high Rb/Sr are relatively more abundant among the plutonic rocks. All these features are opposite those predicted by

the cumulate hypothesis and shown by components of the Fish Canyon Tuff.

Rare earth element (REE) patterns for intermediate rocks from the two groups are summarized in Fig. 5. We use median values to characterize the patterns due to the presence of a small number of samples with high REE contents (e.g., Parker et al. 2010) that greatly skew mean values. The groups show comparable patterns, with median La ~80 times chondrite, Lu ~10 times chondrite, and flat patterns from Dy to Lu. Both groups show modest negative Eu anomalies, with Eu/Eu* for the plutonic group smaller than that for the volcanic group. As with Ba, Zr, and other elements, this difference is opposite that expected from separation of liquid from plagioclase-bearing crystalline remainders.

Data summarized in Figs. 4 and 5 provide a test of the hypothesis that rhyolites are derived

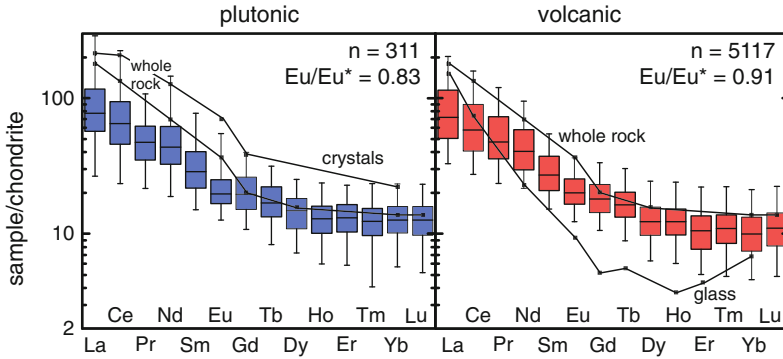


Fig. 5 Box-and-whisker plots summarizing REE data from convergent margins for 311 plutonic and 5117 volcanic rocks with 55–65 wt% SiO₂. Boxes encompass quartiles, median is shown with a horizontal line, and whiskers extends to 95th and 5th percentiles. Although the patterns show great similarity, Eu/Eu* is slightly lower for the plutonic group, opposite the difference

expected if a significant fraction of the plutons are cumulates; this difference passes the rank sum significance test ($p < 10^{-5}$). Patterns for Fish Canyon Tuff whole rock, glass, and calculated crystals are shown by solid lines. Note that displaying the data as box-and-whisker plots obviates the need to subsample the volcanic dataset

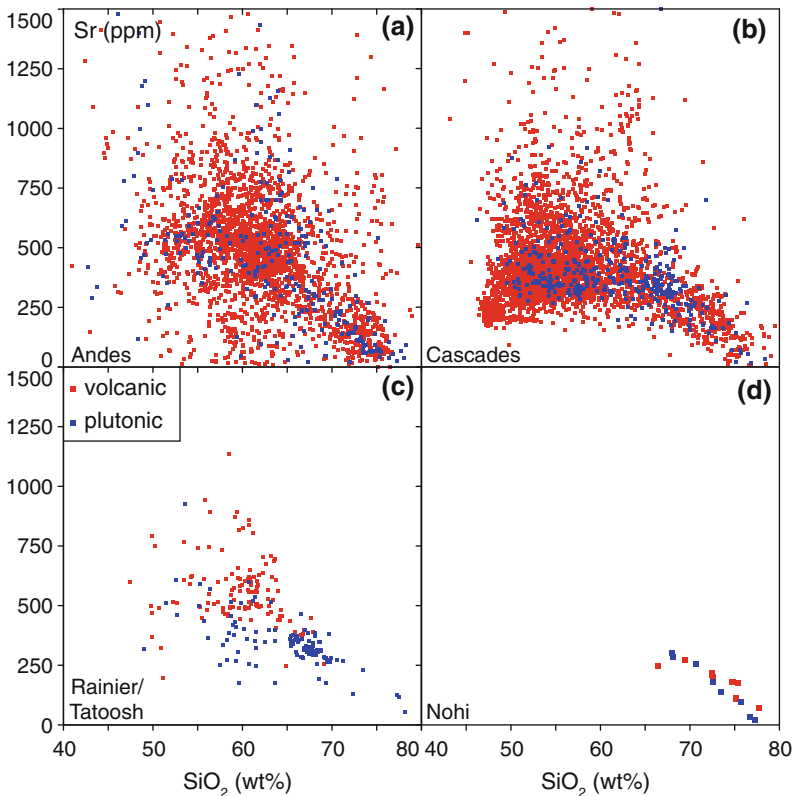


Fig. 6 Sr versus SiO₂ for **a** Cenozoic rocks from the Andes, **b** Cenozoic rocks from the Cascades, **c** Mt. Rainier volcanic field and Tatoosh plutonic complex, Washington, and **d** Nohi Rhyolite and related granitoids, Japan. In none of these successively more localized datasets is there a significant Sr enrichment in plutonic

rocks, as predicted by the mush hypothesis. In **c** most of the plutonic rocks are richer in SiO₂ than the volcanic rocks, precluding a simple fractional crystallization relationship. Other elements (e.g., Ba) as discussed above also lack differences. Data from EarthChem, du Bray et al. (2011), and Sonehara and Harayama (2007)

by separation of liquid from plutonic residuum at shallow levels (Bachmann and Bergantz 2004). These data contradict the hypothesis; there are either no significant differences between the plutonic and volcanic groups, or such differences are opposite those predicted.

4.3 Regional and Local Tests

Global comparisons such as those in Figs. 4 and 5 run the risk of missing fundamental differences due to mixing of different tectonic settings and lithosphere types (Bachmann and Bergantz 2008), although selecting only data from convergent margins mitigates this somewhat. In Fig. 6 we compare Sr concentrations in Cenozoic rocks from the Andes, Cenozoic rocks from the Cascades, Miocene-Recent rocks from the Mt. Rainier, Washington area, and a Cretaceous rhyolite-granitoid association in Japan. Although the number of samples in these datasets becomes progressively more limited as the areal scope is focused down, in none are significant differences evident for Sr or other elements that are predicted to diverge due to crystal-liquid separation.

Gelman et al. (2014) used AFC modeling (DePaolo 1981) to argue that cumulate enrichments in Sr are seen in both a particular plutonic case and in the entire NAVDAT dataset for western North America. Given the large number of free parameters in their modeling and factor-of-five scatter in the data being fit (Bachl et al. 2001), such modeling is not compelling. Lee and Morton (2015) examined geochemical data from the Peninsular Ranges batholith and found only scant evidence of silicic cumulates in the batholith. The inability to find the predicted cumulate geochemical signatures for any elements (and in fact the tendency for data to predict the opposite), as seen in Figs. 4, 5, and 6, argues strongly against the hypothesis that typical granite and granodiorite plutons have lost significant liquid. Hypotheses that consistently fail clear tests should be abandoned, and the concept of plutons as “crystal graveyards” (Gelman et al. 2014) ought to be buried by the weight of contradictory data.

4.4 The Titanite Problem

Eichelberger et al. (2006) proposed a novel connection between rhyolite eruptions and crystallizing magma bodies. They hypothesized that rhyolites can be extracted directly from granitic mushes via pervasive fractures, rather than being stored in magma chambers prior to eruption, and that aplite dikes in plutons are residual magma that failed to escape. Most aplite dikes do have rhyolitic major-element compositions, but Glazner et al. (2008) showed that aplite dikes from the Sierra Nevada batholith in California, and many others worldwide, have trace-element signatures unlike virtually all rhyolites in the EarthChem database. In particular, these aplites have highly depleted middle REE and low Y, consistent with separation from titanite-bearing crystalline material.

Fish Canyon Tuff glass shows this same scoop-shaped pattern and Y depletion (Figs. 4, 5 and 7), consistent with its titanite-bearing crystal assemblage. In sharp contrast, rhyolites from

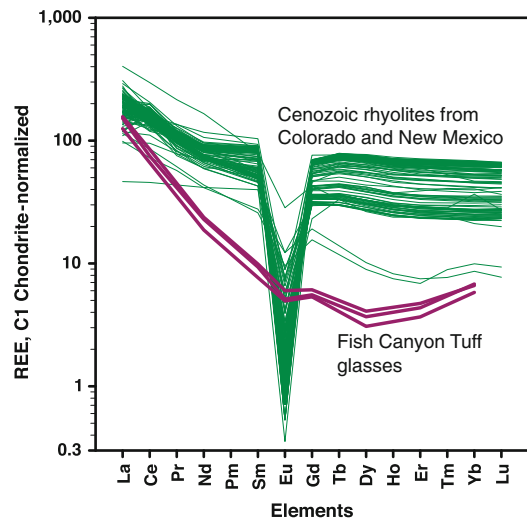


Fig. 7 REE patterns for 118 Cenozoic rhyolites from Colorado and New Mexico (green) plotted with 3 Fish Canyon Tuff glasses (purple) from Bachmann et al. (2005). The remarkable contrast in trace-element patterns indicates that if any rhyolitic liquids like the Fish Canyon glass separated from their coexisting crystals, they did not erupt; see Streck (2014) for more data and a similar analysis. Rhyolite data (volcanic rocks with 74–78 wt% SiO₂) extracted from NAVDAT

Cenozoic volcanic fields in Colorado and New Mexico that surround the Fish Canyon Tuff show “seagull” patterns, with elevated REE and deep negative Eu anomalies (Fig. 7). This indicates that Fish Canyon-type liquid did not erupt to form any of those rhyolites. Streck (2014) came to similar conclusions.

One way to avoid the titanite imprint on rhyolite liquid trace element patterns would be if such liquids separate from their sources before titanite begins crystallization (Glazner et al. 2008; Colombini et al. 2011). However, titanite is not uncommon in dacites and rhyolites in western North America and the Andes, areas where voluminous high-silica rhyolites are abundant (Ewart 1979; Thompson et al. 1986; Best et al. 1989; Warren et al. 1989; Nakada 1991; Wark 1991; de Silva et al. 1994; Chambefort et al. 2008). This suggests that Fish Canyon-type magmas, with both titanite and a relatively large liquid fraction, are not uncommon.

Taylor et al. (1968) and Coleman et al. (2012) found similar systematic trace-element differences between leucogranites and rhyolites. For rocks from Australia and New Zealand, Taylor et al. (1968) noted that the leucogranite compositions are consistent with fractional crystallization but that the rhyolites are not but could have been produced by partial melting. Coleman et al. (2012) suggested that crystal-liquid separation in a granodiorite magma did occur to form the leucogranites, but that the liquids were low-volume and did not entirely escape the crystal mush from which they were separated. This hypothesis accounts for both the occurrence of plutonic rocks with geochemical signatures predicted for fractionated liquids and the absence of such liquids in volcanic rocks.

5 Geochronology

5.1 Magma Flux

Hypotheses for the connection between large-volume ignimbrites and shallow plutons generally make specific predictions about the relative ages of erupted and non-erupted volumes.

We argue that the data consistently fail to support a connection between many ignimbrites and similar-age plutons. Here we make a distinction between large-volume (i.e., $>500 \text{ km}^3$) eruptions and smaller volume eruptions, because there are clear differences in the age systematics between large- and small-volume eruptive systems (Mills and Coleman 2013; Frazer et al. 2014; Caricchi et al. 2014b). Whereas a direct connection between small-volume systems and shallow plutonic rocks is supported by geochronologic data, a connection between large-volume eruptions and large volume plutons is tenuous and has yet to be supported by any high-precision geochronologic data.

The distinction between small- and large-volume systems is evident on plots comparing magma fluxes of volcanic and plutonic systems estimated from U/Pb zircon geochronologic data and geologic mapping (Fig. 8). Below $\sim 500 \text{ km}^3$ both volcanic and plutonic rocks suggest fluxes $<0.005 \text{ km}^3/\text{a}$. For total volumes above 500 km^3 , there is a distinct divergence in flux estimates for volcanic and plutonic systems; the estimated flux for volcanic rocks increases steadily to values $>0.01 \text{ km}^3/\text{a}$, whereas the flux for large plutons remains essentially constant.

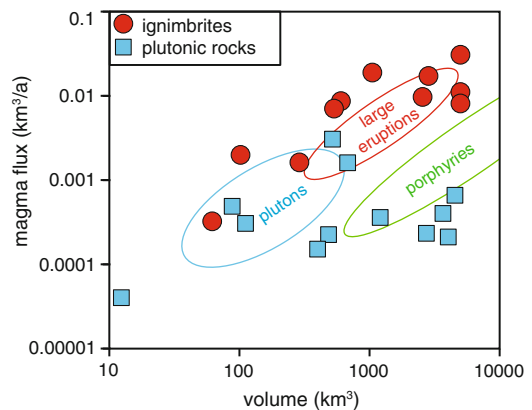


Fig. 8 Compilation, modified from Mills and Coleman (2013) and Frazer et al. (2014), of magma volume and flux estimates for intermediate and felsic plutons and ignimbrites. Ellipses labeled “plutons”, “large eruptions” and “porphyries” are derived from zircon growth modeling results (Caricchi et al. 2014b). Note the divergence of plutonic and ignimbrite systems for large-volume systems

These data are consistent with thermal models (Annen 2009; Gelman et al. 2013) that show a flux of $>0.005 \text{ km}^3/\text{a}$ ($5000 \text{ km}^3/\text{million years}$) as something of a tipping point for accumulating enough magma to generate a large-volume eruption, and are consistent with the rock record. When magmas accumulate in the shallow crust at fluxes greater than $0.005 \text{ km}^3/\text{a}$, they erupt as rare, catastrophic events (Caricchi et al. 2014a). At lower fluxes they are trapped in the crust, forming plutons and producing smaller volcanic eruptions. If the flux is sustained for long enough times (millions of years), large volume plutons may be constructed.

The disconnect between large-volume plutons and erupted rocks is also evident when examining

the zircon systematics of the two (Fig. 9). Zircon U/Pb geochronologic data for plutons with volume estimates greater than 1000 km^3 span many Ma, including for example, the Tuolumne, John Muir, Mount Whitney and Mount Givens suites of the Sierra Nevada batholith in California (Coleman et al. 2004; Davis et al. 2012; Frazer et al. 2014) and the Mount Stuart batholith of the Cascades (Matzel et al. 2006). In sharp contrast, detailed studies of the U/Pb zircon systematics of the Fish Canyon ($\sim 5000 \text{ km}^3$; Lipman 2000) and Bishop ($\sim 700 \text{ km}^3$; Hildreth 1979) Tuffs reveal extremely narrow periods of time for zircon growth (Schmitz and Bowring 2001; Simon and Reid 2005; Bachmann et al. 2007b; Crowley et al. 2007; Wotzlaw et al. 2013). Figure 9 compares

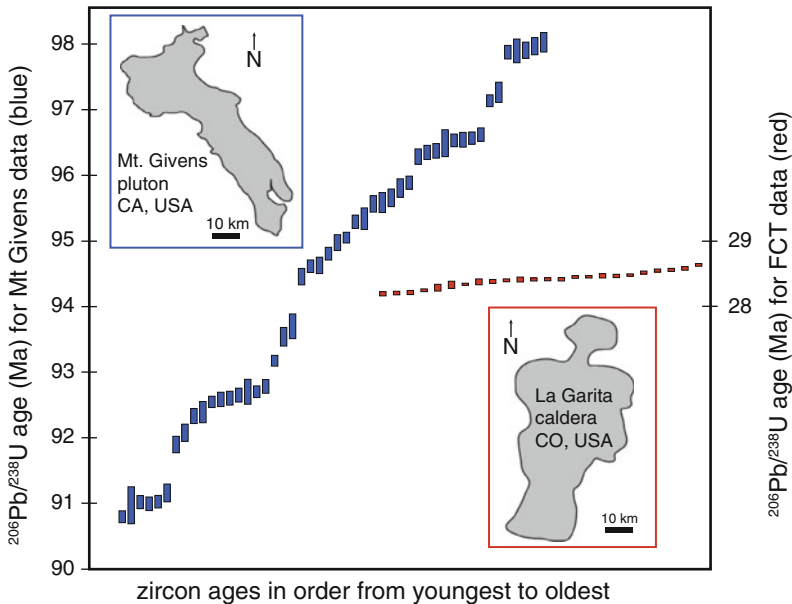


Fig. 9 Summary of all single grain U-Pb zircon analyses for the Mount Givens pluton (blue; Frazer et al. 2014)—note that several multi-grain fractions reported in this contribution are not included here) and Fish Canyon Tuff (red; Wotzlaw et al. 2013). Age is on the vertical axis. The scale for both samples is the same, but note difference in absolute age for the Mount Givens pluton (left ordinate) and Fish Canyon Tuff (right ordinate). Vertical size of symbols reflects uncertainty of the data. Because a significant component of the uncertainties is a function of age, symbols are larger for the older Mount Givens pluton. Horizontal axis sequences analyses from youngest to oldest for one Fish Canyon Tuff sample and 12 Mount Givens samples distributed throughout the

intrusion. Insets show the map outline for the Mount Givens pluton and the La Garita caldera (the source of the Fish Canyon Tuff) at the same scale. These two rock units were selected for comparison because they are comparable compositionally and likely comparable volumetrically. Note that the Mount Givens pluton preserves evidence for zircon growth over orders of magnitude longer times than the Fish Canyon Tuff. This suggests either much lower magma fluxes for the Mount Givens pluton, or very efficient zircon resorption in the Fish Canyon Tuff. The latter interpretation, however, is contradicted by the preservation of zircon interpreted to have crystallized early in the evolution of the Fish Canyon magma body. See text for more discussion

single crystal zircon U/Pb data from plutonic and volcanic rocks with similar compositions and estimated volumes: the Mount Givens Granodiorite and Fish Canyon Tuff. We specifically chose the Mount Givens pluton for comparison because it is cited as potentially analogous to an unerupted Fish Canyon magma body (Bachmann et al. 2007a; Lipman 2007). If all analyses are included, the total range of ages determined for the Mount Givens Granodiorite is > 8 Ma (Frazer et al. 2014), whereas the total range for the Fish Canyon Tuff is 440 ka, about 20 times smaller (Wotzlaw et al. 2013). The data from dated plutonic and volcanic rocks are supported by modeling of timescales of zircon growth (Caricchi et al. 2014b).

In recognition of this conundrum, several authors have speculated that resorption of zircons that grew over millions of years occurred during rejuvenation of the mush immediately prior to eruption (e.g., Barker et al. 2014). However, modeling of zircon resorption demonstrates that the process is slow and cannot occur on the timescales estimated for rejuvenation (Frazer et al. 2013). Furthermore, the preservation of inherited grains and multi-aged antecrysts in ignimbrites offers direct evidence against the efficiency of resorption (Frazer et al. 2013; Wotzlaw et al. 2013).

5.2 Geochronologic Tests for the Link Between Plutons and Large-Volume Ignimbrites

The idea that large-volume eruptions are directly connected to large-volume plutons is predicated on the common spatial and temporal association of the two (Smith 1960; Lipman 2007). This spatial relationship leads to estimation of intrusive: extrusive rock ratios ranging from 10:1 to 2:1 (Smith and Shaw 1979; White et al. 2006). However, such estimates are made with no understanding of the ages of geophysical anomalies (notoriously difficult to date) interpreted to reflect intrusive rocks, or exposed intrusive rocks associated with the volcanic rocks. Without precise ages, it is impossible to establish a direct

genetic link between the two. Whereas it is clear that large-volume ignimbrites are associated with volcanic/plutonic fields that have histories that pre- and post-date ignimbrite eruption (Hildreth 2004; Lipman 2007), a spatial and broad temporal correlation are not sufficient to infer a direct genetic link.

Although it is evident that plutonic systems record a longer history of magma system evolution than the snapshots provided by volcanic rocks, a clear temporal link between the two should include simultaneous growth of zircon in directly related plutonic and volcanic rocks. A small number of studies have focused on dating of spatially associated extrusive and intrusive rocks in an effort to test genetic links, but the scarcity of preserved volcanic-plutonic associations makes this difficult and many such studies lack the precision needed for a true test. In order to achieve age resolution of <100 ka, thermal ionization mass spectrometry (TIMS) on chemically abraded zircons from young (<100 Ma) samples is necessary. Less precise U/Pb methods (ion microprobe and laser-ablation ICPMS) are generally an order of magnitude less precise. For example, Barth et al. (2012) found evidence for coeval volcanism and plutonism in the Mesozoic Sierran arc, but uncertainties on their ages of ± 2 Ma (or more) are far too large to make a definite genetic link between systems that are known to crystallize zircon on timescales an order of magnitude shorter. Zimmerer and McIntosh (2013) obtained laser-ablation ICPMS geochronologic data for volcanic and plutonic rocks of the Oligocene Organ caldera of New Mexico and also concluded that extrusive and intrusive rocks were coeval within ~ 600 ka. More precise TIMS data ($\pm \sim 60$ ka) demonstrate that the assembly of the plutonic rocks dominantly post-dates eruption of the ignimbrite (Wootton 2014; Rioux et al., in review).

At two locations in the southern Rocky Mountain volcanic field (Mt. Princeton magmatic center in Colorado and the Questa-Latir system in New Mexico), precise dating of presumably cogenetic volcanic and plutonic rocks revealed that the only plutonic material with equivalent zircon ages to the ignimbrites are small dikes

with the same chemical composition as the ignimbrite (Tappa et al. 2011; Zimmerer and McIntosh 2012; Mills and Coleman 2013). The vast majority of the plutonic material in these two locations is either older or younger than the caldera-forming ignimbrites. The Mt. Princeton batholith, which had previously been assumed to be the source of the >1000 km³ Wall Mountain Tuff (Chapin and Lowell 1979), was emplaced during a nearly 1 Ma gap in the extensive ignimbrite record from the 39 Mile volcanic field (McIntosh and Chapin 2004).

6 Closing Remarks

A relationship between volcanic and plutonic rocks has been generally accepted for over two centuries, but there is no consensus about the nature of that relationship. A key point concerns the origin of silicic volcanic rocks: are they generally produced by fractional crystallization (down-temperature) or partial melting (up-temperature)? Systematic differences between volcanic and plutonic rocks, such as the bias of volcanic rocks toward mafic compositions (Fig. 3), led to the concept of separate volcanic and plutonic rock series. Kennedy and Anderson (1938) appealed to a primary granodiorite magma produced by partial melting of the “granitic layer” of the Earth, whereas Read (1948) called on metasomatism to produce granitic rocks. Others, going back at least a century, proposed that silicic magmas form by separation of liquids from crystallizing magmas. The experimental work of Tuttle and Bowen (1958) is generally viewed as evidence that fractional crystallization can produce granites and rhyolites, but other experimental work and geochemical datasets point to partial melting as an alternative (Peterson and Roberts 1963; Taylor et al. 1968; Sisson et al. 2005; Frey et al. 2014).

The past decade has seen revitalization and widespread acceptance of the hypothesis, based largely on field association and theory, that rhyolites are produced by shallow separation of high-silica liquid from a crystal mush that freezes as an intermediate pluton (Bachmann and Bergantz 2004; Hildreth 2004). According to this

hypothesis, “low-pressure cumulates (or melting residues) must exist in the shallow crust, weighing in favor of the cumulatic nature of many granitoids” (Gualda and Ghiorso 2013).

This hypothesis makes specific predictions about the geochemical and temporal connections between the separated liquids and residual plutons, and our analysis shows that these predictions are generally not met. The geochemical patterns in Figs. 4 and 5 are striking in their similarity, and doubly so because where differences are apparent the plutonic dataset is more “volcanic” than the volcanic dataset (e.g., Ba, Zr, and Eu in Fig. 4). Furthermore, precise geochronologic data commonly show that ignimbrites and the plutons thought to have been left behind by them are of different ages.

In a review of the plutonic-volcanic connection, de Silva and Gosnold (2007) used as a starting point “the canon that large silicic volcanic fields are the surface manifestation of batholith formation at depth.” Canon can mean “a law, rule, edict,” “a general rule, fundamental principle, aphorism, or axiom,” or “a rule, law, or decree of the Church” (OED Online 2015). We maintain that the true relationships between volcanic and plutonic rocks will be discovered not by adhering to axioms or edicts, but by well-designed experiments. The roughly 20,000,000 geochemical values in Earth-Chem provide ample grist for hypothesis testing, and we have attempted that here.

Like stopping, shallow separation of liquid from cumulate granitoid material to form rhyolite is a logical and sensible idea, yet fails many of the tests applied to it. The genetic relationships between volcanic and plutonic rocks remain a subject of intense research, debate, and significance.

Acknowledgments This work is the product of discussions and debates with colleagues and students too numerous to summarize here. Several, however, warrant special mention. Most importantly, John Bartley has been instrumental in the development of non-axiomatic thinking regarding plutons and pluton-volcano connections. Vigorous discussions with Peter Lipman, Bill McIntosh, Matt Zimmerer, Lang Farmer, and Calvin Miller have significantly influenced our ideas over the past decade. Reviews by Sergio Rocchi and Eric Christiansen helped us to clarify many of the points in the paper and to avoid too many mistakes. This work has been supported by

grants to our students from the University of North Carolina Department of Geological Sciences' Martin Fund, Sigma Xi, the Geological Society of America, and the University of California's White Mountain Research Station. Funding from the National Science Foundation includes awards EAR-0336070, 0538129, 1050215, 1052813, and 1232608. We gratefully acknowledge generous cooperation and logistical support from the U.S. National Park Service and U.S. Geological Survey, in particular Jan van Wagtenonk, Peggy Moore, and Greg Stock. We also thank the staff of the White Mountain Research Center for their generous assistance during field work.

References

- Alidibirov M, Dingwell DB (1996) Magma fragmentation by rapid decompression. *Nature* 380(6570):146–148. doi:[10.1038/380146a0](https://doi.org/10.1038/380146a0)
- Annen C (2009) From plutons to magma chambers: thermal constraints on the accumulation of eruptible silicic magma in the upper crust. *Earth Planet Sci Lett* 284:409–416. doi:[10.1016/j.epsl.2009.05.006](https://doi.org/10.1016/j.epsl.2009.05.006)
- Bachl CA, Miller CF, Miller JS, Faulds JE (2001) Construction of a pluton; evidence from an exposed cross section of the searchlight pluton, Eldorado Mountains, Nevada. *Geol Soc Am Bull* 113:1213–1228
- Bachmann O, Bergantz GW (2004) On the origin of crystal-poor rhyolites: extracted from batholithic crystal mushes. *J Petrol* 45:1565–1582
- Bachmann O, Bergantz GW (2008) Rhyolites and their source mushes across tectonic settings. *J Petrol* 49:2277–2285
- Bachmann O, Dungan MA, Bussy F (2005) Insights into shallow magmatic processes in large silicic magma bodies; the trace element record in the Fish Canyon magma body, Colorado. *Contrib Miner Petrol* 149:338–349
- Bachmann O, Dungan MA, Lipman PW (2000) Voluminous lava-like precursor to a major ash-flow tuff; low-column pyroclastic eruption of the Pagosa Peak Dacite, San Juan volcanic field, Colorado. *J Volcanol Geoth Res* 98:153–171
- Bachmann O, Dungan MA, Lipman PW (2002) The Fish Canyon magma body, San Juan volcanic field, Colorado; rejuvenation and eruption of an upper-crustal batholith. *J Petrol* 43:1469–1503
- Bachmann O, Miller CF, de Silva SL (2007a) The volcanic-plutonic connection as a stage for understanding crustal magmatism. *J Volcanol Geoth Res* 167:1–23. doi:[10.1016/j.jvolgeores.2007.08.002](https://doi.org/10.1016/j.jvolgeores.2007.08.002)
- Bachmann O, Oberli F, Dungan MA, Meier M, Mundil R, Fischer H (2007b) $^{40}\text{Ar}/^{39}\text{Ar}$ and U/Pb dating of the Fish Canyon magmatic system, San Juan volcanic field, Colorado; evidence for an extended crystallization history. *Chemical Geology* 236:134–166. doi:[10.1016/j.chemgeo.2006.09.005](https://doi.org/10.1016/j.chemgeo.2006.09.005)
- Bailey RA, Dalrymple GB, Lanphere MA (1976) Volcanism, structure, and geochronology of Long Valley caldera, Mono County, California. *J Geophys Res* 81:725–744
- Barker SJ, Wilson CJN, Smith EGC, Charlier BLA, Wooden JL, Hiess J, Ireland TR (2014) Post-supereruption magmatic reconstruction of Taupo Volcano (New Zealand), as reflected in zircon ages and trace elements. *J Petrol* 55:1511–1533
- Barth AP, Feilen ADG, Yager SL, Douglas Wooden JL, Riggs NR, Walker JD (2012) Petrogenetic connections between ash-flow tuffs and a granodioritic to granitic intrusive suite in the Sierra Nevada arc, California. *Geosphere* 8:250–264. doi:[10.1130/GES00737.1](https://doi.org/10.1130/GES00737.1)
- Bartley JM, Coleman DS, Glazner AF (2008) Incremental pluton emplacement by magmatic crack-seal. *Trans R Soc Edinb: Earth Sci* 97:383–396
- Bateman PC (1992) Plutonism in the central part of the Sierra Nevada batholith. US Geological Survey Professional Paper, California 1483
- Bateman PC, Chappell BW (1979) Crystallization, fractionation, and solidification of the Tuolumne intrusive series, Yosemite National Park, California. *Geol Soc Am Bull* 90:465–482
- Best MG, Christiansen EH, Blank HR Jr (1989) Oligocene caldera complex and calc-alkaline tuffs and lavas of the Indian Peak volcanic field, Nevada and Utah. *Geol Soc Am Bull* 101:1076–1090
- Boudreau A (2011) The evolution of texture and layering in layered intrusions. *Int Geol Rev* 53:330–353. doi:[10.1080/00206814.2010.496163](https://doi.org/10.1080/00206814.2010.496163)
- Bowen NL (1915) The crystallization of haplobasaltic, haplodioritic, and related magmas. *Am J Sci* 40:161–185
- Branch CD (1967) Genesis of magma for acid calc-alkaline volcano-plutonic formations. *Tectonophysics* 4:83–100
- Buddington AF (1959) Granite emplacement with special reference to North America. *Geol Soc Am Bull* 70:671–747
- Buma G, Frey FA, Wones DR (1971) New England granites; trace element evidence regarding their origin and differentiation. *Contrib Miner Petrol* 31:300–320
- Caricchi L, Annen C, Blundy J, Simpson G, Pinel V (2014a) Frequency and magnitude of volcanic eruptions controlled by magma injection and buoyancy. *Nat Geosci* 7:126–130. doi:[10.1038/NNGEO2041](https://doi.org/10.1038/NNGEO2041)
- Caricchi L, Simpson G, Schaltegger U (2014b) Zircons reveal magma fluxes in the Earth's crust. *Nature* 511(7510):457–461. doi:[10.1038/nature13532](https://doi.org/10.1038/nature13532)
- Chambefort I, Dilles JH, Kent AJR (2008) Anhydrite-bearing andesite and dacite as a source for sulfur in magmatic-hydrothermal mineral deposits. *Geology* 36:719–722. doi:[10.1130/G24920A.1](https://doi.org/10.1130/G24920A.1)
- Chapin CE, Lowell GR (1979) Primary and secondary flow structures in ash-flow tuffs of the Gribbles Run paleovalley, central Colorado. *Spec Pap Geol Soc Am* 180:137–154. doi:[10.1130/SPE180-p137](https://doi.org/10.1130/SPE180-p137)
- Coleman DS, Bartley JM, Glazner AF, Pardue MJ (2012) Is chemical zonation in plutonic rocks driven by

- changes in source magma composition or shallow-crustal differentiation? *Geosphere* 8:1568–1587. doi:[10.1130/GES00798.1](https://doi.org/10.1130/GES00798.1)
- Coleman DS, Gray W, Glazner AF (2004) Rethinking the emplacement and evolution of zoned plutons: geochronologic evidence for incremental assembly of the Tuolumne Intrusive Suite, California. *Geology* 32:433–436
- Colombini LL, Miller CF, Gualda GAR, Wooden JL, Miller JS (2011) Spinel and zircon in the Highland Range volcanic sequence (Miocene, southern Nevada, USA): elemental partitioning, phase relations, and influence on evolution of silicic magma. *Mineral Petrol* 102:29–50. doi:[10.1007/s00710-011-0177-3](https://doi.org/10.1007/s00710-011-0177-3)
- Crowley JL, Schoene B, Bowring SA (2007) U-Pb dating of zircon in the Bishop Tuff at the millennial scale. *Geology* 35:1123–1126. doi:[10.1130/G24017A.1](https://doi.org/10.1130/G24017A.1)
- Daly RA (1914) *Igneous rocks and their origin*. McGraw-Hill, New York
- Daly RA (1917) The geology of Pigeon Point, Minnesota. *Am J Sci* 43:423–448
- Daly RA (1928) Bushveld Igneous Complex of the Transvaal. *Geol Soc Am Bull* 39:703–768. doi:[10.1130/GSAB-39-703](https://doi.org/10.1130/GSAB-39-703)
- Daly RA (1933) *Igneous Rocks and the Depths of the Earth*. McGraw-Hill, New York
- Darwin C (1844) Geological observations on the volcanic islands, visited during the voyage of H.M.S. Beagle: together with some brief notices on the geology of Australia and the Cape of Good Hope. Smith, Elder, London
- Davis JW, Coleman DS, Gracely JT, Gaschnig R, Stearns M (2012) Magma accumulation rates and thermal histories of plutons of the Sierra Nevada Batholith, CA. *Contrib Miner Petrol* 163:449–465. doi:[10.1007/s00410-011-0683-7](https://doi.org/10.1007/s00410-011-0683-7)
- de Silva SL, Gosnold WD (2007) Episodic construction of batholiths: insights from the spatiotemporal development of an ignimbrite flare-up. *J Volcanol Geoth Res* 167:320–335
- de Silva SL, Self S, Francis PW, Drake RE, Ramirez RC (1994) Effusive silicic volcanism in the Central Andes; the Chao Dacite and other young lavas of the Altiplano-Puna volcanic complex. *J Geophys Res, B, Solid Earth Planets* 99:17805–817825
- DePaolo DJ (1981) Trace element and isotopic effects of combined wallrock assimilation and fractional crystallization. *Earth Planet Sci Lett* 53:189–202
- du Bray EA, Bacon CR, John DA, Wooden JL, Mazdab FK (2011) Episodic intrusion, internal differentiation, and hydrothermal alteration of the Miocene Tatoosh intrusive suite south of Mount Rainier, Washington. *Geol Soc Am Bull* 123:534–561. doi:[10.1130/b30095.1](https://doi.org/10.1130/b30095.1)
- Edwards BR, Karson J, Wysocki R, Lev E, Bindeman I, Kueppers U (2013) Insights on lava-ice/snow interactions from large-scale basaltic melt experiments. *Geology* 41:851–854. doi:[10.1130/G34305.1](https://doi.org/10.1130/G34305.1)
- Eichelberger JC, Izbekov PE, Browne BL (2006) Bulk chemical trends at arc volcanoes are not liquid lines of descent. *Lithos* 87:135–154. doi:[10.1016/j.lithos.2005.05.006](https://doi.org/10.1016/j.lithos.2005.05.006)
- Eilers PH, Goeman JJ (2004) Enhancing scatterplots with smoothed densities. *Bioinformatics* 20:623–628. doi:[10.1093/bioinformatics/btg454](https://doi.org/10.1093/bioinformatics/btg454)
- Evans OC, Hanson GN (1993) Accessory-mineral fractionation of rare-earth element (REE) abundances in granitoid rocks. *Chemical Geology* 110:69–93. doi:[10.1016/0009-2541\(93\)90248-H](https://doi.org/10.1016/0009-2541(93)90248-H)
- Evernden JF, Kistler RW (1970) Chronology of emplacement of Mesozoic batholithic complexes in California and western Nevada. United States Geological Survey Professional Paper 623
- Ewart A (1979) A review of the mineralogy and chemistry of Tertiary-Recent dacitic, latitic, rhyolitic, and related salic volcanic rocks. In: Barker F (ed) *Trondhjemites, Dacites and Related Rocks*, pp 13–121
- Farrell J, Smith RB, Husen S, Diehl T (2014) Tomography from 26 years of seismicity revealing that the spatial extent of the Yellowstone crustal magma reservoir extends well beyond the Yellowstone caldera. *Geophys Res Lett* 41:3068–3073. doi:[10.1002/2014GL059588](https://doi.org/10.1002/2014GL059588)
- Faulds JE, Feuerbach DL, Reagan MK, Metcalf RV, Gans P, Walker JD (1995) The Mount Perkins block, northwestern Arizona: an exposed cross section of an evolving preextensional to synextensional magmatic system. *J Geophys Res* 100:15249–15266
- Frazer RE, Coleman DS, Mills RD (2014) Zircon U-Pb geochronology of the Mount Givens Granodiorite: implications for the genesis of large volumes of eruptible magma. *J Geophys Res: Solid Earth* 119:2907–2924. doi:[10.1002/2013JB010716](https://doi.org/10.1002/2013JB010716)
- Frazer RE, Mills RD, Coleman DS (2013) Can a supervolcano eruption eradicate existing zircon? *Abstr with Programs Geol Soc Am* 45:693
- Frey HM, Lange RA, Hall CM, Nelson SA, Delgado-Granados H, Mastin L, Wineberg D (2014) ⁴⁰Ar/³⁹Ar geochronology of Volcan Tepetitiltic, western Mexico: implications for the origin of zoned rhyodacite-rhyolite liquid erupted explosively from an andesite stratovolcano after a prolonged hiatus. *Bull Geol Soc Am* 126:16–30. doi:[10.1130/B30790.1](https://doi.org/10.1130/B30790.1)
- Gelman SE, Deering CD, Bachmann O, Huber C, Gutiérrez FJ (2014) Identifying the crystal graveyards remaining after large silicic eruptions. *Earth Planet Sci Lett* 403:299–306. doi:[10.1016/j.epsl.2014.07.005](https://doi.org/10.1016/j.epsl.2014.07.005)
- Gelman SE, Gutierrez FJ, Bachmann O (2013) On the longevity of large upper crustal silicic magma reservoirs. *Geology* 41:759–762. doi:[10.1130/g34241.1](https://doi.org/10.1130/g34241.1)
- Glazner AF, Bartley JM, Coleman DS, Gray W, Taylor RZ (2004) Are plutons assembled over millions of years by amalgamation from small magma chambers? *GSA Today* 14(4/5):4–11
- Glazner AF, Coleman DS, Bartley JM (2008) The tenuous connection between high-silica rhyolites and granodiorite plutons. *Geology* 36:183. doi:[10.1130/g24496a.1](https://doi.org/10.1130/g24496a.1)
- Gualda GAR, Ghiorso MS (2013) Low-pressure origin of high-silica rhyolites and granites. *J Geol* 121:537–545. doi:[10.1086/671395](https://doi.org/10.1086/671395)

- Hall J (1805) Experiments on whinstone and lava. *Trans R Soc Edinb* 5:43–75
- Hamilton W, Myers WB (1967) The nature of batholiths. U S Geological Survey Professional Paper 554-C
- Hamilton WB (1959) Yellowstone Park area, Wyoming: a possible modern lopolith. *Geol Soc Am Bull* 70:225–228. doi:[10.1130/0016-7606\(1959\)70\[225:YPAWAP\]2.0.CO;2](https://doi.org/10.1130/0016-7606(1959)70[225:YPAWAP]2.0.CO;2)
- Hanson GN (1978) The application of trace elements to the petrogenesis of igneous rocks of granitic composition. *Earth Planet Sci Lett* 38:26–43
- Harris PG, Kennedy WQ, Scarfe CM (1970) Volcanism versus plutonism—the effect of chemical composition. In: Newall G, Rast N (eds) *Mechanism of igneous intrusion, geological journal, special issue 2*. Liverpool Geological Society, Liverpool, pp 187–200
- Higgins MD (1999) Origin of megacrysts in granitoids by textural coarsening; a crystal size distribution (CSD) study of microcline in the Cathedral Peak Granodiorite, Sierra Nevada, California. In: Castro A, Fernandez C, Vigneresse JL (eds) *Understanding granites; integrating new and classical techniques*, Geological Society special publications 168. Geological Society of London, London, pp 207–219
- Hildreth W (1979) The Bishop Tuff; evidence for the origin of compositional zonation in silicic magma chambers. In: Chapin CE, Elston WE (eds) *Ash-Flow Tuffs, special paper—Geological Society of America, vol 180*, pp 3–75
- Hildreth W (1981) Gradients in silicic magma chambers: implications for lithospheric magmatism. *J Geophys Res* 86:10153–10192
- Hildreth W (2004) Volcanological perspectives on Long Valley, Mammoth Mountain, and Mono Craters: several contiguous but discrete systems. *J Volcanol Geoth Res* 136:169–198
- Holtz F, Sato H, Lewis J, Behrens H, Nakada S (2005) Experimental petrology of the 1991–1995 Unzen dacite, Japan: part I, phase relations, phase composition and pre-eruptive conditions. *J Petrol* 46:319–337
- Huang F, Lundstrom CC, Glessner J, Ianno A, Boudreau A, Li J, Ferre EC, Marshak S, DeFrates J (2009) Chemical and isotopic fractionation of wet andesite in a temperature gradient; experiments and models suggesting a new mechanism of magma differentiation. *Geochim Cosmochim Acta* 73:729–749
- Johnson BR, Glazner AF (2010) Formation of K-feldspar megacrysts in granodioritic plutons by thermal cycling and late-stage textural coarsening. *Contrib Miner Petrol* 159:599–619. doi:[10.1007/s00410-009-0444-z](https://doi.org/10.1007/s00410-009-0444-z)
- Johnson MC, Rutherford MJ (1989) Experimentally determined conditions in the Fish Canyon Tuff, Colorado, magma chamber. *J Petrol* 30:711–737
- Kay SM, Coira B, Mpodozis C (2008) Field trip guide; Neogene evolution of the central Andean Puna Plateau and southern Central Volcanic Zone. In: Kay SM, Ramos VA (eds) *Field trip guides to the backbone of the Americas in the Southern and Central Andes: Ridge Collision, Shallow Subduction, and Plateau Uplift: Geological Society of America, vol 13*. Boulder, CO, pp 117–181
- Kennedy WQ, Anderson EM (1938) Crustal layers and the origin of magmas. *Bull Volc* 3:23–82
- Klemetti EW, Grunder AL (2008) Volcanic evolution of Volcan Aucanquilcha: a long-lived dacite volcano in the central Andes of northern Chile. *Bull Volc* 70:633–650
- Kouchi A, Sunagawa I (1983) Mixing of basaltic and dacitic magmas by forced convection. *Nature* 304:527–528
- Lackey JS, Cecil MR, Windham CJ, Frazer RE, Bindeman IN, Gehrels GE (2012) The fine gold intrusive suite; the roles of basement terranes and magma source development in the early Cretaceous Sierra Nevada Batholith. *Geosphere* 8:292–313. doi:[10.1130/GES00745.1](https://doi.org/10.1130/GES00745.1)
- Larsen ES Jr (1948) Batholith and associated rocks of Corona, Elsinore, and San Luis Rey quadrangles. *Memoir—Geological Society of America, Southern California* 29
- Lee C-TA, Morton DM (2015) High silica granites: terminal porosity and crystal settling in shallow magma chambers. *Earth Planet Sci Lett* 409:23–31. doi:[10.1016/j.epsl.2014.10.040](https://doi.org/10.1016/j.epsl.2014.10.040)
- Lipman PW (1984) The roots of ash flow calderas in western North America; windows into the tops of granitic batholiths. *J Geophys Res* 89:8801–8841. doi:[10.1029/JB089iB10p08801](https://doi.org/10.1029/JB089iB10p08801)
- Lipman PW (2000) Central San Juan caldera cluster; regional volcanic framework. *Spec Pap Geol Soc Am* 346:9–69
- Lipman PW (2007) Incremental assembly and prolonged consolidation of Cordilleran magma chambers: evidence from the Southern Rocky Mountain volcanic field. *Geosphere* 3:42–70
- Lofgren G (1980) Experimental studies on the dynamic crystallization of silicate melts. In: Hargraves RB (ed) *Physics of magmatic processes*. University Press of Princeton, New Jersey, pp 487–551
- Lundstrom CC (2009) Hypothesis for the origin of convergent margin granitoids and Earth's continental crust by thermal migration zone refining. *Geochim Cosmochim Acta* 73:5709–5729. doi:[10.1016/j.gca.2009.06.020](https://doi.org/10.1016/j.gca.2009.06.020)
- Lundstrom CC, Chakraborty P, Zambardi T (2013) Isotopic insights into the plutonic-volcanic relationship with proposal of a new eruption mechanism. *Abst with Programs Geol Soc Am* 45:692
- Lyell CS (1838) *Elements of geology*. John Murray, London
- Mahood G, Hildreth W (1983) Large partition coefficients for trace elements in high-silica rhyolites. *Geochim Cosmochim Acta* 47:11–30
- Marsh BD (1988) Crystal size distribution (CSD) in rocks and the kinetics and dynamics of crystallization; 1, theory. *Contrib Miner Petrol* 99:277–291

- Matzel JEP, Bowring SA, Miller RB (2006) Time scales of pluton construction at differing crustal levels; examples from the Mount Stuart and Tenpeak Intrusions, north Cascades, Washington. *Geol Soc Am Bull* 118:1412–1430
- McDonough WF, Sun SS (1995) The composition of the Earth. *Chemical Geology* 120:223–253
- McIntosh WC, Chapin CE (2004) Geochronology of the central Colorado volcanic field. *New Mex Bur Geol Mineral Resour Bull* 160:205–238
- Mills RD, Coleman DS (2013) Temporal and chemical connections between plutons and ignimbrites from the Mount Princeton magmatic center. *Contrib Miner Petrol* 165:961–980. doi:10.1007/s00410-012-0843-4
- Nakada S (1991) Magmatic processes in titanite-bearing dacites, central Andes of Chile and Bolivia. *Am Mineral* 76:548–560
- Nash WP, Crecraft HR (1985) Partition coefficients for trace elements in silicic magmas. *Geochim Cosmochim Acta* 49:2309–2322. doi:10.1016/0016-7037(85)90231-5
- OED Online (2015) “canon, n. 1, 2”. Oxford University Press <http://www.oed.com/view/Entry/27148?rskey=mKfKTq&result=3&isAdvanced=false>
- Ortega-Rivera A, Farrar E, Hanes JA, Archibald DA, Gastil RG, Kimbrough DL, Zentilli M, Lopez Martinez M, Feraud G, Ruffet G (1997) Chronological constraints on the thermal and tilting history of the Sierra San Pedro Martir Pluton, Baja California, Mexico, from U/Pb, ⁴⁰Ar/³⁹Ar, and fission-track geochronology. *Geol Soc Am Bull* 109:728–745. doi:10.1130/0016-7606(1997)109<0728:CCOTTA>2.3.CO;2
- Parker DF, Hodges FN, Perry A, Mitchener ME, Barnes MA, Ren M (2010) Geochemistry and petrology of late Eocene Cascade Head and Yachats Basalt and alkalic intrusions of the central Oregon Coast Range, U.S.A. *J Volcanol Geoth Res* 198:311–324. doi:10.1016/j.jvolgeores.2010.09.016
- Paterson SR, Vernon RH (1995) Bursting the bubble of ballooning plutons: a return to nested diapirs emplaced by multiple processes. *Geol Soc Am Bull* 107:1356–1380
- Perkins P (2006) Plot a smoothed histogram of bivariate data. In: Matlab File Exchange <http://www.mathworks.com/matlabcentral/fileexchange/13352-smoothhist2d>
- Peterson DW, Roberts RJ (1963) Relation between the crystal content and the chemical composition of welded tuffs. *Bull Volc* 26:113–123
- Pirsson LV (1909) *Rocks and rock minerals*. Wiley, New York
- Pitcher WS, Berger AR (1972) *The geology of Donegal: a study of granite emplacement and unroofing*. Wiley, New York
- Piwoński AJ (1968) Experimental studies of igneous rock series, central Sierra Nevada batholith, California. *J Geol* 76:548–570
- Read HH (1948) Granites and granites. *Geol Soc Am Mem* 28:1–19
- Renne PR, Tobisch OT, Saleeby JB (1993) Thermochronologic record of pluton emplacement, deformation, and exhumation at courtright shear zone, central Sierra Nevada, California. *Geology* 21:331–334
- Rioux M, Farmer GL, Bowring SA, Wooton KM, Amato JM, Coleman DS, Verplanck P (in review) The link between volcanism and plutonism in epizonal magma systems: High-precision U-Pb geochronology from the Organ Mountains caldera and batholith, New Mexico. *Contributions to Mineralogy and Petrology*
- Ross DC (1969) Descriptive petrography of three large granitic bodies in the Inyo Mountains. U S Geological Survey Professional Paper, California 601
- Rutherford MJ, Sigurdsson H, Carey S, Davis A (1985) The May 18, 1980, eruption of Mount St. Helens. I. melt composition and experimental phase equilibria. *J Geophys Res* 90:2929–2947
- Scaillot B, Evans BW (1999) The 15 June 1991 eruption of Mount Pinatubo. I. phase equilibria and pre-eruption P-T-fO₂-fH₂O conditions of the dacite magma. *J Petrol* 40:381–411
- Schmitz MD, Bowring SA (2001) U-Pb zircon and titanite systematics of the Fish Canyon Tuff; an assessment of high-precision U-Pb geochronology and its application to young volcanic rocks. *Geochim Cosmochim Acta* 65:2571–2587
- Schöpa A, Annen C (2013) The effects of magma flux variations on the formation and lifetime of large silicic magma chambers. *J Geophys Res: Solid Earth* 118:926–942. doi:10.1002/jgrb.50127
- Simon JJ, Reid MR (2005) The pace of rhyolite differentiation and storage in an “archetypical” silicic magma system, Long Valley, California. *Earth Planet Sci Lett* 235:123–140
- Sisson TW, Ratajeski K, Hankins WB, Glazner AF (2005) Voluminous granitic magmas from common basaltic sources. *Contrib Miner Petrol* 148:635–661
- Smith RL (1960) Ash flows. *Geol Soc Am Bull* 71:795–841
- Smith RL, Shaw HR (1979) *Igneous-related geothermal systems*. Geological Survey Circular, U.S. 790
- Sonehara T, Harayama S (2007) Petrology of the Nohi Rhyolite and its related granitoids: a Late Cretaceous large silicic igneous field in central Japan. *J Volcanol Geoth Res* 167:57–80
- Streck MJ (2014) Evaluation of crystal mush extraction models to explain crystal-poor rhyolites. *J Volcanol Geoth Res* 284:79–94. doi:10.1016/j.jvolgeores.2014.07.005
- Streck MJ, Grunder AL (1997) Compositional Gradients and gaps in high-silica rhyolites of the Rattlesnake Tuff, Oregon. *J Petrol* 38:133
- Tappa MJ, Coleman DS, Mills RD, Samperton KM (2011) The plutonic record of a silicic ignimbrite from the Latir volcanic field, New Mexico. *Geochem Geophys Geosyst* 12:Q10011. doi:10.1029/2011gc003700
- Tarback EJ, Lutgens FK (2008) *Earth: an introduction to physical geology*. Pearson Prentice Hall, New Jersey
- Taylor SR, Ewart A, Capp AC (1968) Leucogranites and rhyolites; trace element evidence for fractional crystallisation and partial melting. *Lithos* 1:179–186

- Thompson RA, Dungan MA, Lipman PW, Hildreth W, Grove TL (1986) Multiple differentiation processes in early-rift calc-alkaline volcanics, northern Rio Grande Rift, New Mexico. *J Geophys Res* 91:6046–6058. doi:[10.1029/JB091iB06p06046](https://doi.org/10.1029/JB091iB06p06046)
- Tuttle OF, Bowen NL (1958) Origin of granite in the light of experimental studies in the system $\text{NaAlSi}_3\text{O}_8$ - KAlSi_3O_8 - SiO_2 - H_2O . Geological Society of America Memoir 74
- Wark DA (1991) Oligocene ash flow volcanism, northern Sierra Madre Occidental; role of mafic and intermediate-composition magmas in rhyolite genesis. *J Geophys Res* 96(13–13):411. doi:[10.1029/90JB02666](https://doi.org/10.1029/90JB02666)
- Warren RG, Byers FM Jr, Broxton DE, Freeman SH, Hagan RC (1989) Phenocryst abundances and glass and phenocryst compositions as indicators of magmatic environments of large-volume ash flow sheets in southwestern Nevada. *J Geophys Res* 94:5987–6020. doi:[10.1029/JB094iB05p05987](https://doi.org/10.1029/JB094iB05p05987)
- White SM, Crisp JA, Spera FJ (2006) Long-term volumetric eruption rates and magma budgets. *Geochem Geophys Geosyst* 7(3). doi:[10.1029/2005gc001002](https://doi.org/10.1029/2005gc001002)
- Whitney JA (1988) The origin of granite: the role and source of water in the evolution of granitic magmas. *Geol Soc Am Bull* 100:1886–1897
- Wootton KM (2014) Organ Needle Pluton, New Mexico: incrementally emplaced from deep crustal sources. OCLC Number: 889066567 In: UNC electronic theses and dissertations collection. University of North Carolina at Chapel Hill, Carolina
- Wotzlaw J-F, Schaltegger U, Frick DA, Dungan MA, Gerdes A, Guenther D (2013) Tracking the evolution of large-volume silicic magma reservoirs from assembly to supereruption. *Geology* 41:867–870. doi:[10.1130/G34366.1](https://doi.org/10.1130/G34366.1)
- Yoder HS Jr (1976) Generation of Basaltic Magma. National Academy of Sciences, Washington, D. C
- Zambardi T, Lundstrom CC, Li X, McCurry M (2014) Fe and Si isotope variations at Cedar Butte Volcano; insight into magmatic differentiation. *Earth Planet Sci Lett* 405:169–179. doi:[10.1016/j.epsl.2014.08.020](https://doi.org/10.1016/j.epsl.2014.08.020)
- Zimmerer MJ, McIntosh WC (2012) The geochronology of volcanic and plutonic rocks at the Questa caldera: constraints on the origin of caldera-related silicic magmas. *Geol Soc Am Bull* 124:1394–1408. doi:[10.1130/B30544.1](https://doi.org/10.1130/B30544.1)
- Zimmerer MJ, McIntosh WC (2013) Geochronologic evidence of upper-crustal in situ differentiation: Silicic magmatism at the Organ caldera complex, New Mexico. *Geosphere* 9:155–169

Structures Related to the Emplacement of Shallow-Level Intrusions

David Westerman, Sergio Rocchi ,
Christoph Breitzkreuz, Carl Stevenson
and Penelope Wilson

Abstract

A systematic view of the vast nomenclature used to describe the structures of shallow-level intrusions is presented here. Structures are organised in four main groups, according to logical breaks in the timing of magma emplacement, independent of the scales of features: (1) Intrusion-related structures, formed as the magma is making space and then develops into its intrusion shape; (2) Magmatic flow-related structures, developed as magma moves with suspended crystals that are free to rotate; (3) Solid-state, flow-related structures that formed in portions of the intrusions affected by continuing flow of nearby magma, therefore considered to have a syn-magmatic, non-tectonic origin; (4) Thermal and fragmental structures, related to creation of space and impact on host materials. This scheme appears as a rational organisation, helpful in describing and interpreting the large variety of structures observed in shallow-level intrusions.

D. Westerman
Norwich University, Northfield, VT, USA

S. Rocchi (✉)
Dipartimento di Scienze della Terra, Università di
Pisa, Via S. Maria 53, Pisa, Italy
e-mail: sergio.rocchi@unipi.it

C. Breitzkreuz
TU Bergakademie, Freiberg, Germany

C. Stevenson
University of Birmingham, Birmingham, UK

P. Wilson
Kingston University, London, UK

Keywords

Magma intrusion · Magma flow · Syn-magmatic deformation · Fragmentation · Geo-logic

1 Introduction

This overview of the fabrics and structures characterizing shallow-level intrusions (SLI) is focused on tabular intrusions recognized as dykes, sills and laccoliths, and related types of bodies. At the grossest scale, shallow-level intrusive bodies are classified based on their aspect ratio and relationship to pre-existing structures in their host, and on their coherent versus clastic texture. The simplest subdivision is generally to separate dykes, with their subparallel contacts cross cutting the host fabric, from sills (*s. l.*). The latter group is further subdivided into sills (*s.s.*), laccoliths, and a host of more esoteric forms (Rocchi and Breitreuz this volume). Sills are, for the most part, defined as tabular igneous intrusions that are concordant with planar structures in the surrounding host rocks (bedding, unconformities, or cleavage) and display large length:thickness ratios. Laccoliths and lopoliths are also concordant intrusions with a convex-upwards upper contact or concave-downwards lower contact, respectively. Laccoliths are distinguished from sills by the non-linear, inelastic, large-scale deflection of roof host rocks that accompanies their emplacement, and by their generally smaller length:thickness ratios (Corry 1988).

Because bodies such as dykes, sills and laccoliths develop by magma propagating along a planar surface, either by brittle or non-brittle failure, it is useful to acknowledge the time frame within which we are concerned. This chapter focuses on the interval between the arrival of the initial magma at its propagating fracture (a time before the igneous body was there at all) and the cessation of magmatic activity with development of younger fractures due to cooling (a time after it was there completely).

This broad scope reflects the transitional role that SLI play as an interface between the hidden kingdom of Pluto below and the fiery realm of Vulcan above. Although nearly all of the features discussed here have been previously recognized and described, including in some of the earliest writings on geology, our organization and coverage of this material can provide a framework to visualize the formation of SLI through time and space.

For the most part, SLI share the characteristic of having distinctive chilled margins, a population of phenocrysts, and generally aphanitic textures in the matrix. The simplest interpretation is that generally euhedral phenocrysts formed prior to arrival at the final emplacement level (Mock et al. 2003), and that solidification of the melt phase was rapid. Exceptions include thick mafic sills that are characterized by phaneritic textures, often with evidence of layering attributed to *in situ* gravity settling (e.g.: 350–450 m-thick Basement Sill, Antarctica; Bédard et al. 2007) and, more rarely, moderately thick (ca. 50 m) rhyolitic sills (Orth and McPhie 2003).

The scales of these features range from structures consisting of sets of intrusive bodies, to shapes and sizes of individual bodies, to scales related to maps, outcrops, hand specimens, thin sections and smaller. Also included are invisible properties such as anisotropy of magnetic susceptibility and chemical zonation.

The value of understanding the physical characteristics of these shallow intrusions lies in large part with the information they can provide about their modes of formation. Often of greatest interest is the use of these characteristics to unravel directions and styles of magma flow so as to understand the growth and development of these bodies.

Major works that bring the understanding of dykes to the forefront include papers collected in proceedings from the International Dyke Conference starting as far back as 1985 (Halls and Fahrig 1987). Papers of this volume, along with volumes resulting from previous LASI conferences since the first in 2002, provide a useful collection of modern work detailing the physical geology of laccoliths, dykes and sills (Breitkreuz and Petford 2004; Rocchi et al. 2010a; Thomson and Petford 2008).

Principally, formation of all fabrics and structures featured here depends on fundamental physical parameters of the emplacing magma, such as temperature, driving pressure, viscosity, volume, ascent/emplacement rate and emplacement level, as well as yield strength and porosity of the host. Many of these parameters have been explored in other chapters of this volume.

Understanding of structures in sub-horizontal tabular intrusions starts with the generalized characteristics that have been addressed by examining expansive databases of sills and laccoliths as reported in the literature. The database of the first encyclopedic work (Corry 1988) recorded 900 laccoliths globally, 600 of which were from North America. The author extrapolated this number to infer that there were actually 5,000–10,000 laccoliths globally. This database has been expanded and diameter and thickness values have been examined, discovering the power law relation between those values (Cruden and McCaffrey 2001; McCaffrey and Petford 1997). Subsequently, an S-shaped power law matching well with plutons of all scales has been proposed (Cruden and McCaffrey 2002), and further augmented and discussed by Cruden et al. this volume. The resulting models show consistent geometric relationships of these parameters.

The multi-layered laccoliths preserved on Elba Island have provided a number of examples that support published models (Cruden and McCaffrey 2001, 2002), but also yield further understanding about the emplacement and inflation processes within such complexes (Rocchi et al. 2002) and the relationships of their geometries to those of assembled plutons (Rocchi et al. 2010b).

The range of features associated with formation of tabular SLI is very broad. During emplacement and solidification, fabrics and structures develop in different locations within the bodies (interior vs. interface), from different driving forces (magmatic flow, solid-state flow, static gravity and thermal), and at various scales (from whole intrusion scale to microscale).

SLI are characterized first by generally having large aspect ratios with overall tabular forms, and second by emplacement into the coolest portion of the crust. These conditions lead to the relatively short “lifetimes” of these bodies between onset of emplacement and complete solidification. Compared to more deep-seated plutons, SLI end up dominated by fabrics and structures directly associated with emplacement since their typical quick crystallization limits the time available to fractionate and develop features associated with *in situ* crystallization. Thus, well-preserved fabrics in SLI are helpful to better understand the early history of deeper-level plutonic complexes in which many textures are erased by prolonged internal movements and crystallization.

2 Structural Subdivisions Scheme

As with many subdivision schemes, the one presented here is fraught with the complexities of mixing description and genesis, together with space and time as they relate to the progressive growth of SLI. We have chosen to first examine structures associated with the openings and modes of magma intrusion-emplacement to build SLI (see overview in Table 1). Our second focus is on structures and fabrics directly related to the growth of the bodies as magma is moving and suspended particles are free to rotate, i.e. the magmatic flow stage (overview in Table 2). Next, we review those fabrics and structures that form after crystals can no longer rotate, but rather respond by solid-state deformation driven by ongoing magmatic processes that are exclusive of external tectonic events (Table 3). Finally, we look at features developing in response to thermal gradients and gravitational forces, as well as

Table 1 Emplacement-related structures of shallow-level intrusive bodies—Intrusion-related structures

Texture type	Description	Location	Figure	Interpretative notes	Examples	References
Steps	Steps are offsets in propagating and transgressing fractures occupied by magma	Leading edge of sills	1a	Helps reconstructing the magma propagation direction and sense	Rockall Trough (NE Atlantic), Rufisque Basin (Senegal)	Rickwood (1990), Hutton (2009), Schofield et al. (2012b)*
Bridges	Sections of wall-rock connecting wall-rock on the two sides of a sill or dyke	Across a dyke or sill	1b	Gives info on brittle propagation of magma-filled fractures	Theron Mts (Antarctica)	Schofield et al. (2012b)*, Hutton (2009)
Broken bridges	Stub of wall-rock projecting from wall-rock into a dyke or sill	In place of a former bridge	1c	Gives info on brittle propagation of magma-filled fractures	Theron Mts (Antarctica)	Hutton (2009)*, Schmiedel et al. (2015), Horsman et al. (2005)
Multiple sheeting	Apparently unique intrusion made of two or more intrusive sheets	Whole intrusion	1d	Evidence for multiple tabular magma pulses in dykes, sills, and laccoliths of any composition	Torres del Paine (Patagonia), Henry Mts (Utah), Elba Island (Tuscany)	Leuthold et al. (2013)*, Horsman et al. (2009), Farina et al. (2010), Rocchi et al. (2010b)
Internal contacts	Sharp to faint, roughly planar boundary between similar units of igneous rock, sometimes marked by planar arrangement of foreign (host) material	At the border between two igneous batches (apparently in the interior of an intrusion)	1e	Evidence for multiple magma pulses in dykes, sills, and laccoliths of any composition	Henry Mts (Utah)	Horsman et al. (2005)*
Magmatic contact	Diffuse, subplanar surface	At the border between two igneous batches (apparently in the interior of an intrusion)	1f	Evidence for short time span between successive intrusions of magma batches	Henry Mts (Utah), Elba Island (Tuscany)	de Saint-Blanquat et al. (2006)*, Farina et al. (2010); this work
Fingers	Discrete, narrow magma-filled fractures developed alongside each other	Lateral contacts between intrusion and host (commonly poorly consolidated sediments)	1g	Evidence for multiple magma batches in the form of fingers in mafic/intermediate sills	Golden Valley (Karoo), Raton Basin (Colorado)	Pollard et al. (1975), Schofield et al. (2010, 2012b)*

(continued)

Table 1 (continued)

Texture type	Description	Location	Figure	Interpretative notes	Examples	References
Boudins (apparent)	Beads or boudins as seen in cross-section	Dykes or sills	1h	Local inflation and/or collapse during or immediately following emplacement in hot country rocks	Cap de Creus (Spain)	Bons et al. (2004)*
Tongues	Bulbous geometry of the lateral termination of igneous rock layer	Sill or laccoliths	1i	Give informations on the number of magma batches and their lateral termination	Henry Mts (Utah)	Horsman et al. (2005), Morgan et al. (2008)*
Lobes	Large elongate lobes, similar to lava flow units	Large intrusions	1j	Evidence for multiple magma batches in the form of lobes in mafic/intermediate sills	Trawenagh Bay (northern Ireland)	Stevenson et al. (2007a)*
Marginal faults	High-angle faults	At the border of an intrusion	1k	Lifting of the country rock, generating a bysmalith	Henry Mts (Utah)	de Saint-Blanquat et al. (2006)*
Plumose structures	Plume-like fractures flanked by one or two fringe zones of small en échelon fractures	Joint surfaces	1l	Formed during early fracture opening by local stress at fracture tip; indicates direction and sense of fracture propagation	S Bohemia (Czech Republic)	Simón et al. (2006)*
Host foliation drag folds	Deflected foliation in the wall rock	Wall rock at the intrusion contact	1m	Flow direction and sense	Henry Mts (Utah)	Correa-Gomes et al. (2001)*
Riedel and P fractures	Fractures at high/low angle with the contact	Chilled margin of the intrusion				

*asterisk indicates the paper from which the artwork or photo in Fig. 1 is derived

marginal structures that help to provide space for magma and that result from fragmentation processes involving igneous and host materials (Table 4).

2.1 Intrusion-Related Structures

At the onset of opening to build a new SLI, the width of the opening, by definition, starts at nothing and eventually reaches a maximum. Of

course subsequent deflation is possible, as back flow in dykes following loss of driving pressure (Philpotts and Asher 1994). Modes of emplacement involve deformation of the host rocks ranging from purely brittle to purely non-brittle (Schofield et al. 2012b). In the well-lithified portion of the crust, crack propagation is the dominant mechanism by which magma advances, with stresses being concentrated at the crack tip. Steps, bridges and broken bridges (Fig. 1a, b and c) collectively constrain

Table 2 Emplacement-related structures of shallow-level intrusive bodies—Magmatic flow-related structures

Texture type	Description	Location	Figure	Interpretation	Examples	References
Linear features	Mesoscopic elongated ornamentations (irregularities) on contacts: fingers/grooves, groove molds, scour marks, cusp axes, ridges-grooves, hot slickenlines	Along intrusion-host rock contact	2a (1m)	Found in dykes of basalt to trachyte composition; lineations are parallel to flow direction	Troodos (Cyprus)	Baer and Reches (1987), Varga et al. (1998)*
Waves	Mesoscopic ornamentations on contacts: elongated, wavy irregularities and drag folds in magmatic rock	Intrusion's outer skin	2b (1m)	Formed early in intermediate to felsic sills and laccoliths; wave axes are orthogonal to flow direction	Elba Island (Tuscany), Henry Mts (Utah)	Tweto (1951); this work*
Lobelets	Mesoscopic ornamentations on contacts: dm-size lobes	Intrusion's outer skin	2c	Formed in felsic sills and laccoliths; interference of disrupting waves	Elba Island (Tuscany)	This work*
Ropes	Mesoscopic ornamentations on contacts: pahoehoe-like ropes with dm-size cross-sections	Intrusion surface	2d	Observed in felsic laccoliths; rope axes orthogonal to flow direction	Elba Island (Tuscany)	This work*
Small ropes	Mesoscopic ornamentations on contacts: pahoehoe-like ropes with cm-size cross-sections, in a series of nested parabolas	In large vesicle, close to the intrusion outer contact	2e	Formed in mafic sills and dykes by shearing of the ropes by the flow of underlying magma; symmetry axes of ropes parallel to flow direction	Holy Island—Harkess Rock (NE England)	Randall and Farmer (1970), Liss et al. (2002)*
Crystal/vesicle shape-preferred orientation (SPO) (foliation, lineation)	Parallel to sub-parallel alignment of undeformed euhedral tabular/prismatic crystals (no solid-state matrix strain) or imbricated oblate/prolate vesicles	(Stronger near contacts)	2f 2g 2h	Evidence for magma flow from visible markers (e.g. in porphyritic rocks); careful consideration of the intrusion setting is needed	Troodos (Cyprus), Henry Mts (Utah), Elba Island (Tuscany), Orciatico (Tuscany)	Paterson et al. (1989), Paterson et al. (1998)*, Vernon (2000), Liss et al. (2002)*, Horsman et al. (2005), Roni et al. (2014)

(continued)

Table 2 (continued)

Texture type	Description	Location	Figure	Interpretation	Examples	References
MME, xenoliths, auloliths trains/elongation/alignment	Elongate microgranular enclaves (crystals not deformed) or fragments of host rock/ auloliths, sometimes organized in trains, sometimes with flow foliation around them	Most common in the central part of dykes	(1m) (3d)	Evidence for magma flow from visible markers	Sandfell (Iceland)	Correa-Gomes et al. (2001)*
Flowage differentiation	Increasing abundance of phenocrysts from the border to interior of a tabular intrusion	Most common in the central part of dykes	2i	Generated by magmatic flow, that concentrates particles in the zones of highest velocity-lowest shear	Rockport (Massachusetts)	Ross (1986), Mock et al. (2003)*
Magmatic folds	Bent planes of markers already existing before the end of flow	Anywhere in the intrusion	2j	Formed late	Elba Island (Tuscany), Sandfell (Iceland)	Paterson et al. (1998), Eriksson et al. 2011; this work*
Crystallographic anisotropy; foliation, lineation	Anisotropy of magnetic susceptibility (AMS)	Anywhere in the intrusion	2k	Evidence for magma flow, also in the absence of visible markers (e.g. in microcrystalline rocks)	Henry Mts (Utah), Elba Island (Tuscany)	Horsman et al. (2005), Roni et al. (2014); this work*

* asterisk indicates the paper from which the artwork or photo in Fig. 2 is derived

the shapes of intrusions occupying the propagating and transgressing fractures, with offsets in an advancing fracture leading to steps (Rocchi et al. 2007; Schofield et al. 2012b; Thomson and Hutton 2004). Then as multiple fractures split off a master fracture in *en echelon* fashion, SLI tend to occur as segments (protolobes) with bridge structures (Fig. 1c) connecting them (Eide et al. 2017; Hutton 2009; Schofield et al. 2012a).

Features occurring at the margins of SLI often reflect geometric patterns associated with the initial emplacement along a developing fracture or fracture system. It is tempting to interpret orientations of forks, branches (apophyses) and anastomosing patterns to constrain flow direction, but such interpretations cannot generally be used reliably (Rickwood 1990). For example, although the front of an advancing intrusion may bifurcate when a new fracture develops with

subparallel orientation, reunion of those fractures along strike would result in not knowing the direction of magma movement.

Dykes can intrude as a single body or as simple sets of dykes, marked by chilled margins on each side. They can also occur as multiple dykes with subsequent intrusion along the same plane producing internal chilled margins of the younger magma. Composite dykes also occur, with distinctly different magmas intruding the same plane more or less synchronously, with or without mixing and mingling effects.

Similarly, subhorizontal sheets can be emplaced as discrete layers, with subsequent sheets above, inside or below previous emplacements (Fig. 1d) (Horsman et al. 2009; Horsman et al. this volume). Contacts between different sheets can be recognized by the occurrence of lithologic variations, chilling effects,

Table 3 Emplacement-related structures of shallow-level intrusive bodies—Solid-state flow-related structures (syn-magmatic)

Texture type	Description	Location	Figure	Interpretation	Examples	References
Large cataclastic bands	cm- to dm-thick cataclastic shear bands separating thick layers of undeformed igneous rock	Petrographic/physical boundaries (magma host-rock contact or contact between successive magma batches)	3a	Boundaries reactivated during successive magma injections	Henry Mts (Utah)	Habert and de Saint-Blanquat (2004)*, de Saint-Blanquat et al. (2006)
Brittle textures—cross section	Stretched/broken/boudinaged/crushed crystal streaks/ribbons with bookshelf structure; rotation tails; delta-shape crystals; sigma-shape crystals; cisaillement-schistosité (C-S) fabrics; recrystallized “tails”	In the chilled margin at magma host-rock contact or at the contact between successive magma batches	3b	Elongation of stretched crystals indicate flow direction at the magma-host contact	Henry Mts (Utah), Elba Island (Tuscany)	Habert and de Saint-Blanquat (2004), Morgan et al. (2005), Horsman et al. (2005)*, de Saint-Blanquat et al. (2006), Morgan et al. (2008); this work*
Brittle textures—plan view	Lineation given by cataclastically stretched crystals	Surface contact	3c	Elongation of stretched crystals indicate flow direction at the magma-host contact	Henry Mts (Utah), Elba Island (Tuscany)	Morgan et al. (2008); this work*
Ductile textures	Bent crystals, flow bands, streaks	In the chilled margin at magma host-rock contact or at the contact between successive magma batches	3d	Indicate flow direction and, if asymmetric, also the flow sense	Henry Mts (Utah)	Horsman et al. (2005); this work*, Eriksson et al. (2011)*

* asterisk indicates the paper from which the artwork or photo in Fig. 3 is derived

Table 4 Emplacement-related structures of shallow-level intrusive bodies—Thermal and fragmental structures

Texture type	Description	Location	Figure	Interpretation	Examples	References
Chilled margin	Fine-grained to glassy intrusion's outermost zone	Intrusion border	4a	Rapid magma cooling	Scrabo (Northern Ireland), Magdeburg (Germany)	This work*
Phenocryst distribution	Differential distribution of abundance and/or size of phenocrysts (e.g. magmatic layering, crystal clusters, etc.)	Intrusion's interior (bottom)	4b	Thermal decay, gravity settling	Gulf of Ajaccio (Corsica)	Galerne and Neumann (this Volume)
Miarolitic cavity	Small cavity into which crystals protrude	Intrusion's interior	4c	Evidence for accumulation of volatiles	Henry Mts (Utah)	de Saint-Blanquat et al. (2006)*
Cooling columns	Columns oriented perpendicular to the contact surface	Country rock	4d	Effect of heating then cooling of host rock	W Magdeburg (Germany)	This work*
Intrusion contact breccia	Breccia composed of clast of the host rock(s)	Host rock at the bottom or top contact of an intrusive sheet	4e	Generated by shear strain at the contact during magma sheet emplacement	Elba Island (Tuscany)	Morgan et al. (2008), Awdankiewicz et al. (2004); this work*
Breccia dyke	Clast-supported small dykelets	In the intrusion surroundings	4f	Phreatic local explosion	Elba Island (Tuscany)	This work*
Pyroclastic dyke	Similar to tabular feeding systems of explosive eruptions	Volcanic edifices, country rock	4g	Welding of pyroclastics occur during upward flow of a dispersion of hot melt fragments and gas	W Dresden (Germany)	Winter et al. (2008); this work*
Peperite	Disintegrated magma mingled with country rock materials	Carapace around the intrusion	4h	Generated by fragmentation of magma during intrusion in wet sediments, coal and hydrous salt	Sag Hegy (Hungary), Raton Basin (Colorado), Herfa-Neurode (Germany)	Skilling et al. (2002), Awdankiewicz et al. (2004), Schofield et al. (2014); this work*
Fluidized material	(i) disaggregated grains (suspended in fluid matrix during fluidization), or (ii) thermally mobilized coal and salt	Carapace around the intrusion (fingers), sometimes connected to hydrothermal vents (4j) throughout breccia dykes (4f)	4i	Generated by (i) flash boiling of pore fluids during intrusion in wet sediments at depth < ~2 km or quick decompression by processes such as faulting, or (ii) thermal mobilization	Whin Sill (England), Witkop (Karoo), Raton Basin (Colorado), Herfa-Neurode (Germany)	Martin and Nemeth (2007) Schofield et al. (2012b)*, Schofield et al. (2014)

(continued)

Table 4 (continued)

Texture type	Description	Location	Figure	Interpretation	Examples	References
Hydrothermal vent complex	Clast-supported pipe-like structures up to several hundred metres in diameter, piercing rock layers overlying the intrusion	In the intrusion surroundings, up to significant distance	4j	Generated by phreatic explosion following heating of sedimentary pore fluids in thermal aureole around a sill, that leads to fragmentation and collapse and/or upward movement of the overlying rock fragments	Witkop (Karoo)	Jamtveit et al. (2004), Svensen et al. (2006)*, Svensen et al. (this volume)
Columnar joints	Parallel prismatic columns	Sills	4k	Generated during subsolidus cooling; columns forms orthogonal to the cooling surface	Colca (Peru), Isle Skye (Scotland)	This work*

* asterisk indicates the paper from which the artwork or photo in Fig. 4 is derived

fragmentation or cataclasis (Fig. 1e). In other instances, the time lag between intrusion of successive sheets can be short enough to prevent the oldest intrusion from cooling below its solidus, giving way to a so-called “magmatic contact” that is a diffuse, yet subplanar, surface (Fig. 1f; Farina et al. 2010; de Saint-Blanquat et al. 2006).

For horizontal sills, the classic model for the propagation of magma is by tensile fracturing in the direction of least resistance (Anderson 1938; Gilbert 1877). Based on examples from the Henry Mountains, Utah (USA), it has been proposed that, for viscous magmas, sill thickness is a function of its length, and once a sill reaches a critical aspect ratio of length to overburden thickness it will inflate vertically (Johnson and Pollard 1973; Pollard and Johnson 1973). This vertical inflation stage then may lead to the

formation of a laccolith. The maximum lateral extent of the initial sill may be controlled by the effective thickness and the elastic properties of the overburden (Jackson and Pollard 1988, 1990; Kerr and Pollard 1998; Koch et al. 1981).

Three models have been proposed for the growth of tabular intrusions such as laccoliths and sills and the expected deformation in the overlying sediments (Corry 1988; Hunt 1953). Model 1 involves a ‘bulldozer’ style of emplacement where the thickness of the intrusion is established early and the magma spreads laterally within a set thickness. This results in extensive disruption of the overlying host rocks, which fold and then unfold as the tip of the advancing magma passes. Model 2 involves simultaneous lateral and vertical growth. This would also result in a deformation history in the roof that records the passage of the magma tip,

although it would perhaps be more subdued than in Model 1. Model 3 is the opposite end-member to Model 1 and involves a distinct two-stage process where a thin protosill would propagate to a maximum lateral extent, followed by vertical inflation. This would result in minimal disruption of the roof except close to the tip where the roof will bend, flex and fold, or will fault in a piston-like vertical growth.

A theoretical model applying continuum mechanics has been developed using field observations from the Henry Mountains (Pollard 1973) to explain the formation of peripheral dykes at the tips of laccolith intrusions. In this model, flexural elastic bending of the overburden controlled the intrusion of dykes at the periphery of a laccolith. The depth of formation has been suggested to exert the main control on the development of faults at sill sheet terminations (Thomson and Schofield 2008). In this model, flexural slip folding at shallower depths would favour mechanical failure of the rock through fracture and faulting (Stearns 1978). More recently it has been proposed that a laccolith grown to a certain maximum thickness may subsequently propagate laterally due to collapse under its own weight, resulting in a larger length: thickness ratio (Bunger and Cruden 2011). Other features associated with such a collapse could include decameter-sized graben-horst-like structures on the top surface of a sill (Awdankiewicz et al. 2004).

In other emplacement modes, advance of the magma may be along discrete narrow fractures that develop alongside each other to produce a pattern of fingers (sometimes also called tongues) (Pollard et al. 1975; Stevenson et al. 2007a; Thomson and Hutton 2004) that may coalesce and preserve marginal features from chilling and/or cataclasis (Fig. 1g). Alternatively, a causal, non-brittle relationship between finger formation and fluidization of country rock has been demonstrated for the Golden Valley Sill in South Africa (Schofield et al. 2010, 2012b). Structures/shapes similar to cross sections of fingers are beads or apparent boudins that may also develop in dykes and sills as a result of local inflation and/or collapse during or immediately

following emplacement in hot country rocks (Fig. 1h) (Bons et al. 2004).

A number of features are seen at a large scale along the margins of sills and laccoliths where the intruding magma defines rounded margins, noted by various authors as tongues (common meaning) and bulbous terminations, sometimes also called lobes (Fig. 1i). These parabolic to semi-circular marginal shapes characterize the lateral and terminal contacts of sheets making up the Maiden Creek and Trachyte Mesa structures in the Henry Mountains, and are thought to reflect the high surface tension of these viscous magmas in relation to the host material that they were invading (Morgan et al. 2005).

Development of sheets from repeated parallel pulses can produce a series of elongate lobes and provide a good example of the combined distribution of these end-member conditions. The flow lobes can be envisaged in the simplest case to be similar to lava flow lobes, where in the core (or along the central axis) there is only constructional flow, and lineations are parallel to the flow direction. Moving away from the core toward the flanks, shearing plays more of a role and planar fabrics become more apparent. At the nose of the lobe only flattening occurs. The disposition of lineations and foliations can be fitted to a series of lobes in this way (Fig. 1j) (Stevenson et al. 2007a, b).

Successive sheet emplacement, leading to subhorizontal SLI such as multi-layered sills and bysmaliths, may involve initial intrusion followed by subsequent intrusion either above or below. Host rock trapped between the resulting layers can generate a sedimentary raft with lateral dimensions in excess of 1 km and thickness >100 m (Schmiedel et al. 2015). Rafts of host material can also develop during dyke formation, and scales of rafts can decrease downward to include screens of wall rock fragments.

Contrasted, but related in scale to large rafts, the arrival of a new magma batch can fail to find a way around or through the initial layer, but can make room by the development of marginal faults along which the body is lifted as a whole (Fig. 1k). For example, the Black Mesa unit in the Henry Mountains is thought to have formed

Fig. 1 Intrusion-related structures. **a** Steps—Three-dimensional sketch of stepped intrusive layer, either a sill or a dyke; cross sections on the *right* refer to the lower sketch on the *left* (Rickwood 1990; Schofield et al. 2012b). **b** Bridges—Sections of wall-rock connecting wall-rock on the two sides of a sill or dyke; cross sections refer to the lower left sketch in (a) (Hutton 2009; Rickwood 1990; Schofield et al. 2012a). **c** Broken bridges—Stubs of wall-rock remaining after merging of two portions of a dyke or sill (sill is 30 m thick; Hutton 2009; Rickwood 1990; Schofield et al. 2012a). **d** Multiple sheeting—An apparently unique intrusion is actually made of two or more intrusive sheets (Leuthold et al. 2012, 2013; Michel et al. 2008). **e** Internal contacts—Sharp to faint, roughly planar boundaries between similar units of igneous rock, detected by lithologic variations (Leuthold et al. 2013), chilling effects, fragmentation or cataclasis along contacts, or marked by planar arrangement of foreign (host) material (Horsman et al. 2005). **f** Magmatic contact—Diffuse, subplanar surface at the border between two igneous batches, apparently in the interior of an intrusion (Farina et al. 2010; de Saint-Blanquat et al. 2006). **g** Fingers—Discrete, flattened cylinders of magma developed alongside each other, eventually coalescing to form a single intrusive layer. **h** Apparent boudins—Beads or apparent boudins in a three-dimensional sketch view of the apparently boudinaged dyke (Bons et al. 2004). **i** Tongues—Bulbous terminations of igneous rock layers, Trachyte Mesa, Henry Mts, Utah (Morgan et al. 2008). **j** Lobes—Elongate lobes similar to lava flow units, making up an intrusive unit, Travenagh Bay Granite (Stevenson et al. 2007a). **k** Marginal fault—High-angle fault developed at the border of an intrusion, giving way to a bysmalith intrusion shape. **l** Plumose structure—Plume-like fractures flanked by one or two fringe zones of small *en échelon* fractures visible on joint surfaces, and formed during early fracture opening by local stress at a fracture tip; useful as an indicator of the direction and sense of fracture propagation. **m** Drag folds, Riedel and P-fractures—Deformation in the host material can be evidenced by deflection/bending/fracturing of the host foliation. Each sketch/picture is after the work indicated by an asterisk in Table 1

by successive underplating of sheets, with the 1.5 km diameter mass rising on an average of 22 mm/year by movement on marginal faults (de Saint-Blanquat et al. 2006).

Under conditions when tensile fractures migrate by brittle failure in a rigid host material, plumose structures (Fig. 1l) may develop with associated hackle steps and their offsets. These feather-like patterns of ridges and grooves expand outward on the fracture surface in the direction of fracture development, and the tips of the ‘feathers’ point in the direction of crack propagation (Simón et al. 2006).

A wide variety of localized brittle fracture and faulting systems are associated with intrusive contacts, as would be expected when the crust must make room for new material. Magmas in most SLI arrive with substantial driving pressure, and the units are thickened as more and more magma arrives. These conditions would predictably create transpressive stresses at the contacts, explaining the bends in truncated host foliation, as well as development of Riedel and P fractures (Fig. 1m) (Correa-Gomes et al. 2001). Well-described examples include the Trachyte Mesa intrusion where conjugate sets of high-angle faults with minor offset are cut by *en-echelon* shear fractures (Morgan et al. 2008). More recently, detailed study of deformation

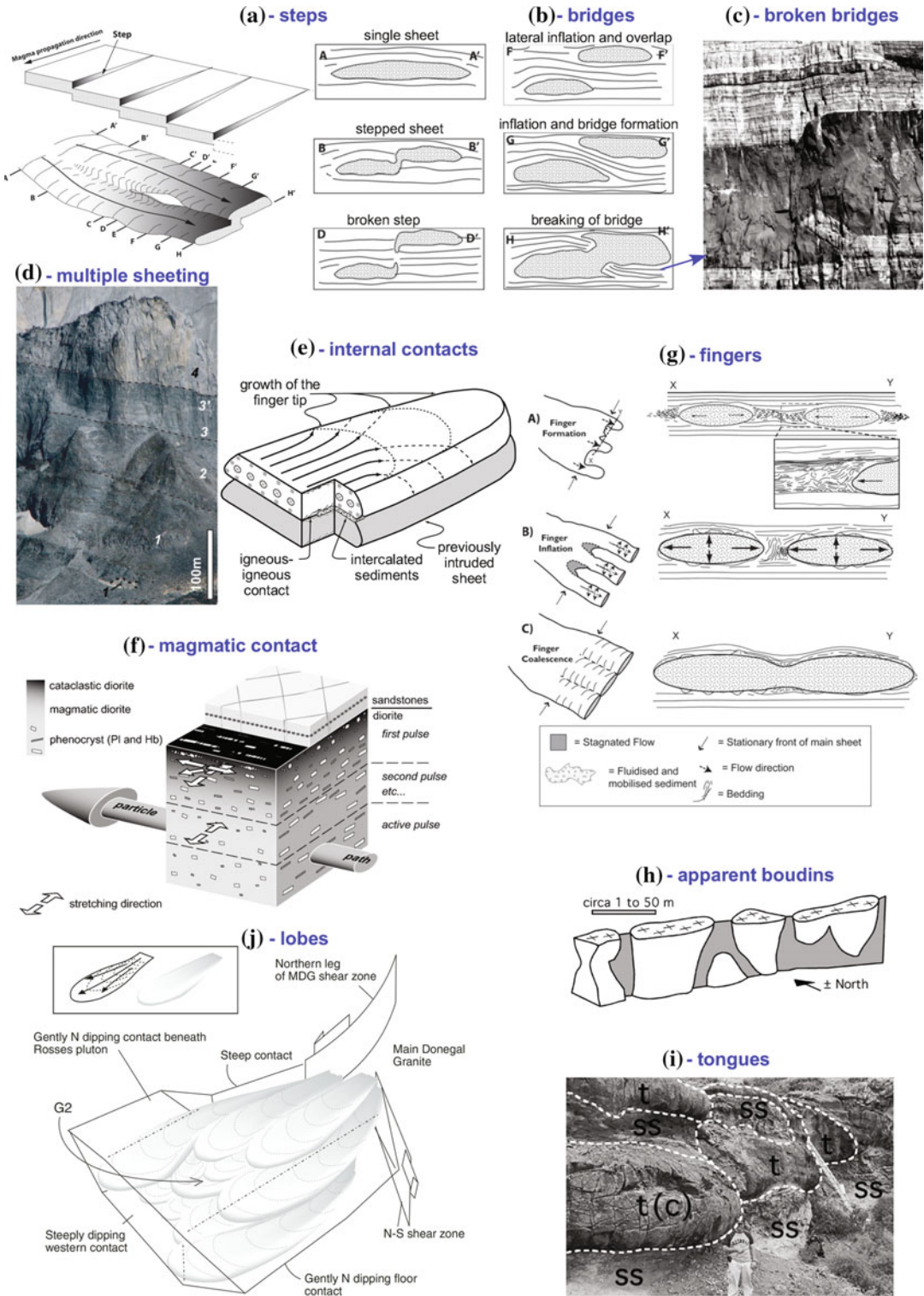
bands, faults and tensile joints during three phases of deformation of country rock surrounding the Trachyte Mesa intrusion have constrained a multi-stage model of emplacement (Wilson et al. 2016). Very similar collections of features are preserved on Elba Island in shoreline exposures at the southern edge of a laccolith (Roni et al. 2014) where cataclastic chilled margins and associated breccia are faulted by sprays of low-offset reverse faults.

2.2 Magmatic Flow-Related Structures

Magmatic flow-related structures result from magmatic flow under conditions where particles can rotate freely in response to directed stress, owing to a sufficient amount of melt available in the system (Vernon 2000). Their recognition can be based on orientation and distribution of readily observable features (i.e. phenocrysts, vesicles, inclusions) or on less tangible characteristics (i.e. AMS, microtextures; Bouchez 1997; Mock and Jerram 2005; Mock et al. 2003).

2.2.1 Surface Structures

Although dykes, sills and laccoliths are, by definition, tabular and sheet-like, detailed



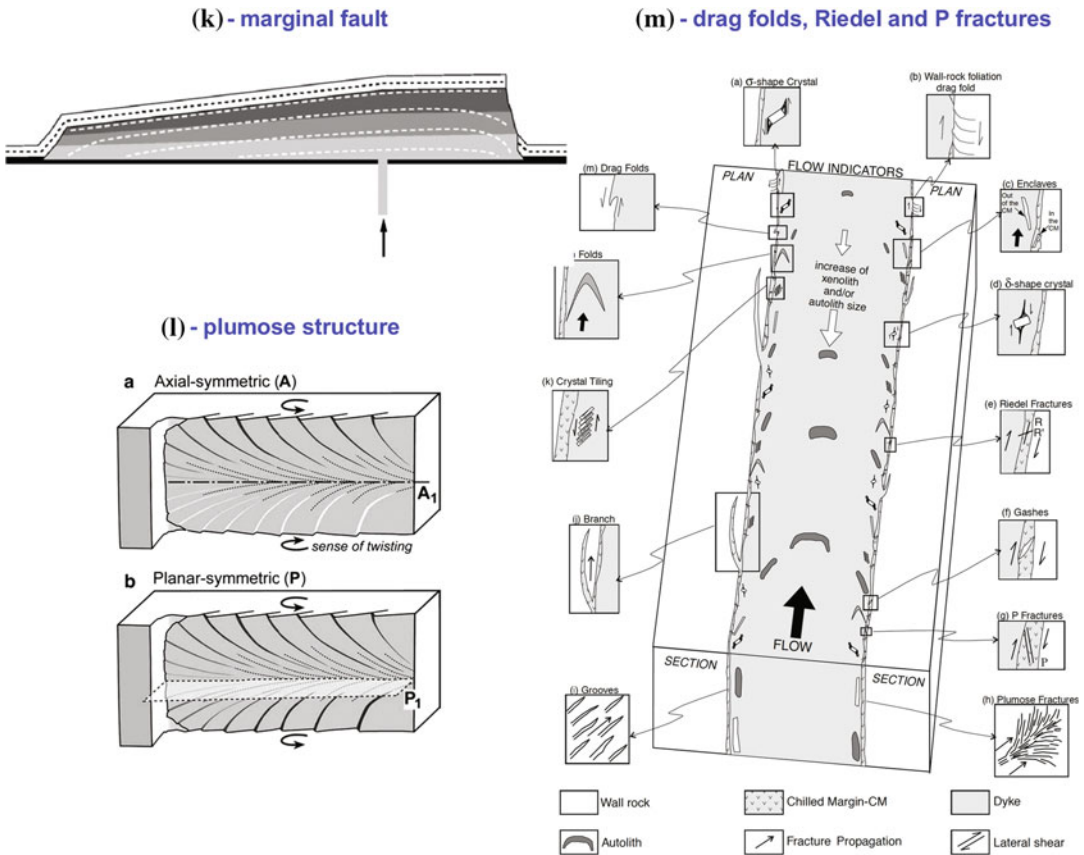


Fig. 1 (continued)

examination of their contact surfaces occasionally shows ornamentation such as raised or indented linear features (Fig. 2a; see also Fig. 11). A number of these parallel linear features are attributed to flow along their alignment (Rickwood 1990; Varga et al. 1998). A group of mesoscopic structures seen most often as flat-topped ridges separated by grooves and termed hot slickenlines are thought to form in the chilled margin as magma moves past irregularities in the wall rock surface with resulting alignment parallel to magma flow (Varga et al. 1998). Earlier workers have described cusps and buds (Pollard et al. 1975), flow lineations (Walker 1987), scour marks (Smith 1987), and fingers (obsolete meaning), grooves and groove molds (Baer and Reches 1987), all thought to form in the direction of flow even if interpretations of formation vary between authors.

An opposing set of linear structures, referred to here as waves and waveforms, also can be found on intrusive surfaces, but aligned at right angles to flow (Fig. 2b). The term ‘wave’ is here used to describe the shape of these structures, but is in no way implying that they ever actively ‘waved’ other than during their in situ growth as standing stationary waveforms. Previous works have shown that shear forces along the intrusive contact can extend into the host, generating asymmetric drag folds of the contact itself (Fig. 11; Correa-Gomes et al. 2001). Reported examples (Rickwood 1990) include: (i) crenulations seen as “microscopic wrinkles to folds a few feet high” on chilled contact surfaces in the Pando porphyry in Colorado (Tweto 1951), and (ii) “flow folds” (Blanchard et al. 1977), “millimetre-high wrinkles projecting out from the glassy surface” (Walker 1987), and

asymmetric folds a few millimeters high, sometimes deformed by interfolding of siltstone with igneous rock at Spanish Peaks, Colorado (Smith 1987). These folds have irregular axes but are generally perpendicular to magma flow directions and their asymmetry preserves the sense of flow. Variations in style include roundness and angularity of crests and troughs, disruption along crests so as to form more lobelets (Fig. 2c), and overrunning of crests to produce ropes (Fig. 2d) that have a distinctive pahoehoe-like appearance. These features are discussed below in greater detail in the case study of coherence of structures observed with different methods at different scales. Much smaller features also attributed to drag in the shearing margin of intrusions occur as ropy structures on the lower walls of large, flattened vesicles in basalt of the Whin Sill in northern England (Fig. 2e; Liss et al. 2002). These have been shown to form with their wave crests perpendicular to flow, and the structures are attributed to shearing of the chilled ductile rind of the vesicles by the underlying magma flow. Similar structures are reported nearby on Holy Island (Liss et al. 2002; Randall and Farmer 1970) and on the Isle of Skye (Schofield et al. this volume).

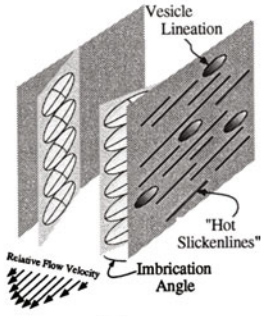
2.2.2 Internal Visibly-Oriented Features

Included in the flow-related features are those that formed during magma flow when suspended objects (crystals, vesicles, xenoliths, enclaves) were able to rotate in the weaker medium, but while the magma viscosity was sufficient to preserve the alignment (Fernandez and Laporte 1991). Most of these features represent processes and products resulting from filling, transport, and stalling of the magma moving between subparallel walls. Extensive efforts, tracing back at least into the 19th Century (Pirsson 1899), have been made to use fabrics in igneous rocks to deduce their history. Magma flow is the most commonly invoked cause, but it is important to consider other possible origins, including tectonic processes (Paterson et al. 1998), and to carefully separate magmatic flow from non-tectonic solid-state flow (Vernon 2000).

Under conditions of uniform coaxial flow of magma (plug flow), tabular and elongated suspended objects have no motivation to orient themselves preferentially. Therefore, development of a magmatic shape-preferred orientation (SPO) fabric is dependent on conditions of non-uniform flow that produce differential stress acting on such suspended objects, i.e. vesicles or crystals (Fig. 2f, g). Non-uniform flow can be thought of with respect to three end-members (Fig. 2h): (i) convergent flow as magma moves through a narrowing region and speeds up, (ii) divergent flow as magma spreads laterally with diverging flow lines and slows down, and (iii) non-coaxial flow caused by drag on a boundary surface (Paterson et al. 1998). We can attempt to look at the distribution of these conditions through space and time as a thickening dyke or sheet develops. Initial conditions are dominated by non-coaxial flow with high drag along contacts, but as a sheet thickens by continuing arrival of magma along the interior plane, marginal effects drop off away from the contacts. The stress ellipsoid generated during convergent flow is elongated parallel to the particle path, causing the long axes of suspended phenocrysts to align parallel to these particle paths, while the shortest crystal axes align parallel to the short axis of the ellipsoid. In contrast, crystal orientations resulting from divergent flow tend to be the opposite, with linear fabric forming parallel to stretching and at right angles to the particle paths, while tabular crystals produce planar fabrics representing flattening perpendicular to particle paths. Both of these conditions include stretching and flattening approaching the mode of pure shear.

Some of the easiest fabrics to see in SLI are coming from incorporated foreign material or vesicles that provide distinctive color contrast, rather than from the minerals making up the main rock. These inclusions can be subdivided into two main groups: xenoliths and mafic microgranular enclaves (MME). Xenoliths include solid rock fragments incorporated in the magma, such as cognate xenoliths or autoliths, which would include fragments of chilled margin material spalled off into the magma. Interpretation of xenolith and autolith distribution can

(a) - linear features



(b) - waves



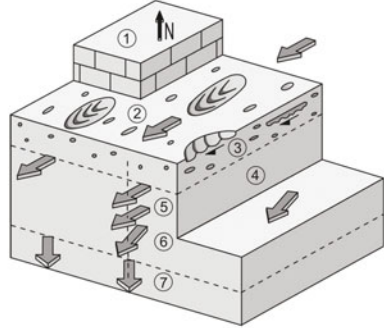
(c) - lobelets



(d) - ropes



(e) - small ropes



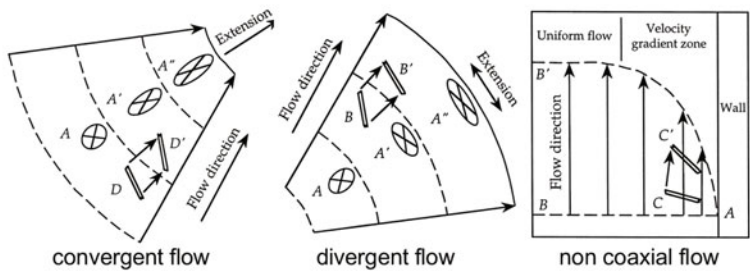
(f) - vesicle SPO



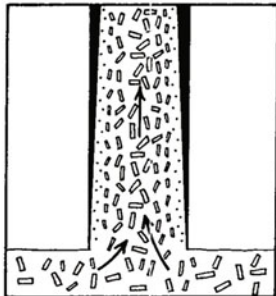
(g) - crystal SPO



(h) - crystal/vesicle SPO



(i) - flowage differentiation



(j) - magmatic folds



◀ **Fig. 2** Magmatic flow-related structures. **a** Linear features—Mesoscopic linear ornamentations on contacts, parallel to magma flow; slickenlines are reported as an example (Varga et al. 1998). **b** Waves—Mesoscopic ornamentations on contacts: elongated, wavy irregularities in the magmatic rock, elongated orthogonal to magma flow; picture from Elba island, Tuscany. **c** Lobelets—Mesoscopic ornamentations on contacts: dm-size lobes; picture from Elba island, Tuscany. **d** Ropes—Mesoscopic ornamentations on contacts: pahoehoe-like ropes with dm-size cross-sections; picture from Elba island, Tuscany. **e** Small ropes—Mesoscopic ornamentations on contacts: pahoehoe-like ropes with cm-size cross-sections, in a series of nested parabolas, typically found in large vesicles, close to the intrusion outer contact (Liss et al. 2002). **f** Vesicle SPO—Parallel to sub-parallel alignment of oblate/prolate vesicles (Liss et al. 2002). **g** Crystal SPO—Parallel to sub-parallel alignment (as a foliation or lineation) of undeformed euhedral tabular/prismatic crystals (no solid-state matrix strain; picture from Elba island, Tuscany. **h** Crystal/vesicle SPO—Alignment controlled by convergent, divergent and non-coaxial flow (Paterson et al. 1998). **i** Flowage differentiation—Variable abundance of phenocrysts, increasing from the border to interior of a tabular intrusion, commonly a dyke. **j** Magmatic folds—Bent planes of markers already existing

before the end of flow; in this picture, planes defined by dark tourmaline clots in a white aplitic intrusions are bent during the latest stages of flow (Elba Island) (Dini et al. 2007). **k** AMS-magnetisation domains. **k.1**: Single-domain and multi-domain configurations serving to minimise the external demagnetising field. **k.2**: Movement of the Bloch wall in multi-domain grains. **l** Magnetic fabric types. **l.1**: Dominantly linear magnetic fabric (similar to an L tectonite). **l.2**: Both magnetic foliation and lineation discerned. **l.3**: Magnetic foliation fabric dominant (similar to an S tectonite). **m** Foliation/lineation patterns. **m.1**: Magnetic fabric pattern of foliations (*dashed lines*) and lineations (*gray lines*) in a magma conduit. **m.2** and **m.3** Fabric patterns proposed for the termination of a sheet in either a viscous or non-brittle propagation mode (Schofield et al. 2010, 2012b) or a brittle (hydrofracture) propagation mode, respectively. **m.4**: End on and plan view magnetic foliations and lineations of a sheet intrusion. **n** AMS data and interpretations from the Trachyte Mesa Sill, Henry Mountains, Utah (Morgan et al. 2008); note plumose splaying of lineation trends. **o** AMS data and interpretations from part of the Trawenagh Bay Granite, NW Ireland (Stevenson et al. 2007a); foliation traces are shown in blue and lineation traces in red. Each sketch/picture is after the work indicated by an asterisk in Table 2

come not only from their alignment as xenolith screens or trains, but also from their tendency to decrease in size in the direction and sense of magma transport (Fig. 11; Correa-Gomes et al. 2001). All these types of xenoliths contrast with MME, which coexisted as partially molten masses within the host magma and have the potential to change shape in response to stresses in the moving magma. The petrologic characteristics of such materials provide abundant and important information beyond the scope of this work, but their spatial distribution is often compatible with the mineral fabrics described above (Tobisch et al. 1997). Distribution patterns of xenoliths and enclaves can potentially be used to determine the line along which particles/melt were moving, as well as the direction of movement where there is an imbricated arrangement of individual fragments. Interpretation of shapes and orientations of MME must be done with care due to the long-lived and variable histories of these masses (Paterson et al. 2004). Because the rheology of enclaves occurring near each other at the emplacement level often vary dramatically, it is unsafe to assume that their shapes reflect strains

associated with development of mineral fabrics. In some cases (Vernon 2000; Vernon et al. 1988), elongation of MME can be demonstrated to correspond to magmatic fabric, with rotation and alignment of plagioclase crystals but without plastic deformation of interstitial quartz. Another caution comes from the recognition that some enclave trains represent a transition from syn-magmatic mafic dykes (Barbarin 2005).

Among the most commonly used mesoscopic-scale structures observable in the field and used as evidence of magma flow are stretched and elongate vesicles (Fig. 2f). These features, presumed to be spherical at the time of inception, deform to define the orientation of the stain ellipsoid in the zone of shear, typically with attitudes corresponding to those revealed by aligned phenocrysts.

Magmatic flow features due to parallel alignment of undeformed phenocrysts and megacrysts, as well as rock fragments (xenoliths) and MME, all in the absence of solid-state matrix strain, may readily be seen at the macroscopic scale. Biotite phenocrysts and microphenocrysts, with their typical oblate shapes, generate a

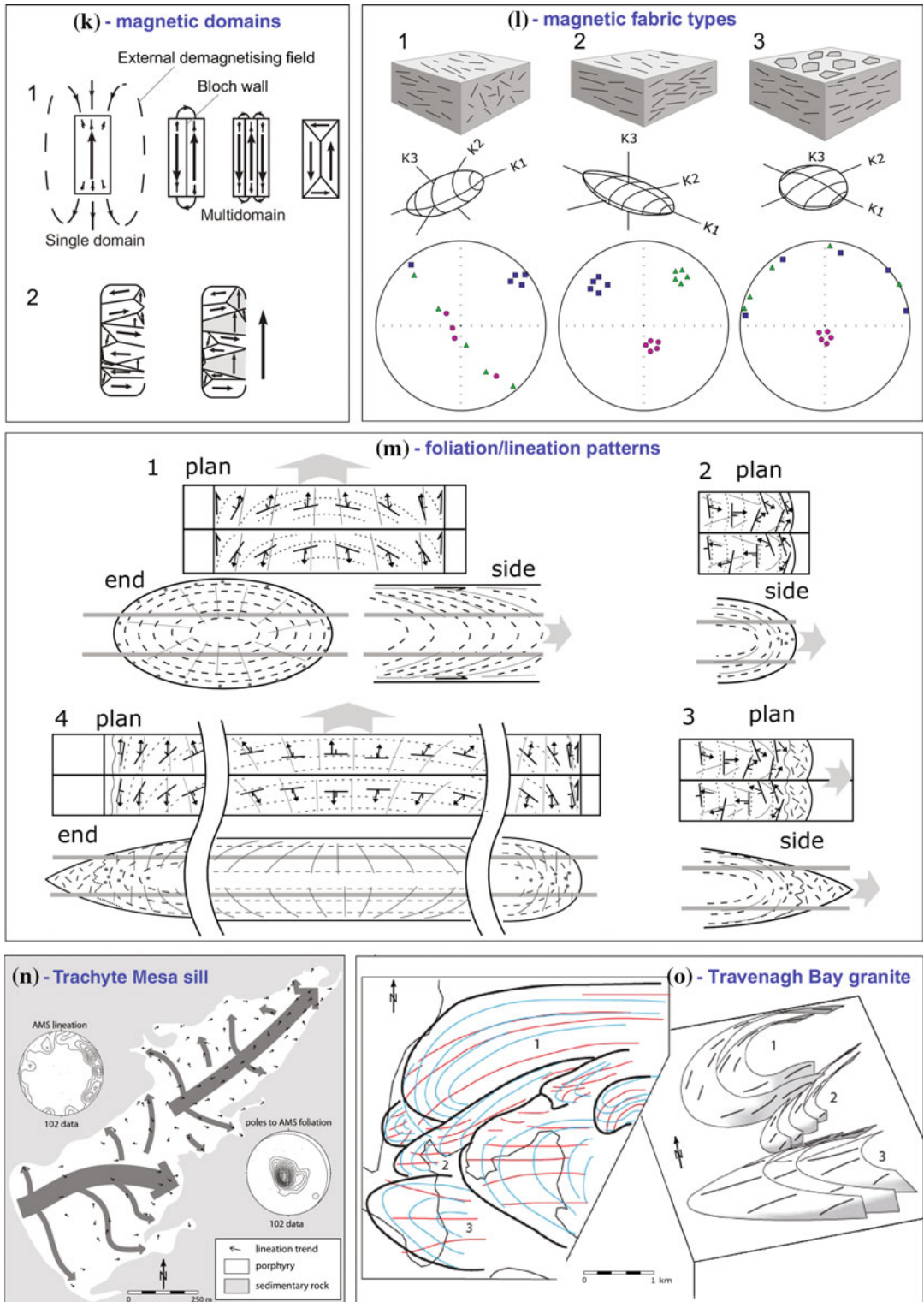


Fig. 2 (continued)

magmatic foliation, while tabular potassium feldspars, and to a lesser degree plagioclase feldspars, generally produce both magmatic foliation and lineation (Fig. 2g). With mafic intrusions, highly elongate minerals such as prismatic amphibole and lath-shaped plagioclase often provide a well-defined magmatic lineation (Fig. 2h). Fabrics near and within xenoliths can help determine a magmatic vs. solid-state origin, since the former produces flow foliation around, rather than through, the xenoliths.

Also associated with the non-coaxial flow regimes along emplacement surfaces are structures related to the process of flowage differentiation (Fig. 2i) by which the percentage of phenocrysts and other suspended objects such as xenoliths and enclaves increases away from the contact (Platten 1995; Ross 1986), generally attributed to the Bagnold effect (Bagnold 1954). Such features are not restricted to dykes, and in fact, are the general rule along the margins of SLI such as the rhyolitic laccolith units of the Halle Volcanic Complex that include thoroughly flow foliated units as well as units with no foliation/alignment (Mock et al. 2003; Schmiedel et al. 2015). These variations are thought to be controlled by viscosity, with flow foliation developing in the less viscous melts where the density of flow planes is greatest; more highly viscous melts, in contrast, emplace by plug flow with all strain accommodated at the margins of the unit (Breitkreuz et al. this volume).

Near intrusive contacts or in any setting where flow is non-coaxial, general orientations of resulting strain ellipsoids have long axes aligned oblique to the intrusive contact and to the particle flow paths, with the intermediate axes parallel to the wall (Correa-Gomes et al. 2001). Resulting fabrics include an imbrication (tiling) of tabular crystals and rock fragments (Figs. 11 and 2h), while highly elongate crystals, including those in the groundmass, define a mineral lineation parallel to the direction of maximum stretching. In order to attribute such fabrics to magmatic flow, it is important to confirm that the aligned crystals are internally undeformed (Rickwood 1990; Vernon 2000). Tabular fragments exhibiting mirrored orientations in opposing chilled

margins, reflective of their ability to rotate in response to the shear along the margin, can be used to constrain flow direction (Correa-Gomes et al. 2001).

Identifying fabrics in the field can be difficult, especially when the grain size is small or when the fabric is weak. Even when the foliation or planar component is clear, it is nevertheless almost always difficult to constrain the linear component with any degree of certainty. Although phenocryst alignment can be statistically constrained in 2D and then extrapolated to 3D with measurements on orthogonal planes (Bouchez 1997), this process is time-consuming and relies on identifying long axes of phenocrysts by eye.

Techniques involving scanning the internal physical properties of a rock using x-rays and quantifying the shape, distribution and orientation of mineral grains using computed tomography (CT scanning) has been making steady progress over the last decade or so (Cnudde and Boone 2013; Cnudde et al. 2006; Ketcham 2005; Ketcham and Carlson 2001). Also, electron backscatter diffraction techniques have improved efficiency and precision, enabling quantitative fabric analysis in a variety of scenarios and contexts (Prior et al. 2009). However, these techniques remain expensive and restrict data to focused analyses on a few samples.

Another set of flow-related structures, namely magmatic “folds” (Fig. 2j), may form as a true fold following development of one of the fabrics above, or directly as a result of alignment due to differential flow. These features are only rarely recognized in SLI, probably due to their fine-grained nature and apparent homogeneity. A spectacular example of a composite dyke where a combination of flow banding and elongated mafic enclaves defines a parabolic foliation trace indicating horizontal flow within the dyke is reported from Iceland (Eriksson et al. 2011). In a totally different lithology, thick sheets of banded aplite preserve internal magmatic folds in the vertical cliffs of Capo Bianco on Elba Island (Fig. 2j; Dini et al. 2007). Other examples of magmatic folds come from observations of symmetrical patterns of imbricated vesicles that

merge across the cores of dykes such that the vesicle fabric defines the fold.

2.2.3 Anisotropy of Magnetic Susceptibility

Some structures in igneous bodies cannot be observed or measured directly, and measurement of anisotropy of magnetic susceptibility (AMS) can be of great help in unravelling them. This method, although first highlighted more than 60 years ago (Graham 1954), has remained a somewhat specialist tool despite the advances in measurement precision, accuracy and efficiency (Borradaile and Henry 1997; Martín-Hernández et al. 2004; O'Driscoll et al. 2015; Tarling and Hrouda 1993). The principle behind AMS measurements relies on the physical property of magnetic susceptibility, K , which is the relationship between the magnetization, M , of a sample in an externally applied magnetic field of strength H . It is assumed that in low field strengths, this relationship is linear such that $M = KH$. The anisotropic response is controlled essentially by the SPO and distribution of Fe-bearing phases, principally magnetite and biotite. Magnetite is usually the dominant controlling phase, despite being an accessory phase, because the susceptibility response of this mineral is up to three orders of magnitude stronger than that of biotite.

Although the physics and application of this technique to fabric analysis can be quite nuanced (e.g. presence of inverse fabrics and distinguishing different carriers), numerous studies have shown that the AMS methodology is a very robust and reliable proxy for petrofabric analysis, principally because magnetite tends to form late and interstitially between the main silicate and fabric-forming phases (Archanjo et al. 1995; Grégoire et al. 1998; O'Driscoll et al. 2007; Stevenson et al. 2007a, b).

The anisotropy is controlled by crystallographic features of the mineral phase. Biotite has a platy crystal structure controlled by sheets of silicate tetrahedra, which results in a minimum susceptibility perpendicular to the [001] crystal face. Crystallographic anisotropy of magnetite is less important but is controlled by the octahedral

lattice with its axis of preferential magnetism, or "easy" axis, oriented through opposite corners. In magnetite, magnetic behaviour is controlled by grain size and shape. Single-domain and multidomain configurations serve to minimise the external demagnetising field (Fig. 2k.1). Movements of the Bloch wall in multi-domain grains give rise to a magnetisation when an external field is applied (Fig. 2k.2).

The data that is produced from AMS measurement may be visualized as a second order tensor with three orthogonal axes representing the maximum (K1), intermediate (K2) and minimum (K3) susceptibility directions. These eigenvalues can be read as a magnetic fabric where the magnetic foliation is the plane containing K1 and K2 (or normal of K3) and the magnetic lineation is parallel to K1 (Fig. 2l). At the sample scale, all magnetic grains create a magnetic fabric. This is similar to tectonic fabrics and may be interpreted in similar ways. If the fabric is dominantly linear, K2 and K3 are least certain and form a girdle, similar to L tectonite or a Flinn plot k value tending to infinity field (Fig. 2l.1; Flinn 1962). With $K1 > K2 > K3$, both a foliation and a lineation may be discerned. This fabric is triaxial, similar to a Flinn plot k value close to 1 field (Fig. 2l.2). When K1 and K2 are equally uncertain and form a girdle, K3 is perpendicular to a foliation, similar to an S tectonite or a Flinn plot k value close to 0 field (Fig. 2l.3).

The most useful aspect of AMS analysis is that it can provide excellent and reliable constraint of the linear fabric component. This element is often very difficult to constrain in the field, even when the planar component is very clear. The linear component is nonetheless necessary to determine the maximum stretching direction, which may be fundamental to understanding transport directions (Stevenson and Bennett 2011; Stevenson et al. 2007a, b). The AMS tensor cannot, however, be assumed to have a linear relationship with strain. This relationship is at best semi-quantitative where the shape of the AMS tensor can usually be trusted, but absolute magnitudes are difficult to correlate with strain (Borradaile 1987, 1988, 1991, 2001;

Borradaile and Henry 1997; Borradaile and Jackson 2004; Hrouda 1993). This is mainly because the way in which magnetic phases behave and crystallize during and after flow is poorly understood. To help constrain the AMS fabric in relation to the petrofabric, or at least understand what is controlling the AMS so that it can be linked more confidently to the silicate fabric, some form of determination of the magnetic carrier phases is required. This is usually done using temperature versus susceptibility analyses that can identify the presence of magnetite or demonstrate a dominant paramagnetic phase (Liss et al. 2004; Magee et al. 2012; O'Driscoll et al. 2015; Orlický 1990), or by using techniques that are able to separate magnetic anisotropy contributions using low and high field measurements (Richter and van der Pluijm 1994; Stevenson et al. 2007a, b) and various methods using remanence in addition to susceptibility.

Fabric pattern relationships can be summarized with respect to magma flow directions in end on, side view or plan (map) view (Fig. 2m). In each diagram the projected foliation trace is marked with dashed lines and the projected lineation trend with grey lines. Map symbols are shown in plan view to establish fabric geometry in the other diagrams. End on and side views show the plane through which the plan view is taken. In each case there is an upper and lower plane shown respectively in upper and lower parts of the relevant diagram. Grey arrows show the magma flow direction where relevant. Fabric pattern in a magma conduit, like a lava tube (Fig. 2m.1), may represent a lobe, tongue or finger. Foliation trace is generally concentric in end on view but shows a parabolic profile in plan view. Lineation tends to be convergent to a central axis in all views. Fabric patterns for the termination of a sheet in a viscous (non-brittle) propagation mode are portrayed in Fig. 2m.2 (Schofield et al. 2010, 2012b). This process may be operating during fluidization of country rocks. Here we assume that sheets take the form of lobes on limited extent along strike, thus in the plan view the lineation trends converge around the nose of the sheet tip. The lobes are flattened in the horizontal plane, so in side view, projected

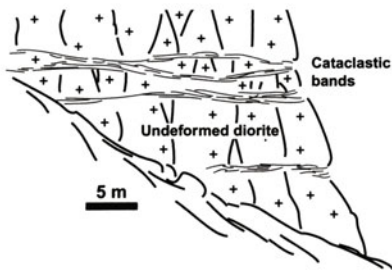
lineation trends are parallel to the foliation trace, while at tip or nose the lineation trends are close to perpendicular to the transport direction. If the structure was more cylindrical we may not expect to see lineation along the axis. The fabric patterns expected for a brittle (hydrofracture) propagation mode (Fig. 2m.3) show that there is a zone at the tip of the sheet that is dominated by fluids and we may not see any continuity in the fabric. For a sheet intrusion, the plumose lineation trend is shown in plan view, where the foliation trace displays a parabolic pattern (Fig. 2m.4). Here the only places where lineation trends parallel to propagation/magma flow is near the margins and along the central axis. Note that foliation planes, imbricated with respect to the margin (roof or floor), may only be used to determine flow direction along the central axis of flow (much like trough cross bedding in fluvial sandstones).

Two examples of AMS fabric data and their interpretations are reported here for reference. The case of Maiden Creek Sill, Henry Mountains, Utah (Fig. 2n) illustrates lineation trends splaying from an axial trend into a plumose pattern in plan view (Horsman et al. 2005). In contrast, Fig. 2o reports AMS data and interpretations from part of the Trawenagh Bay Granite, NW Ireland (Stevenson et al. 2007a). Although not for an SLI per se, the map highlights the way in which lobes were defined in this intrusion based on foliations curving around a lineation axis. In some lobes the lineation trend was parallel to this axis, in some they tended to splay down flow, and in others the lineation trend seemed to converge down flow.

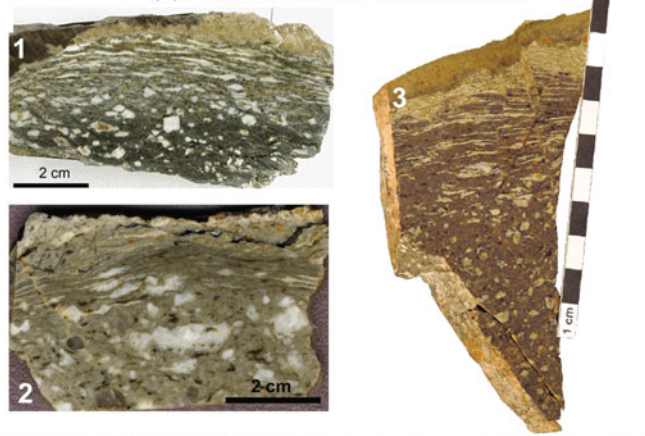
2.3 Solid-State Flow-Related Structures (Syn-magmatic, Non-tectonic)

Solid-state flow in magmatic rocks refers to conditions where the igneous system is subjected to stress when it is either fully solidified, or when the amount of melt available is insufficient for crystals to rotate and, therefore, they deform internally (Vernon 2000). We are concerned here

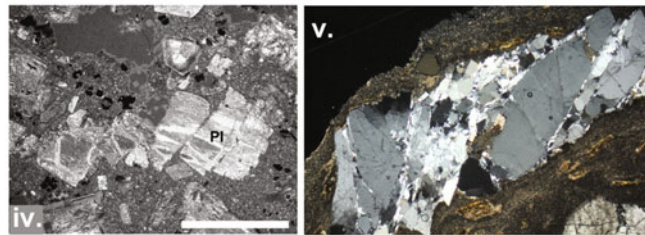
(a) - cataclastic shear bands



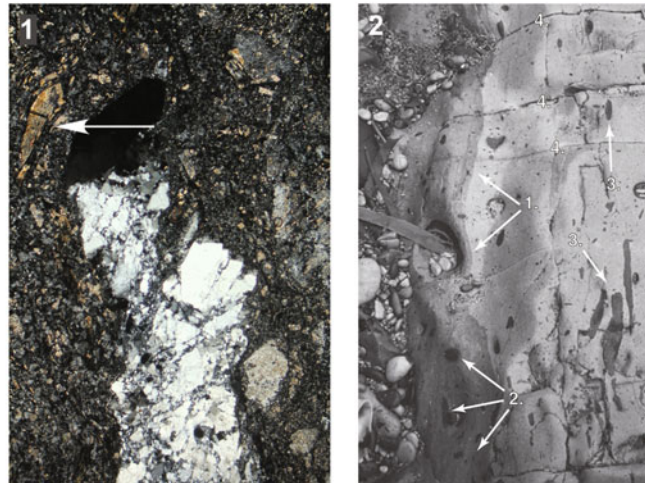
(b) - brittle textures-cross section



(c) - brittle textures-plan view



(d) - ductile textures



with deformation caused by continuing or pulsing emplacement processes rather than from regional tectonic stress. Although this distinction may be difficult to make, examination of fabrics and structures in surrounding host rock is normally sufficient. However, strong differences in rheology, and therefore behavior of the igneous

body and its host, can result in misleading conclusions (Pavlis 1996).

The largest-scale solid-state flow-related features are those that develop along significant expanses of the carapace of SLI as cataclastic shear zones (Fig. 3a; Habert and de Saint-Blanquat 2004; de Saint-Blanquat et al.

◀ **Fig. 3** Solid-state flow-related structures (syn-magmatic). **a** Large cataclastic bands/shear zones—Schematic drawing of the cataclastic bands in the Black Mesa intrusion, Henry Mts, Utah (Habert and de Saint Blanquat 2004). **b** Brittle textures as seen in cross section in the first few cm of the intrusive contact. b.1: Top contact of Trachyte Mesa intrusive sheet against sandstone, illustrating a thin, centimetric, shear zone (Morgan et al. 2008). b.2: Top contact of the Portoferraio laccolith, Elba Island, with centimetric shear zone, where quartz and sanidine are cataclastically deformed. b.3: Top contact of Trachyte Mesa intrusive sheet against country rock, illustrating a centimetric shear zone passing to the normal intrusive porphyritic texture with increasing distance from the contact. b.4: Cataclastically deformed plagioclase at the top of the Black Mesa intrusion, Henry Mts (de Saint-Blanquat et al. 2006). b5: Book-shelf deformed quartz crystal in the vicinity of contact with country rock of Portoferraio Laccolith, Elba Island. **c** Brittle textures as seen in plan view on the contact surface. c.1: Solid-state

lineation on *top* of the intrusion, Maiden Creek sill, Henry Mts (Horsman et al. 2005). c.2: Cataclastically stretched feldspar and quartz crystals on the contact surface of the San Martino laccolith, Elba Island. c.3: Cataclastically stretched feldspar and quartz crystals on the contact surface of the Portoferraio laccolith, Elba Island. **d** Ductile textures. d.1: Bent crystal of biotite within a cataclastically deformed portion of an intrusion very close to the contact, with cataclastically stretched feldspar and quartz crystals on the contact surface of the San Martino laccolith, Elba Island (same as Fig. 3B5). d.2: Flow bands—Flow banding underlined by trains of mafic enclaves occurring in a more felsic intrusion; *arrows* (1.) point to the sharp contact between a hybrid zone showing flow banding features in a homogeneous quartz-porphyry; *arrows* (2.) point to enclaves embedded and flow lineated (Eriksson et al. 2011). Each sketch/picture is after the work indicated by an asterisk in Table 3

2006), but due to erosion and limited exposure, they normally require effort to characterize. Cataclastic shear can be found more locally on opposing walls of dykes, as well as along the roofs and floors of sills (Schmiedel et al. 2015), or they may form relatively late along flow foliation planes inside emplacing viscous magma (Mock et al. 2003).

These deformation structures are thought to develop within highly viscous chilled margin zones as a result of continued magma flow in the interior of the sheet (Fig. 3b). The thickness of such zones tends to be measured in centimeters (Horsman et al. 2005; de Saint-Blanquat et al. 2006). At the mesoscopic scale, textures could appear as ductile shear (Fig. 3b1, 2, 3), yet at the microscopic scale, crystals are clearly cataclastically deformed, and often show bookshelf textures (Fig. 3b4, 5). Seen on contact surfaces, these textures are characterised by stretching lineations formed by cataclastically elongated quartz and feldspar crystals (Fig. 3c.1, .2, .3). At Trachyte Mesa, these lineations on the curving terminations of advancing sheets follow the magma surface and are oriented orthogonal to the axes of folds; within a few cm towards the interior, the magmatic foliation abruptly rotates to perpendicular to the contact (Morgan et al. 2008). Similar relations are observed on Elba Island where cataclastically stretched crystals

align perpendicular to wave crests (Fig. 3c.2, 3). These lineations in the cataclastic skin of a few cm thickness are also at right angles to those that can occur in the interior, reflecting alignment by non-coaxial shear in the former and by coaxial strain in the latter (Fig. 1f; de Saint-Blanquat et al. 2006). More rarely observed, such zones occur within the interior of SLI where they are attributed to multiple injections of discrete sheets or fingers of younger magma (Horsman et al. 2005; Morgan et al. 2005).

Deformation styles within the cataclastic zones are controlled primarily by mineralogy and gradients of temperature and viscosity. Variation in strain rates can also influence the behavior of minerals. The degree of deformation in the shear zones is at a maximum at the contact and decreases inward. Lineations are the dominant deformation features, owing to the high aspect ratios reached by brittlely stretched crystals. A review of sense of motion indicators under magmatic conditions (Blumenfeld and Bouchez 1988) shows that criteria are very similar to those established for solid-state deformation in metamorphic rocks (Simpson and Schmid 1983; Vernon 2004). As implied by referring to these zones as cataclastic, deformation is almost exclusively brittle, but minerals such as biotite can deform plastically as part of a ductile texture (Fig. 3d.1).

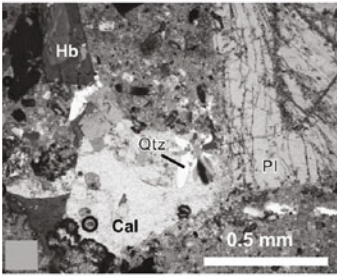
(a) - chilled margin



(b) - phenocryst layering



(c) - miarolitic cavity



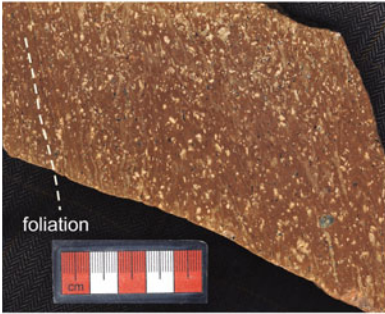
(d) - cooling columns



(e) - contact breccia



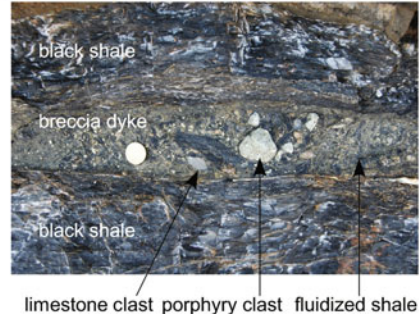
(f) - pyroclastic dyke



(g) - phreatomagmatic dyke



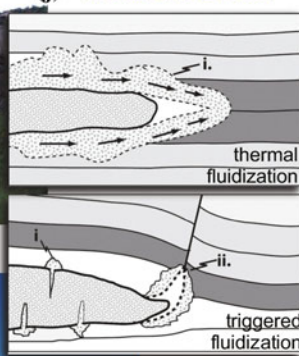
(h) - breccia dyke



(i) - peperite



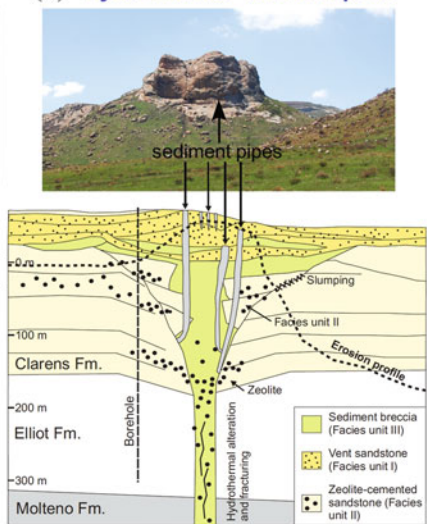
(j) - fluidized material



(l) - columnar joints



(k) - hydrothermal vent complex



◀ **Fig. 4** Thermal and fragmental structures. **a** Chilled margins—Field photo of a Palaeogene sill with a 5–7 cm chilled margin (slightly finer grained and darker) at the contact against Triassic sandstone, Scrabo quarry, northern Ireland (notebook is 20 cm long). Mesoscopic picture of a polished slab of the lower contact against pelitic sediments of a Late Paleozoic andesitic sill, with the sill margin vesiculated and bleached, near Magdeburg, Germany (Awdankiewicz et al. 2004). **b** Phenocryst distribution—Layering of mafic phases in a felsic level inside a fine-grained gabbro, Gulf of Ajaccio, Corsica. **c** Mirolitic cavity—Mirolitic cavity filled with calcite (Cal) and quartz (Qtz) (de Saint-Blanquat et al. 2006). **d** Cooling columns—Host sediments with cooling columns formed by thermal overprint, close to contact with Late Paleozoic andesitic sill from a quarry west of Magdeburg, Germany. **e** Intrusion contact breccia—White aplite brecciated at the intrusive contact with slightly younger light brown porphyritic laccolith below. Clasts are located in the contact zone, with some migrated tens of cm inside the younger porphyry, coin for scale, Elba Island. **f** Breccia dyke—Dyke made of fluidized shale (originally Cretaceous) matrix carrying clasts of late Miocene porphyritic

igneous rock and Cretaceous limestone cropping out in the vicinity, coin for scale, Elba Island. **g** Pyroclastic dyke—Pyroclastic welded domain with vertically (parallel to dyke attitude) oriented fiamme resembling a flow foliation in a dyke related to the Late Carboniferous Tharandt Forest Caldera, west of Dresden, Germany. **h** Breccia dyke—Dyke including fragments of porphyry along with clasts of local and distant host rock, Elba Island, Italy. **i** Peperite—Sill with peperite on both sides, Sag Hegy, Hungary (Martin and Nemeth 2007). **j** Fluidized material—Thermal fluidization (flash boiling within a fluidized mass along the magma contact) and triggered fluidization (rapid release of heated pore-fluids not directly related to magma movement) (Schofield et al. 2012b). **k** Hydrothermal vent complex—Full sketch of a vertical section through a hydrothermal vent complex (Svensen et al. 2006) and field photo of the outcropping portion of the Jurassic Witkop hydrothermal vent complex, Karoo. **l** Columnar joints—Commonly formed in SLI when sheets of solidified magma continue to cool inward from the walls to form parallel prismatic columns like mafic sills, example photo from Colca, Peru. Each sketch/picture is after the work indicated by an asterisk in Table 4

Conditions of non-coaxial flow characterize contact zones where magma drags along the host wall and becomes increasingly viscous due to cooling. This creates a simple shear system parallel to the wall and to the particle paths, but with stretching and flattening at an oblique angle. Flow banding can develop in SLI (Fig. 3d.2), for example where the banding defines the plane of overall flow along the margins of bimodal dykes, preserving intercalated mafic and felsic magmas that intruded quasi-contemporaneously (Eriksson et al. 2011).

2.4 Thermal and Fragmental Structures

Chilled margins are nearly ubiquitous along the contacts of sheet-like bodies emplaced at shallow levels. In fact, initial assumptions about depth of emplacement typically stem from observation of these marginal features that offer evidence of significant temperature contrast between magma and its host. Confirmation of intrusion, as opposed to extrusion, in some cases comes from observing chilled margins on both walls of these tabular bodies rather than on one. Similarly, chilled

margins can be used to unveil post-solidification processes (e.g. faulting) where the margins are truncated. The detailed nature of chilled margins (Fig. 4a), their thickness and degree of crystallinity in particular, is controlled by variables such as magma temperature and composition (and associated viscosity), temperature contrast between magma and host rock, either adjacent to the wall over time or passing along the wall through time. These margins are some of the earliest structures formed during emplacement and often represent the least modified magma.

Another family of features that develop in SLI in response to progressive crystallization involve mineralogical and textural changes producing layering that parallels the tabular forms. Cooling from the walls of dykes or from the roof and floor of sills and laccoliths often produce changes in matrix grain size, as well as phenocryst size and abundance, particularly in more mafic bodies. Given sufficient thickness and low enough viscosity, crystal settling can generate magmatic layering (Fig. 4b). In the same line, high temperature crystallization domains such as spherulites and lithophysae (Breitkreuz 2013) have been observed to form near the margins of SLI, with the domains often arranged parallel to the margin.

In the case of large mafic SLI, extended duration of crystallization promotes fractionation, with associated development of late magmatic features such as granophyres, pegmatites, and miarolitic cavities (Fig. 4c). Late-stage magmatic products also can form systems of dykes and veins, including development of net-veining. Even in more felsic rocks, such as the rhyolitic laccolith units of the Halle Volcanic Complex, whole rock geochemical zonation can develop due to fluid mobility during groundmass crystallization (Słodczyk et al. 2015).

Contact metamorphic effects associated with SLI emplacement are generally minimal, and a decided lack of contact metamorphic effects is reported as a widespread occurrence (Corry 1988). Based on growth of index minerals, even in thick, high-temperature sheets, effects are decidedly less than for plutonic units of similar size. However, contact effects are particularly important and well documented for mafic sills intruded into organic-rich sediments and sedimentary rocks, with aureole thicknesses generally equal the thickness of the sill (Aarnes et al. 2010). Other studies of contact effects in thinly-bedded laminated carbonate mudstones and organic-rich siltstones report aureoles whose full thickness is recognized only by C and O isotope variations (Dutrow et al. 2001).

At the base of mafic sills intruding wet sediments such as in the Karoo and Newark Basins, spherulitic nodules with bullseye patterns have been observed, with pronounced elemental transfer across bleached zones to the newly stable mineral assemblage in the center. In other settings, heated and sintered clastic host sediments can develop cooling columns oriented perpendicular to the contact plane (Fig. 4d; Adamovic 2006). Around most SLI, however, evidence for heated host rock is not visible, perhaps because heat transport away from the SLI contact in porous/permeable host sediments is advective and rapid such that signs of thermal overprint are limited. As an example, vitrinite reflectance from coal seams in the vicinity of large SLI in the Halle Volcanic Complex decreases from values as high as 9% at the contact to background level within 1.5 m of the contact (Schwab 1962).

Fragmentation structures seen as intrusion contact breccias (Fig. 4e) can develop along the propagating fracture beyond the limits of a sill (Tweto 1951), but more commonly they are found in contact with the intrusive rock (Morgan et al. 2008). These fragmented zones can include the intrusive material, the host material, or both (Schmiedel et al. 2015). Igneous breccia made primarily of intrusive material can develop marginally with fragments cemented by sets or networks of quartz and calcite veins (Awdankiewicz et al. 2004). Breccias at the contact can contain shear bands that conform to the overall direction of magma emplacement (Morgan et al. 2008). These breccias are generated by shear strain at the contact during magma sheet emplacement in response to outward translation of individual sheets, with a large degree of frictional coupling between the overlying layers leading to final brecciation.

Pyroclastic dykes (Fig. 4f) have been described as emplacements in volcanic edifices, as well as in country rock. They may resemble tabular feeding systems of explosive eruptions with the exposure level of the dyke being located above the fragmentation level (Almond 1971; Ekren and Byers 1976). “Ignimbritic dykes” have been documented from high-volume caldera complexes of the Sierra Madre Occidental in Mexico (Aguirre-Díaz and Labarthe-Hernández 2003). Common to these is a vertical orientation of pyroclastic welded domains (fiamme) parallel to the attitude of the dyke, resembling a flow foliation. The typically welded pyroclastic rock forms by lateral aggradation during upwardly directed flow of a dispersion of hot melt fragments and gas. Presumably, these feeding systems are being closed due to deflation of the volcanic complex; otherwise, the lack of porosity in these welded pyroclastic dykes is difficult to comprehend.

Other quite frequent types of clastic dykes are phreatic and phreatomagmatic dykes that are cross-cutting lava flows, pyroclastic deposits or country rock. They display vertically aligned, non-welded domains of fine- to coarse-grained volcanoclastic and non-volcanic fragments (Fig. 4g). These dykes are related to phreatic explosions of water bodies (creeks, lakes, wet

substrate) covered by hot lava or pyroclastic flow deposits. Phreatomagmatic dykes may form in the periphery of phreatomagmatic explosions, in and around volcanically active diatremes or emplacing sills and dykes (Martin and Nemeth 2007).

On Elba Island, chaotic breccia zones are preserved with angular fragments of the intruding porphyry and the rigid limestone host material, all 'swimming' in fluidized shale. These types of mixtures can escape the contact zone to form clast-supported breccia dykes (Fig. 4h) in which fragmented intrusive rock mixes with fragmented host rock and intrudes with parallel contacts both into the host and vice versa.

Other pyroclastic systems related to a volcanic vent and formed below the surface may have cone- or pipe-shaped geometry. They range from phreatomagmatic maar-related diatremes to vents related to explosive eruptions of volatile-rich mafic mantle melts (Kano et al. 1997; Reedman et al. 1987). Caution is advised in assuming an intrusive origin when such textures are observed. For example, in the study of a Late Paleozoic silica-rich magmatic system in Burkersdorf, Germany, a detailed 3D data set on orientations of fiamme and cooling columns has been used to justify the interpretation for a welded fall-back breccia in a vent situated on a rhyolitic dyke that propagated subhorizontally through metamorphic country rocks (Winter et al. 2008).

Several variables at the site of emplacement strongly influence the range of disruptive textures that develop in either the intrusive unit or the host, or in both. Foremost among these is the role of fluids, primarily water present in the host, but also as released magmatic fluids. Peperite (Fig. 4i) often forms in adjacent host material when any of a variety of magma types comes in contact with wet sediments, producing a myriad of forms all related as reaction textures that have been well described and illustrated (Martin and Nemeth 2007; Skilling et al. 2002). Peperitic textures are also reported for interactions of magma and both hydrous salt in the Werra-Fulda Basin, Germany (Schofield et al. 2014) and coal in the Raton Basin, Colorado, USA (Schofield et al. 2012b).

Emplacement of sills and laccoliths into the unconsolidated part of the crust occurs by non-brittle opening of the plane of emplacement, initially dominantly as fingers or lobes with a range of interface fabrics and structures produced (Schofield et al. 2012b). Activation of this emplacement mechanism is apparently restricted to the upper 2 km of the crust and is, in most cases, dependent on induced fluidization by buoyant hot water or vapor producing dispersed grains (Fig. 4j), controlled primarily by fluid volume, host strength, vapor velocity, and clast size (Busby-Spera and White 1987). Fluidization can occur as (i) thermal fluidization, a continuous process with flash boiling of pore-fluids within fluidized material flowing along the magma contact, or (ii) triggered fluidization, when heated pore-fluids are rapidly released by a process not directly related to the magma emplacement, such as a fault, leading to rapid expansion of the pore-fluids (Schofield et al. 2010, 2012b). These two processes represent end-members and it is likely that in a given intrusion there will be a combination of both processes operating. Such fluidized mixtures of materials can escape to make dykes or pipes that migrate considerable distance into the overlying host (Platten 1984), or if the available fluids and driving forces are sufficient, to form hydrothermal vent complexes (Fig. 4k) that pierce the overlying strata and sometimes then collapse (Svensen et al. 2006).

As was noted early in this section, chilled margins are characteristic of most SLI, due to the strong temperature contrast with the surrounding host and the generally small volume of many SLI. For similar reasons, formation of post-magmatic, intrusion-scale columnar joints is also common when sheets of solidified magma continue to cool inward from the walls to form parallel prismatic columns. Sets of curved cooling columns can form controlled by non-planar isotherms, parallel to the outer surface of the magma body. Others have examined the detailed fracturing of such jointed rocks in relation to their enhanced porosity in the context of evaluating unconventional hydrocarbon reservoirs (Bermúdez and Delpino 2008).

2.5 Examining Multiple Approaches

Although the above descriptions attempt to simplify the range of conditions and textures, complexity is more likely the norm. Evidence exists for coalescing fingers during dyke and sill formation, and differential rates of flow within a sheet that effectively create magma-magma interface zones in which simple shear and resulting imbrication may occur. Each intrusion needs to be carefully examined to see how the sum of the observations can best be interpreted. As an example, the emplacement history of a giant diabase feeder dyke in Connecticut is reported where seven flow-direction indicators (imbricated phenocrysts, broken and sheared phenocrysts, granophyre wisps emanating from wall rock, granophyre wisps folded by backflow, granophyre segregations attached to phenocrysts, Riedel shears, and ramp structures) have been used to unravel a three-stage model that included back flow (Philpotts and Asher 1994), later confirmed by detailed study of deformed vesicles and AMS analysis (Philpotts and Philpotts 2007).

3 Example of Elba Laccoliths: A Case for Coherence

Many igneous rocks, occurring in dykes and sills in particular, preserve SPO fabrics. However, before concluding that such fabrics are caused by magma flow, other alternatives need to be considered and excluded. If all other reasonable options to generate a fabric are found wanting, then an origin from magma flow becomes most likely. It is worth repeating that the observed fabric mostly represents the flow pattern in the waning stages of movement, and that interpolation to determine earlier patterns during initial emplacement and filling needs to be done with care. On the other hand, given that fabrics are all related to the flow of magma during the waning stage of emplacement, the data describing their geometries should be coherent, as shown by the example of laccoliths from Elba Island.

3.1 Interior Fabrics and Flow

As with many laccoliths and sills, the laccoliths at Elba Island, Tuscany, formed at the transition to horizontal flow following vertical flow in feeder dykes. In such situations, the feeder dykes are characterized by relatively fixed cross sectional area and non-coaxial flow generated by the higher velocity toward the interior, leading to an imbricated fabric. On the other hand, the cross-sectional area of the laccolith bodies continuously increased as the radius and thickness of intrusion increased. Such a transition reoriented the linear and planar fabrics as magma exited the constricting conditions of the dyke and emerged into expanding subhorizontal sheets, a transition similar to that shown experimentally (Kratinová et al. 2006). This observation further underlines that stress fields reconstructed on the basis of mineral fabrics are not sufficient to determine the whole history of flow, because such fabrics represent just the closing stages.

As an example, for the Elba San Martino laccolith, the great coherence between stress fields reconstructed from both (i) orientations of biotite platelets as determined from AMS studies and (ii) aligned tabular K-feldspar megacrysts determined by field analyses (Roni et al. 2014) is nevertheless insufficient to reconstruct the direction and sense of flow. Indeed, the AMS and SPO data provides information about diverging flow lines much like the information provided by simple glacial striations: you know the direction (a line) along which the magma (or ice) moved, but you don't know the sense. Thus, the case of the San Martino laccolith required an initial assumption of overall divergent flow as the laccolith expanded laterally from its feeder dyke, followed by a two-step interpretation. First, the orientation of the flow lines in map view of the laccolith sheets could be determined from the directions of the short axes of the tabular crystals and the weakest AMS direction (K3). Determining the sense of flow along those lines required a second step, namely recognizing that such axes plunged toward or away from flow

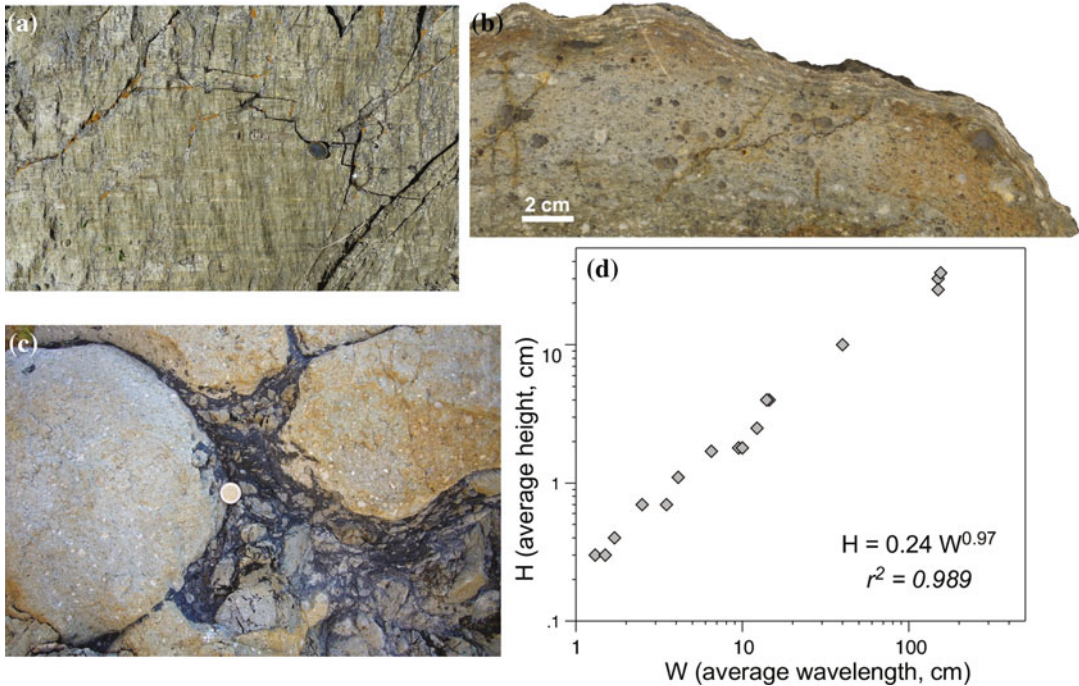


Fig. 5 Elba Island laccoliths—**a** Stretching lineations given by extremely deformed crystals on the exposed outer contact surface of the Portoferraio laccolith; coin for scale. **b** Strongly stretched crystals of quartz and feldspars in the outer “skin” (ca. 2 cm) of the Portoferraio laccolith,

as seen in cross section on a polished slab. **c** Fluidized black shale amidst lobelets of Portoferraio laccolith in the contact zone; coin for scale. **d** Log-log plot of wavelength and wave height of contact waveform sets, measured at five different locations on Elba Island

depending on whether magma was directed toward the base or roof of the laccolith, respectively. The result proved to be a coherent and internally consistent ‘geo-logical’ pattern, compatible with the original position of the primary feeder dyke (Roni et al. 2014), that is known thanks to the post-emplacement lateral displacement of the laccolith layers that left the feeder dyke and laccolith exposed side by side (Westerman et al. this volume).

3.2 Ornamented Waveforms and Disrupted Contacts

A number of well-exposed intrusive contact surfaces in the Elba laccolith complex provides an opportunity to evaluate the relationship of magma flow to the development of waveforms that are ornamented with cataclastically generated mineral lineations in the outer skin of the

porphyries. Observations of these surfaces for both the San Martino and Portoferraio laccoliths show the presence of severely stretched (up to 40:1) phenocrysts of quartz and feldspars (Figs. 3c and 5a). Bookshelf structures in quartz preserve the sense of motion during strain (Fig. 3b5), while feldspar crystals occasionally show similar patterns but are generally characterized by the development of both symmetrical and asymmetrical cataclastic tails of crumbled grains (Roni 2012).

All of these solid-state deformation features, as well as ductile bending of associated biotite microphenocrysts, are restricted to the outer 1–2 cm of the porphyry (Fig. 5b). The groundmass between the deformed crystals shows no evidence of shearing, appearing only slightly finer grained than the groundmass in the interior of the sheets where the phenocrysts are undeformed. Stretching lineations are commonly present on the upper contacts, but are also seen on basal

contacts. Similar structures are reported for shallow intrusions in the Henry Mountains (Horsman et al. 2005; Morgan et al. 2005; de Saint-Blanquat et al. 2006).

All examples of these cataclastic lineations on Elba are seen as ornamentation on waveforms that occur along intrusive contact surfaces of porphyry against highly disrupted, or ‘fluidized,’ shale and serpentinite that has temporarily lost its competence (Fig. 5c). Most commonly, the structures have rounded ‘crests’ and ‘troughs’ best described as sinusoidal, but some sets are characterized by pointy crests and/or troughs (Figs. 2b, 3c.3 and 5b); elsewhere, crests form with an appearance of having ‘overrun’ the troughs, producing a small-scale ropy structure with a ‘pahoe-hoe’ appearance (Fig. 2d).

Exposures at Elba Island allow also more detailed observation: where host rocks became fluidized, wave sets occur across a range of geometries with wavelengths from 1–2 cm up to 1.5 m, and heights from 0.3 to 33 cm. The largest waveforms are associated with thicker sheets, however smaller waveforms can occur either alone or superimposed to produce sets of waveforms of different orders of magnitude. Relationships of wavelength to amplitude tend to be organized and consistent, displaying a power-law relationship (Fig. 5d).

Additionally, these waveforms on contacts of both the Elba Island and Henry Mountains laccoliths (Horsman et al. 2010), show solid-state phenocryst lineations that are characteristically orientated perpendicular to the axes of the waveforms (Figs. 3c.3 and 5a), independent of the regularity of the waveform patterns. And because the lineations wrap on the undulating surfaces, they define the plane perpendicular to those axes. For the Elba laccoliths, the stretching lineation fabric has also been investigated using AMS in the outer 2.5 cm at several contacts, finding that the AMS magnetic lineation (K1) is consistently parallel or sub-parallel to the stretching direction shown by the solid-state fabric on the contacts (Roni 2012). In addition, both of these lineations, whether measured together or alone, are arranged nearly perpendicular to the axes of associated wave crests.

Because the lineation defined by cataclastically stretched crystals is always associated with surface waveforms, and because they invariably occur together, we consider them as directly related to magma flow, with wave crests and troughs aligned perpendicular to flow direction.

Our scenario for the development of these surface features focuses on four elements: fluidization of host rock, sharpness of the contact, freezing the marginal magma, and persisting magma flow. More completely, porphyritic magma enters a brittle fracture, carrying phenocrysts. Host rock is locally fluidized along the fracture but remains “cold” relative to the adjacent, immiscible magma. Magma freezes instantaneously to form a thin skin with embedded phenocrysts. Viscous drag from magma moving against the skin brittly stretches the phenocrysts. The chilled margin thickens incrementally with viscous drag increasing as the sheet also thickens. Crystal stretching extends into the solid and warmer part of the margin, decreasing in intensity. Continued forceful emplacement further thickens the sheet with transpressive forces generating “standing waves” between the warming contact zone and the “soft” host.

With regard to the multiple sets of waveforms, other than having a fluidized host, the main variable most likely controlling both their occurrence and scale is the velocity differential along the flow path, with obstruction of the forward-moving magma causing waveforms to set up behind. In our scenario, lateral propagation was followed by vertical inflation, with two or more episodes during the earliest part of the inflation process. During propagation of the initially thin sheet, the contact surfaces become decorated by centimetric waveforms preserved in the frozen outer skin of the sheet. Then, subsequent inflation stages superimpose decimetric- and even metric-scale waveforms on the contacts of the intrusion.

What remains to be fully understood are the fluid mechanics of the coupled system that control the waveform parameter such that wave height and wavelength correlate. Rheological properties of the fluids vary with distance from the contact and with time, and the forms are

visualized to have formed as stationary features that never propagated.

3.3 Coherence

If fabrics defined by the preferred orientations of undeformed phenocrysts, by waveforms, and by stretched crystals on contacts are all related to the flow of magma, the data describing their geometries should be internally consistent. These relationships are considered here for a diverging set of particle paths with decelerating magma, such as would occur during growth of a laccolith sheet from a central feeder dyke.

On Elba Island, the observed fabrics present a coherent pattern. First, orientations for tabular K-megacrysts (SPO field measurements) and biotite plates (AMS measurements) within the magmatic sheets are similarly aligned and provide a geologically logical ('geo-logical') pattern of overall magma flow in the interior of sheets (Roni et al. 2014). Second, highly elongated phenocrysts in the skin of the intrusions are stretched parallel to the overall flow lines and are in concordance with AMS lineations measured in cores from exposed contacts. Third, waveforms on intrusive surfaces are aligned perpendicular to those interpreted flow lines, suggesting compression in the direction of flow.

Many of the features described above can offer information about magma flow, but when all of them are available, they provide a coherent geometry of fabrics. For the San Martino laccolith system, expanding sheets of magma were being emplaced under conditions of lateral divergence from a feeder dyke resulting in (i) poles perpendicular to aligned tabular crystals defining the flow direction, (ii) fold axes of wave-like structures aligning perpendicular to flow, and (iii) stretched crystals defining a plane that contains the flow direction which is oriented perpendicular to those fold axes.

4 Concluding Summary

Over the past 200 years, a lot of nomenclature has been introduced to describe structures and features of SLIs, often with genetic implications. We have attempted here to organize much of this body of information using logical breaks in the timing of magma emplacement, independent of the scales of features. We started with *Intrusion-related structures* that formed as the magma was initially making space and then developing into its characteristic form. This is followed by a discussion of *Magmatic flow-related structures* that develop as magma moves with suspended crystals that are free to rotate, recognizing that only the final 'snapshot' of this process is preserved. The next set of features were the *Solid-state flow-related structures* (*syn-magmatic, non-tectonic*) that formed in portions of the intrusions impacted by continuing flow of nearby magma. Our final discussion concerned *Thermal and fragmental structures*, less constrained by time of formation than the other features, but related by their association with creation of space and impact on host materials. While this is not the only scheme possible, we find this reasoned and rational organization to be helpful in describing and interpreting the myriad observations that have been reported.

Acknowledgements This work has been partially funded by Università di Pisa, grant PRA_2016_33 to SR.

References

- Aarnes I, Svensen H, Connolly JAD, Podladchikov YY (2010) How contact metamorphism can trigger global climate changes: modeling gas generation around igneous sills in sedimentary basins. *Geochim Cosmochim Acta* 74(24):7179–7195
- Adamovic J (2006) Thermal effects of magma emplacement and the origin of columnar jointing in host sandstone. *Vis Geosci* 72–74
- Aguirre-Díaz GJ, Labarthe-Hernández G (2003) Fissure ignimbrites: fissure-source origin for voluminous

- ignimbrites of the Sierra Madre Occidental and its relationship with Basin and Range faulting. *Geology* 31:773–776
- Almond DC (1971) Ignimbrite vents in the Sabaloka cauldron. *Sudan Geol Mag* 108:159–176
- Anderson EM (1938) The dynamics of sheet intrusion. *Proc R Soc Edinb* 58:242–251
- Archanjo CJ, Launeau P, Bouchez J-L (1995) Magnetic fabric vs. magnetite and biotite shape fabrics of the magnetite-bearing granite pluton of Gameleiras (Northeast Brazil). *Phys Earth Planet Inter* 89:63–75
- Awdankiewicz M, Breikreuz C, Ehling B-C (2004) Emplacement textures in Late Palaeozoic andesite sills of the Flechtingen-Roßlau Block, north of Magdeburg (Germany). In: Breikreuz C, Petford N (eds) *Physical geology of high-level magmatic systems*, vol 234. Geological Society, London, Special Publication, pp 51–66
- Baer G, Reches Z (1987) Flow patterns of magma in dikes, Makhtesh Ramon, Israel. *Geology* 15(6):569–572
- Bagnold RA (1954) Experiments on a gravity-free dispersion of large solid spheres in a Newtonian fluid under shear. *Proc R Soc Lond A* 225:49–63
- Barbarin B (2005) Mafic magmatic enclaves and mafic rocks associated with some granitoids of the central Sierra Nevada batholith, California: nature, origin, and relations with the hosts. *Lithos* 80(1–4):155–177
- Bédard JHJ, Marsh BD, Hersum TG, Naslund HR, Mukasa SB (2007) Large-scale mechanical redistribution of orthopyroxene and plagioclase in the Basement Sill, Ferrar Dolerites, McMurdo Dry Valleys, Antarctica: petrological, mineral-chemical and field evidence for channelized movement of crystals and melt. *J Petrol* 48(12):2289–2326
- Bermúdez A, Delpino D (2008) Concentric and radial joint systems within basic sills and their associated porosity enhancement, Neuquén Basin, Argentina. In: Thomson K, Petford N (eds) *Structure and emplacement of high-level magmatic systems*, vol 302. Geological Society, London, Special Publications, pp 185–198
- Blanchard J-P, Boyer P, Gagny C (1977) Un nouveau critère de sens de mise en place dans une caisse filonienne: le “pincement” des minéraux aux épontes. *Tectonophys.* 53:1–25
- Blumenfeld P, Bouchez J-L (1988) Shear criteria in granite and migmatite deformed in the magmatic and solid states. *J Struct Geol* 10(4):361–372
- Bons PD, Druguet E, Hamann I, Carreras J, Passchier CW (2004) Apparent boudinage in dykes. *J Struct Geol* 26(4):625–636
- Borradaile G (1987) Anisotropy of magnetic susceptibility: rock composition versus strain. *Tectonophys.* 138:327–329
- Borradaile GJ (1988) Magnetic susceptibility, petrofabrics and strain. *Tectonophys.* 156:1–20
- Borradaile GJ (1991) Correlation of strain with anisotropy of magnetic susceptibility (AMS). *Pure appl Geophys* 135:15–29
- Borradaile GJ (2001) Magnetic fabrics and petrofabrics: their orientation distributions and anisotropies. *J Struct Geol* 23:1581–1596
- Borradaile GJ, Henry B (1997) Tectonic applications of magnetic susceptibility and its anisotropy. *Earth Sci Rev* 42(1):49–93
- Borradaile GJ, Jackson M (2004) Anisotropy of magnetic susceptibility (AMS): magnetic petrofabrics of deformed rocks. In: Martín-Hernández F, Lüneburg CM, Aubourg C, Jackson M (eds) *Magnetic fabric: methods and applications*, vol 238. Geological Society, London, Special Publications, pp 299–360
- Bouchez J-L (1997) Granite is never isotropic: an introduction to AMS studies of granitic rocks. In: Bouchez J-L, Hutton DHW, Stephens WE (eds) *Granites: from segregation of melts to emplacement fabrics*. Kluwer, Dordrecht, pp 95–112
- Breikreuz C (2013) Spherulites and lithophysae—200 years of investigation on high-temperature crystallization domains in silica-rich volcanic rocks. *Bull Volc* 75(4):1–16
- Breikreuz C, Petford N (eds) (2004) *Physical Geology of High-Level Magmatic Systems*. In: Geological Society, London, Special Publication, vol 234, p 253
- Bunger AP, Cruden AR (2011) Modeling the growth of laccoliths and large mafic sills: role of magma body forces. *J Geophys Res* 116(B2):B02203
- Busby-Spera CJ, White JDL (1987) Variation in peperite textures associated with differing host-sediment properties. *Bull Volc* 49:765–775
- Cnudde V, Boone MN (2013) High-resolution X-ray computed tomography in geosciences: a review of the current technology and applications. *Earth Sci Rev* 123:1–17
- Cnudde V, Masschaele B, Dierick M, Vlassenbroeck J, Van Hoorebeke L, Jacobs P (2006) Recent progress in X-ray CT as a geosciences tool. *Appl Geochem* 21:826–832
- Correa-Gomes LC, Souza Filho CR, Martins CJFN, Oliveira EP (2001) Development of symmetrical and asymmetrical fabrics in sheet-like igneous bodies: the role of magma flow and wall-rock displacements in theoretical and natural cases. *J Struct Geol* 23(9):1415–1428
- Corry CE (1988) Laccoliths—mechanics of emplacement and growth. *Geol Soc Am Spec Pap* 220:110
- Cruden AR, McCaffrey KJW (2001) Growth of plutons by floor subsidence: implications for rates of emplacement, intrusion spacing and melt-extraction mechanisms. *Phys Chem Earth* 26:303–315
- Cruden A, McCaffrey K (2002) Different scaling laws for sills, laccoliths and plutons: mechanical thresholds on roof lifting and floor depression. In: Breikreuz C, Mock A, Petford N (eds) *Physical geology of subvolcanic systems—Laccolith, Sills and Dykes (LASI)*. Freiberg, 12–14 October 2002, pp 15–17
- de Saint-Blanquat M, Habert G, Horsman E, Morgan SS, Tikoff B, Launeau P, Gleizes G (2006) Mechanisms and duration of non-tectonically assisted magma

- emplacement in the upper crust: the Black Mesa pluton, Henry Mountains, Utah. *Tectonophysics* 428:1–31
- Dini A, Corretti A, Innocenti F, Rocchi S, Westerman DS (2007) Sooty sweat stains or tourmaline spots? The Argonauts on the Island of Elba (Tuscany) and the spread of Greek trading in the Mediterranean Sea. In: Piccardi L, Masse WB (eds) *Myth and geology*, vol 273. Geological Society, Special Publications, London, pp 227–243
- Dutrow BL, Travis BJ, Gable CW, Henry DJ (2001) Coupled heat and silica transport associated with dike intrusion into sedimentary rock: effects on isotherm location and permeability evolution. *Geochim Cosmochim Acta* 65:3749–3767
- Eide CH, Schofield N, Jerram DA, Howell JA (2017) Basin-scale architecture of deeply emplaced sill complexes: Jameson Land, East Greenland. *J Geol Soc* 174(1):23–40
- Ekren EB, Byers FM (1976) Ash-flow fissure vent in west-central Nevada. *Geology* 4(4):247–251
- Eriksson PI, Riishuus MS, Sigmundsson F, Elming SÅ (2011) Magma flow directions inferred from field evidence and magnetic fabric studies of the Streitishvarf composite dike in east Iceland. *J Volcanol Geoth Res* 206(1–2):30–45
- Farina F, Dini A, Innocenti F, Rocchi S, Westerman DS (2010) Rapid incremental assembly of the Monte Capanne pluton (Elba Island, Tuscany) by downward stacking of magma sheets. *Geol Soc Am Bull* 122(9/10):1463–1479
- Fernandez A, Laporte D (1991) Significance of low symmetry fabrics in magmatic rocks. *J Struct Geol* 13:337–347
- Flinn D (1962) On folding during three-dimensional progressive deformation. *Quarterly. Quarterly J Geol Soc* 118(1–4):385–428
- Gilbert GK (1877) Report on the geology of Henry Mountains. In: Department of the Interior, U.S. Geographical and Geological Survey of the Rocky Mountain Region. Washington D.C. Government Printing Office, p 160
- Graham JW (1954) Magnetic susceptibility anisotropy, an unexploited petrofabric element. *Geol Soc Am Bull* 65:1257–1258
- Grégoire V, Darrozes J, Gaillot P, Nédélec A, Launeau P (1998) Magnetite grain shape fabric and distribution anisotropy vs. rock magnetic fabric: A three-dimensional case study. *J Struct Geol* 20(7):937–944
- Habert G, de Saint-Blanquat M (2004) Rate of construction of the Black Mesa bysmalith, Henry Mountains, Utah. In: Breitreuz C, Petford N (eds) *Physical geology of high-level magmatic systems*, vol 234. Geological Society, London, Special Publication, pp 163–173
- Halls H, Fahrig W (1987) Mafic dyke swarms: a collection of papers based on the proceedings of an international conference on mafic dyke swarms held at Erindale College, University of Toronto, Ontario, Canada, 4–7 June 1985. Geological Association of Canada
- Horsman E, Tikoff B, Morgan S (2005) Emplacement-related fabric and multiple sheets in the Maiden Creek sill, Henry Mountains, Utah, USA. *J Struct Geol* 27:1426–1444
- Horsman E, Morgan S, de Saint-Blanquat M, Habert G, Hunter R, Nugent A, Tikoff B (2009) Emplacement and assembly of shallow plutons through multiple magma pulses, Henry Mountains, Utah. *Earth Environ Sci Trans R Soc Edinb* 100:1–16
- Horsman E, Morgan S, de Saint-Blanquat M, Tikoff B (2010) Emplacement and assembly of shallow intrusions, Henry Mountains, Southern Utah. LASI V Conference, Field trip guidebook
- Hrouda F (1993) Theoretical models of magnetic anisotropy to strain relationship revisited. *Phys Earth Planet Inter* 77:237–249
- Hunt CB (1953) Geology and geography of the Henry Mountains region, Utah. U.S. Geological Survey, Professional Paper 228, p 234
- Hutton DHW (2009) Insights into magmatism in volcanic margins: bridge structures and a new mechanism of basic sill emplacement—Theron Mountains, Antarctica. *Petrol Geosci* 15:269–278
- Jackson MD, Pollard DD (1988) The laccolith-stock controversy: new results from the southern Henry Mountains, Utah. *Geol Soc Am Bull* 100:117–139
- Jackson MD, Pollard DD (1990) Flexure and faulting of sedimentary host rocks during growth of igneous domes, Henry Mountains, Utah. *J Struct Geol* 12(2):185–206
- Jamtveit B, Svensen H, Podladchikov YY, Planke S (2004) Hydrothermal vent complexes associated with sill intrusions in sedimentary basins. In: Breitreuz C, Petford N (eds) *Physical Geology of High-Level Magmatic Systems*. Geological Society, London, Special Publication, pp 229–232
- Johnson A, Pollard DD (1973) Mechanics of growth of some laccolithic intrusions in the Henry Mountains, Utah, I. Field observations, Gilbert's model, physical properties and flow of the magma. *Tectonophysics* 18:261–309
- Kano K, Matsuura H, Yamauchi S (1997) Miocene rhyolitic welded tuff infilling a funnel-shaped eruption conduit Shiotani, southeast of Matsue, SW Japan. *Bull Volc* 59(2):125–135
- Kerr AD, Pollard DD (1998) Toward more realistic formulations for the analysis of laccoliths. *J Struct Geol* 20(12):1783–1793
- Ketcham RA (2005) Three-dimensional grain fabric measurements using high-resolution X-ray computed tomography. *J Struct Geol* 27:1217–1228
- Ketcham RA, Carlson WD (2001) Acquisition, optimization and interpretation of X-ray computed tomographic imagery: applications to the geosciences. *Comput Geosci* 27:381–400
- Koch FG, Johnson AM, Pollard DD (1981) Monoclinical bending of strata over laccolithic intrusions. *Tectonophysics* 74(3–4):T21–T31

- Kratinová Z, Závada P, Hrouda F, Schulmann K (2006) Non-scaled analogue modelling of AMS development during viscous flow: a simulation on diapir-like structures. *Tectonophysics* 418(1–2):51–61
- Leuthold J, Müntener O, Baumgartner LP, Putlitz B, Ovtcharova M, Schaltegger U (2012) Time resolved construction of a bimodal laccolith (Torres del Paine, Patagonia). *Earth Planet Sci Lett* 325–326:85–92
- Leuthold J, Müntener O, Baumgartner LP, Putlitz B, Chiaradia M (2013) A detailed geochemical study of a shallow arc-related Laccolith; the Torres del Paine Mafic Complex (Patagonia). *J Petrol* 54(2):273–303
- Liss D, Hutton DHW, Owens WH (2002) Ropy flow structures: a neglected indicator of magma-flow direction in sills and dikes. *Geology* 30(8):715–718
- Liss D, Owens WH, Hutton DHW (2004) New palaeomagnetic results from the Whin Sill complex: evidence for a multiple intrusion event and revised virtual geomagnetic poles for the late Carboniferous for the British Isles. *J Geol Soc Lond* 161:927–938
- Magee C, Stevenson C, O'Driscoll B, Schofield N, McDermott K (2012) An alternative emplacement model for the classic Ardnamurchan cone sheet swarm, NW Scotland, involving lateral magma supply via regional dykes. *J Struct Geol* 43:73–91
- Martin U, Nemeth K (2007) Blocky versus fluidal peperite textures developed in volcanic conduits, vents and crater lakes of phreatomagmatic volcanoes in Mio/Pliocene volcanic fields of Western Hungary. *J Volcanol Geoth Res* 159(1–3):164–178
- Martín-Hernández F, Lüneburg CM, Aubourg C, Jackson M (2004) Magnetic fabric: methods and applications. In: Geological Society, London, Special Publications, vol 238, p 540
- McCaffrey KJW, Petford N (1997) Are granitic intrusions scale invariant? *J Geol Soc Lond* 154:1–4
- Michel J, Baumgartner L, Putlitz B, Schaltegger U, Ovtcharova M (2008) Incremental growth of the Patagonian Torres del Paine laccolith over 90 k.y. *Geology* 36(6):459–462
- Mock A, Jerram DA (2005) Crystal Size Distributions (CSD) in three dimensions: insights from the 3D reconstruction of a highly porphyritic rhyolite. *J Petrol* 46:1525–1541
- Mock A, Jerram DA, Breitzkreuz C (2003) Using quantitative textural analysis to understand the emplacement of shallow-level rhyolitic laccoliths—a case study from the Halle Volcanic Complex, Germany. *J Petrol* 44(5):833–849
- Morgan S, Horsman E, Tikoff B, de Saint Blanquat M, Habert G (2005) Sheet-like emplacement of satellite laccoliths, sills, and bysmaliths of the Henry Mountains, Southern Utah. In: Field guide. Geological Society of America, pp 1–28
- Morgan S, Stanik A, Horsman E, Tikoff B, de Saint Blanquat M, Habert G (2008) Emplacement of multiple magma sheets and wall rock deformation: Trachyte Mesa intrusion, Henry Mountains, Utah. *J Struct Geol* 30(4):491–512
- O'Driscoll B, Ferré EC, Stevenson CT, Magee C (2015) The significance of magnetic fabric in layered mafic-ultramafic intrusions. In: Charlier B, Namur O, Latypov R, Tegner C (eds) Layered intrusions. Springer, pp 295–329
- O'Driscoll B, Hargraves RB, Emeleus CH, Troll VR, Donaldson CH, Reavy RJ (2007) Magmatic lineations inferred from anisotropy of magnetic susceptibility fabrics in Units 8, 9, and 10 of the Rum Eastern Layered Series, NW Scotland. *Lithos* 98(1–4):27–44
- Orlický O (1990) Detection of magnetic carriers in rocks: results of susceptibility changes in powdered rock samples induced by temperature. *Phys Earth Planet Inter* 63:66–70
- Orth K, McPhie J (2003) Textures formed during emplacement and cooling of a Palaeoproterozoic, small-volume rhyolitic sill. *J Volcanol Geoth Res* 128:341–362
- Paterson SR, Vernon RH, Tobisch OT (1989) A review of criteria for the identification of magmatic and tectonic foliations in granitoids. *J Struct Geol* 11(3):349–363
- Paterson SR, Fowler TKJ, Schmidt KL, Yoshinobu AS, Yuan ES, Miller RB (1998) Interpreting magmatic fabric patterns in plutons. *Lithos* 44:53–82
- Paterson SR, Pignotta GS, Vernon RH (2004) The significance of microgranitoid enclave shapes and orientations. *J Struct Geol* 26(8):1465–1481
- Pavlis TL (1996) Fabric development in syn-tectonic intrusive sheets as a consequence of melt-dominated flow and thermal softening of the crust. *Tectonophysics* 253(1):1–31
- Philpotts AR, Asher PM (1994) Magmatic flow-direction indicators in a giant diabase feeder dike, Connecticut. *Geology* 22(4):363–366
- Philpotts AR, Philpotts DE (2007) Upward and downward flow in a camptonite dike as recorded by deformed vesicles and the anisotropy of magnetic susceptibility (AMS). *J Volcanol Geoth Res* 161(1–2):81–94
- Pirsson LV (1899) On the phenocrysts of intrusive igneous rocks. *Am J Sci* 40:271–280
- Platten IM (1984) Fluidized mixtures of magma and rock in a late Caledonian breccia dike and associated breccia pipes in Appin, Scotland. *Geol J* 19:209–226
- Platten IM (1995) The significance of phenocryst distributions in chilled margins of dykes and sills for the interpretation of tip processes. In: Baer G, Heimann A (eds) Physics and chemistry of dykes. Balkema, Rotterdam, pp 141–150
- Pollard DD (1973) Derivation and evaluation of a mechanical model for sheet intrusions. *Tectonophysics* 19:233–269
- Pollard DD, Johnson AM (1973) Mechanics of growth of some laccolithic intrusions in the Henry mountains, Utah, II: Bending and failure of overburden layers and sill formation. *Tectonophysics* 18(3–4): 311–354
- Pollard DD, Muller OH, Dockstader DR (1975) The form and growth of fingered sheet intrusions. *Geol Soc Am Bull* 86(3):351–363

- Prior DJ, Mariani E, Wheeler J (2009) EBSD in the earth sciences: applications, common practice, and challenges. In: Schwartz AJ, Kumar M, Adams BL, Field DP (eds) *Electron backscatter diffraction in materials science*. Springer, pp 345–360
- Randall BAO, Farmer N (1970) The Holy Island dyke. *Nat Hist Soc Northumberland Trans* 16:9–91
- Reedman AJ, Park KH, Merriman RJ, Kim SE (1987) Welded tuff infilling a volcanic vent at Weolseong, Republic of Korea. *Bull Volcanol* 49(3):541–546
- Richter C, van der Pluijm BA (1994) Separation of paramagnetic and ferrimagnetic susceptibilities using low-temperature magnetic susceptibilities and comparison with high field methods. *Phys Earth Planet Inter* 82:113–123
- Rickwood PC (1990) The anatomy of a dyke and the determination of propagation and magma flow directions. In: Parker AJ, Rickwood PC, Tucker DH (eds) *Mafic dykes and emplacement mechanisms*. Balkema, Rotterdam
- Rocchi S, Westerman DS, Dini A, Innocenti F, Tonarini S (2002) Two-stage laccolith growth at Elba Island (Italy). *Geology* 30(11):983–986
- Rocchi S, Mazzotti A, Marroni M, Pandolfi L, Costantini P, Bertozzi G, di Biase D, Federici F, Lô PG (2007) Detection of Miocene saucer-shaped sills (offshore Senegal) via integrated interpretation of seismic, magnetic and gravity data. *Terra Nova* 19:232–239
- Rocchi S, Dini A, Mazzarini F, Westerman DS (2010a) Themed Issue: LASI III—Magma pulses and sheets in tabular intrusions. *Geosphere*
- Rocchi S, Westerman DS, Dini A, Farina F (2010b) Intrusive sheets and sheeted intrusions at Elba Island (Italy). *Geosphere* 6(3):225–236
- Roni E (2012) Magma flow in shallow-level laccoliths and their feeder dykes (Elba island and Orciatico, Tuscany) revealed by AMS and structural data. In: Ph. D. thesis, University of Pisa, p 202
- Roni E, Westerman DS, Dini A, Stevenson C, Rocchi S (2014) Feeding and growth of a dyke–laccolith system (Elba Island, Italy) from AMS and mineral fabric data. *J Geol Soc* 171:413–424
- Ross ME (1986) Flow differentiation, phenocryst alignment, and compositional trends within a dolerite dike at Rockport, Massachusetts. *Geol Soc Am Bull* 97(2):232–240
- Schmiedel T, Breitzkreuz C, Göz I, Ehling BC (2015) Geometry of laccolith margins: 2D and 3D models of the Late Paleozoic Halle Volcanic Complex (Germany). *Int J Earth Sci* 104(2):323–333
- Schofield N, Stevenson C, Reston T (2010) Magma fingers and host rock fluidization in the emplacement of sills. *Geology* 38:63–66
- Schofield N, Heaton L, Holford SP, Archer SG, Jackson CA-L, Jolley DW (2012a) Seismic imaging of ‘broken bridges’: linking seismic to outcrop-scale investigations of intrusive magma lobes. *J Geol Soc* 169(4):421–426
- Schofield NJ, Brown DJ, Magee C, Stevenson CT (2012b) Sill morphology and comparison of brittle and non-brittle emplacement mechanisms. *J Geol Soc* 169(2):127–141
- Schofield N, Alsop I, Warren J, Underhill JR, Lehné R, Beer W, Lukas V (2014) Mobilizing salt: magma-salt interactions. *Geology* 42(7):599–602
- Schwab M (1962) Über die Inkohlung der Steinkohlen im nördlichen Saaletrog bei Halle. *Geologie* 11:917–942
- Simón JL, Arlegui LE, Pocióvi A (2006) Fringe cracks and plumose structures in layered rocks: stepping senses and their implications for palaeostress interpretation. *J Struct Geol* 28(6):1103–1113
- Simpson C, Schmid SM (1983) An evaluation of criteria to deduce the sense of movement in sheared rocks. *Geol Soc Am Bull* 94(11):1281–1288
- Skilling IP, White JDL, McPhie J (2002) Peperite: a review of magma-sediment mingling. *J Volcanol Geoth Res* 114:1–17
- Ślodziński E, Pietranik A, Breitzkreuz C, Pędziwiatr A, Bokła M, Schab K, Grodzicka M (2015) Formation of a laccolith by magma pulses: evidence from modal and chemical composition of the 500 m long borehole section through the Permo-Carboniferous Landsberg laccolith (Halle Volcanic Complex). *Geochem J* 49:523–537
- Smith RP (1987) Dyke emplacement at Spanish Peaks, Colorado. In: Halls HC, Fahrig WH (eds) *Mafic dyke swarms*, vol 34. Geological Association of Canada Special Paper, pp 47–54
- Stearns DW (1978) Faulting and forced folding in the Rocky Mountain foreland. In: Matthews V (ed) *Laramide folding associated with basement block faulting in the Western United States*, vol 151. Geological Society of America Memoir, pp 1–38
- Stevenson CTE, Bennett N (2011) The emplacement of the palaeogene Mourne granite centres, Northern Ireland: New results from the Western Mourne Centre. *J Geol Soc Lond* 168:831–836
- Stevenson CTE, Owens WH, Hutton DHW (2007a) Flow lobes in granite: The determination of magma flow direction in the Travenagh Bay Granite, northwestern Ireland, using anisotropy of magnetic susceptibility. *Geol Soc Am Bull* 119(11):1368–1386
- Stevenson CTE, Owens WH, Hutton DHW, Hood DN, Meighan IG (2007b) Laccolithic, as opposed to cauldron subsidence, emplacement of the Eastern Mourne pluton, N. Ireland: evidence from anisotropy of magnetic susceptibility. *J Geol Soc* 164(1):99–110
- Svensen H, Jamtveit B, Planke S, Chevallier L (2006) Structure and evolution of hydrothermal vent complexes in the Karoo Basin, South Africa. *J Geol Soc Lond* 163:671–682
- Tarling DH, Hrouda F (1993) *The magnetic anisotropy of rocks*. Chapman & Hall, London, p 217

- Thomson K, Hutton DHW (2004) Geometry and growth of sill complexes: insights using 3D seismic from the North Rockall Trough. *Bull Volc* 66:364–375
- Thomson K, Petford N (2008) Structure and emplacement of high-level magmatic systems. In: Geological Society, London, Special Publication, vol 302, p 227
- Thomson K, Schofield N (2008) Lithological and structural controls on the emplacement and morphology of sills in sedimentary basins. In: Thomson K, Petford N (eds) Structure and emplacement of high-level magmatic systems, vol 302. *Geol Soc London Spec Publ*, pp 31–44
- Tobisch OT, McNulty BA, Vernon RH (1997) Microgranitoid enclave swarms in granitic plutons, central Sierra Nevada, California. *Lithos* 40:321–339
- Tweto O (1951) Form and structure of sills near Pando, Colorado. *Geol Soc Am Bull* 62(5):507–532
- Varga RJ, Gee JS, Staudigel H, Tauxe L (1998) Dike surface lineations as magma flow indicators within the sheeted dike complex of the Troodos Ophiolite, Cyprus. *J Geophys Res* 103(B3):5241–5256
- Vernon RH (2000) Review of microstructural evidence of magmatic and solid-state flow. *Vis Geosci* 5(2):1–23
- Vernon RH (2004) A practical guide to rock microstructure. Cambridge University Press, p 594
- Vernon RH, Etheridge MA, Wall VJ (1988) Shape and microstructures of microgranitoid enclaves: indicators of magma mingling and flow. *Lithos* 22:1–11
- Walker G (1987) The dike complex of Koolau volcano, Oahu: internal structure of a Hawaiian rift zone. Volcanism in Hawaii. In: USGS Professional Paper 1350, Volcanism in Hawaii, pp 961–993
- Wilson PI, McCaffrey KJ, Wilson RW, Jarvis I, Holdsworth RE (2016) Deformation structures associated with the Trachyte Mesa intrusion, Henry Mountains, Utah: implications for sill and laccolith emplacement mechanisms. *J Struct Geol* 87:30–46
- Winter C, Breitzkreuz C, Lapp M (2008) Textural analysis of a Late Palaeozoic coherent to pyroclastic rhyolitic dyke system near Burkardsdorf (Erzgebirge, Saxony, Germany). In: Thomson K, Petford N (eds) Structure and emplacement of high-level magmatic systems, vol 302. *Geol Soc London Spec Publ*, pp 197–219

Geochemical Fingerprinting and Magmatic Plumbing Systems

Christophe Y. Galerne and Else-Ragnhild Neumann

Abstract

Subvolcanic systems are characterized by complex combinations of intrusive units (dykes, sills, saucer-shaped sills, cone sheets, etc.) for which genetic relationships are unclear. This chapter explains how whole-rock geochemistry may be used to resolve the genetic relationships of such subvolcanic (and volcanic) systems. We start with a short introduction of the geochemical fingerprinting method with particular emphasis on the statistical refinement method called Forward Stepwise-Discriminant Function Analysis (FS-DFA). Combined with field mapping and structural analysis, geochemical fingerprinting based on major and trace elements and isotope ratios, is a very powerful tool to distinguish between igneous units (lavas, sills, dykes) with subtle (or not so subtle) geochemical differences. Different geochemical fingerprinting or signatures indicate derivation from distinct magma batches. The results from FS-DFA analyses may be used to reveal genetic relationships between geological units, or lack of such, which again may be used to throw light on subvolcanic plumbing systems, the feeding system in sill-dyke complexes, as well as other problems. The method is illustrated by studies of the Golden Valley Sill Complex in the Karoo Basin (South Africa).

1 Introduction

Comprehension of the processes that give rise to different types of units (dykes, sills, lavas) in magmatic domains (flood basalts, sill complexes in sedimentary basins, dyke-lava-sill relationships in volcanoes, etc.) depends strongly on information about the genetic relationships between different units. Important information may be obtained from field observations and geophysical imaging (e.g. seismic analyses). However, although the physical relationships

C.Y. Galerne (✉)
GeoModellingSolutions GmbH,
Hardturmstraße 120, 8005 Zurich, Switzerland
e-mail: christophe.y.galerne@googlemail.com

E.-R. Neumann
Physics of Geological Processes,
University of Oslo, Oslo, Norway
e-mail: e.r.neumann@geo.uio.no

between units may be identified by these methods, their genetic relationships are not ascertained. This is true for units that appear to be in direct physical contact, as well as for units that are not. An important additional method is to establish the geochemical signatures of the geological units in the area in question. Different geochemical signatures of two units imply derivation from different magma batches, whereas identical signatures imply derivation from the same, or chemically identical, magma batches. Further analysis of the geochemical signatures of the units in an area may be used to establish the evolutionary histories of the magmatic rocks (the causal mechanisms for observed compositional variations), and possible genetic relationships between the units.

This chapter gives a presentation of different methods for geochemical fingerprinting; the statistical method Forward Stepwise-Discriminant Function Analysis (FS-DFA) is described in some detail. The methods are illustrated by examples from the Karoo Large Igneous Province (South Africa), with emphasis on the results obtained in the Golden Valley Sill Complex (GVSC).

The chapter ends with a discussion of how geochemical fingerprinting may be used to throw light on feeding mechanisms between different units (sill-sill, dyke-lava, dyke-sill), and subsurface plumbing systems.

2 Chemical Fingerprinting

2.1 Element Ratios

Chemical fingerprinting was originally developed in order to map distinct lava flows in igneous provinces dissected by erosion and/or poorly exposed. The basic method is to use ratios between incompatible trace elements to identify different magmatic units (lavas, dykes, sills). The term “incompatible trace elements” is generally

used for elements that fit very poorly into the minerals in the mantle (where basaltic magmas are formed) and in minerals forming in a basaltic magma (e.g. Rb, Th, U, Nb, Ta, Zr, P, rare earth elements [REE], Zr, Ti, Y). In a magma, ratios between pairs of strongly and moderately incompatible or pairs of moderately and mildly incompatible trace elements will therefore not change during moderate degrees of fractional crystallization. This means that samples derived from the same magma reservoir will have similar ratios, whereas different batches generally will have different ratios. Other processes (contamination, assimilation, mixing between chemically distinct magmas, separation of a fluid phase, etc.), will generally modify ratios between incompatible trace elements.

Figures 1 and 2 show the use of geochemical fingerprinting on lavas in the Lesotho Lava Plateau (the Drakensberg Group) in the Karoo Basin (Marsh et al. 1997). Whole-rock analyses on lavas from numerous isolated sections (Fig. 1a) show slightly different ratios between pairs of incompatible elements, i.e. different geochemical fingerprints. These differences are expressed in ratio-ratio diagrams in Fig. 2. In ratio-ratio diagrams samples from the same unit are expected to plot in a tight cluster. Samples from different units may overlap in one diagram, but be separated in another, revealing different geochemical characteristics. By the help of several ratio-ratio diagrams it may be possible to distinguish the chemical identities of different magmatic units within the same area. Fig. 2 shows the results for lavas in the Lesotho Formation and in the Barkly East Formation in the Drakensberg Group. Lavas in the Barkly East formation form separate clusters in the two ratio-ratio diagrams, demonstrating different geochemical signatures. The chemical variations among the Lesotho lavas (Fig. 2), however, are too subtle to be differentiated in the ratio-ratio diagram and overlap in the grey field in Fig. 2. Based on ratio-ratio diagrams Marsh et al. (1997) were able to correlate lavas in

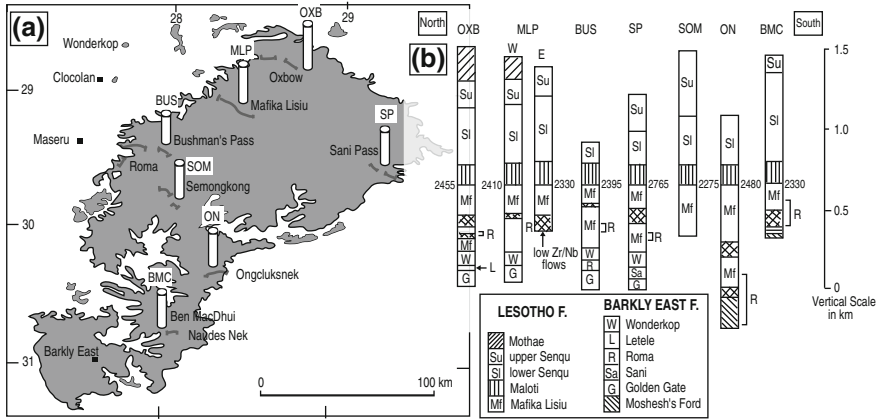


Fig. 1 Chemical fingerprinting of the Drakensberg lava sequence showing the correlation between the lava units at different localities. **a** Schematic map of the

Drakensberg flood basalts. **b** Summary of the stratigraphic columns in each location based on geochemistry after Marsh et al. (1997)

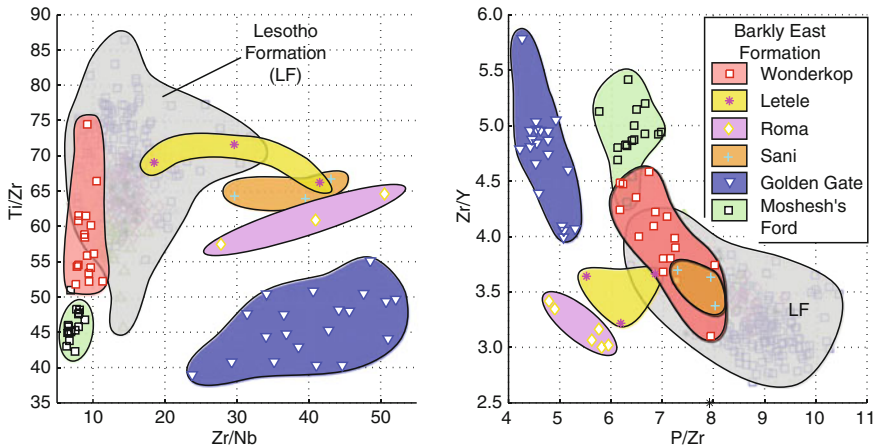


Fig. 2 Plots of ratio between strongly incompatible elements (Ti/Zr vs. Zr/Nb, Zr/Y vs. P/Zr) for lavas from the Lesotho Formation (*grey field*) and Barkly East

formation within the Drakensberg lava sequence (Marsh et al. 1997). See text for discussion

the Lesotho Formation and in the Barkly East Formation from one outcrop to the next (Fig. 1b). In this way they managed to map the extent of different lava flows, as well as time-related compositional variations.

Although ratios between highly incompatible elements are useful in revealing chemical contrasts in some cases, they clearly do not resolve subtle chemical contrasts. A more robust method is to use a statistical approach.

2.2 Statistical Methods

Statistical methods have proven to be excellent tools for distinguishing different geochemical signatures among magmatic rock units with small compositional contrasts (e.g. Duncan et al. 1984; Sheth et al. 2004). One such method is the Forward Stepwise-Discriminant Function Analysis (FS-DFA; Hill and Lewicki 2007; StatSoft 2013). Discriminant function analysis is a statistical

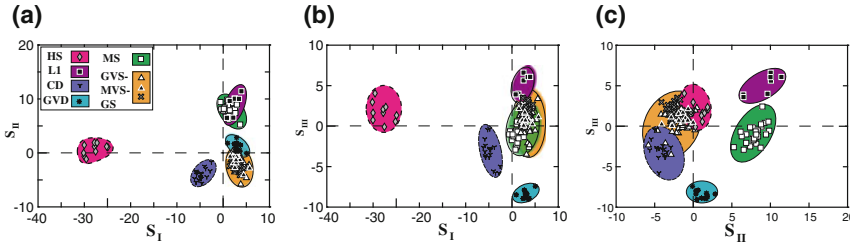


Fig. 3 Principal Component diagrams obtained from the FS-DFA method applied to the GVSC after Galerne et al. (2008). **a**, **b** and **c** show the best results for the sample populations used as input data. The applications of these

discriminant functions on samples from localities with too few samples to use statistics gave additional details on the GVSC geochemical architecture (see Fig. 10 d–f in Galerne et al. 2008)

analysis to predict a categorical dependent variable (called a *grouping variable*) on the basis of a set of independent variables (called *predictor variables*). Discriminant analysis is used when groups are known a priori (unlike in cluster analysis). It works by creating one or more linear combinations of predictors, called *discriminant functions* (or *principal component functions*). The number of discriminant functions possible is either $n - 1$ ($n =$ number of groups), or p (the number of predictors), whichever is smaller. The first function created maximizes the differences between groups on that function. The second function maximizes differences on that function, but also must not be correlated with the previous function. This continues with subsequent functions with the requirement that the new function is not correlated with any of the previous functions.

In geological fingerprinting by the FS-DFA method, n is a set of known sample populations or groups (i.e. lavas, dykes, sills); the predictor variables, p , are chemical variables within each population (major elements, trace elements, isotope ratios). The higher p , the more detailed and reliable are the results. Using such input information the FS-DFA evaluates the compositional variations within each sample population, and the geochemical differences between the sample populations. The resulting basis functions are based on the most discriminative predictor variables, m ($< p$), weighted by the coefficients, W , that maximize the variance between the populations relative to the

variance within them. These weighted variables are combined in $n - 1$ basis functions (assuming that $n < m$). An example of such statistical analysis can be found in Table 3 in Galerne et al. (2008). The general formulation of the discriminant (or principal component) function is:

$$S_i = C_i + W_i^1 \cdot X_i^1 + W_i^2 \cdot X_i^2 + \dots + W_i^m \cdot X_i^m \quad (1)$$

where C is a constant specific to the i th discriminant function S ; X is the measured concentration of a given element, weighted by the coefficient W specific to that element X in the i th discriminant function. The subscript i refers to the relative importance of the discriminant functions, 1 giving the best discrimination, $n - 1$ the poorest; the superscripts 1 to m refer to the predictors (elements, isotope ratios) included in the final model. The statistical method has the advantage that it can deal with large data sets and produce quick and robust results (see Fig. 11 in Galerne et al. 2008).

The result may be presented in two-dimensional plots using the best discriminative functions as main axes (Fig. 3). It is also possible to show the populations in a hierarchical diagram which displays the relative compositional differences between the populations (Fig. 4). Below we show the use of the FS-DFA method on the Golden Valley Sill Complex in the Karoo Basin, South Africa.

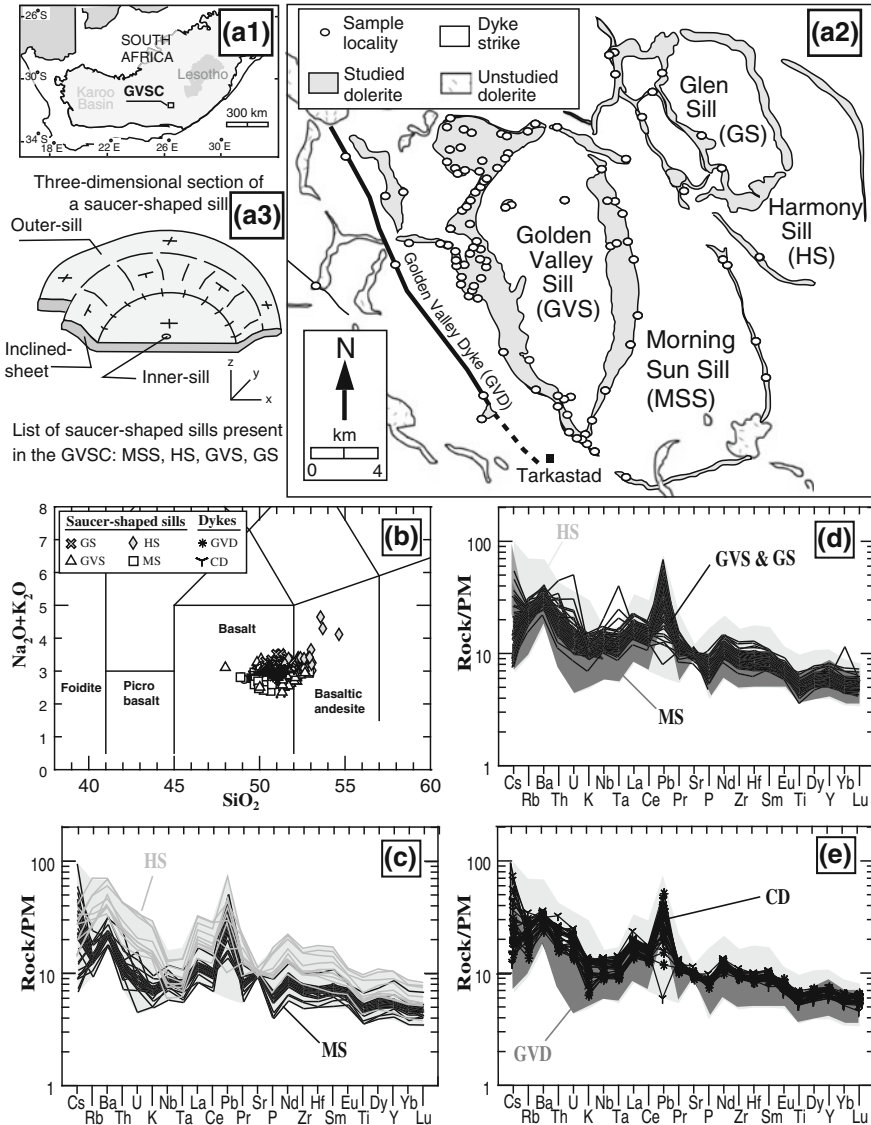


Fig. 5 **a1** Location of the GVSC in the Karoo Basin, South Africa. **a2** Simplified geological map of the GVSC showing sample locations (after Galerne et al. 2008). **a3** Schematic illustration of saucer-shaped sill in three-dimensional cross-section. **b** Total Alkali Silica (TAS)

diagram **c–e** Trace element concentrations (normalized to Primitive mantle, PM, as given by McDonough and Sun 1995) for rocks in the golden valley Sill Complex (Galerie et al. 2008)

All the rocks in the GVSC are basaltic to basaltic-andesitic (Fig. 5b) and the compositional range is generally small (Fig. 5b–e). The samples show essentially parallel trace-element patterns which might be explained by different degrees of fractional crystallization from a common initial magma. The southern part of the Karoo Basin is

underlain by the Namaqua-Natal Mobile Belt in which the lithosphere acquired an arc-like signature (enriched Sr–Nd isotope ratios, negative Nb–Ta anomalies) during former orogenic events (e.g., Catuneanu 2004); Strong enrichment in Pb indicates crustal contamination (Fig. 5d–e). However, plots of ratios between pairs of incompatible

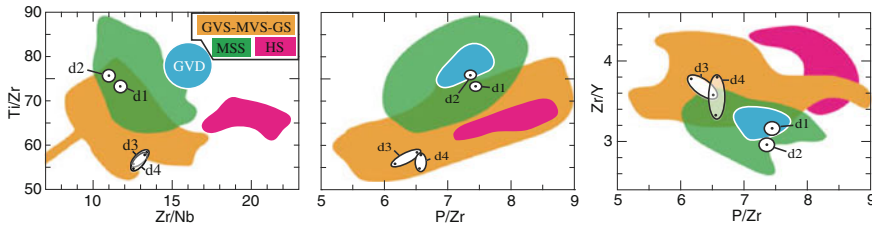


Fig. 6 Plots of strongly incompatible element ratios (Ti/Zr vs. Zr/Nb, Ti/Zr vs. P/Zr, and Zr/Y vs. P/Zr) in dolerites from the GVSC (modified after Galerne et al. 2008, 2011). Data published in Fig. 15 of Galerne et al.

(2008) are completed with the data published as supplementary material by Galerne et al. (2008). The colored fields represent the distinct magma batches involved in the emplacement of major sills and dykes of the GVSC

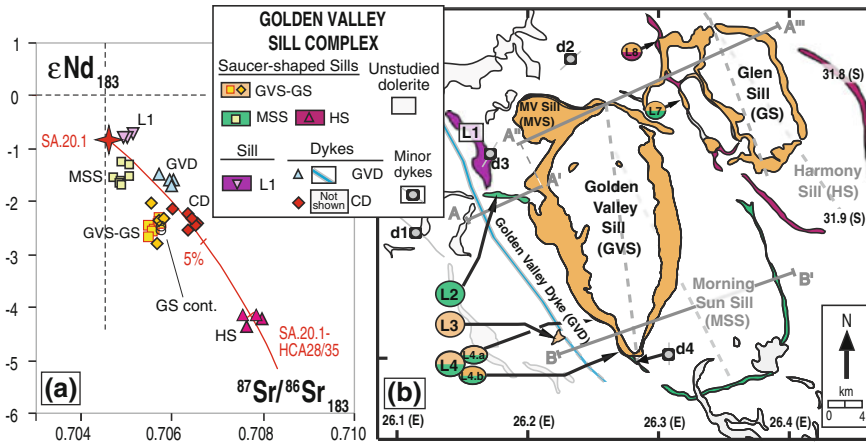


Fig. 7 a Variations in initial Sr–Nd isotopes among the GVSC units (after Neumann et al. 2011), assuming the age of 183 Ma determined for sills in the Karoo Basin (Svensen et al. 2007, 2012). The trend is estimated on the basis of the EC-RAFC model of Spera and Bohrsen (2004) using dyke SA.20.1 from southern KwaZulu-Natal, South Africa (Riley et al. 2006) as initial-melt

model and a combination of the Proterozoic mafic granulite xenoliths HCA28 and HCA35 from the northern Lesotho/central Cape province (Huang et al. 1995). **b** Map view of the Geochemical architecture of the GVSC (Galerie et al. 2008). Different colors reflect different chemical signatures

elements (Fig. 6) show clear distinctions between some of the populations. It is particularly evident that the geochemical characteristics of the HS and the GVD are different from those of the other units. However, the FS-DFA statistical method, based on 47 major and trace elements, reduced to 19 most discriminative predictor variables (*m*) by the PCA algorithm, gives an excellent separation of the populations (Fig. 3). Although some populations overlap in some diagrams, they are separated in others, showing that the units, or sample populations, are separated in *m*-dimensional space. The results are presented in map view in Fig. 7b. The

degree of chemical diversity among the populations is shown in the hierarchical diagram, Fig. 4. Two units, the Golden Valley Sill (GVS) and the Glen Sill (GS) overlap in all diagrams, and are shown as identical in the hierarchal diagram, the other units have different chemical fingerprinting. This means that GVS and GS must originate in the same, or identical, magma batches, whereas the other populations in the GVSC were derived from separate magma batches.

The FS-DFA method also helped in the study of the GVSC regarding some units for which there were too few analyses to give a statistical

basis. Once the basis functions were established, it was possible to estimate the positions of samples from these units in the Principal Component diagrams and thus test their possible affinity to the other units (and magma batches; see Fig. 10 in Galerne et al. 2008). This increased the details of known genetic relationships in the GVSC. The overall result is the comprehensive geochemical architecture shown in map view in Fig. 7b.

In the GVSC the results obtained by the FS-DFA method were later confirmed by Sr–Nd isotope data (Fig. 7a; Neumann et al. 2011). Each unit that was given a unique geochemical identity by the FS-DFA method based on major and trace element data, covered a very limited range in $^{87}\text{Sr}/^{86}\text{Sr}$ and $^{143}\text{Nd}/^{144}\text{Nd}$ ratios, defining a small domain different from those of the other units. Furthermore, like in the Principal Component diagram (Fig. 3), the GVS and GS showed identical Sr–Nd isotope ratios, confirming derivation from the same (or identical) magma batches.

4 Implications

4.1 Genetic Relationship and Evolutionary History

Geochemical fingerprinting can reveal details about the genetic relationships between magmatic rocks in an area, and about their evolutionary history. Based on major and trace element and Sr–Nd isotope data Neumann et al. (2011) concluded that the different geochemical signatures in the different units in the Golden Valley Sill Complex were caused by a combination of interaction with the lithospheric mantle and fractional crystallization and contamination in the deep crust. The ascending magmas lost their buoyancy when passing from the dense upper mantle into the less dense lower crust, and ponded there. The hot magmas heated the crustal wall-rocks beyond their solidus temperatures, causing partial melting. At the same time the magmas cooled and started to crystallize. Different degrees of hybridism of crustal melts with strong arc-type geochemical signature,

accompanied by fractional crystallization (AFC processes) changed the major and trace element, and the Sr–Nd isotope compositions of the magmas, thus causing their different geochemical fingerprinting (Figs. 6 and 7). Hybridism of lower crustal melts led to different degrees of enrichment in strongly incompatible elements, enriched Sr–Nd isotopic ratios, and relative depletion in Nb and Ta relative to REE. In summary the different magmas appear to be derived from a common, or identical, primary melt(s). Entering the lower crust the melt(s) formed magma chambers where they were subjected to different degrees of fractional crystallization and contamination. This gave rise to magma batches with different chemical fingerprinting which have given very important information about the feeding mechanisms and plumbing system in the upper crust.

4.2 Emplacement Mechanism of the GVSC Plumbing System

Saucer-shaped sills are tabular intrusions observed worldwide in volcanic margins and sedimentary basins (e.g., offshore Norway, Karoo Basin). Although they are common, their feeding mechanisms are poorly known, mainly because the relationships between sills and their feeders are rarely exposed (e.g., Hyndman and Alt 1987), and difficult to image on seismic data. The emplacement mechanism of sills and saucer-shaped sills in sedimentary basins are therefore mostly debated on the basis of theoretical models. Some models propose that sill intrusions occur along the level of neutral buoyancy of the magma, and the feeders are expected to be located below the outer sill at one side of the saucer (Fig. 8a; e.g., Bradley 1965; Francis 1982; Chevallier and Woodford 1999; Gouly 2005); other models propose that saucers are fed from below through a central feeder dyke (Fig. 8b; Galland et al. 2009, and references therein). In the latter models, the feeders are expected to be situated beneath the central part of the inner sills (Fig. 8b).

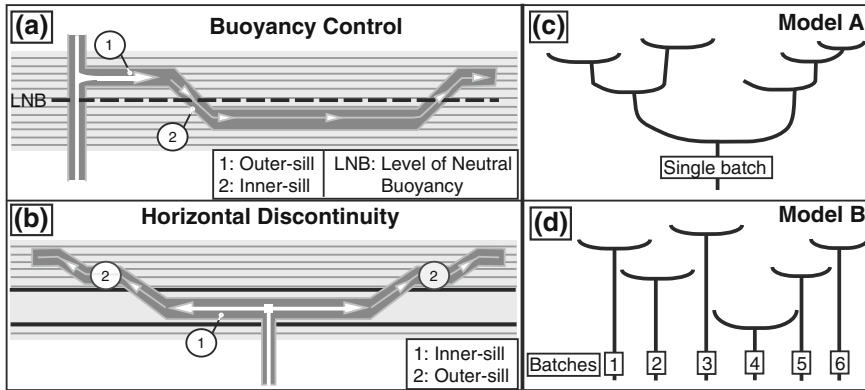


Fig. 8 **a** and **b** are theoretical models of saucer-shaped sill emplacement mechanisms. Numbers (1) and (2) indicate the steps of emplacement. **a**. Model of emplacement controlled at the level of neutral buoyancy (LNB), modified from Francis (1982). Sills are fed laterally from one part of the outer sill. **b** Model of emplacement along horizontal discontinuity, modified after Malthe-Sørenssen

et al. (2004). Sills are fed radially from the inner sill. **c** and **d** are geochemical end-member plumbing system scenarios for sill complexes. **c** Model A: a single batch of magma forms a network of interconnected (nested) sills. **d** Model B: each saucer-shaped sill represents a geochemical distinct magma batch that has entered the upper crust through separate channels

The application of the geochemical fingerprinting method to saucer-shaped sill complexes may help deciphering which of these theoretical models works in nature. The problem is reformulated as follows: are the sills in saucer-shaped sill complexes formed by a single magma batch through an interconnected network (Model A; Fig. 8c), or is each unit in such a complex fed by an individual magma batch (Model B; Fig. 8d)? The first hypothesis implies that the sills fed each other through an interconnected sill network (Fig. 8c); the second hypothesis implies that each sill is fed through a distinct conduit (Fig. 8d).

In the GVSC a small part of the vertical section is exposed, revealing part of the 3-D relationship between sills and dykes. Combined with field relationships, structural observations and mechanical considerations, the application of chemical fingerprinting provides an important tool to establish the architecture of the upper parts of plumbing systems and the feeding relationship between different units.

As shown above, the FS-DFA statistical method revealed that in the GVSC the two major saucers at the upper stratigraphic level (GVS and GS) have identical chemical fingerprinting (Figs. 4 and 5). This indicates that, although they are not presently in physical contact, they

originate from the same, or identical, magma batches. All other major intrusions yield distinctive geochemical signatures. This implies that the sills at the upper (GVS and GS) and lower levels (HS and MSS) were not connected in a sill-feeding-sill relationship while emplaced in the Karoo Basin (Fig. 9a, b).

Some minor sills are in physical contact with major sills or dykes (L3-GVD, L4-GVS, L7-GS and L8-GS; Fig. 7b), suggesting sill-feeding-sill relationships. However, the FS-DFA results show that L4, L7 and L8 consist of two parts, an upper part with GVS-GS geochemical signature and a lower part with MSS signature (Galerie et al. 2008). These locations reveal that the MSS at the lower stratigraphic level locally came into contact with the GVS-GS at the higher stratigraphic level, but there is no sill-feeding-sill relationship (Figs. 8 and 9).

There are, however, close associations between one elliptical sill (the GVS) and a small dyke (d4): the dyke is exposed underneath the southern tip of the sill, and is parallel to the long axis of the GVS sill (dashed line in Fig. 7b). Unfortunately only two analyses with significantly fewer trace elements than in the main data set were available on d4. To determine their geochemical relationship the GVS and dyke d4

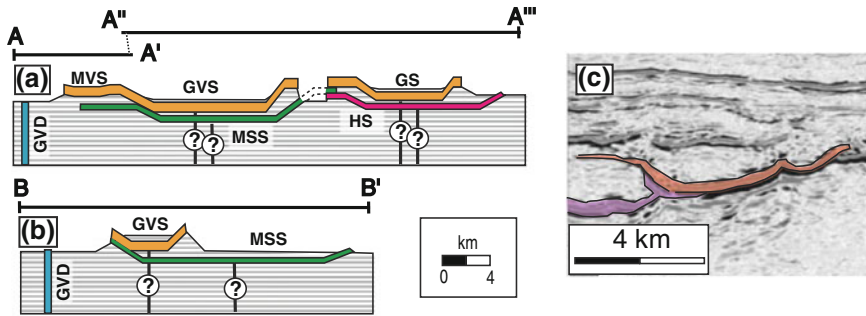


Fig. 9 Geological cross-sections **a** A-A''' and **b** B-B'. Figure after Galerne et al. (2011), see Fig. 6 for colour legend. **c** Example of seismic image showing contact between two saucer-shaped sills, interpreted as feeding relationship by Hansen et al. (2004). A comparison

between this image and the geological cross section of the GVSC suggests that the contact between the two sills may not reflect a feeding relationship, but is accidental, as suggested by the different colors in this hypothetical re-interpretation

data were compared on the basis of element ratios (Fig. 6). In all diagrams d4 falls within the field defined by the GVS-GS magma batch. Having the same geochemical signature as the GVS, the d4 dyke covers all fundamental criteria required for being the feeder of the overlying saucer-shaped GVS sill: it is stratigraphically below the GVS, aligned along the long axis of the sill, and has identical geochemical signatures.

The above discussion shows that the plumbing system in the GVSC closely resembles Model B in Fig. 9d with each unit being fed by a separate batch of magma (Galerne et al. 2008, 2011). However, their identical geochemical signatures leave the possibility that GVS fed GS through a lateral overflow and that a former contact between the two sills has been erased by erosion (Galerne et al. 2008). This possibility was, however, made unlikely by laboratory experiments combined with recent field work in the GVSC (Galerne et al. 2011). Experiments on the relationships between type of feeder (one-dimensional or dyke) and the shape of saucer-shaped sills suggest that the most likely feeder to an elliptical saucer-shaped sill is a dyke located underneath the sill, oriented parallel to the long axis of the elliptical sill (Galerne et al. 2011). The experimental results show strong similarities to the GVS-d4 relationships and thus support the proposition that dyke d4 is the feeder to the GVS sill (Galerne et al. 2011). Also the other saucer-shaped sills in the GVSC are elliptical. Based on

these experiments it seems likely that all the GVSC sills are fed by separate dykes. Despite identical geochemical signatures of the GVS and GS, these two sills may also have had separate feeder dykes in the upper crust.

The experimental technique and apparatus used in the laboratory experiments that gave rise to the dyke-feeding-elliptical-sill hypothesis were developed by Galland et al. (2009). Details on this method may be found in “Laboratory experiments” in the present volume (Galland et al. 2014). This is important information also when it comes to interpreting saucer-shaped sills that appear to be nested in images based on seismic data (Fig. 9c). Saucer-shaped sills showing contact in seismic images are generally interpreted in terms of sill-feeding-sill (Hansen et al. 2004). However, the results from the GVSC strongly suggest that such contacts may be accidental, and have no bearing on the genetic relationship between the sills. The alternative interpretation of two sills in contact but genetically unrelated are suggested in Fig. 9c.

5 Summary and Perspectives

Chemical fingerprinting is an old method in geochemistry. Since the work of Pearce and Cann (1971, 1973) this method has kept evolving as the resolution of chemical analyses increase. Technical improvements have brought geochemical

fingerprinting into a new era where it can be used to distinguish magmatic units emplaced or erupted in restricted areas within a given tectonic setting on the basis of subtle geochemical contrasts.

Theoretical models based on mechanistic approaches and/or observations often result in numerous competing models. Geochemical fingerprinting provides a tool to identify the geochemical architecture of magmatic systems. This technique appears to be a robust method to support or reject theoretical models. We have provided two examples of successful application of the geochemical fingerprinting method to flood basalts and a sill complex emplaced in sedimentary basin. In the case of the flood basalts, the results provided the possibility of correlating lavas in stratigraphic sections that are separated by erosion and spread over distances of 100s of km. The results gave information on time-related compositional variations on the same scale, and confirmed the large extent of surface eruptions of the same magma batch, either through continuous connection or separate co-eruptive fissures. In the case of sill complex emplacements in a sedimentary basin, geochemical fingerprinting showed that a large complex of apparently interconnected sills (saucer-shaped sills) were not feeding one another but formed from separate magma batches, and that one of the major sills was fed by a dyke.

References

- Bradley J (1965) Intrusion of major dolerite sills. *Trans R Soc NZ* 3:27–55
- Catuneanu O (2004) Retroarc foreland systems—evolution through time. *J Afr Earth Sc* 38(3):225–242
- Chevallier L, Woodford A (1999) Morpho-tectonics and mechanism of emplacement of the dolerite rings and sills of the western Karoo, South Africa. *S Afr J Geol* 102(1):43–54
- Duncan AR, Erlank AJ, Marsh JS (1984) Regional geochemistry of the Karoo igneous province. In: Erlank AJ (ed) *Petrogenesis of the volcanic rocks of the Karoo province*. Geol Soc of S Afr Spl Pub, pp 355–388
- Encarnación J, Fleming TH, Eales HV (1996) Synchronous emplacement of Ferrar and Karoo dolerites and the early breakup of Gondwana. *Geology* 24:535–538
- Francis EH (1982) Magma and sediment—I. Emplacement mechanism of late Carboniferous tholeiite sills in northern Britain. *J Geol Soc* 139(1):1–20
- Galerne CY, Neumann ER, Planke S (2008) Emplacement mechanisms of sill complexes: information from the geochemical architecture of the golden valley sill complex South Africa. *J Volcanol Geoth Res* 177(2):425–440
- Galerne CY, Neumann ER, Aarnes I, Planke S (2010) Magmatic differentiation processes in saucer-shaped sills: Evidence from the golden valley sill in the Karoo Basin, South Africa. *Geosphere* 6(3):163–188
- Galerne CY, Galland O, Neumann ER, Planke S (2011) 3D relationships between sills and their feeders: evidence from the golden valley sill complex (Karoo Basin) and experimental modelling. *J Volcanol Geoth Res* 202(3–4):189–199
- Galland O, Holohan E, van Wyk de Vries B, Burchardt S (2014) Laboratory modelling of volcano plumbing system. In: Breitreuz C, Rocchi S (eds) *Laccoliths, sills and dykes—physical geology of shallow level magmatic systems*. Advances in volcanology
- Galland O, Planke S, Neumann ER, Malthe-Sørensen A (2009) Experimental modelling of shallow magma emplacement: application to saucer-shaped intrusions. *Earth Planet Sci Lett* 277(3–4):373–383
- Gouly NR (2005) Emplacement mechanism of the Great Whin and Midland Valley dolerite sills. *J Geol Soc* 162:1047–1056
- Hansen DM, Cartwright JA, Thomas D (2004) 3D seismic analysis of the geometry of igneous sills and sill junctions relationships. In: Davies RJ, Cartwright JA, Stewart SA, Lappin M, Underhill JR (eds) *3D Seismic technology: application to the exploration of sedimentary basins*. Geological Society, London, Memoirs pp 199–208
- Hill T, Lewicki P (2007) *STATISTICS: methods and applications*. StatSoft, Tulsa
- Huang Y, van Calsteren P, Hawkesworth C (1995) The evolution of the lithosphere in southern Africa: A perspective on the basic granulite xenoliths from kimberlites in South Africa. *Geochim Cosmochim Acta* 59(23):4905–4920
- Hyndman DW, Alt D (1987) Radial dikes, laccoliths, and gelatin models. *J Geol* 95:763–774
- Jourdan F, Feraud G, Bertrand H, Kampunzu AB, Tshoso G, Le Gall B, Tiercelin JJ, Capiez P (2004) The Karoo triple junction questioned: evidence from Jurassic and Proterozoic Ar-40/Ar-39 ages and geochemistry of the giant Okavango dyke swarm (Botswana). *Earth Planet Sci Lett* 222(3–4):989–1006
- Jourdan F, Feraud G, Bertrand H, Kampunzu AB, Tshoso G, Watkeys MK, Le Gall B (2005) Karoo large igneous province: Brevity, origin, and relation to mass extinction questioned by new Ar-40/Ar-39 age data. *Geology* 33(9):745–748
- Jourdan F, Feraud G, Bertrand H, Watkeys MK (2007) From flood basalts to the inception of oceanization: Example from the Ar-40/Ar-39 high-resolution picture

- of the Karoo large igneous province. *Geochem Geophys Geosyst* 8(2):1–20
- Le Gall B, Tshoso G, Jourdan F, Feraud G, Bertrand H, Tiercelin JJ, Kampunzu AB, Modisi MP, Dymont J, Maia M (2002) Ar-40/Ar-39 geochronology and structural data from the giant Okavango and related mafic dyke swarms, Karoo igneous province, northern Botswana. *Earth Planet Sci Lett* 202(3–4):595–606
- Malthe-Sørenssen A, Planke S, Svensen H, Jamtveit B (2004) Formation of saucer-shaped sills. In: Breikreuz C, Petford N (eds) *Physical geology of high-level magmatic systems*. Geological Society, London, *Spl Pub* pp 215–227
- Marsh JS, Hooper PR, Rehacek J, Duncan RA, Duncan AR (1997) Stratigraphy and age of Karoo basalts of Lesotho and implications for correlations within the Karoo igneous province. In: Mahoney JJ, Coffin MF (eds) *Large igneous provinces: continental, oceanic, and planetary flood volcanism*. Geophysical Monographs Series. American Geophysical Union, pp 247–272
- McDonough WF, Sun SS (1995) The composition of the earth. *Chem Geol* 120(3–4):223–253
- Neumann ER, Svensen H, Galerne CY, Planke S (2011) Multistage evolution of dolerites in the Karoo Large Igneous Province, Central South Africa. *J Petrol* 52(5):959–984
- Pearce J, Cann J (1971) Ophiolite origin investigated by discriminant analysis using Ti, Zr and Y. *Earth Planet Sci Lett* 12(3):339–349
- Pearce J, Cann J (1973) Tectonic setting of basic volcanic-rocks determined using trace-element analyses. *Earth Planet Sci Lett* 19(2):290–300
- Riley TR, Curtis ML, Leat PT, Watkeys MK, Duncan RA, Millar IL, Owens WH (2006) Overlap of Karoo and Ferrar magma types in KwaZulu-Natal, South Africa. *J Petrol* 47(3):541–566
- Sheth HC, Mahoney JJ, Chandrasekharam D (2004) Geochemical stratigraphy of Deccan flood basalts of the Bijasan Ghat section, Satpura Range, India. *J Asian Earth Sci* 23(1):127–139
- Spera F, Bohron W (2004) Open-system magma chamber evolution: an energy-constrained geochemical model incorporating the effects of concurrent eruption, recharge, variable assimilation and fractional crystallization (EC-E RA chi FC). *J Petrol* 45(12):2459–2480
- StatSoft Inc (2013) *Electronic statistics textbook*. Tulsa, OK. <http://www.statsoft.com/textbook/>
- Svensen H, Corfu F, Polteau S, Hammer O, Planke S (2012) Rapid magma emplacement in the Karoo Large Igneous Province. *Earth Planet Sci Lett* 325:1–9
- Svensen H, Planke S, Chevallier L, Malthe-Sørenssen A, Corfu F, Jamtveit B (2007) Hydrothermal venting of greenhouse gases triggering early Jurassic global warming. *Earth Planet Sci Lett* 256(3–4):554–566
- Svensen H, Polteau S, Cawthorn S, Planke S (2014) Subvolcanic intrusions in the Karoo Basin, South Africa. In: Breikreuz C, Rocchi S (eds) *Laccoliths, sills and dykes—physical geology of shallow magmatic systems*. *Advances in Volcanology*

Geophysics and Remote Sensing

Sverre Planke, Henrik Svensen, Reidun Myklebust,
Stephen Bannister, Ben Manton, and Lars Lorenz

Abstract

Igneous sheet intrusions such as sills, dikes, and laccoliths are abundant in volcanic basins. Mafic intrusions are characterized by high P-wave seismic velocities in the range from 5.0 to 7.0 km/s. Velocity aureoles with a thickness comparable to the sill intrusion are commonly identified on sonic log data above and below the intrusions. Sills as thin as 10 m may be detected by conventional seismic reflection data, whereas sills with a thickness above about 40 m are resolvable. Offset-dependent tuning of sill reflections is expected due to the high velocity of the intrusions. Deep sills are difficult to image by reflection methods but can be identified from wide-angle seismic data. Sill reflections are interpreted based on characteristic features such as their high amplitudes and saucer-shaped geometries. Sill complexes are further well-suited for 3D visualization techniques. Potential field and electromagnetic data may improve the reliability of the igneous intrusion interpretation; however such data have poor resolution if sills are buried below more than a few kilometers of sediments. Andesitic and felsic intrusions and laccoliths are less abundant than sills in volcanic basins, and few well-documented geophysical interpretation studies of such intrusions or dykes are published.

S. Planke (✉) · H. Svensen
Centre for Earth Evolution and Dynamics (CEED),
University of Oslo, Oslo, Norway
e-mail: planke@vbpr.no

S. Planke
Volcanic Basin Petroleum Research (VBPR),
Oslo Science Park, Oslo, Norway

R. Myklebust
TGS, Asker, Norway

S. Bannister
GNS Science, Lower Hutt, New Zealand

B. Manton
Cardiff University, Cardiff, UK

L. Lorenz
EMGS, Oslo, Norway

1 Introduction (F1-3)

Igneous sheet intrusions are commonly present in sedimentary basins world-wide, and are associated with continental and volcanic rifted margin Large Igneous Provinces (LIPs). The intrusions are dominantly mafic in composition, however ultramafic, andesitic, and felsic LIPs are also identified (Bryan and Ernst 2008; Bryan and Ferrari 2013). The subvolcanic intrusions in sedimentary basins are dominantly tabular in shape, whereas laccoliths and plutons are less abundant. Smaller volume igneous intrusions are

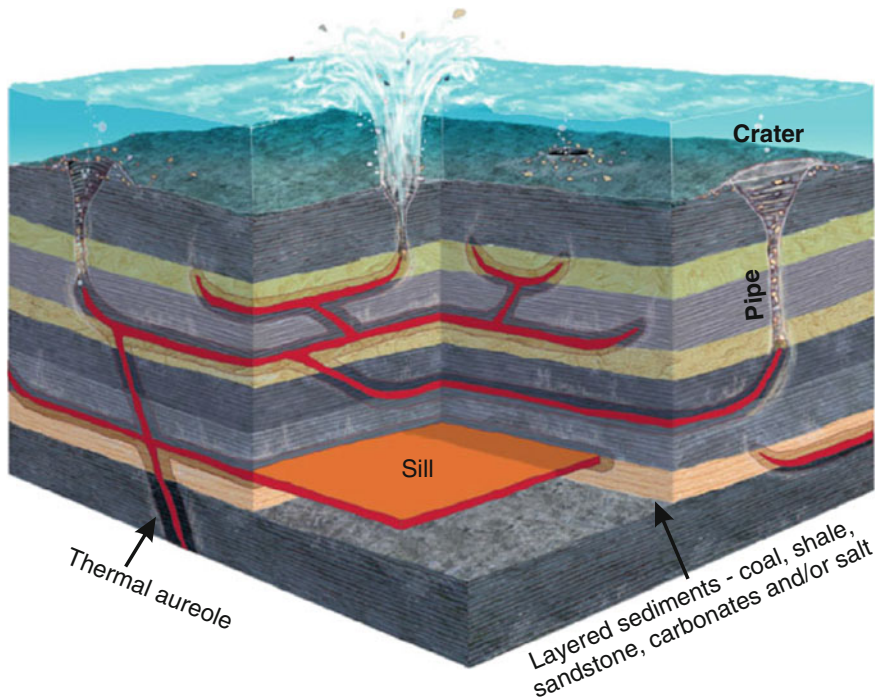


Fig. 1 Sketch of a volcanic basin showing a sill complex (red), thermal aureoles and associated hydrothermal vent complexes. The vent complexes are typically located

above the tip of transgressive sills, and consist of a vertical pipe and a crater at the seabed

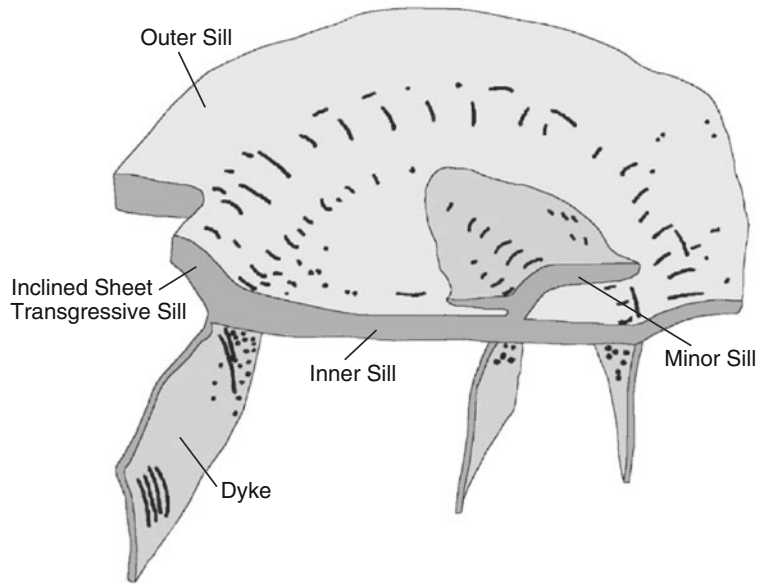
also present in sedimentary basins and sedimentary sequences above oceanic crust.

The emplacement of magma into sedimentary basins causes heating and deformation of the host rocks. Metamorphic reactions may lead to the formation of large volumes of greenhouse gases such as methane and carbon dioxide, or ozone-depleting gases such as chlorinated and brominated halocarbons if evaporite basins are intruded. It has been suggested that rapid release of such gases to the atmosphere may have triggered rapid global warming and mass-extinction events several times during Earth history (e.g., Svensen et al. 2004). The igneous intrusions also have an impact on the petroleum and mineral prospectivity of sedimentary basins. The sill complexes may represent long-lasting barriers to fluid flow, whereas fracture contact zones and hydrothermal vent complexes may lead to focused fluid flow. The permeable zones are good targets for water exploration drilling in dry

regions such as the Karoo of South Africa (Chevallier and Woodford 1999).

Volcanic basins are sedimentary basins with major components of intrusive and/or extrusive igneous rocks. Figure 1 shows a sketch of a subvolcanic complex in a typical volcanic basin. Deep seated sills are dominantly layer parallel, whereas saucer-shaped sills are more common in the shallow intervals. The sills may form interconnected complexes, whereas dykes are less common. Metamorphic aureoles develop around the cooling intrusions. The heating causes devolatilization reactions, leading to overpressure by the formation of gases such as methane, carbon dioxide, and/or boiling of water below the critical pressure. Hydrothermal vent complexes are formed if sufficiently large pressures are generated to fracture the overburden in low-permeability sequences. The vent complexes commonly originate from the upper terminations of transgressive sill segments, and consist of a

Fig. 2 Morpho-structural diagram of a typical saucer-shaped dolerite sill of the Karoo Basin. Note that the feeder dykes are often difficult to identify in the field. Modified from Chevallier and Woodford (1999)



pipe connecting the aureole to a crater at the paleo-surface.

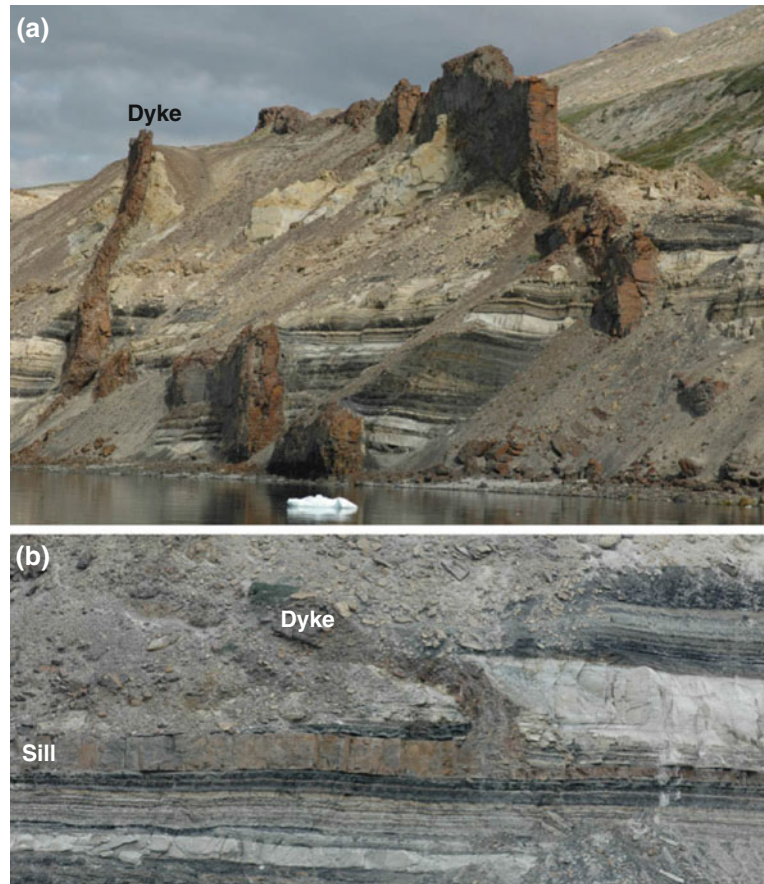
The sills commonly display a saucer-shaped geometry in layered sedimentary basins (Polteau et al. 2008). Field and borehole studies in the Karoo Basin reveal that the saucer-shaped sills consist of three main components: a sub-horizontal inner sill, inclined sheets (transgressive sills), and outer sills (Fig. 2). Minor sills and dykes are sometimes also present, but the feeding relationships of dykes and sills are often difficult to document. Figure 3 shows small-scale outcrops of near-vertical dykes and a rare occurrence of a sill-dyke connection in the Nuussuaq Basin, west-central Greenland.

Sub-horizontal sheet intrusions are well imaged on seismic reflection data as the sill-sediment contacts are high-impedance boundaries. Major sill complexes were identified on 2-D seismic data in the Northeast Atlantic in the 1980s and 1990s (e.g., Gibb and Kanaris-Sotiriou 1988; Skogseid and Eldholm 1989; Skogseid et al. 1992). During the past decade numerous detailed 3-D seismic studies of sill complexes have been published, in particular from the West of Shetland region (e.g., Bell and Butcher 2002; Trude 2004;

Hansen et al. 2004; Thomson 2004; Smallwood and Harding 2009). Saucer-shaped sill complexes are now identified in numerous sedimentary basins world-wide, including offshore West Africa (e.g., Rocchi et al. 2007) and Australia (Schofield and Totterdell 2008; Magee et al. 2013). In contrast, identification of dykes or intrusive bodies such as laccoliths, stocks and plutons is less common.

The aim of this contribution is to show how igneous intrusions are identified and interpreted on remote sensing geophysical data. The focus of the paper is on seismic imaging and interpretation of mafic sill complexes, as mafic intrusions are abundant in sedimentary basins and the seismic reflection method represents the most useful geophysical method currently available. However, potential field data (gravity, magnetic), wide-angle velocity data, electromagnetic data, and satellite imaging data are occasionally used to identify and interpret subvolcanic intrusions and will therefore also be briefly discussed. The examples are mainly from the Vøring Basin offshore mid-Norway, where extensive Paleogene breakup-related sill complexes intrude dominantly Cretaceous sequences.

Fig. 3 Paleogene sills and dykes intruding sandstones, shales and coals of the deltaic Cretaceous Atane Formation at Atanikerluk on the Nuussuaq Peninsula, west-central Greenland. The dykes in **a** are about 3.5 m wide. The sill in **b** is about 1 m wide



2 Seismic Reflection Method

A high-quality 2-D seismic reflection profile across the northern Vøring Basin is shown in Fig. 4a. This profile reveals an extensive, dominantly layer-parallel sill complex that was intersected by exploration well 6607/5-2 on the Utgard High in 1991. The well drilled a 91 m thick Upper Sill (US) and terminated 50 m into a Lower Sill (LS). In addition, a 3 m thick sill was penetrated 370 m above the US. The Upper and Lower sills are accurately dated by the TIMS zircon U-Pb method at 55.6 ± 0.3 and 56.3 ± 0.4 Ma, respectively (Svensen et al. 2010). A detailed geochemical study of borehole cuttings shows that the dolerites were formed by fractional crystallization of melt in the lower

crust with minor assimilation of crustal melts, leaving a >320 m thick unit of ultramafic cumulates (Neumann et al. 2013).

The Upper Sill correlates with a high amplitude reflection, S1, in the Någrind Syncline, whereas the Lower Sill is less-well imaged in the Utgard High but can be correlated with S2 in the Någrind Syncline. Two deeper levels of sills, S3 and S4, are interpreted in the central part of the syncline. The imaging is not sufficiently good to determine if any deeper sills are present. Thin and small sills are also difficult to image, and the uppermost 3 m thick sill drilled in 6607/5-2 is too small to be imaged on available data. The vertical resolution limit of sills is discussed in Sect. 2.2. Note that no sills were intersected by the nearby well 6607/5-1, about 10 km to the southeast. No sill reflections are identified in this area.

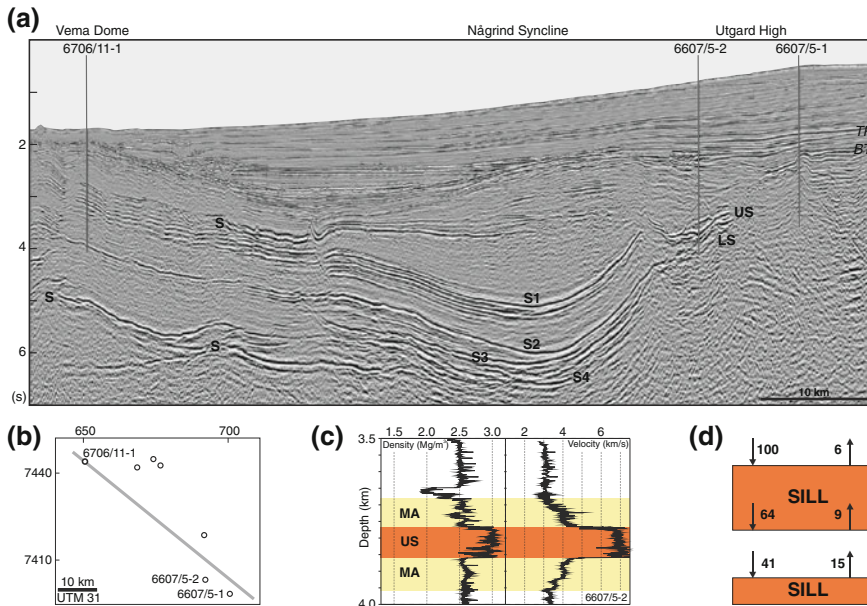


Fig. 4 Seismic reflection profile across the north Vøring Basin in the Norwegian Sea. **a** 2D seismic reflection profile. **b** Location map; selected wells and seismic profile in **a** shown as circles and a grey line, respectively. **c** Wire line log data of the Upper Sill. **d** Normalized amplitude of transmitted and reflected normal incidence wave based on

Zoeppritz equations. Velocities of the host rock and sill are 3.0 and 5.5 km/s, respectively, whereas the corresponding densities are 2.5 and 2.9 Mg/m³. Modified from Planke et al. (2005). *S* sill; *US* upper sill; *LS* lower sill; *TP* top palaeocene; *BT* base tertiary

2.1 Petrophysics

The wire line logs from well 6607/5-2 document the characteristic petrophysical properties of dolerite intrusions. The sonic log shows a box like character, with a rapid increase of P-wave velocity at the top of the sill and a correspondingly rapid decrease at the base of the sill (Fig. 4c). The sill velocity is very high, about 7.0 km/s, and fairly constant throughout. A few zones of lower velocities correlate with increase in borehole size measured by the caliper log, and is likely related to hole washout, possibly related to fracturing of the dolerite.

The P-wave velocity of the intruded Upper Cretaceous sediments in the Utgard well is about 3.0 km/s. However, there is a distinct increase of P-wave velocity towards the sill both from the top and the bottom, reaching more than 4.0 km/s near the contact. The thickness of the interval with increased P-wave velocity is about 100 m both above and below the Upper Sill, defining a

high velocity contact metamorphic aureole around the intrusion (MA).

The entire suite of conventional log curves from the well is available from the Norwegian Petroleum Directorate (www.npd.no). Other porosity-dependent logs (bulk density, neutron porosity, resistivity) reveal the same general trend as the sonic log. The dolerite density is as high as 3.0 Mg/m³, whereas the porosity is very low, typically <5 %. The deep resistivity is very high (2,000 Ω-m; ca. 1–5 m depth of investigation), whereas the medium resistivity is somewhat lower (300–1,000 Ω-m). Shear wave velocity logs are not available, but Vp/Vs ratios of 1.8–2.0 are assumed based on downhole measurements of massive basalts in Ocean Drilling Program boreholes offshore southeast Greenland (Planke and Cambray 1998). The natural gamma ray log correlates well with the box-like velocity response, with a typical value of 30 GAPI in the dolerite. In the host rocks there is a well-defined intermediate resistivity aureole both above and below the

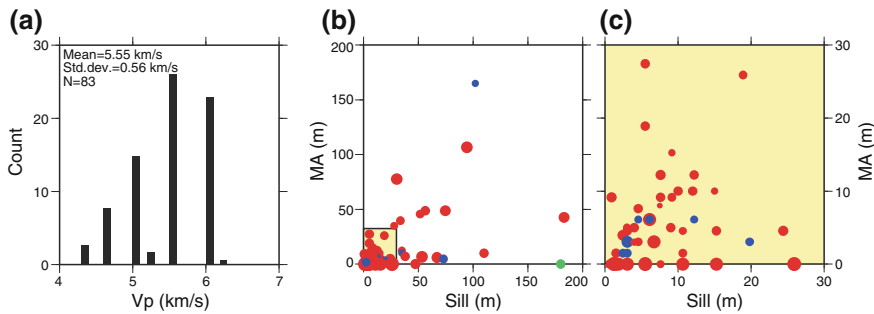


Fig. 5 **a** Average P-wave wireline log velocities of 83 sills drilled West of Shetland. The average sill thickness is 35 m. **b**, **c** Sill versus metamorphic aureole (MA) thickness of the same sills. The sill and aureole thicknesses are interpreted from log data. *Red circles*

fine-grained clastic host rocks; *blue circles* limy fine-grained clastic host rocks. The symbol sizes are scaled according to the host rock velocity (mean of 3.55 km/s). Modified from Skogly (1998)

intrusion. No aureoles are identified on the gamma ray, density, and porosity logs.

Well log data from 83 sills drilled in the West of Shetland region reveal sonic velocities of 4.5–6.2 km/s, and a mean velocity of 5.55 km/s (Fig. 5a). These velocities are significantly lower than the Utgard sill velocities. The difference is possibly related to thickness, grain size, and compositional variations, with the Utgard sills being thicker and more iron-rich (Berndt et al. 2000). A plot of the sill versus the aureole thicknesses in the West of Shetland area displays a broad 1:1 correlation, however there is a large scatter of data and several intrusions with no detectable velocity aureoles.

Sill velocities may also be measured by wide-angle seismic experiments. A multi-layered sill complex, similar to the one in the Någrind Syncline, is found in the Hel Graben, about 50 km to the northwest. Berndt et al. (2000) modelled ocean bottom seismometer data across the Hel Graben, and obtained P-wave velocities of 7.4 km/s at ca. 5 km depth (Fig. 6), which is even higher than the 7.0 km/s sonic velocity of the Upper Sill of the Utgard well.

In summary, mafic sills represent high-velocity and high-density sheets in sedimentary basins. Seismically, they can be viewed as homogenous, isotropic layers. The intrusions are commonly associated with a velocity aureole of similar thickness to that of the sills, as confirmed by both mineralogical and thermal modelling (Aarnes et al. 2010). A caveat is that shallow sills and

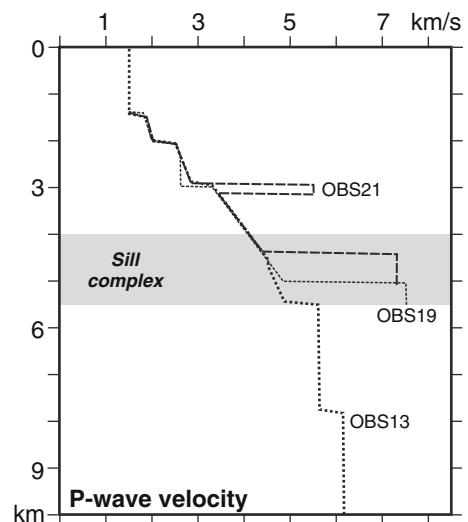


Fig. 6 Seismic wide-angle velocity-depth profiles in the Hel Graben, about 50 km NW of the Vema Dome (Fig. 4). A layered sill complex intruded into Cretaceous sediments is associated with high P-wave velocities. *OBS* ocean bottom seismometer. Modified from Berndt et al. (2000)

invasive flows emplaced into unconsolidated sediments may have significantly lower velocities due to intense fracturing or the development of peperitic layers.

2.2 Seismic Imaging

High velocity tabular sill intrusions emplaced in low velocity host rocks represent easy targets for seismic imaging. Sub-sill imaging is, however,

more difficult, partly due to transmission loss across high-impedance contrast boundaries. This is clearly illustrated in Fig. 4a where the Upper Sill is much better imaged than the Lower Sill even though the sill-sediment impedance contrasts and the sill thicknesses are similar. The sketch in Fig. 4d shows the sub-sill decrease of reflection amplitude of a normal incidence plane-wave with a relative amplitude of 100. Based on Zoeppritz equations, the amplitude of the reflected wave from the top of the upper sill is six times greater than the amplitude of the reflected wave from the top of the lower sill. The figure shows that the relative amplitude of the wave reflected from the top of the lower sill is only 6 % of the amplitude of the incoming wave at the top of the upper sills.

Other factors influencing the seismic imaging are related to the geometry of the sills (e.g., thickness, areal extent, and dip). Additionally, the seismic acquisition parameters, such as the source pulse and streamer length, as well as seismic processing have an important impact on the imaging.

The seismic detection and resolution limits of sills depend on the signal/noise ratio and bandwidth of the data. In simple terms, detection is the ability to identify a sill, whereas resolution is the ability to determine the thickness of the intrusion. The vertical detection limit is perhaps as low as 1/30 of the dominant wavelength, or ca. 6 m for a 30 Hz wavelet and a sill velocity of 5.5 km/s. The horizontal detection limit is somewhat more difficult to assess. Pant and Greenhalgh (1989) used physical 2D seismic modelling to determine that targets as small as 1/30 of a wavelength are detectable, but the amplitude, polarity and frequency of the event is modified if the reflecting layer is less than one wavelength. The nature of the reflection is dependent on a volume integration of the properties of the media above and below the sill interface. The lateral extent of the integration volume corresponds to the first Fresnel zone at the sill-sediment interface (approximately 400–700 m radius for a 30 Hz reflection at 2–6 s depth and an average velocity of 3 km/s) (Favretto-Cristin et al. 2009). 3D migration is very

important for improved horizontal resolution, essentially for collapsing the Fresnel zone to a much smaller area.

The vertical seismic resolution of a thin bed is often determined by the classic quarter wavelength criterion. Thus, the vertical resolution of a sill with a velocity of 5.5 km/s is 46 and 69 m for a 30 and 20 Hz Ricker wavelet, respectively. However, thinner layers may be resolved down to 1/16 of a wavelength using spectral inversion methods (Purvey and Castagna 2008; Zhang and Castagna 2011). For real data, it is often the signal/noise ratio and the wavelet spectrum that determine the obtainable resolution limit.

Sill tuning and resolution aspects are explored using the classic wedge model of Widess (1973) and a 20 Hz zero-phase Ricker wavelet (Fig. 7). Note strong interference and tuning effects for sill thicknesses up to 120 m with destructive interference of <20 m thick sills and a maximum constructive interference for ca. 50 m thick sills.

Sills in volcanic basins are thin, high-velocity layers which lead to source-receiver offset dependent tuning of reflected waves. The tuning effects can be explored by full elastic wave-equation modelling of simplified Earth models and typical seismic acquisition parameters (Fig. 8). A 100 m thick sill is clearly resolved at short offsets for a 30 Hz Ricker wavelet. However, strong tuning effects are observed at offsets >2 km, and only one reflection is visible beyond 3 km offset. There is a clear amplitude-versus-offset (AVO) increase, with a peak near the critical offset. The tuning effects are similar for the sill and the sill+aureole models (Fig. 8c, d), however the maximum amplitude and the critical offset are slightly different with a lower near-offset amplitude and a greater critical distance of the sill +aureole model. Similar wave-equation modelling of 15–50 m thick sills show only one reflection at all offsets, and a clear AVO decrease.

Kinematic ray-tracing can be used to show how the distance between the top sill and base sill travel-time curves is reduced towards the critical point (Fig. 9). The decreasing separation between the two travel-time curves makes it more difficult to distinguish individual reflections with increasing offset and leads to offset-depending tuning.

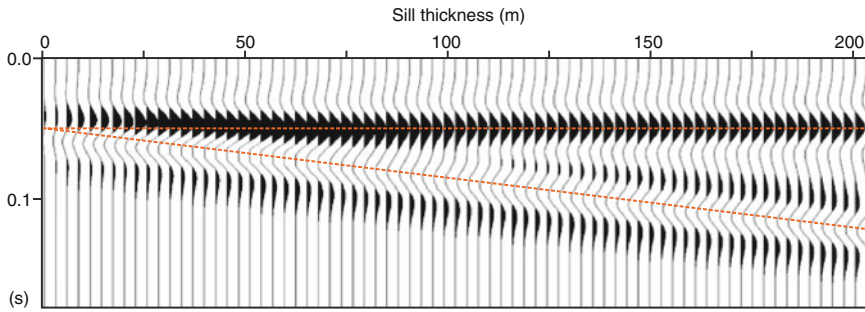


Fig. 7 Plot of 1-D synthetic seismograms for sills with systematically increasing thicknesses from 0 to 205 m. The *top* and *bottom* sill contacts are shown by *dashed orange lines*. The section corresponds to perfectly

migrated reflection data. Calculations were done using a 20 Hz zero-phase Ricker wavelet and no transmission losses. Velocities of the host rock and sill are as in Fig. 4d

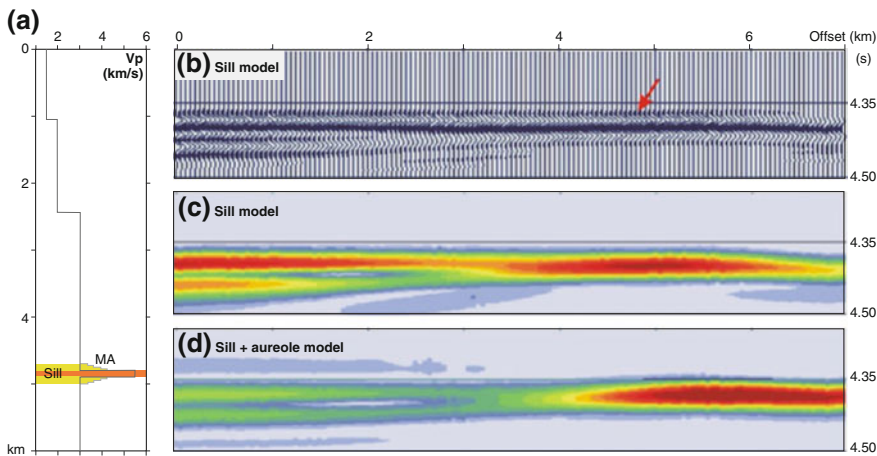


Fig. 8 Synthetic wave-equation seismograms for a simplified 1-D Earth model showing strong source-receiver offset dependent tuning for a 100 m thick sill using a 30 Hz Ricker source wavelet. **a** P-wave velocity (V_p) models of a 100 m thick sill with and without a metamorphic aureole (MA). Sediment layers $\rho = 2.2 \text{ Mg/m}^3$, $Q_p = Q_s = 250$; $V_p/V_s = 1.8$ in upper sediment layer, 1.75 otherwise. Sill

intrusion $\rho = 2.9 \text{ Mg/m}^3$, $Q_p = Q_s = 1,000$, $V_p/V_s = 1.9$. **b** Synthetic seismograms of the sill model. Red arrow critical offset (4.8 km). The data are plotted after applying a static time-shift operator to align the sill reflections (i.e. no moveout stretching). **c, d** Instantaneous amplitude response of the sill model and sill + aureole model, respectively (red is high, blue is low; y-axis in seconds)

The wide-angle data from the Hel Graben (Fig. 6; Berndt et al. 2000) documents that sufficient seismic energy to be detected is transmitted through a sill-sediment complex with a wave velocity representing the high-velocity end-member ($>7 \text{ km/s}$). The measured high velocity of the layered sill-sediment complex suggests that lower-crustal high velocity bodies imaged by wide-angle seismic data may not represent massive underplated material, but rather a complex of lower crustal intrusions mixed with sedimentary rocks (White et al. 2008).

2.3 Seismic Interpretation

The determination of lithology from seismic reflection data is challenging, in particular in frontier volcanic basins with limited well control. Igneous intrusions are, however, good imaging targets and have some deterministic features that make it possible to interpret them with high confidence in many basins. However, it is important to have consistent and reliable criteria to interpret intrusions and to avoid misinterpretation of similarly imaged geological features

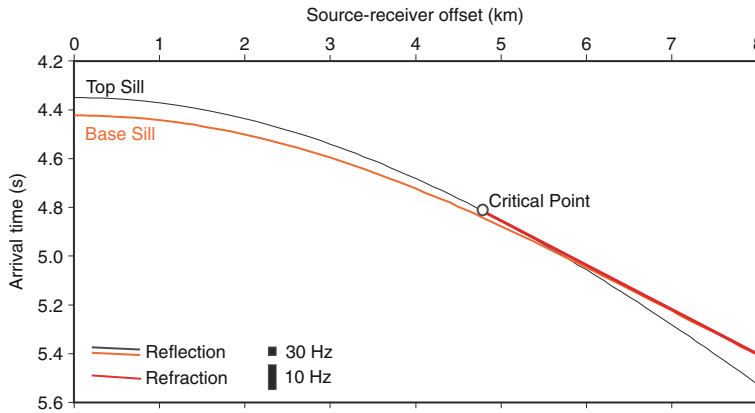


Fig. 9 Kinematic ray-tracing of a four-layer Earth model (see Fig. 8a) with a 200 m thick sill. Note that the time-difference between the reflection curves from the upper

and lower surfaces decreases with offset. The critical offset for the top sill reflection is 4.8 km. Vertical length of 10 and 30 Hz wavelets shown

such as high-velocity carbonate layers, sediment intrusions, or gas-charged sandstones. Thin or small intrusions, dykes and other steeply dipping sheet intrusions, and intrusions below the uppermost igneous unit are also difficult to identify in many basin provinces.

A combination of methods is commonly used for interpretation of sill complexes in volcanic basins (Planke et al. 2005):

- horizon and attribute mapping,
- interpretation of sill reflections,
- 3D voxel visualization,
- seismic facies analyses, and
- integration with well, geological and other geophysical data.

The seismic interpretation is normally done in a workstation environment using software such as the Kingdom Suite (www.ihs.com) and Petrel (www.software.slb.com). These software packages are well-suited for conventional mapping of time horizons and reflection attributes. Such data form an important stratigraphic framework for subsequent mapping of igneous intrusive units and associated hydrothermal vent complexes and lava flows.

Sill reflections are characterized by four distinct features:

- high positive reflection amplitudes,
- abrupt reflection terminations,
- saucer shape, and/or

- cross-cutting of layered sedimentary sequences (“transgressive sheets”).

The most diagnostic features are the high amplitude and the saucer-shape or transgressive nature of the sill reflections. 3D seismic data or grids of 2D seismic data are important to increase the confidence of the interpretation. An improved reliability can also be obtained by borehole calibration (e.g., Fig. 4), integration with other geophysical data (Sect. 3), and the identification of related igneous features in the basin.

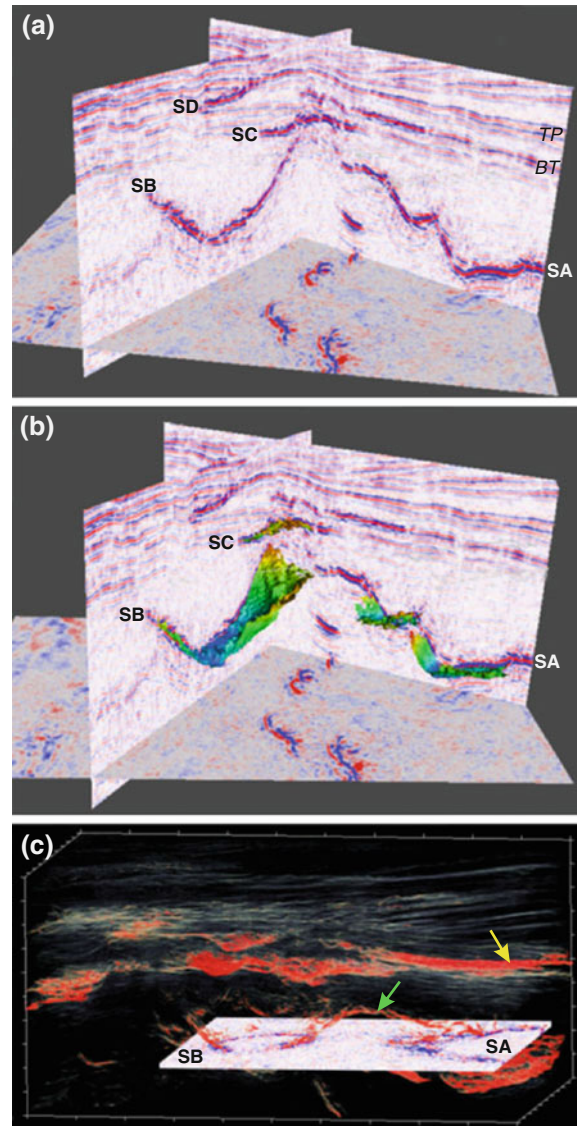
Sill complexes consist of splitting and merging sheets, and conventional horizon picking is therefore complicated. Normally, numerous horizons must be generated representing individual sill segments. In contrast, sill reflections are well suited for 3D visualization methods because of their high amplitudes and complicated shapes. Proper scaling of the data is obviously important, and true amplitude data or scaling using a long time window is useful for 3D visualization of sills.

Figure 10 shows the 3D interpretation of the Gleipne Sill Complex in the Outer Vøring Basin. Two saucer-shaped, positive high-amplitude reflections with abrupt terminations, SA and SB, are well-defined on seismic cross-sections and time slices (Fig. 10a). Two sub-horizontal high-amplitude events, SC and SD, are identified above the saucers. Both events are locally cross-cutting the uppermost Cretaceous and Palaeocene

Fig. 10 3-D visualization and interpretation of the Gleipne Sill Complex, outer Vøring Basin.

a Seismic profiles showing two well-defined saucer-shaped sills (*SA* and *SB*) and shallow sub-horizontal sills (*SC* and *SD*). The saucer-shaped sill *SB* is approximately 3×4 km wide and 0.5 km high.

b Horizon interpretation of three sills. **c** Semi-transparent voxel rendering of reflection amplitudes. High amplitudes are shown in red. Green arrow possible link between *SA* and *SB*. Yellow arrow shallow sills



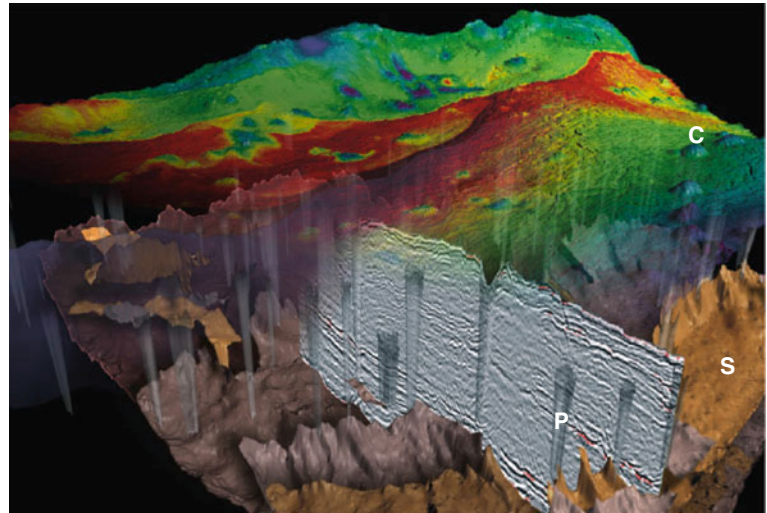
sequences below the Top Palaeocene (TP) paleosurface. These events are also interpreted as sills. A few discontinuous, high-amplitude layer-parallel events are also present in the Palaeocene sequence. No clear cross-cutting relationships are identified, and these events are therefore possibly sedimentary reflections.

The result of automatic horizon mapping of the two elliptical saucers, *SA* and *SB*, and the *SC* event, is shown in Fig. 10b. Semi-transparency amplitude voxel rendering reveal the saucer shape of *SA* and *SB* (Fig. 10c). These two saucers are

locally connected with an outer sill (green arrow). A visualization of the Stetind Sill Complex in the central Vøring Basin is shown in Fig. 11. Individual sills are picked and plotted as horizons. The sills are shown together with numerous vertical pipe structures terminating at kilometre-sized craters on the paleosurface. Mound structures are commonly present above the craters, both as domes near the Top Palaeocene horizon and in the overlying Eocene sequences.

Detailed sill interpretation, attribute analyses, and volume rendering techniques have

Fig. 11 3-D visualization of the Stetind Sill Complex in the central Vøring Basin. The interpreted sills (*S*) are associated hydrothermal vent complexes (*P* pipe; *C* crater/mound), and rms amplitudes of an Eocene time horizon. Visualization of Audun Groth, Statoil

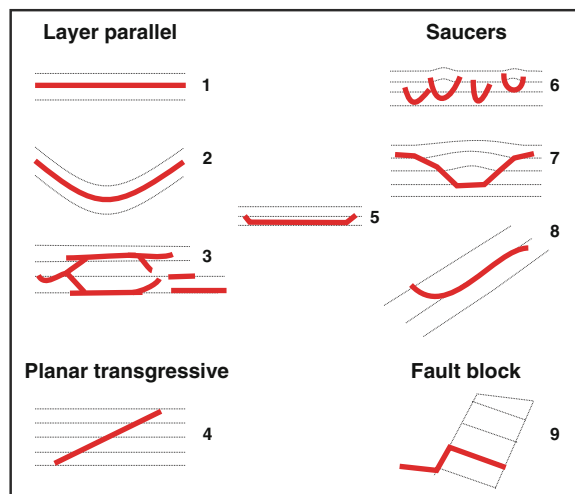


particularly been applied to 3D seismic data in the Northeast Atlantic to gain a better understanding of sill geometries and emplacement processes. Flow morphologies, magma tubes, and feeding systems have been mapped in detail (e.g., Trude 2004; Thomson 2004, 2007; Hansen et al. 2004; Cartwright and Hansen 2006; Hansen and Cartwright 2006a; Thomson and Schofield 2008; Smallwood and Harding 2009; Miles and Cartwright 2010; Schofield et al. 2012; Holford et al. 2012). The data document that sill complexes may form inter-connected plumbing systems with outward flow of magma in tubes and lobes. The sill emplacement leads to doming and deformation of sediments above saucer-shaped sills, forming

so-called forced-folds (Trude et al. 2003; Hansen and Cartwright 2006b). The Tulipan well in the Outer Møre Basin offshore mid-Norway made a small gas discovery in such a dome above a saucer-shaped sill (Polteau et al. 2008).

Sill reflections display a range of characteristic geometries that can be classified and mapped as facies units (Fig. 12; Planke et al. 2005). Saucer-shaped sills are formed when magma is injected into layered sedimentary basins due to uplift and elastic deformation of the overburden sediments (Polteau et al. 2008). The size of the saucer is a function of the emplacement depth, with small saucers or cone sheets formed at shallow depths whereas large saucers with minor

Fig. 12 Sketch showing the geometries of sill facies units 1–9 in the Vøring Basin. Modified from Planke et al. (2005)



transgressive sheets are found at larger depths. Magma may also exploit weak sediment layers (e.g., shales) and fractures (e.g., faults) forming layer-parallel tabular sheets (Magee et al. 2013). Sub-horizontal invasive or hybrid flows and associated peperites are formed when magma intrudes unconsolidated sediments at very shallow emplacement depths (e.g., the yellow arrow shows high-amplitude shallow sills in Fig. 10c and Miles and Cartwright 2010).

Dykes and laccoliths are rarely identified in seismic data, even in high-quality 3D cubes. Dykes are frequently thin and steeply dipping (Fig. 3a) and are therefore difficult to image by the seismic reflection method. However, dyke swarms would be easily visible as linear amplitude anomalies on 3D time and horizon maps if they were abundant in the imaged areas. Laccoliths are mainly formed by low-volume injection of andesitic and felsic melt batches. Up to 500 m thick laccoliths are present in the Neuquén Basin, Argentina (Rodríguez Monreal et al. 2009). The laccoliths form an integrated part of the petroleum system in this basin, both by influencing the maturation of intruded immature source rocks and by forming fractured hydrocarbon reservoirs. Unfortunately, few seismic profiles are published from this region.

3 Other Geophysical Methods

The confidence of interpreted sill reflections can be increased through integration with other geophysical methods such as gravity, magnetic, wide-angle velocity and electromagnetic methods, and geological data. However, the resolution and detection limit of these data types are often insufficient to identify sheet intrusions in volcanic basins.

3.1 Integrated Seismic, Gravity, Magnetic Interpretation

Mafic igneous intrusions are characterized by high magnetic susceptibilities and densities. However, sheet intrusions are normally quite thin, and give rise to small potential field

anomalies, particularly when the sheets are deeply buried in sedimentary basins. Anomalies are typically associated with rapid thickness variations or are edge effects. However, it is possible to image steeply dipping intrusions, such as dykes, or thick laccolith intrusions with high-resolution magnetic data.

Integrated seismic, gravity, and magnetic interpretation is done in a seismic workstation environment. High-pass filtered potential field data are scaled to two-way travel time, and imported as grids. This approach allows for plotting of the data as maps and curves on the seismic reflection data.

A seismic profile and 50-km high-pass filtered Bouguer gravity and magnetic anomaly maps are shown in Fig. 13. The profile is located in the Gjallar Ridge region in the outer Vøring Basin. Strong northeast trending magnetic anomalies, M1 and M2, are associated with the kilometre high Vøring Escarpment where subaerially emplaced basalt thins rapidly (Fig. 13a, b). The gravity anomaly displays a major sub-rounded positive anomaly associated with the Gjallar Ridge (Fig. 13c). Gravity modelling suggests that this anomaly is related to a deep density increase across the T-Reflection (Planke and Myklebust 1999; Gernigon et al. 2003). There is no good correlation between the gravity and magnetic anomaly, suggesting the body is non-magnetic. The interpretation of this high-density body is controversial, and several different models have been proposed including serpentinized mantle, a lower-crustal sill complex, a massive gabbroic magmatic underplate, and retrograde high-grade metamorphic rocks (Gernigon et al. 2004).

The seismic reflection data reveal several transgressive planar sheet intrusions climbing towards the Gjallar Ridge from the south and east. A deep sill intrusion is also imaged just northwest of the ridge. A minor magnetic anomaly, M3, is associated with the western edge of the sills in the Vigrid Syncline. The northeast trending anomaly extends along the eastern flank of the Gjallar Ridge for >10 km (Fig. 13b). Magnetic modelling suggests that the transgressive sills may be the cause of the M3 anomaly. Note that no gravity anomaly is associated with the sill terminations.

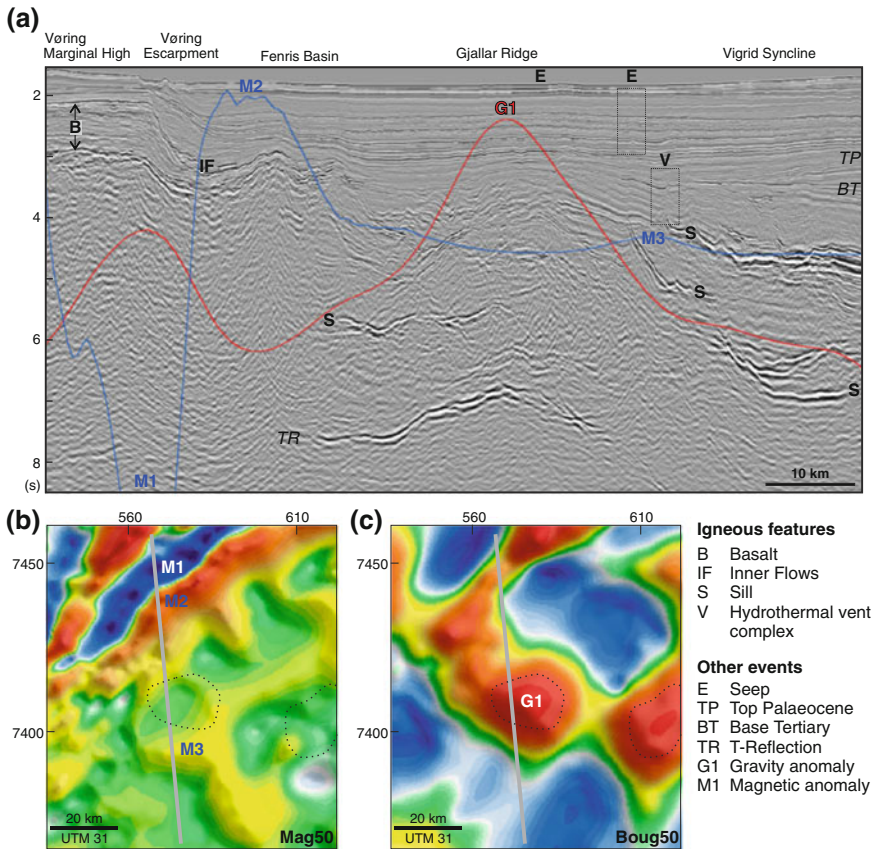


Fig. 13 Integrated seismic-gravity-magnetic interpretation of the Gjallar Ridge, outer Vøring Basin. **a** Seismic profile extending from the Vøring Marginal High into the Vigrid Syncline. Gridded high-pass filtered gravity and magnetic data are converted to pseudo-time and displayed

as red and blue curves, respectively. **b** 50-km high-pass filtered aeromagnetic data. *Dashed lines* correspond to gravity anomalies. **c** 50-km high-pass filtered marine Bouguer gravity data

3.2 Wide-Angle Seismic and Electromagnetic Data

High-velocity and high-resistivity sill complexes can be imaged by wide-angle seismic profiling and electromagnetic data. However, the intrusions are commonly too thin to be detected by these methods, especially when they are deeply buried in sedimentary basins. A high-velocity sill complex is identified by wide-angle data in the northern Vøring Basin (Fig. 6), supporting the igneous interpretation of the high-amplitude reflections in the Hel Graben. A major sill complex below thin basalts is similarly imaged on electromagnetic data on the Vøring Marginal High (Fig. 14).

3.3 Satellite Images and Topography

Satellite images and topographic data can be used to identify erosional resistant igneous intrusions. The mafic intrusions have different mechanical and chemical properties than the intruded host rocks, and sills and dykes form characteristic erosional highs in arid and Arctic environments (Fig. 3a). Google Earth images from the Karoo Basin, South Africa, and the Sverdrup Basin, Arctic Canada, reveal numerous well-defined saucer-shaped sill intrusions (Fig. 15). The mafic nature of these outcrops is confirmed by field studies (e.g., Polteau et al. 2008; Evenchick and Embry 2012).

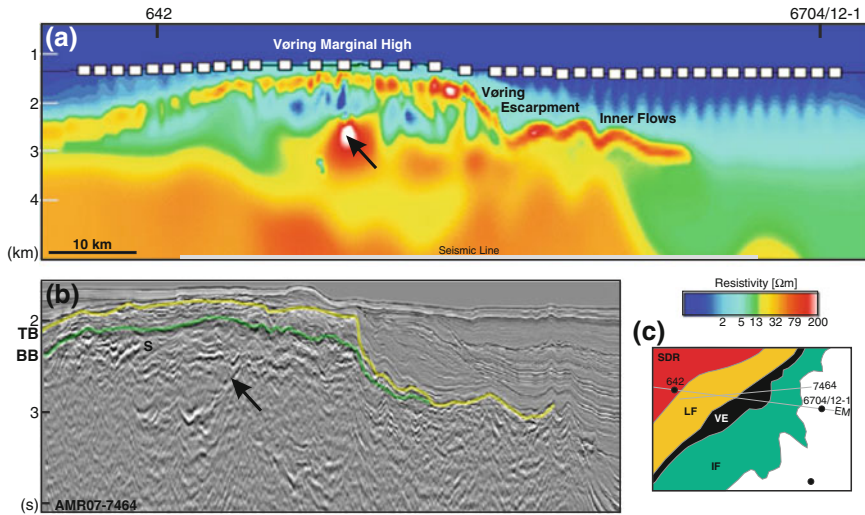


Fig. 14 a Resistivity structure of a 2D profile across the outer Vøring Basin derived from CSEM inversion by EMGS. A thin, ca. 0.5 km, basalt sequence is identified as a high resistivity unit at 1.5–3.0 km depth. Low resistivities below this unit suggest the presence of kilometre thick sub-basalt sedimentary sequences. This interpretation is corroborated by interpretation of nearby seismic

profiles (b *TB* top basalt, *BB* base basalt, *S* sill). A very high resistive unit in the middle of the profile (*black arrow*) corresponds to a high-amplitude saucer-shaped reflection interpreted as a major sill. The map, c, shows the location of the profiles, wells and volcanic seismic facies units (*IF* inner flows, *VE* Vøring escarpment, *LF* landward flows, *SDR* seaward dipping reflections)

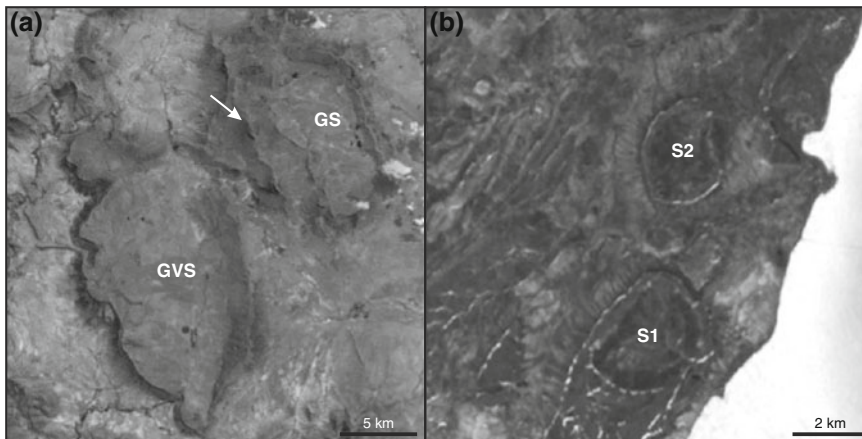


Fig. 15 Modified Google Earth images of erosional remnants of saucer-shaped sills. a The Golden Valley Sill Complex (31.9S, 26.3E), Karoo Basin, South Africa. *GVS* Golden Valley Sill; *GS* Glen Sill. *Arrow* shows shallow-

level sills between *GVS* and *GS* possibly linking the intrusions. b Ellef Ringnes sill complex (79.0N, 102.8W), Sverdrup Basin, Canada. *S1*, *S2* Saucer-shaped sills

4 Summary

Igneous intrusions such as sills, dykes, and laccoliths are abundant in sedimentary basins, and are often associated with continental and volcanic rifted margin Large Igneous Provinces. Mafic igneous intrusions are characterized by high seismic velocities in the range from 5.0 to 7.0 km/s. Velocity aureoles with a thickness comparable to the sill intrusion are commonly identified on sonic log data above and below the intrusions. Sills as thin as 10 m may be detected by conventional seismic reflection data, whereas sills with a thickness above about 40 m are resolvable. Deeper sills are more difficult to image as the wave amplitudes decay across the uppermost sill due to transmission losses across the high-impedance boundaries at the top and the base of the sills. Offset-dependent tuning is expected for high-velocity sills due to the high-velocity of the intrusions. The velocity of intrusions in sill-sediment complexes can be derived from wide-angle ocean bottom seismometer data if the sills are sufficiently abundant.

Sill reflections are interpreted based on characteristic features such as high amplitude reflections with saucer-shaped geometries. Sill complexes are well-suited for 3D visualization techniques and abundant new information about sill geometries and emplacement dynamics have been obtained by such methods over the past decade. Potential field and electromagnetic data may improve sill interpretation; however such data have a poor resolution if sills are buried below more than a few kilometres of sediments. In contrast, field studies of volcanic basins such as the Karoo Basin in South Africa have provided a lot of complementary information about intrusive sill complexes. Dykes and laccoliths are less abundant than sills in volcanic basins, and few well-documented geophysical interpretation studies of such intrusions are published. Geophysical interpretation studies of andesitic and felsic intrusions are also rare.

Acknowledgments Special thanks to Audun Groth, Statoil, and VoxelVision for seismic visualization. Seismic data were kindly provided by TGS and EM data by

EMGS. This work was partly supported by the Research Council of Norway through its Centres of Excellence funding scheme, project number 223272.

References

- Aarnes I, Svensen H, Connolly JAD, Podladchikov YP (2010) How contact metamorphism can trigger global climate changes: modeling gas generation around igneous sills in sedimentary basins. *Geochim Cosmochim Acta* 74:7179–7195
- Bell B, Butcher H (2002) On the emplacement of sill complexes: evidence from the Faroe-Shetland basin. *Geol Soc, London, Spec Publ* 197:307–329
- Berndt C, Skogly O, Planke S et al (2000) High-velocity breakup-related sills in the Vøring Basin, off Norway. *J Geophys Res: Solid Earth* 105:28443–28454
- Bryan SE, Ernst RE (2008) Revised definition of large igneous provinces (LIPs). *Earth Sci Rev* 86:175–202
- Bryan SE, Ferrari L (2013) Large igneous provinces and silicic large igneous provinces: progress in our understanding over the last 25 years. *Geol Soc Am Bull* 125:1053–1078. doi:10.1130/B30820.1
- Cartwright J, Hansen DM (2006) Magma transport through the crust via interconnected sill complexes. *Geology* 34:929–932
- Chevallier L, Woodford A (1999) Morpho-tectonics and mechanism of emplacement of the dolerite rings and sills of the western Karoo, South Africa. *S Afr J Geol* 102:43–54
- Evenchick CA, Embry AF (2012) *Geology, Ellef Rignes Island north Nunavut: Map 86 (preliminary)*. In: Canadian geoscience. Geological Survey of Canada
- Favretto-Cristin N, Cristini P, Bazelaire E (2009) What is a seismic reflector like? *Geophysics* 74:T13–T23
- Gernigon L, Ringenbach JC, Planke S, Le Gall B, Jonquet-Kolstø H (2003) Extension, crustal structure and magmatism at the outer Vøring Basin, Norwegian margin. *J Geol Soc London* 160:197–208
- Gernigon L, Ringenbach JC, Planke S, Le Gall B (2004) Deep structures and breakup along volcanic rifted margins: insights from integrated studies along the outer Vøring Basin (Norway). *Mar Pet Geol* 21:363–372
- Gibb F, Kanaris-Sotiriou R (1988) The geochemistry and origin of the Faeroe-Shetland sill complex. *Geol Soc, London, Spec Publ* 39:241–252
- Hansen DM, Cartwright J (2006a) Saucer-shaped sill with lobate morphology revealed by 3D seismic data: implications for resolving a shallow-level sill emplacement mechanism. *J Geol Soc* 163:509–523
- Hansen DM, Cartwright J (2006b) The three-dimensional geometry and growth of forced folds above saucer-shaped igneous sills. *J Struct Geol* 28:1520–1535
- Hansen DM, Cartwright JA, Thomas D (2004) 3D seismic analysis of the geometry of igneous sills and sill junction relationships. *Geol Soc, London, Memoirs* 29:199–208

- Holford SP, Schofield N, Macdonald JD et al (2012) Seismic analysis of igneous systems in sedimentary basins and their impacts on hydrocarbon prospectivity: examples from the southern Australian margin. *APPEA J* 52:229–252
- Magee C, Jackson CA-L, Schofield N (2013) The influence of normal fault geometry on igneous sill emplacement and morphology. *Geology* 41:407–410
- Miles A, Cartwright J (2010) Hybrid flow sills: a new mode of igneous sheet intrusion. *Geology* 38:343–346
- Neumann ER, Svensen H, Tegner C et al (2013) Sill and lava geochemistry of the mid-Norway and NE Greenland conjugate margins. *Geochem Geophys Geosyst* 14:3666–3690
- Pant DR, Greenhalgh SA (1989) Lateral resolution in seismic reflection—a physical model study. *Geophys J* 97:187–198
- Planke S, Cambray H (1998) Seismic properties of flood basalts from hole 917A downhole data, Southeast Greenland Volcanic Margin. *Proc ODP Sci Results* 152:453–462
- Planke S, Myklebust R (1999) Når seismikken kommer til kort. *GEO, Trondheim* 10:20–22
- Planke S, Rasmussen T, Rey S et al (2005) Seismic characteristics and distribution of volcanic intrusions and hydrothermal vent complexes in the Vøring and Møre basins. In: Geological Society, London, petroleum geology conference series. Geological Society of London, pp 833–844
- Polteau S, Mazzini A, Galland O et al (2008) Saucer-shaped intrusions: occurrences, emplacement and implications. *Earth Planet Sci Lett* 266:195–204
- Puryear CI, Castagna JP (2008) Layer-thickness determination and stratigraphic interpretation using spectral inversion. *Geophysics* 73:R37–R48
- Rocchi S, Mazzotti A, Marroni M et al (2007) Detection of Miocene saucer-shaped sills (offshore Senegal) via integrated interpretation of seismic, magnetic and gravity data. *Terra Nova* 19:232–239
- Rodriguez Monreal F, Villar HJ, Baudino R, Delpino D, Zencich S (2009) Modeling an atypical petroleum system: a case study of hydrocarbon generation, migration and accumulation related to igneous intrusions in the Neuquén Basin, Argentina. *Mar Pet Geol* 26:590–605
- Schofield A, Totterdell JM (2008) Distribution, timing and origin of magmatism in the Bight and Eucla basins. In: *Geoscience Australia*, p 19
- Schofield NJ, Brown DJ, Magee C et al (2012) Sill morphology and comparison of brittle and non-brittle emplacement mechanisms. *J Geol Soc* 169:127–141
- Skogseid J, Eldholm O (1989) Vøring Plateau continental margin: seismic interpretation, stratigraphy and vertical movements. *Proc Ocean Drill Program Sci Results* 104:993–1030
- Skogseid J, Pedersen T, Eldholm O et al (1992) Tectonism and magmatism during NE Atlantic continental break-up: the Vøring Margin. *Geol Soc, London, Spec Publ* 68:305–320
- Skogly OP (1998) Seismic characterization and emplacement of intrusives in the Vøring Basin. Cand Scient thesis, Department of Geology, University of Oslo
- Smallwood J, Harding A (2009) New seismic imaging methods, dating, intrusion style and effects of sills: a drilled example from the Faroe-Shetland basin. In: Varming T, Ziska H (eds) *Second Faroe Islands exploration conference*. Sindri–Jardfeingi, Torshavn, Faroe Islands, pp 104–123
- Svensen H, Planke S, Malthe-Sørensen A et al (2004) Release of methane from a volcanic basin as a mechanism for initial Eocene global warming. *Nature* 429:542–545
- Svensen H, Planke S, Corfu F (2010) Zircon dating ties NE Atlantic sill emplacement to initial Eocene global warming. *J Geol Soc* 167:433–436
- Thomson K (2004) Sill complex geometry and internal architecture: a 3D seismic perspective. *Physical geology of high-level magmatic systems*. *Geol Soc, London, Spec Publ* 234:229–232
- Thomson K (2007) Determining magma flow in sills, dykes and laccoliths and their implications for sill emplacement mechanisms. *Bull Volc* 70:183–201
- Thomson K, Schofield N (2008) Lithological and structural controls on the emplacement and morphology of sills in sedimentary basins. *Geol Soc, London, Spec Publ* 302:31–44
- Trude K (2004) Kinematic indicators for shallow level igneous intrusions from 3D seismic data: evidence of flow direction and feeder location. *Geol Soc, London, Memoirs* 29:209–218
- Trude J, Cartwright J, Davies RJ et al (2003) New technique for dating igneous sills. *Geology* 31:813–816
- Widess MB (1973) How thin is a thin bed. *Geophysics* 38:1176–1254
- White R, Smith L, Roberts A et al (2008) Lower-crustal intrusion on the North Atlantic continental margin. *Nature* 452:460–464
- Zhang R, Castagna J (2011) Seismic sparse-layer reflectivity inversion using basis pursuit decomposition. *Geophysics* 76:147–158

Laboratory Modelling of Volcano Plumbing Systems: A Review

Olivier Galland, Eoghan Holohan,
Benjamin van Wyk de Vries and Steffi Burchardt

Abstract

We review the numerous experimental studies dedicated to unravelling the physics and dynamics of various parts of a volcanic plumbing system. Section 1 lists the model materials commonly used for model magmas or model rocks. We describe these materials' mechanical properties and discuss their suitability for modelling sub-volcanic processes. Section 2 examines the fundamental concepts of dimensional analysis and similarity in laboratory modelling. We provide a step-by-step explanation of how to apply dimensional analysis to laboratory models in order to identify fundamental physical laws that govern the modelled processes in dimensionless (i.e. scale independent) form. Section 3 summarises and discusses the past applications of laboratory models to understand numerous features of volcanic plumbing systems. These include: dykes, cone sheets, sills, laccoliths, caldera-related structures, ground deformation, magma/fault interactions, and explosive vents. We outline how laboratory models have yielded insights into the main geometric and mechanical controls on the development of each part of the volcanic

O. Galland (✉)

Physics of Geological Processes (PGP), Department
of Geosciences, University of Oslo, Oslo, Norway
e-mail: olivier.galland@fys.uio.no

E. Holohan

German Research Centre for Geosciences (GFZ),
Helmholtz Zentrum Potsdam, Potsdam, Germany

B. van Wyk de Vries

Observatoire de Physique du Globe de
Clermont-Ferrand, Blaise Pascal University,
Clermont-Ferrand, France

S. Burchardt

Department of Earth Sciences, Center for
Experimental Mineralogy, Petrology and
Geochemistry, University of Uppsala, Uppsala,
Sweden

plumbing system. We conclude with some perspectives on the limitations of past and current analogue modelling approaches, and on challenges to be addressed by future research.

1 Introduction

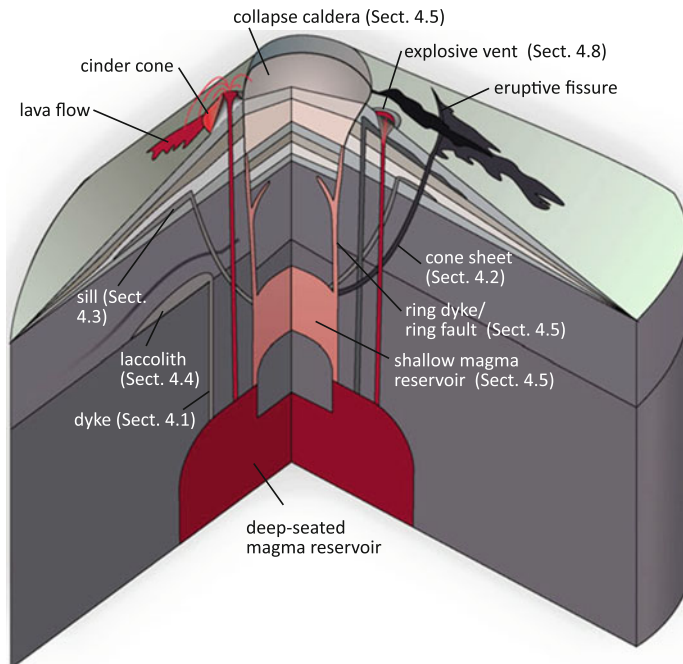
Volcanic plumbing systems set the stage for volcanic eruptions, by controlling the flow of magma into the vent. The term ‘volcano plumbing system’ is here broadly defined as the structural framework of pathways and storage regions through which magma travels on its journey from its source region to the Earth’s surface. As the metaphor of a plumbing system suggests, the focus here is primarily on the transport and storage of magma within relatively solid or brittle Earth materials that characterise the upper part of the Earth’s lithosphere.

The huge scale ranges that characterise volcano plumbing systems represent a challenge for unravelling the complexity of underlying processes. These processes act at length scales of microns to thousands of kilometres, and over time

scales of milliseconds to millions of years. Our observational range is limited, e.g. to the human life (and working) time and the geological processes are often hidden under ground (Fig. 1). Earth scientists try to overcome these obstacles by studying geological systems as observed in the field. However, field examples are commonly the compound result of a series of past and/or on-going geological events and processes. This aggregation of effects can make it difficult to grasp clearly the roles of individual physical processes in the geological system’s evolution as a whole.

One way to tackle these obstacles is to replicate geological processes in controlled laboratory experiments. Hall (1815) conducted one of the first such experiments to provide a qualitative physical explanation (horizontal shortening) for folded rock strata observed in Scotland. By designing experiments to study the formation of

Fig. 1 Schematic drawing illustrating the main characteristics of volcano plumbing systems. These include dykes (Sect. 4.1), cone sheets (Sect. 4.2), sills (Sect. 4.3), laccoliths (Sect. 4.4), caldera-related structures and intrusions (Sect. 4.5), magma-fault interactions (Sect. 4.7), and explosive volcanic vents (Sect. 4.8). See text for details



diatremes, Daubrée (1891) first simulated processes underlying the development of volcano plumbing systems. Since then, laboratory models have been a key tool for scientists seeking to unravel the physical processes that control the development and behaviour of volcanic and magmatic systems (Fig. 2).

In this chapter, we provide a review of how laboratory models, also called analogue models, have been designed and adapted to unravel the dynamics of shallow magmatic systems. We also describe and discuss the application of the laboratory results to various features and stages in these systems' evolution. As with other disciplines in Earth Sciences, laboratory modelling has evolved to become increasingly quantitative in recent years. As we highlight below, this has drastically increased the capacity of analogue models to aid the interpretation of not only intrusive and structural relationships in 'fossilised' field examples, but also geodetic and geophysical data from active volcanoes.

2 Model Materials

An important technical aspect of laboratory models of volcanic plumbing systems is a relevant choice of model materials. Before starting an experimental project, it is very important to know exactly the mechanical properties of the model materials to be used. This step is crucial for: (i) designing the experimental apparatus, (ii) setting the initial and boundary conditions of the models, and (iii) quantitatively interpreting the model results. A wide range of materials with known mechanical properties is available from the literature, both for model magmas and model host rocks (Figs. 3 and 4; Tables 1, 2, 3 and 4).

2.1 Model Magma

In nature, magma viscosity depends on many factors, such as chemical composition, temperature, dissolved volatile content (e.g. water), and total crystal content. Magma viscosity hence has a wide range, within which a lowest viscosity end

member would be a high temperature, crystal-poor, 'wet' mafic magma ($\eta \sim 10\text{--}100$ Pa s) (Dingwell et al. 1993), and a highest viscosity end member be a low-temperature, crystal-rich, 'dry' granite magma (η up to $10^{17\text{--}18}$ Pa s) (Scaillet et al. 1997). Such wide range means that different materials are required to simulate magmas of high or low viscosity (Table 2).

2.1.1 "High" Viscosity Magma

The most commonly used material for simulating high viscosity magma is a silicone polymer or putty called Polydimethylsiloxane (PDMS; Figs. 3 and 4a). The advantage of PDMS is that it is a Newtonian fluid at typical laboratory strain rates and temperatures (Weijermars 1986; ten Grotenhuis et al. 2002; Boutelier et al. 2008). This means that the relationship of the applied shear stress to resultant shear strain rate follows a power law of exponent of 1 (i.e. is linear). Its viscosity is hence a constant at a given temperature and has been measured at $\sim 1\text{--}3 \times 10^4$ Pa s at room temperature (Table 2; e.g. Weijermars 1986; Corti et al. 2005). As temperature varies, the viscosity of PDMS follows an Arrhenius law (Hailemariam and Mulugeta 1998; Cagnard et al. 2006), i.e., it decreases exponentially with increasing temperature. The viscosity of PDMS can be easily measured by using a cylindrical viscometer, as described by e.g. Cobbold and Jackson (1992) and Reber et al. (2013), or a capillary (extrusion) viscometer, as described by e.g. Hailemariam and Mulugeta (1998).

According to experimental requirements, the viscosity of PDMS can also be increased or decreased by the addition of other materials. Increasing PDMS viscosity is achieved by mixing it with different proportions of small mineral particles (inert fillers). The resulting mixture is a suspension of particles within a viscous matrix, the viscosity of which follows the Einstein-Roscoe law (Einstein 1906; Weijermars 1986). Depending on the specific gravity of the particles used, the bulk density of such a mixture can be increased or decreased with respect to pure PDMS. For example, addition of BaSO₄ increases the bulk density (ten Grotenhuis et al. 2002), whereas addition of fine hollow glass

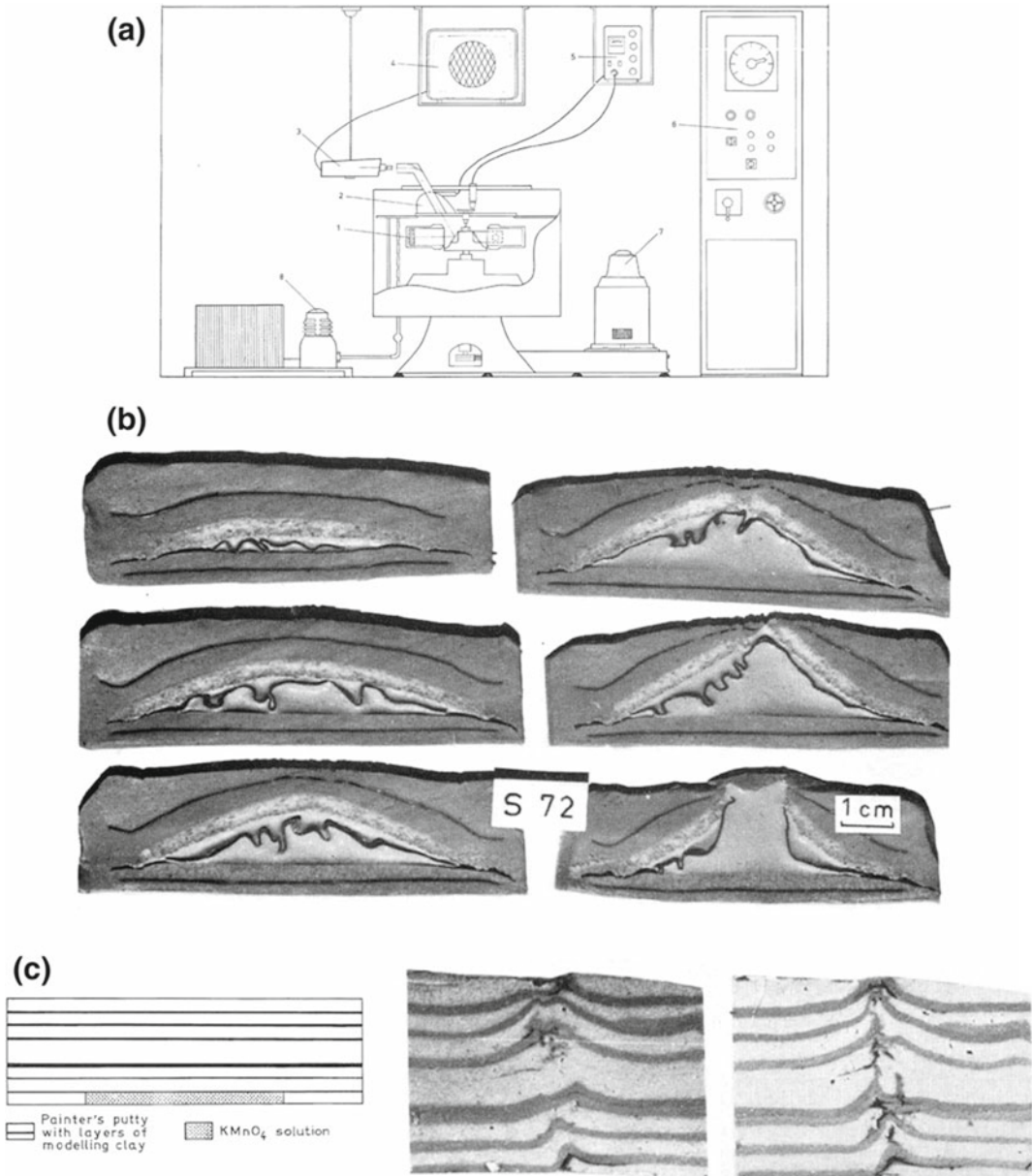


Fig. 2 **a** Drawing of the pioneering experimental apparatus designed by Hans Ramberg, at the University of Uppsala, Sweden. 1 model in centrifuge cup; 2 stroboscopic light reflector; 3 TV camera; 4 TV receiver; 5 stroboscope; 6 temperature and speed control cabinet; 7 motor; 8 refrigerator unit. **b** Sections through Ramberg's centrifuged model of silicone putty with powdered-wax layer above, embedded in painter's putty with sheets of modelling clay. Run 10 min at 1300 g, the experiment was intended to model diapir rise. Nevertheless, the

similarity between the model outcome and igneous laccoliths suggests that such models can be applied to these igneous features. **c** Ramberg's model of magma rise due to buoyant forces. **Left** Initial arrangement of model. **Centre and right** Cross-sections through vent of a $KMnO_4$ solution through overburden in model shown in left. The vent runs vertically from one edge of the collapsed original "magma" chamber. Run less than 1 min at some 1000 g. After Ramberg (1967)

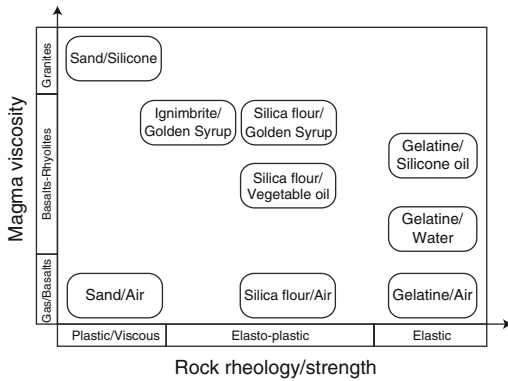


Fig. 3 Qualitative diagram representing the mechanical properties of the main model materials that have been used in laboratory models of volcano plumbing systems (see Tables 1, 2, 3 and 4). Note that for model rocks, the elastic, elasto-plastic and viscous/plastic rheologies correspond to the dominant behaviours of the corresponding model materials. See Sect. 2.2 for explanations

beads (Boutelier et al. 2008) decreases it. For large contents of inert fillers, however, the mixture becomes non-Newtonian and its stress to strain relationship may instead follow a power law with an exponent greater than 1. At very large contents of fillers, the mixture may become visco-elastic (i.e. display substantial elastic or recoverable strains). Decreasing the viscosity of PDMS is achieved by mixing it with oleic acid, such as described by e.g. Corti et al. (2005) and Reber et al. (2013), although the PDMS-oleic acid mixture becomes sticky and challenging to handle. These two procedures provide an enlarged analogue magma viscosity range of between $\sim 7 \times 10^3$ and $\sim 5 \times 10^5$ Pa s, i.e. almost two orders of magnitude.

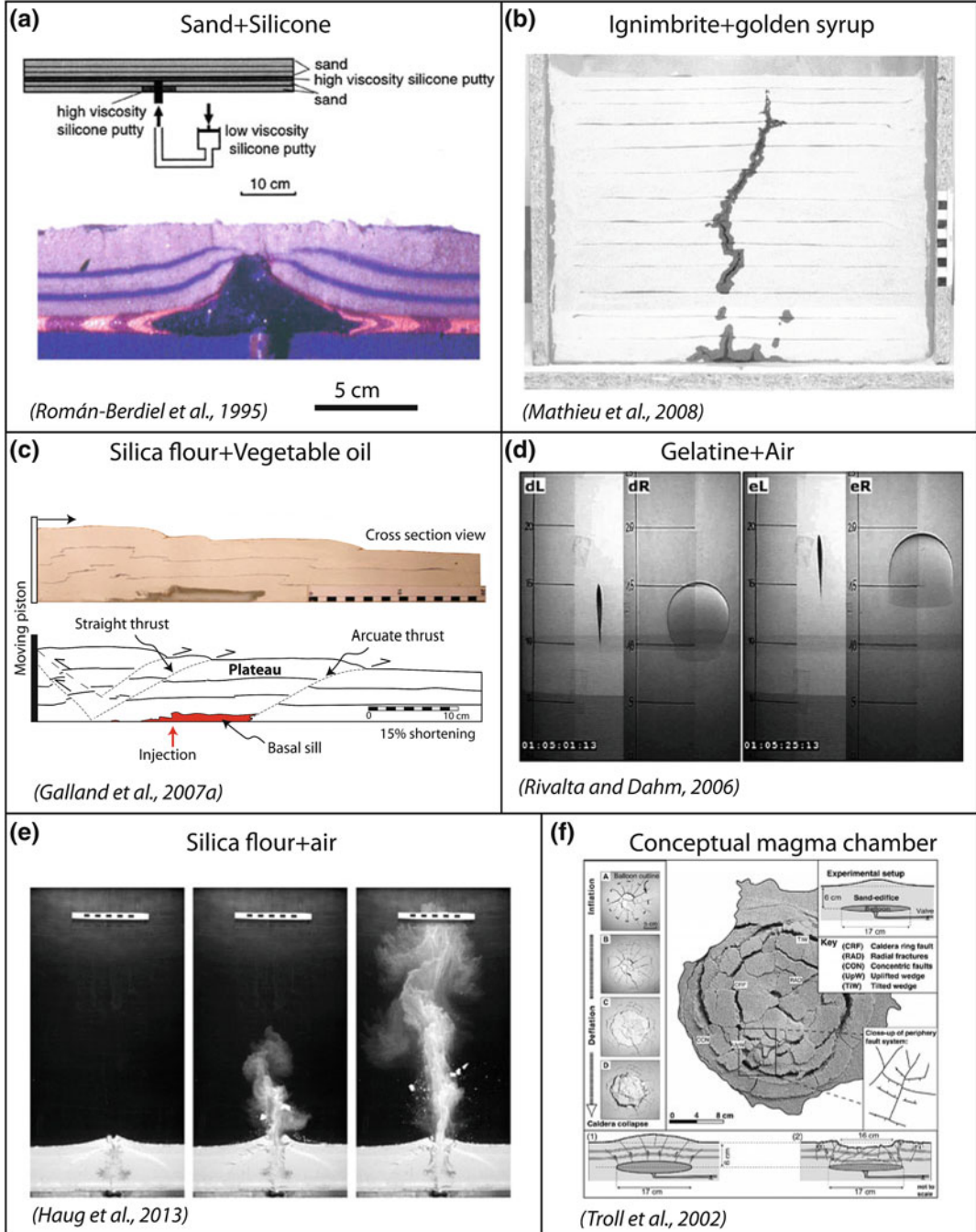
In addition, the commonly-used stiff PDMS putty is an end member of a suite of silicone oil products of variable, controlled viscosities (Takada 1990, 1994b; de Bremond d’Ars et al. 2001; Watanabe et al. 2002). Those used by these authors range between 0.8×10^{-3} and 1.337 Pa s, but products with a still-broader viscosity range are available on the market. Given their wide range of viscosities, silicone oils can hence be used to simulate both high viscosity and low viscosity magmas without the need for adding other materials (cf. Table 2).

2.1.2 “Low” Viscosity Magma

During the last two decades, several experimental techniques have been developed to simulate low-viscosity magmas. The simplest model magma is water; it has been mostly used for simulating dyke and sill emplacement in gelatine (Tables 1 and 2; Hyndman and Alt 1987; McLeod and Tait 1999; Menand and Tait 2002; Walter and Troll 2003; Kavanagh et al. 2006; Menand 2008; Kervyn et al. 2009; Le Corvec et al. 2013). Water is an incompressible Newton fluid of viscosity $\sim 10^{-3}$ Pa s. It is often dyed, such that an intruding dyke can be optically tracked through models made of transparent gelatine. In these models, the density of the intruding water is very similar to that of the hosting gelatine. Consequently, an internal fluid pressure imposed by the experimentalist is required to trigger the propagation of the neutrally buoyant intrusion.

To study buoyancy-driven fracturing, air is used as the intruding fluid (Table 2; Figs. 3 and 4d–e). Air has a density of 1.2×10^{-3} kg m⁻³ and a viscosity of $\sim 2 \times 10^{-6}$ Pa s at room temperature (e.g. Rivalta et al. 2005; Rivalta and Dahm 2006). In addition to being much less dense than the host materials, air is compressible, such that a rising experimental dyke is subject to pressure decrease, and so to volume increase. In nature, magma compressibility (Rivalta 2010) and fluid exsolution (Menand and Tait 2001; Rivalta and Dahm 2006; Taisne and Jaupart 2011) are expected to lead to volume increase of propagating dykes, which is likely to affect their propagation dynamics. At the scale of the experiments, however, Rivalta and Dahm (2006) estimated that this effect is negligible.

Air has also been used to study the formation of shallow magma conduits resulting from explosive processes due to rapid gas exsolution of the rising magma (Haug et al. 2013; Galland et al. 2014b), with applications to maar-diatremes (e.g. Woolsey et al. 1975) (see also Table 1; Figs. 3 and 4e), kimberlite pipes (e.g. Gernon et al. 2009), hydrothermal vent complexes (Nermoen et al. 2010a), and mud volcanoes (e.g. Mazzini et al. 2009).



◀ **Fig. 4** Characteristic examples of laboratory models of volcano plumbing systems made by using various model materials. **a** Schematic drawing of experimental setup (*top*) and photograph of model cross section (*bottom*) of the sand + silicone experiments of Román-Berdiel et al. (1995). **b** Side view photograph of ignimbrite + Golden Syrup experiment (Mathieu et al. 2008). Ignimbrite powder simulates elasto-plastic rocks, whereas Golden Syrup simulates magma of intermediate viscosity. **c** Photograph and corresponding drawing of a cross-section of silica-flour + vegetable oil model (Galland et al. 2007a). The silica flour simulates the behaviour of the brittle crust, and exhibits faults, whereas the oil simulates magma of typical viscosity. The cohesion of the silica flour allows the oil to form sheet intrusion. Note that the oil solidifies, such

that it becomes possible to make cross-sections through the models. **d** Time series of side- and front-view photographs of gelatine + air experiments (Rivalta and Dahm 2006). The gelatine simulates elastic rock, whereas the air simulates low viscosity magma. These experiments only simulate sheet intrusions (dyke and sills). **e** Time series of side-view photographs of silica flour + air 2D experiments (Haug et al. 2013). The silica flour represents brittle cohesive rock, and the air represents rapidly degassing magma or phreatomagmatically-generated water vapour. **f** Surface view photograph of model using conceptual magma chamber (Troll et al. 2002). The inflation/deflation of a balloon represents the replenishment and draining of a magma chamber, and the deformation induced in the overburden is observed at the surface of the models

Model rocks in some models are made of granular media (see below and Table 4). In these models, very low viscosity fluids like air and water are unsuitable for the simulation of magma intrusion, because they flow through the pores between the grains in addition to intruding the model. Moreover, the most commonly used granular media are made of silica, which is hydrophilic, such that the percolation of water through the pores is enhanced by surface tension. Therefore, other fluids such as oil (Grout 1945), honey, or Golden Syrup, have been used in this case (Table 2; Figs. 3 and 4b). The latter's viscosity is 50 Pa s at room temperature, and its density is 1400 kg m⁻³ (Mathieu et al. 2008; Kervyn et al. 2009; Abdelmalak et al. 2012).

Limiting the percolation of model magma in its host granular medium requires the use of a fluid that is chemically incompatible with its host, i.e. high surface tension. Good examples are greases (Johnson and Pollard 1973; Pollard and Johnson 1973), which are hydrophobic, such as the vegetable oil sold in France under the name *Végétaline* (Table 2; Figs. 3 and 4c) (Galland et al. 2006, 2009; Galland 2012). This fluid offers several advantages:

- its viscosity is low ($\eta = 2 \times 10^{-2}$ Pa s at 50 °C), such that it is suitable for simulating low viscosity magmas (Galland et al. 2006);
- it is solid at room temperature, and its melting temperature is 31 °C. It hence can be injected at molten state at a relatively low temperature (50 °C), that is technically easy to handle;

- it percolates very little into a very fine-grained granular host medium;
- at the end of the experiments, it solidifies after 15–30 min such that (i) the intrusions can be excavated and their shapes analysed in 3D (Galland et al. 2009; Galland 2012), or (ii) the models can be cut to reveal how intrusions relate to surrounding structures and overlying surface morphology (Galland et al. 2003, 2007a, 2008).

The vegetable oil's viscosity was measured via a rotary viscometer (Galland et al. 2006), which is a standard device to measure fluids of relatively low viscosities.

Finally, room temperature vulcanization (RTV) silicone (Gressier et al. 2010) has also been used as a model magma (Table 2). Its viscosity is 25 Pa s. RTV silicone solidifies after approximately five hours, such that the simulated intrusions can be excavated.

2.1.3 Conceptual Magma Chambers

Some experimental studies of volcanic plumbing systems do not focus on the magma emplacement mechanisms, but on the deformation patterns induced by inflating or deflating magma bodies (Table 1). In these cases, an inflating/deflating magma chamber is conceptually simulated with a balloon (Martí et al. 1994; Walter and Troll 2001; Troll et al. 2002; Geyer et al. 2006) or a moving piston (Acocella et al. 2001; Burchardt and Walter 2010). Although these experiments do not

Table 1 List of analog 'rock'-'magma' combinations used in the experimental studies referenced in this chapter

Rock analogue	Magma analogue	Part of plumbing system and dynamic regime modelled	References
<i>Gels</i>			
Gelatin	Air	Ascent of low viscosity dykes (buoyancy driven)	Takada (1990), Bons et al. (2001), Menand and Tait (2001), Muller et al. (2001), Ito and Martel (2002), Rivalta et al. (2005), Rivalta and Dahm (2006), Le Corvec et al. (2013)
	Hexane	Interactions between two ascending dykes	Ito and Martel (2002)
	Water	Propagation or ascent of intermediate viscosity dykes and sills (internal pressure driven)	Fiske and Jackson (1972), McGuire and Pullen (1989), Takada (1990), McLeod and Tait (1999), Menand and Tait (2001, 2002), Walter and Troll (2003), Kavanagh et al. (2006), Menand (2008); Kervyn et al. (2009), Tibaldi et al. (2014), Daniels and Menand (2015)
	Water-gelatin solution	Dyke, sill and laccolith emplacement under volcanic cone	Hyndman and Alt (1987)
	Mud	Hydraulic fracturing in different stress fields	Hubbert and Willis (1957)
	Water-Natrosol solution	Dyke nucleation from model magma reservoir	McLeod and Tait (1999)
	Water-Sugar solutions	Propagation and arrest of buoyancy-driven dyke	Taisne and Tait (2009), Taisne et al. (2011)
	Water-Glycerin	Dyke propagation and nucleation, and composite dyke emplacement	Koyaguchi and Takada (1994), McLeod and Tait (1999), Takada (1999)
	Molten wax	Cooling effects on dyke propagation	Taisne and Tait (2011)
	Vegetable oil	Cooling effects on dyke and sill emplacement	Chanceaux and Menand (2014)
	Silicone oils	Dyke propagation and nucleation	Takada (1990, 1994b), McLeod and Tait (1999), Watanabe et al. (2002)
	Grease	Sill and laccolith emplacement	Johnson and Pollard (1973), Pollard and Johnson (1973)
	Silicone putty	Dyke nucleation	Cañón-Tapia and Merle (2006)
Acryl gel	Air	Dyke propagation driven by magma pulses	Maaløe (1987)
	Oil	Dyke propagation	Maaløe (1987)
Agar-sugar gel	Water-glycerol solution	Dyke propagation along level of neutral buoyancy	Lister and Kerr (1991)

(continued)

Table 1 (continued)

Rock analogue	Magma analogue	Part of plumbing system and dynamic regime modelled	References
<i>Granular materials</i>			
Sand or sand with silicone layers	Silicone putty	Inflating or deflating laccoliths or stock-like intrusions, driven by internal overpressures or underpressures	Merle and Vendeville (1995), Román-Berdiel et al. (1995, 1997), Benn et al. (1998, 2000), Román-Berdiel (1999), Acocella et al. (2000, 2001, 2004), Roche et al. (2000, 2001), Girard and van Wyk de Vries (2005)
	Rigid piston	Deflating stock-like or sill-like intrusions	Burchardt and Walter (2010)
	Balloon	Deflating sill-like or laccolithic intrusions	Walter and Troll (2001), Lavallée et al. (2004), Geyer et al. (2006)
	Silicone-Oleic acid mix	Magma emplacement in deforming crust	Corti et al. (2005), Musumeci et al. (2005), Mazzarini et al. (2010), Montanari et al. (2010a, b), Ferré et al. (2012)
	Glycerol	Magma emplacement in tectonic extension	Bonini et al. (2001), Corti et al. (2001)
	Air	Explosive fragmentation of near vent region	Walters et al. (2006)
Wheat flour	Balloon	Deflating and/or inflating (cyclic) sill-like or laccolithic intrusions	Walter and Troll (2001)
Glass beads	Air	Formation of hydrothermal vent complex	Nermoen et al. (2010a)
	Air + glass beads	Diatreme formation	Ross et al. (2008a, b)
Crushed cohesive sand	Sleeve + plates	Opening of dyke and associated surface deformation	Trippanera et al. (2014)
Sand-plaster mix	Golden syrup	Caldera collapse and dyke propagation	Roche et al. (2001), Kervyn et al. (2009), Delcamp et al. (2012b)
	“Creamed” honey	Deflating sill-like intrusions	Holohan et al. (2008a, b, 2013)
Ignimbrite powder	Golden Syrup	Propagation and inflation of dykes, sills, and saucer-shaped intrusions driven by internal pressure	Mathieu et al. (2008), Mathieu and van Wyk de Vries (2009)
Sand-flour mix	Silicone putty	Inflating intra-edifice stock-like intrusions (cryptodomes), driven by internal overpressures. Deflating sill or stock-like magma chambers	Donnadiou and Merle (1998), Roche et al. (2000), Merle and Donnadiou (2000)
	Balloon	Deflating laccolithic magma chambers	Holohan et al. (2005)
Fused alumina powder	Balloon	Deflating and/or inflating laccolithic magma chambers	Martí et al. (1994)
Diatomite powder	RTV silicone	Dyke and sill propagation in the presence of pore fluid overpressure	Gressier et al. (2010)

(continued)

Table 1 (continued)

Rock analogue	Magma analogue	Part of plumbing system and dynamic regime modelled	References
Silica powder	Air	Explosive fragmentation of near vent region	Haug et al. (2013), Galland et al. (2014b)
	Vegetable oil	Propagation and inflation of dykes, sills, and saucer-shaped intrusions driven by internal pressure	Galland (2005, 2012), Galland et al. (2003, 2006, 2007a, 2008, 2009, 2011, 2014a), Ferré et al. (2012)
	Golden Syrup	Propagation and inflation of dykes driven by internal pressure	Abdelmalak et al. (2012)
Sand-Powdered clay mix	Rigid body	Deflating or inflating intrusions (idealised as sphere)	Komuro et al. (1984), Komuro (1987)
	Balloon	Deflating and/or inflating (cyclic) sill-like or laccolithic intrusions	Walter and Troll (2001), Troll et al. (2002)
Clay	Aqueous KMnO ₄	Buoyancy-driven dyke ascent through brittle crust	Ramberg (1970, 1981)
<i>Others</i>			
Rigid walls	Air + glass beads	Mixing of materials in vents and conduits by gas-driven fluidization	Gernon et al. (2008, 2009)
	Wet plaster	AMS analysis on analogue intrusion	Závada et al. (2006, 2009, 2011)
Rigid piston	Aqueous corn-syrup solutions	Ring dyke intrusion and internal flow synchronous with a deflating sill-like intrusion	Kennedy et al. (2008)
Plasticine-wax	Silicone putty	Laccolith formation	Dixon and Simpson (1987)
Wet clay	Air	Diatreme formation	Grout (1945)
Water-corn syrup mix	Air	Diatreme formation	Grout (1945)

simulate the complexity of volcanic plumbing systems, the phenomenological results can be very inspiring for understanding geological structures observed in the field (Figs. 3 and 4f).

2.2 Model Rocks

Like magmas, rocks exhibit various mechanical behaviours depending on their lithology and on the scales (both length and time) of the simulated processes (Tables 3 and 4). Natural rocks exhibit complex rheologies, which combine elastic, viscous and plastic properties. Elastic deformation is reversible and usually occurs at low stresses/strains. If the stress/strain exceeds the rocks' elastic limit, they deform in an irreversible

manner. They can do so by viscous behaviour, where the strain rate is a linear or power law function of the applied stress, or by plastic behaviour where the strain is a function of the applied stress. Various rheological laws describing these end member behaviours exist (Turcotte and Schubert 2002; Jaeger et al. 2009). In nature, rock rheology combines these different end members in a non-trivial manner, such that the complete rock behaviour is extremely challenging to characterise. Nevertheless, under given pressure and temperature conditions, length-scales and time-scales (strain rates), rock behaviour is dominated by one or the other end member. Different laboratory materials are available to simulate these dominant rock-mechanical behaviours.

Table 2 Types and mechanical properties of analogue ‘magmas’ used in laboratory models of volcanic plumbing systems

Model magma	Macroscopic behaviour	Viscosity	Density	References
<i>Silicone polymers</i>				
PDMS (silicone putty)	Stiff Newtonian fluid at low strain rates (power law fluid at high strain rates) Rigidity (shear modulus) $G = 2.6 \times 10^5$ Pa	$1-3 \times 10^4$ Pa s (at room temperature)	$965-1140$ kg m ⁻³	Weijermars (1986), Acocella et al. (2001); ten Grotenhuis et al. (2002), Corti et al. (2005)
PDMS + inert fillers	Stiff Newtonian fluid if low filler content Stiff non-Newtonian fluid if high filler content	3×10^4 to 5×10^5 Pa s	Variable	Weijermars (1986), Boutelier et al. (2008), Reber et al. (2013)
PDMS + oleic acid	Sticky Newtonian fluid	7×10^2 to 1×10^4 Pa s	1060 kg m ⁻³	Corti et al. (2003, 2005), Reber et al. (2013)
RTV silicone	Viscous fluid Solidifies in contact with air	25 Pa s	1500 kg m ⁻³	Gressier et al. (2010)
Silicone oil	Viscous Newtonian fluid Incompressible	Used: 0.8×10^{-3} to 1.337 Pa s (can cover broader range of viscosities)	$800-965$ kg m ⁻³	Takada (1990, 1994a, b), de Bremond d’Ars et al. (2001), Watanabe et al. (2002)
<i>Water-sugar solutions</i>				
Corn-syrup	Viscous Newtonian fluid	81 Pa s at 26 °C	1425 kg m ⁻³	Kennedy et al. (2008)
“Creamed” honey	Intermediate viscosity, non-Newtonian (thixotropic) fluid	$150-400$ Pa s at 20 °C, decreasing with increased rotary shear rate	1350 kg m ⁻³	Holohan et al. (2008a, b)
Golden syrup	Sticky viscous fluid Incompressible Near Newtonian fluid	$30-500$ Pa s	1400 kg m ⁻³	Mathieu et al. (2008), Kervyn et al. (2009), Beckett et al. (2011), Schellart (2011), Abdelmalak et al. (2012), Delcamp et al. (2012b)
Aqueous corn-syrup solutions	Low viscosity Newtonian fluid	$0.0155-0.127$ Pa s	$1211-1305$ kg m ⁻³	Kennedy et al. (2008)
Glycerin–water solutions	Low viscosity Newtonian fluid	10^{-3} to 10 Pa s	$1000-1260$ kg m ⁻³	Takada (1990), Koyaguchi and Takada (1994), Bonini et al. (2001)
Concentrated sugar-water solutions	Low viscosity Newtonian fluid Incompressible	–	$1102-1373$ kg m ⁻³	Taisne and Tait (2009)
Water	Low viscosity Newtonian fluid Incompressible	10^{-3} Pa s	1000 kg m ⁻³	Hyndman and Alt (1987), Takada (1990), Menand and Tait (2002), Kavanagh et al. (2006)

(continued)

Table 2 (continued)

Model magma	Macroscopic behaviour	Viscosity	Density	References
<i>Oils and waxes</i>				
Grease	Viscous fluid	–	–	Johnson and Pollard (1973)
Molten vegetable oil	Low viscosity Newtonian fluid Solid at room temperature Incompressible	2×10^{-2} Pa s at 50 °C	890 kg m^{-3}	Galland et al. (2006)
Molten wax	Low viscosity Newtonian fluid Solid at room temperature Incompressible	4×10^{-4} to 7×10^{-2} Pa s	$1100\text{--}1335 \text{ kg m}^{-3}$	Taisne and Tait (2011)
<i>Others</i>				
Mud	Viscous fluid, non Newtonian	–	–	Hubbert and Willis (1957)
Wet plaster	Bingham pseudoplastic fluid	0.8–6 Pa s	–	Závada et al. (2009)
Water– Natrosol solution	Low viscosity fluid	0.001–0.5 Pa s	–	McLeod and Tait (1999)
Aqueous KMnO ₄ solution	Low viscosity dyed Newtonian fluid Incompressible	10^{-3} Pa s	–	Ramberg (1970, 1981)
Aqueous methylene blue-sodium polytungstate solution	Low viscosity dyed Newtonian fluid, Incompressible, adjustable density	10^{-3} Pa s	$996\text{--}1010 \text{ kg m}^{-3}$	Hallot et al. (1994, 1996)
Hexane	Low viscosity Newtonian fluid (toxic for long-term exposure)	3×10^{-4} Pa s	1330 kg m^{-3}	Ito and Martel (2002)
Air	Low viscosity gas Compressible Low density	2×10^{-6} Pa s	$1.2 \times 10^{-3} \text{ kg m}^{-3}$	Takada (1990), Rivalta et al. (2005)

2.2.1 Plasticity-Dominated Materials (Weak Materials)

The most commonly used material for simulating model rocks is dry, loose, quartz sand (Tables 3 and 4; Figs. 3 and 4). Its cohesion is negligible (Schellart 2000; Mourgues and Cobbold 2003), such that (i) it fails along shear zones (mode II fractures), thereby simulating faults, and (ii) it does not allow open fractures (mode I fractures) to form. Failure of cohesion-less dry sand occurs according to a Mohr-Coulomb criterion that is

defined, in theory, only by the angle of internal friction (ϕ). Dry sand is most applicable for simulating: (i) relatively low cohesion host materials in nature, such as unconsolidated or weakly lithified sediments or tuffs, and/or (ii) large-scale (several to 100s of km) processes involving regional-tectonic deformation (Corti et al. 2001, 2003, 2005; Musumeci et al. 2005; Mazzarini et al. 2010; Montanari et al. 2010a, b), whereby the material strength is assumed to decrease relative to the increasing length-scale (Schultz 1996).

Table 3 Types and mechanical properties of non-granular viscoelastic and viscoplastic materials used as analogue ‘rock’ in laboratory models of volcanic plumbing systems

Rock analogue	Macroscopic behaviour	Elastic properties	Fracture toughness	Density	Viscosity	References
<i>Gels</i>						
Gelatin	Viscoelastic solid Properties depend on: temperature, gelatin concentration, strain rate, and age (time elapsed after setting)	E = 390–16,000 Pa $\nu = 0.5$	28–200 Pa m ^{1/2}	1000–1010 kg m ⁻³	Complex viscosity at concentration of 2.5 wt% temperature of 10 °C (gel-state), and strain rate of 10 ⁻² s ⁻¹ is c. 50 Pa s. At 30–40 °C (sol-state), the viscosity lies between 0.36–0.0015 Pa s, decreasing with increased strain rate in the range 0.01–12 s ⁻¹	Djabourov et al. (1988b), Takada (1990), Rivalta and Dahm (2006), Di Giuseppe et al. (2009), Kavanagh et al. (2013)
Acryl amid gel	Gel of variable rheology from nearly liquid to nearly brittle material (poisonous)	–	–	–	–	Maaløe (1987)
Aqueous sugar-agar gels	Viscoelastic solid Properties depend on: temperature, gel and sugar concentrations, waiting time	E = 1000 Pa	20 Pa m ^{1/2}	1066–1310 kg m ⁻³	–	Lister and Kerr (1991)
Water	Newton viscous fluid	–	–	1000 kg m ⁻³	10 ⁻³ Pa s	Grout (1945)
<i>Others</i>						
Silicone putty	Newton viscous fluid	G = 3 × 10 ⁴ to 2.6 × 10 ⁵ Pa	–	–	10 ⁴ Pa s	Ramberg (1981), Román-Berdiel et al. (1995), Corti et al. (2003), Boutelier et al. (2008)
Plasticine	Power law material (exponent n = 6–9.5)	–	–	1770 kg m ⁻³	–	McClay (1976), Weijermars (1986), Dixon and Simpson (1987)
Wax	Power law material (exponent n = 2)	E = 2 × 10 ⁶ to 10 ⁷ Pa	–	950 kg m ⁻³	–	Dixon and Simpson (1987)
Water-Corn syrup mix	Viscous fluid Temperature-dependent viscosity	–	–	1211–1305 kg m ⁻³	0.3–20 Pa s	Grout (1945), Kennedy et al. 2008)
Wet clay	Visco-elasto-plastic material	–	–	–	–	Grout (1945)

Table 4 Types and mechanical properties of granular materials used as analogue ‘rock’ in laboratory models of volcanic plumbing systems

Rock analogue	Macroscopic behaviour	Cohesion (estimated)	Friction angle	Density	References
Sand	Loose Coulomb material	12–123 Pa	25–35°	1300–1700 kg m ⁻³	Schellart (2000), Lohrmann et al. (2003), Mourgues and Cobbold (2003)
Wheat flour	Slightly cohesive Coulomb material	40–50 Pa (likely underestimated)	33°	570 kg m ⁻³	Walter and Troll (2001), Holohan et al. (2008a)
Sand-Plaster mix	Slightly cohesive Coulomb material	40–100 Pa (likely underestimated)	36°	1360–1560 kg m ⁻³	Roche et al. (2001), Kervyn et al. (2009, 2010)
Glass beads	Loose Coulomb material	64–137 Pa	20°	1547–1905 kg m ⁻³	Schellart (2000), Nermoen et al. (2010a, b)
Ignimbrite powder	Cohesive Coulomb material	100–230 Pa	38°	1400 kg m ⁻³	Mathieu et al. (2008)
Sand-flour mix	Cohesive Coulomb material	200 Pa	40°	1200–1400 kg m ⁻³	Donnadieu and Merle (1998), Holohan et al. (2005)
Fused alumina powder	Cohesive Coulomb material	200 Pa	38°	–	Marti et al. (1994)
Diatomite powder	Low density cohesive Coulomb material	300 Pa	–	400 kg m ⁻³	Gressier et al. (2010)
Silica flour	Cohesive fine-grained Coulomb material	300–400 Pa	40°	1050–1700 kg m ⁻³	Galland et al. (2006, 2009), Abdelmalak et al. (2012)
Sand-powdered clay	Cohesive Coulomb material Likely anisotropic	500–1300 Pa (likely overestimated)	26–31°	1500–1700 kg m ⁻³	Komuro (1987), Walter and Troll (2001)

Note that although dry sand is very weak, it does not exhibit a purely or ideally plastic behaviour. At low stresses and strains, it holds some reversible, elastic deformation, as demonstrated by the measurements of, e.g. Lohrmann et al. (2003) and Panien et al. (2006). Moreover, under loading conditions typical of laboratory

experiments, dry sand fails in a semi-brittle fashion characterised by a stress drop that reflects a difference in static and dynamic friction coefficients. Such properties can become important in, e.g. models made of dry rice, which intend to simulate stick-slip faulting (Rosenau et al. 2010).

2.2.2 Elasticity-Dominated Materials (Strong Materials)

While sand is a weak end member of model rocks, the strong end member is gelatine (Table 3; Figs. 3 and 4d). At the scales of laboratory models, gelatine fails through the formation of open cracks (mode I fractures). In these models, gelatine behaves elastically, except locally at the tips, where complex viscoelastic processes occur. Hence gelatine is suitable for simulating: (i) natural host rocks of relatively high cohesion, such as well-consolidated sedimentary rocks or crystalline igneous or metamorphic basement rocks, and/or (ii) relatively small-scale processes (10s of m to a few km). Another advantage of gelatine, and gels in general, is that they become birefringent when strained (e.g. Dupré and Lagarde 1997; Dupré et al. 2010). When the models are placed between crossed polarizers, the strained domains of the models appear as coloured fringes, whereas unstrained domains appear dark (Richards and Mark 1966; Pollard and Johnson 1973; Taisne and Tait 2009, 2011).

The stiffness (Young's modulus, E) and the strength (fracture toughness, K_c) of gelatine can be jointly tuned by varying the gelatine concentration (Di Giuseppe et al. 2009; Kavanagh et al. 2013), while the Poisson's ratio is constant at $\nu = 0.5$ (Djabourov et al. 1988a, b). K_c can be calculated by measuring the fluid pressure required to propagate an existing crack (Menand and Tait 2002; Kavanagh et al. 2013). Systematic measurements show that E is a linear function of the gelatine concentration (Kavanagh et al. 2013). Nevertheless, for a given gelatine concentration, E is also time-dependent (Kavanagh et al. 2013), as the gelification process continues long time after the gelatine becomes solid. The value of K_c is a function of \sqrt{E} , and therefore of the gelatine concentration also (Kavanagh et al. 2013). This means that the preparation of gelatine models must follow a rigorous procedure, during which the waiting time between the preparation of the model and the experimental run is constant to ensure repeatable mechanical properties of the models.

2.2.3 Elasto-Plastic (Intermediate Strength) Materials

Dry sand and gelatine are the end members of rock mechanical behaviours, being plasticity- and elasticity-dominated, respectively. Nevertheless, it is known that complex processes, in which elastic and plastic behaviours are balanced, can govern natural rock deformation. Therefore, other model materials are needed to explore the effects of such complex rock rheology on magma emplacement in the Earth's crust. Good examples are cohesive granular materials (Table 4; Fig. 4b, c, e, f), such as ignimbrite powder (Mathieu et al. 2008, 2011; Mathieu and van Wyk de Vries 2011), fine-grained silica flour (Galland et al. 2006, 2009; Galland 2012), diatomite powder (Gressier et al. 2010), or sand-plaster mixtures (Roche et al. 2001), among others. When deformed, these materials typically exhibit both open (mode I) and shear (mode II) fractures at shallow and deep levels, respectively (Holland et al. 2006; Kettermann and Urai, 2015). Although their elastic properties remain challenging to estimate, these granular materials thus appear to be most suitable for reproducing the complex elasto-plastic mechanical behaviour of natural rocks.

Such cohesive granular materials also fail according to a Mohr-Coulomb criterion, but one that is defined by the material's tensile strength (T), cohesion (C) and its angle of internal friction (ϕ). These parameters control the depth of the transition from Mode 1 to Mode 2 fracturing. The cohesion and the angle of internal friction are properties that are measured indirectly. Firstly, a Mohr-Coulomb failure envelope is constructed via numerous shear tests conducted by using either a Hubbert-type shear box (Hubbert 1937; Mourgues and Cobbold 2003; Galland et al. 2006) or a Casagrande shear box (Rossi and Storti 2003). These apparatuses measure the shear strength τ of the tested material for variable normal stress σ_n . In a diagram displaying τ as a function of σ_n , many measurements exhibit a positive correlation. By fitting a function or 'failure envelope' to the data, it is possible to calculate C as being the intercept of the fitting function with the shear stress axis (typically the

y-axis in such a diagram; e.g. Schellart 2000; Mourgues and Cobbold 2003). The slope of the envelope, which is typically linear for most of its length, is the tangent of Φ . The tensile strength can be measured directly (Schweiger and Zimmermann 1999), but this requires specific devices, such that tensile strengths are rarely reported (Galland et al. 2006; Holland et al. 2006).

The degree of compaction (or closeness of packing) of a granular material strongly influences its mechanical properties (Lohrmann et al. 2003; Galland et al. 2006; Schreurs et al. 2006). Increased compaction leads to an increased density, cohesion and friction coefficient. The degree of compaction is controlled by the procedure of emplacing the material in the experimental apparatus. Compaction can be increased by shaking the model before running it, especially if the material is cohesive (Galland et al. 2009; Galland 2012), or by sifting the material if it is cohesionless (Lohrmann et al. 2003; Maillot 2013). Simply pouring the granular material in the experimental box is to be avoided as it leads to inhomogeneity in initial packing and hence in mechanical properties (Lohrmann et al. 2003).

2.2.4 Other Materials

Some of the first experiments of magma emplacement considered the whole crust as a viscous fluid. Grout (1945) injected air into media of various viscosities, such as wet clay, corn syrups and water-diluted syrups in order to simulate structures related to batholith emplacement. The rheologies of these pioneering model materials were not accurately measured, however. Silicone putty (Fig. 4a) is commonly used to simulate viscously deforming rock strata or formations, such as evaporite and shale (Román-Berdiel et al. 1995, 1997; Román-Berdiel 1999; Corti et al. 2001, 2003). Nevertheless, it becomes technically challenging to simulate both viscous host rock and the injection of viscous magma in the same experiments.

2.2.5 Summary

Most existing experimental studies of volcanic plumbing systems have used end member model rock materials with rheologies that are

elasticity-dominated, plasticity-dominated, or viscous. Recently, the introduction of cohesive granular materials has allowed for exploring the effect of complex elasto-plastic behaviour of host rock on magma transport and emplacement. Moreover, although highly concentrated gels are elasticity-dominated, low-concentration gels (e.g. laponite, gelatine, agarose) exhibit viscoelastic behaviour at the length and time scales of laboratory experiments (e.g. Hallot et al. 1996; Di Giuseppe et al. 2009; Ruzicka and Zaccarelli 2011) and offer the possibility to explore experimentally the emplacement mechanism of magma into viscoelastic rocks, which is an essential step toward more geologically realistic models.

3 A Crucial Starting Point: The Model “Scaling”

The main advantage of laboratory modelling, i.e. that geological processes are simulated within the limits of a laboratory and the working time of the researcher, at the same time represents the method’s biggest problem: the difference in scale between natural and laboratory volcanic plumbing systems. It is the scale gap between small models and huge intrusions that often leads to scepticism among Earth scientists regarding the applicability of laboratory models. Following the pioneering 19th century work that impressively reproduced natural structures, however, the 20th century saw a breakthrough with the development of the concept of scaling, with particular application to experimental models.

In 1937, Marion King Hubbert introduced the “theory of scale models” to the geological community and thereby shifted phenomenological analogue experiments from a qualitative to a quantitative approach. According to Hubbert (1937) and his followers (e.g. Ramberg 1970, 1981), laboratory models should be geometrically, kinematically, and dynamically similar to the natural system under investigation. Scaling is therefore an essential part for any laboratory study and needs to be considered to justify the applicability of the model results. Nevertheless,

there is a lot of confusion among Earth scientists about correct scaling of laboratory models to geological systems, and first of all about the meaning of “scaling”.

The main confusion is related to the misunderstanding of the goals of laboratory models. They are not designed to exactly mimic a given geological system, as many Earth scientists think, but to understand underlying generic processes, either individually or in combination, and to identify or demonstrate physical laws governing these processes. In order to prove that any physical laws identified in laboratory experiments apply to geological systems, these laws should be dimensionless, i.e. they are independent of the length scale, time scale, etc., which is why they are often called scaling laws.

The procedure for establishing dimensionless scaling laws involves two steps: (i) a *dimensional analysis* of the considered physical problem, to identify the dimensionless governing parameters, and (ii) a *comparison of laboratory and geological values of these dimensionless parameters* to test the geological relevance of the experimentally-derived physical laws.

3.1 Dimensional Analysis

The principles of dimensional analysis are described in detail by e.g. Barenblatt (2003). The first applications of such an approach in laboratory experiments of volcanic processes has been conducted by Tibaldi (1995) and Merle and Borgia (1996). The approach consists of identifying the dimensionless physical parameters that govern the processes to be addressed.

The first step is to list the n parameters *with dimensions* that are relevant for the processes to be studied. In mechanical systems, usual dimensions are those of length [L], mass [M] and time [T]. An analysis of thermo-mechanical systems requires the addition of the dimension of temperature [K].

Let us consider a simple conceptual example: the stability of a volcanic edifice. The aim of the following paragraphs is only to provide an illustrative example of dimensional analysis. In the case of edifice stability, the effect of the

coefficient of friction is obvious, however it is not suitable for illustrating the implementation of dimensional analysis. Instead, we will consider the effect of material cohesion on edifice stability, which has not been considered. In the following sections, we will thus assume that the coefficient of friction is taken as a constant, and it will be ignored despite its established relevance. The dimensional analysis developed in the following sections thus only aim at assessing the effects cohesion on edifice stability.

The edifice has a height h ($[h] = L$), diameter D ($[D] = L$), a density ρ ($[\rho] = M L^{-3}$), and the material making the edifice has a cohesion C ($[C] = M L^{-1} T^{-2}$). The square brackets here represent the dimension, not the unit, of each parameter. The volcano is exposed to gravitational acceleration g ($[g] = L T^{-2}$). Again for illustrative purpose, we consider the coefficient of friction to be a dimensionless constant and we will ignore it during the following analysis, despite its established relevance. From this list of parameters, the experimentalist should separate the governing parameters, i.e. those known and controlled, from the parameters to measure. To study the stability of a volcanic edifice in the laboratory, two approaches can be developed. A first approach (example 1) consists of controlling both the height and diameter of the edifice, such that h , D , ρ , g and C are governing parameters. The experimentalist builds volcanic edifices of controlled sizes using model materials of varying cohesions, and observes whether they are stable or not. A second approach (example 2) consists of controlling the height of the edifice only, and measuring the diameter, such that h , ρ , g and C are the governing parameters and D the measured quantity. The experimentalist gradually builds the cone with model materials of varying cohesions at a critically stable slope to a given height h , and measures the diameter D of the cone, as in the experiments of Ramos et al. (2009). We base the following sections on these examples.

The second step is to identify the number k of the governing parameters with *independent dimensions*. A set of parameters has independent dimensions if their dimensions cannot be

expressed as a function of each other's (Barenblatt 2003). For instance, the height of a volcanic edifice and the density of the rock have independent dimensions, because the dimension of the density ($[\rho] = \text{M L}^{-3}$) cannot be expressed as a function of the dimension of the depth ($[h] = \text{L}$) only. In contrast, the rock cohesion ($[C] = \text{M L}^{-1} \text{T}^{-2}$), the density ($[\rho] = \text{M L}^{-3}$), the gravity ($[g] = \text{L T}^{-2}$) and the height of a volcanic edifice ($[h] = \text{L}$) do not have independent dimensions, given that the dimension of C is a function of the dimensions of ρ , g and h :

$$\begin{aligned} [C] &= \text{M L}^{-1} \text{T}^{-2} = [\rho] \times [g] \times [h] \\ &= (\text{M L}^{-3}) \times (\text{L T}^{-2}) \times (\text{L}) \end{aligned} \quad (1)$$

In example 1, it is thus possible to show that ρ , g , h are governing parameters with independent dimensions, whereas the dimensions of C and D can be expressed as functions of those of ρ , g , and h . Note that the selection of the governing parameters with independent dimensions is not unique. For instance, one can choose ρ , g , and D as governing parameters with independent dimensions, C and h being the others. But in both cases, among the set of $n = 5$ governing parameters, $k = 3$ parameters have independent dimensions. In example 2, there is only one possibility: ρ , g , and h are the governing parameters with independent dimensions, C is the other governing parameter, and D is the measured quantity. Therefore, among $n = 4$ governing parameters, $k = 3$ parameters have independent dimensions.

The third step is to calculate the number m of dimensionless parameters that characterise the physical system to be simulated in the experiments. This number is easily calculated by using the Π -theorem (or Buckingham Π -theorem), which is the central theorem in dimensional analysis. It states that “a physical relationship between some dimensional (generally speaking) quantity and several dimensional governing parameters can be rewritten as a relationship between a dimensionless parameter and several dimensionless products of the governing parameters; the number of dimensionless products is equal to the total number of governing

parameters minus the number of governing parameters with independent dimensions” (Barenblatt 2003). This means that the number m of dimensionless parameters to be defined is given by $m = n - k$.

In example 1, ignoring the coefficient of friction, the total number of governing parameters being $n = 5$, and the number of governing parameters with independent dimensions being $k = 3$, the number of dimensionless parameters governing the physics of a volcanic edifice is $m = n - k = 2$. If ρ , g and h are chosen as the governing parameters with independent dimensions, the two dimensionless parameters are:

$$\Pi_1 = \frac{C}{\rho \times g \times h} \quad (2)$$

$$\Pi_2 = \frac{h}{D} \quad (3)$$

In example 2, again ignoring the coefficient of friction, $n = 4$ and $k = 3$, therefore the number of dimensionless parameters governing the defined physical system is $m = 1$. A clear choice for this parameter is simply:

$$\Pi_1 = \frac{C}{\rho \times g \times h} \quad (4)$$

In order to test the relevance of the dimensional analysis, the defined dimensionless numbers should have a physical meaning. In example 1, the physical meanings of Π_1 and Π_2 are straightforward. Π_2 expresses the slope of the volcanic edifice. Π_1 expresses whether the volcanic edifice is gravity-controlled ($\Pi_1 \rightarrow 0$) or strength-controlled ($\Pi_1 \rightarrow \infty$). In the first case, the material that composes the edifice is macroscopically loose, such as sand, and the edifice is expected to collapse under its own weight along shear planes (i.e. faults). Conversely, in the second case the material is macroscopically cohesive, and the edifice is expected to be stable.

Several widely used dimensionless numbers are called by the name of their discoverer. A good example is the Reynolds number (Re), which quantifies the ratio between the inertial

forces in a flowing fluid and the viscous forces. A critical value of the Reynolds number sets the boundary between the laminar flow regime and the turbulent flow regime. This number is thus highly relevant for magma flow. Another example is the Rayleigh number (Ra), which quantifies the ratio between the buoyancy forces of a heated fluid and the viscous forces (i.e. those forces resisting flow). A critical value of the Rayleigh number sets the boundary between a convective system and a non-convective system: this has high relevance for mantle convection and the dynamics of magma chambers.

In example 2, we note that the measured quantity D has not been used in the definition of the dimensionless parameter Π_1 . At this stage, we can define a dimensionless parameter Π , which is defined as a ratio between the measured quantity D and a function of the governing parameters with independent dimensions. Here a definition is given by $\Pi = D/h$. The Π -theorem implies that a dimensionless quantity Π to be measured in the experimental study can be rewritten as a function of the other m Π -numbers, such as:

$$\Pi = F(\Pi_1, \Pi_2, \dots, \Pi_m) \tag{5}$$

The function F is the physical law that governs the simulated processes. This relationship between the dimensionless output and the dimensionless input parameters should dictate the experimental strategy. In order to test the effects of each dimensionless parameter Π_i during an experimental project, the dimensional experimental parameters should be varied such that Π_i is systematically varied, while the others are kept constant. Applied to each Π_i -number and so by constraining the function F , the experimental results will contribute to deriving the physical laws that govern the investigated processes.

This strategy can be adapted to two different approaches depending on the nature of the model outputs.

If the model output is not a measured quantity, but contrasting physical behaviours, the aim of the experimental procedure will be to explore the parameter space, i.e. to vary systematically the values of the dimensionless parameters Π_i , to map under which conditions these contrasting physical behaviours occur (Fig. 5a). This procedure is equivalent to building a phase diagram, the contrasting physical behaviours being physical phases. Let us illustrate this approach with our example 1. An experimental procedure would

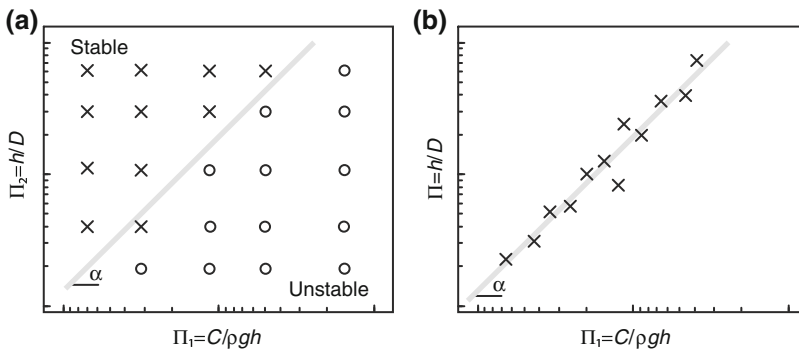


Fig. 5 Qualitative diagrams illustrating the two main experimental strategies defined from dimensional analysis. **a** Example 1, when the model output is not a measured quantity but a number of physical behaviours, each behaviour (here stability or collapse of a volcanic edifice; see Sect. 3.1 for explanation) is plotted in a diagram with the dimensionless input parameters as x- and y-axes. This so-called phase diagram maps the physical fields, in which the observed behaviours are

expected. The field transitions are commonly described by power laws of the form $\Pi_2 \propto \Pi_1^z$. **b** Example 2, i.e. when the model output is a measured quantity Π (here the slope $\Pi = h/D$ of a volcanic edifice at stability criterion; see text for explanation), it is plotted as a function of the dimensionless input parameters (here $\Pi_1 = C/\rho gh$, see text for explanation). The correlation between Π and Π_1 is usually a power law of the form $\Pi \propto \Pi_1^z$

consist of building a model volcanic edifice of given and controlled height h and width D , with materials of given cohesions C (and a constant coefficient of friction). Once the edifice is built, one can see if it is stable or unstable (collapses). The experimental strategy would be to run many experiments by varying systematically and independently Π_1 and Π_2 to explore how these parameters control the stability of a volcanic edifice. By plotting all the experiments in a diagram of Π_1 against Π_2 , and by indicating the corresponding physical behaviour with e.g. different data point symbols, it is possible to identify physical fields, or phases, separated by transitions. The transitions between the fields are mostly expected to be power laws of the form: $\Pi_2 \propto \Pi_1^\alpha$.

If the model output is a measured quantity, the aim of the experimental procedure will be to establish a correlation between the measured dimensionless parameter Π and the dimensionless input parameters Π_i (Fig. 5b). In our example 2, an experimental procedure would consist of gradually building model volcanic edifices of given height h with materials of given cohesions C , and measure the final diameter D of the edifices. The experimental strategy would be to run many experiments by systematically varying Π_1 to explore how these parameters control the output parameter Π . If the parameters Π and Π_i are well defined, they are expected to correlate, and most likely following a power law. Hence the correlation should appear as a straight line of slope α in a log-log plot, showing that the physical law linking Π and Π_i is a power law of the form: $\Pi \propto \Pi_i^\alpha$.

3.2 Similarity to Geological Systems

After performing the dimensional analysis, identifying the Π -numbers, and obtaining the experimental results, the geological relevance of the experimentally-defined scaling laws needs to be tested. In other words, we need to test whether the processes simulated in the laboratory are physically similar to the geological processes. This concept of *physically similar phenomena* is central to geological laboratory modelling. “Two systems are considered similar if the values of

the dimensionless parameters are identical, even if the values of the governing dimensional parameters differ greatly” (Barenblatt 2003). It means that although the scales of the laboratory models are drastically different to the scales of the geological systems they aim to simulate, the laboratory models will be physically similar to their geological equivalents if their respective Π -numbers have the same values. Therefore, the experimentalist must compare the values of each Π -number in the laboratory with the values of these numbers in the geological system: if the ranges of values overlap, the two systems are similar, and the experimental results are relevant to the geological system.

The principle of similarity can be also strictly applied if we consider the physical meaning of the Π -numbers. Let us consider the height-to-diameter ratio of a volcanic edifice $\Pi = h/D$. In geological settings, Π is typically 0.12–0.6 (Grosse et al. 2012). In laboratory experiments, the resulting values of Π will be larger or smaller than the geological values of Π , if the model material is too cohesive or too loose, respectively. In this case, the laboratory volcanic edifices are not rigorously similar to the geological edifices. Nevertheless, in our example 2 if a plot of the laboratory and geological values of Π against $\Pi_1 = C/\rho gh$ shows an alignment along the same scaling law (Fig. 6), it would mean that both edifice types are governed by the same physical law. Consequently, in both the laboratory and geological systems, the physical regimes are the same, and the law identified in the laboratory model of volcano edifice can be considered physically relevant to geological edifices. In our example 1, it is also important to consider the physical regime (i.e. the physical ‘phase’ in the phase diagram): if the geological edifice and the laboratory edifices have different values of Π_1 and Π_2 , but if both are in the stable field, they can be considered physically equivalent, without being similar *sensu stricto*. Likewise, the Reynolds numbers related to magma flow in the laboratory and its geological prototype can be different, but if both are way below the critical value, the flow regimes are both laminar (see discussion in, e.g. Galland et al. 2009).

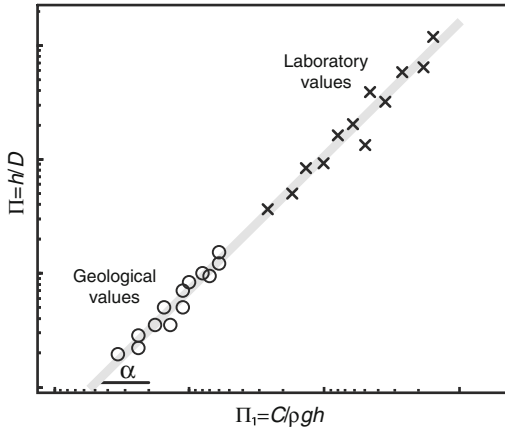


Fig. 6 Schematic diagram illustrating a potential mismatch between laboratory and geological values of the slope h/D against $C/\rho gh$ for a volcanic edifice (see text for explanation). The model and geological edifices exhibit different values, implying that they are not strictly similar. Nevertheless, they plot on the same scaling law, showing that they result from the same physical processes. Therefore, such diagram shows that the laboratory models are physically equivalent to the geological systems, without being strictly similar

4 Geological Applications

There is an extensive literature on laboratory experiments of volcanic plumbing systems. We structure our review of these past studies according to the simulated geological structures or processes, which include: (1) dykes, (2) cone sheets, (3) sills, (4) laccoliths, (5) caldera-related structures and intrusion, (6) ground deformation associated with shallow intrusions, (7) magma/fault interactions and (8) explosive volcanic vents.

4.1 Dyke Formation

Dykes are the most common magma conduits in the Earth. They are steeply inclined sheet-like intrusive bodies that are discordant to any mechanical stratigraphy in their host rocks, and that usually exhibit a very small thickness-to-length ratio (between 10^{-4} and 10^{-2} , Rubin 1995). The latter characteristic means that model dykes in experiment set-ups of a few decimetres in length should theoretically be very thin (between 1 and 10^{-3} mm). This is very challenging to achieve.

Magmatic dykes are commonly assumed to be emplaced by hydraulic fracturing (Pollard 1987; Lister and Kerr 1991). One of the first experiments that intended to simulate hydraulic fracturing consisted of elastic gelatine as the model rock, and mud as the model magma (Fig. 7) (Hubbert and Willis 1957). Although the motivation of these experiments was to simulate hydraulic fracturing in boreholes, the experimental results are relevant for igneous dykes and sills. These experiments demonstrated that the stress field applied to the model controlled the orientation of hydraulic fractures nucleating from a vertical pipe: the fracture planes were always perpendicular to the least principal stress σ_3 , and parallel to the $(\sigma_1-\sigma_2)$ plane (Sibson 2003). In addition, these experiments demonstrated qualitatively the strong effect of mechanically layered host rocks on dyke propagation.

Experiments with gels have since been used extensively to unravel various aspects of dyke propagation through the Earth's crust. Gels are transparent, so it is possible to track the evolution of growing intrusions. This has proven very practical for unravelling the physical processes governing dyke nucleation and propagation. The following provides a short summary of our understanding of the physics of dykes from gel experiments.

4.1.1 Dyke Nucleation from a Magma Reservoir

An important aspect of dyke formation is their nucleation from a magma reservoir. Using gel +silicone experiments, Cañón-Tapia and Merle (2006) simulated dyke nucleation from an over-pressurised magma reservoir made of silicone putty. The silicone putty was injected at a constant flow rate via a computer-controlled piston. The results suggest that dykes nucleate in response to the overpressure in the reservoir, rather than because of buoyancy forces arising from the density difference between the silicone and the gel. Interestingly, these experiments highlight the discontinuous behaviour of dyke propagation from a magma reservoir, which results from a competition between the strain energy accumulated in the gel and the pressure evolution in the reservoir.

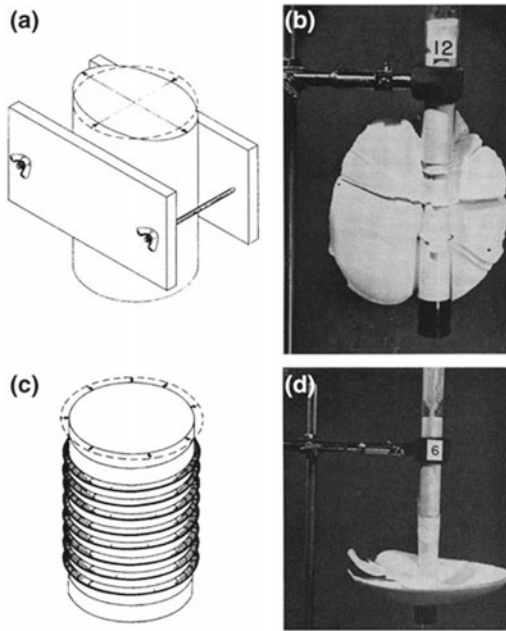


Fig. 7 Characteristic results of pioneering experiments of Hubbert and Willis (1957) to address the mechanics of hydraulic fracturing. **a** Drawing of experimental setup with anisotropic horizontal stress. A cylinder of gelatine is compressed in one direction between two plates. Mud is injected in the gelatine, and form hydraulic fractures. **b** Photograph of vertical hydraulic fracture obtained from experimental setup displayed in **a**. The fracture is perpendicular to the least principal stress, which is horizontal and parallel to the plates. **c** Drawing of experimental setup with isotropic horizontal stress. A cylinder of gelatine is compressed horizontally in every direction by a series of elastic strings. **d** Photograph of horizontal hydraulic fracture obtained from experimental setup displayed in **c**. The fracture is perpendicular to the least principal stress, which is vertical

Further to the above experiments, McLeod and Tait (1999) investigated the effects of magma viscosity on dyke nucleation (Fig. 8a). By controlling the injection pressure rather than the injection flow rate, McLeod and Tait (1999) showed that for an instantaneous increase in model magma pressure, the time delay required to nucleate a dyke from a reservoir in a gelatine host increases with increased fluid viscosity (Fig. 8a). In addition, for gradually increasing pressure in the reservoir, the critical pressure required to nucleate a dyke is larger when the magma is more viscous. These results suggest

that the pressures required to form felsic dykes are much higher than for mafic dykes.

4.1.2 Dyke Propagation in a Homogeneous and Isotropic Medium—The Effects of Buoyancy

Fundamental mechanisms controlling the propagation of dykes have also been studied by using simple gel experiments that take advantage of the gel's isotropic and homogeneous nature. This nature means that effects on propagation that are related solely to buoyancy, i.e. the force arising from the difference in density between the magma and its host rock, can be isolated and understood.

Takada (1990) concluded that the shapes and velocities of propagating dykes depend largely on the density difference between the intruding fluid and the gel—i.e. that they are buoyancy-controlled (Fig. 8b). In Takada's (1990) experiments, the liquid was injected with a needle, either from the side or the bottom of the models. Thus, the dykes were of controlled volumes, and neither the applied overpressure nor the injection flow rate was controlled. Takada (1990) concluded that: (i) Intrusion shapes are governed by the balance between the buoyancy forces and the strength of the gel. If buoyancy is small, the dykes are symmetrical penny-shaped, whereas if the buoyancy is large, the dykes are vertically asymmetrical in transverse section where they exhibit a tear drop shape with a fat curved upper tip and a sharp straight lower tip. (ii) The propagation direction is governed by the balance between the buoyancy forces and the strength of the gel: if buoyancy is small, the dyke propagates in all directions, whereas if the buoyancy is large, the dyke propagates dominantly upward. (iii) A buoyant crack of constant volume propagates itself only if it is larger than a critical length (see also Algar et al. 2011). (iv) The propagation velocity of the dyke is correlated to the density difference between the gel and the injected fluid. (v) When buoyancy forces are higher, the leading edge of the intrusion becomes broad, leading to the splitting of the dyke tip.

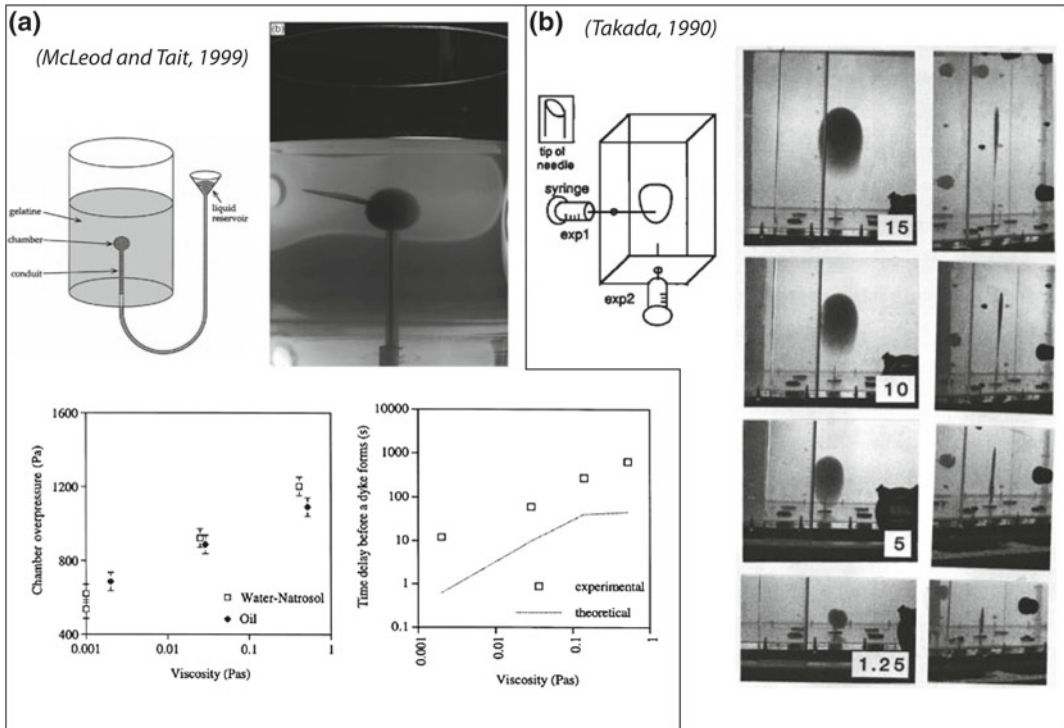


Fig. 8 a Schematic drawing of experimental setup (upper left) and photograph of a characteristic experiments of dyke nucleation from a magma reservoir (upper right; McLeod and Tait 1999), in which fluids of various viscosities are injected at controlled pressures in a gelatine model from a cavity. The lower left graph shows how the viscosity controls the fluid pressure required to nucleate a dyke, whereas the lower right graph shows how the viscosity of the injected fluid controls the time scale of

dyke nucleation from a reservoir. b Experimental setup (left) of Takada’s (1990) experimental study of dyke propagation. Liquids of various densities and viscosities were injected via a syringe, and their subsequent propagation was monitored with photographs. The series of photographs show profile (left) and front (right) views of the time evolution of a propagating dyke during a characteristic experiment

In addition to examining buoyancy on dyke propagation, Menand and Tait (2002) investigated the effect of overpressure in a magma reservoir. They imposed an overpressure by placing a water reservoir at given vertical distances above the model. They show that dyke propagation exhibits two regimes: (i) an initial overpressure-dominated regime during which the dyke propagates both vertically and laterally, and (ii) a subsequent buoyancy-dominated regime during which the dyke propagates mostly vertically. The transition between both regimes is controlled by a critical size of the dyke, in agreement with Takada’s (1990) experiments.

Finally, buoyancy-driven cracks of constant volume in gelatine experiments accelerate as they

approach the free surface (Rivalta and Dahm 2006). Such a phenomenon has also been observed in volcanoes, such as Piton de la Fournaise, Réunion Island (Battaglia 2001), and appears crucial for forecasting the timing of volcanic eruptions by means of dyke-induced seismicity (Rivalta and Dahm 2006). Interestingly, the experiments show that the free surface effects are larger when the fracture is ascending more slowly (i.e. when the buoyancy forces are smaller).

4.1.3 Effects of Contrasting Magma Viscosities on Composite Dyke Propagation

Magma batches of different compositions, and so of different viscosities, can lead to the formation

of composite dykes, the cores of which are felsic and the rims are mafic (Walker and Skelhorn 1966). A spectacular example is the Streitishorn dyke, Eastern Iceland (Paquet et al. 2007). Koyaguchi and Takada (1994) simulated the propagation of a dyke from a magma reservoir containing two fluids of contrasting viscosities within an isotropic gelatine medium. They show that low viscosity fluid (mafic magma) at the dyke tip controls the tip's propagation. This lower viscosity fluid in the dyke tip lubricates the subsequent flow of the higher viscosity fluid (felsic magma) into the middle of the dyke. Such process may considerably enhance the drainage of a silicic magma chamber and the flow of viscous felsic magmas over large distances.

4.1.4 Effects of Mechanical Heterogeneity (Preexisting Dykes or Layering) on Dyke Propagation

The medium through which dykes propagate in nature, the Earth's lithosphere, is neither isotropic nor homogeneous. Two first-order planar heterogeneities that can greatly influence dyke propagation include pre-existing dykes and sedimentary layering. Experiments investigating the effects of such heterogeneities (Maaløe 1987; Bons et al. 2001; Rivalta et al. 2005; Kavanagh et al. 2006) show that they represent fundamental features controlling the average dyke propagation velocity, the propagation direction, and possibly also dyke geometry.

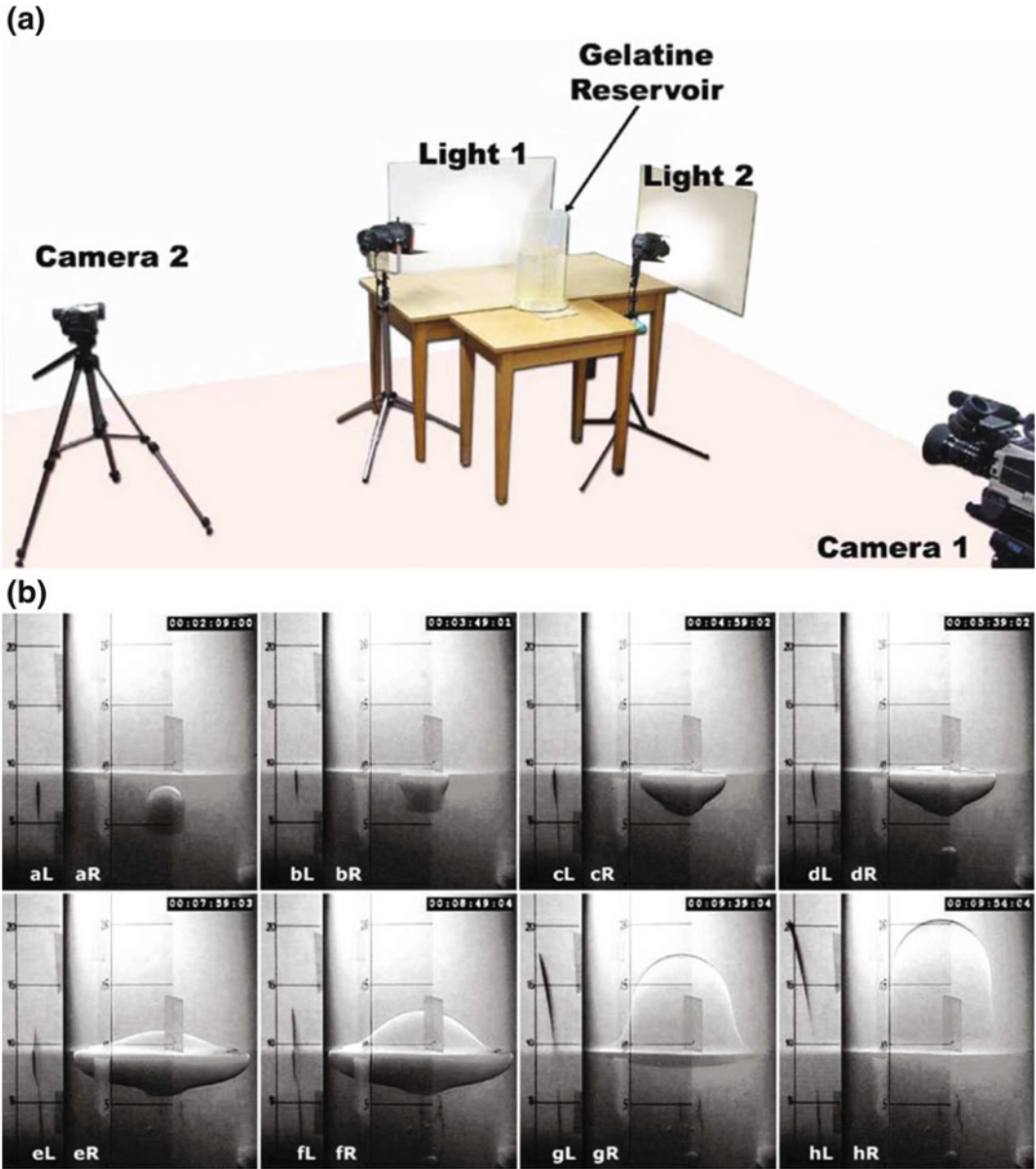
Maaløe (1987) and Bons et al. (2001) conducted gelatin and air/water model experiments that suggest that dykes propagate in a stepwise manner due to successive magma batches. Maaløe (1987) showed that an initial magma batch forms a dyke, which stops after some distance. This initial dyke only propagates further if a new magma batch reaches it. Bons et al. (2001) simulated dyke propagation in heterogeneous gelatine, and showed that the path of an initial dyke greatly controls the propagation of subsequent dykes. In addition, Bons et al. (2001) show that local heterogeneities stopped a propagating dyke, which only continues propagating if it is fed by a new magma batch.

Rivalta et al. (2005) and Kavanagh et al. (2006) addressed the mechanisms of dyke propagation through mechanically-layered media, which are common in sedimentary basins and lava piles. They show that the velocity of the propagating dyke is correlated with the strength and Young's modulus of the host: a dyke decelerates when it reaches a stronger layer, and vice versa. In addition, the nature of the layer interface can considerably affect the 3-dimensional shape of a dyke (Fig. 9). For instance, if a dyke reaches a very strong layer interface, its vertical propagation is arrested and it propagates laterally. If the driving pressure in the dyke is large enough, the dykes can turn into horizontal sills at such interfaces (see also the Sect. 4.3 below).

4.1.5 Effects of Anisotropic Stress Fields (From Regional Tectonics or Local Topography) on Dyke Propagation

It has been long hypothesised from field relationships that dyke emplacement is greatly controlled by the regional stress field (Hubbert and Willis 1957; Sibson 2003; Takada 1999). If the stress field is homogeneous but anisotropic (i.e., the magnitudes of the principal stresses differ), dykes are expected to be parallel to each other, and perpendicular to the least principal stress, σ_3 (Anderson 1936). In addition, topographic features, such as volcanic edifices, are thought to produce local anomalous stress fields that can greatly affect the propagation of dykes (Odé 1957; Johnson 1970; Nakamura 1977). This effect of gravitational stresses related to topography on dyke geometry and propagation has been subject of numerous experimental studies.

Gelatine experiments have been used to investigate how the stress generated by the load of a volcanic edifice affects dyke propagation in the region around the edifice. Muller et al. (2001) and Watanabe et al. (2002) used injected dykes at varying distances from a load, and observed that dykes close to the load were attracted toward it, whereas dykes far away from the load were not (Fig. 10). They show that the critical distance at which a dyke is affected by the load is correlated



(Rivalta et al., 2005)

Fig. 9 a Experimental apparatus designed by Rivalta et al. (2005) to study dyke propagation through layered media. The model magma is air, and the model rock consists of two layers of gelatine of different concentrations. **b** Time series of photographs of a characteristic experiment of dyke propagation in a layered medium. Here the upper layer is more resistant than the lower layer.

When the rising dyke reaches the interface between the layers, it is temporarily stopped upward but propagates laterally (*photographs* bR, cR, dR), until the dyke tip starts piercing through the upper, tougher layer (*photograph* eR). Interestingly, the dyke is wider in the upper layer than in the lower layer, although it has the same volume

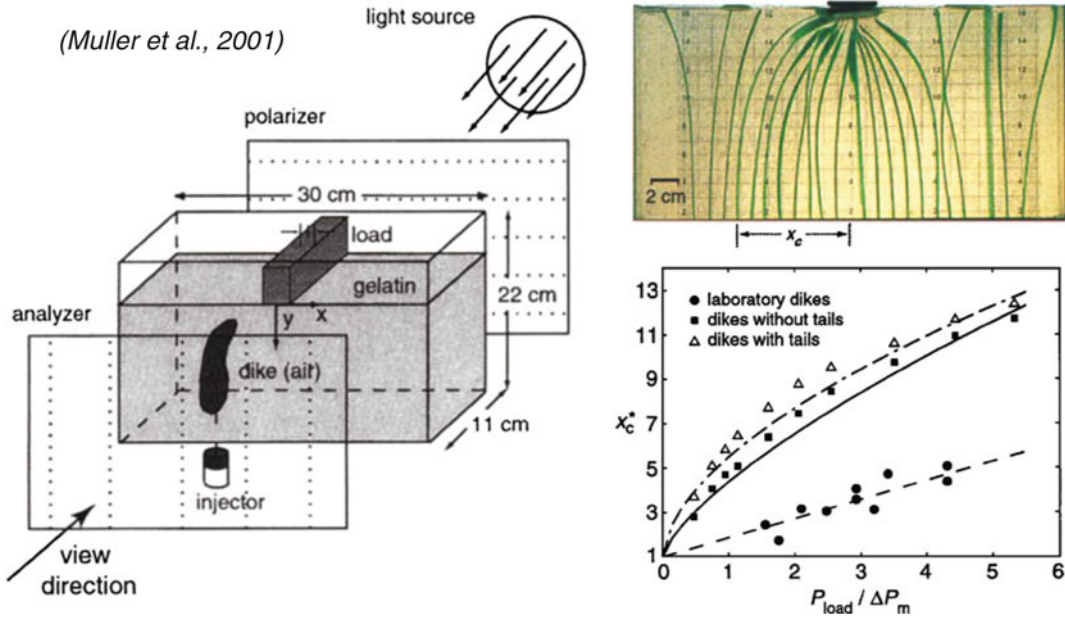


Fig. 10 Experimental study of Muller et al. (2001), in which air-filled dykes are injected in a gelatine model, at the surface of which a load is placed. Dyke injection is successively performed at an increased lateral distance x from the position of the load. The *upper right* photograph shows dyke trajectories during an experiment: the dyke closer to a critical distance x_c are attracted toward the load, whereas the other dykes are not attracted by the

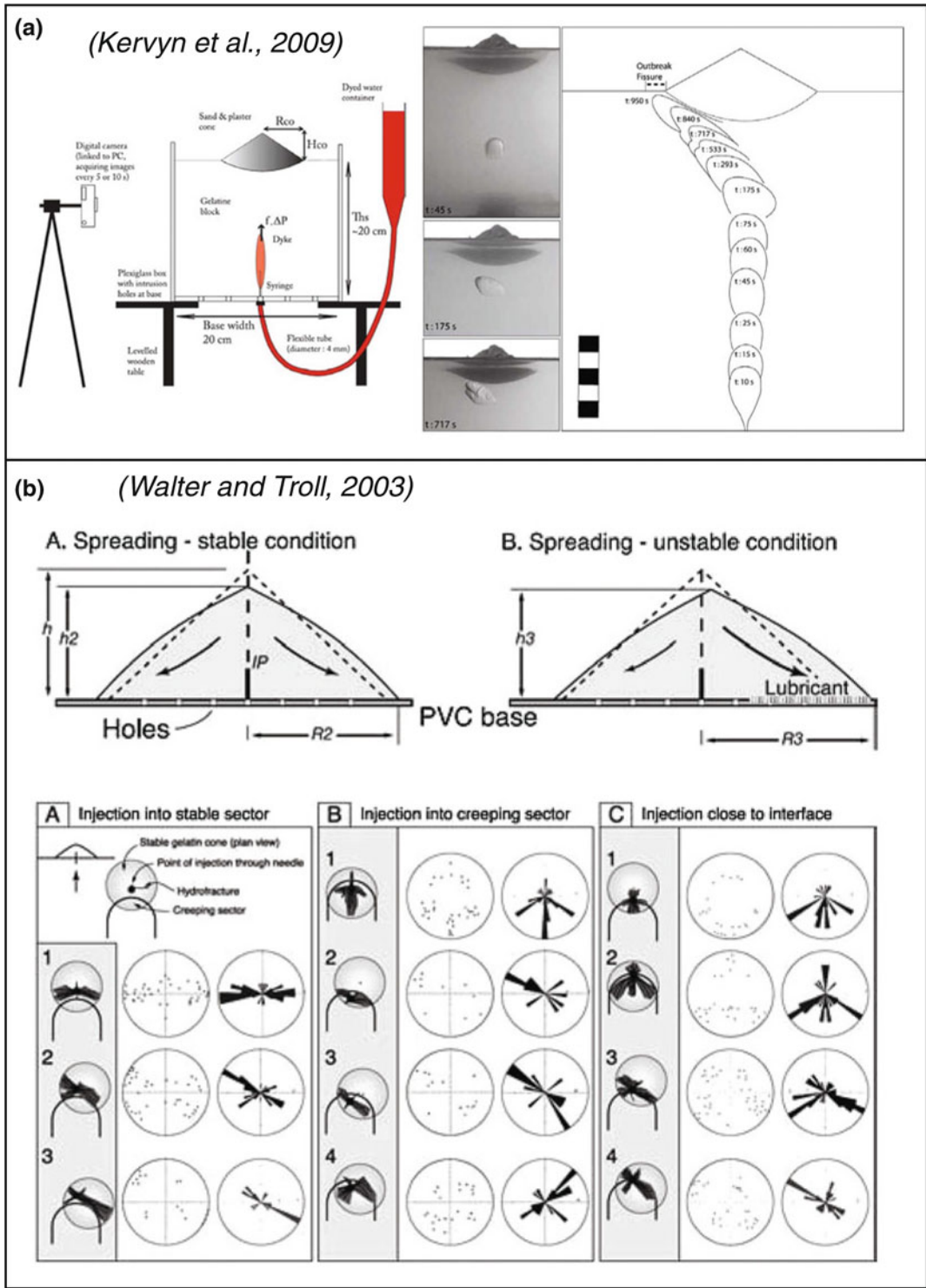
load. The *lower right* diagram shows that the critical distance x_c in the experiments (*black discs*) is a linear function of the ratio between the pressure induced by the load (P_{load}) and the excess pressure in the dyke (ΔP_m). Muller et al. (2001) also performed numerical modelling, and obtained different behaviours of x_c as a function of $P_{load}/\Delta P_m$ (see results in *lower right* graph.)

with the ratio of average pressure at the base of the load (i.e. the height of the edifice) to the dyke driving pressure: larger loads attract more distanced dykes. The particular trajectories taken by attracted dykes are also affected by this ratio. This attraction of dykes rising through the crust by volcanic loads may help to explain the absence of volcanism between large volcanoes.

Laboratory experiments of dyke emplacement also show that topography-derived stresses can greatly control the orientation of dykes *within* volcanic edifices (Fiske and Jackson 1972). Gelatine experiments by Hyndman and Alt (1987), McGuire and Pullen (1989), Delcamp et al. (2012b), for instance, show that dykes orientate along the long axis of an elongated volcanic edifice, albeit with some divergence at the edifice periphery (Tibaldi et al. 2014). In addition, the experiments of McGuire and Pullen (1989) show that: (i) shallow dykes below edifices stop propagating upward, and start

propagating laterally to give rise to a lateral fissure eruption, and (ii) the behaviours of intruding dykes differ according to their initial position with respect to the summit of the edifice. Kervyn et al. (2009) show a similar deflection of the dyke away from the summit of an edifice standing on a brittle substratum of controlled thickness (Fig. 11a); deflection depends on the thickness of the substratum, on the edifice slope, and on the overpressure within the dyke. These experimental results are consistent with lateral dyke propagation observed in many volcanoes, and corroborate well the theoretical analyses of Pinel and Jaupart (2000, 2004).

Rapidly constructed topographic loads like volcanoes can be unstable and sectors of an edifice can tend toward collapse. Walter and Troll (2003) used gelatine experiments to investigate the effect of a volcano sector instability on the formation of dyke swarms (Fig. 11b). At the base of a gelatine edifice, they simulated a



◀ **Fig. 11** **a** Experimental study of Kervyn et al. (2009), in which an water-filled or an air-filled dyke was injected into a gelatine model, at the surface of which was a volcanic edifice made of sand. *Left* Drawing of experimental setup. *Centre* Time series photographs of a characteristic experiment of dyke rising under a volcanic edifice. *Right* Evolution of the dyke outline illustrating that the dyke rise velocity decreases when approaching the cone base. **b** Experimental study of Walter and Troll (2003), in which dyed water was injected into a volcanic edifice made of gelatine. *Top* Geometry of experimental cones in stable situation (A) and unstable situation (B). Due to gravity, the cones spread outward, partially sliding on a basal lubricant. In the unstable situation, only one flank was lubricated. *IP* injection point (10 mm above

base), basal radii $R_3 > R_2 > R_1$; cone height $h > h_2 > h_3$. Through small holes drilled in the basal plate, injection was possible at various positions. *Bottom* Summarized arrangement of hydro-fractures propagating in locally destabilized edifices relative to injection point and eccentricity of a creeping sector. *A* Injection into stable sector. *B* Injection into creeping sector. *C* Injection close to the interface stable/unstable sector. Stereoplots illustrate the statistic orientation of fractures: each black dot in pole plots refers to the distal locality of an experimental fracture, measured in azimuth and distance from the point of injection. In frequency–azimuth (rose) diagrams (polar lines, sector size = 8°), the length of each rose sector is proportional to the frequency of orientation that lies within that sector (Walter and Troll 2003)

localised décollement, above which the sector of the edifice was considered unstable. They showed that: (i) injection into the stable sector of the edifice results in two main radial dyke swarms, (ii) injection into the unstable sector of the edifice results in swarms reflecting the extent of the unstable sector, and (iii) injection close to the transition between the stable and the unstable sectors mainly produce three swarms, two of which follow the stable/unstable discontinuity. These results corroborate geological observations from volcanic centres exhibiting triaxial rift zones, such as Tenerife, Canary Islands (e.g. Delcamp et al. 2012a).

Sector instability and sliding have been linked with active intrusion or the presence of intrusive complexes at several volcanoes. Models studying the interaction between gravitational instability and intrusions have been conducted by Mathieu and van Wyk de Vries (2009), Delcamp et al. (2012b), and by Norini and Acocella (2011). Mathieu and van Wyk de Vries (2009) modelled the development of the Mull centre in Scotland, showing how large intrusions could develop dykes along gravity slides. Delcamp et al. (2012b) found that dykes would propagate out of a central intrusion into rift zones and applied their models to the distribution of inclined dykes and intrusive bodies on La Reunion Island, France. Norini and Acocella (2011) used a combination of high viscosity silicone and low viscosity oils to study the relationship between magma intrusion, gravity sliding and tectonic extension at Mt. Etna, Italy. They conclude that

the magmatic forcing and gravity effects greatly outweigh the regional tectonics in controlling intrusion and instability on Mt. Etna.

4.1.6 Interaction of Coevally Propagating Dykes

Laboratory experiments enable the emplacement of several coeval dykes to see how they interact. It is expected that the stress field induced by propagation of one dyke would influence the propagation of another (Delaney and Pollard 1981). Takada (1994a, b) carried out gelatine experiments, in which he injected two coeval dykes. The experiments show that: (i) two propagating liquid-filled cracks are likely to coalesce; (ii) a propagating liquid-filled crack is unlikely to coalesce with a nearby solidified crack; (iii) large regional differential stresses impede the coalescence of magma-filled cracks, and control the formation of parallel dykes; (iv) a large magma supply rate can produce a complete stress field rearrangement that overcomes the regional stress field, leading to the formation of radial dykes, as observed in many exhumed volcano plumbing systems (Odé 1957; Nakamura 1977).

In other gelatine experiments, Ito and Martel (2002) tested the effect of the critical dyke spacing x_c on dyke interaction: if the distance x between the dykes is smaller than x_c , the dykes coalesce, whereas if $x > x_c$, the dykes do not coalesce (Fig. 12). Also, increasing the regional differential stress reduces the value of x_c . The experiments show that when regional differential stresses are small, x_c scales with only a few times

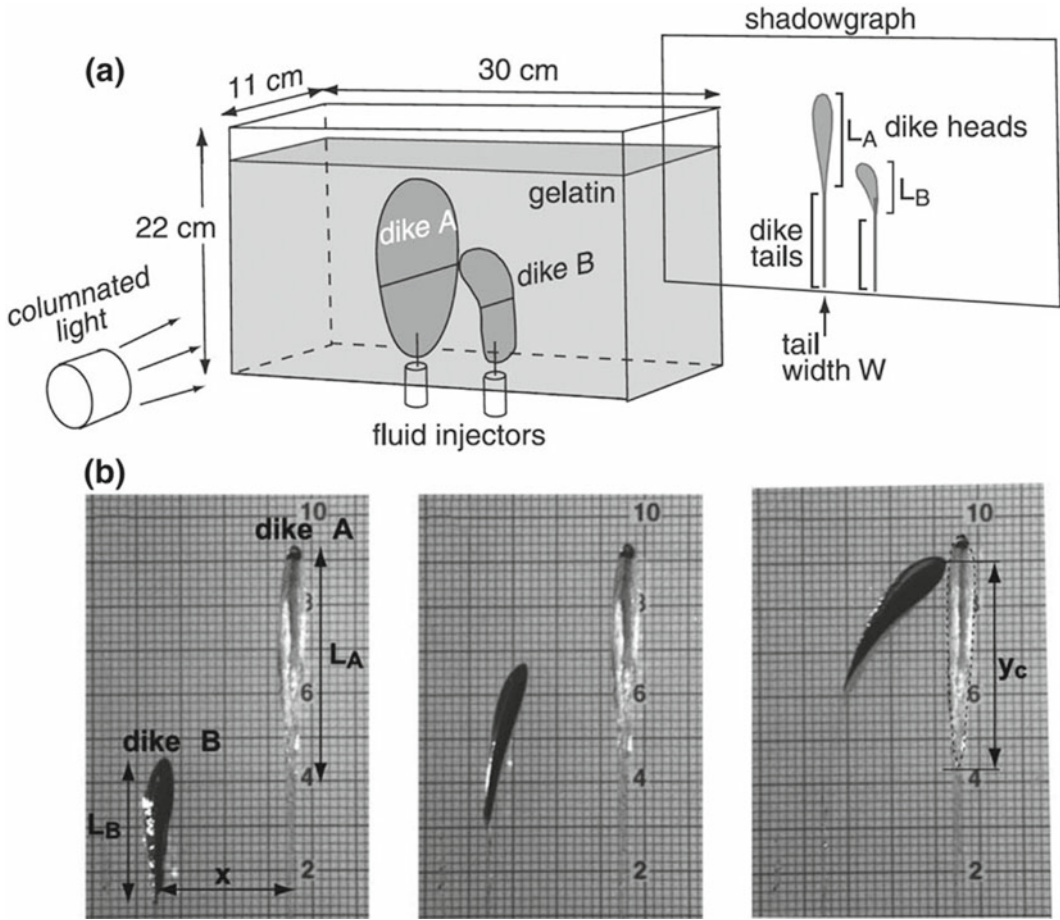


Fig. 12 a Schematic drawing of the experimental setup of Ito and Martel (2002) for studying dyke interactions. b Time series of photographs of a characteristic

experiment illustrating the interaction and coalescence of two propagating parallel dykes

the dyke height, i.e. dyke interaction can potentially focus magma transport over large vertical distances. Such a process can help explain the critical distance observed between volcanoes at the Earth’s surface, even though these volcanoes are fed from broad melting zones in the mantle.

4.1.7 Inelastic Processes Associated with Dyke Propagation

With gelatine experiments, one assumes that the model host rock behaves as a nearly purely elastic solid, and that dykes propagate according to the Linear Elastic Fracture Mechanics (LEFM) theory. Nevertheless, field observations (Mathieu et al. 2008; Kavanagh and Sparks 2011; Daniels

et al. 2012) suggest that host rock behaviour during dyke emplacement is substantially inelastic. Such inelastic processes can be addressed in laboratory models made of cohesive granular materials.

The experiments of Mathieu et al. (2008) and Kervyn et al. (2009), which use ignimbrite powder and Golden Syrup, show qualitatively that shear bands form at the tips of propagating dykes, leading to the splitting of the dyke tips to form V-shaped (cup-shaped) intrusions. Such dyke tip splitting has also been observed in the 3D experiments of Galland et al. (2009) and Galland (2012), which used silica flour and vegetable oil. These results suggest that dykes may propagate as viscous indenters, where the

viscous material penetrates the cohesive granular material like a chisel pushed into plaster or a spade pushed into the ground (Donnadieu and Merle 1998), rather than as a simple mode I fracture, particularly if the host rock cohesion is relatively low. Quantitative 2D experimental results of Abdelmalak et al. (2012) (Fig. 13a) further show that: (i) small-scale reverse shear bands form at the vicinity of the propagating dyke tip, and (ii) the model surface lifts up due to dyke emplacement (Fig. 13b). These two observations are incompatible with the LEFM theory, and the results suggest that models made of cohesive granular materials may provide important insights into the complex mechanics governing dyke emplacement in low strength rock masses. Given that these models have been designed only recently, they offer broad possibilities for future experimental studies of dyke emplacement.

4.1.8 Effects of Cooling on Dyke Propagation

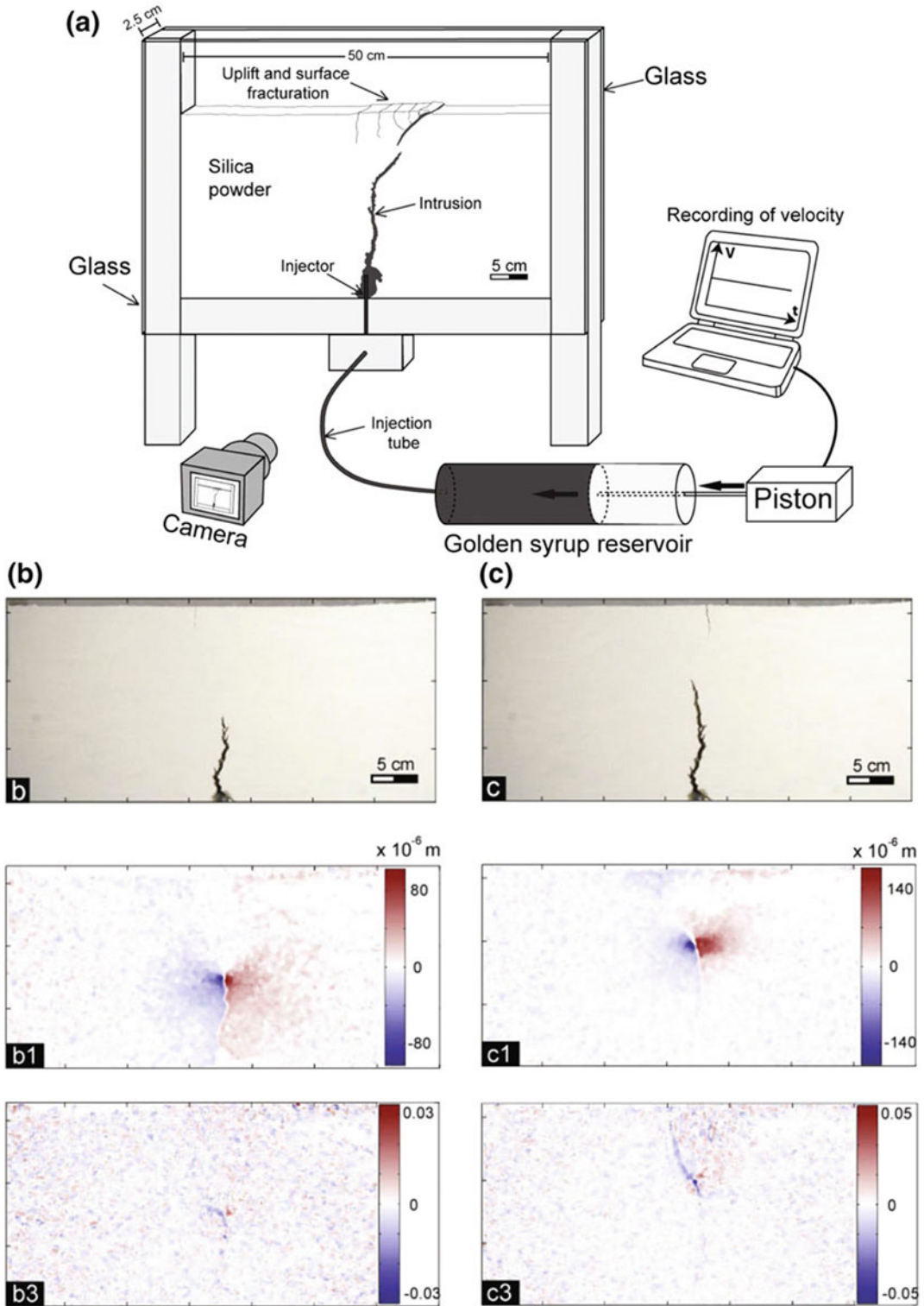
A critical aspect of magma intrusion is the effect of cooling, which is usually neglected in laboratory experiments (e.g., Galland et al. 2009), because it is technically challenging to control. Taisne and Tait (2011) performed experiments in which they injected a wax into a model made of gelatine; the gelatine temperature was lower than the solidus temperature of the wax. The temperature difference between the injected wax and the host gelatine was varied, as was the balance between the heat injected into the system and the heat diffusing from the wax into the gelatine host. Three main behaviours were observed: (i) when the injected wax temperature was large compared to its solidus temperature, and when the heat influx was large compared to the diffusive heat loss, the dyke propagated continuously, like a non-solidifying dyke; (ii) when the injected wax temperature was close to its solidus temperature, and when the heat influx was small compared to the diffusive heat loss, the dyke did not propagate; (iii) when the wax temperature and the heat fluxes lay between the above end members, the dyke propagates in a stepwise, intermittent,

manner due to local clogging of the dyke tip. This intermittent behaviour may help explain the occurrence of seismic bursts recorded during dyke emplacement in volcanoes (Hayashi and Morita 2003; White et al. 2011) as a consequence of the thermo-mechanical interaction of the dyke and its host rocks.

4.2 Cone Sheet Emplacement

Cone sheets are prominent features in many volcanoes on Earth. In eroded volcanoes, these sheet-like intrusions strike concentrically about and dip in toward the volcano centre, and they commonly occur as dense swarms. Like dykes, they are typically discordant to any mechanical stratigraphy in their host rocks. A classic example of a cone sheet swarm is found in the Ardnamurchan intrusive complex, NW Scotland (Richey et al. 1930; O'Driscoll et al. 2006; Burchardt et al. 2013). Other good examples are found in the Canary Islands (Ancochea et al. 2003), Galápagos Islands (Chadwick and Howard 1991; Chadwick and Dieterich 1995), and Iceland (e.g. Schirnack et al. 1999; Walker 1999; Klausen 2004; Burchardt et al. 2011).

Despite the prominence of cone sheets, little is known about their much-debated emplacement mechanisms (e.g. Phillips 1974; Klausen 2004; Burchardt et al. 2013). One reason is that laboratory cone sheets rarely occur in gelatine experiments, which mostly simulate either dykes (Takada 1990; Lister and Kerr 1991; Dahm 2000; Rivalta and Dahm 2006; Le Corvec et al. 2013) or sills (Kavanagh et al. 2006; Menand 2008). To our knowledge, the only cone sheet-like intrusions recorded in gelatine models developed from a pressurised cavity simulating a magma reservoir (McLeod and Tait 1999) (Fig. 8a; see Sect. 4.1). Theoretical studies suggest that shear failure, absent in gelatine experiments, might be important for cone sheet formation (Phillips 1974). Indeed, experiments using cohesive granular materials, which undergo shear failure, have produced dykes and/or cone sheets (Mathieu et al. 2008; Galland et al. 2009) (Fig. 14).



◀ **Fig. 13 a** Experimental setup of Abdelmalak et al. (2012) designed to study the small-scale deformation induced by dyke emplacement. The experiments are 2D, such that the propagation of the dyke was monitored from the side of the box with digital camera. The resulting images were processed using Digital Image Correlation algorithm to compute the displacement field associated with dyke emplacement. **b** Photograph (*top*), horizontal displacement field (*middle*) and strain field (*bottom*) of an

experimental dyke during experiment. The strain field highlights small-scale shear bands rooted at the tip of the dyke. **c** Photograph (*top*), horizontal displacement field (*middle*) and strain field (*bottom*) of an experimental dyke during the same experiment than in **b**, but later. The strain field showed that substantial shear bands connected the dyke tip to the model surface. These experimental results suggest that dykes propagate as a viscous indenter, not as linear elastic hydraulic fracture

Galland et al. (2014a) recently identified two dimensionless numbers that control the formation of either cone sheets or dykes in such cohesive granular materials (Fig. 14a). The first number Π_1 is a geometric ratio between the depth of emplacement and the width of the magmatic source. The second number Π_2 is a dynamic ratio between the viscous stresses within the flowing magma and the strength (cohesion) of the host rock. Plotted in a dimensionless phase diagram with Π_1 and Π_2 as the vertical and horizontal axes, respectively, the experimental data define dyke and cone sheet regimes in a phase diagram, separated by a transition that fits a power law (Fig. 14a). This result shows that cone sheets preferentially form (i) from shallow magma feeders (small value of Π_1), in agreement with the results of Mathieu et al. (2008), and (ii) when magma is viscous, or when the injection velocity is high, and/or when the host rock is weak (large value of Π_2).

This experimental phase diagram (Fig. 14a) also explains why gelatine experiments rarely simulate cone sheets: the large cohesion of the gelatine generally leads to small values of Π_2 , i.e. in the dyke field of the phase diagram. In the exceptional gelatine experiments of McLeod and Tait (1999), the cavity from which cone sheets formed was large and shallow (Fig. 8a), corresponding to small values of Π_1 , i.e. to the cone sheet field of the phase diagram.

These 3D experiments with cohesive granular materials did not allow for imaging the small-scale processes controlling the formation of dykes versus cone sheets, given that processes at work are buried and thus invisible. Such a limitation is overcome by using ‘2D’ experiments, whereby the intrusion propagates upward against a glass plate (Fig. 14b) (Mathieu et al.

2008; Abdelmalak et al. 2012; Mourgues et al. 2012). This allows the growth of sheet intrusions to be monitored directly. Boundary effects from the glass plate are found to be minimal. Abdelmalak et al. (2012) and Mourgues et al. (2012) applied Digital Image Correlation (DIC) to photographs of their experiments to quantitatively map the small-scale 2D deformation field induced by intrusion (Fig. 13). In good agreement with the conclusions of Mathieu et al. (2008) and Kervyn et al. (2009) (Fig. 14b), their results show that dykes propagating towards the model surface can trigger the formation of shear fractures, which control the formation of V-shaped sheet intrusions. This supports the hypothesis of Phillips (1974) that cone sheet emplacement is mainly controlled by shear failure in the host rocks.

4.3 Sill Formation

Igneous sills are another form of sheet intrusion that is very common in the Earth. Unlike dykes or cone sheets, to which they are nonetheless closely related, sills are typically concordant with the mechanical stratigraphy in their host rocks. Igneous sills represent substantial volumes of volcanically-influenced sedimentary basins, good examples being the Karoo Basin, South Africa (Chevallier and Woodford 1999; Svensen et al. 2012), and the North Atlantic volcanic margins (e.g. Vøring and Møre Basins, off Norway; Berndt et al. 2000; Planke et al. 2005). Their emplacement likely triggered the release of gigantic volumes of greenhouse and poisonous gases in the atmosphere, leading to mass extinctions (Svensen et al. 2004, 2007). In addition, sills have a large impact on petroleum systems as (i) they provide heat that enhances the

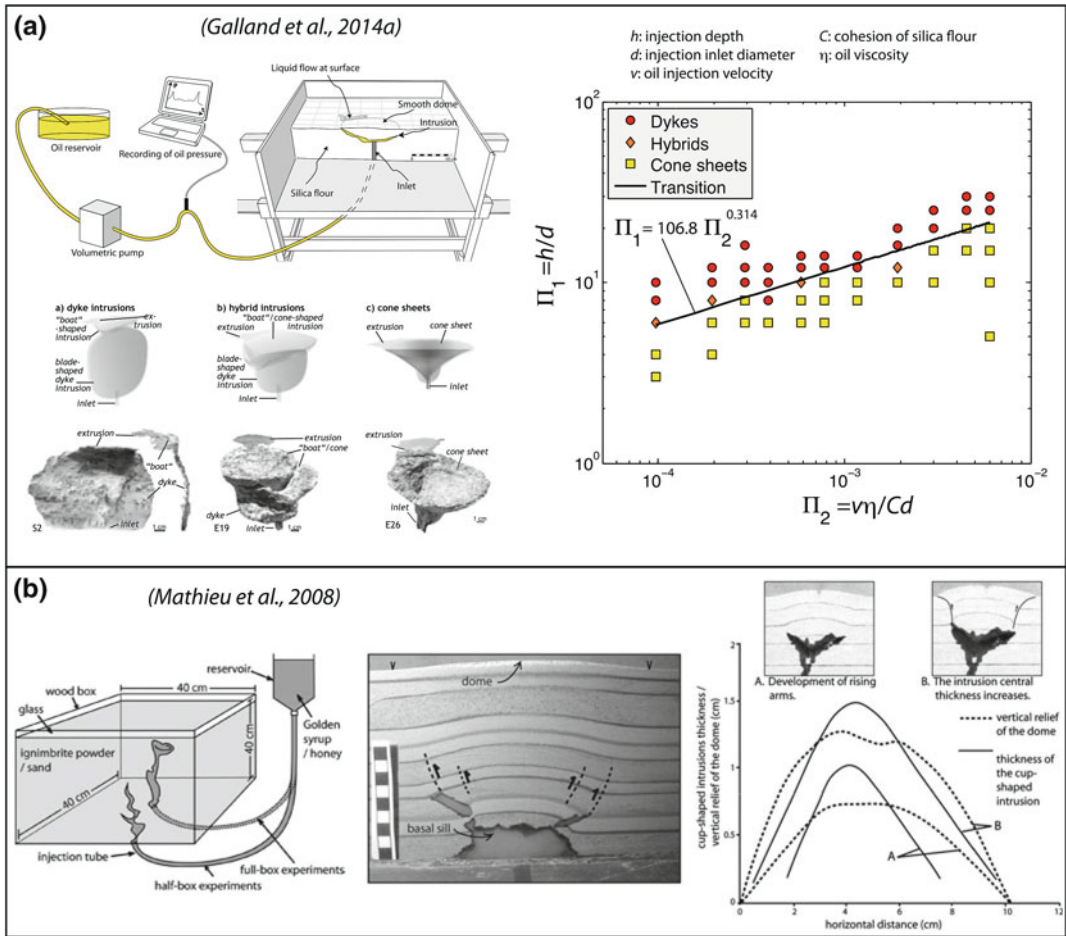


Fig. 14 Characteristic experimental studies of cone sheet emplacement. **a** Experimental setup (upper left), typical modelled intrusions (lower left) and experimental phase diagram (right) of the experimental study of Galland et al. (2014a), which used fine-grained silica flour and molten vegetable oil. The apparatus allows flow rate-controlled injection of the oil, and pressure measurements. Varying systematically the depth of injection (h), the diameter of the injection inlet (d) and the injection fluid velocity (v), the models produced dykes, cone sheets or hybrid intrusions. Plotting the experiments in a phase diagram with $\Pi_1 = h/d$ and $\Pi_2 = v\eta/Cd$ as y- and x-axes, respectively, the dykes and cone sheets group in two fields, separated by a transition that fits a power law. Notice that the hybrid intrusions always plot between the

dyke and cone sheet fields. Here, η and C are the oil viscosity and flour cohesion, respectively. **b** Experimental setup (left), cross section of a typical model (centre) and measurements (right) of the experimental study of Mathieu et al. (2008) using ignimbrite powder and Golden Syrup. This experimental apparatus allows pressure-controlled injection of Golden Syrup. The cross section exhibits the main features obtained in the models of Mathieu et al. (2008), which are V-shaped conduits connected to shear bands, these later being at the edges of a dome structure in the intrusion's overburden. The graph on the right exhibits comparison between the along-strike thickness of the V-shaped intrusions and the amplitude of the overlying dome, showing a non-simple relationship between them

maturation of organic matter in surrounding rocks (e.g. Aarnes et al. 2011a, b), (ii) they generate dome structures (also called forced folds) in their overburden strata (e.g. Trude et al. 2003; Hansen and Cartwright 2006b; Jackson

et al. 2013; van Wyk de Vries et al. 2014, Magee et al. 2014) that can be hydrocarbon traps (Polteau et al. 2008b), and (iii) cooling and solidification of the magma triggers intense fracturing of the solidified sills, which can be excellent

hydrocarbon reservoirs (Rossello et al. 2002; Rodriguez Monreal et al. 2009; Witte et al. 2012).

4.3.1 Formation of Sills from Vertically-Propagating Dykes

For many decades, it had been assumed that sills were emplaced from dykes that stalled in their ascent and intruded along a level of neutral buoyancy (LNB) (e.g. Francis 1982; Lister and Kerr 1991). However, no laboratory models have managed to simulate sill emplacement as fed from a dyke along a LNB; instead, a feeder dyke reaching a LNB stops propagating upwards and starts propagating laterally with dip unchanged (Lister and Kerr 1991). All laboratory experiments that simulated the emplacement of sills required the presence of mechanical layering of the host, i.e. layers of different strengths, such as is commonly observed in sedimentary basins and volcanic sequences.

In pioneering gelatine experiments by Pollard and Johnson (1973) and Hyndman and Alt (1987), sills formed from a dyke either (i) along a weak interface between two gelatine layers of similar strength (Pollard and Johnson 1973), or (ii) at the base of a gelatine layer that is stronger than the underlying layer (Hyndman and Alt 1987). Kavanagh et al. (2006) and Menand (2008) later conducted more quantitative experiments with water injected at constant pressure (Fig. 15a). These authors systematically varied: (i) the input pressure scaled by the resisting pressure (i.e. the pressure required to propagate a crack of given size) and (ii) the rigidity contrast between upper and lower gelatine layers.

All experiments started with a vertical dyke propagating upward to the interface between the two gelatine layers. Several behaviours were then observed (Fig. 15a).

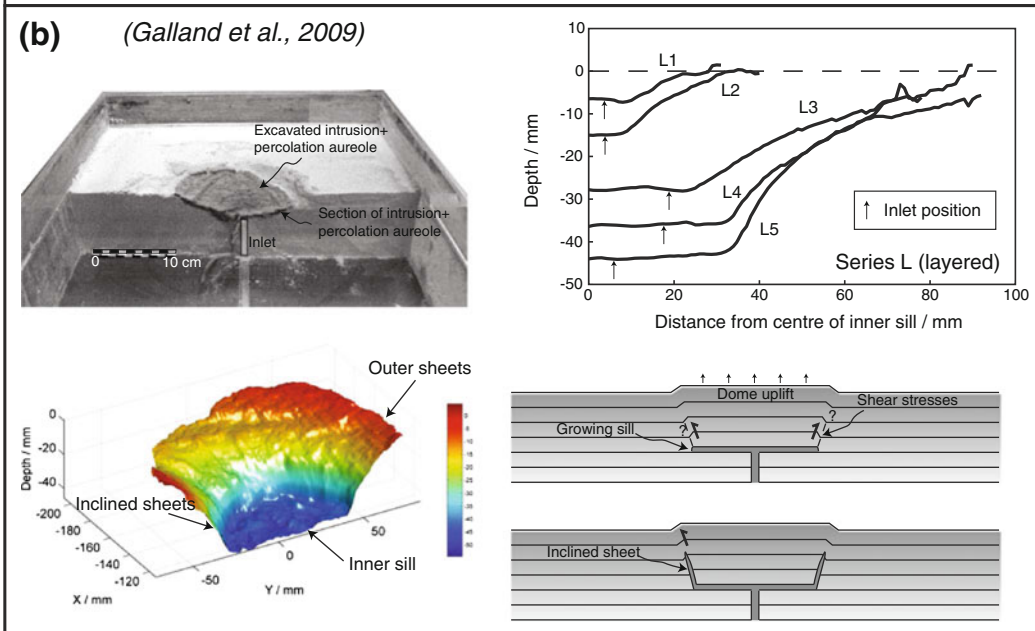
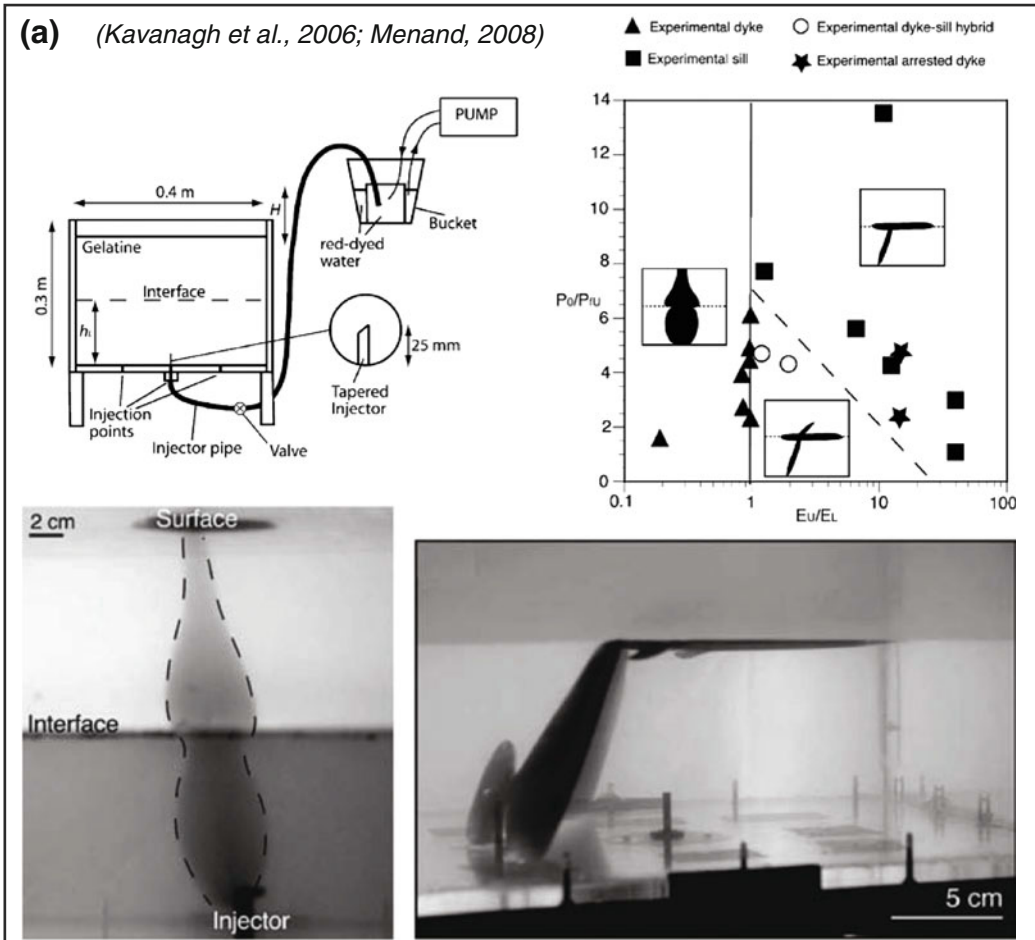
With a more rigid lower layer, the dyke always simply propagated through the upper layer and never turned into a sill. With a more rigid upper layer and a strong interface, the dyke was arrested. With a more rigid upper layer and a weak interface, two varieties of sills were obtained. First, with a high rigidity contrast

between the layers and with a high driving pressure, the dyke completely turned into a sill. Second, with a low rigidity contrast between the layers and with a low driving pressure, a hybrid intrusion formed that comprised a dyke in the upper layer and a sill along the interface. These experiments therefore can explain the transition of dykes into sills at layers in the host rock as a consequence of particular combinations of rigidity or strength contrasts between layers, of the strength of the interface between the layers, and of the driving pressure in the magma.

4.3.2 Formation of Saucer-Shaped Sills

Seismic data (Thomson and Hutton 2004; Planke et al. 2005; Hansen and Cartwright 2006a; Thomson 2007; Hansen et al. 2008) and geological observations (Chevallier and Woodford 1999; Polteau et al. 2008a, b), show that from their initiation point at a flat layer interface, sills can develop segments that cut up at an angle through the layering and then flatten again. This gives the sheet-intrusion a peculiar saucer-like shape. A correlation between their diameters and depths led Malthe-Sørenssen et al. (2004) to suggest that saucer shaped sills result from a mechanical interaction with the deformable free surface during sill growth.

Galland et al. (2009) and Galland (2012) tested this hypothesis by using models made of silica flour and vegetable oil (Fig. 15b). The oil was injected directly along a flexible net that simulated a horizontal sedimentary layer. The oil initially formed a sub-circular sill along the layer. The model surface subtly lifted up above the sill, forming a smooth sub-circular dome, or forced fold (Hansen and Cartwright 2006b; Jackson et al. 2013; Magee et al. 2014). Finally, the oil erupted, always at the edge of the dome. After solidification, a saucer-shaped intrusion was excavated (Fig. 15b), the flat inner sill being under the dome centre, and the inclined sheets being under the dome edges. Galland et al. (2009) showed that the diameter of the inner sill correlated well with the depth of injection, i.e. the transition from horizontal to inclined intrusion is depth-controlled (Fig. 15b). In good



◀ **Fig. 15 a** Experimental study of Kavanagh et al. (2006) and Menand (2008) on sill emplacement in layered media, here made of gelatine. Setup for pressure-controlled intrusion (*upper left*), characteristic experimental dyke (*lower left*) and dyke-fed sill (*lower right*), and experimental phase diagram showing the parameters controlling the formation of dykes, sills, hybrid dyke-sills, or arrested dykes in layered media (*upper right*). Here E_U and E_L denote the Young modulus of the upper and lower layers, respectively, and P_0 and P_{fU} denote the water overpressure and the fracture pressure (i.e. the strength) of the

upper layer. **b** Experimental study of Galland et al. (2009) and Galland (2012) on the emplacement of saucer-shaped sills, using silica flour and vegetable oil. The experimental setup is displayed in Fig. 14. Experimental box exhibiting excavated solidified intrusion (*upper left*), 3D model of an excavated experimental saucer-shaped sill (*lower left*), averaged profiles of experimental saucer-shaped sills emplaced at various depths (*upper right*), and conceptual model of saucer-shaped sill emplacement (*lower left*). The averaged profiles show that saucer-shaped sills are larger when they are deeper

agreement with the numerical results of Malthé-Sørensen et al. (2004) and the theoretical analysis of Goultly and Schofield (2008) and Galland and Scheibert (2013), these experiment results demonstrate how shallow intrusions dynamically interact with the free surface. As a shallow sill grows laterally, it deforms its overburden by doming. When the sill reaches a critical diameter, shear stresses at the edges of the dome deflect the crack tip and so initiate an inclined sheet (Fig. 15b). This scenario illustrates that the free surface exerts a positive mechanical feedback on a growing intrusion.

While some saucer-shaped sills are perfectly circular, others are markedly elliptical (Chevalier and Woodford 1999). Galerne et al. (2011) tested the hypothesis that elliptical saucer-shaped sills result from the planar geometry of a feeder dyke. They performed experiments with either pipe-like or planar injection inlets, and found that the former leads to sub-circular sills, whereas the latter leads to elliptical sills. The long axis of the elliptical sills is superimposed on the trace of the planar feeder dyke, in very good agreement with geological observations (Galerie et al. 2011). The 3-dimensional form of saucer-shaped sills therefore reflects the geometry of their feeders.

4.3.3 Effects of Cooling on Sill Emplacement

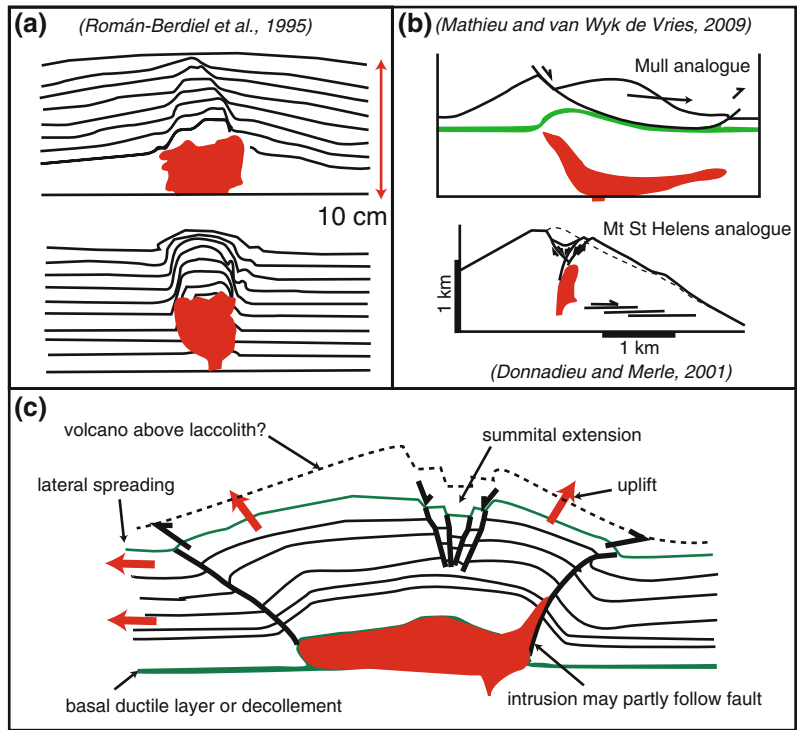
As for dykes, cooling effects are neglected in most past studies of sill emplacement. However, Chanceaux and Menand (2014) recently adopted Taisne and Tait's (2011) approach (see #4.1.8 above) to investigate thermal controls on sill initiation. In these experiments, a molten vegetable oil was injected at a controlled temperature

into a gelatine host made of two layers. The experiments highlight various behaviours of the intruding oil according to the dimensionless temperature, $\theta = (T_s - T_g) / (T_i - T_g)$, where T_s is the solidification temperature of the intruding fluid, T_g is the temperature of the host and T_i is the temperature of the injected fluid. When both θ and injection flux are low, solidification effects are extreme and so intrusion is inhibited. When θ and injection flux are high, solidification effects are limited and dykes pass through the interface between the two layers of gelatine. For intermediate values of θ and injection flux, either dykes terminate at the interface (high solidification effect) or else sills form along it (moderate solidification effect).

4.4 Laccoliths, Stocks and Cryptodomes

Laccoliths are igneous intrusions exhibiting a flat lower margin and a domed, convex upper margin. The Henry Mountains of Utah are the classic type locality (Gilbert 1877; Johnson and Pollard 1973; Pollard and Johnson 1973; Jackson and Pollard 1990; de Saint-Blanquat et al. 2006; Morgan et al. 2008), where multiple stacks of laccoliths have developed in individual magmatic centres. Laccoliths in Elba, Tuscany and in Central Europe are other good examples (Rocchi et al. 2002; Breitreuz and Mock 2004; Westerman et al. 2004). In most cases, laccoliths are intrusions emplaced at shallow depth into layered sedimentary rocks. Laccoliths tend to be thick in relation to their width, compared with sills and saucer-, or cup-shaped intrusions (Corry 1988; Bungler and Cruden 2011). The host rock around a laccolith is typically

Fig. 16 **a** Analogue model cross sections of a laccolith from Román-Berdiel et al. (1995). **b** Laccolith-like intrusion schematic cross-section from Mathieu and van Wyk de Vries (2009) and steep cryptodome intrusion modelled by Donnadieu and Merle (2001) for Mt. St. Helens. **c** Cross-section of the generalised features of a laccolith intrusion developed from analogue models studies, showing the uplift caused by the intrusion and possible lateral spreading



domed, and often at least one, usually steep, side of the laccolith exhibits faulting that also accommodates uplift of the host rock (Fig. 16).

Stocks are steep sided, vertically-elongated intrusions that have roughly equal horizontal dimensions and that truncate any mechanical stratigraphy in the host rock. The term cryptodome refers to a viscous laccolithic or stock-like intrusion that remains hidden below the updomed overburden. The development of cryptodomes may culminate in eruption of typically highly viscous silicic lava, either effusively as in the Showa-Shinzan uplift and dome at Usu Volcano, Japan (Corry 1988; Breikreuz and Mock 2004) or explosively as in the 1980 eruption of Mt. St. Helens, U.S.A (Lipman et al. 1981).

4.4.1 General Development of Laccolith Emplacement and Controls from Host Rock Layering

The first systematic experimental investigation of laccolith emplacement was carried out by Dixon and Simpson (1987). Their experiments ran in a

centrifuge; the model magma was silicone putty, which was injected at the base of elastoplastic parafin layers. The experiments allowed for reconstructing the time sequence of laccolith emplacement: (i) a sill forms between two layers; (ii) the sill spreads and thickens as the overburden bends upward; (iii) the overburden kinks above the laccolith tip and eventually fails. Dixon and Simpson (1987) showed that the bending phase is enhanced by thicker and stronger overburden, as expected by theory (e.g. Pollard and Johnson 1973; Galland and Scheibert 2013).

The experiments of Román-Berdiel et al. (1995), who simulated the emplacement of a laccolith along a ductile layer below a brittle overburden, produced similar results (Fig. 16a). Using silicone for both magma and the ductile layer, and sand for the brittle overburden, they found that: (i) a critical thickness of ductile layer for laccolith formation was reduced with increasing overburden thickness; (ii) laccolith height to width ratio decreased with increasing thickness of overburden (i.e. deeper laccoliths are flatter); (iii) and the laccolith diameter was also linked to overburden

thickness. They also noted that asymmetric laccoliths could be linked to synchronous gravitational sliding along the ductile layer. Intrusion of silicone in the absence of a ductile layer produced piercing, stock-like intrusions, rather than laccoliths (see also Acocella et al. 2001).

4.4.2 Controls of Regional Tectonics or Gravitational Spreading on Laccolith Emplacement

Benn et al. (1998, 2000) modelled granitic intrusion within a transpressive tectonic regime by using similar materials to Román-Berdiel et al. (1995). Their models also produced laccoliths on which thrust faults nucleated to accommodate both the intrusion-related inflation and the regional-tectonic deformation. They again found that laccoliths formed at greater depths were flatter. Using different materials (cohesive silica flour and vegetable oil), Galland (2005) produced laccoliths at the interface between two brittle layers of different cohesions, without requiring a ductile layer like in the experiments of Román-Berdiel et al. (1995). The laccoliths in the above three studies all have a domed overburden that is uplifted on a shear zone that surrounds the intrusion and has a reverse slip sense. This doming leads to extension and normal faulting on the apex of the dome (Fig. 16b, c). In addition, the experiments of Galland et al. (2007a) show that compressional tectonics are likely to enhance the uplift of the laccolith's roof, and so greatly control the final thickness of laccoliths.

If the surface and overburden can move laterally to accommodate intrusion, as in a volcano flank or in gravitational spreading, then a laccolith can also easily develop. This association of intrusion with large-scale lateral deformation was studied by Merle and Vendeville (1995). They injected silicone putty into a sand pack contained between glass walls and constrained by a fixed wall on one side. The models produced extensive lateral movement and thrusting that accommodated magma emplacement far from the point of intrusion. Subsequently, Mathieu et al. (2008) and Delcamp et al. (2012b) explicitly modelled magma intrusion into spreading volcanic edifices

(Fig. 16b). In their models, a basal silicone layer below the volcanic edifice was intruded by a Golden syrup magma analogue. These models produced laccolith-like intrusion shapes, as would be predicted for these conditions by Román-Berdiel et al. (1995), and were characterised by considerable edifice and substrata deformation. These models raise the possibility that some laccoliths may propagate by lateral spreading as well as by vertical uplift.

4.4.3 Formation of Stocks or Cryptodomes

Donnadieu and Merle (1998) intruded silicone putty into sand cones, and produced cryptodomes or stocks that caused considerable surface deformation (see Fig. 22a). In these models, and in those of Román-Berdiel et al. (1995), Román-Berdiel (1999), Mathieu et al. (2008) and Galland (2005), there was no ductile stratum to intrude into and the viscosity of injected silicone was high relative to the host material strength. As a result, the intrusions formed in a viscous indenter style on reverse and normal faults that developed synchronously with intrusion into the edifice.

4.4.4 The Roles of Magma Viscosity and Host Rock Strength in the Formation of Laccoliths, Stocks and Cryptodomes

The scaled viscosity in which the analogue laccolith or stock-like intrusions have been formed is significantly higher than those of sills and saucer-shaped intrusions. Equally, in natural cases laccoliths are overwhelmingly produced with intermediate to felsic magmas. Thus, viscosity is a critical controlling factor on the type of intrusion (see Galland et al. 2014a). If the magma is of low viscosity it will tend to form a thin sill, and then it will intrude fractures climbing towards the surface to create saucers (Galland et al. 2009). If the magma is of high viscosity, it will tend to propagate less rapidly along décollements and fractures, and will tend to uplift the host rock. If this uplift predominates over lateral or included injection, a laccolith or a stock like intrusion will

develop. In addition, magma cooling at the margins may seal the edges, increasing uplift, and multiple pulses may be trapped below or within the growing intrusion (e.g. Torres del Paine Laccolith; Michel et al. 2008).

In addition to a relatively viscous magma, the general conditions for the formation of laccoliths and stock-like (cryptodome) intrusions, as established by analogue modelling, include a relatively weak host rock and a shallow emplacement depth (a few hundred metres to a few kilometres below the surface). The key condition controlling which intrusion type forms is the presence (or absence) of mechanical layering of the host rock, with laccoliths favoured by the presence of weak interfaces or ductile layers of sufficient thickness. Both intrusion types develop by roof uplift.

4.5 Caldera-Related Structures and Intrusions

Collapse calderas are enclosed volcano-related topographic depressions of >1 km diameter that have typically sharply-defined, steep walls and nearly flat bottoms (Lipman 1997) (e.g. Fig. 17). They occur in all volcanic settings on Earth and other planets and with all magma types (e.g. Crumpler et al. 1996; Geyer and Martí 2008; Hansen and Olive 2010). Both ancient geological evidence and recent observations from active volcanoes indicate that calderas form through subsidence of the roof of a sub-surface magma body, as a consequence of magma withdrawal from that body (Fouqué 1879; Verbeek 1884; Clough et al. 1909; Williams 1941; Smith and Bailey 1968; Druitt and Sparks 1984; Lipman 1984, 1997; McBirney 1990; Geshi et al. 2002; Cole et al. 2005; Michon et al. 2011). Subsidence usually occurs along a ring fault; magma may intrude this fault to form a ring dyke and may ultimately erupt from it. Caldera collapse may thus lead to the partial or complete destruction of the volcanic edifice and to a dramatic alteration of the shallow plumbing system. Moreover, post-collapse magmatic plumbing systems may become controlled by caldera-related structures.

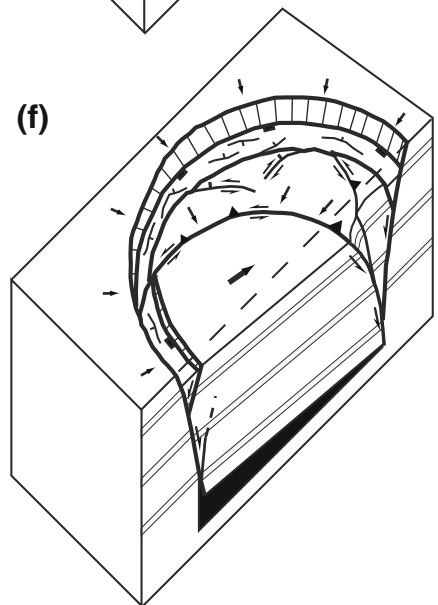
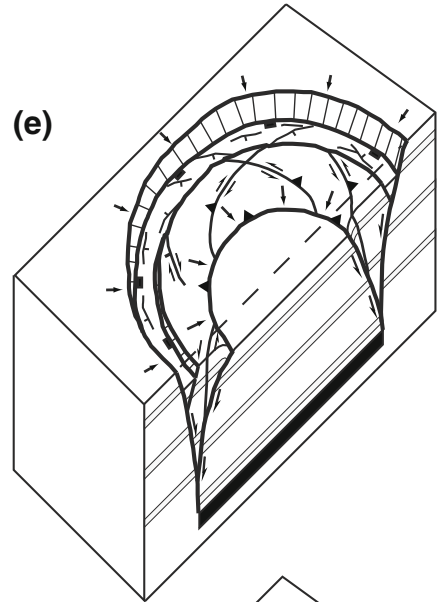
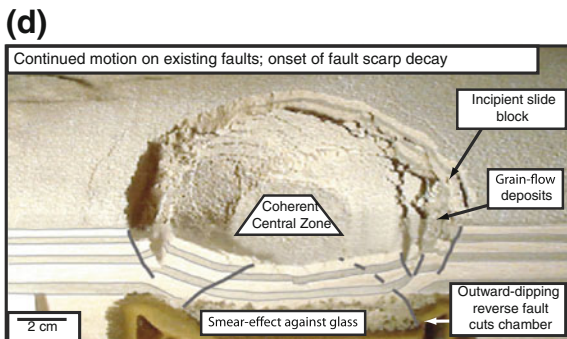
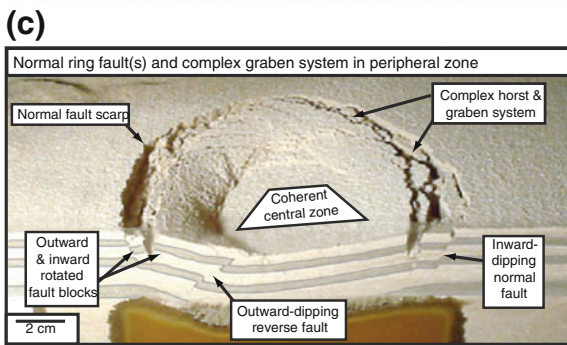
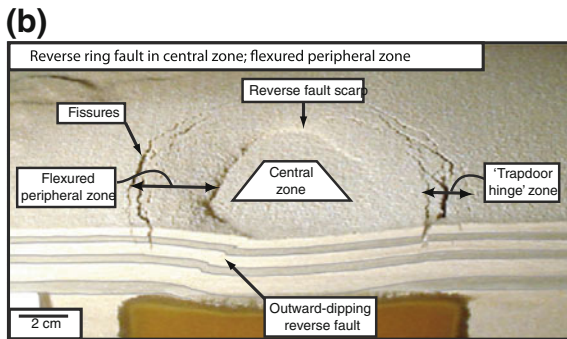
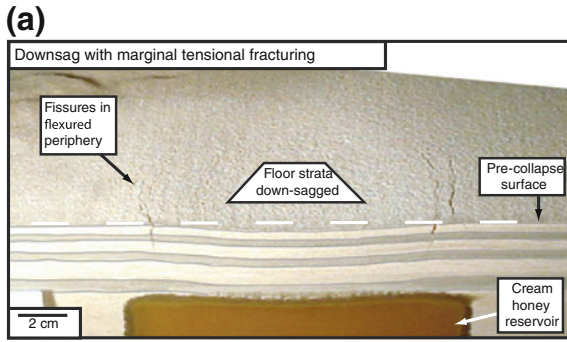
Analogue studies have mainly aimed to study the nature of caldera fault structures, which are thought to provide the primary pathways for syn-and post-collapse intrusion and eruption, and how they relate to the attributes of the underlying magma body. Their results have contributed substantially to our current understanding of the process of caldera collapse and its impact on sub-volcanic plumbing systems.

4.5.1 Generalised Geometry and Kinematics of Ring-Fault Related to Caldera Subsidence

The vast majority of past studies have primarily addressed the question of how caldera subsidence is structurally accommodated. One motivation for this is a so-called ‘space problem’ arising from many field reports of ring faults that only dip inward, toward the caldera centre (Lipman 1984, 1997; Branney 1995; Cole et al. 2005), in contrast with only a few reports of ring faults that dip outward, at least partly (Clough et al. 1909; Mori and McKee 1987). While subsidence along an outward-dipping fault represents a kinematically reasonable geometry, and one predicted from analytical solutions (Anderson 1936), subsidence accommodated only by an entirely inward-dipping fault is kinematically unfeasible.

Analogue experiments have helped resolve this ‘space problem’ by showing that subsidence into a depleted reservoir is typically accommodated by a ring-fault system that consists of outward-dipping and inward-dipping faults or fault segments (Fig. 17) (Komuro 1987; Martí et al. 1994; Branney 1995; Roche et al. 2000). The outward-dipping faults usually form further toward the central part of the reservoir roof than the inward-dipping faults. Their position and geometry means that outward-dipping faults have a poorer preservation potential, which may account for their under reportage in field studies (Branney 1995).

In terms of kinematics, the outward-dipping (reverse) faults always form first in experiment. Analytical solutions and numerical models show that this is a consequence of ‘arching’ of the



(Modified after Holohan et al., 2013)

◀ **Fig. 17 a–d** Structural evolution of a representative experimental caldera collapse. The experiment was conducted against a glass pane to gain simultaneous access to the structural development both in cross-section and in plan-view. The analogue magma reservoir is a sill-like half-cylinder of cream honey that is 10 cm in diameter and has 3.5 cm thick roof with an initially flat ceiling. This model hence has a reservoir roof thickness/diameter ratio of 0.3. The sand/gypsum cohesion is a little higher than ideal here (for illustration), and so marginal tensile fracturing is a slightly exaggerated. In addition, the sticky honey causes some smearing effects against the glass that become more pronounced with greater subsidence. However, the geometry, kinematics, and complexity of structures are overall very similar to most past analogue studies (cf. Martí et al. 1994; Branney 1995; Roche et al. 2000; Walter and Troll 2001; Kennedy et al. 2004). Note the formation of outward- and inward-dipping ring faults. Note also that in this example the sense of subsidence

‘asymmetry’ has reversed in later subsidence phases. **e** Block diagrams showing 3D fault geometry and slip-sense of experimental caldera centred (‘symmetric’) subsidence. **f** Block diagrams showing 3D fault geometry and slip-sense of experimental caldera off-centred (‘asymmetric’ or ‘trapdoor’) subsidence. In both cases, *half arrows* show fault slip sense; full arrows schematically show horizontal movements. The horizontal movements during collapse are directed radially-inward throughout the roof if collapse is centred, but may show a significant bulk translation in the roof centre if collapse is off-centred. These horizontal motions give rise to strike-slip components of fault slip-sense. Note that in the off-centred case, the strong horizontal motion toward the area of maximum subsidence favours the development of a normal ring fault (or ring-fault segment) in the ‘hinge-zone’ area on the opposite side of the roof. Modified after Holohan et al. (2013)

principal stress trajectories above the deflating reservoir (Anderson 1936; Sanford 1959; Holohan et al. 2011, 2013). The inward-dipping (normal) faults form later as the hanging-wall of the outward-dipping ring fault becomes gravitationally unstable (e.g. Martí et al. 1994; Roche et al. 2000) and/or if the subsidence becomes off-centred reservoir (trapdoor-like or ‘asymmetric’; e.g. Holohan et al. 2011, 2013) (Fig. 17c). Slip sense on these faults may not be entirely dip-slip (Holohan et al. 2013) (Fig. 17e–f). As subsidence progresses, retreat of the ring fault scarps widens the model caldera diameter and forms a funnel-shaped caldera margin containing topographic embayments—as in nature (Branney 1995; Lipman 1997; Geshi et al. 2012).

4.5.2 Effects of Initial Geometric Parameters on Collapse

Two key geometric parameters in the structural evolution of collapse are: (i) the *ratio of reservoir roof thickness to roof diameter (T/D)* in cross-section (Roche et al. 2000; Kennedy et al. 2004; Geyer et al. 2006) and (ii) the *ratio of roof long axis to roof short axis (A/B)* in plan-view (Roche et al. 2000; Holohan et al. 2008a).

T/D ratio affects the structural style of roof subsidence (Fig. 18). At very low T/D ratios (<0.3), sagging of the roof, and not just ring faulting, plays an important role in accommodating subsidence (Roche et al. 2000; Kennedy

et al. 2004; Holohan et al. 2013) (Fig. 18a). As T/D increases, sagging diminishes. At intermediate T/D ratios ($0.3 < T/D < 1.0$), the roof typically subsides along one main outward-dipping fault and one main inward-dipping fault. At high T/D (>1), the roof subsides via a complex system of mainly outward-dipping, but also locally inward-dipping, fractures (Fig. 18b, c). These fractures form in a sequence that migrates upward from the reservoir to the surface (Burchardt and Walter 2010). A sub-surface column of multiple fault blocks hence develops; the complexity of this column increases with increasing T/D ratio (Roche et al. 2000). Once deformation reaches the surface, the usual pattern of central outward-dipping faults and peripheral inward-dipping faults is established there (Roche et al. 2000; Burchardt and Walter 2010). This upward migration of faulting in experiments with high T/D ratios is remarkably similar to an apparent upward migration of seismicity recorded prior to the collapse of Miyakejima caldera, Japan, in 2000 (Geshi et al. 2002; Burchardt and Walter 2010; Ruch et al. 2012).

T/D ratio also affects the percentage of reservoir depletion required to develop collapse. For a given reservoir shape and size, higher T/D necessitates greater reservoir depletion to cause the onset of collapse and to attain each stage in the structural evolution thereafter (Geyer et al. 2006). These findings are similar to those of analytical

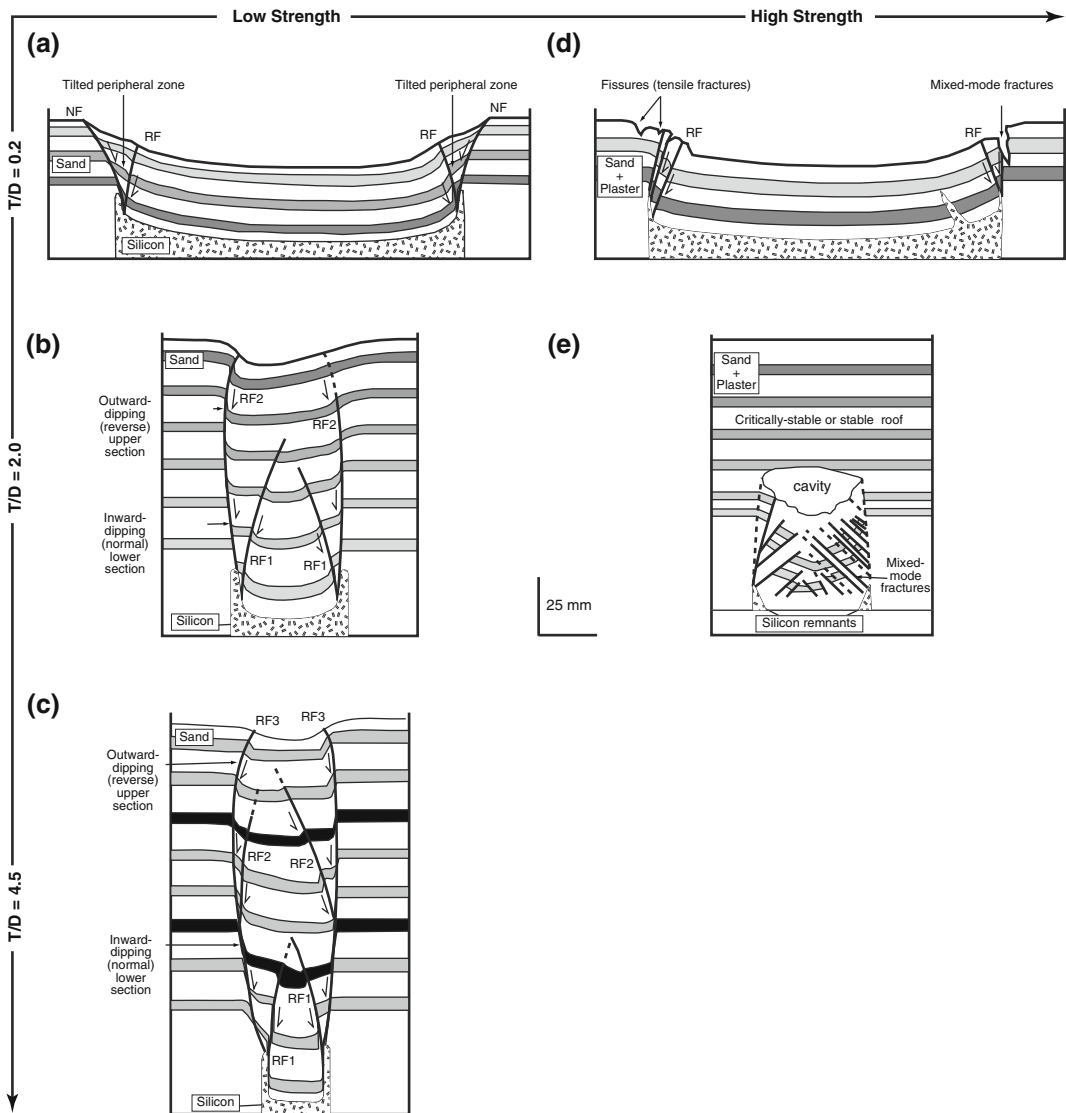


Fig. 18 How varying roof thickness/diameter (T/D) ratio and material strength may influence caldera collapse structure. To the *left* are results of analogue models with low-cohesion sand and with: **a** $T/D = 0.2$; **b** $T/D = 2.0$; **c** $T/D = 4.0$ (modified from Roche et al. 2000). To the *right* are results of models with a higher cohesion sand/plaster mix and with: **d** $T/D = 0.2$; **e** $T/D = 2.0$ (modified from Roche et al. 2001). NF = Normal fault; RF = Reverse fault. If present, numbers indicate order of

fault localisation. All drawings are to the same scale. Note that the models in parts **a**, **b**, and **c** were run in '2D' between two glass panes, whereas those in **d** and **e** were run in '3D'. Low cohesion models run in '3D' produce very similar structural developments to the 2D ones (cf. Roche et al. 2000), however, and so the variations in the results shown here stem mainly from differing roof geometry and strength

studies (e.g. Roche and Druitt 2001) and numerical models (Holohan et al. 2011, 2013).

A/B ratio affects the three-dimensional collapse structure and the lateral propagation of ring faults (Fig. 19). At high A/B ratios, and for a uniform

roof thickness, the T/D ratio is at a maximum along the short axis and a minimum along the long axis. The structural style in cross-section can thus be more fault-controlled along the short axis and more sagging-affected along the long axis

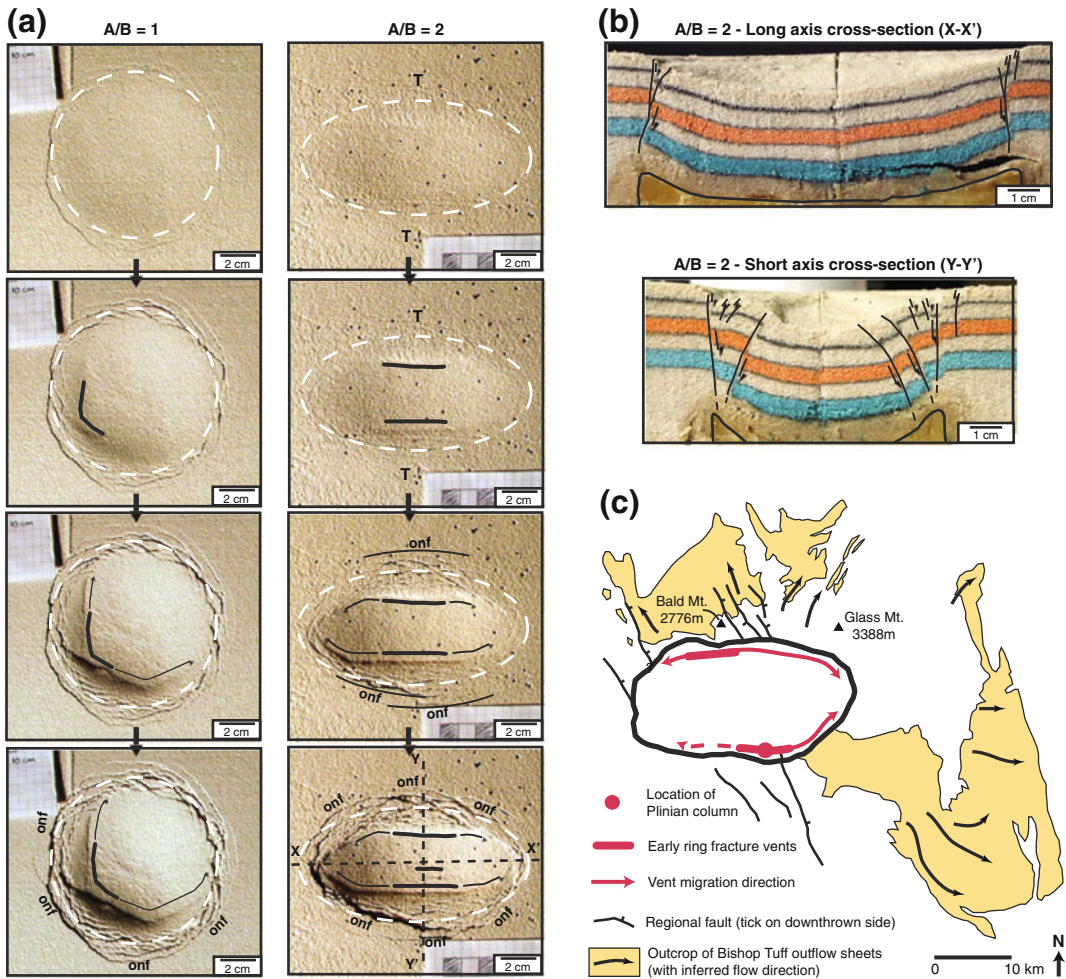


Fig. 19 How varying magma chamber’s plan-view long to short axis (A/B) ratio may influence caldera collapse structure. **a** Evolutions of collapse into a cream honey reservoir with $A/B = 1.0$ (i.e., circular in plan-view) in the left-hand column and with $A/B = 2.0$ (i.e., highly elliptical in plan-view) in the right-hand column. **b** Cross-sections through the long and short axes of the model with $A/B = 2.0$ in part **a**. Note the greater roles played by

sagging versus faulting in accommodating vertical displacement on the long and short axes, respectively. This reflects the variation in T/D along either axis in a roof that is elongate in plan-view. **c** Outline map of Long Valley caldera with inferred migration of vents feeding syn-collapse outflow ignimbrite sheets. Modified from Wilson and Hildreth (1997) and Holohan et al. (2008a)

(Holohan et al. 2008a) (Fig. 19b). For a reservoir that is circular in plan-view ($A/B = 1$), ring faults typically localise at one random point in the reservoir roof and then propagate bi-directionally around the reservoir circumference (Roche et al. 2000; Holohan et al. 2008a). For a reservoir that is highly elliptical in plan-view ($A/B \geq 2$), and has a relatively low T/D ratio ($T/D < 0.4$), the ring faults systematically localise as separate segments near

the opposite ends of the reservoir roof’s short axis. Each fault segment then propagates bi-directionally toward the roof’s long axis, where they link to form a single ring fault. This experimental ring fault propagation pattern at high A/B results from a higher shear strain along the short axis during reservoir depletion, as here the same vertical displacement is accommodated over a shorter horizontal distance than on the long axis.

This effect of roof geometry may explain the emplacement mechanism inferred for the highly elliptical Slaufudalur pluton, Iceland (Burchard et al. 2012) and the vent migration pattern inferred during the formation of the highly elliptical Long Valley caldera, USA (Wilson and Hildreth 1997; Holohan et al. 2008a) (Fig. 19c).

4.5.3 Effects of Host-Rock Cohesion on Collapse

As in the case of intrusions, host-rock strength affects the nature of collapse structures (Roche et al. 2000, 2001) (Fig. 18). At low material strength, peripheral extension near the surface is accommodated only by shear fracturing (normal faults), but at high material strength, and especially at low T/D ratios, opening-mode or mixed-mode fractures play more of a role (Fig. 18d). Changing the material strength also alters the sub-surface fracturing process seen at high T/D ratios ($T/D > 1.2$). At low material strength, the multiple sub-surface blocks are delimited by shear fractures. At high strength, however, near-horizontal opening-mode fractures may form in the centre of the roof and grow to form quasi-stable, sub-surface cavities (Fig. 18e). Detachment of material from a cavity roof forms numerous smaller blocks and causes the cavity to migrate upward. Consequently, the high-strength reservoir roofs may disintegrate into a column of coarse, loosely-fitting, rubble. In some cases, the roof above a sub-surface cavity may remain stable, in which case the collapse process halts underground.

These strength-related effects in experiments are remarkably similar to those reported in studies of mining-induced collapse (Reddish and Whittaker 1989), and have been observed at basaltic volcanoes (Rymer et al. 1998; Carter et al. 2006). Moreover, the experimental results support Anderson's (1936) postulate that high rock strength is required to develop the near-horizontal, opening-mode 'cross-fracture' that defines the upper cap of a complete subterranean 'ring dyke' (Clough et al. 1909; Richey 1932) formed in the case of magma emplacement by cauldron subsidence.

4.5.4 Effects of Topography and Regional Tectonics on Collapse Structures

Pre-collapse topography has little or no effect on experimental collapse structures when a magma reservoir resides inside, and is thus smaller than, a conical edifice (Walter and Troll 2001). On the other hand, when the reservoir is centred below and is significantly larger than a conical edifice, the topographic load causes steepening of the outward-dipping faults and more focussed subsidence (Lavallée et al. 2004). Where regional faults formed in pre-collapse extensional or strike-slip tectonic regimes are near to or coincide with the reservoir margins in experiments, they are at least partly reactivated as subsidence-guiding faults, thereby deflecting or even halting the propagation of caldera-related ring faults (Acocella et al. 2004; Holohan et al. 2005, 2008b). These results provide insight into how regional-tectonic faults may act as conduits and venting sites during caldera-forming eruptions, as inferred at, e.g., Glencoe caldera, Scotland (Moore and Kokelaar 1998).

4.5.5 Effects of Caldera Collapse on Magma Chamber Dynamics and Ring-Dyke Intrusion

Kennedy et al. (2008) modelled the effects of caldera collapse on magma chamber dynamics and ring-dyke intrusion through laboratory experiments of a rigid, cylindrical piston sinking into a slightly larger cylinder filled with corn syrup (Fig. 20a). The process can be described by two dimensionless geometrical parameters, describing subsidence and tilt of the subsiding magma reservoir roof, and by one dimensionless parameter, the Reynolds number, describing the influence of inertial and viscous forces on flow, mixing, and stirring (Fig. 20b–d). The experimental results illustrate how caldera collapse likely causes magma in the reservoir to mix and overturn and to have complex flow paths (hence emplacement directions) within a ring dyke. These effects account for compositional zonation of many ignimbrites (Hildreth and Wilson 2007),

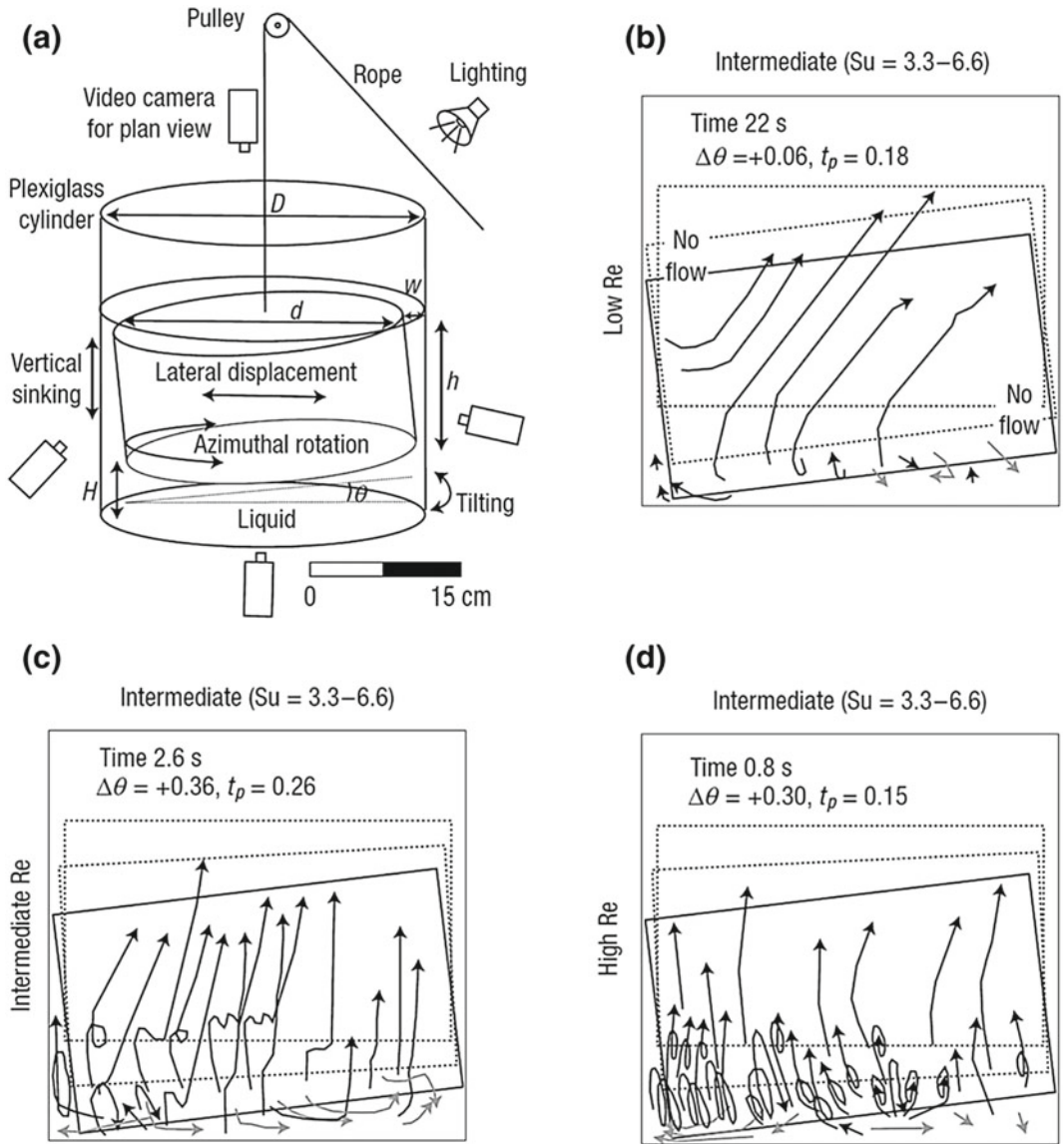


Fig. 20 How variation in the Reynolds number (Re) may affect magma flow dynamics in a reservoir and ring conduit during caldera collapse. **a** Sketch of experimental set-up involving the sinking of a cylindrical block into a cylindrical reservoir of larger diameter. The liquid in the reservoir contains neutrally buoyant marker particles that enable tracking of the liquid flow paths. **b** Results for low Re . Flow is predominantly laminar, but involves a large lateral component within the dyke due to the tilting of the downgoing block. **c** Results for intermediate Re . Some kinking and local overturning of flow paths are observed.

Flow in the ring conduit tends to be more vertical overall. **d** Results for high Re . Flow paths show multiple and much tighter overturns. Onset of such turbulent behaviour occurs as the liquid transitions from reservoir into the ring conduit. All results shown here are representative and for an intermediate subsidence stage as denoted by the subsidence number (Su), which is the block diameter normalised to block subsidence. Some further variations, e.g. in ring conduit flow directions, are also seen as Su increases. From Kennedy et al. (2008)

and for mingled magmas observed in many exposed ring dykes (Sparks 1988).

4.5.6 Kinematics of Pre-collapse ‘Tumescence’ and Post-collapse Caldera ‘Resurgence’

For many large (>c. 10 km diameter) silicic magmatic systems, caldera formation is one of three main stages in their evolution (Smith and Bailey 1968; Lipman 1984, 1997). In *Stage 1*, voluminous intrusion of less-evolved magmas into the crust eventually leads to the development of a larger, more-evolved magma reservoir (Fig. 21a). As the magma-reservoir grows, the overlying host rocks may be uplifted, a phenomenon termed ‘tumescence’. In *Stage 2*, a caldera forms when the magma reservoir roof

subsides rapidly during eruption (Fig. 21b). During *Stage 3*, renewed intrusion of magma rejuvenates the sub-caldera plumbing system. Growth of a new or remobilised sub-caldera pluton may cause uplift of the overlying caldera floor and infill, a phenomenon termed ‘resurgence’ (Fig. 21c; Kennedy et al. 2012).

Analogue modelling studies that superimposed deformation of some or all of these three stages indicate that structures inherited from previous stages affect the kinematics of later stages. Low-cohesion models showed that an initial uplift phase generates peripheral *inward-dipping reverse ring faults* (Martí et al. 1994) (Fig. 21a). With large uplift relative to reservoir diameter, central *outward-dipping normal faults* may also form (Acocella et al. 2000, 2001). During the collapse phase, these reactivate

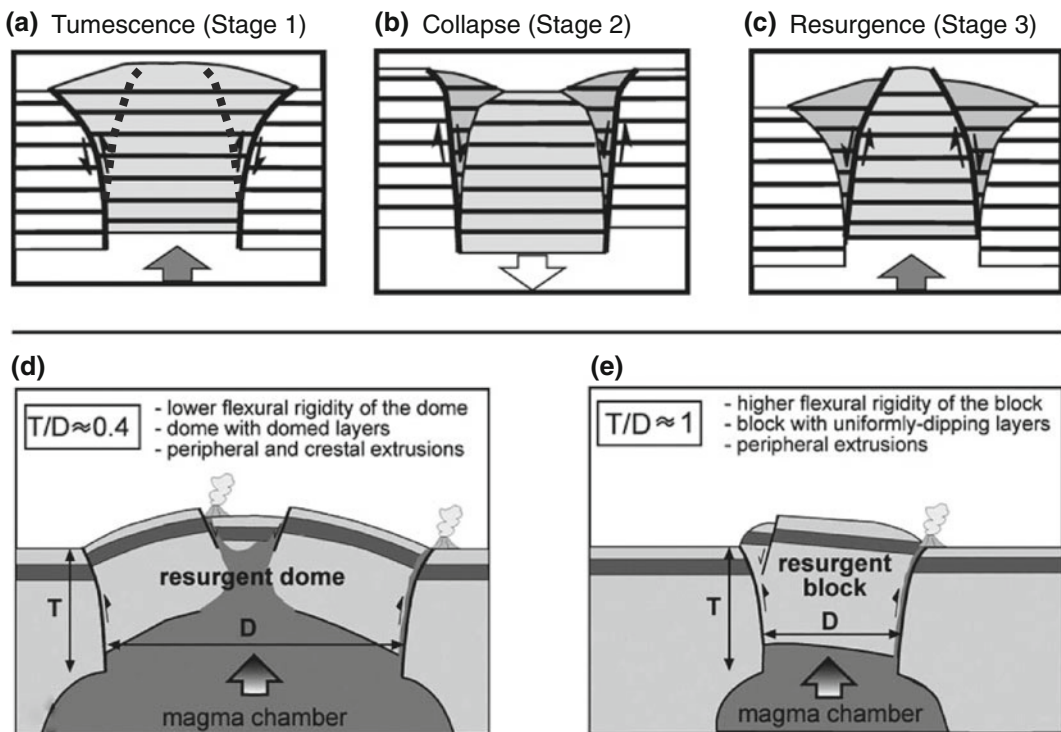


Fig. 21 Schematically-drawn section-view results of analogue models illustrating the three stages in caldera development. **a** Geometry and slip-sense of ring faults formed during pre-collapse tumescence. **b** Reactivation (inversion) of tumescence-related ring fault(s) during collapse. **c** Further inversion of collapse-related ring

faulting during post-collapse resurgence. Note the greater basal displacement here compared to that in part **a**. Also shown here are the effects of **d** low T/D ratio and **e** high T/D ratio on the structural style of resurgence. Similar effects are seen for the collapse stage (see Fig. 18). Modified from Acocella et al. (2000, 2001)

(Fig. 21b). Further uplift during resurgence may lead to complete inversion of the movements during the collapse phase (Fig. 21c). Structural relationships very similar to those in such models exist at the exhumed Rum caldera volcano, Scotland, where evidence for pre-collapse uplift is atypically clear (Holohan et al. 2009). Higher-cohesion models superimposing multiple cycles of tumescence, collapse and resurgence developed a complex ‘piecemeal’ jigsaw of roof blocks delimited by intersecting radial and concentric faults (Walter and Troll 2001). Structural relationships similar to these occur at Tejada caldera, Gran Canaria (Troll et al. 2002).

Acocella et al. (2000, 2001) show that the T/D ratio affects the structural development of resurgence similarly to that of collapse. At low T/D ratios, upwarping plays a major role in roof uplift and forms an apical graben (Fig. 21d), a structural style comparable to that at Valles caldera, New Mexico. At high T/D ratios, the roof uplift is accommodated by a more piston-like inversion of the collapse-related ring faults (Fig. 21e), a style comparable to block-like resurgence at Ischia Island, Italy.

4.5.7 Limitations of Caldera-Related Experiments

Although past experiments have simulated the development of fracture systems that likely act as magma pathways, magma intrusion into these systems, as well as interaction between fracturing and intrusion, were not simulated. Where fluid analogue reservoirs were employed, viscosities were too high to allow fluid intrusion into dilatant faults. Where a balloon or a solid piston was used, such intrusion was impossible. To our knowledge, only one study (Kennedy et al. 2008) has directly simulated coupled collapse and intrusion into caldera-related faults, albeit under highly predefined conditions.

A second common limitation is that fluid withdrawal from the analogue reservoir was not through the roof and so did not result in eruption at surface. Consequently, effects of synchronous in-filling of the caldera by erupted material are unaccounted for. The experimental procedure

instead more closely approximates caldera collapse triggered by lateral withdrawal and occurring without much in-fill by erupted material—as has occurred at e.g., Katmai caldera, Alaska (Hildreth and Fierstein 2000) and Miyakejima caldera, Japan (Geshi et al. 2002).

A third limitation is that the fluids used are single phase (liquid) only. Gas exsolution during magma intrusion and eruption may strongly affect collapse dynamics, especially with more evolved magma compositions (Stix and Kobayashi 2008; Michon et al. 2011). Such effects remain to be examined experimentally.

It should be noted that the fixed balloons or piston-like set-ups in studies of resurgence enforce a complete remobilisation of the pre-caldera magma reservoir, rather than allowing for the generation of new intrusion geometry. As a consequence, ring faults formed during a preceding phase were commonly inverted entirely along their circumferences during the succeeding phase. While this may be valid for some resurgent calderas, such a close, reactivation-based relationship between collapse- and resurgence-related structures is not so apparent at others (e.g. Long Valley caldera, California—Wilson and Hildreth 1997). ‘Resurgence’ in the latter cases may take the form of newly-generated sub-caldera intrusion geometries, which require a less constrained model set up to develop.

4.6 Ground Deformation Induced by Intrusions

Ground displacements measured at volcanoes have become very important for unravelling the dynamics of active volcano plumbing systems. This is because the monitored ground deformation patterns reflect the shape and dynamics of the underlying volcano plumbing system. Ground displacements measured during magma intrusion can range from a few centimetres, such as those induced by the emplacement of dykes and sills (e.g. Amelung et al. 2000; Sigmundsson et al. 2010), to several hundred meters, such as that induced by the emplacement of cryptodomes (e.g., the 1980 Mount St. Helens eruption; Lipman et al. 1981).

Geodetic monitoring systems that measure such displacements have become very important and increasingly sophisticated tools for monitoring and unravelling the dynamics of volcano plumbing systems. Geodetic measurement methods such as GPS, InSAR, photogrammetry, tilt, and precise levelling, now provide accurate and high-resolution time-series maps of displacements at many active volcanoes. They are able to detect even subtle ground movements induced by changes in magma pressure or distribution at depth. Data from these methods are widely used to (i) forecast that an eruption is imminent (Sigmundsson et al. 2010) and (ii) infer the geometry of volcanic plumbing system components, such as dykes (Wright et al. 2006; Fukushima et al. 2010), cone sheets (Chadwick et al. 2011), sills (Amelung et al. 2000; Sigmundsson et al. 2010) and magma reservoirs (Chang et al. 2007).

Geodetic data is routinely analysed by fitting displacement data predicted from analytical or numerical models to the measured data. The best fit thus provides insights into the depth, shape and orientation of underlying magma body responsible for the observed ground movements. Such deformation sources are usually interpreted in terms of magma bodies or pathways. These analyses have several limitations: (i) The modelled sources usually have highly simplified shapes to make inversion of observed displacements computationally tractable and efficient. Field observations show that the shapes of natural magma intrusions are more diverse and complex. (ii) The source models are consequently also a highly simplified representation of the geological process(es) and their development, and of how these affect ground displacements. (iii) Many source modelling studies only take into account the elastic response of the host rock, while plastic deformation, such as faulting, may play a major role in nature.

The interpretation of the underlying cause(s) of ground displacements at volcanoes in terms of the plumbing system attributes is a challenge that also can be addressed by laboratory models. Firstly, as shown in the preceding sections (see above), analog models are capable of reproducing

the complex geometries of various kinds of igneous intrusion. Secondly, they are capable of simulating more complex elasto-plastic host-rock rheology. Thirdly, a range of photogrammetric and other techniques (e.g. laser scanning, structured light) for measuring surface displacements, can be applied to laboratory models. Therefore, if they are set up appropriately (see below), such models carry the advantage of being a geologically representative physical system in which both the shape of the plumbing system and the resulting pattern of free surface displacement are known.

4.6.1 Surface Deformation Related to Dykes

The first laboratory study addressing surface deformation induced by dykes considered a pseudo-2-dimensional, vertically-elongated cell filled with a cohesive flour-sugar mix; the “dyke” was modelled by two moving rigid sleeves, the distance between which was increased by inserting sheets of cardboard (Mastin and Pollard 1988). Very similar experiments with ground sand have been conducted recently in three dimensions by Trippanera et al. (2014). In agreement with the theoretical results of Pollard and Holzhausen (1979), geodetic data and field observations (e.g. Pallister et al. 2010), these laboratory experiments produce a surface depression above the tip of the opening dyke. In addition, a broad area of surface uplift occurs marginal to the depression as the dyke opens. The laboratory models show that subsidence to form the depression is accommodated by central sagging, block rotation and/or reverse faulting, as well as by tension fractures (crevasse) or normal faults that bound the depression.

The experiments of Mastin and Pollard (1988) and Trippanera et al. (2014), like the corresponding analytical or numerical models, represent the inflation of an already emplaced dyke, rather than a full consideration of dyke propagation.

In order to simulate and measure the surface deformation associated with dyke propagation, Abdelmalak et al. (2012) and Galland (2012) designed 2-dimensional and 3-dimensional experiments, respectively, in which dyke emplacement

is simulated by the injection of a viscous fluid into cohesive granular material. Surface uplift is induced by the emplacement of a dyke, but the character and cause of the uplift is drastically different with respect to that in the experiments of Tripanera et al. (2014). The uplifted area is much narrower and is focussed directly above the tip of the propagating dyke; no depression forms. Like the 2-D experiments of Mathieu et al. (2008), this dyke-induced uplift results from a viscous indenter process of propagation. The models show that reverse faults steeply dipping toward the dyke tip accommodate the uplift.

These differing models of dyke-related surface displacement results hence form a basis for discriminating dyke inflation versus viscous indentation from geodetic data sets. Future work might consider analysis of surface displacements induced in gelatine models, which offer the possibility of quantifying such behaviour for a more elasticity-dominated dyke propagation process.

4.6.2 Surface Deformation Related to Saucer-Shaped Sills or Cone Sheets

Galland (2012) used silica flour and végétaline oil models (Fig. 22a) to quantify a time series of 3D surface displacement related to the emplacement of cone sheets of saucer-shaped sills. Intrusion of the oil triggered subtle deformation of the flat model surface, which was monitored by using a structured light-based system, combining a video-projector and a CCD camera (Brèque et al. 2004; Galland 2012). This system allows fast (<1.5 s) and accurate measurements of the model surface, and produced topographic maps through time.

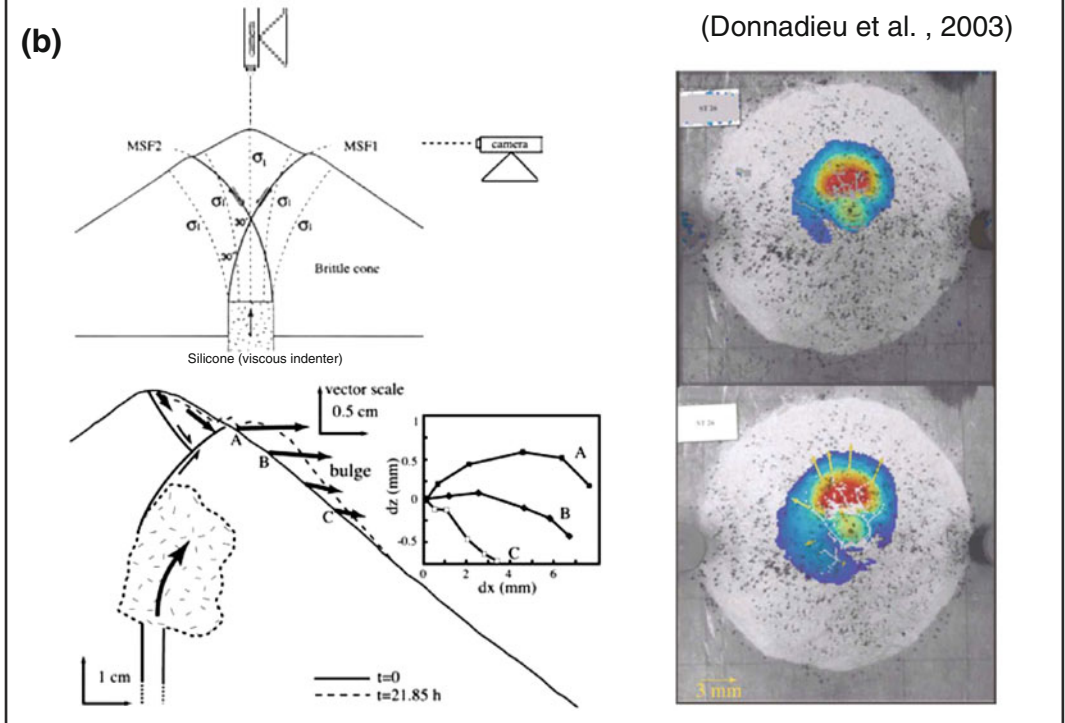
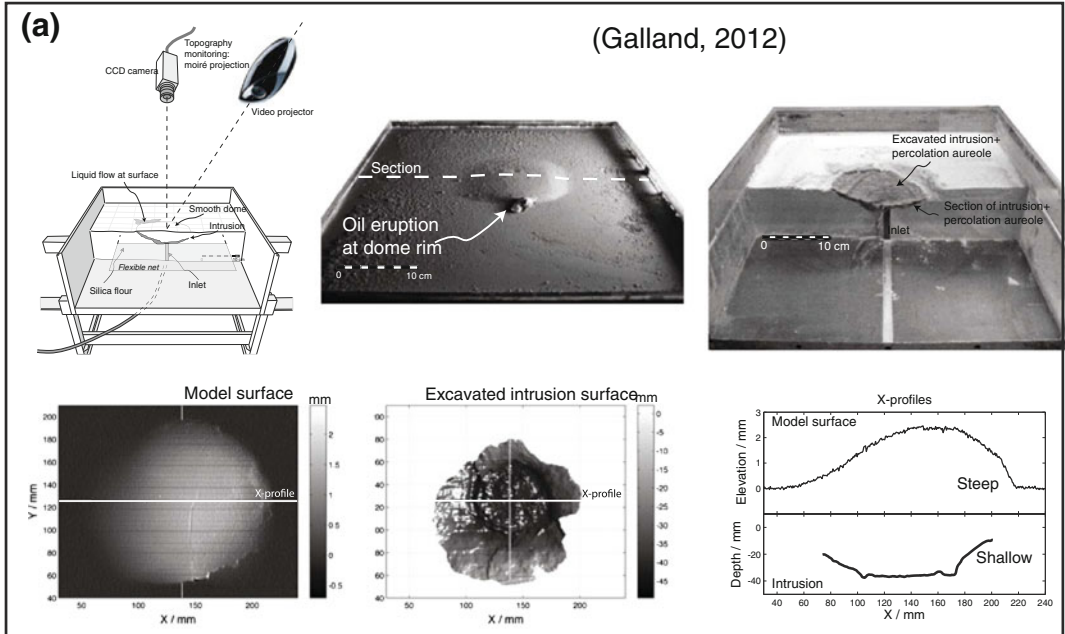
After the experiments were run, the oil solidified in the models, and the intrusion was excavated. If the intrusion was flat-lying, the shape of its upper surface was also measured with the same system, such that the ground deformation pattern could be directly compared to its associated underlying magma conduit.

The experiment results show a remarkable correlation between the asymmetry of the ground deformation pattern and the asymmetry of the underlying intrusion (Fig. 22a). In particular, the

steepest edges of the uplifted zones at the model surface were always located above the shallowest parts of the underlying intrusion. Given that the asymmetry of the ground deformation developed relatively early during the experiments, it was thus possible to detect well before the eruption where the oil was rising towards the surface (see also the 2D dyke results of Abdelmalak et al. 2012). These experiments thus show that real-time analysis of asymmetrical development of ground deformation patterns in volcanoes could be used as a predictive tool to forecast the location of an impending volcanic eruption.

4.6.3 Surface Deformation Related to Cryptodomes

Cryptodome-induced deformation has been studied in the laboratory by Donnadiu and Merle (1998, 2001), who used silicone as model magma and a cohesive pack of granular material to simulate a volcanic edifice (Fig. 22b). They show that the early emplacement of the cryptodome generates curved inward-dipping major shear zones that affect the flanks of the edifice. As intrusion proceeds, the magma deviates toward the flanks by following these shear zones, such that it grows laterally and leads to a bulge on the flank of the edifice. Merle and Donnadiu (2000) and Donnadiu et al. (2003) applied digital photogrammetry to their experiments in order to quantify the horizontal displacements of the flanks of a volcanic edifice intruded by a cryptodome. They show that the expected displacement is clearly asymmetrical, such that most of the flank is affected by a substantial bulging (Fig. 22b). These results are in very good agreement with the geodetic observations collected before the 1980 eruption of Mount St. Helens (Lipman et al. 1981). In addition, these results explain how the processes controlling the emplacement of cryptodomes also govern lateral volcanic blasts resulting from a volcano flank collapse. As for the other intrusions types described above, such quantitative laboratory model results therefore provide a basis for linking ground displacements at volcanoes to an underlying physical process and so can assist in real time hazard assessment.



◀ **Fig. 22** Characteristic experimental studies of ground deformation induced by magma intrusions. **a** Experimental study of Galland (2012). *Upper left* Drawing of experimental setup. *Upper central* Oblique photograph of model surface at the end of an experiment. *Upper right* Intrusion partly excavated after oil solidification. *Lower left* Topographic map of model surface during an experiment, made by using a moiré projection device (Brèque et al. 2004). *Lower central* Topographic map of top surface of excavated intrusion, again made by using the moiré projection device. *Lower right* Comparison between corresponding profiles of the model surface (*top*) and underlying intrusion (*bottom*). The positions of the

profiles are indicated with the white lines on the maps to the right (X-profile). **b** Experimental study of Donnadiou et al. (2003). *Upper left* Drawing of experimental setup, silicone putty being injected at the base of a cone made of sand. The deformation of the cone can be monitored from a side camera or a top camera. *Lower left* Results from side observations of volcanic edifice deformation in experiments (Donnadiou and Merle 1998; Merle and Donnadiou 2000). *Right* Horizontal displacement maps of volcanic edifice deformation at two time steps of an experiment, computed using digital photogrammetry (Donnadiou et al. 2003)

4.7 Magma Intrusions in Deforming Crust (Magma-Fault Interactions)

Volcanic activity concentrates at tectonic plate boundaries, where the Earth's crust is actively deforming. Good examples are active margins, which host 75 % of volcanic eruptions and 90 % of earthquakes. Understanding how magmatic intrusions are affected, or interact, with tectonic deformation of the crust is thus a key aspect of the dynamics of volcanic plumbing systems.

To address this aspect, the experimental setups need to properly simulate both the mechanical behaviour of the magma and the deforming host rocks. In particular, a major challenge is to account for faulting. Gelatine, for example, is not suitable, as the high strength of the gelatine does not allow shear failure under the low stresses applied in the models. Gelatine only enables to simulate a stressed crust (Hubbert and Willis 1957; Watanabe et al. 2002; Kervyn et al. 2009; Menand et al. 2010; Daniels and Menand 2015) or a crust with pre-existing fracture planes (Le Corvec et al. 2013).

In contrast, granular materials are suitable for addressing the interactions between faults and magmatic intrusion. Sand/silicone models, for example, have been extensively used to constrain the emplacement of high viscosity magma in the brittle crust in any kind of tectonic settings, from pure extension (Fig. 23a) (Román-Berdiel 1999; Bonini et al. 2001; Corti et al. 2003), transtension (Corti et al. 2001), strike-slip faulting (Fig. 23b) (Román-Berdiel et al. 1997; Román-Berdiel 1999; Corti et al. 2005; Holohan et al. 2008b),

transpression (Benn et al. 1998, 2000), to pure compression (Fig. 23c, d) (Musumeci et al. 2005; Mazzarini et al. 2010; Montanari et al. 2010a, b). All these models produced two fundamental findings: (i) the shapes of magma intrusions are controlled by the deformation, and (ii) vice versa the development of the deformation patterns is perturbed by the presence of a viscous heterogeneity.

These studies demonstrate that the elongation (i.e. orientation) of magma bodies is governed by the far field principal components of the deformation field. In extension, the model intrusions are elongated such that the short axis is perpendicular to the direction of extension. In strike-slip and compressional settings, the intrusions are also elongated, but in contrast to the extensional case, the short axis is perpendicular to the main shortening direction. This implies that in strike-slip and transpressional regimes, intrusions are elongated oblique to the main strike-slip faults. In these models, it is noticeable that faults exert only a very local effect on intrusions, which develop small sharp edges at the roots of faults. Conversely, faults tend to nucleate at the edges of intrusions, which represent rheological discontinuities that localise strain in the models.

Sand/silicone models, however, suffer from some limitations. The scaling of these experiments is such that: (i) the silicones only simulates very high viscosity magmas, i.e. between 10^{16} and 10^{17} Pa s, which is way above the range of common basaltic to rhyolitic magmas between 100 and 10^8 Pa s; and (ii) sand is too loose and only simulates shear failure (faulting), but not

tensile or mixed-mode fracturing that may arise as magmas interact with a pre-existing failure surface (Fig. 23b, c). Consequently, these models do not simulate the formation of magmatic sheet intrusions such as dykes and sills, which are fundamental magma pathways, and their ability to simulate the effects of the faults on intrusions are rather limited.

In order to overcome these limitations, other materials are required. Model magmas need to have lower viscosities than silicone putty, and the model crust needs to be more cohesive than dry sand. As noted in previous sections (Sects. 2.1.2 and 2.2.3), suitably low viscosity model magmas include Golden Syrup, molten vegetable oil, and RTV silicone, while suitable rock analogues include sieved ignimbrite, fined-grained silica flour and diatomite powder (Galland et al. 2006; Mathieu et al. 2008; Gressier et al. 2010; Abdelmalak et al. 2012).

In contrast to sand-silicone models, the models with these alternative materials clearly highlight the prominent effects of faults on magma transport (Fig. 23a, d). The experiments of Galland et al. (2007a) and Ferré et al. (2012), for instance, show that thrust faults localise magma transport both when the faults are active and inactive. These models highlight that gently-dipping faults facilitate substantial horizontal transport of magma in compressional settings, with important implications for magma plumbing systems in active margins, which are currently still considered as simplistic sub-vertical pathways.

Similarly to sand-silicone models, silica flour-vegetable oil models also show that intrusions greatly affect the tectonic pattern, as they correspond to weak heterogeneities that concentrate stresses and nucleate deformation, in a similar manner to a velocity discontinuity (Barrier et al. 2002). Consequently, intrusions locally perturb regional tectonic structures (Fig. 23d) (Galland et al. 2007a). These experimental results are corroborated by geological examples of orogenic fronts curved around batholiths (e.g., Boulder Batholith, Montana, USA; Kalakay et al. 2001; Lageson et al. 2001) and volcanoes, such as Tromen Volcano, Northern Patagonia,

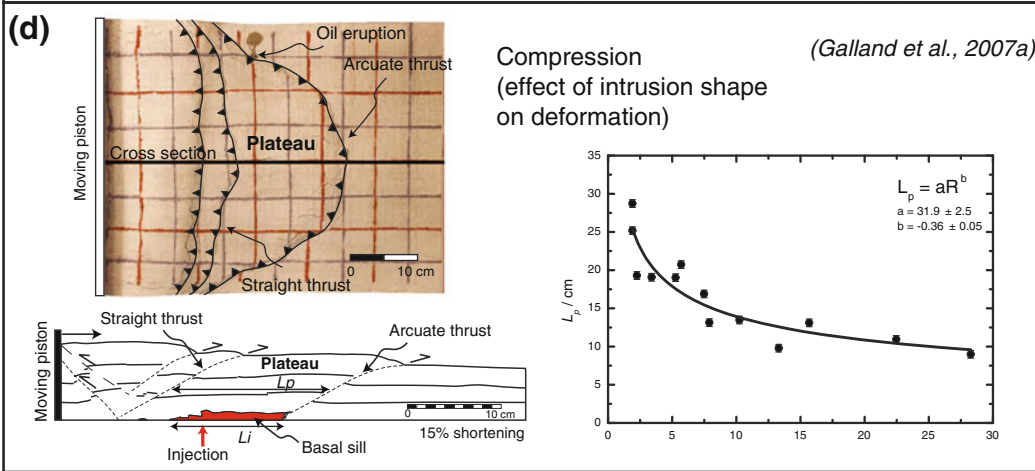
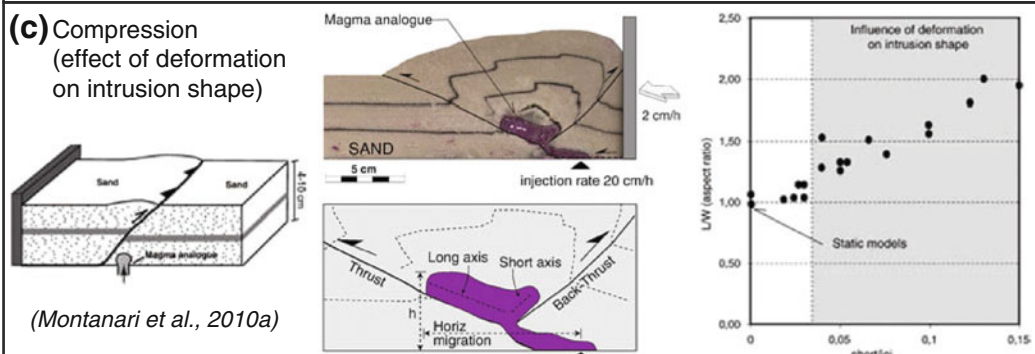
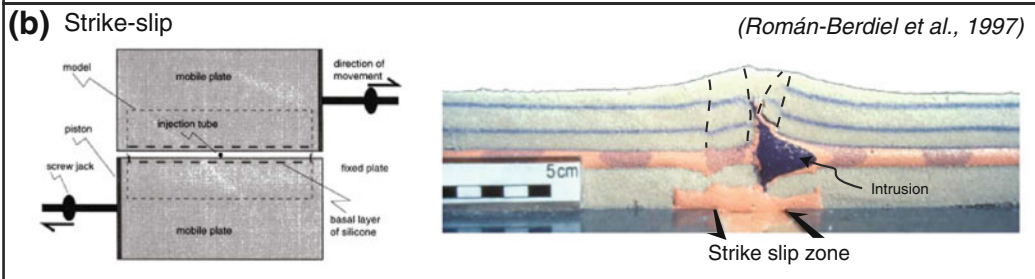
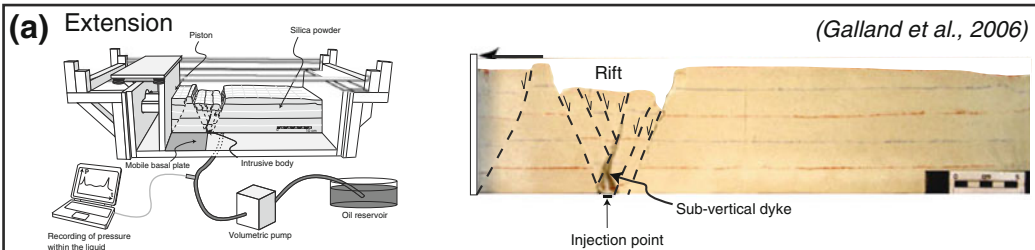
Argentina (Marques and Cobbold 2006; Galland et al. 2007b; Llambías et al. 2011), Guagua Pichincha Volcano, Ecuador (Legrand et al. 2002), and El Reventador Volcano, Ecuador (Tibaldi 2005; Tibaldi et al. 2010).

4.8 Explosive Volcanic Vents

All the experimental studies described above deal with magma transport and emplacement at depth. To ultimately feed a volcanic eruption, however, the volcano plumbing system must intersect the Earth's surface. Therefore, understanding how magma flows through and exits the plumbing system to reach the Earth's surface is a critical factor for assessing volcanic hazards. Laboratory experiments have been also designed to study the dynamics of the shallowest parts of volcano plumbing systems—i.e. the part leading into the eruptive vent.

Most vent-related experiments address the dynamics of explosive processes that arise from large magma overpressures and that result in piercement structures, such as diatremes and breccia pipes. These overpressures can result from: (i) gas exsolution during magma ascent and decompression, leading to the development of kimberlites (Sparks et al. 2006; Brown et al. 2007); (ii) phreatomagmatism due to explosive magma–water interactions, leading to the formation of maar-diatremes (Lorenz and Kurszlauskis 2007; White and Ross 2011); or (iii) rapid generation of gas due to accelerated maturation of organic-rich rocks in the surrounding of magma intrusions, producing hydrothermal vent complexes (Svensen et al. 2004, 2006; Aarnes et al. 2011b, 2012).

The first qualitative laboratory study of piercement structures was conducted by Daubrée (1891) to investigate the formation of diatremes. These pioneering experiments did not address fluidisation processes, however, which geological observations suggest is prominent during diatreme and breccia pipe formation. In contrast, the later experiments of Woolsey et al. (1975) and McCallum (1985) did so. These authors used granular materials of various grain sizes (clay to gravels) and cohesions to simulate the behaviour



◀ **Fig. 23** Characteristic experimental studies of magma-fault interactions in various tectonic settings. **a** Experimental study of magma intrusion in extension (Galland et al. 2006). *Left* Experimental setup. *Right* Typical longitudinal cross section, displaying the normal fault pattern and the intrusion. The latter is a dyke that follows a normal fault. **b** Experimental study of magma intrusion in strike slip (Román-Berdiel et al. 1997). *Left* Drawing of experimental setup viewed from above. *Right* Typical cross section perpendicular to the strike slip fault. **c** Experimental study of magma intrusion in compression made by using sand/silicone models (Montanari et al. 2010a). *Left* Experimental setup. *Centre* Photograph (*top*) and corresponding drawing (*bottom*) of a typical longitudinal cross section, on which the faults and the length (L) of the intrusion can be observed. Serial cross sections can also be made to reconstruct the intrusion in 3D, and so to estimate its width (W). *Right*: Correlation between the length-to-width (L/W) aspect ratio of the intrusion and the

shortening velocity-to-injection velocity ratio. The plot demonstrates that the shape of the intrusion is controlled by this dynamic ratio. **d** Experimental study of magma intrusion in compression made of silica flour/vegetable oil models (Galland et al. 2007a). *Left* View of the model surface, displaying the fault trace pattern. A strongly arcuate thrust forms when oil is injected in the models. The *black straight line* locates the drawing (*bottom*) of a typical longitudinal cross section, displaying the oil intrusion and the faults. Note that the arcuate thrust is rooted at the tip of the intrusion. A non-deformed plateau lies between the arcuate thrust and the thrusts rooted at the bottom of the moving piston. Both the length of the intrusion (L_i) and of the plateau (L_p) can be measured. *Right* Correlation between the length of the plateau (L_p) and the dynamic ratio R quantifying the ratio between the shortening and injection rates. It demonstrates that the deformation pattern is strongly influenced by the occurrence of magma injection

of different rock types. They performed both 3D and 2D experiments, in which pressurised air was injected at the bottom of a pack of granular material. The initial stages of the models consisted of a bulging of the model surface and associated uplift of the granular material above the pressure source along reverse shear fractures. Following the initial doming, the pressurised air broke through to surface and fluidised the material. This produced a maar-type crater. During fluidization, material convected upward in the middle of the conduits and downward along their sides. The latter movement resulted in inward-dipping layers along the sides of the conduits. With layers of different materials, fluidization caused complex mixing of the materials and led to secondary segregation along the walls of the conduits. The top part of the model conduits exhibits a funnel shape. Although these experiments look simple, they managed to reproduce most of the first-order geological features observed in maar-diatremes and hydrothermal vent complexes, and so suggest that fluidization processes are likely to be important in the shallow parts of volcano plumbing systems.

Similar experiments addressed aspects of the formation and evolution of kimberlite pipes. Walters et al. (2006) studied the complex distribution of fluid flow across pipes filled with a mixture of granular materials. A detailed analysis of the experimental conduit morphologies shows

that the fluid velocity maximised in the conduit centre and decreased towards the conduit sides following a Gaussian law. In addition, reducing the fluid flow rate reduced the size of the fluidizing conduits, leading to complex pipes-within-pipes structures, as observed in natural kimberlite pipes.

The results of Walters et al. (2006) suggest that the shape of the fluidised conduits control the complex distribution of fluid pressure and flow rate. Gernon et al. (2008) quantified this effect of conduit morphology in a series of fluidization experiments with (i) confined vertical walls, and (ii) tapered walls of varying dip angle (Fig. 24a). They show that the fluidization in vertical conduits is homogeneous, whereas fluidization in tapered conduits is heterogeneous and mainly confined to the conduit centre. In these latter experiments, the width of the fluidised region is positively correlated to the fluid flow rate. The results of Gernon et al. (2008) also show that fluctuating fluid flow during kimberlite pipe formation can produce complex internal boundaries, as observed in the field.

Analyses of kimberlite volcanoclastic deposits show that they are made of mixtures of fragments of very different sizes (from 10 mm to several cm; e.g. Walters et al. 2006). Gernon et al. (2009), and Nermoen et al. (2010b) studied the complex fluidization processes of mixtures of fine-grained and coarse-grained granular

◀ **Fig. 24** Characteristic experiments of explosive volcanic vents. **a** Experiments of Gernon et al. (2008). *Left* Drawing of experimental setup. *Right* Schematic diagram of the general behaviour of a tapered fluidised bed. The fluidised region, A is divided into (A1) a central core of dilute flow and upward particle transport, and (A2) a region dominated by the net downward movement of particles. B is the unfluidised or static region, where (1) frictional drag, and (2) shear occur at high flow rates. Particles are elutriated at C, and deposit on the surface, both at D, and the top of zone B. **b** Experiments of Ross et al. (2008a). *Left* Drawing of experimental setup. *Right* Time series of photographs of a characteristic experiment. The *upper left image* shows initial conditions. After 156 ms (*upper right image*), a ‘bubble’ grows, the density of the gas-particle mixture decreases as more gas arrives, and the base of the ‘bubble’ starts to pinch noticeably

because of inward movement of granular host (*white beads*). After 316 ms (*lower left image*), *red beads* setting forms a vertical cylindrical body. After 436 ms (*lower right image*), the model exhibits the final “crater” aspect of the surface, due to subsidence of particles into the crucible underlying the rectangular container of the host (cf. Ross et al. 2008a). **c** Experiments of Nermoen et al. (2010a). *Upper left* Drawing of the experimental setup. *Lower left* Time series of photographs of an experiment, from initial state (*left*) to final state (*right*). *Right* Dimensionless plot of the critical fluid velocity at onset of fluidization v_f , scaled by the Darcy velocity of the model granular medium, against the inlet depth-to-width ratio (h/w). The graph displays experimental results (*black*) and results from analytical model (*red*), and shows a linear relationship between v_f and h/w (cf. Nermoen et al. 2010a)

materials. Their results show that fluidization of the granular mixture triggers local segregation and a concentration of coarser grains. Consequently, this locally produces a higher permeability anomaly, which focuses further fluid flow and fluidization. This self-focusing fluidization process likely explains the strong textural variations observed within kimberlite pipes.

Similar experiments with gas and granular material have been used to study the formation of phreatomagmatic underground explosions and their associated deposits. Such explosive processes have been simulated by injecting a mixture of overpressurised gas and red glass beads into a model made of white glass beads (Ross et al. 2008a, b). A high-speed camera was necessary to monitor the evolution of the models. In the early stages of the experiments, a bubble rose towards the surface, entrained the injected and host materials, and domed the surface of the models (Fig. 24b). The injected material sometimes erupted at the surface, but other times did not. The experiments show that eruption is favoured if: (i) the initial fluid pressure is high; and (ii) the thickness and the permeability of the bed into which the material is injected are low, which is in good agreement with the theoretical analysis of Jamtveit et al. (2004). In all experiments, after the fluid escaped, the red injected material appeared as a steep-sided conduit, similar to those observed in the field.

In all of the experiments mentioned above, the pressures applied to the models were large

enough to form piercement structures, whether the surface was breached or not. Many volcanic conduits do not exhibit piercement structures, however. A key question is thus: what is the critical pressure required to form piercement structures? To answer this question, Nermoen et al. (2010a) injected pressurised air at the base of a bed of glass beads through an injector of variable depth (h) and width (w) (Fig. 24c). The air’s pressure and velocity were gradually increased until fluidization of the bed occurred. By independently varying h and w , Nermoen et al. (2010a) established that the critical pressure for fluidization, scaled by the intrinsic permeability of the material, is a linear function of h/w . Given that the experimental results were presented in dimensionless form, they are applicable to piercement structures of different scales, from small pockmarks to kimberlite pipes.

Field studies highlight that explosive volcanic vents exhibit various shapes, regardless the origin of the explosion (magmatic, phreatomagmatic or phreatic): these shapes include vertical pipes and V-shaped vents (Jamtveit et al. 2004; Sparks et al. 2006; Svensen et al. 2007; White and Ross 2011). The integrated laboratory and numerical study of Galland et al. (2014b) demonstrates that the shape of explosive vents is governed by two dimensionless parameters, (1) the fluid pressure-to-gravitational stress ratio ($P/\rho gh$) and (2) the fluid pressure-to-host rock strength ratio (P/C). Through dimensionless phase diagrams, Galland et al. (2014b) show that

vertical vents correspond to a high-energy physical regime (high values of $P/\rho gh$ and P/C), whereas the V-shaped vents correspond to a lower-energy regime (lower values of $P/\rho gh$ and P/C). In addition, numerical simulations show that the vertical vents in the experiments result from plasticity-dominated yielding of the host rock, whereas the V-shaped vents result from elasticity-dominated failure of the overburden. In other words, V-shaped vents form as a result of obliquely propagating fractures (low energy regime), whereas vertical vents form as a result of plastic indenting (high energy regime). Though these experiments and simulations are 2-dimensional, this latter mechanism significantly differs from fracturing and is likely to explain the 3-dimensional circular shapes of vertical pipes.

5 Conclusions and Perspectives

Analogue models conducted over the past few decades have yielded a wealth of insights into most aspects of the geometric and kinematic development of sub-volcanic plumbing systems. Most works have, for practical reasons, focussed on one type of intrusion, be it dyke, sill or laccolith, but the ensemble of works allows us to make some statements on the general conditions that control intrusion type and processes. The models, taken together, have shown how the growth and final geometries of sub-volcanic intrusions are largely governed by an interplay between several key factors that include:

- the mechanical properties of the host rocks, in particular strength and elastic modulus;
- the presence or absence of heterogeneities or discontinuities, such as mechanical layering, weak interfaces or faults, within the host rocks;
- the depth of magma emplacement;
- the shape and relief of surface topography and the proximity of related topographic loads;

- the physical properties of the intruding magma(s), in particular magma viscosity and density relative to those of the surrounding host rocks.

Analogue models also show how many of the same parameters often play similar roles in the disruption and reorganisation of the plumbing system that occurs during the course of caldera collapse, related ring fault intrusion, and the re-establishment of a ‘resurgent’ magmatic system. Lastly, analogue models have also helped to unravel the complex structural and geometric effects of fluidisation and explosion that occur where magmas and magmatic fluids pass through and exit the shallowest part of the plumbing system and finally reach the surface.

- (1) Despite advances from the numerous existing laboratory studies, this chapter highlights the future key challenges of experimental modelling of volcano plumbing systems. These are:
- (2) A rigorous mechanical characterisation of some of the model magmas and model rocks. The properties of, e.g. ignimbrite powder, cream honey and sand-gypsum mixtures, are poorly constrained. Model magma characterisation is usually focussed on viscosity and density, but other magma properties like shear thinning, compressibility and multi-phase behaviour are rarely considered.
- (3) The use of model materials of complex, and more geologically relevant rheologies. Good examples are elasto-plastic cohesive granular materials, which have demonstrated their suitability and adaptability for simulating rocks of the brittle crust. In addition, currently used materials do not enable the modelling of magma—host rock interactions, such as fluidisation, fine scale fracturing, and margin cooling that may be important in developing intrusions. Thus, magma advance by fingering and/or fluidisation are currently not modelled (cf. e.g. Schofield et al. 2010), nor is the possibility of multiple injections (Menand 2008).

- (4) The design of models accounting for two-phase or even three-phase magmas. The rheology of such complex materials is drastically different than those of the model magmas commonly used in the literature, which can appear somewhat simplistic.
- (5) A better integration of laboratory modelling results in multidisciplinary research on volcano plumbing systems (e.g. Galland et al. 2013). This step requires rigorous dimensional analysis of the modelled processes, such that the experimental results are displayed in dimensionless form to overcome the scale problem often highlighted for laboratory models.
- (6) A more quantitative description (measurements) of experimental results in order to better constrain the physics of the modelled processes and the physical laws identified from the dimensional analysis. Modern tools, such as Digital Image Correlation (White et al. 2003; Leever et al. 2011) and X-CT scanners (Adam et al. 2013) produce quantitative kinematic data sets that prove essential to unravel the complex processes simulated for the host rock (Leever et al. 2014). For better quantifying magma flow in growing or inflating intrusions more complex models, such as those of Závada et al. (2006, 2009, 2011), which used magnetic particles to track magma flow in a progressively solidifying laccolith analogue, are required. In addition, these data make the integration of laboratory models with numerical models and geological/geophysical data more quantitative.
- (7) The prediction of the type and geometry of plumbing system components (e.g. dykes, sills, laccoliths, plutons, etc.). While they are mostly addressed through separate models, they all result from the intrusion of a viscous magma into a solid rock of complex rheology. The next challenge of laboratory models will be to establish a unified mechanical model of magma emplacement in the Earth's crust that predicts under which conditions intrusions of given shapes form (Galland et al. 2014a), although, as the

geological system is highly variable and very complicated, this final goal will be no simple task.

References

- Aarnes I, Fristad K, Planke S, Svensen H (2011a) The impact of host-rock composition on devolatilization of sedimentary rocks during contact metamorphism around mafic sheet intrusions. *G3* 12(10):Q10019. doi:[10.1029/2011gc003636](https://doi.org/10.1029/2011gc003636)
- Aarnes I, Svensen H, Polteau S, Planke S (2011b) Contact metamorphic devolatilization of shales in the Karoo Basin, South Africa, and the effects of multiple sill intrusions. *Chem Geol* 281(3–4):181–194. doi:[10.1016/j.chemgeo.2010.12.007](https://doi.org/10.1016/j.chemgeo.2010.12.007)
- Aarnes I, Podladchikov YY, Svensen H (2012) Devolatilization-induced pressure build-up: implications for reaction front movement and breccia pipe formation. *Geofluids* 12(4):265–279. doi:[10.1111/j.1468-8123.2012.00368.x](https://doi.org/10.1111/j.1468-8123.2012.00368.x)
- Abdelmalak MM, Mourgues R, Galland O, Bureau D (2012) Fracture mode analysis and related surface deformation during dyke intrusion: results from 2D experimental modelling. *Earth Planet Sci Lett* 359–360:93–105. doi:[10.1016/j.epsl.2012.10.008](https://doi.org/10.1016/j.epsl.2012.10.008)
- Acocella V, Cifelli F, Funicello R (2000) Analogue models of collapse calderas and resurgent domes. *J Volcanol Geotherm Res* 104(1–4):81–96
- Acocella V, Cifelli F, Funicello R (2001) The control of overburden thickness on resurgent domes: insights from analogue models. *J Volcanol Geotherm Res* 111(1–4):137–153
- Acocella V, Funicello R, Marotta E, Orsi G, de Vita S (2004) The role of extensional structures on experimental calderas and resurgence. *J Volcanol Geotherm Res* 129(1–3):199–217
- Adam J, Klinkmüller M, Schreurs G, Wieneke B (2013) Quantitative 3D strain analysis in analogue experiments simulating tectonic deformation: integration of X-ray computed tomography and digital volume correlation techniques. *J Struct Geol* 55:127–149. doi:[10.1016/j.jsg.2013.07.011](https://doi.org/10.1016/j.jsg.2013.07.011)
- Algar CK, Boudreau BP, Barry MA (2011) Initial rise of bubbles in cohesive sediments by a process of viscoelastic fracture. *J Geophys Res* 116(B4):B04207. doi:[10.1029/2010jb008133](https://doi.org/10.1029/2010jb008133)
- Amelung F, Jonsson S, Zebker H, Segall P (2000) Widespread uplift and “trapdoor” faulting on Galápagos volcanoes observed with radar interferometry. *Nature* 407(6807):993–996. doi:[10.1038/35039604](https://doi.org/10.1038/35039604)
- Ancochea E, Brändle JL, Huertas MJ, Cubas CR, Hernan F (2003) The felsic dikes of La Gomera (Canary Islands): identification of cone sheet and radial dike swarms. *J Volcanol Geotherm Res* 120(3–4):197–206

- Anderson EM (1936) The dynamics of the formation of cone sheets, ring dykes and cauldron subsidences. *Proc R Soc Edin* 56:128–163
- Barenblatt GI (2003) *Scaling*. Cambridge University Press, Cambridge
- Barrier L, Nalpas T, Gapais D, Proust JN, Casas A, Bourquin S (2002) Influence of syntectonic sedimentation on thrust geometry. Field examples from the Iberian Chain (Spain) and analogue modelling. *Sediment Geol* 146(1–2):91–104
- Battaglia J (2001) Quantification sismique des phénomènes magmatiques sur le Piton de la Fournaise entre 1991 et 2000. PhD thesis, Université Paris, 7 Denis Diderot, Paris
- Beckett FM, Mader HM, Phillips JC, Rust AC, Witham F (2011) An experimental study of low-Reynolds-number exchange flow of two Newtonian fluids in a vertical pipe. *J Fluid Mech* 682:652–670. doi:10.1017/jfm.2011.264
- Benn K, Odonne F, de Saint Blanquat M (1998) Pluton emplacement during transpression in brittle crust: new views from analogue experiments. *Geology* 26(12):1079–1082
- Benn K, Odonne F, Lee SKY, Darcovich K (2000) Analogue scale models of pluton emplacement during transpression in brittle and ductile crust. *Trans R Soc Edin Earth Sci* 91:111–121
- Berndt C, Skogly OP, Planke S, Eldholm O, Mjelde R (2000) High-velocity breakup-related sills in the Vøring Basin, off Norway. *J Geophys Res* 105(B12):28443–28454
- Bonini M, Sokoutis D, Mulugeta G, Boccaletti M, Corti G, Innocenti F, Manetti P, Mazzarini F (2001) Dynamics of magma emplacement in centrifuge models of continental extension with implications for flank volcanism. *Tectonics* 20(6):1053–1065
- Bons PD, Dougherty-Page J, Elburg MA (2001) Stepwise accumulation and ascent of magmas. *J Metamorphic Geol* 19(5):625–631
- Boutelier D, Schrank C, Cruden A (2008) Power-law viscous materials for analogue experiments: new data on the rheology of highly-filled silicone polymers. *J Struct Geol* 30(3):341–353. doi:10.1016/j.jsg.2007.10.009
- Branney MJ (1995) Downsag and extension at calderas: new perspectives on collapse geometries from ice-melt, mining, and volcanic subsidence. *Bull Volcanol* 57(5):303–318. doi:10.1007/bf00301290
- Breitkreuz C, Mock A (2004) Are laccolith complexes characteristic of transensional basin systems? Examples from the permo-carboniferous of Central Europe. *Geol Soc London Spec Pub* 234(1):13–31. doi:10.1144/gsl.sp.2004.234.01.03
- Brèqre C, Dupré J-C, Brémand F (2004) Calibration of a system of projection moiré for relief measuring: biomechanical applications. *Opt Las Engin* 41(2):241–260
- Brown RJ, Kavanagh J, Sparks RSJ, Tait M, Field M (2007) Mechanically disrupted and chemically weakened zones in segmented dike systems cause vent localization: evidence from kimberlite volcanic systems. *Geology* 35(9):815–818
- Bunger AP, Cruden AR (2011) Modeling the growth of laccoliths and large mafic sills: role of magma body forces. *J Geophys Res* 116(B2):B02203. doi:10.1029/2010jb007648
- Burchardt S, Walter TR (2010) Propagation, linkage, and interaction of caldera ring-faults: comparison between analogue experiments and caldera collapse at Miyakejima, Japan, in 2000. *Bull Volcanol* 72(3):297–308. doi:10.1007/s00445-009-0321-7
- Burchardt S, Tanner DC, Troll VR, Krumbholz M, Gustafsson LE (2011) Three-dimensional geometry of concentric intrusive sheet swarms in the Geitafell and the Dyrhöll volcanoes, eastern Iceland. *G3* 12(7):Q0AB09. doi:10.1029/2011gc003527
- Burchardt S, Tanner D, Krumbholz M (2012) The Slaufudalur pluton, southeast Iceland—an example of shallow magma emplacement by coupled cauldron subsidence and magmatic stoping. *Geol Soc Am Bull* 124(1–2):213–227. doi:10.1130/b30430.1
- Burchardt S, Troll VR, Mathieu L, Emeleus HC, Donaldson CH (2013) Ardnamurchan 3D cone-sheet architecture explained by a single elongate magma chamber. *Sci Rep* 3. doi:10.1038/srep02891. <http://www.nature.com/srep/2013/131008/srep02891/abs/srep02891.html-supplementary-information>
- Cagnard F, Brun J-P, Gapais D (2006) Modes of thickening of analogue weak lithospheres. *Tectonophysics* 421(1–2):145–160
- Cañón-Tapia E, Merle O (2006) Dyke nucleation and early growth from pressurized magma chambers: insights from analogue models. *J Volcanol Geotherm Res* 158(3–4):207–220. doi:10.1016/j.jvolgeores.2006.05.003
- Carter A, Wyk Van, de Vries B, Bachèlery P, Briole P (2006) Pits, rifts and slumps: the summit structure of Piton de la Fournaise. *Bull Volc* 67:741–756
- Chadwick WWJ, Howard KA (1991) The pattern of circumferential and radial eruptive fissures on the volcanoes of Fernandina and Isabela islands, Galápagos. *Bull Volcanol* 53(4):259–275. doi:10.1007/bf00414523
- Chadwick WWJ, Dieterich JH (1995) Mechanical modeling of circumferential and radial dike intrusion on Galápagos volcanoes. *J Volcanol Geotherm Res* 66:37–52
- Chadwick WWJ, Jonsson S, Geist DJ, Poland M, Johnson DJ, Batt S, Harpp KS, Ruiz A (2011) The May 2005 eruption of Fernandina volcano, Galápagos: the first circumferential dike intrusion observed by GPS and InSAR. *Bull Volcanol* 73(6):679–697. doi:10.1007/s00445-010-0433-0
- Chanceaux L, Menand T (2014) Solidification effects on sill formation: an experimental approach. *Earth Planet Sci Lett* 403:79–88. doi:10.1016/j.epsl.2014.06.018
- Chang W-L, Smith RB, Wicks C, Farrell JM, Puskas CM (2007) Accelerated uplift and magmatic intrusion of the Yellowstone caldera, 2004 to 2006. *Science* 318(5852):952–956. doi:10.1126/science.1146842

- Chevallier L, Woodford A (1999) Morpho-tectonics and mechanism of emplacement of the dolerite rings and sills of the western Karoo, South Africa. *South Afr J Geol* 102(1):43–54
- Clough CT, Maufe HB, Bailey EB (1909) The cauldron subsidence of glencoe and the associated igneous phenomena. *J Geol Soc London* 65:611–678
- Cobbold PR, Jackson MPA (1992) Gum rosin (colophony): a suitable material for thermomechanical modelling of the lithosphere. *Tectonophysics* 210(3–4):255–271. doi:[10.1016/0040-1951\(92\)90325-Z](https://doi.org/10.1016/0040-1951(92)90325-Z)
- Cole JW, Milner DM, Spinks KD (2005) Calderas and caldera structures: a review. *Earth-Sci Rev* 69(1–2):1–26. doi:[10.1016/j.earscirev.2004.06.004](https://doi.org/10.1016/j.earscirev.2004.06.004)
- Corry CE (1988) Laccoliths; mechanisms of emplacement and growth, vol 220. Geological Society of America Special Paper
- Corti G, Bonini M, Innocenti F, Manetti P, Mulugeta G (2001) Centrifuge models simulating magma emplacement during oblique rifting. *J Geodyn* 31:557–576
- Corti G, Bonini M, Conticelli S, Innocenti F, Manetti P, Sokoutis D (2003) Analogue modelling of continental extension: a review focused on the relations between the patterns of deformation and the presence of magma. *Earth-Sci Rev* 63(3–4):169–247
- Corti G, Moratti G, Sani F (2005) Relations between surface faulting and granite intrusions in analogue models of strike-slip deformation. *J Struct Geol* 27(9):1547–1562
- Crumpler LS, Head JW, Aubele JC (1996) Calderas on Mars: characteristics, structure, and associated flank deformation. *Geol Soc Lond Spec Pub* 110(1):307–348. doi:[10.1144/gsl.sp.1996.110.01.24](https://doi.org/10.1144/gsl.sp.1996.110.01.24)
- Dahm T (2000) Numerical simulations of the propagation path and the arrest of fluid-filled fractures in the Earth. *Geophys J Int* 141(3):623–638
- Daniels KA, Menand T (2015) An experimental investigation of dyke injection under regional extensional stress. *J Geophys Res: Solid Earth* JB011627. doi:[10.1002/2014jb011627](https://doi.org/10.1002/2014jb011627)
- Daniels KA, Kavanagh JL, Menand T, R. Stephen JS (2012) The shapes of dikes: evidence for the influence of cooling and inelastic deformation. *Geol Soc Am Bull* 124(7–8):1102–1112. doi:[10.1130/b30537.1](https://doi.org/10.1130/b30537.1)
- Daubrée A (1891) Recherches expérimentales sur le rôle possible des gaz à hautes températures doués de très fortes pressions et animés d'un mouvement fort rapide dans divers phénomènes géologiques. *Bulletin de la Société géologique de France* 19:313–354
- de Bremond d'Ars J, Arndt NT, Hallot E (2001) Analog experimental insights into the formation of magmatic sulfide deposits. *Earth Planet Sci Lett* 186(3–4):371–381. doi:[10.1016/S0012-821X\(01\)00254-0](https://doi.org/10.1016/S0012-821X(01)00254-0)
- de Saint-Blanquat M, Habert G, Horsman E, Morgan SS, Tikoff B, Launeau P, Gleizes G (2006) Mechanisms and duration of non-tectonically assisted magma emplacement in the upper crust: the Black Mesa pluton, Henry Mountains, Utah. *Tectonophysics* 428(1–4):1–31. doi:[10.1016/j.tecto.2006.07.014](https://doi.org/10.1016/j.tecto.2006.07.014)
- Delaney PT, Pollard DD (1981) Deformation of host rocks and flow of magma during growth of Minette dikes and breccia-bearing intrusions near Ship Rock, New Mexico, vol 1202. U.S. Geological Survey Professional Paper
- Delcamp A, Troll VR, Wyk de Vries B, Carracedo JC, Petronis MS, Pérez-Torrado FJ, Deegan FM (2012a) Dykes and structures of the NE rift of Tenerife, Canary Islands: a record of stabilisation and destabilisation of ocean island rift zones. *Bull Volcanol* 74(5):963–980. doi:[10.1007/s00445-012-0577-1](https://doi.org/10.1007/s00445-012-0577-1)
- Delcamp A, Wyk de Vries B, James MR, Gailler LS, Lebas E (2012b) Relationships between volcano gravitational spreading and magma intrusion. *Bull Volcanol* 74(3):743–765. doi:[10.1007/s00445-011-0558-9](https://doi.org/10.1007/s00445-011-0558-9)
- Di Giuseppe E, Funicello F, Corbi F, Ranalli G, Mojoli G (2009) Gelatins as rock analogs: a systematic study of their rheological and physical properties. *Tectonophysics* 473(3–4):391–403. doi:[10.1016/j.tecto.2009.03.012](https://doi.org/10.1016/j.tecto.2009.03.012)
- Dingwell DB, Bagdassarov NS, Bussov GY, Webb SL (1993) Magma rheology. In: Luth RW (ed) Experiments at high pressure and applications to the Earth's mantle, vol 21. Mineralogists Association of Canada Short Course Handbook, pp 131–196
- Dixon JM, Simpson DG (1987) Centrifuge modelling of laccolith intrusion. *J Struct Geol* 9:87–103
- Djabourov M, Leblond J, Papon P (1988a) Gelation of aqueous gelatin solutions. I. Structural investigation. *J Phys France* 49(2):319–332
- Djabourov M, Leblond J, Papon P (1988b) Gelation of aqueous gelatin solutions. II. Rheology of the sol-gel transition. *J Phys France* 49(2):333–343
- Donnadiou F, Kelfoun K, van Wyk de Vries B, Cecchi E, Merle O (2003) Digital photogrammetry as a tool in analogue modelling: applications to volcano instability. *J Volcanol Geotherm Res* 123(1–2):161–180. doi:[10.1016/s0377-0273\(03\)00034-9](https://doi.org/10.1016/s0377-0273(03)00034-9)
- Donnadiou F, Merle O (1998) Experiments on the indentation process during cryptodome intrusions: new insights into Mount St. Helens deformation. *Geology* 26(1):79–82
- Donnadiou F, Merle O (2001) Geometrical constraints of the 1980 Mount St. Helens intrusion from analogue models. *Geophys Res Lett* 28(4):639–642. doi:[10.1029/2000gl011869](https://doi.org/10.1029/2000gl011869)
- Druitt TH, Sparks RSJ (1984) On the formation of calderas during ignimbrite eruptions. *Nature* 310:679–681
- Dupré JC, Lagarde A (1997) Photoelastic analysis of a three-dimensional specimen by optical slicing and digital image processing. *Exp Mech* 37(4):393–397. doi:[10.1007/bf02317303](https://doi.org/10.1007/bf02317303)
- Dupré JC, Valle V, Jarny S, Monnet P (2010) Fringe analysis by phase shifting technique for birefringent fluid studies. *Opt Las Engin* 48(1):37–42. doi:[10.1016/j.optlaseng.2009.07.015](https://doi.org/10.1016/j.optlaseng.2009.07.015)
- Einstein A (1906) Eine neue Bestimmung der Moleküldimensionen. *Ann Phys* 324(2):289–306. doi:[10.1002/andp.19063240204](https://doi.org/10.1002/andp.19063240204)

- Ferré E, Galland O, Montanari D, Kalakay T (2012) Granite magma migration and emplacement along thrusts. *International J Earth Sci* 1–16. doi:[10.1007/s00531-012-0747-6](https://doi.org/10.1007/s00531-012-0747-6)
- Fiske RS, Jackson ED (1972) Orientation and growth of Hawaiian volcanic rifts: the effect of regional structure and gravitational stresses. *Proc R Soc Lond Ser A (Math Phys Sci)* 329(1578):299–326
- Fouqué F (1879) Santorin et ses éruptions. G. Masson
- Francis EH (1982) Magma and sediment—I. Emplacement mechanism of late Carboniferous tholeiite sills in northern Britain. *J Geol Soc London* 139(1):1–20
- Fukushima Y, Cayol V, Durand P, Massonnet D (2010) Evolution of magma conduits during the 1998–2000 eruptions of Piton de la Fournaise volcano, Réunion Island. *J Geophys Res* 115(B10):B10204. doi:[10.1029/2009jb007023](https://doi.org/10.1029/2009jb007023)
- Galerne CY, Galland O, Neumann ER, Planke S (2011) 3D relationships between sills and their feeders: evidence from the Golden Valley Sill Complex (Karoo Basin) and experimental modelling. *J Volcanol Geotherm Res* 202(3–4):189–199. doi:[10.1016/j.jvolgeores.2011.02.006](https://doi.org/10.1016/j.jvolgeores.2011.02.006)
- Galland O (2005) Interactions mécaniques entre la tectonique compressive et le magmatisme: expériences analogiques et exemple naturel. PhD thesis, Université de Rennes I, Mémoires de Géosciences-Rennes, n°116
- Galland O (2012) Experimental modelling of ground deformation associated with shallow magma intrusions. *Earth Planet Sci Lett* 317–318:145–156. doi:[10.1016/j.epsl.2011.10.017](https://doi.org/10.1016/j.epsl.2011.10.017)
- Galland O, Scheibert J (2013) Analytical model of surface uplift above axisymmetric flat-lying magma intrusions: implications for sill emplacement and geodesy. *J Volcanol Geotherm Res* 253:114–130. doi:[10.1016/j.jvolgeores.2012.12.006](https://doi.org/10.1016/j.jvolgeores.2012.12.006)
- Galland O, de Bremond d’Ars J, Cobbold PR, Hallot E (2003) Physical models of magmatic intrusion during thrusting. *Terra Nova* 15:405–409
- Galland O, Cobbold PR, Hallot E, de Bremond d’Ars J, Delavaud G (2006) Use of vegetable oil and silica powder for scale modelling of magmatic intrusion in a deforming brittle crust. *Earth Planet Sci Lett* 243:786–804
- Galland O, Cobbold PR, de Bremond d’Ars J, Hallot E (2007a) Rise and emplacement of magma during horizontal shortening of the brittle crust: Insights from experimental modeling. *J Geophys Res* 112. doi:[10.1029/2006JB004604](https://doi.org/10.1029/2006JB004604)
- Galland O, Hallot E, Cobbold PR, Ruffet G, de Bremond d’Ars J (2007b) Volcanism in a compressional Andean setting: a structural and geochronological study of Tromen volcano (Neuquén province, Argentina). *Tectonics* 26:TC4010. doi:[10.1029/2006TC002011](https://doi.org/10.1029/2006TC002011)
- Galland O, Cobbold PR, Hallot E, De Bremond d’Ars J (2008) Magma-controlled tectonics in compressional settings: insights from geological examples and experimental modelling. *Bolletino della Società Geologica Italiana* 127(2):205–208
- Galland O, Planke S, Neumann ER, Malthe-Sørenssen A (2009) Experimental modelling of shallow magma emplacement: application to saucer-shaped intrusions. *Earth Planet Sci Lett* 277(3–4):373–383
- Galland O, Burchardt S, Troll VR (2013) Volcanic and igneous plumbing systems: state-of-the-art and future developments. *Eos, Trans Am Geophys Union* 94(18):169. doi:[10.1002/2013eo180008](https://doi.org/10.1002/2013eo180008)
- Galland O, Burchardt S, Hallot E, Mourgues R, Bulois C (2014a) Dynamics of dikes versus cone sheets in volcanic systems. *J Geophys Res: Solid Earth* JB011059. doi:[10.1002/2014jb011059](https://doi.org/10.1002/2014jb011059)
- Galland O, Gisler GR, Haug ØT (2014b) Morphology and dynamics of explosive vents through cohesive rock formations. *J Geophys Res* 119. doi:[10.1002/2014JB011050](https://doi.org/10.1002/2014JB011050)
- Gernon TM, Gilbertson MA, Sparks RSJ, Field M (2008) Gas-fluidisation in an experimental tapered bed: insights into processes in diverging volcanic conduits. *J Volcanol Geotherm Res* 174(1–3):49–56. doi:[10.1016/j.jvolgeores.2007.12.034](https://doi.org/10.1016/j.jvolgeores.2007.12.034)
- Gernon TM, Gilbertson MA, Sparks RSJ, Field M (2009) The role of gas-fluidisation in the formation of massive volcanoclastic kimberlite. *Lithos* 112 Supplement 1(0):439–451. doi:[10.1016/j.lithos.2009.04.011](https://doi.org/10.1016/j.lithos.2009.04.011)
- Geshi N, Acocella V, Ruch J (2012) From structure- to erosion-controlled subsiding calderas: evidence thresholds and mechanics. *Bull Volcanol* 74(6):1553–1567. doi:[10.1007/s00445-012-0617-x](https://doi.org/10.1007/s00445-012-0617-x)
- Geshi N, Shimano T, Chiba T, Nakada S (2002) Caldera collapse during the 2000 eruption of Miyakejima Volcano, Japan. *Bull Volcanol* 64(1):55–68. doi:[10.1007/s00445-001-0184-z](https://doi.org/10.1007/s00445-001-0184-z)
- Geyer A, Folch A, Martí J (2006) Relationship between caldera collapse and magma chamber withdrawal: an experimental approach. *J Volcanol Geotherm Res* 157(4):375–386. doi:[10.1016/j.jvolgeores.2006.05.001](https://doi.org/10.1016/j.jvolgeores.2006.05.001)
- Geyer A, Martí J (2008) The new worldwide collapse caldera database (CCDB): a tool for studying and understanding caldera processes. *J Volcanol Geotherm Res* 175(3):334–354. doi:[10.1016/j.jvolgeores.2008.03.017](https://doi.org/10.1016/j.jvolgeores.2008.03.017)
- Gilbert GK (1877) Report on the geology of the Henry Mountains. U.S. Geographical and Geological Survey, Rocky Mountain Region (Powell)
- Girard G, van Wyk de Vries B (2005) The Managua Graben and Las Sierras-Masaya volcanic complex (Nicaragua); pull-apart localization by an intrusive complex: results from analogue modeling. *J Volcanol Geotherm Res* 144(1–4):37–57. doi:[10.1016/j.jvolgeores.2004.11.016](https://doi.org/10.1016/j.jvolgeores.2004.11.016)
- Goultly NR, Schofield N (2008) Implications of simple flexure theory for the formation of saucer-shaped sills. *J Struct Geol* 30(7):812–817
- Gressier JB, Mourgues R, Bodet L, Matthieu JY, Galland O, Cobbold PR (2010) Control of pore fluid pressure on depth of emplacement of magmatic sills: an experimental approach. *Tectonophysics* 489(1–4):1–13

- Grosse P, van Wyk de Vries B, Euillades PA, Kervyn M, Petrinovic IA (2012) Systematic morphometric characterization of volcanic edifices using digital elevation models. *Geomorphology* 136(1):114–131. doi:10.1016/j.geomorph.2011.06.001
- Grout FF (1945) Scale models of structures related to batholiths. *Am J Sci* 243A:260–284
- Haillemariam H, Mulugeta G (1998) Temperature-dependent rheology of bouncing putties used as rock analogs. *Tectonophysics* 294(1–2):131–141. doi:10.1016/S0040-1951(98)00124-3
- Hall J (1815) II. On the Vertical Position and Convolutions of certain Strata, and their relation with Granite. *Earth Environ Sci Trans R Soc Edinburgh* 7(1):79–108. doi:10.1017/S0080456800019268
- Hallot E, Auvray B, de Bremond d’Ars J, Martin H, Davy P (1994) New injection experiments in non-Newtonian fluids. *Terra Nova* 6(3):274–281. doi:10.1111/j.1365-3121.1994.tb00495.x
- Hallot E, Davy P, de Bremond d’Ars J, Auvray B, Martin H, Van Damme H (1996) Non-Newtonian effects during injection in partially crystallised magmas. *J Volcanol Geotherm Res* 71(1):31–44
- Hansen DM, Cartwright JA (2006a) Saucer-shaped sill with lobate morphology revealed by 3D seismic data: implications for resolving a shallow-level sill emplacement mechanism. *J Geol Soc London* 163:509–523
- Hansen DM, Cartwright JA (2006b) The three-dimensional geometry and growth of forced folds above saucer-shaped igneous sills. *J Struct Geol* 28(8):1520–1535
- Hansen DM, Redfern J, Federici F, di Biase D, Bertozzi G (2008) Miocene igneous activity in the Northern Subbasin, offshore Senegal, NW Africa. *Mar Pet Geol* 25(1):1–15
- Hansen VL, Olive A (2010) Artemis, Venus: the largest tectonomagmatic feature in the solar system? *Geology* 38(5):467–470
- Haug ØT, Galland O, Gisler GR (2013) Experimental modelling of fragmentation applied to volcanic explosions. *Earth Planet Sci Lett* 384:188–197. doi:10.1016/j.epsl.2013.10.004
- Hayashi Y, Morita Y (2003) An image of a magma intrusion process inferred from precise hypocentral migrations of the earthquake swarm east of the Izu Peninsula. *Geophys J Int* 153(1):159–174. doi:10.1046/j.1365-246X.2003.01892.x
- Hildreth W, Fierstein J (2000) Katmai volcanic cluster and the great eruption of 1912. *Geol Soc Am Bull* 112(10):1594–1620. doi:10.1130/0016-7606(2000)112<1594:kvcats>2.0.co;2
- Hildreth W, Wilson CJN (2007) Compositional Zoning of the Bishop Tuff. *J Petrol* 48(5):951–999. doi:10.1093/petrology/egm007
- Holland M, Urai JL, Martel S (2006) The internal structure of fault zones in basaltic sequences. *Earth Planet Sci Lett* 248(1–2):301–315
- Holohan EP, Troll VR, Walter TR, Munn S, McDonnell S, Shipton ZK (2005) Elliptical calderas in active tectonic settings: an experimental approach. *J Volcanol Geotherm Res* 144(1–4):119–136
- Holohan EP, Troll VR, van Wyk de Vries B, Walsh JJ, Walter TR (2008a) Unzipping Long Valley: an explanation for vent migration patterns during an elliptical ring fracture eruption. *Geology* 36(4):323–326. doi:10.1130/g24329a.1
- Holohan EP, Wyk de Vries B, Troll VR (2008b) Analogue models of caldera collapse in strike-slip tectonic regimes. *Bull Volcanol* 70(7):773–796. doi:10.1007/s00445-007-0166-x
- Holohan EP, Troll VR, Errington M, Donaldson CH, Nicoll GR, Emeleus CH (2009) The Southern Mountains Zone, Isle of Rum, Scotland: volcanic and sedimentary processes upon an uplifted and subsided magma chamber roof. *Geol Mag* 146(3):400
- Holohan EP, Schöpfer MPJ, Walsh JJ (2011) Mechanical and geometric controls on the structural evolution of pit crater and caldera subsidence. *J Geophys Res* 116(B7):B07202. doi:10.1029/2010jb008032
- Holohan EP, Walter TR, Schöpfer MPJ, Walsh JJ, van Wyk de Vries B, Troll VR (2013) Origins of oblique-slip faulting during caldera subsidence. *J Geophys Res* 118(4):1778–1794. doi:10.1002/jgrb.50057
- Hubbert MK (1937) Theory of scale models as applied to the study of geologic structures. *Geol Soc Am Bull* 48:1459–1520
- Hubbert MK, Willis DG (1957) Mechanics of hydraulic fracturing. In: Hubbert MK (ed) *Structural geology*. Hafner Publishing Company, New York, pp 175–190
- Hyndman DW, Alt D (1987) Radial dikes, laccoliths, and gelatin models. *J Geol* 95:763–774
- Ito G, Martel SJ (2002) Focusing of magma in the upper mantle through dike interaction. *J Geophys Res* 107(B10):2223. doi:10.1029/2001jb000251
- Jackson CAL, Schofield N, Golenkov B (2013) Geometry and controls on the development of igneous sill-related forced-folds: a 2D seismic reflection case study from offshore southern Australia. *Geol Soc Am Bull* 125(11–12):1874–1890
- Jackson MD, Pollard DD (1990) Flexure and faulting of sedimentary host rocks during growth of igneous domes, Henry Mountains, Utah. *J Struct Geol* 12(2):185–206
- Jaeger JC, Cook NGW, Zimmerman RW (2009) *Fundamentals of rock mechanics*. Blackwell Publishing Ltd., Oxford
- Jamtveit B, Svensen H, Podladchikov YY, Planke S (2004) Hydrothermal vent complexes associated with sill intrusions in sedimentary basins. In: Breiterkreuz C, Petford N (eds) *Physical geology of high-level magmatic systems*, vol 234. Geological Society, London, Special Publication, London, pp 233–241
- Johnson AM (1970) *Physical processes in geology*. Freeman, Cooper & Company, San Francisco
- Johnson AM, Pollard DD (1973) Mechanics of growth of some laccolithic intrusions in the Henry Mountains, Utah, I. Field observations, Gilbert’s model, physical properties and flow of the magma. *Tectonophysics* 18:261–309

- Kalakay TJ, John BE, Lageson DR (2001) Fault-controlled pluton emplacement in the Sevier fold-and-thrust belt of southern Montana. *J Struct Geol* 23:1151–1165
- Kavanagh JL, Menand T, Daniels KA (2013) Gelatine as a crustal analogue: determining elastic properties for modelling magmatic intrusions. *Tectonophysics* 582:101–111. doi:10.1016/j.tecto.2012.09.032
- Kavanagh JL, Menand T, Sparks RSJ (2006) An experimental investigation of sill formation and propagation in layered elastic media. *Earth Planet Sci Lett* 245(3–4): 799–813
- Kavanagh JL, Sparks RSJ (2011) Insights of dyke emplacement mechanics from detailed 3D dyke thickness datasets. *J Geol Soc London* 168(4):965–978. doi:10.1144/0016-76492010-137
- Kennedy B, Stix J, Vallance JW, Lavallée Y, Longpré M-A (2004) Controls on caldera structure: results from analogue sandbox modeling. *Geol Soc Am Bull* 116 (5–6):515–524. doi:10.1130/b25228.1
- Kennedy BM, Jellinek AM, Stix J (2008) Coupled caldera subsidence and stirring inferred from analogue models. *Nature Geo* 1(6):385–389
- Kennedy B, Wilcock J, Stix J (2012) Caldera resurgence during magma replenishment and rejuvenation at Valles and Lake City calderas. *Bull Volcanol* 74 (8):1833–1847. doi:10.1007/s00445-012-0641-x
- Kervyn M, Boone MN, van Wyk de Vries B, Lebas E, Cnudde V, Fontijn K, Jacobs P (2010) 3D imaging of volcano gravitational deformation by computerized X-ray micro-tomography. *Geosphere* 6(5):482–498. doi:10.1130/ges00564.1
- Kervyn M, Ernst GJJ, van Wyk de Vries B, Mathieu L, Jacobs P (2009) Volcano load control on dyke propagation and vent distribution: insights from analogue modeling. *J Geophys Res* 114(B3):B03401. doi:10.1029/2008jb005653
- Kettermann M, Urai JL (2015) Changes in structural style of normal faults due to failure mode transition: first results from excavated scale models. *J Struct Geol* 74:105–116. doi:10.1016/j.jsg.2015.02.013
- Klausen MB (2004) Geometry and mode of emplacement of the Thverartindur cone sheet swarm, SE Iceland. *J Volcanol Geotherm Res* 138(3–4):185–204
- Komuro H (1987) Experiments on cauldron formation: a polygonal cauldron and ring fractures. *J Volcanol Geotherm Res* 31(1–2):139–149
- Komuro H, Fujita Y, Kodama K (1984) Numerical and experimental models on the formation mechanism of collapse basins during the Green Tuff orogenesis of Japan. *Bull Volcanol* 47(3):649–666. doi:10.1007/bf01961233
- Koyaguchi T, Takada A (1994) An experimental study on the formation of composite intrusions from zoned magma chambers. *J Volcanol Geotherm Res* 59 (4):261–267. doi:10.1016/0377-0273(94)90081-7
- Lageson DR, Schmitt JG, Horton BK, Kalakay TJ, Burton BR (2001) Influence of Late Cretaceous magmatism on the Sevier orogenic wedge, western Montana. *Geology* 29:723–726
- Lavallée Y, Stix J, Kennedy B, Richer M, Longpré M-A (2004) Caldera subsidence in areas of variable topographic relief: results from analogue modeling. *J Volcanol Geotherm Res* 129(1–3):219–236. doi:10.1016/S0377-0273(03)00241-5
- Le Corvec N, Menand T, Lindsay J (2013) Interaction of ascending magma with pre-existing crustal fractures in monogenetic basaltic volcanism: an experimental approach. *J Geophys Res: Solid Earth* 118(3):968–984. doi:10.1002/jgrb.50142
- Leever KA, Gabrielsen RH, Sokoutis D, Willingshofer E (2011) The effect of convergence angle on the kinematic evolution of strain partitioning in transpressional brittle wedges: insight from analog modeling and high-resolution digital image analysis. *Tectonics* 30(2):TC2013. doi:10.1029/2010tc002823
- Leever KA, Galland O, Acocella V (2014) The Science behind laboratory-scale models of the earth. *Eos, Trans Am Geophys Union* 95(3):30. doi:10.1002/2014eo030008
- Legrand D, Calahorrano A, Guillier B, Rivera L, Ruiz M, Villagomez D, Yepes H (2002) Stress tensor analysis of the 1998–1999 tectonic swarm of northern Quito related to the volcanic swarm of Guagua Pichincha volcano, Ecuador. *Tectonophysics* 344(1–2):15–36
- Lipman PW (1984) The roots of ash flow calderas in western North America: windows into the tops of granitic batholiths. *J Geophys Res* 89(B10):8801–8841. doi:10.1029/JB089iB10p08801
- Lipman PW (1997) Subsidence of ash-flow calderas: relation to caldera size and magma-chamber geometry. *Bull Volcanol* 59(3):198–218. doi:10.1007/s00445050186
- Lipman PW, Moore JG, Swanson DA (1981) bulging of the north flank before the May 18 eruption: geodetic data. *US Geol Surv Prof Pap* 1250:143–156
- Lister JR, Kerr RC (1991) Fluid-mechanical models of crack propagation and their application to magma transport in dykes. *J Geophys Res* 96(B6):10049–10077
- Lambías EJ, Leanza HA, Galland O (2011) Agrupamiento volcánico Tromen-Tilhue. Paper presented at the Geología y recursos naturales de la Provincia del Neuquén, XVIII Congreso Geológico Argentino, Relatorio, Neuquén, Argentina
- Lohrmann J, Kukowski N, Adam J, Onken O (2003) The impact of analogue materials properties on the geometry, kinematics, and dynamics of convergent sand wedges. *J Struct Geol* 25:1691–1711
- Lorenz V, Kurszlauskis S (2007) Root zone processes in the phreatomagmatic pipe emplacement model and consequences for the evolution of maar-diatreme volcanoes. *J Volcanol Geotherm Res* 159(1–3):4–32. doi:10.1016/j.jvolgeores.2006.06.019
- Maaløe S (1987) The generation and shape of feeder dykes from mantle sources. *Contr Mineral and Petrol* 96(1):47–55. doi:10.1007/bf00375524
- Magee C, Jackson CAL, Schofield N (2014) Diachronous sub-volcanic intrusion along deep-water margins:

- insights from the Irish Rockall Basin. *Basin Res* 26 (1):85–105. doi:[10.1111/bre.12044](https://doi.org/10.1111/bre.12044)
- Maillet B (2013) A sedimentation device to produce uniform sand packs. *Tectonophysics* 593:85–94. doi:[10.1016/j.tecto.2013.02.028](https://doi.org/10.1016/j.tecto.2013.02.028)
- Malthe-Sørenssen A, Planke S, Svensen H, Jamtveit B (2004) Formation of saucer-shaped sills. In: Breithreuz C, Petford N (eds) *Physical geology of high-level magmatic systems*, vol 234. Geological Society of London Special Publication, London, pp 215–227
- Marques FO, Cobbold PR (2006) Effects of topography on the curvature of fold-and-thrust belts during shortening of a 2-layer model of continental lithosphere. *Tectonophysics* 415(1–4):65–80
- Martí J, Ablay GJ, Redshaw LT, Sparks RSJ (1994) Experimental studies of collapse calderas. *J Geol Soc London* 151(6):919–929. doi:[10.1144/gsjgs.151.6.0919](https://doi.org/10.1144/gsjgs.151.6.0919)
- Mastin LG, Pollard DD (1988) Surface deformation and shallow dike intrusion processes at Inyo craters, Long Valley, California. *J Geophys Res* 93(B11):13221–13235
- Mathieu L, van Wyk de Vries B (2009) Edifice and substrata deformation induced by intrusive complexes and gravitational loading in the Mull volcano (Scotland). *Bull Volcanol* 71(10):1133–1148. doi:[10.1007/s00445-009-0295-5](https://doi.org/10.1007/s00445-009-0295-5)
- Mathieu L, van Wyk de Vries B (2011) The impact of strike-slip, transtensional and transpressional fault zones on volcanoes. Part I: scaled experiments. *J Struct Geol* 33(5):907–917. doi:[10.1016/j.jsg.2011.03.002](https://doi.org/10.1016/j.jsg.2011.03.002)
- Mathieu L, van Wyk de Vries B, Holohan EP, Troll VR (2008) Dykes, cups, saucers and sills: analogue experiments on magma intrusion into brittle rocks. *Earth Planet Sci Lett* 271(1–4):1–13
- Mathieu L, van Wyk de Vries B, Pilato M, Troll VR (2011) The interaction between volcanoes and strike-slip, transtensional and transpressional fault zones: analogue models and natural examples. *J Struct Geol* 33(5):898–906. doi:[10.1016/j.jsg.2011.03.003](https://doi.org/10.1016/j.jsg.2011.03.003)
- Mazzarini F, Musumeci G, Montanari D, Corti G (2010) Relations between deformation and upper crustal magma emplacement in laboratory physical models. *Tectonophysics* 484(1–4):139–146
- Mazzini A, Nermoen A, Krotkiewski M, Podladchikov Y, Planke S, Svensen H (2009) Strike-slip faulting as a trigger mechanism for overpressure release through piercement structures. Implications for the Lusi mud volcano, Indonesia. *Mar Pet Geol* 26(9):1751–1765
- McBirney AR (1990) An historical note on the origin of calderas. *J Volcanol Geotherm Res* 42(3):303–306
- McCallum ME (1985) Experimental evidence for fluidization processes in breccia pipe formation. *Econ Geol* 80(6):1523–1543. doi:[10.2113/gsecongeo.80.6.1523](https://doi.org/10.2113/gsecongeo.80.6.1523)
- McClay KR (1976) The rheology of plasticine. *Tectonophysics* 33(1–2):T7–T15. doi:[10.1016/0040-1951\(76\)90047-0](https://doi.org/10.1016/0040-1951(76)90047-0)
- McGuire WJ, Pullen AD (1989) Location and orientation of eruptive fissures and feeder dykes at Mount Etna; influence of gravitational and regional tectonic stress regimes. *J Volcanol Geotherm Res* 38(3–4):325–344
- McLeod P, Tait S (1999) The growth of dykes from magma chambers. *J Volcanol Geotherm Res* 92:231–245
- Menand T (2008) The mechanics and dynamics of sills in layered elastic rocks and their implications for the growth of laccoliths and other igneous complexes. *Earth Planet Sci Lett* 267(1–2):93–99
- Menand T, Daniels KA, Benghiat P (2010) Dyke propagation and sill formation in a compressive tectonic environment. *J Geophys Res* 115. doi:[10.1029/2009JB006791](https://doi.org/10.1029/2009JB006791)
- Menand T, Tait S (2001) A phenomenological model for precursor volcanic eruptions. *Nature* 411:678–680
- Menand T, Tait S (2002) The propagation of a buoyant liquid-filled fissure from a source under constant pressure: an experimental approach. *J Geophys Res* 107(B11):2306
- Merle O, Borgia A (1996) Scaled experiments of volcanic spreading. *J Geophys Res* 101(B6):13, 805–813, 817
- Merle O, Donnadiou F (2000) Indentation of volcanic edifices by the ascending magma. *Geol Soc London Spec Pub* 174(1):43–53. doi:[10.1144/gsl.sp.1999.174.01.03](https://doi.org/10.1144/gsl.sp.1999.174.01.03)
- Merle O, Vendeville B (1995) Experimental modelling of thin-skinned shortening around magmatic intrusions. *Bull Volcanol* 57:33–43
- Michel J, Baumgartner L, Putlitz B, Schaltegger U, Ovtcharova M (2008) Incremental growth of the Patagonian Torres del Paine laccolith over 90 k.y. *Geology* 36(6):459–462. doi:[10.1130/g24546a.1](https://doi.org/10.1130/g24546a.1)
- Michon L, Massin F, Famin V, Ferrazzini V, Roul G (2011) Basaltic calderas: collapse dynamics, edifice deformation, and variations of magma withdrawal. *J Geophys Res* 116(B3):B03209. doi:[10.1029/2010jb007636](https://doi.org/10.1029/2010jb007636)
- Montanari D, Corti G, Sani F, Ventisette CD, Bonini M, Moratti G (2010a) Experimental investigation on granite emplacement during shortening. *Tectonophysics* 484(1–4):147–155
- Montanari D, Corti G, Simakin A (2010b) Magma chambers and localization of deformation during thrusting. *Terra Nova* 22(5):390–395. doi:[10.1111/j.1365-3121.2010.00962.x](https://doi.org/10.1111/j.1365-3121.2010.00962.x)
- Moore I, Kokelaar P (1998) Tectonically controlled piecemeal caldera collapse: a case study of Glencoe volcano, Scotland. *Geol Soc Am Bull* 110(11):1448–1466. doi:[10.1130/0016-7606\(1998\)110<1448:tcpcca>2.3.co;2](https://doi.org/10.1130/0016-7606(1998)110<1448:tcpcca>2.3.co;2)
- Morgan SS, Stanik A, Horsman E, Tikoff B, de Saint Blanquat M, Habert G (2008) Emplacement of multiple magma sheets and wall rock deformation: Trachyte Mesa intrusion, Henry Mountains, Utah. *J Struct Geol* 30(4):491–512. doi:[10.1016/j.jsg.2008.01.005](https://doi.org/10.1016/j.jsg.2008.01.005)
- Mori J, McKee C (1987) Outward-dipping ring-fault structure at Rabaul Caldera as shown by earthquake locations. *Science* 235(4785):193–195. doi:[10.1126/science.235.4785.193](https://doi.org/10.1126/science.235.4785.193)

- Mourgues R, Bureau D, Bodet L, Gay A, Gressier JB (2012) Formation of conical fractures in sedimentary basins: experiments involving pore fluids and implications for sandstone intrusion mechanisms. *Earth Planet Sci Lett* 313–314:67–78. doi:[10.1016/j.epsl.2011.10.029](https://doi.org/10.1016/j.epsl.2011.10.029)
- Mourgues R, Cobbold PR (2003) Some tectonic consequences of fluid overpressures and seepage forces as demonstrated by sandbox modelling. *Tectonophysics* 376:75–97
- Muller JR, Ito G, Martel SJ (2001) Effects of volcano loading on propagation in an elastic half-space. *J Geophys Res* 106:11101–11113
- Musumeci G, Mazzarini F, Corti G, Barsella M, Montanari D (2005) Magma emplacement in a thrust ramp anticline: the Gavorrano Granite (northern Apennine, Italy). *Tectonics* 24. doi:[10.1029/2005TC001801](https://doi.org/10.1029/2005TC001801)
- Nakamura K (1977) Volcanoes as possible indicators of tectonic stress orientation—principle and proposal. *J Volcanol Geotherm Res* 2(1):1–16
- Neremoen A, Galland O, Jettestuen E, Fristad K, Podladchikov YY, Svensen H, Malthe-Sørenssen A (2010a) Experimental and analytic modeling of piercement structures. *J Geophys Res* 115(B10):B10202. doi:[10.1029/2010jb007583](https://doi.org/10.1029/2010jb007583)
- Neremoen A, Raufaste C, deVilliers SD, Jettestuen E, Meakin P, Dysthe DK (2010b) Morphological transitions in partially gas-fluidized granular mixtures. *Phys Rev E* 81(6):061305
- Norini G, Acocella V (2011) Analogue modeling of flank instability at Mount Etna: understanding the driving factors. *Journal of Geophysical Research: Solid Earth* 116(B7):B07206. doi:[10.1029/2011jb008216](https://doi.org/10.1029/2011jb008216)
- O'Driscoll B, Troll VR, Reavy RJ, Turner P (2006) The Great Euclid intrusion of Ardnamurchan, Scotland: reevaluating the ring-dike concept. *Geology* 34(3):189–192
- Odé H (1957) Mechanical analysis of the dike pattern of the Spanish Peaks area, Colorado. *Geol Soc Am Bull* 68:567–576
- Pallister JS, McCausland WA, Jonsson S, Lu Z, Zahran HM, Hadidy SE, Aburukbah A, Stewart ICF, Lundgren PR, White RA, Moufti MRH (2010) Broad accommodation of rift-related extension recorded by dike intrusion in Saudi Arabia. *Nature Geosci* 3(10):705–712. doi:<http://www.nature.com/ngео/journal/v3/n10/abs/ngео966.html#supplementary-information>
- Panien M, Schreurs G, Pfiffner A (2006) Mechanical behaviour of granular materials used in analogue modelling: insights from grain characterisation, ring-shear tests and analogue experiments. *J Struct Geol* 28(9):1710–1724. doi:[10.1016/j.jsg.2006.05.004](https://doi.org/10.1016/j.jsg.2006.05.004)
- Paquet F, Dauteuil O, Hallot E, Moreau F (2007) Tectonics and magma dynamics coupling in a dike swarm of Iceland. *J Struct Geol* 29(9):1477–1493. doi:[10.1016/j.jsg.2007.06.001](https://doi.org/10.1016/j.jsg.2007.06.001)
- Phillips WJ (1974) The dynamic emplacement of cone sheets. *Tectonophysics* 24:69–84
- Pinel V, Jaupart C (2000) The effect of Edifice load on magma ascent beneath a volcano. *Philos Trans: Math Phys Eng Sci* 358(1770):1515–1532
- Pinel V, Jaupart C (2004) Magma storage and horizontal dyke injection beneath a volcanic edifice. *Earth Planet Sci Lett* 221(1–4):245–262
- Planke S, Rasmussen T, Rey SS, Myklebust R (2005) Seismic characteristics and distribution of volcanic intrusions and hydrothermal vent complexes in the Vøring and Møre basins. In: Doré AG, Vining BA (eds) *Proceedings of 6th Petroleum Geology Conference*. Geological Society, London
- Pollard DD (1987) Elementary fracture mechanics applied to the structural interpretation of dikes. In: Halls HC, Fahrig WF (eds) *Mafic dyke swarms*, vol 34. Geological Association of Canada Special Paper, pp 5–24
- Pollard DD, Holzhausen G (1979) On the mechanical interaction between a fluid-filled fracture and the Earth's surface. *Tectonophysics* 53(1–2):27–57
- Pollard DD, Johnson AM (1973) Mechanics of growth of some laccolithic intrusions in the Henry Mountains, Utah, II. Bending and failure of overburden layers and sill formation. *Tectonophysics* 18:311–354
- Polteau S, Ferré EC, Planke S, Neumann E-R, Chevalier L (2008a) How are saucer-shaped sills emplaced? Constraints from the Golden Valley Sill, South Africa. *J Geophys Res* 113
- Polteau S, Mazzini A, Galland O, Planke S, Malthe-Sørenssen A (2008b) Saucer-shaped intrusions: occurrences, emplacement and implications. *Earth Planet Sci Lett* 266(1–2):195–204
- Ramberg H (1967) Gravity, deformation and the Earth's crust as studied by centrifuge models. Academic Press, New York
- Ramberg H (ed) (1970) Model studies in relation to intrusion of plutonic bodies, vol 2. Mechanism of igneous intrusion. *Geol J Spec Iss*
- Ramberg H (1981) Gravity, deformation and the Earth's crust. Academic Press, New York
- Ramos O, Altshuler E, Måløy KJ (2009) Avalanche prediction in a self-organized pile of beads. *Phys Rev Lett* 102(7):078701
- Reber JE, Galland O, Cobbold PR, Carlier Le, de Veslud C (2013) Experimental study of sheath fold development around a weak inclusion in a mechanically layered matrix. *Tectonophysics* 586:130–144. doi:[10.1016/j.tecto.2012.11.013](https://doi.org/10.1016/j.tecto.2012.11.013)
- Reddish DJ, Whittaker BN (1989) Subsidence: occurrence, prediction and control, vol 56. Elsevier, Amsterdam
- Richards RJ, Mark R (1966) Gelatin models for photoelastic analysis of gravity structures. *Exp Mech* 6(1):30–38. doi:[10.1007/bf02327111](https://doi.org/10.1007/bf02327111)
- Richey JE (1932) The tertiary ring complex of Slieve Gullion (Ireland), with petrological notes by Herbert Henry Thomas. *Q J Geol Soc* 88(1–4):776–849
- Richey JE, Thomas HH, Radley EG, Dixon BE (1930) The geology of Ardnamurchan, North-West Mull and Coll: a description of Sheet 51 and part of sheet 52 of

- the Geological Map. Printed under the authority of HM Stationery Office
- Rivalta E (2010) Evidence that coupling to magma chambers controls the volume history and velocity of laterally propagating intrusions. *J Geophys Res* 115 (B7):B07203. doi:[10.1029/2009jb006922](https://doi.org/10.1029/2009jb006922)
- Rivalta E, Böttlinger M, Dahm T (2005) Buoyancy-driven fracture ascent: experiments in layered gelatine. *J Volcanol Geotherm Res* 144:273–285
- Rivalta E, Dahm T (2006) Acceleration of buoyancy-driven fractures and magmatic dikes beneath the free surface. *Geophys J Int* 166(3):1424–1439. doi:[10.1111/j.1365-246X.2006.02962.x](https://doi.org/10.1111/j.1365-246X.2006.02962.x)
- Rocchi S, Westerman DS, Dini A, Innocenti F, Tonarini S (2002) Two-stage growth of laccoliths at Elba Island, Italy. *Geology* 30(11):983–986. doi:[10.1130/0091-7613\(2002\)030<0983:tsgola>2.0.co;2](https://doi.org/10.1130/0091-7613(2002)030<0983:tsgola>2.0.co;2)
- Roche O, Druitt TH (2001) Onset of caldera collapse during ignimbrite eruptions. *Earth Planet Sci Lett* 191 (3–4):191–202. doi:[10.1016/S0012-821X\(01\)00428-9](https://doi.org/10.1016/S0012-821X(01)00428-9)
- Roche O, Druitt TH, Merle O (2000) Experimental study of caldera formation. *J Geophys Res: Solid Earth* 105 (B1):395–416. doi:[10.1029/1999jb900298](https://doi.org/10.1029/1999jb900298)
- Roche O, van Wyk de Vries B, Druitt TH (2001) Sub-surface structures and collapse mechanisms of summit pit craters. *J Volcanol Geotherm Res* 105(1–2):1–18. doi:[10.1016/S0377-0273\(00\)00248-1](https://doi.org/10.1016/S0377-0273(00)00248-1)
- Rodriguez Monreal F, Villar HJ, Baudino R, Delpino D, Zencich S (2009) Modeling an atypical petroleum system: a case study of hydrocarbon generation, migration and accumulation related to igneous intrusions in the Neuquén Basin, Argentina. *Mar Pet Geol* 26(4):590–605. doi:[10.1016/j.marpetgeo.2009.01.005](https://doi.org/10.1016/j.marpetgeo.2009.01.005)
- Román-Berdiel T (1999) Geometry of granite emplacement in the upper crust: contribution of analogue modelling. In: Castro A, Fernández C, Vignerresse JL (eds) *Understanding granites: integrating new and classical techniques*, vol 174. Geological Society of London, Special Publications, London, pp 77–94
- Román-Berdiel T, Gapais D, Brun J-P (1995) Analogue models of laccolith formation. *J Struct Geol* 17 (9):1337–1346
- Román-Berdiel T, Gapais D, Brun JP (1997) Granite intrusion along strike-slip zones in experiment and nature. *Am J Sci* 297(6):651–678. doi:[10.2475/ajs.297.6.651](https://doi.org/10.2475/ajs.297.6.651)
- Rosenau M, Nerlich R, Brune S, Oncken O (2010) Experimental insights into the scaling and variability of local tsunamis triggered by giant subduction megathrust earthquakes. *J Geophys Res* 115(B9):B09314. doi:[10.1029/2009jb007100](https://doi.org/10.1029/2009jb007100)
- Ross PS, White JDL, Zimanowski B, Büttner R (2008a) Multiphase flow above explosion sites in debris-filled volcanic vents: insights from analogue experiments. *J Volcanol Geotherm Res* 178(1):104–112. doi:[10.1016/j.jvolgeores.2008.01.013](https://doi.org/10.1016/j.jvolgeores.2008.01.013)
- Ross PS, White JDL, Zimanowski B, Büttner R (2008b) Rapid injection of particles and gas into non-fluidized granular material, and some volcanological implications. *Bull Volcanol* 70(10):1151–1168. doi:[10.1007/s00445-008-0230-1](https://doi.org/10.1007/s00445-008-0230-1)
- Rossello EA, Cobbold PR, Diraison M, Arnaud N (2002) Auca Mahuida (Neuquén basin, Argentina): a quaternary shield volcano on a hydrocarbon-producing substrate. Paper presented at the 5th ISAG, Extended Abstracts, Toulouse
- Rossi D, Storti F (2003) New artificial granular materials for analogue laboratory experiments: aluminium and siliceous microspheres. *J Struct Geol* 25:1893–1899
- Rubin AM (1995) Propagation of magma-filled cracks. *Annu Rev Earth Planet Sci* 23:287–336
- Ruch J, Acocella V, Geshi N, Nobile A, Corbi F (2012) Kinematic analysis of vertical collapse on volcanoes using experimental models time series. *J Geophys Res: Solid Earth* 117(B7):B07301. doi:[10.1029/2012jb009229](https://doi.org/10.1029/2012jb009229)
- Ruzicka B, Zaccarelli E (2011) A fresh look at the Laponite phase diagram. *Soft Matter* 7(4):1268–1286
- Rymer H, Wyk Van, de Vries B, Stix J (1998) Pit Crater structure and persistent volcanic activity at Masaya, Nicaragua. *Bull Volcanol* 59:345–355
- Sanford AR (1959) Analytical and experimental study of simple geologic structures. *Geol Soc Am Bull* 70 (1):19–52. doi:[10.1130/0016-7606\(1959\)70\[19:aaesos\]2.0.co;2](https://doi.org/10.1130/0016-7606(1959)70[19:aaesos]2.0.co;2)
- Scaillet B, Holtz F, Pichavant M (1997) Rheological Properties of Granitic Magmas in Their Crystallization Range. In: Bouchez JL, Hutton DHW, Stephens WE (eds) *Granite: from segregation of melt to emplacement fabrics*, vol 8. Petrology and structural geology. Springer, Netherlands, pp 11–29. doi:[10.1007/978-94-017-1717-5_2](https://doi.org/10.1007/978-94-017-1717-5_2)
- Schellart WP (2000) Shear test results for cohesion and friction coefficients for different materials: scaling implications for their usage in analogue modelling. *Tectonophysics* 324:1–16
- Schellart WP (2011) Rheology and density of glucose syrup and honey: determining their suitability for usage in analogue and fluid dynamic models of geological processes. *J Struct Geol* 33(6):1079–1088. doi:[10.1016/j.jsg.2011.03.013](https://doi.org/10.1016/j.jsg.2011.03.013)
- Schirnick C, van den Bogaard P, Schmincke H-U (1999) Cone sheet formation and intrusive growth of an oceanic island—the Miocene Tejada complex on Gran Canaria (Canary Islands). *Geology* 27(3):207–210. doi:[10.1130/0091-7613\(1999\)027<0207:csfaig>2.3.co;2](https://doi.org/10.1130/0091-7613(1999)027<0207:csfaig>2.3.co;2)
- Schofield N, Stevenson CT, Reston T (2010) Magma fingers and host rock fluidization in the emplacement of sills. *Geology* 38(1):63–66. doi:[10.1130/g30142.1](https://doi.org/10.1130/g30142.1)
- Schreurs G, Buitter SJH, Boutelier D, Corti G, Costa E, Cruden AR, Daniel JM, Hoth S, Koyi HA, Kukowski N, Lohrmann J, Ravaglia A, Schlichte RW, Withjack MO, Yamada Y, Cavozi C, Del Ventisette C, Brady JAE, Hoffmann-Rothe A, Mengus JM, Montanari D, Nilforoushan F (2006) Analogue benchmarks of shortening and extension experiments. *Geol Soc London Spec Pub* 253(1):1–27. doi:[10.1144/gsl.sp.2006.253.01.01](https://doi.org/10.1144/gsl.sp.2006.253.01.01)

- Schultz RA (1996) Relative scale and the strength and deformability of rock masses. *J Struct Geol* 18 (9):1139–1149. doi:[10.1016/0191-8141\(96\)00045-4](https://doi.org/10.1016/0191-8141(96)00045-4)
- Schweiger A, Zimmermann I (1999) A new approach for the measurement of the tensile strength of powders. *Powder Technol* 101(1):7–15. doi:[10.1016/S0032-5910\(98\)00117-X](https://doi.org/10.1016/S0032-5910(98)00117-X)
- Sibson RH (2003) Brittle-failure controls on maximum sustainable overpressure in different tectonic regimes. *AAPG Bull* 87(6):901–908
- Sigmundsson F, Hreinsdóttir S, Hooper A, Arnadóttir T, Pedersen R, Roberts MJ, Óskarsson N, Auriac A, Decriem J, Einarsson P, Geirsson H, Hensch M, Ófeigsson BG, Sturkell E, Sveinbjörnsson H, Feigl KL (2010) Intrusion triggering of the 2010 Eyjafjallajökull explosive eruption. *Nature* 468(7322):426–430. doi:[10.1038/nature09558](https://doi.org/10.1038/nature09558)
- Smith RL, Bailey RA (1968) Resurgent Cauldrons. *Geological Society of America Memoirs* 116:613–662. doi:[10.1130/MEM116-p613](https://doi.org/10.1130/MEM116-p613)
- Sparks RSJ (1988) Petrology and geochemistry of the Loch Ba ring-dyke, Mull (N.W. Scotland): an example of the extreme differentiation of tholeiitic magmas. *Contr Mineral and Petrol* 100(4):446–461. doi:[10.1007/bf00371374](https://doi.org/10.1007/bf00371374)
- Sparks RSJ, Baker L, Brown RJ, Field M, Schumacher J, Stripp G, Walters A (2006) Dynamical constraints on kimberlite volcanism. *J Volcanol Geotherm Res* 155 (1–2):18–48. doi:[10.1016/j.jvolgeores.2006.02.010](https://doi.org/10.1016/j.jvolgeores.2006.02.010)
- Stix J, Kobayashi T (2008) Magma dynamics and collapse mechanisms during four historic caldera-forming events. *J Geophys Res: Solid Earth* 113(B9):B09205. doi:[10.1029/2007jb005073](https://doi.org/10.1029/2007jb005073)
- Svensen H, Corfu F, Polteau S, Hammer Ø, Planke S (2012) Rapid magma emplacement in the Karoo Large Igneous Province. *Earth Planet Sci Lett* 325–326:1–9. doi:[10.1016/j.epsl.2012.01.015](https://doi.org/10.1016/j.epsl.2012.01.015)
- Svensen H, Jamtveit B, Planke S, Chevallier L (2006) Structure and evolution of hydrothermal vent complexes in the Karoo Basin, South Africa. *J Geol Soc London* 163:671–682
- Svensen H, Planke S, Chevallier L, Malthe-Sørenssen A, Corfu F, Jamtveit B (2007) Hydrothermal venting of greenhouse gases triggering Early Jurassic global warming. *Earth Planet Sci Lett* 256(3–4):554–566
- Svensen H, Planke S, Malthe-Sørenssen A, Jamtveit B, Myklebust R, Eldem TR, Rey SS (2004) Release of methane from a volcanic basin as a mechanism for initial Eocene global warming. *Nature* 429 (6991):542–545
- Taisne B, Jaupart C (2011) Magma expansion and fragmentation in a propagating dyke. *Earth Planet Sci Lett* 301(1–2):146–152. doi:[10.1016/j.epsl.2010.10.038](https://doi.org/10.1016/j.epsl.2010.10.038)
- Taisne B, Tait S (2009) Eruption versus intrusion? Arrest of propagation of constant volume, buoyant, liquid-filled cracks in an elastic, brittle host. *J Geophys Res: Solid Earth* 114(B6):B06202. doi:[10.1029/2009jb006297](https://doi.org/10.1029/2009jb006297)
- Taisne B, Tait S (2011) Effect of solidification on a propagating dike. *J Geophys Res: Solid Earth* 116 (B1):B01206. doi:[10.1029/2009jb007058](https://doi.org/10.1029/2009jb007058)
- Taisne B, Tait S, Jaupart C (2011) Conditions for the arrest of a vertical propagating dyke. *Bull Volcanol* 73 (2):191–204. doi:[10.1007/s00445-010-0440-1](https://doi.org/10.1007/s00445-010-0440-1)
- Takada A (1990) Experimental study on propagation of liquid-filled crack in gelatin: shape and velocity in hydrostatic stress condition. *J Geophys Res* 95 (B6):8471–8481
- Takada A (1994a) Accumulation of magma in space and time by crack interaction. In: Michael PR (ed) *International geophysics*, vol 57. Academic Press, New York, pp 241–257. doi:[10.1016/S0074-6142\(09\)60099-1](https://doi.org/10.1016/S0074-6142(09)60099-1)
- Takada A (1994b) Development of a subvolcanic structure by the interaction of liquid-filled cracks. *J Volc Geothermal Res* 62:207–224
- Takada A (1999) Variations in magma supply and magma partitioning: the role of tectonic settings. *J Volcanol Geotherm Res* 93(1–2):93–110. doi:[10.1016/S0377-0273\(99\)00082-7](https://doi.org/10.1016/S0377-0273(99)00082-7)
- ten Grotenhuis SM, Piazzolo S, Pakula T, Passchier CW, Bons PD (2002) Are polymers suitable rock analogs? *Tectonophysics* 350(1):35–47. doi:[10.1016/S0040-1951\(02\)00080-X](https://doi.org/10.1016/S0040-1951(02)00080-X)
- Thomson K (2007) Determining magma flow in sills, dykes and laccoliths and their implications for sill emplacement mechanisms. *Bull Volcanol* 70(2):183–201
- Thomson K, Hutton D (2004) Geometry and growth of sill complexes: insights using 3D seismic from the North Rockall Trough. *Bull Volcanol* 66(4):364–375
- Tibaldi A (1995) Morphology of pyroclastic cones and tectonics. *J Geophys Res: Solid Earth* 100 (B12):24521–24535. doi:[10.1029/95jb02250](https://doi.org/10.1029/95jb02250)
- Tibaldi A (2005) Volcanism in compressional tectonic settings: is it possible? *Geophys Res Lett* 32(L06309)
- Tibaldi A, Bonali FL, Corazzato C (2014) The diverging volcanic rift system. *Tectonophysics* 611:94–113. doi:[10.1016/j.tecto.2013.11.023](https://doi.org/10.1016/j.tecto.2013.11.023)
- Tibaldi A, Pasquarè F, Tormey D (2010) Volcanism in Reverse and Strike-Slip Fault Settings. In: Cloetingh S, Negendank J (eds) *New frontiers in integrated solid earth sciences*. Springer, Netherlands, pp 315–348. doi:[10.1007/978-90-481-2737-5_9](https://doi.org/10.1007/978-90-481-2737-5_9)
- Tripanera D, Acoella V, Ruch J (2014) Dike-induced contraction along oceanic and continental divergent plate boundaries. *Geophys Res Lett* GL061570. doi:[10.1002/2014gl061570](https://doi.org/10.1002/2014gl061570)
- Troll VR, Walter TR, Schmincke HU (2002) Cyclic caldera collapse: piston or piecemeal subsidence? Field and experimental evidence. *Geology* 30(2):135–138
- Trude J, Cartwright J, Davies RJ, Smallwood J (2003) New technique for dating igneous sills. *Geology* 31 (9):813–816
- Turcotte DL, Schubert G (2002) *Geodynamics –*, 2nd edn. Cambridge University Press, Cambridge

- van Wyk de Vries B, Marques A, Herrera R, Granjas JL, llanes P, Delcamp (2014) Craters of elevation revisited: forced folds, bulges and uplift of volcanoes (2014) *Bull Volcanol*. doi:[10.1007/s00445-014-0875-x](https://doi.org/10.1007/s00445-014-0875-x)
- Verbeek R (1884) The Krakatoa eruption. *Nature* 30:10–15
- Walker GL, Skelhorn RR (1966) Some associations of acid and basic igneous rocks. *Earth-Sci Rev* 2:93–109. doi:[10.1016/0012-8252\(66\)90024-9](https://doi.org/10.1016/0012-8252(66)90024-9)
- Walker GPL (1999) Volcanic rift zones and their intrusion swarms. *J Volcanol Geotherm Res* 94(1–4):21–34
- Walter TR, Troll VR (2001) Formation of caldera periphery faults: an experimental study. *Bull Volcanol* 63:191–203
- Walter TR, Troll VR (2003) Experiments on rift zone evolution in unstable volcanic edifices. *J Volcanol Geotherm Res* 127(1–2):107–120
- Walters AL, Phillips JC, Brown RJ, Field M, Gernon T, Stripp G, Sparks RSJ (2006) The role of fluidisation in the formation of volcanoclastic kimberlite: grain size observations and experimental investigation. *J Volcanol Geotherm Res* 155(1–2):119–137. doi:[10.1016/j.jvolgeores.2006.02.005](https://doi.org/10.1016/j.jvolgeores.2006.02.005)
- Watanabe T, Masuyama T, Nagaoka N, Tahara T (2002) Analog experiments on magma-filled cracks: competition between external stresses and internal pressure. *Earth Planets Space* 54:1247–1261
- Weijermars R (1986) Flow behaviour and physical chemistry of bouncing putties and related polymers in view of tectonic laboratory applications. *Tectonophysics* 124(3–4):325–358. doi:[10.1016/0040-1951\(86\)90208-8](https://doi.org/10.1016/0040-1951(86)90208-8)
- Westerman DS, Dini A, Innocenti F, Rocchi S (2004) Rise and fall of a nested Christmas-tree laccolith complex, Elba Island, Italy. *Geol Soc London Spec Pub* 234(1):195–213. doi:[10.1144/gsl.sp.2004.234.01.12](https://doi.org/10.1144/gsl.sp.2004.234.01.12)
- White DJ, Take WA, Bolton MD (2003) Soil deformation measurement using particle image velocimetry (PIV) and photogrammetry. *Géotechnique* 53(7):619–631. doi:[10.1680/geot.2003.53.7.619](https://doi.org/10.1680/geot.2003.53.7.619)
- White JDL, Ross PS (2011) Maar-diatreme volcanoes: a review. *J Volcanol Geotherm Res* 201(1–4):1–29. doi:[10.1016/j.jvolgeores.2011.01.010](https://doi.org/10.1016/j.jvolgeores.2011.01.010)
- White RS, Drew J, Martens HR, Key J, Soosalu H, Jakobsdóttir SS (2011) Dynamics of dyke intrusion in the mid-crust of Iceland. *Earth Planet Sci Lett* 304(3–4):300–312. doi:[10.1016/j.epsl.2011.02.038](https://doi.org/10.1016/j.epsl.2011.02.038)
- Williams H (1941) Calderas and their origin 25:239–346
- Wilson CJN, Hildreth W (1997) The Bishop Tuff: new insights from eruptive stratigraphy. *J Geol* 105(4):407–440
- Witte J, Bonora M, Carbone C, Oncken O (2012) Fracture evolution in oil-producing sills of the Rio Grande Valley, northern Neuquén Basin, Argentina. *AAPG Bull* 96(7):1253–1277. doi:[10.1306/10181110152](https://doi.org/10.1306/10181110152)
- Woolsey TS, McCallum ME, Schumm SA (1975) Modeling of diatreme emplacement by fluidization. *Phys Chem Earth* 9:29–42
- Wright TJ, Ebinger C, Biggs J, Ayele A, Yirgu G, Keir D, Stork A (2006) Magma-maintained rift segmentation at continental rupture in the 2005 Afar dyking episode. *Nature* 442(7100):291–294. doi:[10.1038/nature04978](https://doi.org/10.1038/nature04978)
- Závada P, Dedecek P, Mach K, Lexa O, Potuzák M (2011) Emplacement dynamics of phonolite magma into maar-diatreme structures—correlation of field, thermal modeling and AMS analogue modeling data. *J Volcanol Geotherm Res* 201(1–4):210–226
- Závada P, Kratinová Z, Kusbach V, Hrouda F (2006) Analogue modeling of AMS development during emplacement of shallow level volcanic bodies (Extrusive Domes and Laccoliths). *Geolines* 206(5):136–137
- Závada P, Kratinová Z, Kusbach V, Schulmann K (2009) Internal fabric development in complex lava domes. *Tectonophysics* 466(1–2):101–113. doi:[10.1016/j.tecto.2008.07.005](https://doi.org/10.1016/j.tecto.2008.07.005)

Catastrophic Collapse Features in Volcanic Terrains: Styles and Links to Subvolcanic Magma Systems

David B. Hacker, Peter D. Rowley and Robert F. Biek

Abstract

Catastrophic structural slope failures of large volcanic landforms, notably volcanoes, are among the most sudden agents of landscape change, producing large-scale landslide features. Some of these volcanic landslides rank among the largest and most devastating natural hazards encountered on Earth. Following the 1980 landslide and directed blast that destroyed the northern flank of Mount St. Helens, there has been an increased awareness and study of flank and sector collapses of stratovolcanoes worldwide. Collapse features have now been observed on hundreds of volcanoes and it is now widely accepted that such events are common recurrent phenomena during the evolution of many volcanoes. Although most studies of structural failure have concentrated on volcanoes, it is important to note that two other volcanic landforms in volcanic terrains have experienced collapse events at scales equivalent to, and sometimes exceeding, the scale of landslides on volcanoes. These include slope failures from intrusive laccoliths and from partial collapse of volcanic fields. Volcanic landslides from these less familiar sources share many morphological and textural similarities as landslides from volcanoes and could be mistaken as a volcano-derived deposit. Subvolcanic magma systems play an integral part in the collapse process from these three volcanic source types (volcanoes, laccoliths, and volcanic fields) by creating elevated landforms with steep slopes, aiding in destabilization of

D.B. Hacker (✉)
Department of Geology, Kent State University, Kent,
OH, USA
e-mail: dhacker@kent.edu

P.D. Rowley
Geologic Mapping Inc., New Harmony, UT, USA

R.F. Biek
Utah Geological Survey, Salt Lake City, UT, USA

the slopes, and often triggering a slope failure. We therefore introduce a new concept that volcanic collapse landslide features should be viewed as involving multiple sources within volcanic terrains instead of from only volcanoes.

1 Introduction

Volcanic terrains are the surface expressions of magma reaching the surface of our planet from the interior, often through a complex subsurface plumbing system. These dynamic terrains consist of a great variety of volcanic rock types, from lavas and explosive pyroclastics to secondary epiclastic deposits. They also contain a wide variety of volcanic landforms, consisting largely of volcanoes of diverse shapes and forms, including calderas, lava domes, outflow tuff plains, and lava plateaus. Also present is a pervasive array of shallow subvolcanic intrusions of dikes, sills, and laccoliths, many of which were themselves conduits for explosive or effusive volcanic eruptions. Prior to significant buildout of volcanic landforms, early ash deposited in lake, stream, and marine environments may in time break down into soft expansive clays and therefore result in a weak foundation for the later rapid and voluminous accumulation of heavy volcanic deposits on this foundation. During the evolution of a volcanic field, its growth (constructive buildup phases) of surface volcanic features is constantly under attack by gravity and erosion that acts to reduce them (destructive phases). As part of this interplay of volcanic growth and erosion, elevated volcanoes have frequently been punctuated by catastrophic gravitational collapse of their edifices, producing volcanic landslides that moved large rock masses kilometers to hundreds of kilometers from their source.

Interest in volcanic landslides took off over the past few decades following the spectacular 1980 sector collapse and eruption of Mount St. Helens volcano (Fig. 1). Subsequent studies have recognized collapse events on more than 400

volcanoes worldwide (Siebert et al. 2006). Terrestrial volcano collapses can produce large volumes (greater than several km³) of rock material that move downslope at high velocities (greater than 100 m/s) and travel distances sometimes exceeding 50 km, forming deposits spread over areas of hundreds to thousands of km² (Ui 1983; Siebert 1984, 1992, 1996, 2002; Schuster and Crandell 1984; Ui et al. 2000; van Wyk de Vries and Davies 2015). Large sector collapses have occurred at a rate of approximately 4–5 per century over the last 500 years, a rate roughly double that of caldera collapse following magma chamber evacuation during the same interval (Siebert et al. 2010). Discovery of submarine volcanic and non-volcanic landslides has shown that they are even larger, with volumes of as much as 5000 km³, travel distances exceeding 200 km, and have depositional areas of as much as 23,000 km² (Moore et al. 1989, 1994; Carracedo 1994). Similarly, volcano collapses are not confined to Earth, but have also been discovered on both Mars (Crumpler et al. 1996) and Venus (Bulmer and Guest 1996).

However, we are now becoming aware that not all volcanic landslides necessarily originate only from collapse of volcanoes. Intrusive laccoliths, and even large portions of volcanic fields have experienced structural failure in the past leading to catastrophic volcanic landslides and initiation of volcanic eruptions (Hacker 1998; Hacker et al. 2007; Rowley et al. 2006; Biek et al. 2009, 2015). Batholiths beneath volcanic fields can produce the rapid and considerable relief necessary for slope failure, whether by feeding shallow, higher level laccoliths, or by uplifting and tilting (magma inflation) a large portion of a volcanic field itself. We emphasize here that recognition of ancient landslides in a



Fig. 1 North Fork Toutle River valley, Mount St. Helens, Washington. A scientist stands on one of the many hummocks that form the chaotic surface of a massive volcanic landslide deposit in the upper North Fork Toutle River valley below Mount St. Helens volcano (10 km in distance). Before the landslide and eruption on

May 18, 1980, a forest grew on this part of the valley floor. The landslide deposit extends about 22 km from the volcano and buries the river valley to an average depth of about 45 m. In places, the deposit is nearly 200 m thick. The landslide covers an area of about 60 km². Photograph by L. Topinka in 1981, courtesy of the USGS

volcanic terrain need not automatically be attributed to collapse of an individual volcano, especially in the absence of a documented edifice, but could also have originated from alternative volcanic causes whose modern hazard assessment is still in its infancy.

The growing need for better understanding of landslide processes operating in volcanic terrains stems from the societal need of protecting human populations from these rare but high impact hazards. Volcanic landslide generation poses a considerable hazard for inhabited areas around volcanoes, either directly or through secondary events, such as tsunamis (Keating and McGuire 2000), lahars (Scott et al. 2005), or magmatic eruptions (Lipman et al. 1991). They have caused approximately 20,000 casualties in the last 400 years (Siebert 1984) and millions of people currently live on top of volcanic landslide deposits (Siebert 2002), where recurrent

collapses are possible (e.g., Komorowski et al. 2005). Studies in both modern and ancient volcanic terrains have contributed to the major growth of understanding the physical processes involved in volcanic landslides. Although the studies of volcano collapse hazards are highly warranted, awareness of collapse from other volcanic sources should be kept in mind when documenting and assessing the geologic structure and evolution of modern volcanic fields. Although large-scale catastrophic collapse of volcanic fields are rare, they represent the largest known subaerial volcanic landslides on Earth (Hacker et al. 2014).

In this short overview, we introduce the concept of volcanic landslides originating from multiple volcanic landform sources within volcanic terrains. Collapses due to volcano buildup, laccolith emplacement, and deposition of large parts of volcanic fields themselves will be

emphasized. Although volcanic landslides from laccoliths and volcanic fields are less well known, they have produced similar volcanic landslide deposits as those from volcanoes, but often on a much larger scale. We will concentrate on the subaerial volcanic landslides and collapse events generated from three volcanic landform types (i.e., volcanoes, laccoliths, and volcanic fields) and review the common causes and triggers of collapse related to magmatic activity within the subvolcanic plumbing system. A review of collapse features and submarine volcanic landslides from marine volcanoes can be found in McGuire (2006).

2 Volcanic Landslides

Catastrophic structural failure (collapse) from volcanoes, laccoliths, and volcanic fields generate many types of similar landslides. Engineering geologists include as landslides all types of mass movements, including falls, topples, slides (including slumps), spreads, and flows (Varnes 1978;

Cruden and Varnes 1996). In volcanic terrains, the full spectrum of these “landslide” movements occur, but the most common catastrophic collapse mass movements involve slides and flows. Major volcanic, as well as nonvolcanic, mass movements are typically complex, involving various combinations of slide and flow processes within different parts of the moving mass during different stages of development (Varnes 1978; Voight 1978). Volcanic landslides have been variably called a flank failure, flank collapse, sector collapse, rockslide, debris avalanche, rockslide-debris avalanche, rockslide-avalanche, and gravity slide (e.g., Crandell et al. 1984; Siebert 1984, 2002; Glicken 1996; van Wyk de Vries and Francis 1997; Hacker 1998). The term “volcanic landslide” used here describes a variety of slide and flow processes and mass movements involving gravity-driven, downward and outward transfer of wet or dry slope-forming materials (rock, debris, soil, etc.) from its collapsed source to an area of deposition. Therefore we include three depositional types, namely slide, debris avalanche, and debris flow in the term volcanic landslide (Fig. 2).

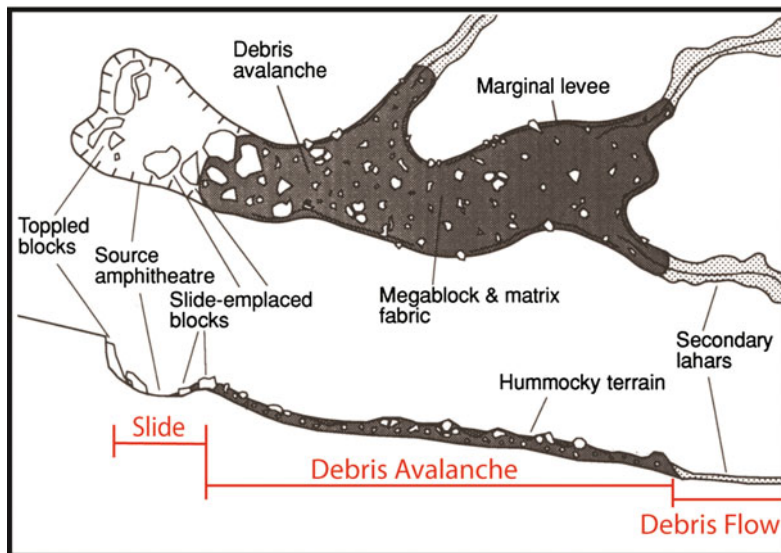


Fig. 2 Anatomy of a volcanic landslide illustrating the slide-debris avalanche-debris flow transitions (*above* map view; *below* schematic section). Characteristic features include a slide zone of relatively coherent blocks (or toveva blocks) emplaced by sliding or toppling in the

source area; a debris avalanche zone containing megablocks and matrix facies forming a hummocky terrain bounded by marginal levees; a debris flow zone (or secondary lahars) flowing in channels. Modified from McGuire (1996)

Volcanic mass movements commonly begin with a sliding mass, although flow soon dominates in the form of debris avalanches and/or debris flows as movement progresses (Fig. 2). Large segments of volcanic material can slide downslope without transforming into debris avalanches. In most cases, disaggregation rapidly transforms movement into fragmental flow of debris avalanches that rapidly attain high velocities over low-angle terrains. Therefore, volcanic landslides can be viewed as a continuous sequence of emplacement events with the resulting deposit being dominated by one type, or in some cases, a combination of all three (i.e., slide, debris avalanche, and debris flow). Most often, the lines of separation are blurred and there is a gradation between them. However, these three types display distinct structural patterns and kinetic behavior and will be discussed separately below.

2.1 Volcanic Slides

The volcanic landslide sequence outlined above begins with sliding of a large mass of rock from a source area. In volcanic slides, the displaced rock mass moves as an essentially coherent unit or units of broken blocks under the influence of gravity while maintaining contact with the substrate as it shears over it (Fig. 2). Barely perceptible movements of a rock mass can pass through a stage of accelerating creep into a rapid downward and outward displacement of a rock slide mass along one or several surfaces. Initial movements can be divided into translational (block slide) or rotational (slump) types that involve lateral movement of the slide mass or individual discrete slide blocks bounded by normal (extensional) faults. Slides in volcanic terrains should be very common due to steep slopes and the interbedding of mechanically diverse lithologies such as pyroclastic, epiclastic, and lava flow units. Being relatively coherent, slides retain elements of original stratigraphy with some degree of internal deformation such as minor faults and folds. The source area will often be marked by a scar that is commonly concave in

the direction of movement. Stranded detached slabs, or blocks, may mark a trail of the slide mass back to the scar (see Fig. 2). Nonvolcanic slides share similarities with volcanic slides and have been well documented in the subaerial and subaqueous environments (e.g. Voight 1978).

Large backward tilted and rotated blocks on the scale of several kilometers have been termed “toreva blocks” and can travel several kilometers in a nearly coherent manner. At Socampa volcano in Chile, toreva blocks traveled 7 km from their source without disaggregating into an avalanche deposit (Francis et al. 1985; Wadge et al. 1995) and 9 km at Barú volcano in Panama (Herrick et al. 2013).

2.2 Volcanic Debris Avalanches

A debris avalanche is a common middle stage in the transformation sequence from slide to debris flow (Fig. 2). A volcanic debris avalanche is referred to as a rapidly moving heterogeneous, unsorted mass of rock and soil mobilized by gravity from its source (Schuster and Crandell 1984). Volcanic debris avalanches form when frontal sections of the slide mass disintegrates upon continued movement through shear under gravity. As the slide mass section leaves the source area it collapses into a granular flow and travels over the landscape at high velocities (as much as ~ 100 m/s) spreading and thinning as it moves (Davies et al. 2010). After traveling many kilometers, the mass decelerates to rest, leaving a deposit (may be over 100 km long) containing all or some of the following features: (1) highly comminuted debris, (2) prominent hummocky terrain consisting of conical to elongated mounds on the surface, (3) raised marginal edges forming levees (see Fig. 2; McGuire 1996; Davies et al. 2010). Hummocks are often an indicator of extensional spreading (e.g., Voight 1981; Glicken 1998; Ponomareva et al. 2006; Shea et al. Shea et al. 2008). Detailed deposit descriptions exist for debris avalanche events such as Mount St. Helens (Glicken 1998), Socampa (van Wyk de Vries et al. 2001), Mombacho (Shea et al. 2008), and Parinacota (Clavero et al. 2002).

In general the moving rock mass flows, rather than slides, and the shearing action with the substrate is low (Hsü 1975, 1978; Ui 1983; Siebert 1984). Pervasive internal deformation occurs during movement, and the resultant clasts have a degree of relative motion and freedom between each other. The inertial Bagnoldian grain flow mechanics of avalanches means that grain support, grain momentum, and flow momentum are all maintained by grain-to-grain collisions leading to a progressive transfer of momentum through the flow (Hsü 1978; Pierson and Costa 1987; Iverson 1997). Avalanches are therefore incoherent and have considerable interactions between clasts, making the flow highly mobile. Deposition takes place through frictional freezing of the rock mass as it loses momentum, showing that the avalanche flow has a relatively high bulk viscosity and a high degree of clast interaction.

2.3 Volcanic Debris Flows

Debris flows are commonly the final stage of transformation within the volcanic landslide sequence (Fig. 2). A debris flow is typically a flowing mixture of debris and water, with sediment concentrations between 70 and 90% by weight (Pierson and Costa 1987). Volcanic debris flows are commonly referred to as lahars and can transform to even more dilute flows called hyperconcentrated flows with the addition of more water. If the landslide is large enough and contains a high-enough percentage of water and fine material (typically, >3–5% of clay-sized particles), these secondary flows can reach longer distances than the debris avalanches, sometimes traveling as much as 200 km downstream.

Volcanic debris flows owe much of their behavior to excess pore-water pressure and a pore fluid that is viscous and contains fine sediment. In cases of very hot lahars, steam may contribute to mobility (Arguden and Rodolfo 1990). A moving lahar looks like a roiling rapid slurry of wet concrete. As it travels downstream, the size, speed, and amount of material carried can constantly change. The initial flow may be

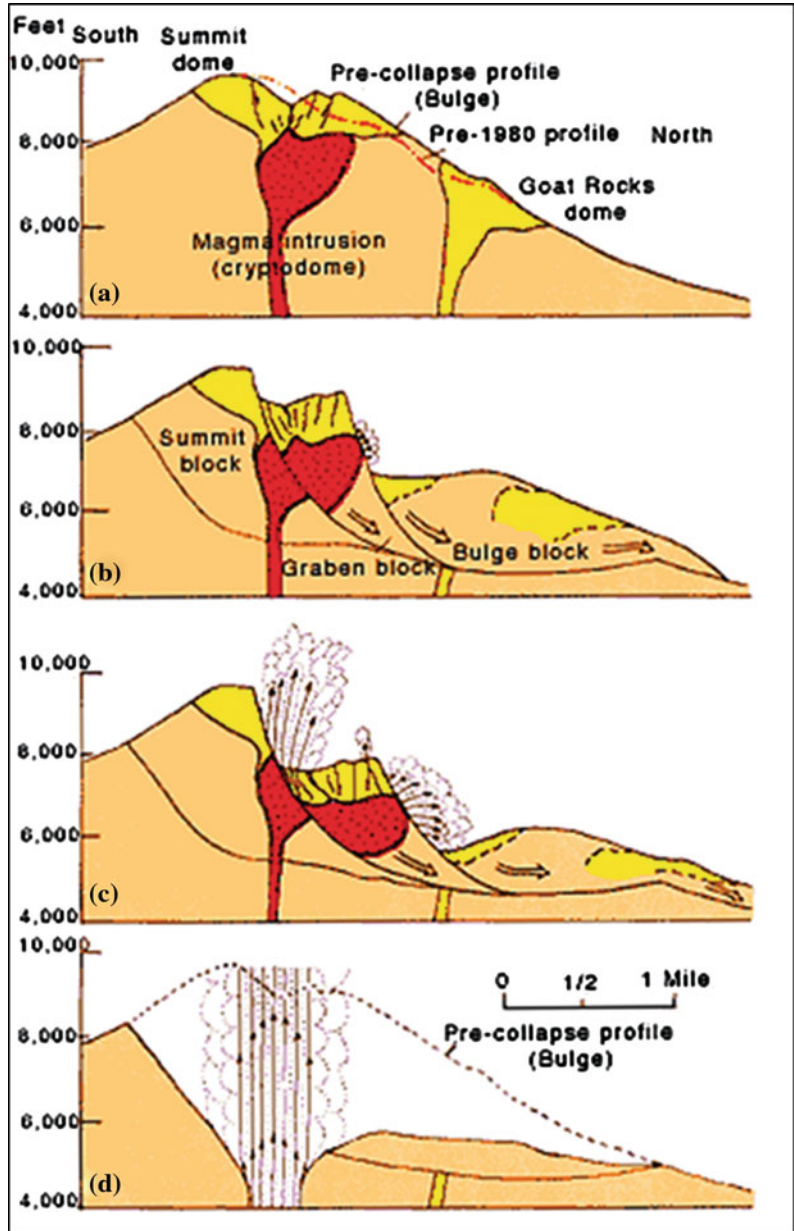
relatively small, but a debris flow may grow in volume as it entrains (called bulking) and incorporates anything in its path, including rocks, soil, vegetation; and even buildings, cars, and bridges. The flowing slurry may consume additional water through melting of snow and ice or by engulfing river or lake water and can grow to more than 10 times its initial size as it moves downslope. In steep areas lahar speeds can exceed 55 m/s.

Debris flows associated with volcanic landslides originate from: (1) direct transformation of a debris avalanche during its long transport (Scott et al. 2002); (2) transformation of the distal portion of a more water-saturated debris avalanche (Palmer and Neall 1989); (3) post-depositional remobilization of water-saturated parts of a debris avalanche (Glicken 1998; Pulgarin et al. 1999); and (4) subsequent rupture of natural dams formed by the earlier obstruction of drainages during the emplacement of a debris-avalanche deposit (Costa 1988; Costa and Shuster 1988). The first two types take place during the related collapse event or maybe some hours later. In contrast, the last two types can occur following an indeterminate lapse of time ranging from hours to years (Costa and Shuster 1988).

2.4 Mount St. Helens, USA: Classic Case Study of Cataclysmic Collapse and Eruption

The largest and best known historically witnessed volcanic landslide in a volcanic terrain was the catastrophic event that initiated the devastating 1980 eruption of Mount St. Helens (Cascade Range, USA). On May 18, 1980, the northern sector of Mount St. Helens failed retrogressively and led to the formation of a 2.5 km³ volcanic landslide (Lipman and Mullineaux 1981; Voight 1981; Glicken 1998). Magma began intruding into the Mount St. Helens edifice in early spring of 1980 and by May 18, a cryptodome (forming the “bulge”) on the northern flank (Fig. 3a) had deformed the edifice to the point of instability. By that time,

Fig. 3 Schematic cross sections of Mount St. Helens showing the cryptodome of magma that produced the bulge and the three major blocks that collapsed retrogressively to form the debris avalanche. **a** The volcano in the early morning of May 18, 1980; the bulging of the north flank is shown by the pre-1980 and pre-collapse profiles. **b** and **c** (within 30 s after the collapse) shows the progressive development of the debris avalanche and the beginning of both the lateral blast and vertical eruption, as the cryptodome was exposed; the Bulge block was the first to slide, followed by the Graben block. **d** (30 s later), by now the Summit block had slid and the lateral blast had stopped; the vertical eruption was now in full fury. After USGS Professional Paper 1250, courtesy of USGS



the northern flank had grown outward about 140 m at consistent rates of about 2 m per day and was creeping more rapidly toward failure.

At 8:32 a.m. on May 18, 1980, a magnitude 5.1 earthquake triggered the volcano's northern bulge and summit to fail and slide away as a huge landslide, first as slide blocks that quickly transformed into a debris avalanche (Fig. 3b). The debris avalanche swept around and up bedrock

ridges as far as 8 km north of the volcano crater, but most of it turned westward and flowed 25 km down the valley of the North Fork Toutle River (Fig. 4) and formed a hummocky deposit (see Fig. 1). The initial slide masses accelerated to an average of 45 m/s 10 s after detachment and increased to 70–80 m/s during the following 10 s. The avalanche flow, with maximum velocities around 90 m/s, took about 10 min to travel the

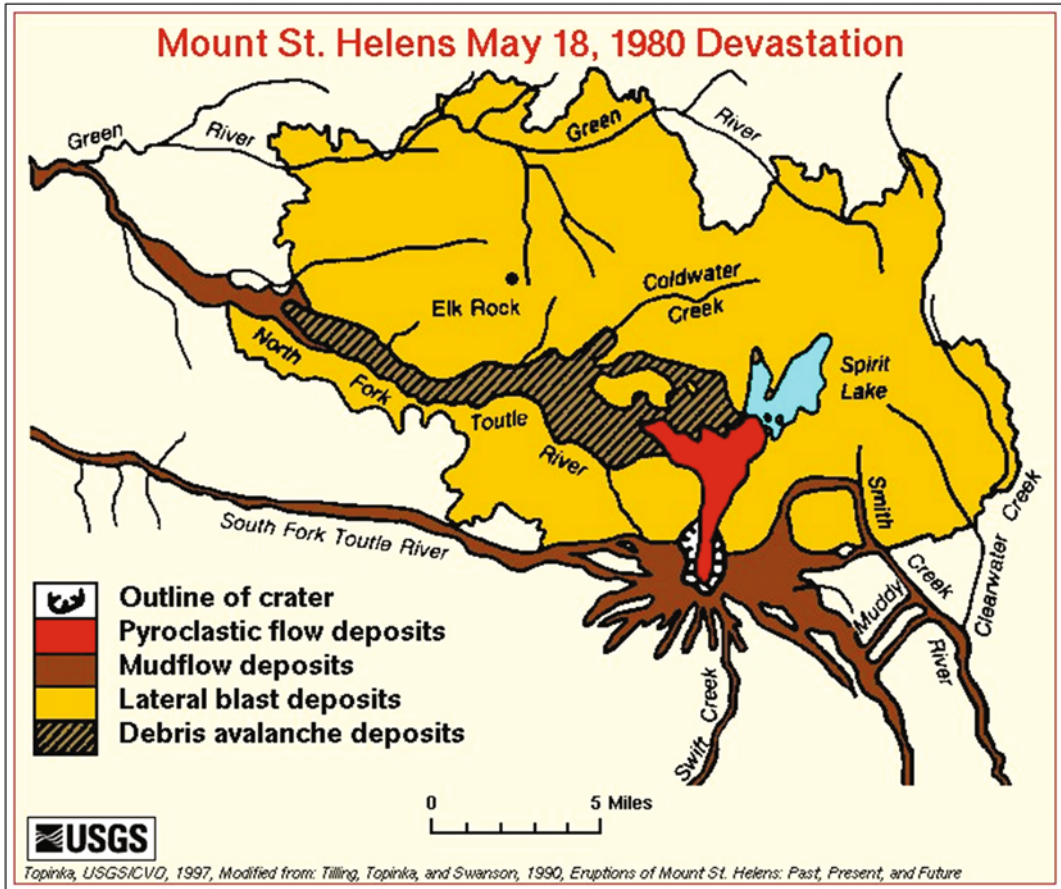


Fig. 4 Generalized geologic map showing the impact and deposits of the climatic eruption in the vicinity of Mount St. Helens volcano. Courtesy of USGS

25 km down the Toutle River (Voight et al. 1981). About 60 km² of the North Fork Toutle River valley system was choked with avalanche debris to an average depth of 45 m.

The landslide removed Mount St. Helens' northern flank, resulting in immediate depressurization of the volcano's magmatic system and triggering a powerful magmatic explosion that blasted laterally through the sliding debris (Fig. 3c). This directed blast consisted of hot juvenile material, the initial volcanic unit of May 18, that accelerated to at least 480 km/hr and overtook the debris avalanche and created a 600 km² blast zone that devastated the forest and blanketed it with a deposit of hot debris for as far as 25 km north and northwest of the crater

(Hoblitt et al. 1981). With this release of pressure on the volcano's plumbing system (Fig. 3d), which caused a depressurization wave to propagate down the conduit to the subsurface magma reservoir, a 9-h long Plinian eruption immediately followed, with its huge vertical eruption plume and by far the largest of the six 1980 pyroclastic-flow events (Rowley et al. 1981, 1985; Kuntz et al. 1990).

During the first few minutes of the eruption, parts of the blast cloud and pyroclastic flows surged over the crater rim and down the west, south, and east sides of the volcano and quickly eroded and melted the snow and ice on the volcano, creating surges of water that eroded and mixed with loose rock debris so as to form lahars

that poured down the volcano into river valleys, ripping up trees and destroying roads and bridges (see Fig. 4). The largest and most destructive debris flow occurred in the North Fork Toutle River after the debris avalanche came to a halt and some of the material was remobilized hours later. The debris flow that formed by water (originally groundwater and melting blocks of glacier ice) escaping from inside the avalanche deposit through most of the day, created a powerful slurry that eroded material from both the landslide deposit and from the channel bed of the North Fork Toutle River. The debris flow increased in size as it traveled downstream, eventually reaching its maximum size at about 80 km downstream from the volcano (Voight et al. 1981, 1983; Glicken 1998).

3 Collapse Styles in Volcanic Terrains

Sources of structural collapse leading to volcanic landslides have typically been recognized as the “volcano type” similar to that described from Mount St. Helens. However, other volcanic landform collapse types have been recognized in the geologic past that produced similar volcanic landslides (e.g., Mackin 1960; Hacker et al. 2002, 2014; Rowley et al. 2006; Biek et al. 2015). These include the collapse of growing laccoliths not associated with volcano edifice intrusions, as well as collapse of large portions of the volcanic field itself during volcanic buildup (Fig. 5). Nomenclature varies widely on the use of the terms flank versus sector collapses within the “volcano” literature. Flank collapses do not usually involve the magmatic conduit, while sector collapses do, and usually involve taking most of the volcano summit off in the process. In the broadest meaning, a sector collapse is defined as a gravity-driven movement of a portion of a volcano, independent of its size, origin, and type (Acocella 2005). Flank collapses would then fall within the definition of a sector collapse. Without introducing new nomenclature to collapses produced from laccoliths and volcanic fields, we have adopted the volcano collapse terminology

for all three (volcano, laccolith, and volcanic field) collapse types.

Smaller-scale failures are here referred to as flank collapses that mostly produce debris avalanche deposits from shallow slope failures (Fig. 5). The larger-scale failures are referred to as sector collapses and involve larger sections of a volcano’s or volcanic field’s substrate, or a laccolith’s laterally buttressed country-rock area. With this usage, sector collapses from the three collapse types involve movement along deep-seated failure surfaces where the displaced mass laterally ramps onto the land surface and takes on the geometry of an extensional looking “thrust fault” complete with a bedding-plane fault (younger on older strata), ramp fault, and former land-surface fault (older on younger strata).

3.1 Volcano Collapse Type

Structural slope failures at volcanoes are the most recognized and studied of the three collapse types (see Fig. 5). Once considered rare, volcanic collapse is now recognized to be a common process in the evolution of volcanoes. Landslides from volcanoes occur in many different settings and scales, independent of their composition (mafic and silicic), shape (cinder cones, strato-volcanoes, and shield volcanoes), and geodynamic setting (divergent and convergent margins, hot spots). Volcanic edifices are the result of the repeated emplacement, usually within time spans of many thousands of years, of magmatic products in a limited area. As a consequence of this relatively rapid construction, any volcanic edifice with significant height can become unstable and fail.

Structural failure at large volcanoes may be confined to a volcano flank, or may involve a large portion of the edifice (sector collapse). Besides Mount St. Helens, there are several well-known examples of volcanic landslides during the twentieth century such as Bezymianny (Gorshkov 1959; Belousov 1996), Shiveluch (Gorshkov and Dubik 1970; Belousov 1995), and the Soufriere Hills volcano in Montserrat

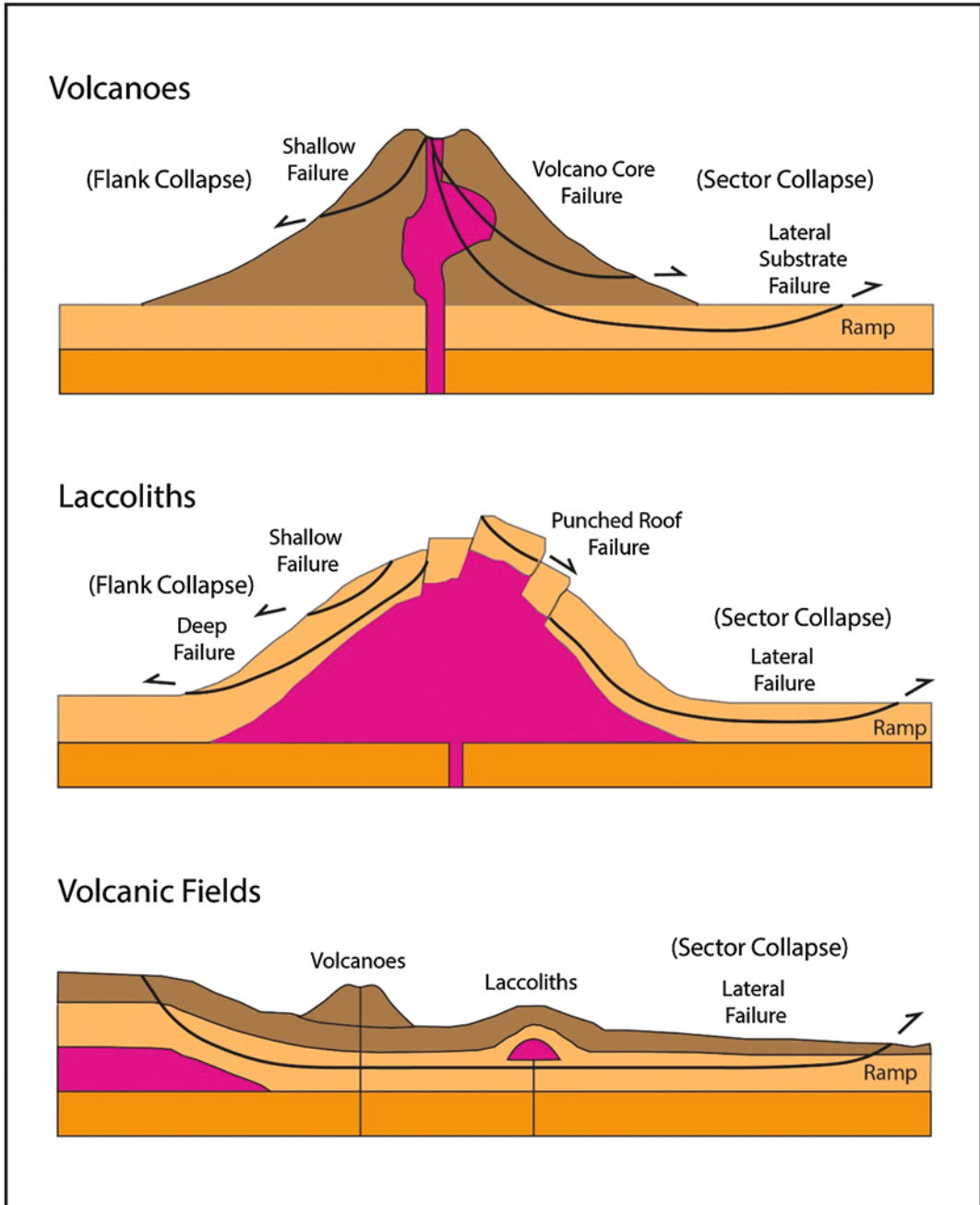


Fig. 5 Schematic diagram of collapse styles associated with volcanoes, laccoliths, and volcanic fields. Upper volcanoes diagram modified from van Wyk de Vries and Delcamp (2015)

(Voight et al. 2002). Sector collapses from volcanoes have also produced very large prehistoric subaerial landslides: the 2200 km², 22–33 km³ Nevado de Colima event, Mexico (Stoopes and

Sheridan 1992); the 500 km², 36 km³ Socompa event, Chile (van Wyk de Vries et al. 2001); the 990 and 1200 km², ~30 km³ Barú events, Panama (Herrick et al. 2013), and the 450 km²,

26 km³ Mt. Shasta event, USA (Crandell et al. 1984).

Volcano-generated landslides generally range in size from less than 1 km³ to more than 100 km³. The high velocity and great momentum of landslides allows them to cross valley divides and run up slopes several hundred meters high, as at Mount St. Helens where its 2.5 km³ landslide reached speeds of 50–80 m/s and surged up and over a 400 m high ridge located about 5 km from the cone. Another remarkable feature derived from volcanic sector collapses of volcanoes is the source area. Because most large volcanic landslides remove the summit of the failed volcano, a horseshoe-shaped crater or semi-amphitheater is formed that varies in size based on the volume of the removed slide, typically from more than 1 km³ up to several tens of km³ (Carrasco-Núñez et al. 2011).

By removing a large portion of a volcano's cone, a landslide may abruptly decrease pressure on the shallow magmatic and hydrothermal systems, which can generate explosions ranging from a small steam explosion to large steam and magma driven directed blasts. These result in tephra and ash-fall-tuff hazards for surrounding areas. Collapse events can be grouped into three types: those involving a magmatic eruption, those involving non-magmatic explosions, and those that are 'cold' and have no volcanic activity associated with them (Siebert 1984; Carrasco-Núñez et al. 2011). The first type is called a *Bezymianny*-type, which refers to the magmatic eruption and collapse of the Bezymianny volcano in Russia in 1956 similar to Mount St. Helens, where magma intruded the cone and destabilized the flank. The second is called a *Bandai*-type, which refers to the Bandai volcano in Japan, whose flank collapsed in 1888 and produced a phreatic eruption. In this case, magma did not intrude the cone and the collapse depressurized an active hydrothermal system, producing vigorous phreatic eruptions without magma reaching the surface. The third type is generally referred to as an *Unzen*-type after a sector collapse in Japan occurred in 1792 but did not involve any volcanic activity.

3.2 Laccolith Collapse Type

Historic growth of laccoliths in volcanic fields has been observed in the form of cryptodome growth in the landscape surrounding volcanoes, such as the classic growth of the Showa-Shinzan dome in Japan in the mid-1940s (Yokoyama 2002). A postmaster, Masao Minatsu, in a nearby village documented its growth by drawing its slowly changing shape on a paper window of his office. He showed that over a years' time (from August 1944 to September 1945) magma caused the 100 m thick sedimentary cover to be uplifted over 200 m. The top of the roof contained a punched section that continued to rise like a piston above the main dome, yet the roof did not collapse to trigger a volcanic eruption.

The idea of volcanic landslides generated from laccoliths was first described by J. Hoover Mackin, who showed that laccoliths can produce large landslides (Mackin used the term gravity slide) on the scale of collapsing volcanoes during the vertical growth of the laccolith (Fig. 6; Mackin 1960). Laccolith intrusions "make room" for themselves in the shallow crust and thus must deform and inflate the surface considerably, in places producing steep unstable slopes. Most of the instructive field studies of laccoliths have been made where erosion has stripped most of the cover and surrounding strata to expose their intrusive cores. Therefore, most evidence of volcanic landsliding has been eroded from the record of most exposed laccoliths. However, studies from laccoliths in the Iron Axis magmatic province in southwestern Utah have revealed evidence of multiple collapse structures that led to volcanic landsliding as well as to initiation of volcanic eruptions (Fig. 5; Hacker et al. 2002, 2007; Rowley et al. 2006; Biek et al. 2009).

The Iron Axis laccolith group consists of a series of lower Miocene calc-alkaline hypabyssal laccoliths and associated volcanic rocks located just west of the present Colorado Plateau (Fig. 7). During Iron Axis magmatic activity, ascending quartz monzonite to granodiorite porphyry magma from a deep batholith complex intruded along one or more northeast-striking,

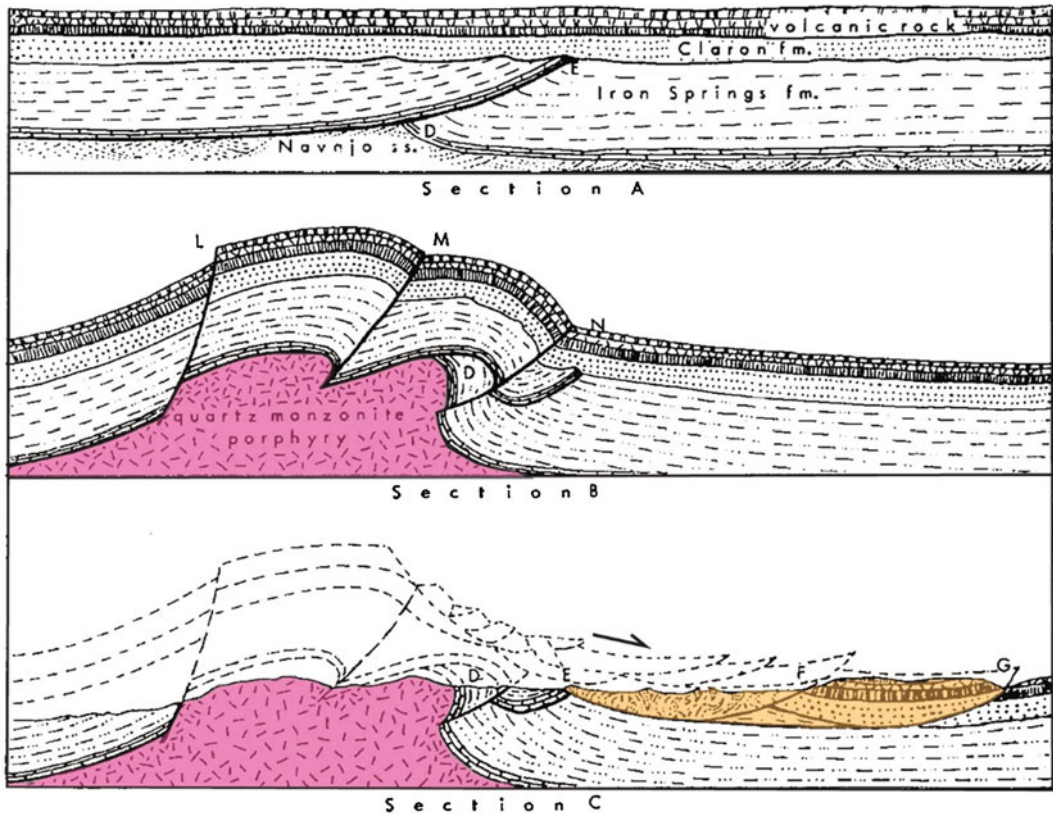


Fig. 6 Structural features associated with the Iron Mountain laccolith, Iron Axis, Utah. **a** Restoration of pre-intrusive structure showing east verging Cretaceous Sevier thrust sheet eroded and unconformably overlain by Tertiary sedimentary and volcanic strata. **b** Restoration

after emplacement of Iron Mountain intrusion along former thrust fault and vertical inflation. **c** Same as **b** but showing gravity slides (remaining erosional remnants colored) formed by collapse of oversteepened eastern flank. Modified from Mackin (1960)

east-verging Cretaceous Sevier thrust faults before being emplaced as bulbous laccoliths within Mesozoic and Tertiary sedimentary rock units (Mackin 1960; Blank and Mackin 1967; Blank et al. 1992; Rowley et al. 1998; Rowley 1998). More than a dozen exposed intrusions have been mapped within the magmatic province and others are inferred from structures in the roof rock, geophysical data, and drilling (Rowley et al. 2006; Biek et al. 2009). The intrusions occur in a northeast-trending belt that follows the trend of the Sevier orogenic front. The intrusions were forcibly emplaced into sedimentary rocks at depths ranging mostly between 2.5 and 0.25 km and deformed their roofs by upward folding and faulting.

Detailed studies show that the laccoliths in the Iron Axis form a continuum from sill injection to domed laccolith structures through a rapid incremental, or even a single-pulse growth (Hacker 1998; Hacker et al. 2002, 2007; Petronis et al. 2004). Structural and topographic relief produced by the emplacement of laccoliths progressed in stages, beginning with initial sill formation that was either laterally fed by transport of magma along pre-laccolith thrust faults or vertically through feeder dikes, followed by subsequent inflation of the sill by forcible intrusion of continuous or multi pulses of magma (Fig. 8). Bending of the entire roof overburden began as magma was continually added to the base of the laccoliths to forcibly thicken the intrusions

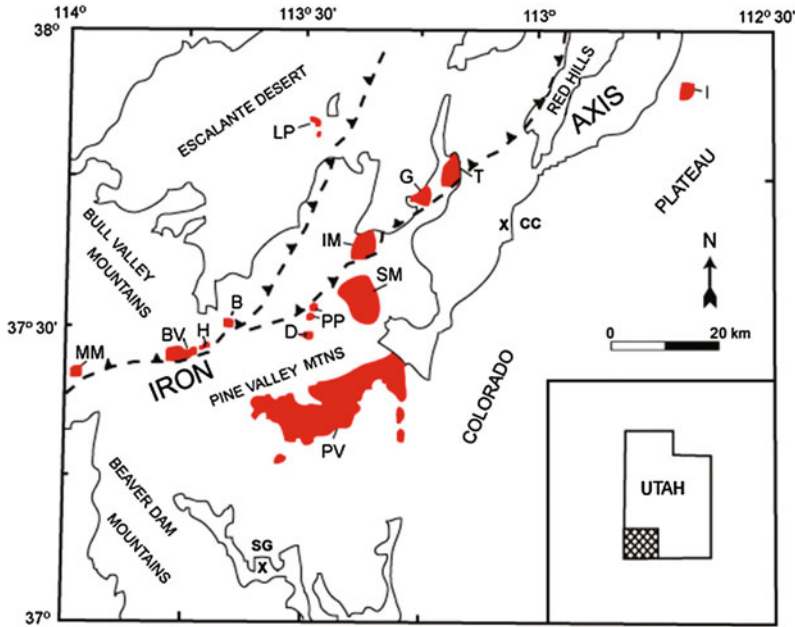


Fig. 7 Map of southwest Utah, USA, showing intrusions of the Iron Axis magmatic province: *B*—Big Mountain; *BV*—Bull Valley; *D*—The Dairy; *G*—Granite Mountain; *H*—Hardscrabble Hollow; *I*—Iron Peak; *IM*—Iron Mountain; *LP*—Lookout Point; *MM*—Mineral mountain;

PP—Pinto Peak; *PV*—Pine Valley; *SM*—Stoddard Mountain; *T*—Three Peaks. General trend of Sevier age thrust faults shown as dashed lines with saw-teeth. Towns: *CC*—Cedar City; *SG*—St. George. Modified from Hacker et al. (2007)

vertically. As intrusions inflated, the overlying host rocks were gently rotated and arched into doubly hinged flexures around the periphery. Due to the shallow emplacement (thin overburden), extension over the up-arched area was accommodated by brittle fracturing and high-angle reverse and normal faulting of the roofs. The geometry of most laterally fed laccoliths is asymmetrical in cross section, with the over-steepened flank of the laccolith occurring on the side farthest from the source area (to the east), which corresponds to where the sill stopped. Thus the laccolith is thickest where magma piled up, so to speak, from continued lateral injections.

The unusual aspect of laccolith growth in the Iron Axis group is the catastrophic structural collapse of some of the laccoliths flanks and roofs and subsequent venting of pyroclastic flows (ash flows) and lava flows. As the concordant intrusions continued their vertical growth, the limbs of the overlying peripheral flexure steepened as the hinges tightened. Extensional faulting

at the hinge crest most likely reduced the lateral support of the limb on an otherwise already steepened and unstable slope. The resulting slabs of host rock detached within shale units of the sedimentary rocks and slid onto the former land surface below (see Hacker et al. 2002, 2007). The sudden loss of peripheral overburden greatly reduced the lithostatic pressure that was essentially holding the roof “down” in advance of the upward loading forces applied by the thickening magma. This sudden release of overburden by sliding most likely resulted in immediate frothing of the magma due to massive pressure release, as with the 1980 Mount St. Helens eruptions (Lipman and Mullineaux 1981).

Field evidence clearly shows that intrusive doming produced by the growing laccoliths created unstable slopes from which large segments of host rock material were catastrophically sloughed by sliding prior to volcanic eruptions. This sequence of events (i.e., doming, then gravity sliding, then volcanism) indicates that volcanism

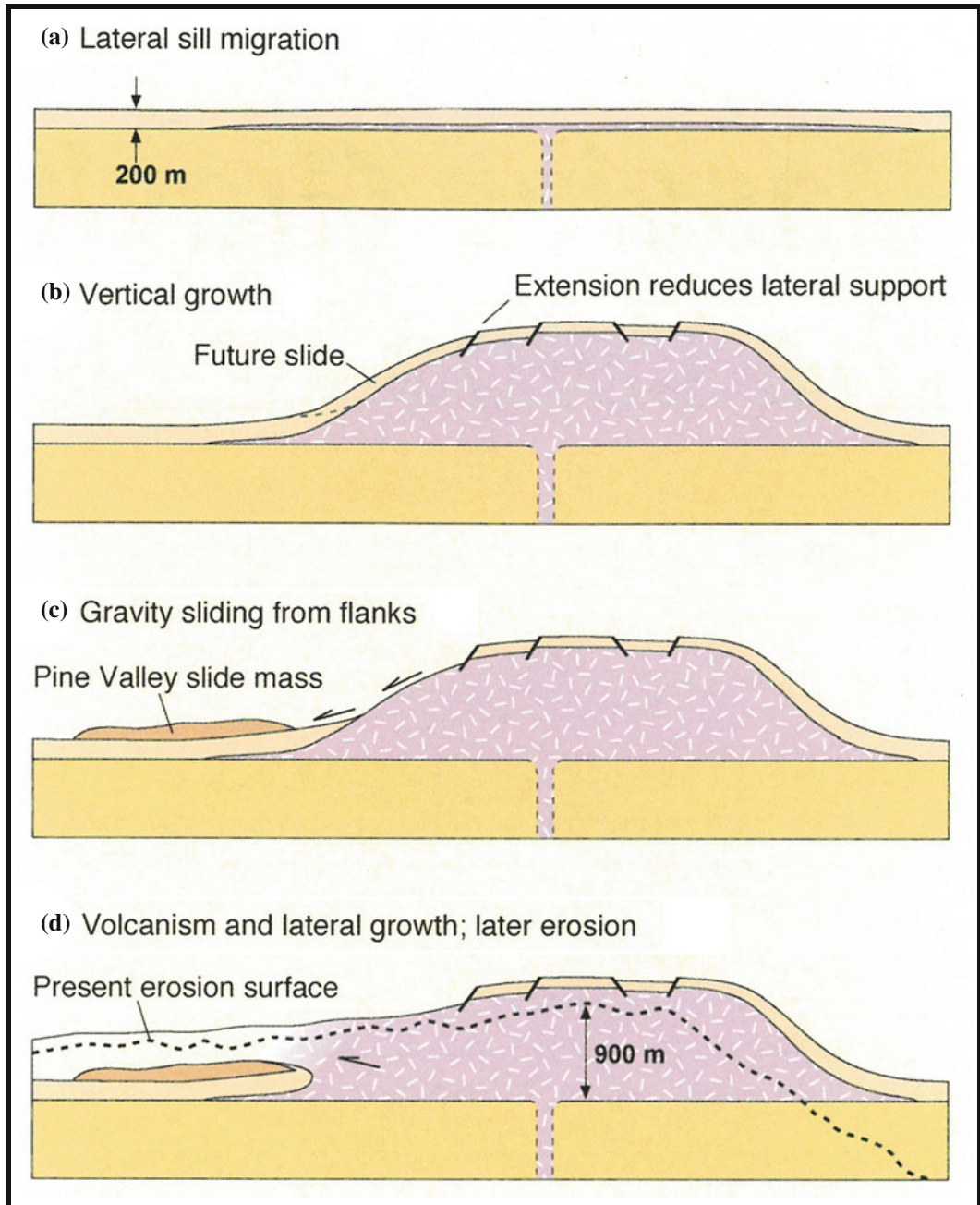
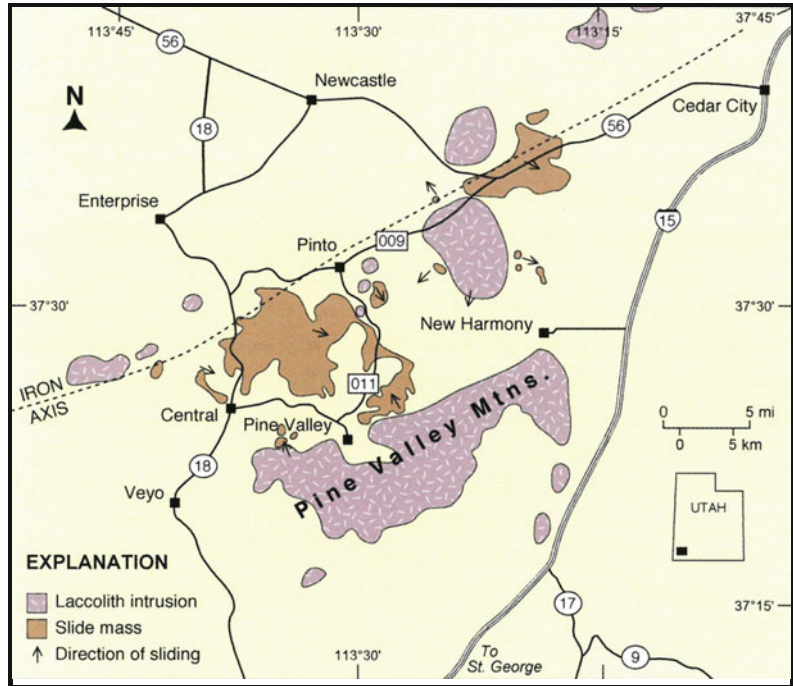


Fig. 8 Schematic model for evolution of laccoliths in Iron Axis using the Pine Valley laccolith as a proxy. Cross-section is north-south through laccolith. Emplacement and growth is envisioned to be a continuum from one stage to the next. **a** Stage 1—ascend of magma through en echelon dike system followed by lateral migration of sill to its fullest extent. **b** Stage 2—vertical laccolith growth by continued sill emplacements at the

base of the intrusion. **c** Stage 3—gravity sliding from laccolith by flank failure and continued growth. **d** Stage 4—volcanic eruptions of pyroclastic flows (or in the case of the Pine Valley laccolith, lava flows) onto the landslide and surrounding surface, followed by continued lateral laccolith growth. Modified from Hacker et al. (2007), courtesy of Utah Geological Survey

Fig. 9 Laccolith intrusions and slide masses within the central area of the Iron Axis. Arrows indicate primary direction of slide movement away from source intrusion. Largest slide mass is the Big Mountain slide. Modified from Hacker et al. (2002), courtesy of Utah Geological Survey



was initiated by gravity sliding. At least seven major collapse episodes in the Iron Axis can be attributed to the rapid emplacement of laccoliths (Lookout Point, Pinto Peak, Bull Valley-Big Mountain, Iron Mountain, Stoddard Mountain, and Pine Valley; Fig. 7) with at least five (Pinto Peak, Bull Valley-Big Mountain, Stoddard Mountain, and Pine Valley) triggering a volcanic eruption event (Blank et al. 1992; Hacker 1998; Hacker et al. 1996, 2002, 2007). The volcanic landslides were generated by three types of slope failure (Fig. 5): (1) flank failure where sedimentary host rocks failed on the over-steepened slopes of the laccolith, (2) punched roof failure where large block sections of the host-rock were faulted upward in piston fashion by the magma to the point that they lost lateral support and failed, and (3) sector collapse where a thicker section of the laccolith's flank and surrounding buttressed sedimentary strata failed laterally away from the laccolith (similar to the substrate failure type of volcanoes). Most of the volcanic landslides generated were composed of slides, with minor portions of the debris-avalanche component occurring in more distal regions.

The largest slide mass (Big Mountain event), with a volume of ~ 50 to 60 km^3 , covers $>150 \text{ km}^2$, is more than 550 m thick in places and it extends more than 25 km from its parent laccolith dome (Figs. 9 and 10). The Big Mountain event represents a sector collapse type, which makes this laccolith collapse event larger than the Mount St. Helens volcano event.

The transported stratigraphic units within slide masses show attenuation and exhibit various internal structural complexities; however, normal internal stratigraphic succession is maintained. Typically, the strata exhibit pervasive internal fracturing and shattering but are well indurated. Some members and formations are brecciated and consist of pebble-to-boulder-sized, angular to subangular rock fragments with a crushed matrix of the same composition as the fragments (Fig. 11). The brecciated zones are commonly matrix-poor, with the fragments commonly tightly packed in a jigsaw-puzzle mosaic separated by a cataclastically generated sand-to-granule-size matrix. Most fragments have moved slightly relative to their neighbors, while others show some rotation. Rocks from adjacent

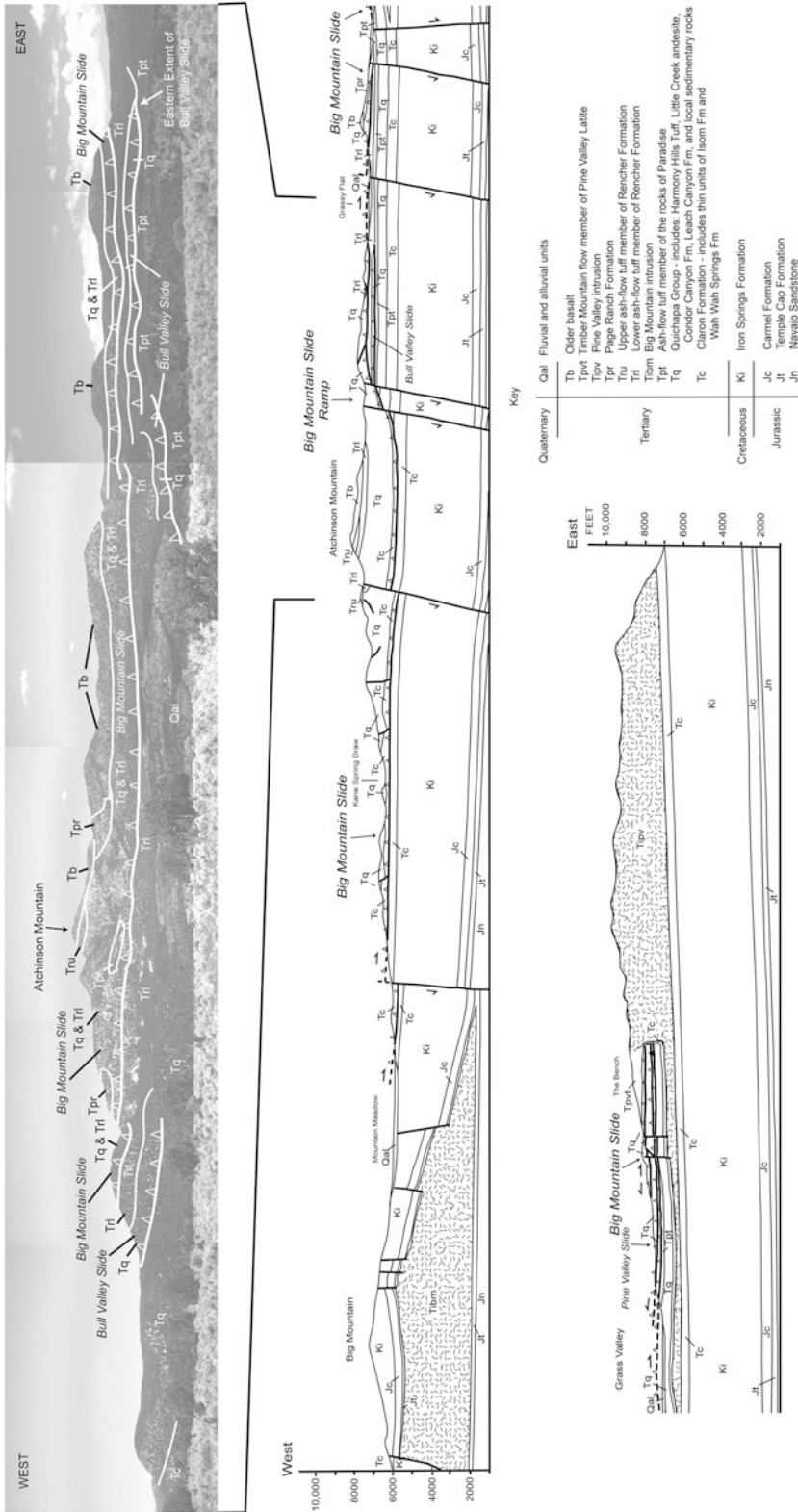


Fig. 10 Geologic cross section (east-west) through the Big Mountain gravity slide showing the ramp just to the east of Atchinson Mountain. Modified from Hacker et al. (2002)



Fig. 11 Outcrop of pre-collapse welded tuff exhibiting pervasive internal fracturing with angular to subrounded fragments in a crushed matrix formed during slide transport within Bull Valley gravity slide

stratigraphic units are usually not mixed, but locally are chaotically juxtaposed along close-spaced shear domains. Omission or smearing out of stratigraphic units takes place along low-angle shear zones or bedding-plane faults. Mechanically, the character of the internal deformation varies with rock lithology. Softer, moderately welded ash-flow tuffs deformed along sheared zones as much as 3 cm thick that contain pulverized rock flour material (cataclasite) formed by the mechanical breakdown by crushing and grinding of the tuff. In contrast, the more competent highly welded tuffs and lava flows deformed along brittle intersecting or anastomosing sets of shear fractures, which resulted in brecciation of the rocks. In addition to internal deformation fabrics of the rock units, many structurally complex areas within the slide masses contain extensively faulted and folded strata. Faulting occurs along: (1) local tear faults oriented

parallel to transport direction, and (2) high-to low-angle normal and reverse faults oriented mostly perpendicular to transport direction.

Overall, the slide masses closely resemble remnants of “erosional thrust sheets” in form. All deformation is confined to the slide masses themselves and abruptly terminates downward at low-angle, basal-bounding gravity-slide faults (analogous to attenuation or denudation faults or to non-rooted detachment faults). The basal gravity-slide faults are a composite of four types of fault surfaces. They include: (1) a subhorizontal “bedding fault” (decollement) within shale-rich sedimentary rocks in which younger rocks overlie older rocks, (2) subvertical “flanking faults,” which are lateral bounding tear faults with strike-slip movement, (3) a transgressive “ramp fault” that cuts upward across bedding, and (4) a subhorizontal “land surface fault,” which is a fault between the slide mass and the pre-existing land surface of that time, in which older rocks overlie younger rocks. All four fault components are not necessarily preserved beneath every slide mass due to differential erosion, especially at the proximal ends of the slide masses where the bedding and ramp structures were mostly located at higher elevations on the intrusive domes and therefore were more susceptible to erosion. Alternatively, some of the components were destroyed by subsequent extrusion of magma. The Big Mountain slide is the most complete structure, for it retains a set of all four bounding faults (see Fig. 15 for illustration of fault types).

The relationship of gravity sliding as triggers for volcanic eruptions is evident in the Iron Axis laccoliths. The areas of structural and topographic relief that were necessary for the formation of gravity slide structures were formed by the forceful intrusion of quartz monzonite magma into sedimentary rocks and structurally uplifting these host rocks by laccoliths. The close timing between sliding and volcanism suggests that eruptions from the laccoliths could not take place until the initiation of gravity sliding. Sloughing off part of the roof of some of the laccoliths reduced the overburden pressure on the magma, leading to violent magma frothing

(vesiculation) and explosive eruptions. Most initial volcanic activity was of the pyroclastic flow type. The pyroclastic flows traveled laterally outward over the landscape in the direction of the slide movement, immediately burying most of the slide deposits and surrounding landscape. The largest pyroclastic deposit covered an area of $>1000 \text{ km}^2$. The volumes of the volcanic deposits do not appear to correspond to the size of the collapse features, that is, the smallest of failures (the punched roof block failure) could release enough pressure to initiate the same size eruption as the larger lateral failure.

3.3 Volcanic Field Collapse Type

Volcanic field collapses are the supervolcanoes (e.g., Yellowstone caldera type eruptions) of the volcanic landslide world. Although these volcanic field collapses are rare and the least recognized, due in part to the lack of modern analogs, they have formed the largest subaerial volcanic landslides on Earth (Hacker et al. 2014; Biek et al. 2015). This type of collapse involves shear failure along a large portion of the substrate of a volcanic terrain, resulting in mass movement of gigantic sections of the volcanic field (a mega-sector collapse). Collapse of a volcanic field can incorporate not only multiple volcanoes, but also shallow or older stocks, laccoliths, sills, and dikes, as well as any volcanic landform associated with the field's evolution (Fig. 5).

A volcanic field is an area of the Earth's crust that is prone to localized volcanic activity and generally contains numerous volcanoes of either the monogenetic or polygenetic type. A polygenetic volcanic field contains polygenetic vents, each of which erupts repeatedly over long periods of time. Unlike monogenetic volcanoes, polygenetic volcanoes reach massive sizes, such as Mauna Loa, which is the world's largest active volcano. Polygenetic volcanoes include stratovolcanoes, complex volcanoes, shield volcanoes and calderas. The Marysvale volcanic field is a polygenetic field located in southwestern Utah and is one of the largest volcanic fields in the western United States (Rowley et al. 1998, 2002,

2005). Most of its volcanism took place from early Oligocene to late Miocene (about 32 to 14 Ma).

Partial collapse of the southwestern part of the Marysvale volcanic field produced a volcanic landslide, the Markagunt gravity slide, with an areal extent of at least 5000 km^2 (dimensions revised from Hacker et al. 2014), making it the largest known subaerial gravity slide on Earth. It is larger than the famous 3400 km^2 Heart Mountain gravity slide of Eocene age in the Absaroka volcanic field of northwestern Wyoming, long considered to be the largest subaerial landslide (e.g., Malone and Craddock 2008; Beutner and Hauge 2009; Craddock et al. 2009). The Markagunt gravity slide took place at about 21.5 Ma, prior to basin-range tectonism. Basin-range faulting, which produced north-trending basins and ranges that form the present topography, overprinted those structures formed during gravity sliding. Nonetheless, grooves, striations, Riedel shears, pseudotachylite (Fig. 12), crushed and rehealed clasts, basal cataclastic breccia, and clastic dikes that we have identified provide strong evidence of southward catastrophic emplacement by gravity sliding. The uniformity of directional indicators, the stratigraphic sequence of volcanic rocks that make up upper-plate strata, and the overall geometry of the gravity slide show that it represents a single emplacement event (Biek et al. 2014, 2015; Hacker et al. 2014).

From its mapped breakaway zone in the central Tushar Mountains and central Mineral Mountains to the southern limit of its debris avalanche deposits in the northern Markagunt Plateau and eastern Black Mountains, the gravity slide is presently about 95 km long and at least 65 km wide at the latitude of the ramp (Fig. 13). Southward transport after the ramp of at least 32 km occurred over the former Miocene land surface. The southwestern part of the Marysvale volcanic field, which consists of clustered stratovolcanoes and subordinate yet important calderas, is built on a weak substrate of mostly fine-grained volcanoclastic strata of the Brian Head Formation, which to this day are famously prone to modern landsliding. We remain uncertain what triggered the giant gravity slide, but



Fig. 12 *Upper image* Pseudotachylyte on secondary shear plane along sharp contact between highly fractured sandstone of the Bear Valley Formation below and volcanic deposits of the Mount Dutton Formation above.

Lower image close-up of pseudotachylyte-filled dike injected downward into sandstone at GPS receiver in center of photo

suggest that it was triggered by pre-caldera inflation of the 20–18 Ma Mount Belnap caldera (Fig. 14) or perhaps by earthquakes associated with this inflation.

At its simplest form, the gravity slide is a great sheet of volcanic rock that slid many km southward and at its distal southern end placed older rock on younger rock above a

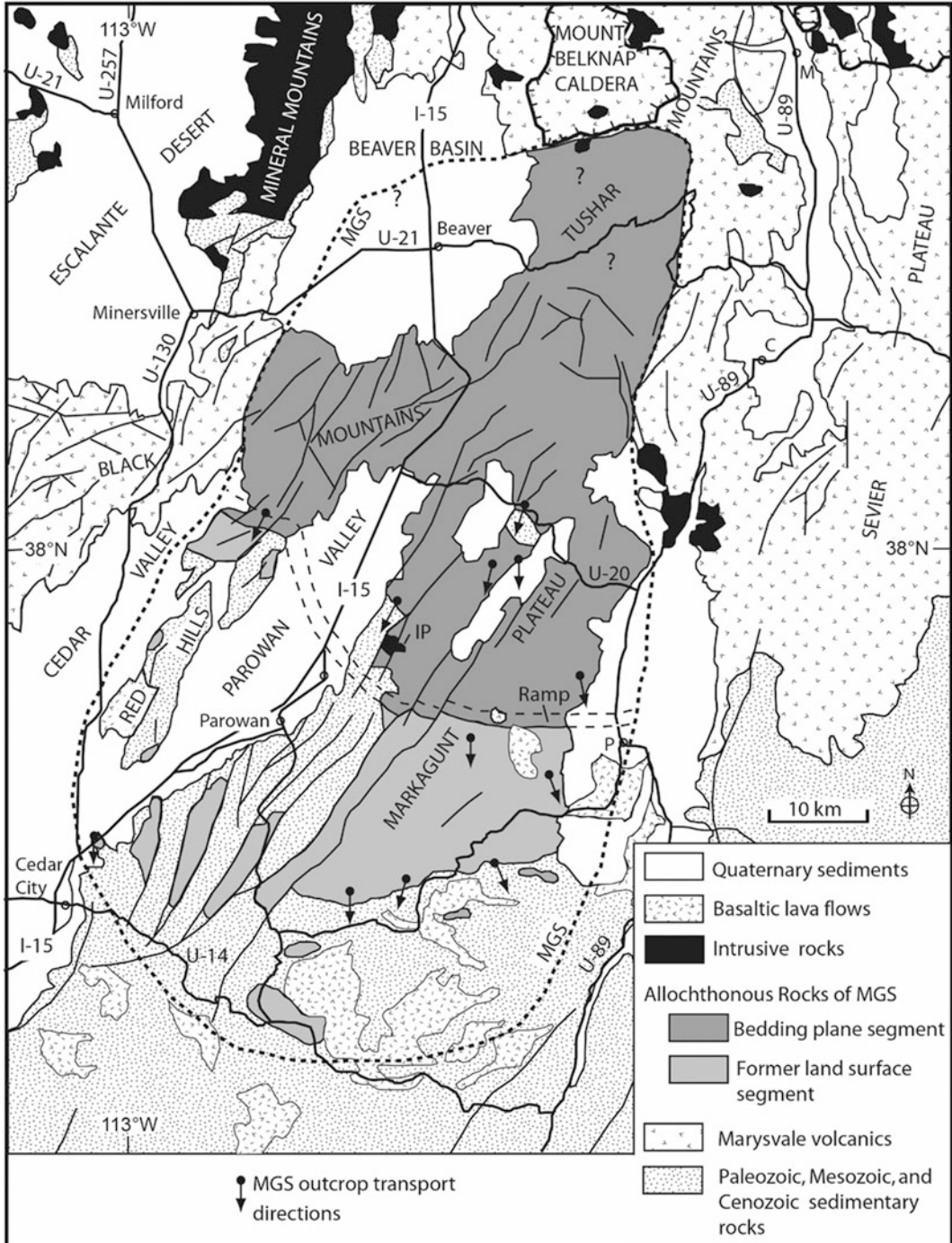


Fig. 13 Simplified geologic map showing extent (*heavy dashed line*) and features of the Markagunt gravity slide (MGS). C Circleville; IP Iron Peak intrusion; M Marysvale; P Panguitch. Modified from Hacker et al. (2014)

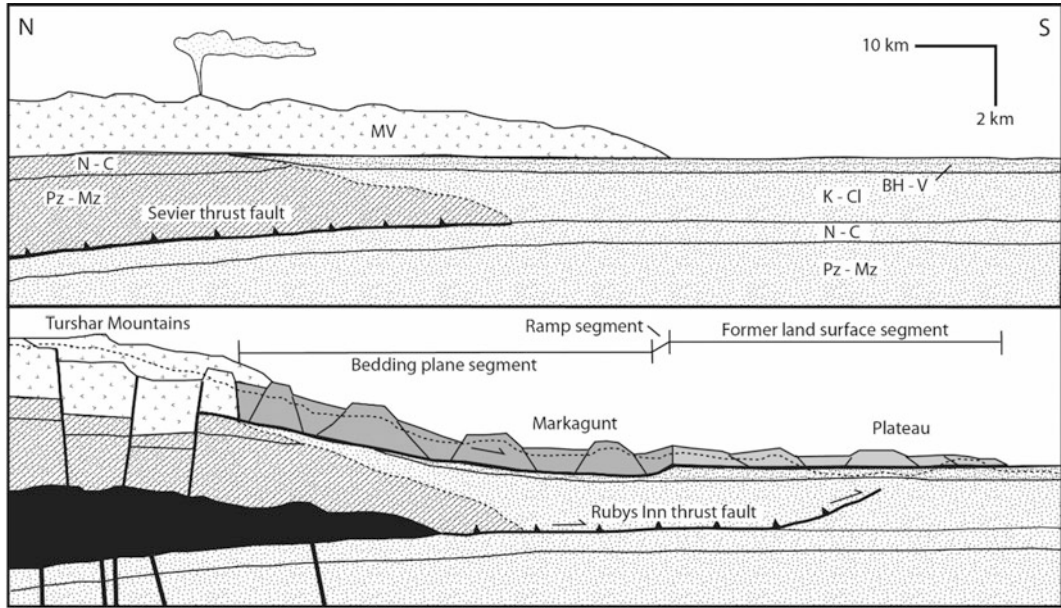


Fig. 14 Diagrammatic N-S cross section of Markagunt gravity slide before and after sliding; Although interpretive (based on cross sections using petroleum exploration wells), late-stage intrusions (area shown in *black* in lower cross section) utilized Sevier thrust faults, doming the overlying volcanic field. Pz-Mz, Paleozoic and Mesozoic

sedimentary rocks; N-C, Jurassic Navajo Sandstone and Carmel Formation; K-CL, Cretaceous and Claron Formation sedimentary rocks; BH-V, Brian Head Formation and oldest regional ash-flow tuffs; MV, Marysvale volcanics. Modified from Hacker et al. (2014)

subhorizontal surface (Fig. 15). It blankets the entire central and northern Markagunt Plateau and adjacent areas and consists of large blocks many square km in size of Miocene and Oligocene regional ash-flow tuffs and local volcanic and volcanoclastic rocks (derived from the Marysvale volcanic field stratovolcanoes and calderas). One way to think of the Markagunt gravity slide is as a thick stack of playing cards representing the volcanic stratigraphy of the volcanic field that are intensely deformed along shears between individual sheets but remain relatively undisturbed in the interior of the sheet (or blocks). The fact that the gravity slide consists mostly of undeformed large blocks above the bedding plane segment, bounded below by an inconspicuous shear plane, is one of the reasons it remained undiscovered for so long. The land-surface segment, however, is structurally more chaotic and consists of large tilted blocks of volcanic rocks in a more brecciated and sheared matrix, thus representing a more debris avalanche zone of the landslide (Fig. 16).

Characteristics of these astonishingly large gravity slides suggest that these types of volcanic fields are preconditioned for gigantic displacements by virtue of their: (1) large volume of available slide material that rapidly accumulated during volcanism, creating a thick, potentially unstable wedge, (2) a possible substrate of subhorizontal sedimentary strata containing early ash from the start of volcanism that weathers to incompetent beds, (3) an underlying batholith whose growth tilts rocks outward from the center of the volcanic pile, (4) shallow intrusive complexes (mostly laccoliths and dike systems) that rose from the batholith to feed the volcanism and which add lateral stress, and (5) possible pre-collapse development of summit fractures and normal faults by intrusive doming or during gradual lateral spreading on deeper-seated thrust faults that weaken the structural integrity of the volcanic field. Recognition of these features in modern volcanic fields could aid in potential hazard assessments.

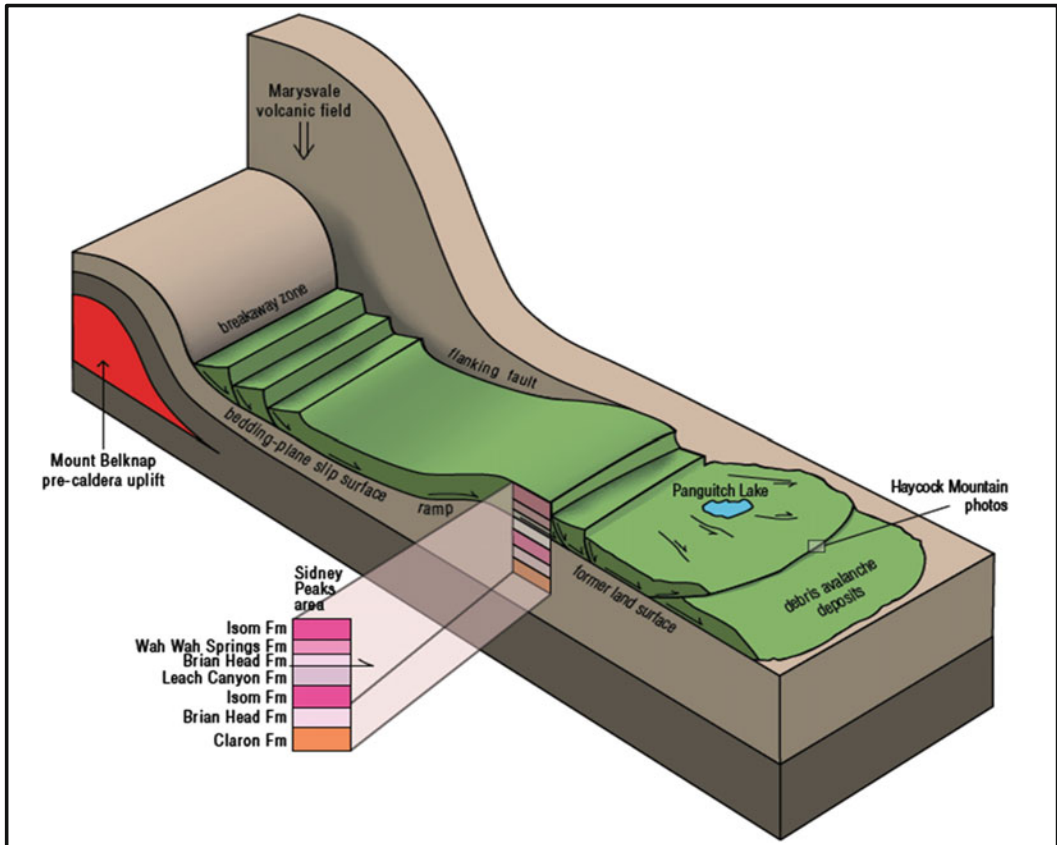


Fig. 15 Vertically exaggerated block diagram of an idealized gravity slide. Here, we suggest that the trigger is pre-caldera inflation of the Mount Belknap area, causing arching of overlying strata and consequent failure on over-steepened slopes. Note the four main bounding surfaces: the bedding-plane slip surface in mechanically weak clay-rich rocks of the Brian Head Formation; the ramp, where the slide mass breaks upward to the surface; the former land surface, now covered by the slide mass; and the flanking failure that bounds the margin of the slide. The basal slip surface resembles shallow low-angle faults, complete with slickensided and striated surfaces, cataclastic zones, local pseudotachylyte, and brittle microfabrics. Extensional deformation characterizes the

upper part of the slide, whereas compressional deformation characterizes the toe area. The main part of the gravity slide remains mostly intact with individual blocks as much as several square km in size, preserving a stratigraphy inherited from the source area. Distal portions of the slide mass disaggregate into debris avalanche deposits. Because gravity is the ultimate driver of landslides, the dip of the slip surface must be sufficient such that the downslope component of the weight of the slide mass overcomes the frictional resistance to sliding at the detachment layer. Once moving, however, the slides can travel many km over former land surfaces. Haycock Mountain photos shown in Figs. 16 and 18. Modified from Biek et al. (2015)

4 Volcanic Landslide Features and Deposits

Large volcanic landslides from the three main collapse types described (i.e., volcanoes, laccoliths, and volcanic fields) share a number of

morphological and fabric-related features that developed during transformation of slides to debris avalanches to debris flows. Unlike individual volcanic deposits such as pyroclastic flows, recognition of prehistoric volcanic landslide deposits may be easier to identify by large-scale properties rather than by

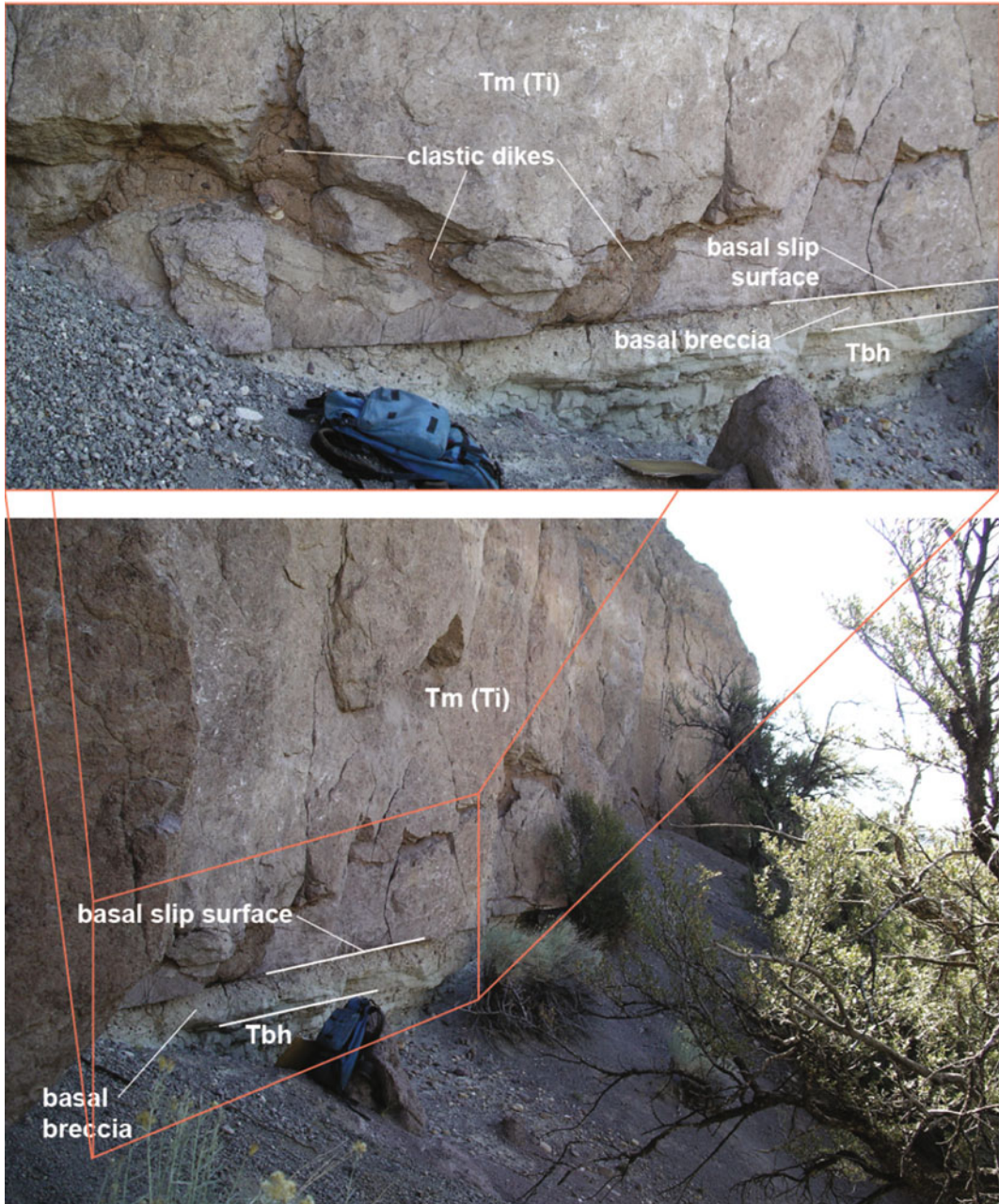


Fig. 16 Markagunt gravity slide exposure just south of Haycock Mountain. Note planar basal slip surface and underlying thin basal breccia, which in turn overlies similarly dipping volcanoclastic pebbly sandstone of the Brian Head Formation (Tbh). Basal breccia is light-reddish-brown and consists of both angular (Isom Formation) and rounded (intermediate volcanics and quartzite) clasts floating in a well-cemented sandy matrix; the breccia is texturally similar to concrete or glacial till and was derived from pulverized Isom Formation and

underlying strata immediately above and below the slip surface. This breccia is injected as clastic dikes into the basal part of the gravity slide, which here consists of resistant Isom Formation (Tm[Ti]) cataclasite. This pulverized and silicified Isom Formation forms a cliff 5–10 m high and grades upward into fractured but otherwise undisturbed Isom Formation. *Inset* shows close-up of clastic dikes and cataclastic Isom Formation. Modified from Biek et al. (2014)

outcrop-scale structures or lithologies, although these are important where erosion has stripped away major portions of a slide mass.

4.1 Slide Zone

The slide zone of the three collapse types includes the area at the head of the slide mass where large slide blocks are displaced downslope as largely intact masses from the horseshoe shaped scar of the breakaway area. The large blocks are bounded by large high-angle normal faults, not only the major breakaway fault but faults that are antithetic and synthetic to it, that may form a wide variety of structures and landforms, including horsts and grabens. In edifice-scale collapses, slide blocks (toreva blocks) may show backward tilting. These high-angle faults pass into a low-angle, downslope-dipping plane or strata of weakness, especially in the case of volcanic field collapses. Typical planar surfaces in the breakaway area and downslope are disrupted by small high-angle normal and echelon faults that strike perpendicular to the downslope direction. Most graben areas are filled in with post collapse erosional debris. This zone of the landslide is preserved only in the largest sector collapses where the landslide cuts deeply into volcanic landforms. Flank collapses are generally smaller and lack the slide blocks, so the main products preserved are debris avalanche or flow deposits. Slide-zone runout lengths vary greatly depending on the distance between the head breakaway scarp and where the slide plane daylight at the surface farther downslope, where it is a ramp fault in deep-seated collapses. Volcanic field collapses contain the largest slide zones with the Markagunt gravity slide bedding plane slip surface reaching over 60 km in length. The sides of the slide, parallel to the slide direction, represent strike-slip movement, and in the case of volcanic-field collapses may be represented by a subvertical lateral fault, much of which is a broad subvertical zone of tectonic breccia.

4.2 Debris Avalanche Zone

The surface morphology of most younger volcanic debris avalanche deposits is characterized by a hummocky terrain with numerous hills and closed depressions (Fig. 17). Hummocks (also called mounds) may form by extension as the laterally spreading avalanche produces horst and graben structures, or the hummocks may represent the surface topography of the deposit produced by avalanche blocks rafted within finer material (Voight et al. 1981, 1983; Glicken 1986, 1996; Crandell 1989). The long axis of hummocks are mostly oriented parallel or perpendicular to transport direction; some deposits contain hundreds to thousands of closely spaced hummocks. Hummock size ranges from ~1 m to several hundred meters in height and >1 km in length, with height and density generally decreasing toward its distal area, reflecting progressive disintegration of internal blocks (Ui 1983; Siebert 1984, 2002; Glicken 1986, 1996; Crandell 1989). Distally, areas of flat surfaces may increase as the hummocky morphology becomes subdued and longitudinal ridges become prominent. Avalanche deposits also generally have sharply defined edges, with marginal levees and a steep terminus, although levees may be subdued or absent in avalanches that contain a higher water content.

Internally, most debris avalanche deposits are poorly sorted and poorly graded, with particle sizes ranging from silt size to extremely coarse blocks. They typically have a more bimodal fabric, consisting of a block facies and a mixed facies (also referred to as a matrix facies) (Crandell et al. 1984; Glicken 1991; Mehl and Schmincke 1999). Block (or megaclasts) dimensions range from meters to hundreds of meters in diameter and represent fragments of highly brecciated and fragmented segments of volcanic material transported relatively intact and surrounded by matrix. Block-facies material, which dominates in most hummocks, can consist of one large clast, multiple clasts of the same lithology, or multiple deformed and faulted clast



Fig. 17 The catastrophic debris avalanche at Mount Shasta showing hummocky terrain. The deposits of an exceptionally large debris avalanche extend from the base of Mount Shasta volcano northward across the floor of Shasta Valley in northern California. The

debris-avalanche deposits covers an area of about 675 km², and their estimated volume is at least 45 km³. Dating methods suggest that the debris avalanche occurred between about 300,000 and 380,000 years ago. (Image courtesy of USGS)

groups of different lithologies (Siebert 2002). Mixed-facies material consists of poorly sorted angular lithic fragments, in which the frequency and size of blocks decreases with increasing distance from the source and the matrix proportion rises.

Clasts in all facies are angular to subangular, highly fractured, and pervasively shattered, forming a “jigsaw” texture (both jigsaw cracked and jigsaw-fit textures) in which fragments of adjacent clasts can be visually refitted across fractures (Shreve 1968; Ui 1983). Fractured clasts of one lithology surrounded by crushed fragments of the same lithology represent the crushing of individual blocks or stratigraphic layers and are usually stretched or smeared in the direction of transport. Fracturing of crystals, glass, and lithic fragments extends to the microscopic level (Komorowski et al. 1991).

The basal region experiences high normal and shear stresses that result in intense comminution (the action of reducing a material to minute particles or fragments). Basal zones of both debris avalanches and slide zones show more penetrative shear fracturing of clasts and a smeared-out fabric of blocks, thus producing a crude layering. Pervasive shearing usually decreases in extremely short distances vertically. Clastic dikes formed by injection of matrix material into fractures during movement are commonly observed in basal regions (see Fig. 16). Basal contacts of debris avalanches show evidence of either relatively passive transport or erosive scour, as observed by lengthy contacts above largely undeformed soft sediment substrate, or striations and grooves found on substrate material or in the base of the mass (Fig. 18), along with incorporation of substrate material.



Fig. 18 Close-up of slickenlines exposed at the base of the Markagunt gravity slide at Haycock Mountain. Riedel shears and slickenlines at the base of the gravity slide demonstrate transport from north to south

Where large blocks are not present, avalanche deposits resemble angular breccias with larger clasts supported by a matrix of finer material that in most places shows evidence of intense shearing. Although a wide range of clast sizes may be present at any one location, their composition is usually not random and homogenization is far from complete. The spatial distribution of clast types reflects the original stratigraphy of the collapsing source mass, thus broad stratigraphic relationships in the source rocks are generally preserved, a fact that indicates that debris avalanche emplacement involves laminar flow rather than turbulent flow (Fig. 19).

4.3 Debris Flow Zone

Where sufficient water is present during flow, debris avalanche deposits generally grade downslope into debris flows. Such a transition has been observed at Mount St. Helens and Mount Shasta, USA, where the two types of flow deposits are distinguished on the basis of sedimentological differences (Crandell 1989). Scott et al. (2002) divide debris flows into cohesive

and noncohesive types. Most debris flows contain less than 3% of the clay fraction in the weight of the matrix (sand + silt + clay) and are referred to as non-cohesive debris flows. When the clay content is >3%, they are known as cohesive debris flows, which are distinguished by the fact that they do not change their character throughout their runout as non-cohesive types do (Scott and Vallance 1995). The higher clay content in cohesive debris flows is in most cases due to hydrothermal alteration within the volcanic landform, and therefore the resulting clay-rich debris flows originate from volcanic collapses, in contrast with non-cohesive flows, which originate as meltwater surges during eruptions or during excessive precipitation.

5 Causes of Volcanic Collapse in Volcanic Terrains

Volcanic terrains are inherently susceptible to instabilities by nature of their basic materials and structures. Structural failure and collapse is a common outcome of this slope instability. As with nonvolcanic landslides, collapse of volcanic



Fig. 19 Outcrop of slide block within the Big Mountain slide showing fractured and sheared nature of the rock units and preservation of original stratigraphy. Outcrop approximately 6 m high

landforms is produced by a combination of circumstances rather than any single process or cause. For conventional landslides, causes of slope instability have been divided into factors that produce an increase in shear stress (or driving forces) on the slope and into factors that contribute to the reduction in material shear strength and/or friction (e.g., Varnes 1978; Voight and Elsworth 1992). Slope angle is clearly an important factor for increasing shear stress that causes slope instability, especially on stratovolcanoes, as indicated by the frequency of their major slope failures. Precipitation and seismic loading are important destabilizing causes of reducing a material's shear strength on a slope by increasing pore pressures. In many situations, it is the combination of both stress-increasing and strength-decreasing factors that lead to major volcanic landform instabilities.

Once a segment of a volcanic landform has become destabilized, it becomes susceptible to failure in response to one or more internal or external “triggers” that may initiate collapse. This trigger process may operate in the short term (collapse during or immediately after a volcanic event) or with delayed reaction (collapse many years following an event). A comprehensive review of the possible causes and triggers of volcanic landslides can be found in Voight and Elsworth (1997) and del Potro et al. (2013).

5.1 Role of Magma in Volcanic Destabilization

Causes of slope instabilities are inherently due to the nature of the slope, rock composition, layering in relation to strength and permeability zones,

bedding planes, joints, faults, etc. and their orientation relative to the slope (del Potro et al. 2013). Intrusions have a significant role as a primary cause of large volcanic landslides by contributing to these slope instabilities. Intrusions cause intense deformation and visible bulging in all three styles of collapses, as well as producing seismicity and elevated pore-fluid pressure. The internal structure of a volcanic landforms can exhibit intense fracture and faulting caused by intrusions that enhance instability. Hydrothermal alteration affects large segments of volcanic landforms, producing clay minerals that increase permeability and elevate pore-fluid pressures. Such effects can drastically lower shear strength of the rocks, thus weakening the edifice (Lopez and Williams 1993; Frank 1995; Day 1996). Fluid pressure can also be enhanced by hydrothermal waters accompanying large intrusions and dikes (Voight et al. 1983; Elsworth and Voight 1996). Volcanic eruptions continuously add material that lead to oversteepening and overloading at the surface.

The behavior of the subvolcanic substrate is also important, in both subsidence and uplift of the volcanic landforms, to produce slope instabilities. Also, the growth of volcanoes or a volcanic field onto a sloping or weak substrate (e.g., rich in clay or gypsum) enhances the development of lateral spreading and produces instability within and below the volcanic landforms (McGuire 1996).

5.2 Triggers

Destabilization of volcanic landforms may occur over a period of weeks or months, as was the case for the rapid-onset instability produced by the cryptodome intrusion at Mount St. Helens, or destabilization may develop over thousands to tens of thousands of years (McGuire 1996; van Wyk de Vries and Francis 1997). However, once a part of a volcanic terrain has become unstable by one or more causes, it becomes susceptible to failure due to one or more of many triggers that

initiate collapse and generate a volcanic landslide. The introduction of new magma within dikes, sills, and laccoliths can trigger structural failure due to increasing pore pressure and reducing shear strength or to over-steepening of surface slopes (Elsworth and Voight 1996). The large amounts of internal and surface deformation produced by intrusions both increases shear stress on the slope and reduces rock shear strength through the creation of shear zones and pervasive brecciation. Changes in the hydrothermal groundwater system increases pore pressure and causes fluid migration. Because the hydrothermal system is driven by intrusions, new intrusions may be responsible for disturbances in the system and thus trigger a landslide (van Wyk de Vries and Davies 2015). Additional extrusive material added onto already heavily loaded volcanic landforms may also initiate failure and collapse. Other triggers involve earthquakes (typically > M5) that may quickly change pore pressure (Acocella et al. 2003), and displacements associated with long-term structural spreading (van Wyk de Vries and Francis 1997). Environmental factors may also be important triggers, such as large precipitation events or higher sea levels at island volcanoes, both of which may elevate pore pressures.

6 Volcanic Landslide Transport and Mobility Mechanisms

Once failure has been initiated, the failed mass moves with considerable inertial energy and may travel in a largely coherent manner, or the mass may be totally disaggregated with travel velocities of over 100 m/s during catastrophic failure. Velocities of volcanic debris avalanches have been calculated in the order of 50–150 m/s (Ui et al. 1986; Siebert et al. 1995), whereas direct measurements of the only observed avalanche (from Mount St. Helens), provides an average velocity of 35 m/s and initial velocities ranging from 70 to 80 m/s (Voight et al. 1981).

One of the first approaches used to determine debris avalanche mobility was based on the apparent coefficient of friction (H/L), using the relationship between the drop height and the maximum runout length of the flow (Hsü 1975). This parameter has been largely used to describe flow mobility, which generally increases as the mass (volume) increases (Dade and Huppert 1998). Therefore, larger volumes generally mean longer runouts as well as higher velocities. Some large avalanches have been known to carry blocks as long as three kilometers several kilometers from their source (Francis 1993).

Despite our observations on volcanic landslides, understanding the physical processes operating during exceptionally long run-out distances is still problematic. Several dynamic models about flow behavior and mechanism of emplacement have been proposed, ranging from fluidized granular flow (Bagnold 1954; Melosh 1983; Davies 1982; Campbell 1990) to plug flow (Takarada et al. 1999). Movement occurs over a lubricated, shearing basal layer that allows much of the mobility yet has minimal frictional effects (Voight et al. 1983; Reubi and Hernandez 2000; Clavero et al. 2002; Shea et al. 2008). A large list of transport mechanisms has been proposed to explain reduced friction of large avalanches, including fine basal powders, interstitial fluids, pore-fluid pressure, an air cushion, dispersive grain flow, local steam generation, frictional melting, lubrication, fluidization, entrainment, oscillation, and dynamic fragmentation (Kent 1966; Shreve 1968; Howard 1973; Hsü 1975; Lucchitta 1978; McSaveney 1978; Davies 1982; McEwen 1989; Iverson 1997; Davies and McSaveney 1999; van Wyk de Vries et al. 2001; Legros 2002; Collins and Melosh 2003; Aharonov and Anders 2006; Campbell 2006; Mangeney et al. 2007; Pudasaini and Hutter 2007; Deganutti 2008; Cagnoli and Quarenì 2009; McSaveney and Davies 2009; Davies et al. 2010). Of these different mechanisms, no one dominant mechanism stands out as an explanation for the hypermobility of huge slides and avalanches (Pudasaini and Miller 2013).

7 Hazards

The hazards that volcanic landslides at volcanoes, laccoliths, and volcanic fields can produce are numerous. Landslides can travel large distances and destroy everything in their paths, and they can dam rivers and lakes to produce flooding. It has been shown that landslides can lead to a decrease in magma pressure and cause an explosive volcanic eruption. The mixture of water with debris from an avalanche may produce debris flows that have much greater mobility, so can affect people living in valley areas far away from the source of the avalanche.

Hazards of volcanic landslides can be amplified by eruptions that are triggered by, or accompany, collapse of their unstable slopes. These associated eruptions can range from mild to moderate phreatic explosions to major Plinian eruptions, along with powerful lateral blasts from sudden depressurization of hydrothermal-magmatic systems.

Debris avalanches may convert to debris flows that travel considerably farther than avalanches and cover broad valley areas with great impact. Debris flows can form directly by transformation from debris avalanches during displacement, from dewatering of debris avalanche deposits shortly after emplacement, or from breakouts of avalanche-dammed lakes weeks to years after the avalanche (Pierson 1985; Fairchild 1987; Scott et al. 1995; Vallance and Scott 1997; Siebert 2002).

Another important hazard that can be produced from volcanic landslides are tsunamis. Historically, the most deadly volcanic landslide occurred in 1792 when sliding debris from Mt. Mayu-yama near Unzen Volcano in Japan plummeted into the Ariaka Sea and generated a tsunami that reached the opposite shore 20 km away, killing nearly 15,000 people in the process (Siebert 2002). The effect of tsunamis generated by volcanic landslides entering the seas or lakes is considerable. Nearly 80% of the ~25,000 historical fatalities from volcanic landslides came from those that generated tsunamis upon entering the water.

8 Summary

Most studies of volcanic structural failure and collapse have concentrated on volcano flanks, yet other volcanic landforms in volcanic terrains have produced collapse features that rival or surpass them in scale. These include slope failures from laccoliths and volcanic fields, both of which produced volcanic landslides that share many morphological and textural similarities with volcanic landslides from volcanoes. Subvolcanic magma systems may play an integral part in the collapse of all three volcanic collapse types by creating elevated landforms with steep slopes, by aiding in destabilizing slopes, and locally by triggering a slope failure. Some slope failures even triggered volcanic eruptions similar to, but larger than, those produced at Mount St. Helens. Although large-scale catastrophic collapse of volcanic fields are rare, they represent the largest known subaerial volcanic landslides on Earth.

Acknowledgements We gratefully acknowledge support from the Utah Geological Survey, the U.S. Geological Survey (National Cooperative Geologic Mapping Program) through a number of USGS STATEMAP grants, and the Kent State University Research Council. We also are grateful for generous cooperation and logistical support from the U.S. Forest Service and U.S. Geological Survey through the BARCO (Basin and Range–Colorado Plateau transition area) project. We would also like to thank Lee Siebert and Christoph Breitzkreuz for helpful reviews of this manuscript.

References

- Acocella V (2005) Modes of sector collapse of volcanic cones: Insights from analogue experiments. *J Geophys Res. Solid Earth* 110(B2)
- Acocella V, Behncke B, Neri M, D'Amico S (2003) Link between large-scale flank slip and 2002–2003 eruption at Mt. Etna (Italy). *Geophys Res Lett* 30(24):2286
- Aharonov E, Anders MH (2006) Hot water: a solution to the Heart Mountain detachment problem? *Geology* 34(3):165–168
- Arguden AT, Rodolfo KS (1990) Sedimentologic and dynamic differences between hot and cold laharc debris flows of Mayon Volcano, Philippines. *Geol Soc Am Bull* 102(7):865–876
- Bagnold RA (1954) Experiments on a gravity-free dispersion of large solid spheres in a Newtonian fluid under shear. *Proc R Soc Lond Ser A* 225:49–63
- Belousov AB (1995) The Shiveluch volcanic eruption of 12 November 1964—explosive eruption provoked by failure of the edifice. *J Volcanol Geotherm Res* 66:357–365
- Belousov AB (1996) Deposits of the 30 March 1956 directed blast at Bezmyianny volcano, Kamchatka, Russia. *Bull Volcanol* 57:649–662
- Beutner EC, Hauge TA (2009) Heart Mountain and South Fork fault systems—architecture and evolution of the col-lapse of an Eocene volcanic system, northwest Wyoming. *Rocky Mt Geol* 44(2):147–164
- Biek RF, Rowley PD, Hayden JM, Hacker DB, Willis GC, Hintze LF, Anderson RE, Brown KD (2009) Geologic Map of the St. George and East Part of the Clover Mountains 30' × 60' quadrangles, Washington and Iron Counties, Utah. Utah Geological Survey Map 242, scale 1:100,000
- Biek RF, Hacker DB, Rowley PD (2014) New constraints on the extent, age, and emplacement history of the early Miocene Markagunt Megabreccia, southwest Utah—the deposit of one of the world's largest subaerial gravity slides. In: MacLean JS, Biek RF, Huntoon JF (eds) *Geology of Utah's far south*, vol 43. Utah Geological Association Publication, pp 565–598
- Biek RF, Rowley PD, Anderson JJ, Maldonado F, Moore DW, Hacker DB, Eaton JG, Hereford R, Sable EG, Filkorn HF, Matyjasik B (2015) Geologic map of the Panguitch 30' × 60' quadrangle, Garfield, Iron, and Kane Counties, Utah. Utah Geological Survey Map 270DM, scale 1:62,500
- Blank HR, Rowley PD, Hacker DB (1992) Miocene monzonitic intrusions and associated megabreccias of the Iron Axis region, southwestern Utah. In: Wilson JR (ed) *Field guide to geologic excursions in Utah and adjacent areas of Nevada, Idaho, and Wyoming*. Utah Geological Survey Miscellaneous Publication 92-3, pp 399–420
- Blank Jr HR, Mackin JH (1967) Geologic interpretation of an aeromagnetic survey of the Iron Springs district, Utah. U.S. Geological Survey Professional Paper, 516-B
- Bulmer, MH, Guest, JE (1996) Modified volcanic domes and associated debris aprons on Venus. In: McGuire WJ, Jones AP, Neuberg J (eds) *Volcano instability on the Earth and Other planets*. Geological Society Special Publication
- Cagnoli B, Quarenzi F (2009) Oscillation-induced mobility of flows of rock fragments with quasi-rigid plugs in rectangular channels with frictional walls: a hypothesis. *Eng Geol* 103(1–2):23–32
- Campbell CS (1990) Rapid granular flows. *Annu Rev Fluid Mech* 22(1):57–90

- Campbell CS (2006) Granular material flows—an overview. *Powder Technol* 162:208–229
- Carracedo JC (1994) The Canary Islands: an example of structural control on the growth of large oceanic-island volcanoes. *J Volcanol Geotherm Res* 60:225–241
- Carrasco-Núñez G, Siebert L, Capra L (2011) Hazards from volcanic avalanches. *Horizons in earth science research*. Nova Science Publishers, New York
- Clavero JE, Sparks RSJ, Huppert HE (2002) Geological constraints on the emplacement mechanism of the Parinacota debris avalanche, northern Chile. *Bull Volcanol* 64:40–54
- Collins GS, Melosh HJ (2003) Acoustic fluidization and the extraordinary mobility of sturzstroms. *J Geophys Res* 108(B10):2473
- Costa JE (1988) Floods from dam failures. In: Baker VR, Kochel RC, Patton PC (eds) *Flood geomorphology*. Wiley, New York, pp 439–463
- Costa JE, Shuster RL (1988) The formation and failure of natural dams. *Geol Soc Am Bull* 100:1054–1068
- Craddock JP, Malone DH, Magloughlin J, Cook AL, Rie-ser ME, Doyle JR (2009) Dynamics of the emplacement of the Heart Mountain allochthon at White Mountain—constraints from calcite twinning strains, anisotropy of magnetic susceptibility, and thermodynamic calculations. *Geol Soc Am Bull* 121(5/6):919–938
- Crandell DR (1989) Gigantic debris-avalanche of Pleistocene age from ancestral Mount Shasta volcano, California, and debris avalanche hazard zonation. *Bulletin of the US Geological Survey*, 1861
- Crandell DR, Miller CD, Glicken HX, Christiansen RL, Newhall CG (1984) Catastrophic debris avalanche from ancestral Mount Shasta volcano, California. *Geology* 12:143–146
- Cruden DM, Varnes DJ (1996) Landslide types and processes. In: Turner AK, Schuster RL (eds) *Landslides investigation and mitigation*. Transportation Research Board, U.S. National Research Council, Special Report 247, chap. 3, pp 36–75
- Crumpler LS, Head JW, Aubele JC (1996) Calderas on Mars: characteristics, structure, and associated flank deformation. In: McGuire WJ, Jones AP, Neuberg J (eds) *Volcano instability on the Earth and other planets*. Geological Society Special Publication
- Dade WB, Huppert HE (1998) Long-runout rockfalls. *Geology* 26(9):803–806
- Davies TRH (1982) Spreading of rock avalanche debris by mechanical fluidization. *Rock Mech* 15:9–24
- Davies TR, McSaveney MJ (1999) Runout of dry granular avalanches. *Can Geotech J* 36(2):313–320
- Davies T, McSaveney M, Kelfoun K (2010) Runout of the Socompa volcanic debris avalanche, Chile: a mechanical explanation for low basal shear resistance. *Bull Volc* 72(8):933–944
- Day S (1996) Hydrothermal pore fluid pressure and the stability of porous, permeable volcanoes. In: McGuire WJ, Jones AP, Neuberg J (eds) *Volcano instability on the Earth and other Planets*. Geological Society London Special Publication, vol 110, pp 77–94
- Deganutti AM (2008) The hypermobility of rock avalanches. (PhD Dissertation, Università degli Studi di Padova)
- del Petro R, Hürlimann M, Pinkerton H (2013) Modelling flank instabilities on stratovolcanoes: parameter sensitivity and stability analyses of Teide, Tenerife. *J Volcanol Geotherm Res* 256:50–60
- Elsworth D, Voight B (1996) Evaluation of volcano flank instability triggered by dyke intrusion. *Spec Pub Geol Soc Lond* 110:45–54
- Fairchild LH (1987) The importance of lahar initiation processes. *Rev Eng Geol* 7:51–61
- Frank D (1995) Surficial extent and conceptual model of hydrothermal system at Mount Rainier, Washington. *J Volcanol Geotherm Res* 65:51–80
- Francis P (1993) *Volcanoes, a planetary perspective*. Oxford University Press, Oxford, p 443
- Francis PW, Gardeweg M, Ramirez CF, Rothery DA (1985) Catastrophic debris avalanche deposit of Socompa volcano, northern Chile. *Geology* 13:600–603
- Glicken H (1986) Rockslide—debris avalanche of May 18, 1980, Mount St. Helens volcano. PhD dissertation, Univ Santa Barbara, 303 p
- Glicken H (1991) Rockslide-debris avalanche of May 18th, 1980, Mount St. Helens volcano. US Geological Survey Professional Paper, Washington, p 1488
- Glicken H (1996) Rockslide-debris avalanche of May 18, 1980, Mount St. Helens Volcano, Washington. U.S. Geological Survey Open-File Report 96-677, 90 p
- Glicken H (1998) Rockslide-debris avalanche of May 18, 1980, Mount St. Helens Volcano, Washington. *Bull Geol Surv Japan* 49(2/3):55–106
- Gorshkov GS (1959) Gigantic eruption of the volcano Bezymianny. *Bull Volcanol* 20:77–109
- Gorshkov GS, Dubik YM (1970) Gigantic directed blast at Shiveluch volcano (Kamchatka). *Bull Volcanol* 34:261–288
- Hacker DB, (1998) Catastrophic gravity sliding and volcanism associated with the growth of laccoliths—examples from early Miocene hypabyssal intrusions of the Iron Axis magmatic province, Pine Valley Mountains, southwestern Utah. Kent, Ohio, Kent State University, Ph.D. dissertation, 258 p
- Hacker DB, Rowley PD, Blank HR, Snee LW (1996) Early Miocene catastrophic gravity sliding and volcanism associated with intrusions of the southern Iron Axis region, southwest Utah. *Geol Soc Am Abstr Programs* 29:511
- Hacker DB, Holm DK, Rowley PD, Blank HR (2002) Associated Miocene laccoliths, gravity slides, and volcanic rocks, Pine Valley Mountains and Iron Axis region, south-western Utah. In: Lund WR (ed) *Field guide to geo-logic excursions in southwestern Utah and adjacent areas of Arizona and Nevada*. U.S.

- Geological Survey Open-File Report OF 02-0172, pp 235–283
- Hacker DB, Petronis MS, Holm DK, and Geissman JW (2007) Shallow level emplacement mechanisms of the Miocene Iron Axis laccolith group, southwest Utah. In: Lund WR (ed) Field guide to geologic excursions in southern Utah. Utah Geological Association Publication vol 35, p 49
- Hacker DB, Biek RF, Rowley PD (2014) Catastrophic emplacement of the gigantic Markagunt gravity slide, southwest Utah (USA). Implications for hazards associated with sector collapse of volcanic fields. *Geology* 42(11):943–946
- Herrick JA, Siebert L, Rose WI (2013) Large-volume Barriles and Caisán debris avalanche deposits from Volcán Barú, Panama. *Geol Soc Am Spec Pap* 498:141–162
- Hoblitt RP, Miller CD, Vallance JW (1981) Origin and stratigraphy of the deposit produced by the May 18 directed blast. In: Lipman PW, Mullineaux DR (eds) The 1980 eruptions of Mount St. Helens, Washington, vol 1250. U.S. Geol Surv Prof Paper, pp 401–419
- Howard KA (1973) Avalanche mode of motion: implications from lunar examples. *Science* 180:1052–1055
- Hsü KJ (1975) Catastrophic debris stream (Sturzstroms) generated by rockfalls. *Geol Soc Amer Bull* 86:129–140
- Hsü KJ (1978) Albert Heim: observations on landslides and relevance to modern interpretations. *Rocks and Avalanches*. 1:71–93
- Iverson RM (1997) The physics of debris flows. *Rev Geophys* 35:245–296
- Keating BH, McGuire WJ (2000) Island edifice failures and associated tsunami hazards. *Pure appl Geophys* 157(6-8):899–955
- Kent PE (1966) The transport mechanism in catastrophic rock falls. *J Geol* 74:79–83
- Komorowski JC, Boudon G, Semet M, Beauducel F, Anténor-Habazac C, Bazin S, Hammouya G (2005) Guadeloupe. In: Lindsay J, Robertson R, Shepherd J, Ali S (eds) Volcanic hazard atlas of the Lesser Antilles. University of the West Indies, Seismic Research Unit, Trinidad and IAVCEI, pp 65–102
- Komorowski JC, Glicken HX, Sheridan MF (1991) Secondary electron imagery of microcracks and hackly fracture surfaces in sand-size clasts from the 1980 Mount St. Helens debris-avalanche deposit: implications for particle-particle interactions. *Geology* 19(3):261–264
- Kuntz MA, Rowley PD, MacLeod NS (1990) Geologic maps of pyroclastic-flow and related deposits of the 1980 eruptions of Mount St. Helens, Washington. U. S. Geological Survey Miscellaneous Investigations Series Map I-1950, scale 1:12,000
- Legros F (2002) The mobility of long runout landslides. *Eng Geol* 63:301–331
- Lipman PW, Mullineaux D (eds) (1981) The 1980 eruptions of Mount St. Helens. US Geological Survey Professional Paper, 1250
- Lipman PW, Rhodes JM, Dalrymple GB (1991) The Ninole Basalt—implications for the structural evolution of Mauna Loa volcano, Hawaii. *Bull Volcanol* 53:1–19
- Lopez DL, Williams SN (1993) Catastrophic volcanic collapse: relation to hydrothermal processes. *Science* 260:1794–1796
- Lucchitta BK (1978) A large landslide on Mars. *Geol Soc Am Bull* 89:1601–1609
- Mackin JH (1960) Structural significance of Tertiary volcanic rocks in southwestern Utah. *Am J Sci* 258(2):81–131
- Malone DH, Craddock JP (2008) Recent contributions to the understanding of the Heart Mountain detachment, Wyoming. *Northwest Geol* 37:21–40
- Mangeny A, Tsimring LS, Volfson D, Aranson IS, Bouchut F (2007) Avalanche mobility induced by the presence of an erodible bed and associated entrainment. *Geophys Res Lett* 34:L22401
- McEwen AS (1989) Mobility of large rock avalanches: evidence from Valles Marineris, Mars. *Geology* 17:1111–1114
- McGuire WJ (1996) Volcano instability: a review of contemporary themes. In: McGuire WJ, Jones AP, Neuberg J (eds) Volcano instability on the earth and other planets. Geological Society Special Publication
- McGuire WJ (2006) Lateral collapse and tsunamigenic potential of marine volcanoes. *Geol Soci London Spec Publ* 269(1):121–140
- McSaveney MJ (1978) Sherman glacier rock avalanche, Alaska, U.S.A. In: Voight B (ed) Natural phenomena. *Rocks and avalanches*, vol 1. Elsevier Sci., New York, pp 197–258
- McSaveney MJ, Davies TRH (2009) Surface energy is not one of the energy losses in rock comminution. *Eng Geol* 109:109–113
- Mehl KW, Schmincke HU (1999) Structure and emplacement of the Pliocene Roque Nublo debris avalanche deposit, Gran Canaria, Spain. *J Volcanol Geoth Res* 94(1):105–134
- Melosh HJ (1983) Acoustic fluidization: can sound waves explain why dry rock debris appears to flow like a fluid in some energetic geologic events? *Am Sci* 71:158–165
- Moore JG, Clague DA, Holcomb RT, Lipman PW, Normark WR, Torresan ME (1989) Prodigious submarine landslides on the Hawaiian Ridge. *J Geophys Res* 94:17465–17484
- Moore JG, Normark WR, Holcomb RT (1994) Giant Hawaiian landslides. *Ann Rev Earth Planet Sci* 22:119–144
- Palmer BA, Neall VE (1989) The Murimotu Formation—9500 year old deposits of a debris avalanche and associated lahars, Mount Ruapehu, North Island, New Zealand. *J Geol Geophys* 32:477–486
- Petronis MS, Hacker DB, Holm DK, Geissman JW, Harlan SS (2004) Magmatic flow paths and paleomagnetism of the Miocene Stoddard Mountain Laccolith, Iron Axis region, southwest Utah, USA.

- In: Martin-Hernandez F, Luneburg CM, Aubourg C, Jackson M (eds) *Magnetic fabric: methods and applications*, vol 238. The Geological Society of London, Special Publications, pp 251–283
- Pierson TC (1985) Initiation and behavior of the 1980 Pine Creek and Muddy River lahars, Mount St. Helens, Washington. *Geol Soc Am Bull* 96:1056–1069
- Pierson TC, Costa JE (1987) A rheologic classification of subaerial sediment-water flows. In: Costa JE, Wicczorek GF (eds) *Debris flows/Avalanches: process, recognition, and mitigation*. *Geol. Soc. Am. Rev. Eng. Geol.*, pp 1–12
- Ponomareva VV, Melekestsev IV, Dirksen OV (2006) Sector collapses and large landslides on late Pleistocene-Holocene volcanoes in Kamchatka, Russia. *J Volc Geotherm Res* 158:117–138
- Pulgarin B, Macas JL, Cepeda H (1999) Secondary debris flow originated from the dam failure of a Pleistocene debris avalanche deposit, Nevado del Huila Volcanic Complex, Colombia. *Am. Geophys. Union Fall Meeting*. *Eos, Trans. Am. Geophys. Union*, San Francisco, CA, p. V31D-02
- Pudasaini SP, Hutter K (2007) *Avalanche dynamics: dynamics of rapid flows of dense granular avalanches*. Springer, Berlin, New York
- Pudasaini SP, Miller SA (2013) The hypermobility of huge landslides and avalanches. *Eng Geol* 157:124–132
- Reubi O, Hernandez J (2000) Volcanic debris avalanche deposits of the upper Maronne valley (Cantal volcano, France): evidence for contrasted formation and transport mechanism. *J Volcanol Geotherm Res* 102:271–286
- Rowley PD (1998) Cenozoic transverse zones and igneous belts in the Great Basin, western United States: their tectonic and economic implications. *Special Papers-Geological Society of America*, pp 195–228
- Rowley PD, Cunningham CG, Steven TA, Mehnert HH, Naeser CW (1998) Cenozoic igneous and tectonic setting of the Marysvale volcanic field and its relation to other igneous centers in Utah and Nevada. In: *Laccolithic complexes of southeastern Utah: time of emplacement and tectonic setting—workshop proceedings*, pp 167–201
- Rowley PD, Cunningham CG, Steven TA, Workman JB, Anderson JJ, Theissen KM (2002) Geologic map of the central Marysvale volcanic field, southwestern Utah. U.S. Geological Survey Geologic Investigations Series Map I-2645-A, scale 1:100,000
- Rowley PD, Kuntz MA, MacLeod NS (1981) Pyroclastic-flow deposits. In: Lipman PW, Mullineaux DR (eds) *The 1980 eruptions of Mount St. Helens, Washington*. U.S. Geological Survey Professional Paper, vol 1250, pp 489–512
- Rowley PD, MacLeod NS, Kuntz MA, Kaplan AM (1985) Proximal bedded deposits related to pyroclastic flows of May 18, 1980, Mount St. Helens, Washington. *Geol Soc Am Bull* 96:1373–1383
- Rowley PD, Vice GS, McDonald RE, Anderson JJ, Machette MN, Maxwell DJ, Ekren EB, Cunningham CG, Steven TA, Wardlaw BR (2005) Interim geologic map of the Beaver 30' × 60' quadrangle, Beaver, Piute, Iron, and Garfield Counties, Utah. Utah Geological Survey Open-File Report 454, scale 1:100,000
- Rowley PD, Williams VS, Vice GS, Maxwell DJ, Hacker DB, Snee LW, Mackin JH (2006) Interim geologic map of the Cedar City 30' × 60' quadrangle, Iron and Washington Counties, Utah. Utah Geological Survey Open-File Report 476DM, scale 1:100,000
- Schuster RL, Crandell, DR, (1984) Catastrophic debris avalanches from volcanoes. In: *IV international symposium on landslide proceedings*, Toronto, vol 1, pp 567–572
- Scott KM, Vallance JW (1995) Debris flow, debris avalanche, and flood hazards at and downstream from Mount Rainier, Washington. U.S. Geological Survey Hydrologic Investigations Atlas 729: 2 Sheets and Accompanying Pamphlet
- Scott KM, Vallance JW, Pringle PT (1995) Sedimentology, behavior and hazards of debris flows at Mount Rainier, Washington. U.S. Geological Survey Professional Paper 1547, 56 p
- Scott KM, Macias JL, Vallance JW, Naranjo JA, Rodriguez-Elizarraras SR, McGeehin JP (2002) Catastrophic debris flows transformed from landslides in volcanic terrains: mobility, hazard assessment, and mitigation strategies. *US Geological Survey Professional Paper*, 1630
- Scott KM, Vallance JW, Kerle N, Luis Macías J, Strauch W, Devoli G (2005) Catastrophic precipitation-triggered lahar at Casita volcano, Nicaragua: occurrence, bulking and transformation. *Earth Surf Proc Land* 30(1):59–79
- Shea T, van Wyk de Vries B, Pilato M (2008) Emplacement mechanisms of contrasting debris avalanches at Volcan Mombacho (Nicaragua), provided by structural and facies analysis. *Bull Volcanol* 70:899–921
- Shreve RL (1968) The Blackhawk landslide. *Geol Soc Am Spec Pap* 108:47
- Siebert L (1984) Large volcanic debris avalanches: characteristics of source areas, deposits, and associated eruptions. *J Volcanol Geotherm Res* 22:163–197
- Siebert L (1992) Threats from debris avalanches. *Nature* 356:658–659
- Siebert L (1996) Hazards of large volcanic debris avalanches and associated eruptive phenomena. In: Scarpa T, Tilling RI (eds) *Monitoring and mitigation of volcanic hazards*. Springer, Berlin, pp 541–572
- Siebert L (2002) Landslides resulting from structural failure of volcanoes. In: Evans SG, De Graff JV (eds) *Catastrophic landslides: effects, occurrence, and mechanisms*, vol 15. *Geol Soc Amer Rev Eng Geol*, pp 209–235
- Siebert L, Glicken H, Ui T (1987) Volcanic hazards from Bezymianny- and Bandai-type eruptions. *Bull Volcanol* 49:435–459
- Siebert L, Béget JE, Glicken H (1995) The 1883 and late-prehistoric eruptions of Augustine volcano, Alaska. *J Volcanol Geotherm Res* 66:367–395

- Siebert L, Alvarado GE, Vallance JW, van Wyk de Vries B (2006) Large-volume volcanic edifice failures in Central America and associated hazards. In: Rose WI, Bluth GJS, Carr MJ, Ewert JW, Patino LC, Vallance JW (eds) *Volcanic hazards in Central America*, Geological Society of America Special Paper, vol 412, pp 1–26
- Siebert L, Simkin T, Kimberly P (2010) *Volcanoes of the World*, 3rd edn. University of California Press, Berkeley, p 551
- Stoopes GR, Sheridan MF (1992) Giant debris avalanches from the Colima Volcanic Complex, Mexico: implications for long runout landslides (>100 km) and hazard assessment. *Geology* 20:299–302
- Takarada T, Ui T, Yamamoto H (1999) Depositional features and transportation mechanism of valley filling Iwasegawa and Kaida debris avalanches, Japan. *Bull Volcanol* 60:508–522
- Ui T (1983) Volcanic debris avalanche deposits—identification and comparison with non-volcanic debris stream deposits. *J Volcanol Geotherm Res* 18:135–150
- Ui T, Yamamoto H, Suzuki-Kamata K (1986) Characterization of debris avalanche deposits in Japan. *J. Volcanol Geotherm Res* 29:231–243
- Ui T, Takarada S, Yoshimoto M (2000) Debris avalanches. *Encycl Volcanoes* 617–626
- Vallance JW, Scott KM (1997) The Osceola Mudflow from Mount Rainier: sedimentology and hazard implications of a huge clay-rich debris flow. *Geol Soc Am Bull* 109:143–163
- van Wyk de Vries B, Francis P (1997) Catastrophic collapse at stratovolcanoes induced by gradual volcano spreading. *Nature* 387:387–390
- van Wyk de Vries B, Self S, Francis, PW Keszthelyi L (2001) A gravitational spreading origin for the Socompa debris avalanche. *J Volcanol Geotherm Res* 105:225–247
- van Wyk de Vries B, Davies T (2015) Landslides, debris avalanches and volcanic gravitational deformation. In: Sigurdsson H, Houghton B, McNutt S, Rymer H, Stix J (eds) *The encyclopedia of volcanoes*, 2nd edn, pp 665–685
- van Wyk de Vries B, Delcamp A (2015) Chapter 5—volcanic debris avalanches. In: *Landslide hazards, risks and disasters*. Academia Press
- Varnes DJ (1978) Slope movement types and processes. In: Schuster RL, Krizek RJ (eds) *Landslides, analysis and control*. National Research Council, Transportation Research Board, Special Report, vol 176, pp 11–33
- Voight B (ed) (1978) *Rockslides and avalanches 1, natural phenomena*. Elsevier, Amsterdam, 826 p
- Voight B (1981) Time scale for the first movements of the May 18 eruption. In: Lipman PW, Mullineaux DR (eds) *The 1980 eruptions of Mount St. Helens*, Washington. US Geological Survey Professional Paper, vol 1250, pp 69–86
- Voight B, Elsworth D (1992) Resolution of mechanics problems for prodigious Hawaiian landslides: magmatic intrusions simultaneously increase driving force and reduce driving resistance by fluid pressure enhancement (abstract). *Eos Trans. AGU* 73 43, 506, Fall Meeting suppl
- Voight B, Elsworth D (1997) Failure of volcano slopes. *Geotechnique* 47(1):1–31
- Voight B, Glicken H, Janda RJ, Douglass PM (1981) Catastrophic rockslide avalanche of May 18. In: Lipman PW, Mullineaux DR (eds) *The 1980 eruptions of Mount St. Helens*, Washington. US Geological Survey Professional Paper, vol 1250, pp 347–348
- Voight B, Janda RJ, Glicken H, Douglass PM (1983) Nature and mechanics of the Mount St. Helens rockslide-avalanche of 18 May 1981. *Geotechnique* 33:243–273
- Voight B, Komorowski J C, Norton G E, Belousov A, Belousova M, Boudon G, Francis PW, Franz W, Heinrich P, Sparks RSJ, Young SR (2002) The 26 December (Boxing Day) 1997 sector collapse and debris avalanche at Soufrière Hills Volcano, Montserrat. In: Druitt TH, Kokelaar P (eds) *The eruption of Soufrière Hills Volcano, Montserrat, from 1995 to 1999*. The Geoll Soc London, Mem, vol 21, pp 363–407
- Wadge G, Francis PW, Ramirez CF (1995) The Socompa collapse and avalanche event. *J Volcanol Geotherm Res* 66:309–336
- Yokoyama I (2002) Growth mechanism of the 1944 lava dome of Usu volcano in Hokkaido, Japan. *Proc Japan Acad, Ser B* 78(1):6–11

Sub-Volcanic Intrusions and the Link to Global Climatic and Environmental Changes

Henrik H. Svensen, Sverre Planke,
Else-Ragnhild Neumann, Ingrid Aarnes, Julian S. Marsh,
Stéphane Polteau, Camilla H. Harstad and Luc Chevallier

Abstract

Most of the Large Igneous Provinces (LIPs) formed during the last 260 million years are associated with climatic changes, oceanic anoxia, or extinctions in marine and terrestrial environments. Current hypotheses involve (1) degassing of carbon from either oceans or shallow sea-bed reservoirs, (2) degassing from flood basalts, or from (3) sedimentary basins heavily intruded by LIP-related sills. These hypotheses are based on detailed geological and geochemical studies from LIPs or relevant proxy data sequences. Here we present new data on gas generation and degassing from a LIP, based on the LA1/68 borehole north of the Ladybrand area in the Karoo Basin, South Africa. The borehole was drilled in the middle of a phreatic breccia pipe and penetrated 11 sills before reaching the basement at 1710 m depth. We present new data on the lowermost 15 m thick sill emplaced in shale, and on the breccia comprising the uppermost 154 m of the core. We show that (1) a reduction in organic matter within a contact aureole can be explained by heating and the formation of CH₄, (2) a phreatic eruption and breccia formation was

H.H. Svensen (✉) · S. Planke · E.-R. Neumann
Centre for Earth Evolution and Dynamics (CEED),
University of Oslo, Oslo, Norway
e-mail: hensven@fys.uio.no

S. Planke · S. Polteau
Volcanic Basin Petroleum Research (VBPR), Oslo
Innovation Centre, Oslo, Norway

I. Aarnes
Roxar Software Solutions, AS, Oslo, Norway

J.S. Marsh
Rhodes University, Grahamstown, South Africa

C.H. Harstad
AGR Petroleum Services, Oslo, Norway

L. Chevallier
Council for Geoscience, Bellville, South Africa

initiated from pore fluid boiling around sills emplaced in Beaufort Group sandstones at 420–570 m depth, (3) the phreatic eruption cut through a cover of solidified and partly molten lava flows that subsequently filled the crater, and (4) the pipe has been used as a fluid flow pathway for millions of years, demonstrated by fossil and active oil seeps. We conclude that the sub-volcanic LIP environment hold the key to understand the relationships between large scale volcanism and rapid environmental perturbations.

1 LIPs and the Environment

The causal relationships between Large Igneous Provinces (LIPs) and environmental changes and mass extinctions are debated. There is a broad correlation between LIPs and global carbon isotope excursions (i.e., global warming), oceanic anoxic events, and extinctions in the oceans and on the continents. Examples of events include the North Atlantic volcanic province and the Paleocene-Eocene thermal maximum (55.6 Ma), the Karoo LIP and the Toarcian event (182.6 Ma), the Siberian Traps and the end-Permian (252 Ma), and the Central Atlantic magmatic province and the end-Triassic (201 Ma) (e.g., Bond and Wignall 2014; Courtillot and Renne 2003; Stothers 1993; Svensen and Jamtveit 2010; Wignall 2001).

Since the 1980s, Large Igneous Provinces were regarded as key players in triggering mass extinctions. Degassing from subaerial lava flows could lead to short term global cooling and long term global warming (Caldeira and Rampino 1990). However, the increasing interest in sedimentary sections and proxy data measurements in the 1990s, especially carbon isotope data, suggested that large quantities of ^{12}C -enriched carbon was needed to explain events such as the PETM and the end-Permian (Bernier 2002; Dickens et al. 1997). As basaltic systems contain too little and too ^{13}C -enriched carbon, LIP lava degassing was not consistent with available proxy data.

Following the work on marine gas hydrates in the 1990s, rapid environmental changes and carbon isotope excursions were almost exclusively explained by gas hydrate dissociation (e.g., Cohen et al. 2007; Dickens et al. 1997;

Hesselbo et al. 2000; Kemp et al. 2005). LIP volcanism was not considered as a relevant part of the long term climate system.

In 2004 it was suggested that the sub-volcanic parts of LIPs may mobilize sedimentary carbon during interaction between sills, dykes, and carbon-rich sedimentary rocks (Svensen et al. 2004). This hypothesis, often referred to as ‘the thermogenic gas hypothesis’, provided a new framework for investigating the environmental consequences of LIPs, volcanism, and metamorphic processes. The cornerstones of the 2004 hypothesis can be summarized as:

- Sill emplacement in organic-bearing sedimentary units lead to heating and devolatilization of the contact aureole, usually to a distance equal to the sill thickness on both sides of the sill.
- Generation of CH_4 and CO_2 from heating of organic matter and carbonates, with ^{12}C -enriched isotopic signatures.
- Degassing to the atmosphere following release of overpressure, either during the formation of breccia pipes and hydrothermal vent complexes, or during long term seepage.
- Whereas carbon gases derived from organic matter and limestone can contribute to climate changes, sulfur- and halogen-bearing gases formed during magma-evaporite interactions may have led to mass extinction due to atmospheric ozone depletion. Thus the environmental effects of sill emplacement depend on the type of sedimentary rocks intruded.

As sedimentary basins represent a vast reservoir of organic carbon, rapid heating events in the

sub-volcanic domain of a LIP may generate sufficient ^{12}C -enriched gas to explain available proxy data and carbon cycle models for past warming events (Bernier 2002). Recent results have suggested that the hypothesis can be applied to most of the major rapid climate and extinction events since 260 Ma, including the Toarcian (Lower Jurassic), the Triassic-Jurassic, the end-Permian, the end-Guadalupian, and the Miocene climatic optimum (e.g., Armstrong et al. 2014; Beerling et al. 2007; Ganino and Arndt 2009; McElwain et al. 2005; Retallack and Jahren 2008; Ruhl and Kürschner 2011; Svensen et al. 2007, 2009a; van de Schootbrugge et al. 2009).

This study is a part of a large project at the University of Oslo targeted at understanding sub-volcanic processes and the link to global environmental changes. Projects include sill geochemistry and emplacement mechanisms, contact metamorphism and organic maturation, venting processes, extinction mechanisms, chemostratigraphy and tephra geochronology (Aarnes et al. 2010, 2011a, b, 2012; Galerne et al. 2008; Grab and Svensen 2011; Jamtveit et al. 2004; Malthe-Sørenssen et al. 2004; Mazzini et al. 2010; Neumann et al. 2011; Polteau et al. 2008a, 2008b; Roscher et al. 2011; Svensen and Jamtveit 2010; Svensen et al. 2006, 2007, 2009a, b, 2010, 2012).

The aim of this study is to present new data and interpretations that show how geological processes in a sedimentary basin can be used to understand the environmental consequences of LIP formation, in particular the sub-volcanic parts. We present new data from the Karoo Basin on (1) contact metamorphism of black shale, including volatile generation, and (2) formation of a basalt-dominated breccia pipe, including a comparison of the basalt breccia geochemistry with that of the nearby Lesotho basalts.

2 Sills and Pipes in the Karoo Basin

The Upper Carboniferous to Triassic Karoo Supergroup in South Africa is divided in five groups (the Dwyka, Eccca, Beaufort, Stormberg

and Drakensberg groups) with a postulated maximum cumulative thickness of 12 km and a preserved maximum thickness of 5.5 km (Tan-kard et al. 2009). The depositional environments range from marine and glacial (the Dwyka Group), marine to deltaic (the Eccca Group), to fluvial (the Beaufort Group) and finally aeolian (the Stormberg Group) (Catuneanu et al. 1998, 2005). The Karoo Basin is overlain by 1.65 km of preserved volcanic rocks of the Drakensberg Group, consisting mainly of stacked basalt flows erupted in a continental and dry environment (Bristow and Saggerson 1983; Duncan and Marsh 2006; Marsh and Eales 1984). The plumbing system of the Karoo continental flood basalts is a basin-scale intrusive complex consisting of sills and dykes of varying thickness (Fig. 1) (Chevallier and Woodford 1999; du Toit 1920; Marsh and Eales 1984) emplaced at about 182.6 Ma (Svensen et al. 2012).

The sedimentary rocks hosting the sill complexes are affected by contact metamorphism. Contact aureoles around the sills are particularly well developed in the Eccca Group, and are characterized by bleached hornfels where the organic carbon content is reduced to zero near the sill contacts (Aarnes et al. 2010, 2011b; Svensen et al. 2007). Model simulations of methane generation from dispersed organic matter in black shale from the Karoo Basin suggests a production potential of 50–500 kg/m³ in the inner contact aureole (Aarnes et al. 2011b). In shales with very high organic carbon contents, the resulting pressure increase during gas formation is substantial, making it more likely that fracturing and degassing take place compared to a shale with no or little organic matter (Aarnes et al. 2012). During fracturing, the fluids produced vertical breccia pipes and hydrothermal vent craters at the surface. Hundreds of such pipes and vents crop out in the Karoo Basin (Dingle et al. 1983; Gevers 1928; Jamtveit et al. 2004; Svensen et al. 2006, 2007). The breccia pipes are confined to the Eccca and Beaufort groups, whereas the hydrothermal vent complexes are present within the uppermost group, the Stormberg Group (Fig. 1), formed during shallow boiling of pore fluids. Figure 2 shows a

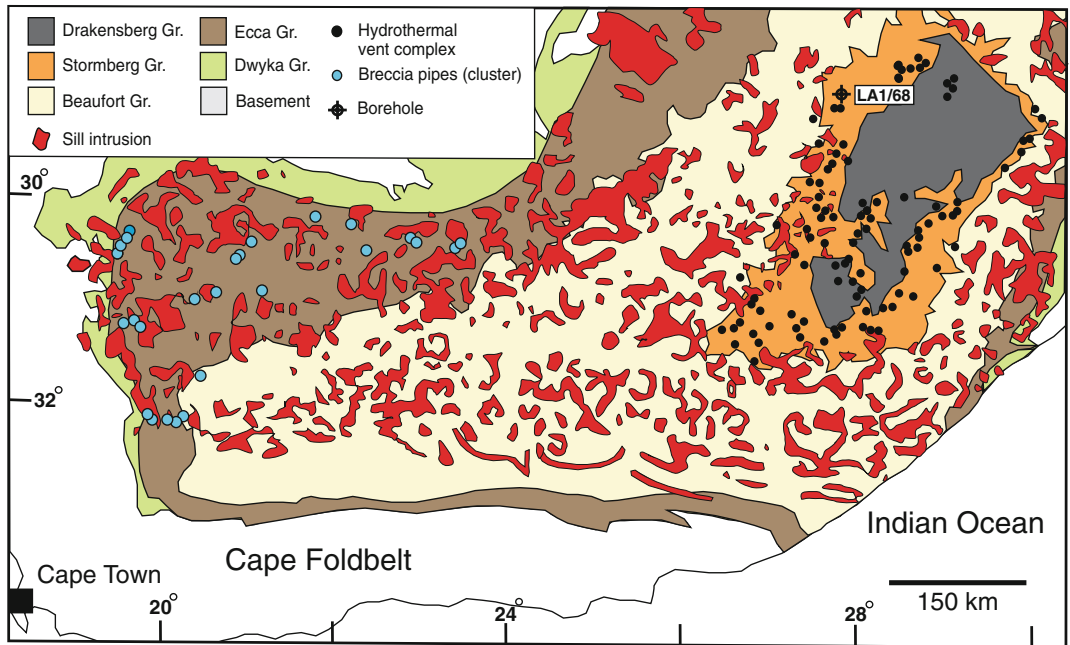


Fig. 1 Geological map of the Karoo Basin showing the distribution of sill intrusions and the locations of the LA1/68 borehole used in this study. Other localities refer to the vent structures presented in Fig. 3

selection of outcrops of pipes and hydrothermal vent complexes. In addition, large phreatomagmatic complexes are present in the Stormberg Group (McClintock et al. 2008). The latter contain a range of rock types (lava, sedimentary fragments, and pyroclastic rocks) and formed during interactions between magma and surface water. Thus the Karoo Basin contains a remarkable range of combined magmatic, metamorphic and sedimentary degassing structures that were active in the Early Jurassic.

This study presents another type of degassing structure that has received only minor attention so far: circular pipe structures dominated by volcanic breccia infill with a varying degree of sedimentary fragments and intercalations. We focus on a key area north of Ladybrand (Figs. 2a and 3) where we have borehole and field constraints from such a volcanic-dominated pipe. In addition, numerous sills are present in the borehole. The organic-rich Eccla Formation is thermally affected and methane generation in the contact aureole could have played a part in the Early Jurassic climate change (cf. Svensen et al. 2007).

3 Methods

The LA1/68 borehole was drilled by Soekor between 1968 and 1972 at the Olney farm 16 km NW of Ladybrand (−29.09, 27.48) (Roux 1972). The borehole was drilled in the middle of a basalt breccia in the Elliot Formation, the Stormberg Group (Figs. 3 and 4). The reason for choosing this particular location for drilling was presumably the discovery of an active oil seep within the breccia when it was quarried in the 1960s. The borehole reached the base of the Eccla Formation at 1710 m depth, terminated at 2002 m depth within basement gneiss and is fully cored. Both the core and the original logs were obtained at the Council for Geoscience in Pretoria, South Africa. Fieldwork at Olney and borehole sampling in Pretoria was done in the period 2002–2011.

Thin sections of selected basalt and sediment samples were studied and analysed using a Cameca SX100 electron microprobe with integrated energy dispersive spectrometer and five

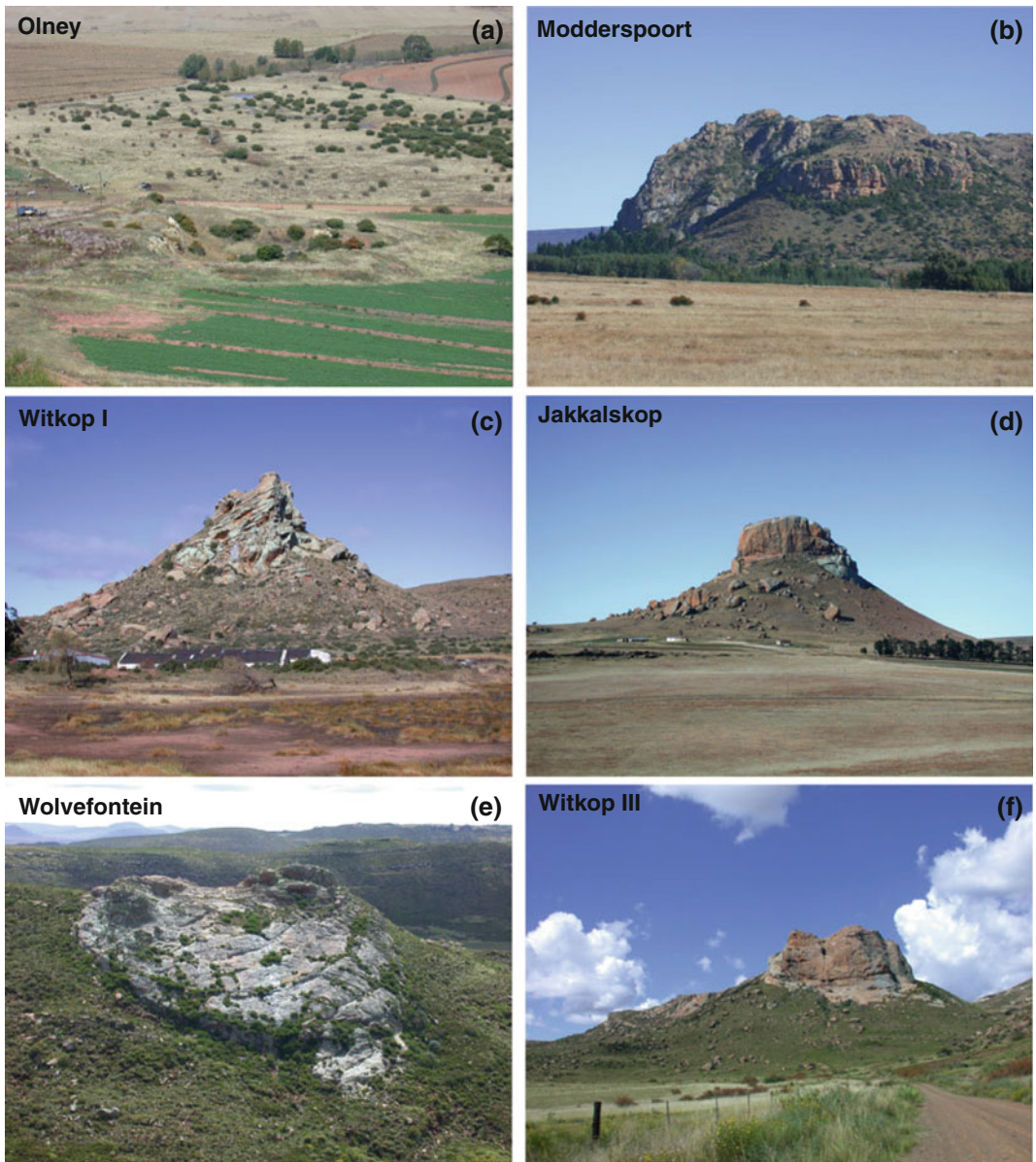


Fig. 2 Overview of selected pipe structures and hydrothermal vent complexes in the Karoo Basin. **a** The Olney breccia pipe, this study. **b** The modderspoort hydrothermal vent complex (see Fig. 4 for location). **c** The witkop I hydrothermal vent complex. **d** The Jakkalskop hydrothermal vent complex (see Lock et al. 2007). **e** The

wolffontein hydrothermal vent complex, representing a sandstone-filled crater in the Elliot Formation, but never subjected to detailed studies. **f** The witkop III hydrothermal vent complex, representing a crater filled with sediment breccias and sandstone (Svensen et al. 2006)

wavelength-dispersive crystal spectrometers at the Department of Geosciences, University of Oslo.

A selection of dolerite and lava samples from the borehole and outcrops were analyzed for major and trace elements by inductively coupled

plasma atomic emission spectrometry (ICP-AES) and inductively coupled plasma mass spectrometry (ICP-MS) at the University of London, Royal Holloway. See Neumann et al. (2011) for analytical details. We have compared the

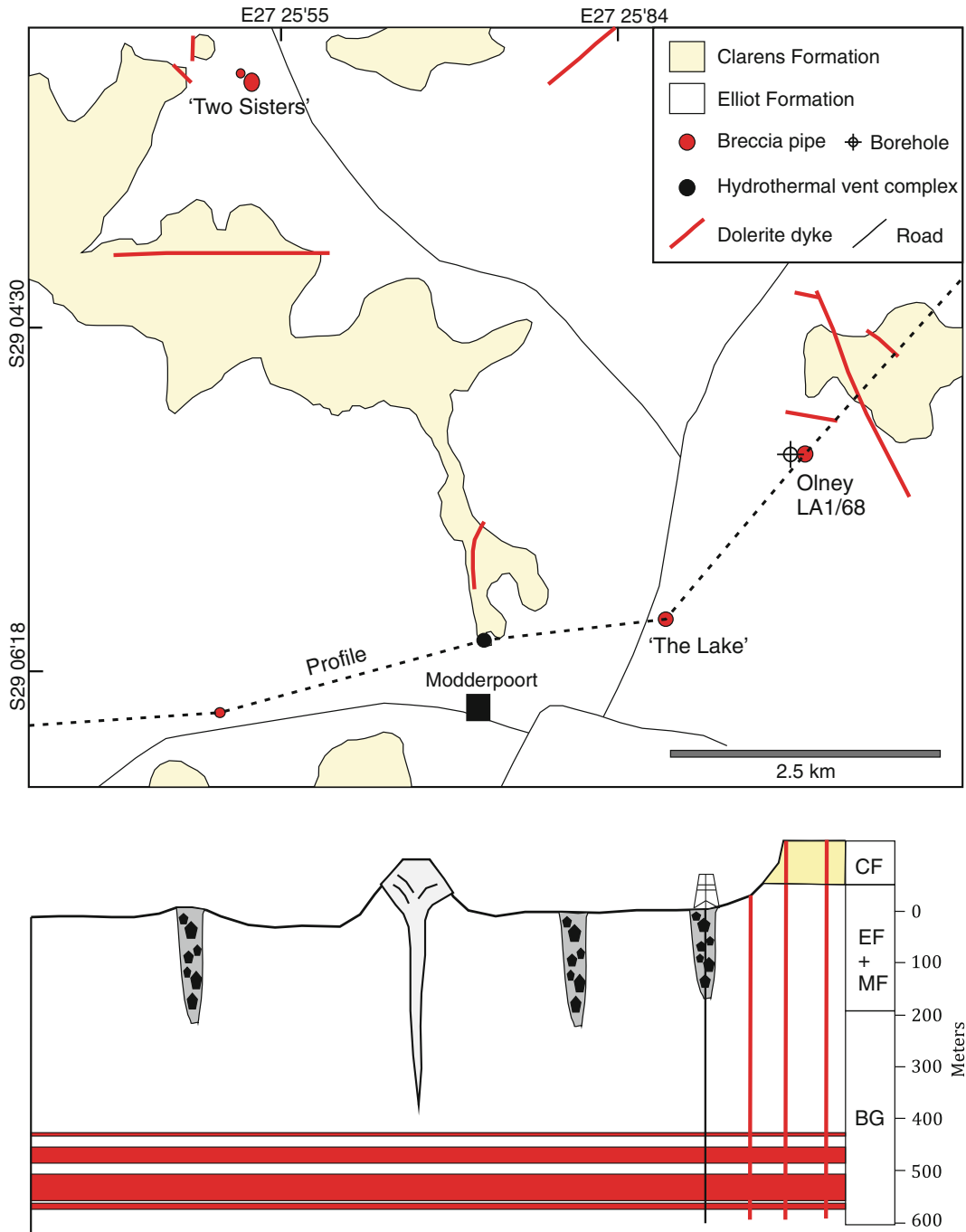


Fig. 3 Geological map of the Modderspoort-area north of Ladybrand. The map is based on Google Earth images, ground-truthing and scouting and mapping of breccia

structures. The composite cross section is based on the LA1/68 borehole log and surface geology

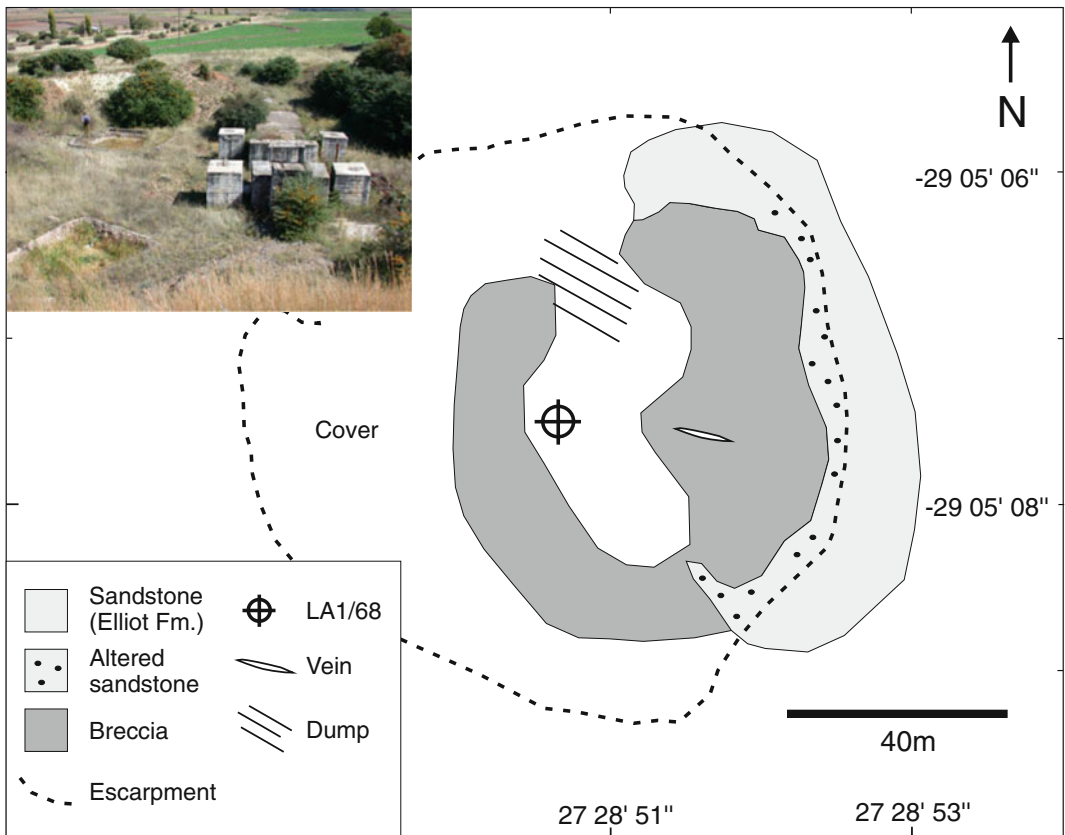


Fig. 4 Detailed map of the Olney breccia pipe showing the outline of the pipe, the main rock types, and the position of the LA1/68 borehole. The escarpment is due to excavation of the basalt material

geochemistry of our samples with the geochemistry of Drakensberg lavas from the Moteng-Oxbow section in Lesotho. Data from this section was published in Marsh et al. (1997) but was recently resampled in more detail by J.S. Marsh and data from this new collection is used in this study.

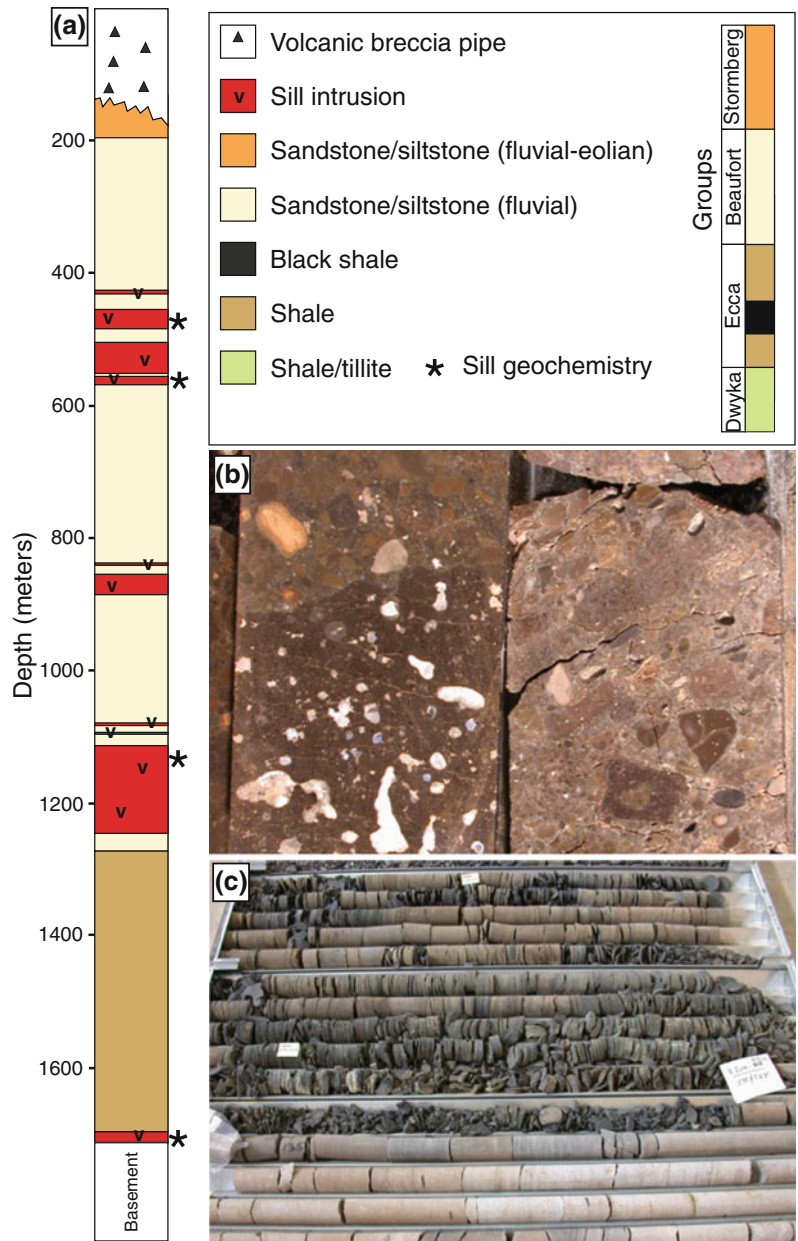
Shale samples from the lowermost contact aureole in LA1/68 were analysed for total organic carbon (TOC), Rock Eval, and vitrinite reflectance. Total organic carbon (TOC) measurements were conducted at the Department of Geosciences, University of Oslo on a Carbon Analyzer LECO (CR-412) instrument. The analytical details for the vitrinite and Rock Eval analyses are given in Aarnes et al. (2011b).

Carbon isotopes on calcite were measured at the Institute for Energy Technology, Kjeller,

Norway. Organic material was removed prior to carbonate stable isotope analysis by vacuum heating the samples in a furnace for 4 h at 400 °C. Rock samples were ground and digested with a 0.1 ml 100 % H_3PO_4 solution for two hours at 30 °C under vacuum. The released CO_2 was transferred to a FinniganMAT Delta XP isotope ratio mass spectrometer (IRMS) for determination of $\delta^{13}C$. The performance of instrument was monitored using in-house calcite standards. Results are reported in δ notation, as per-mil (‰) deviation relative to the VPDB standard. The precision for $\delta^{13}C$ is ± 0.1 ‰.

The 1D numerical modelling of heat transport and organic maturation in contact aureoles around sills was done using the model and procedure described by Aarnes et al. (2010, 2011b).

Fig. 5 **a** Simplified log of the LA1/68 borehole as based on our own logging and on Roux (1972). There are 11 sills in the borehole but note that only 10 are shown in the log as one of the sills is very thin (1.6 m thick at 1093.9–1095.5 m). **b** Close-up of the basalt breccia showing vesicular basalt to the left and a sediment-dominated breccia to the right. **c** LA1/68 core trays from the Ecça group showing shale (*upper*) and coarse sandstone (*lower*)



4 Results

4.1 Geology of the Ladybrand Area

Several pipe structures are located in the Modderpoort area north of Ladybrand (Figs. 2a, b and 3). Two of these, the Olney pipe and the

Modderpoort vent structure are briefly mentioned in the literature. Four others (Two Sisters, The Lake, and one un-named pipe) were discovered during fieldwork in the area (Fig. 3). The LA1/68 borehole was drilled by Soekor in 1968–1972 in the middle of the Olney pipe.

The Olney pipe is a circular structure cutting through the Elliot Formation sandstone (Figs. 4 and 5). The outcrop is described below. Three

other basalt-dominated breccias crop out in the same region, but have never been subjected to detailed studies. We briefly describe them here and have included samples from these localities into our analytical program. The Two Sisters locality (local name), The Lake, and the un-named pipe represent pipes filled with breccias of basalt and varying amount of sedimentary rock fragments. Calcite veins cutting matrix-dominated zones are common. To the west of Olney, next to the Mooderpoort community, a structural sandstone-anomaly crops out at the edge of the Clarens Formation plateau (Figs. 2b and 3). This structure resembles the hydrothermal vent complexes found further to the south-west in the Karoo Basin (Svensen et al. 2006), thus likely representing a phreatic explosion crater subsequently filled with sediment breccias and sand from the Clarens Formation.

4.2 The Olney Breccia

The Olney pipe is a circular depression in the Elliot Formation sandstone and is about 120 m in diameter (Fig. 4). The exposed part of the breccia is dominated by lava blocks up to 40–50 cm in diameter. Both fine-grained lava and vesicular lava is common. Partly altered Elliot Fm. sandstone surrounds the breccia. In the central parts of the pipe, calcite- and quartz-bearing veins are common, as are 2–3 cm large fragments of black volcanic glass. The glass demonstrates that partially molten lava was present during breccia formation. The contact between the breccia and the Elliot Fm. sandstone is sharp, locally with sediment veinlets extending from the margin into the breccia.

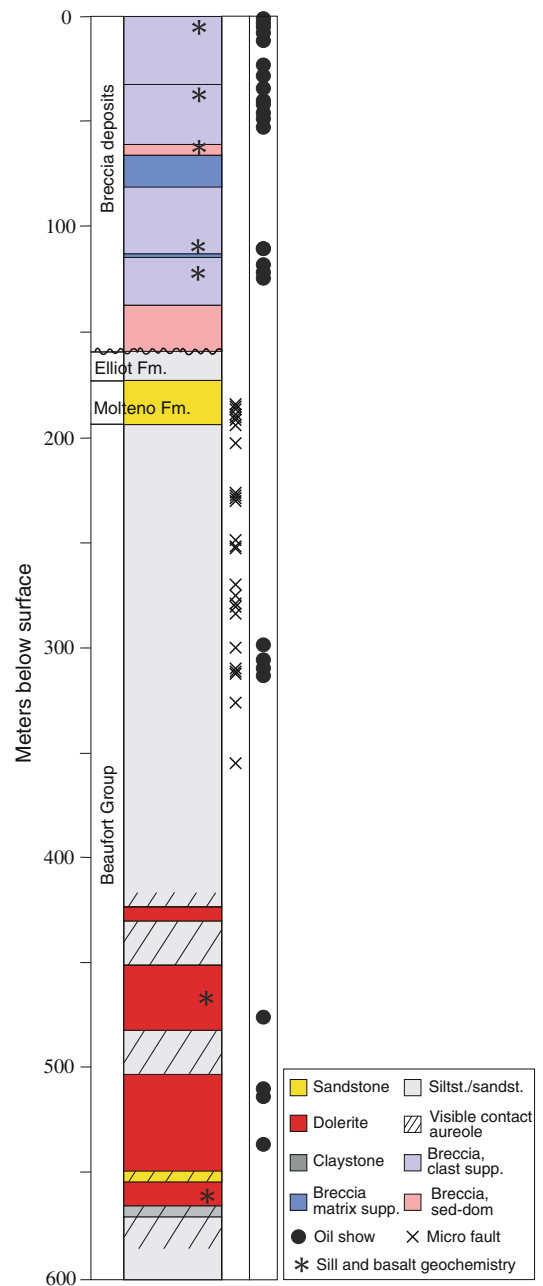
Based on the outcrops and the LA1/68 core, the breccia can be grouped in three main classes: (1) matrix-supported basalt breccia, (2) clast-supported basalt breccia, and (3) sediment-dominated matrix-supported breccia (Figs. 5 and 6). The clast-supported breccias are the most abundant, as seen in Fig. 6. This interpretation is supported by breccia logging done by Woodford et al. (2002). Locally, both volcanic glass (Fig. 7) and calcite veins with bitumen are abundant (Fig. 8), mostly in the clast-supported parts. The

breccia is cemented by calcite with abundant authigenic pyrite (Fig. 8b). Note there is an absence of high temperature (>250 °C) minerals such as epidote, pyroxene, or biotite.

The basal part of the breccia is dominated by sediment fragments with minor volcanic clasts, and gradually fades into normal-faulted and distorted host sedimentary rocks at about 154 m depth. Based on the outcrops of the nearby Clarens Formation (Fig. 3), we infer that the base of the Drakensberg flood basalts were located at least 120 m above the current pipe outcrop. Thus the pipe extended to a depth of at least 270 m deep at the time of formation, with a crater of perhaps 240 m in diameter (double the current pipe width). Deformed sedimentary rocks with micro-faults are common in the 180–350 m interval in the core, with displacements in the centimeter to millimeter range. Note that dolerite dykes have not been found in the immediate surroundings of the pipe.

The log in Fig. 6 shows the visible oil shows in the LA1/68 core. Oil is abundant in four intervals, including the upper 50 m of the breccia. The oil is viscous and thus likely affected by near-surface bacterial degradation. Figure 9 shows a close-up of a calcite and quartz vein from the upper 20 m of the core, where light brown liquid oil is present in fluid inclusions, and black bitumen fills the pore space in the vein. The bitumen in this sample (OL11-2) has a bulk $\delta^{13}\text{C}$ value of -28.0 permil, suggesting bacterial degradation which results in ^{13}C enrichment (Table 1). Isotope analyses on the matrix calcite, calcite veins and calcite nodules in the Elliot Formation document fluid flow and precipitation during a range of temperatures (Fig. 9). The trend towards more depleted carbon and oxygen isotopes seen in Fig. 9 is consistent with a thermogenic and organic source of carbon with increasing temperatures, giving low $\delta^{18}\text{O}$ values. Most of the $\delta^{13}\text{C}$ values from the breccia have values between -10 and -12 permil, which is generally too ^{12}C -enriched to be explained by a mantle or marine source for the carbon. Compared with reference samples of calcite veins in dolerite from various localities show comparable sources of carbon but also suggests that sill-hosted veins were formed at slightly higher temperatures.

Fig. 6 Log of the upper 600 m of the LA1/68 core showing the breccia and the main sills in the Beaufort Group. Note the presence of micro faults and oil shows



4.3 Basalt and Dolerite Geochemistry

The compositions of dolerites and a sedimentary rock in the LA1/68 core were presented and discussed by Neumann et al. (2011). Data on magmatic fragments in the LA1/68 and Two

Sisters breccias, together with data on a sedimentary rock, are given in Table 2 together with representative data on LA1/68 dolerites.

The LA1/68 dolerites have relatively uniform basaltic compositions (e.g. MgO 6.1–7.8 wt%; $mg\# = \text{cation ratio } Mg^*100/[Mg + Fe_{\text{total}}]$: 49–59) and belong to the low-Ti Karoo series. The

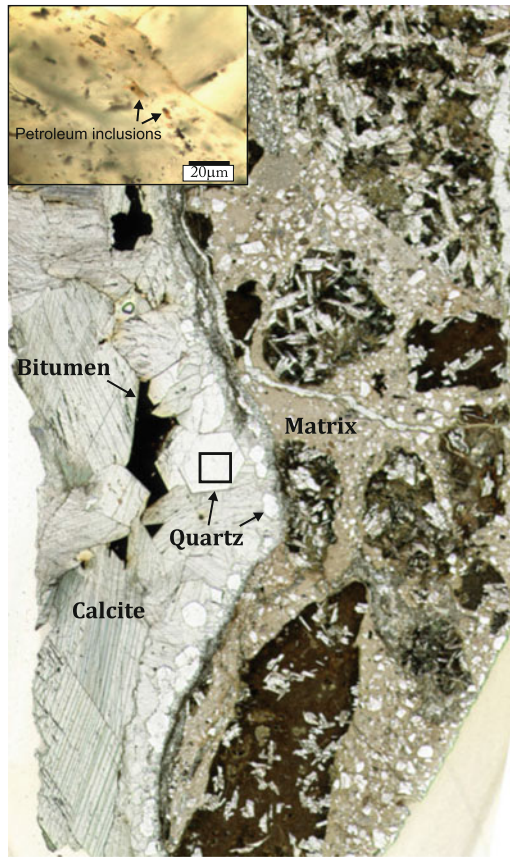


Fig. 7 Thin section scan (1.5 cm across) of a quartz and calcite vein from the upper 12 m of the breccia. Not the dark fragments (glass-rich basalt) and the bitumen in the

vein. The inserted picture shows liquid oil inclusions in quartz from the vein

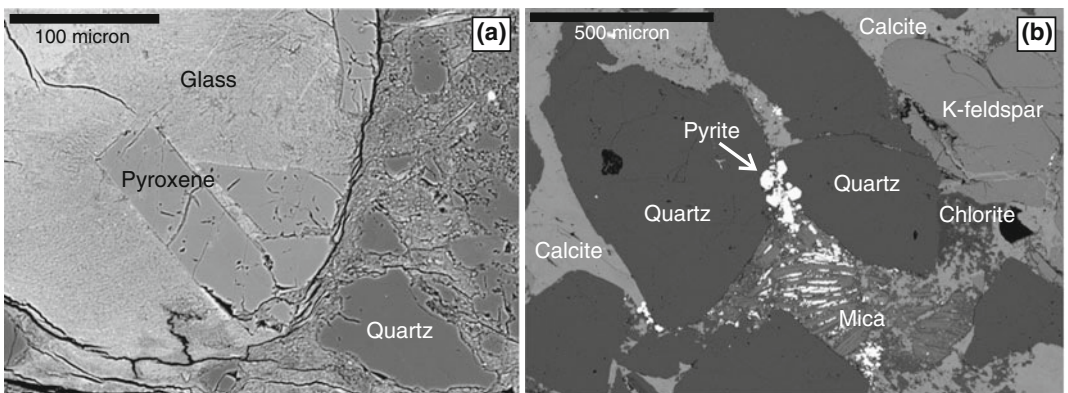


Fig. 8 Electron microprobe backscatter images. **a** Volcanic glass in the breccia, with pyroxene crystals. **b** Sediment grains (quartz and feldspar) cemented by calcite and locally pyrite

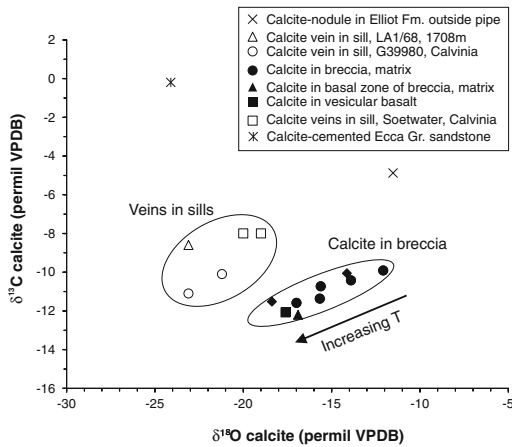


Fig. 9 Carbon and oxygen isotope systematics from calcite in the Olney breccia. Samples from veins in dolerite and carbonate in surrounding sedimentary rocks are included for comparison. See Svensen et al. (2007) for information about the G39980 borehole. The Soetwater sample is from a calcite alteration zone in a thick sill west of Calvinia (S31°32', E19°24')

lowermost sill at the base of the Ecce Group is slightly more evolved than those emplaced into the overlying Beaufort Group.

The geochemistry of the dolerite fragments in the breccia is similar to those of the dolerite sills in LA1/68 and the LOI (loss on ignition) is low (Table 2, Fig. 10). The basalt fragments, however, have significant LOI (3.9–14.3 wt%) and show increasing CaO with increasing LOI. The highest LOI and CaO are found in a tuff fragment in the Two Sisters breccia. The basalt and tuff fragments with the highest LOI and CaO contents also have significantly lower Rb, Ba and K₂O contents than the least altered basalt (LA-413). These features strongly suggest alteration by Ca-rich hydrothermal fluids.

4.4 Contact Metamorphism of Ecce Shale

A total of 11 sills are present in the LA1/68 borehole, with a cumulative thickness of 266 m. The thickest sill is 199 m (Fig. 5). Note that the base of the Karoo stratigraphy is located at 1710 m depth, and that the Dwyka Group is absent. The Ecce Group is shale-dominated and

Table 1 Stable isotope analysis of calcite and organic matter

Sample	Setting	Depth LAI/68 (m)	δ ¹³ C		δ ¹⁸ O	
			VPDB (permil)			
LA1/68-HS1	Matrix calcite in breccia	6.0	-10.4	-13.9		
LA1/68-HS6	Matrix calcite in breccia	88.1	-12.0	-17.0		
LA1/68-HS7A	Matrix calcite in breccia	125.6	-11.4	-15.7		
LA1/68-HS2B	Matrix calcite outside calcite vein	6.0	-9.9	-12.1		
LA1/68-HS4	Matrix calcite in breccia	6.1	-10.7	-15.6		
LA1/68-HS2A	Calcite vein with asphaltene	6.0	-11.5	-18.4		
LA1/68-HS5	Calcite vein in sandstone clast	34.4	-10.1	-14.1		
LA1/68-HS7B	Calcite vesicles in basalt	125.6	-12.1	-17.6		
OL11-2	Bulk oil in breccia		-28.0		-	
OL11-3	Carbonate nodule in Elliot Fm.		-4.9		-11.5	
LAI/68-07	Calcite vein in dolerite	1798.8	-8.6		-23.1	
LAI/68-07	Calcite cemented basal breccia	149.7	-12.2		-16.9	
LA1/68-HS38	Calcite cemented coarse ecce ss	1566.4	-0.2		-24.1	
K04HS-26	Soetwater calcite in dolerite, Ecce		-8.0		-19.0	
K04HS-30	Soetwater calcite in dolerite, Ecce		-8.0		-20.0	
G39980-92,9	Fractured and brecciated dolerite		-11.1		-23.1	
G39980-133,7	Brecciated dolerite, close to lower contact		-10.1		-21.2	

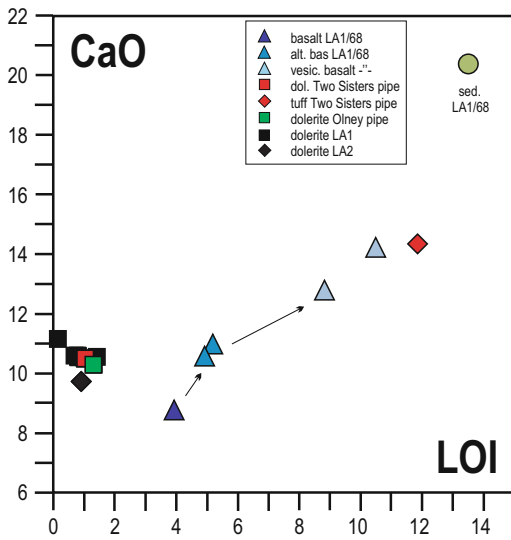


Fig. 10 CaO and volatile content (LOI) in the basalt on one sedimentary rock sample from the Olney pipe and the LA1/68 core. Samples from two sisters are shown for comparison

438 m thick (Fig. 5c). Figure 12 shows pictures from the contact aureole above the 15 m thick sill at the base of the Eccca Group. Note the sharp contacts, the fractured upper contact, and the

variation in textures and color of the hornfels (coarse grained to light brown to grey). Also, note the chilled fine-grained margin of the sill contacts.

The measured total organic carbon (TOC) in the whole Eccca Group varies from zero close to the sill contacts, to maximum values above 4 wt % in the lower half of the group (the local equivalent of the Whitehill Formation). Note that the organic-rich part of the Eccca Group is virtually unaffected by contact metamorphism and that metamorphism is restricted to a zone of equal thickness to the sill. Total organic carbon, vitrinite reflectance and temperature estimated based on the thermal modelling are presented in Fig. 13. Vitrinite reflectance ranges from 1.0 in the background, to 5.7 %Ro at 9.2 m above the sill. Our model calculations show that the observed TOC profile can be explained by generation of methane from and reduction in TOC from calculated background values (2.3 wt% TOC in the lower parts of the group). The maximum temperature obtained from the modelled contact aureole is about 550 °C (Fig. 13) compared to an estimated background temperature of about 150 °C.

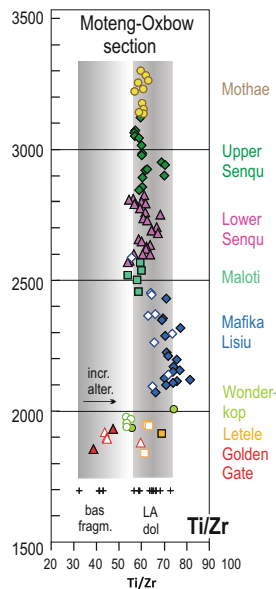


Fig. 11 Comparison of the geochemistry of magmatic rocks in the LA1/68 (Olney pipe) with the Drakensberg Group lavas as present in the Moteng-Oxbow profile (Marsh et al. 1997; JS Marsh, unpublished data). Samples from the Moteng section are show as filled symbols, from the Oxbow section as open symbols with Moteng fill colors

on the rims. Notice that the altitude intervals are slightly different along the two sections. The overlap in altitude between samples from the thin lowermost units is due to sampling difficulties along the lower part of the road that undulates up and does not have continuous exposures. This made it difficult to piece together a continuous stratigraphy

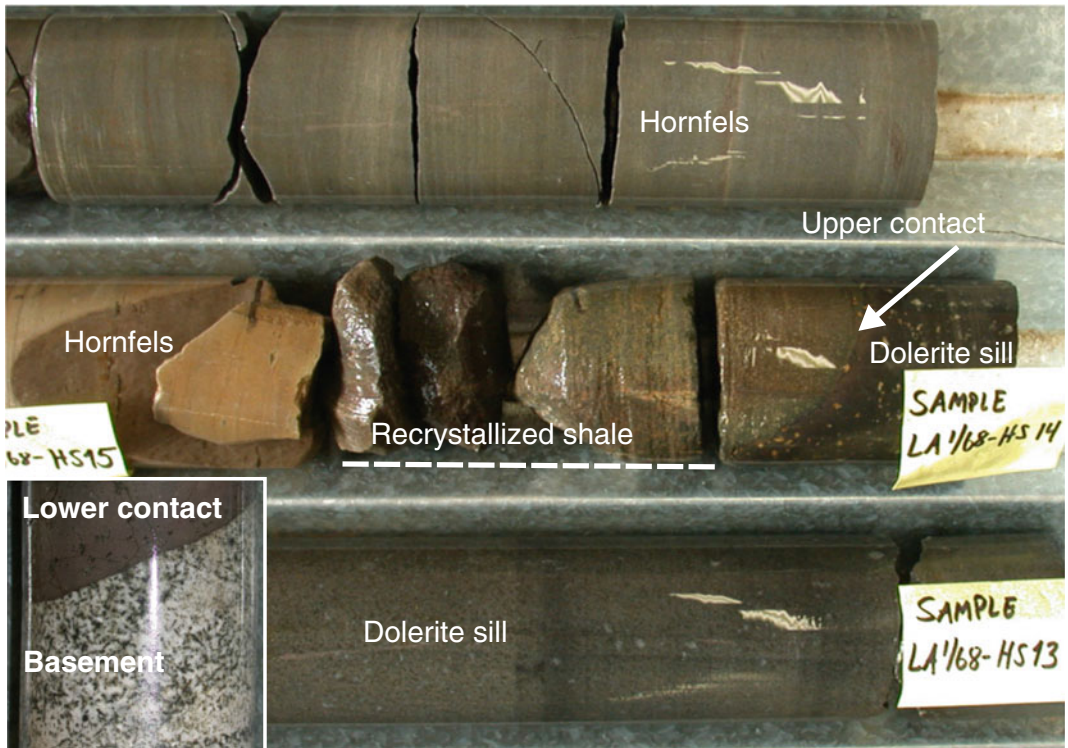


Fig. 12 Images from the lowermost sill in the LA1/68 borehole showing the hornfels zone and the chilled glassy contact zone of the sill

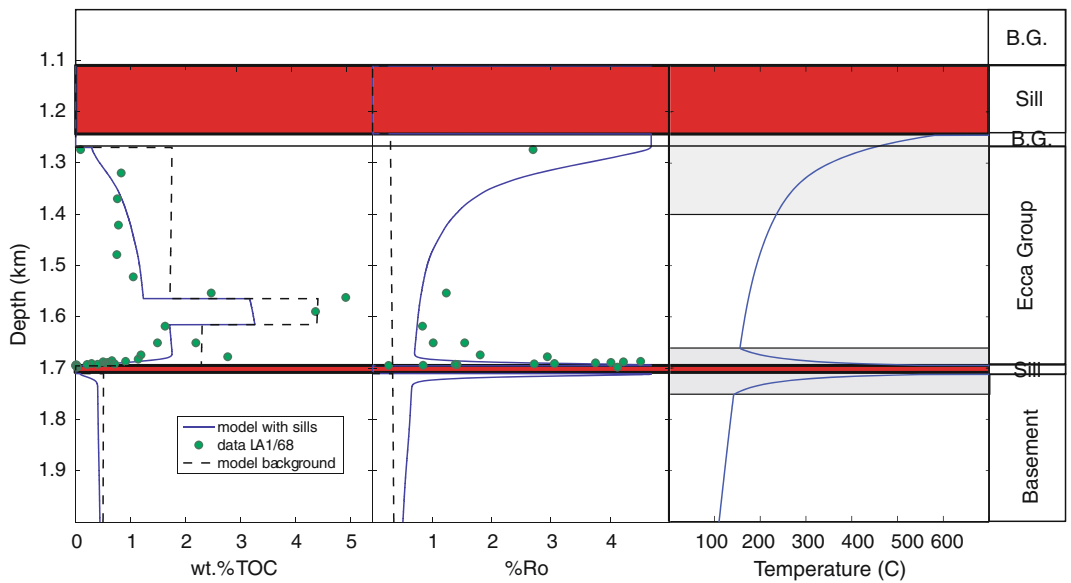


Fig. 13 Results from thermal modelling of the Eccla Group contact aureoles compared with TOC and vitrinite reflectance data. Grey boxes show the thicknesses of the interpreted contact aureoles. B.G.: Beaufort Group

5 Discussion

In this study, we have presented a case study that demonstrates various aspects of the thermogenic gas hypothesis that links sub-volcanic intrusions to global environmental changes. In the following, we discuss our data into the context of three key processes: (1) Estimates of gas volumes from contact aureoles, (2) timing of gas release, and (3) long-term fluid flow. We conclude the discussion with summarizing the current and future research directions needed for further testing the link between LIPs and environmental changes.

5.1 Aureole Thickness and Gas Volume

The aureole thickness around sills has been a source of confusion in the literature. Some sills have thick visible aureoles whereas others have thin visible aureoles, sometimes used as an argument against widespread gas generation during contact metamorphism (e.g., (Gröcke et al. 2009). However, there is nothing mysterious about contact metamorphism. Even very thin sills show well-developed contact aureoles (e.g., Senger et al. 2014). The most important factors controlling the aureole thickness, as stressed by Aarnes et al. (2010), are: (1) sill thickness, (2) sill temperature, (3) emplacement depth and geothermal gradient (higher background T gives thicker aureole), (4) type of host rock (porosity and thermal conductivity properties). Additionally, long-term magma flow in a sill will result in a thicker aureole (although this is poorly documented in the literature), and significant fluid flow in the aureole will cool the aureole quicker but also result in a thicker aureole. Note that aureole thickness can be measured by a wide range of methods with contrasting results.

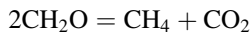
The thickness of aureoles also depends on the measuring method. The most widely used

methods are vitrinite reflectance (measures the organic matter, but usually poor data quality in the inner aureole), petrography and mineral isograds (difficult in the fine grained rocks of the outer aureole), bleaching and visible effects (pronounced in inner aureoles, limited value further out), total organic carbon measurements (need to know the background variation), and finally petrophysical measurements (for instance seismic velocity and density, mostly measured in boreholes). Geochemical analyses of elements and isotopes can be useful in many cases, especially around dykes where sampling of a specific sedimentary rock unit can be done, but is of limited use when sampled across layered units as the natural background variation is usually unknown. A rare example, where the geochemistry of a sedimentary sequence and the metamorphic equivalent both were studied, is the KL1/78 and DP1/78 boreholes from the northern parts of the Karoo Basin (Aarnes et al. 2011b). Bulk carbon isotope systematics of organic matter during contact metamorphism is usually not fractionated beyond 1–2 permil, where case studies show that the remaining carbon can be either mildly ^{12}C -enriched or depleted (Arneth and Matzigkeit 1986; Meyers and Simoneit 1999; Peters et al. 1981). As a consequence, carbon isotopes cannot be used to infer aureole width or gas volumes generated during heating.

Our data from LA1/68 shows that the 15 m thick sill at the base of the Eccia Group resulted in intense high temperature metamorphism of the shale. Background vitrinite reflectance values from parts of the borehole unaffected by sills, is from 1.0 %Ro (Table 3). In the outer aureole, there is an increase to 5.7 at about 9 m from the contact. At the same time, the total organic carbon content decreases to 0.7 wt%. Our modelling results have captured the coupled vitrinite and TOC trends, which show that methane generation took place according to the reaction:

Table 3 LAI/68: TOC, Rock-Eval and vitrinite reflectance

Depth (m)	S1 (mg/g)	S2 (mg/g)	S3 (mg/g)	Tmax (°C)	PP (mg/g)	PI (wt ratio)	HI*	OI**	TOC (wt. %)	% Ro	std	#
637.2	0.00	0.04	0.11	349	0.04	0.09	80	220	0.05	1.33	0.18	5
1553.6	0.17	0.96	0.15	447	1.13	0.15	39	6	2.47	1.24	0.12	20
1598.8	0.33	3.00	0.36	464	3.33	0.10	69	8	4.37	1.11	0.09	33
1618.3	0.08	0.94	0.22	455	1.02	0.08	58	13	1.63	0.84	0.08	21
1650.8	0.06	0.86	0.24	458	0.92	0.07	58	16	1.49	1.02	0.09	21
1650.8	0.07	0.83	0.07	458	0.90	0.08	38	3	2.19	1.55	0.12	22
1674.4	0.03	0.15	0.12	547	0.18	0.14	13	10	1.19	1.81	0.12	9
1677.9	0.06	0.11	0.10	605	0.17	0.34	4	4	2.77	2.94	0.37	23
1682.5	0.12	0.12	0.22	330	0.24	0.49	11	19	1.14	5.46	0.40	3
1685.5	0.09	0.28	0.10	471	0.37	0.24	42	15	0.66	5.65	0.68	14
1686.9	0.47	0.21	0.35	323	0.68	0.70	23	38	0.91	4.51	0.41	24
1687.8	0.32	0.14	0.08	326	0.45	0.70	28	16	0.50	4.22	0.28	21
1689.0	0.53	0.43	0.16	408	0.96	0.55	73	27	0.59	4.01	0.44	20
1689.8	0.43	0.40	0.13	409	0.83	0.52	72	24	0.55	3.75	0.72	21
1691.0	0.11	0.26	0.09	482	0.38	0.30	90	31	0.29	3.06	0.30	20
1691.7	0.45	0.47	0.26	436	0.93	0.49	67	37	0.71	2.72	0.53	21
1692.6	0.22	0.26	0.09	343	0.48	0.46	64	23	0.40	1.39	0.14	20
1692.9	0.12	0.18	0.04	432	0.30	0.40	87	19	0.21	1.42	0.14	4
1693.5	0.01	0.02	0.09	482	0.02	0.24	160	900	0.01			
1694.5	0.00	0.03	0.02	373	0.03	0.06	1	1	0.00	0.85	0.05	2
1694.8	0.01	0.04	0.03	377	0.05	0.11	200	150	0.02	0.27	0.07	3
1695.0	0.00	0.05	0.17	361	0.05	0.08	225	850	0.02			
1695.6	0.00	0.03	0.00	373	0.04	0.11	1		0.00			
1689.0	0.00	0.05	1.01	439	0.05	0.02	157	3367	0.03	4.12	0.27	22

^amg HC/gTOC^bmg CO₂/g TOC1710.1 m *upper contact*1698.0 m *lower contact*

CH₂O is an approximation to the composition of organic matter. Organic parameters, such as S2 (mg generated hydrocarbons during pyrolysis per g rock), also follows the same trend as the TOC, showing that the remaining organic matter has lost the hydrocarbon productivity following heating. Note that the thick sill in the lower Beaufort Group is included in the thermal calculations, showing that almost half of the Ecca Group is thermally affected by the two sills.

The mass of methane generated from the contact aureole can be calculated from the missing organic material in the contact aureole using the following relationship (Svensen et al. 2007).

$$\text{WC} = \text{FC} * \text{A} * \text{h} * \text{d},$$

where WC is the total mass of carbon generated in contact aureole. WC also depends on the contact aureole volume (area A * sill thickness h), the amount of carbon in wt% converted to methane or carbon dioxide (FC) and the rock density (d; 2400 kg/m³). The thickness h of the

contact aureole can be estimated from field and seismic observations or TOC and vitrinite reflectance data. The total mass of carbon produced, WC, can be converted to equivalents of methane ($= WC * 1.34$) and carbon dioxide ($= WC * 3.66$).

If only 1 wt% of the organic carbon in shale or siltstone is transformed into gaseous carbon compounds, the gas production potential associated with a cumulative volume of 5,000–10,000 km³ sill intrusion is 230–460 Gt C (corresponding to 310–600 Gt CH₄).

5.2 Relative Age of Sills, Phreatomagmatism, and Lavas

The phreatic explosion that formed the Olney breccia pipe was likely initiated by boiling and pore fluid expansion around the intrusion of the sills in the Beaufort Group sandstones. In the model by Jamtveit et al. (2004), boiling is most efficient around thick sills emplaced within the upper 1000 m of the basin where the pore fluid content is high and the volume contrast between vapor and liquid phase water is the greatest. In order to form lava fragments inside the explosion breccia, the lava source must have been present in the area before the explosion, and thus the lava must be older than the sill(s) that caused the boiling. The lava fragments must consequently be older than the LA1/68 sills, and the lower part of the Lesotho lava units. This reinforces the notion of contemporaneity of lava eruptions and sill emplacement.

The age of emplacement of the magmatic rocks in the breccia pipes, relative to the Drakensberg lava units, has been tested on the basis of “geochemical fingerprinting”, that is plots of ratios between incompatible elements that are relatively insensitive to weathering and alteration. The Drakensberg lavas have relatively uniform major element compositions, but Marsh et al. (1997) showed that most lava units may be identified on the basis of the “geochemical fingerprinting” method. We use geochemical data

on the Drakensberg Group lavas for comparison with the volcanic fragments in the LA1/68 breccia. The present areal extent of the Drakensberg lavas (Fig. 1) is very limited due to erosion (Eales et al. 1984). However, the original extent of the lava cover has been estimated to about 1 million km², covering most of South Africa and Namibia (Richardson 1979; Chevalier and Woodford 1999). This means that the lava cover extended far beyond the Olney pipe and LA1/68 borehole. In order to have the most realistic basis for comparison with magmatic rocks in the LA1/68 borehole, we use only data on lavas sampled in the northwestern part of the Drakensberg Group, the Moteng-Oxbow section.

The lava fragments in the LA1/68 pipe differ from most of the Drakensberg lavas by having low Ti/Zr (Fig. 11) and P/Zr, and high Zr/Nb ratios. This is particularly the case for the least altered basalt sample. The closest chemical characteristics are presented by the Golden Gate unit at the base of the Barkly East Formation. Other ratios between incompatible elements gave similar results but are not shown. An alternative possibility is that the lava fragments represent basalts now removed from the Drakensberg Group by erosion (cf. Marsh et al. 1997).

The LA1/68 dolerite sills show no affinity to lavas in the Barkly East Formation (Golden Gate, Letele, Wonderkop), nor to the lava fragments. However, they closely resemble lava units in the younger Lesotho Formation (Fig. 11). The closest similarity is with the Senqu unit (Lower and Upper) in the central part of the Lesotho Formation.

The relative sequence of emplacement of the 11 sills in LA1/68 cannot be further constrained, but we emphasize that a cover of flood basalts would make it more likely that sills are emplaced shallow in the stratigraphy (upper Beaufort Group or shallower). Late sill emplacement is however not regarded as common in the Karoo Basin due to the absence of sills within the Drakensberg Group and the absence of basalt fragments in hydrothermal vent complexes (Svensen et al. 2006).

5.3 Short- and Long Term Fluid Flow

The whole pipe system likely originated from contact metamorphic boiling of pore fluids around the LA1/68 sills 420–550 m interval (Jamtveit et al. 2004), suggesting that the pipe system cut across at least 570 m of basin stratigraphy at the time of formation. Quartz and calcite veins show that fluid flow took place during cooling. The presence of oil, both liquid and solid bitumen, demonstrates a long-lived petroleum system that could only have originated from the organic-rich parts of the Ecca Group. No other parts of the stratigraphy are capable of generating petroleum. Rowsell and De Swardt (1976) compiled borehole data from LA1/68 including oil and gas shows in the borehole. Their data is shown in Fig. 14 as a histogram of depths of oil and gas shows. Even though the base of the Karoo sequence is located as shallow as 1710 m, the petroleum in the lower half of the borehole is present as gas. This indicates a very high thermal gradient in the region, either explained by heating from the sill intrusions or the presence of a very thick paleo lava cover. The abundant quartz cementation in the shallow Molteno Formation in the Karoo Basin is most likely due to burial under thick lava flows

(Svensen et al. 2008), although we cannot rule out that the sills played a prominent role in the Ecca Group maturations, as indicated by both our data and model calculations (Fig. 13).

5.4 Perspectives on Sills, Aureoles, Venting and the Environment

Contact metamorphism in the Karoo Basin has been studied for a range of purposes in the last decades. In the 1960s and 70s, there were concerns about the influence of sills on the petroleum systems, with focused reports from the Council for Geoscience (Mills and Fourie 1976). Rowsell and De Swardt (1976) compiled borehole data demonstrating the effect of sills on clay minerals and petroleum systems. Coal mining has also triggered many studies about contact metamorphism in the Ecca Group coal deposits and the coal rank in aureoles, especially in the eastern parts of the basin (de Oliveira and Cawthorn 1999). During the latest years, several studies have been done on the details of Karoo sills and lavas aiming at investigating the role of degassing on the Toarcian climate (Aarnes et al. 2010, 2011a; Gröcke et al. 2009; Jourdan et al. 2005; Mazzini et al. 2010; Svensen et al. 2007).

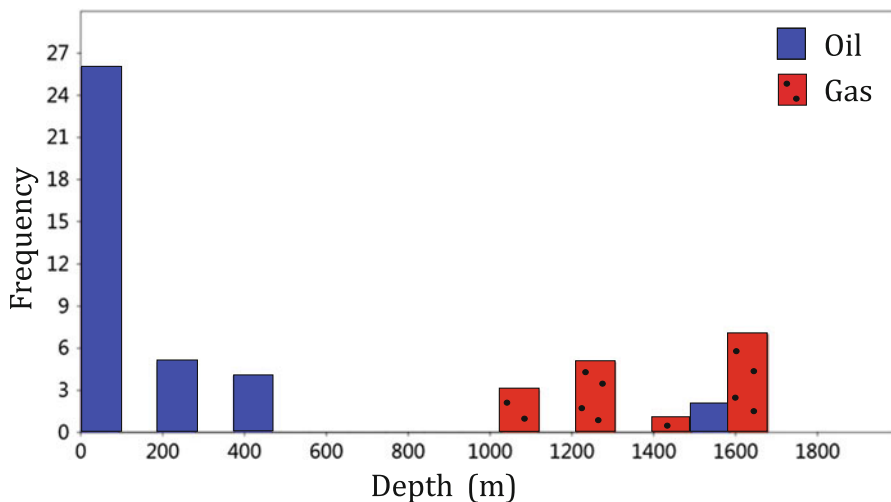


Fig. 14 Compilation of gas and oil shows in the LA1/68 borehole, from Rowsell and DeSwardt (1976)

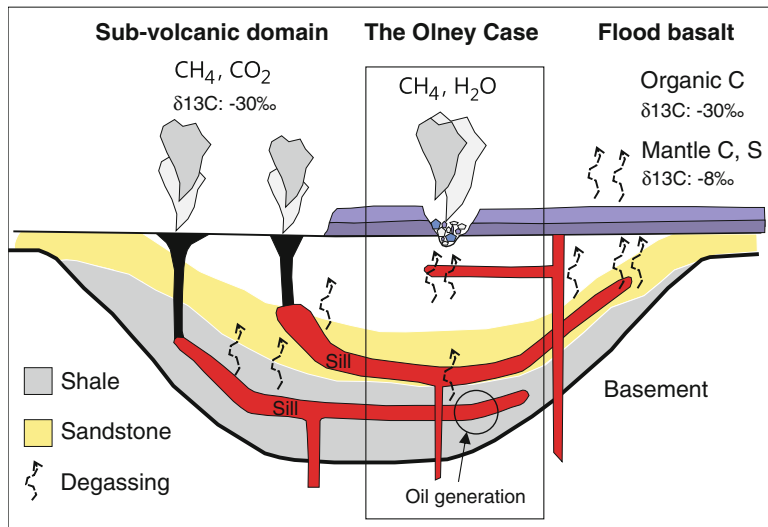


Fig. 15 Schematic cross section through a large igneous province showing surface flood basalts and an extensive sub-volcanic complex of dolerite sills and dykes. The Olney and LA1/68 case is highlighted in the box. Pervasive heating of the sedimentary rocks around the intrusions lead to widespread gas generation from organic

matter and carbonate-bearing lithologies, subsequently released and emitted to the atmosphere via seepage or violent venting through breccia pipes and hydrothermal vent complexes. Note that the isotopic composition of the emitted carbon gases is determined by the composition of the mantle or the original sedimentary carbon

These studies have used a combination of field data, borehole data, geochemistry and numerical modeling. In addition, the recent interest in shale gas in the Karoo Basin has led to a new focus on the role of contact metamorphism.

Our data shows that contact metamorphism around sill intrusions must be taken into account when considering the climatic effects of Large Igneous Provinces. Figure 15 summarizes the three main degassing systems during LIP emplacement, where deep sills lead to breccia pipe formation, shallow sills lead to boiling and phreatic eruptions, and lava flows lead to sub-aerial degassing. The Olney case, as presented here, represents an example of a phreatic eruption at the time of lava emplacement.

during LIP formation. Based on fieldwork, core studies, petrography, organic and inorganic geochemistry, and thermal modelling, we conclude that:

- A phreatic eruption followed boiling around sills emplaced at shallow levels.
- The resulting pipe cut through a partially molten lava cover, likely representing the basal flows of the Drakensberg Group.
- Geochemistry of contact metamorphic Ecca Group, and thermal modelling, shows widespread gas generation and temperatures up to 550 °C during peak metamorphic conditions.
- The breccia contains abundant calcite cement and oil trapped in inclusions and in veins. Isotope analyses of the calcite suggest a thermogenic origin. The oil can only be explained by a source within the middle Ecca Group that migrated at least 1500 m toward the surface long after the breccia formed.
- The studied area in the Karoo Basin holds a key to understand the geological processes taking place following intrusive volcanism in

6 Conclusions

The Olney pipe and the LA1/68 borehole represent a unique case in demonstrating the effects of sill emplacement for gas generation and release

a sedimentary basin: (1) contact metamorphism of organic-bearing sedimentary rocks, (2) rapid gas generation and migration, (3) explosive venting of gases to the atmosphere, and (4) long-term re-use of fractures and pipe systems for fluid migration. We suggest that the sill-induced processes contributed to the climate change and mass extinction during the Toarcian, Early Jurassic.

Acknowledgments We gratefully acknowledge support from the Norwegian Research Council (grant to H.H. Svensen and a Centre of Excellence grant to CEED, grant number 223272). We also would like to thank Council of Geoscience and the National Core Library in Pretoria for providing borehole material and logs from LA1/68, and to Doug Cole for discussions about Karoo geology.

References

- Aarnes I, Fristad K, Planke S, Svensen H (2011a) The impact of host-rock composition on devolatilization of sedimentary rocks during contact metamorphism around mafic sheet intrusions. *Geochem Geophys Geosyst* 12(10)
- Aarnes I, Podladchikov Y, Svensen H (2012) Devolatilization-induced pressure build-up: implications for reaction front movement and breccia pipe formation. *Geofluids* 12(4):265–279
- Aarnes I, Svensen H, Connolly JAD, Podladchikov YY (2010) How contact metamorphism can trigger global climate changes: modeling gas generation around igneous sills in sedimentary basins. *Geochim Et Cosmochim Acta* 74(24):7179–7195
- Aarnes I, Svensen H, Polteau S, Planke S (2011b) Contact metamorphic devolatilization of shales in the Karoo Basin, South Africa, and the effects of multiple sill intrusions. *Chem Geol* 281(3–4):181–194
- Armstrong MKDI, Tyrrell T, Wilson PA, Foster GL (2014) Estimating the impact of the cryptic degassing of large igneous provinces: a mid-Miocene case-study. *Earth Planet Sci Lett* 403:254–262
- Arneth JD, Matzigkeit U (1986) Laboratory-simulated thermal maturation of different types of sediments from the Williston Basin, North America—effects on the production rates, the isotopic and organo-geochemical composition of various pyrolysis products. *Chem Geol Isot Geosci Sect* 58(4):339–360
- Beerling DJ, Harfoot M, Lomax B, Pyle JA (2007) The stability of the stratospheric ozone layer during the end-Permian eruption of the Siberian Traps. *Philos Trans R Soc Math Phys Eng Sci* 365:1843–1866
- Berner RA (2002) Examination of hypotheses for the Permo-Triassic boundary extinction by carbon cycle modeling. *Proc Natl Acad Sci USA* 99(7):4172–4177
- Bond DPG, Wignall PB (2014) Large igneous provinces and mass extinctions: an update. *Geol Soc Am Spec Pap* 505:29–55
- Bristow JW, Saggerson EP (1983) A review of Karoo volcanicity in Southern Africa. *Bull Volcanologique* 46(2):135–159
- Caldeira K, Rampino MR (1990) Carbon dioxide emissions from Deccan volcanism and a K/T boundary greenhouse effect. *Geophys Res Lett* 17:1299–1302
- Catuneanu O, Hancox PJ, Rubidge BS (1998) Reciprocal flexural behaviour and contrasting stratigraphies: a new basin development model for the Karoo retroarc foreland system, South Africa. *Basin Res* 10(4):417–439
- Catuneanu O, Wopfner H, Eriksson PG, Cairncross B, Rubidge BS, Smith RMH, Hancox PJ (2005) The Karoo basins of south-central Africa. *J Afr Earth Sci* 43(1–3):211–253
- Chevallier L, Woodford A (1999) Morpho-tectonics and mechanism of emplacement of the dolerite rings and sills of the western Karoo, South Africa. *S Afr J Geol* 102(1):43–54
- Cohen AS, Coe AL, Kemp DB (2007) The late Palaeocene-Early Eocene and Toarcian (Early Jurassic) carbon isotope excursions: a comparison of their time scales, associated environmental changes, causes and consequences. *J Geol Soc* 164:1093–1108
- Courtillot VE, Renne PR (2003) On the ages of flood basalt events. *CR Geosci* 335(1):113–140
- de Oliveira DPS, Cawthorn RG (1999) Dolerite intrusion morphology at Majuba Colliery, northeast Karoo Basin, Republic of South Africa. *Int J Coal Geol* 41(4):333–349
- Dickens GR, Castillo MM, Walker JCG (1997) A blast of gas in the latest Paleocene: simulating first-order effects of massive dissociation on oceanic methane hydrate. *Geology* 25(3):259–262
- Dingle RV, Siesser WG, Newton AR (1983) Mesozoic and tertiary geology of Southern Africa, Rotterdam, Balkema, 375 p
- du Toit AI (1920) The Karoo dolerites of South Africa: a study in hypabyssal injection. *Trans Geol Soc S Afr* 23:1–42
- Duncan AR, Marsh JS (2006) The karoo igneous province. In: Johnson MR, Anhaeusser CR, RJ T (eds) *The geology of South Africa*, geological society of South Africa, Johannesburg/Council for Geoscience, Pretoria, pp 501–519
- Eales HV, Marsh JS, Cox KG (1984) The Karoo igneous province: an introduction. In: Erlank AJ (ed) *Petrogenesis of the volcanic rocks of the Karoo Province*, vol 13. Geological Society Special Publication of South Africa, pp 1–26
- Galerne CY, Neumann ER, Planke S (2008) Emplacement mechanisms of sill complexes: information from the geochemical architecture of the Golden Valley Sill

- Complex, South Africa. *J Volcanol Geoth Res* 177 (2):425–440
- Ganino C, Arndt NT (2009) Climate changes caused by degassing of sediments during the emplacement of large igneous provinces. *Geology* 37(4):323–326
- Gevers TW (1928) The volcanic vents of the Western Stormberg. *Trans Geol Soc S Afr* 31:43–62
- Grab S, Svensen H (2011) Rock doughnut and pothole structures of the Clarens Fm. Sandstone in the Karoo Basin, South Africa: Possible links to Lower Jurassic fluid seepage. *Geomorphology* 131(1–2):14–27
- Gröcke DR, Rimmer SM, Yoksoulia LE, Cairncross B, Tsikos H, van Hunen J (2009) No evidence for thermogenic methane release in coal from the Karoo-Ferrar large igneous province. *Earth Planet Sci Lett* 277(1–2):204–212
- Hesselbo SP, Grocke DR, Jenkyns HC, Bjerrum CJ, Farrimond P, Bell HSM, Green OR (2000) Massive dissociation of gas hydrate during a Jurassic oceanic anoxic event. *Nature* 406(6794):392–395
- Jamtveit B, Svensen H, Podladchikov Y, Planke S (2004) Hydrothermal vent complexes associated with sill intrusions in sedimentary basins. *Phys Geol High-Level Magmatic Syst* 234:233–241
- Jourdan F, Feraud G, Bertrand H, Kampunzu AB, Tshoso G, Watkeys MK, Le Gall B (2005) Karoo large igneous province: brevity, origin, and relation to mass extinction questioned by new Ar-40/Ar-39 age data. *Geology* 33(9):745–748
- Kemp DB, Coe AL, Cohen AS, Schwark L (2005) Astronomical pacing of methane release in the Early Jurassic period. *Nature* 437(7057):396–399
- Lock BE, Robey JA, Svensen H, Planke S, Jamtveit B, Chevallier L (2007) Discussion on structure and evolution of hydrothermal vent complexes in the Karoo Basin, South Africa—Journal, Vol. 163, 2006, 671–682. *J Geol Soc* 164:477–479
- Malthe-Sørenssen A, Planke S, Svensen H, Jamtveit B (2004) Formation of saucer-shaped sills. In: Breiterreuz C, Petford N (eds) *Physical geology of high-level magmatic systems*, vol 234., Geological society London, Special Publications, pp 215–227
- Marsh JS, Eales HV (1984) The chemistry and petrogenesis of igneous rocks of the Karoo central area, Southern Africa. *Spec Publ Geol Soc S Afr* 13:27–67
- Marsh JS, Hooper PR, Rehacek J, Duncan AR and Duncan RA (1997) Stratigraphy and age of Karoo basalts of Lesotho and implications for correlations within the Karoo igneous province. In: Mahoney JJ and Coffin MF (eds) *Large igneous provinces: continental, oceanic and planetary flood volcanism*. *Geophysical Monograph* 100, pp 347–272
- Mazzini A, Svensen H, Leanza HA, Corfu F, Planke S (2010) Early Jurassic shale chemostratigraphy and U-Pb ages from the Neuquén Basin (Argentina): implications for the Toarcian Oceanic Anoxic event. *Earth Planet Sci Lett* 297(3–4):633–645
- McClintock M, White JDL, Houghton BF, Skilling IP (2008) Physical volcanology of a large crater-complex formed during the initial stages of Karoo flood basalt volcanism, Sterkspruit, Eastern Cape, South Africa. *J Volcanol Geoth Res* 172(1–2):93–111
- McElwain JC, Wade-Murphy J, Hesselbo SP (2005) Changes in carbon dioxide during an oceanic anoxic event linked to intrusion into Gondwana coals. *Nature* 435(7041):479–482
- Meyers PA, Simoneit BRT (1999) Effects of extreme heating on the elemental and isotopic compositions of an upper Cretaceous coal. *Org Geochem* 30(5):299–305
- Mills SR, Fourie ET (1976) A review of the heat effects of dolerite intrusions on oil accumulations in the Middle Ecca of the Northern Karoo
- Neumann ER, Svensen H, Galerne CY, Planke S (2011) multistage evolution of dolerites in the karoo large igneous province, Central South Africa. *J Petrol* 52 (5):959–984
- Peters EK, Rohrbach BG, Kaplan IR (1981) Carbon and hydrogen stable isotope variations in kerogen during laboratory-simulated thermal maturation. *AAPG Bull* 65:501–508
- Polteau S, Mazzini A, Galland O, Planke S, Malthe-Sørenssen A (2008a) Saucer-shaped intrusions: Occurrences, emplacement and implications. *Earth Planet Sci Lett* 261:195–204
- Polteau S, Ferre EC, Planke S, Neumann ER, Chevallier L (2008b) How are saucer-shaped sills emplaced? constraints from the Golden Valley Sill, South Africa. *J Geophys Res Solid Earth* 113(B12)
- Retallack G, Jahren AH (2008) Methane release from igneous intrusion of coal during late permian extinction events. *J Geol* 116(1):1–20
- Richardson SH (1979) Chemical variation produced by flow differentiation in an extensive Karoo dolerite sheet, southern Namibia. *Geochim Cosmochim Acta* 43:1433–1441
- Roscher M, Stordal F, Svensen H (2011) The effect of global warming and global cooling on the distribution of the latest Permian climate zones. *Palaeogeogr Palaeoclimatol Palaeoecol* 309(3–4):186–200
- Roux HJ (1972) Geological well completion report of LA1/68
- Rowell DM, De Swardt AMJ (1976) Diagenesis in Cape and Karoo sediments, South Africa and its bearing on their hydrocarbon potential. *Trans Geol Soc S Afr* 79:81–145
- Ruhl M, Kürschner WM (2011) Multiple phases of carbon cycle disturbance from large igneous province formation at the Triassic-Jurassic transition. *Geology* 39(5):431–434
- Senger K, Planke S, Polteau S, Ogata K, Svensen H (2014) Sill emplacement and contact metamorphism in a siliciclastic reservoir on Svalbard, Arctic Norway. *Norw J Geol* 94(2–3):155–169
- Stothers RB (1993) Flood basalts and extinction events. *Geophys Res Lett* 20(13):1399–1402
- Svensen H, Bebout G, Kronz A, Li L, Planke S, Chevallier L, Jamtveit B (2008) Nitrogen geochemistry as a tracer of fluid flow in a hydrothermal vent complex in the Karoo Basin, South Africa. *Geochim Et Cosmochim Acta* 72(20):4929–4947

- Svensen H, Corfu F, Polteau S, Hammer O, Planke S (2012) Rapid magma emplacement in the Karoo large igneous province. *Earth Planet Sci Lett* 325:1–9
- Svensen H, Jamtveit B (2010) Metamorphic fluids and global environmental changes. *Elements* 6(3):179–182
- Svensen H, Jamtveit B, Planke S, Chevallier L (2006) Structure and evolution of hydrothermal vent complexes in the Karoo Basin, South Africa. *J Geol Soc* 163:671–682
- Svensen H, Planke S, Chevallier L, Malthe-Sorensen A, Corfu F, Jamtveit B (2007) Hydrothermal venting of greenhouse gases triggering Early Jurassic global warming. *Earth Planet Sci Lett* 256(3–4):554–566
- Svensen H, Planke S, Corfu F (2010) Zircon dating ties NE Atlantic sill emplacement to initial Eocene global warming. *J Geol Soc* 167(3):433–436
- Svensen H, Planke S, Malthe-Sorensen A, Jamtveit B, Myklebust R, Rasmussen Eidem T, Rey SS (2004) Release of methane from a volcanic basin as a mechanism for initial Eocene global warming. *Nature* 429(6991):542–545
- Svensen H, Planke S, Polozov AG, Schmidbauer N, Corfu F, Podladchikov YY, Jamtveit B (2009a) Siberian gas venting and the end-Permian environmental crisis. *Earth Planet Sci Lett* 277(3–4):490–500
- Svensen H, Schmidbauer N, Roscher M, Stordal F, Planke S (2009b) Contact metamorphism, halocarbons, and environmental crises of the past. *Environ Chem* 6:466–471
- Tankard A, Welsink H, Aukes P, Newton R, Stettler E (2009) Tectonic evolution of the Cape and Karoo basins of South Africa. *Mar Pet Geol* 26(8):1379–1412
- van de Schootbrugge B, Quan TM, Lindstrom S, Puttmann W, Heunisch C, Pross J, Fiebig J, Petschick R, Rohling HG, Richoz S, Rosenthal Y, Falkowski PG (2009) Floral changes across the Triassic/Jurassic boundary linked to flood basalt volcanism. *Nat Geosci* 2(8):589–594
- Wignall PB (2001) Large igneous provinces and mass extinctions. *Earth Sci Rev* 53(1–2):1–33
- Woodford AC, Chevallier L (2002) Hydrogeology of the main Karoo Basin: current knowledge and research needs: Pretoria, South Africa, Water Research Commission Report, p 310

Sills in Sedimentary Basins and Petroleum Systems

Nick Schofield, Dougal A. Jerram, Simon Holford, Stuart Archer, Niall Mark, Adrian Hartley, John Howell, David Muirhead, Paul Green, Donny Hutton and Carl Stevenson

Abstract

Our knowledge of igneous emplacement in sedimentary basins has been revolutionised by studies of offshore 3D seismic reflection data, where large scale structures and relationships are realised. These offshore data sets require detailed information from onshore analogues to fully understand subsurface structure of such intrusions and their potential effect on petroleum systems. The Inner Hebrides of Western Scotland, which contains an onshore record of the extensive Palaeogene magmatic activity that affected much of the North Atlantic, allows us to examine some of the classic sill geometries on a seismic to sub-seismic (outcrop) scale. As hydrocarbon exploration moves to more challenging basins, it is clear the need exists for us to fully understand the role in which intrusive volcanism plays in active hydrocarbon systems. Intrusions in general can have major effects on prospective sedimentary basins by forming interconnected low-permeability zones which can compartmentalise significant volumes of source and reservoir rock. We present a series of outcrop case studies which allow the potential influences of sills on what would represent potential source and reservoir rock intervals to be addressed and discuss the wider implications for sill emplacement in such basins.

N. Schofield (✉) · N. Mark · A. Hartley · J. Howell

D. Muirhead

Geology and Petroleum Geology, School of Geosciences, University of Aberdeen, Meston Building, Aberdeen AB24 3UE, UK

e-mail: n.schofield@abdn.ac.uk

<http://www.dougalearth.com>

D.A. Jerram

Centre for Earth Evolution and Dynamics (CEED), University of Oslo, Oslo, Norway

D.A. Jerram

DougalEARTH Ltd., Solihull, UK

D.A. Jerram

Earth, Environmental and Biological Sciences, Queensland University of Technology, Brisbane, QLD, Australia

S. Holford

Australian School of Petroleum, University of Adelaide, Adelaide, SA 5005, Australia

S. Archer

Dana Petroleum, Aberdeen AB10 IRS, UK

P. Green

Geotrack International, Brunswick West, VIC 3055, Australia

D. Hutton · C. Stevenson

Earth Sciences, University of Birmingham, Birmingham B15 2TT, UK

1 Introduction

Volcanic margins are found globally and are characterised by large volumes of extrusive volcanism and associated intrusions (Mahoney and Coffin 1997; Jerram and Widdowson 2005). Their associated continental flood basalts represent some of the largest outpourings of volcanism on the planet (e.g. Bryan et al. 2010). Such volcanism and magma fluxes involve the movement of significant volumes of material from deep within the earth to the surface through magma plumbing systems, in the form of dykes, sill complexes and intrusive centres (e.g. Jerram and Bryan 2015, this volume). Volcanic rifted margins themselves are partitioned into sedimentary basins, and it is often through these basins that shallow level magma systems migrate (Cartwright and Hansen 2006) and where intrusions, commonly found as complexes of interconnected sills, are concentrated in volume. Magma that migrates through such basins can often come into direct contact with both hydrocarbon reservoir and source rock regions (e.g. Rateau et al. 2013), leading potentially to a profound impact on petroleum systems within a sedimentary basin (e.g. Holford et al. 2012).

Our knowledge of igneous emplacement in sedimentary basins has been revolutionised by studies of offshore seismic reflection data (Thomson 2005; Cartwright and Hansen 2006; Jerram et al. 2009; Schofield et al. 2012a; Wright et al. 2012; Schofield et al. 2015). New and enhanced imaging techniques (Thomson 2005; Archer et al. 2005), in conjunction with the proliferation of 3D seismic data sets acquired in volcanic basins (e.g. Schofield et al. 2015), have enabled the imaging of large parts of these magmatic systems. Many of these studies have been focussed on offshore late-Cretaceous to Eocene aged sill complexes along the Northwest Atlantic margin (e.g. Schofield et al. 2012a; Magee et al. 2014), from the South Rockall Basin to the Norwegian margin (e.g. Planke et al. 2015, this volume).

The Inner Hebrides of Western Scotland, which contains an onshore record of this extensive

magmatic activity such as the Palaeogene aged Trotternish/Minch Sill Complex, Isle of Skye, allows us to examine some of the classic sill geometries on a seismic to sub-seismic (outcrop) scale. Linking from seismic to sub-seismic scales is valuable as it allows us to relate the bigger structures that we see in 3D seismic reflection data, to what might be happening in areas below the resolution of seismic reflection data (commonly 20–40 m). These outcrops therefore, provide a detailed understanding of the structure of the sill complexes and the sub-seismic interaction between volcanic rocks and host rock strata. This is particularly important, as the basins situated along the Northwest Atlantic margin represent particularly challenging hydrocarbon exploration environments due to the presence of areally and vertically extensive sills, which inhibit seismic imaging within underlying sequences, such as those of Jurassic age, which may contain organic-rich source rocks. This makes it difficult to predict the potential interaction that the sill intrusions may have had with both reservoir, but particularly source rock intervals within the sedimentary basins along the Northwest Atlantic margin.

We present a series of outcrop case studies which allow the potential influences of sills on what would represent potential source and reservoir rock intervals to be addressed. It is important to note that the Isle of Skye has undergone previous hydrocarbon exploration, including the drilling of an onshore exploration well, meaning that unlike many other areas with exposed sills, direct outcrop-to-subsurface comparisons can be made. The associated seismic exploration and also recent studies of other remote geophysical techniques such as magnetotelluric data (e.g. Hautot et al. 2007) mean that detailed knowledge of the hydrocarbon aspects of the area are at least partly known, allowing comparison with the hydrocarbon systems present within the Northwest Atlantic margin basins. The discussion is focused around the petroleum implications of such sill complexes in the Northwest Atlantic margin and volcanic margins in general.

2 Geological Summary of the Isle of Skye of Skye

The Isle of Skye and its surrounding basins have been documented in terms of their regional structural geology (e.g. Stein and Blundell 1990), burial/uplift history (e.g. England et al. 1993) and the igneous/volcanic rocks that form the expression of the North Atlantic Igneous Province (NAIP) in this area (e.g. Williamson and Bell 1994; Single and Jerram 2004; Emeleus and Bell 2005; Nelson et al. 2011). The geological context of the Isle of Skye is complex and diverse (Fig. 1), and contains a number of geological units from the Precambrian to Quaternary (Fig. 1). The continental crust in Skye underwent several rifting episodes, with associated sediment

fills, before the final rifting and opening of the NE Atlantic. These include pre-Cambrian (Torridonian), lower Palaeozoic, and a sequence of Triassic—Mid Jurassic rifting, late Jurassic subsidence and Late Cretaceous uplift (and erosion) before Eocene break-up (Stein and Blundell 1990; England et al. 1993). During the Palaeogene, Skye was subject to volcanism in the form of intrusive sills and dykes, eruption of lava (Skye Main Lava Series) and the emplacement at depth of gabbros and granites (the Cuillins).

The Isle of Skye is bounded by two major structural lineaments; the Outer Hebrides fault zone (also known as the Minch Fault) to the NW and the Moine Thrust to the SE (see Fig. 1). The basement rocks of the region consist of pre-Cambrian Lewisian Gneiss, which are thought to underlie most of

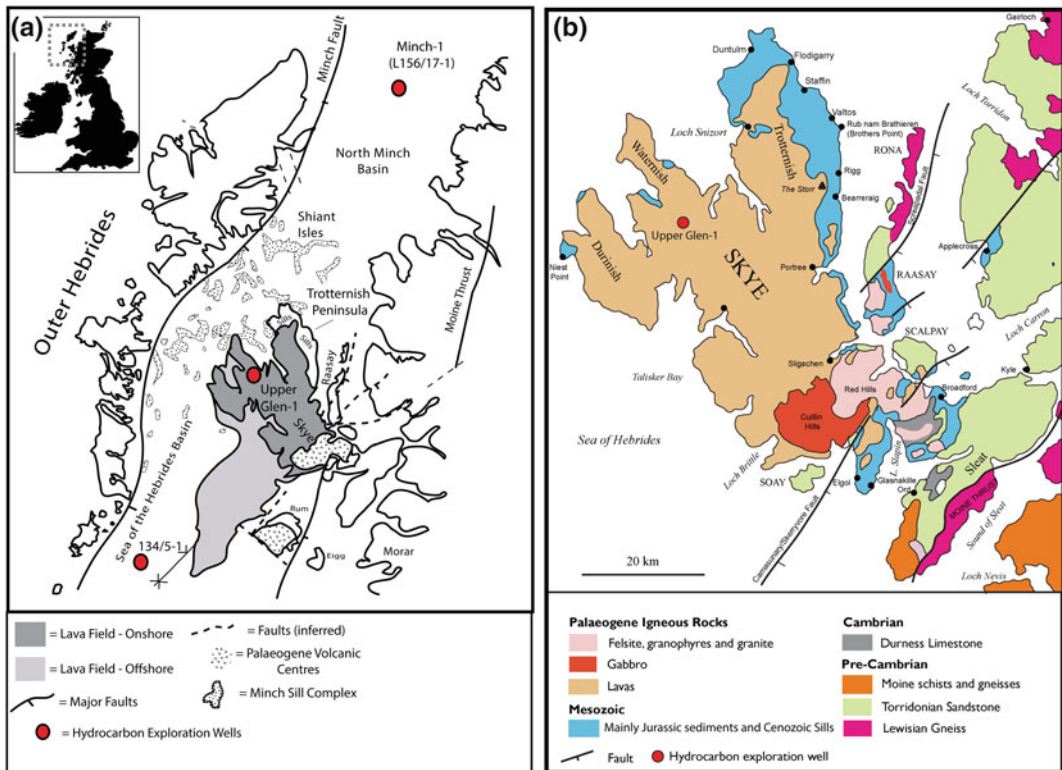


Fig. 1 a Overview map of Skye and the Sea of Hebrides basin (modified from Schofield 2009), showing main tectonic and volcanic elements. Note the

Trotternish/Minch Sill Complex extending into the Sea of Hebrides and North Minch Basin. b Simplified geological map of Skye

the area (Emeleus and Bell 2005) and form the majority of the Outer Hebrides landmass.

The dolerite sills of the Minch Sill Complex, exposed extensively around the Trotternish Peninsula, locally cut the Skye Main Lava Series at the base of the sequence, and are thought to post-date the eruption of the lava flows, but pre-date the last generation of dykes which cross-cut the area (Anderson and Dunham 1966; Emeleus and Bell 2005). The chronological relationship of the sills and the lavas is corroborated by geochemical analysis of the sills which show that they are contaminated by upper crustal rocks, compared to the lava field which displays mostly lower crustal contamination, suggesting that the lavas and sills were fed from two separate magma sources (Kerr 1993), and that interaction has occurred with different potential crustal contaminants highlighting a complex petrogenesis and magma migration pathway (Font et al. 2008).

3 Petroleum Geology of the Isle of Skye/Sea of Hebrides

To assess the potential impact of intrusions on sedimentary basins it is important to understand the basin stratigraphy and petroleum potential. In the case of Skye, it is necessary to consider and understand this region and the offshore Sea of Hebrides Basin in terms of its known stratigraphy from both outcrop and any available well data.

The Isle of Skye and Sea of Hebrides Basins were the focus of hydrocarbon exploration in the late 1980s and early 1990s, which culminated with two wells being drilled: Upper Glen-1 onshore in North Skye by Pentex Oil Ltd. (Figure 2), and the offshore Sea of Hebrides well (134/5-1), drilled by Chevron in the southern Sea of Hebrides. Although both wells were ultimately unsuccessful, the data from the drilling demonstrated that Skye and the Inner Hebrides have many elements needed for a successful petroleum system to operate, including good source rock and reservoir potential. Below we

will briefly consider the detailed information from the Skye based Upper Glen-1 well and onshore sequences, in the context of a petroleum system.

3.1 The Upper Glen-1 Well

The Upper Glen-1 well was drilled on Waternish Peninsula, Northern Skye in 1989 by Pentex Oil Ltd (Fig. 2; see location on Fig. 1), and much of the information in the section below is taken from the final well report. The well was a wildcat exploration well, designed to test the hydrocarbon potential of the Sea of Hebrides Basin, which up to that point was largely unknown. The primary objective of the well was to target Jurassic and Triassic sands within the up-dip portion of the Sea of Hebrides half-graben basin. The secondary target was Carboniferous (Westphalian) coal measures. The pre-drill plan was to drill to a total depth of 1676 m, terminating in the Carboniferous, however on drilling, the pre-drill prognosis was found to be incorrect, with the Jurassic and Triassic sequences coming in much deeper than anticipated and the hole was temporarily abandoned, at a depth of 1829 m, before being re-entered to drill to a total depth of 2682 m, terminating within the Triassic. The well penetrates all sequences which can be seen at outcrop onshore Skye and Raasay to the Triassic, giving a unique opportunity to study outcrop to well relationships. This detailed stratigraphy and its relationships to the outcrop geology is presented in Fig. 2 and discussed below.

The well penetrated ~600 m of the Skye Main Lava series, and basal intrusions, before entering into 320 m of the Middle Jurassic Great Estuarine Group, which displayed several moderate porosity reservoir sections (e.g. Elgol Sandstone) (Fig. 2). The well then penetrated ~400 m of the Bearraig Sandstone Formation, which showed moderate reservoir quality in the uppermost sequences. The well then encountered ~90 m of early Jurassic Lower Toarcian shales with high total organic carbon (TOC), before penetrating

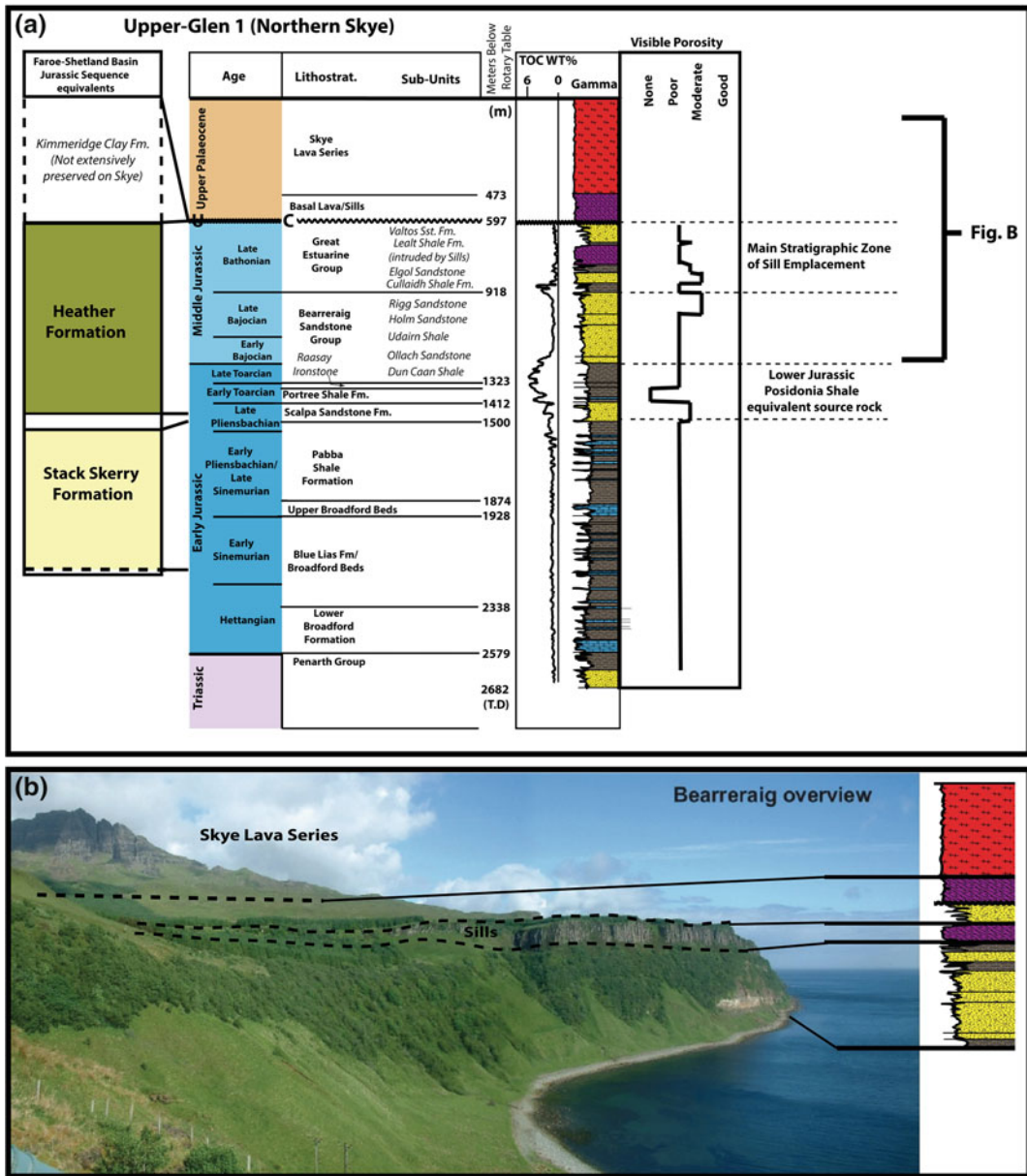


Fig. 2 a Figure showing detailed stratigraphy of the Upper Glen-1 well, with accompanying Faroe-Shetland basin time equivalent sequences and also the relative visible porosity

recorded in sequences from the well. b Figure showing coastal section on Skye with equivalent sequences penetrated by the Upper Glen-1 well highlighted

the Lower Jurassic Pabba and Broadford Formations, eventually terminating within the Triassic.

The well did not encounter any liquid hydrocarbon accumulations, but a gas peak was detected in the Lower Jurassic Broadford Formation/Top Triassic. The volcanic and intrusive units can be

identified from the well log using their characteristic rock property profiles (e.g. Nelson et al. 2009). Subsequent Drill Stem Tests (DST's) to assess the hydrocarbon viability and producibility of the particular zone proved inconclusive, due to technical issues with the DST's.

In terms of reservoirs, the Middle Jurassic Great Estuarine and Berreraig sandstone group were found to possess good reservoir quality, displaying moderate visual porosity, interspersed with mudstone forming potential for reservoir-seal pairs.

3.2 The Potential Petroleum System Across the Sea of Hebrides/Malin Basins

The source rock potential of the Jurassic sequences on Skye and in the Inner Hebrides is good, with the lower Jurassic containing high TOC (2–6 %) early Toarcian shales (Butterworth et al. 1999), equivalent to the Posidonia Shale, which forms a highly prospective hydrocarbon producing sequence across large parts of Northern Europe (Rohl et al. 2001). These potential source rocks are areally extensive onshore through the Inner Hebrides (Emeleus and Bell 2005), although their offshore distribution in the Sea of Hebrides/Malin basins is less well understood. Other source rock regions also occur in the Great Estuarine Group, in the form of the Lealt Shale (0.5–2.4 % TOC) and Cullaidh Shale Formation (up to 4.5 % TOC) (Butterworth et al. 1999).

Onshore sections of the Jurassic source rocks are immature for hydrocarbons, except where directly adjacent to igneous intrusions, where localized cracking of the kerogens has occurred (Thrasher 1992; Muirhead 2011). This highlights the potential of intrusive rocks to raise the maturation of otherwise immature source rocks. Burial history diagrams suggest that in the onshore sections, no part of the Jurassic has ever been buried deeper than a few km's (Morton and Hudson 1992; Holford et al. 2010). The potential lack of burial of the Jurassic sequences (although exact knowledge of this is still poor), remains a major limitation to the working hydrocarbon system and exploitation of the inshore basins West of Scotland. Potentially, offshore, within the Sea of Hebrides and adjacent Malin basins, next to some of the major graben and half-graben bounding-faults, source rock sequences may

have been buried deeply enough to enter the oil window. Equally, igneous intrusions in both the form of large igneous centres (e.g. the offshore Blackstones igneous centre) and sills, may play an important role in helping bring the close to mature source rocks to maturity by localized heating (e.g. Thrasher 1992).

4 The Trotternish/Minch Sill Complex

The Trotternish Sill Complex, and sills on Raasay and the Shiant Isles represent a small onshore exposure of the much more extensive but mainly submarine, Minch Sill Complex (sometimes referred to as the Shiant Isle Sill Complex) which covers an area of ~4000 km² (Gibson and Jones 1991) (see Fig. 1). Onshore, although it is best seen on the Trotternish Peninsula, prominent isolated outcrops of the complex also occur on the Duirinish Peninsula (e.g. Neist Point). Offshore, the complex which is generally exposed at or just below the sea bed, often forming prominent bathymetric features, extends into the NW portion of the Sea of Hebrides Basin and SW portion of the North Minch Basin (Fig. 1). The sills of the Trotternish peninsula form the largest single on-land expression of the Minch Sill Complex with individual sills ranging in average thickness between 10 and 120 m (Emeleus and Bell 2005).

The sill complex as a whole is both structurally and petrologically complicated. Previous studies have been concerned predominantly with field relationships, petrography and geochemistry of the sill complex (Anderson and Dunham 1966; Gibson and Jones 1991; Emeleus and Bell 2005). Gibson and Jones (1991) provide a comprehensive petrographic and geochemical investigation of sills of the Trotternish Peninsula. As yet no published studies have dealt with the structure, emplacement and effect of intrusions on the petroleum system in detail.

The sills within the Trotternish complex do not possess a clear saucer-shaped morphology such as those imaged in offshore seismic data

(Thomson and Hutton 2004). Although local transgressions of the sills do occur, most notably at Kilt Rock, the sills are generally tabular and sheet like in nature, being approximately concordant with the Jurassic host rocks.

The emplacement of sills into Jurassic host rock is associated with the development of several structural and morphological features that are related to the mechanism of magma emplacement and flow within the sills. These structures mainly take the form of bridge structures, which have been shown to form perpendicular to the axis of magma flow (e.g. Hutton 2009; Schofield et al. 2012a, b). The formation of these structures is presented in Fig. 3 in both 2D section and 3D schematic. These structures and how they are visualised in 2D and 3D will become important as we consider the Skye case studies.

5 Key Outcrops and Structures

Case Study 1 (Intrusion into potential source rocks) At low tide the foreshore on the northern side of the Rubha nam Brathairean (Brothers Point) peninsula (Figs. 4 and 5) exposes a series of dolerite sills intruding into the Middle Jurassic Lealt Shale Formation, which possesses relatively high TOC (0.5–2.4 %), and represents one of the potential source rock units within the Inner Hebrides region (Butterworth et al. 1999).

On the foreshore, inclined rafts of Lealt shale can be seen separating bodies of dolerite (Figs. 4 and 5). Figure 4 shows a 2 m thick raft of shale sandwiched between two dolerite sills which have intruded on separate stratigraphic horizons. Evidence of re-orientation of the Lealt shale raft as a

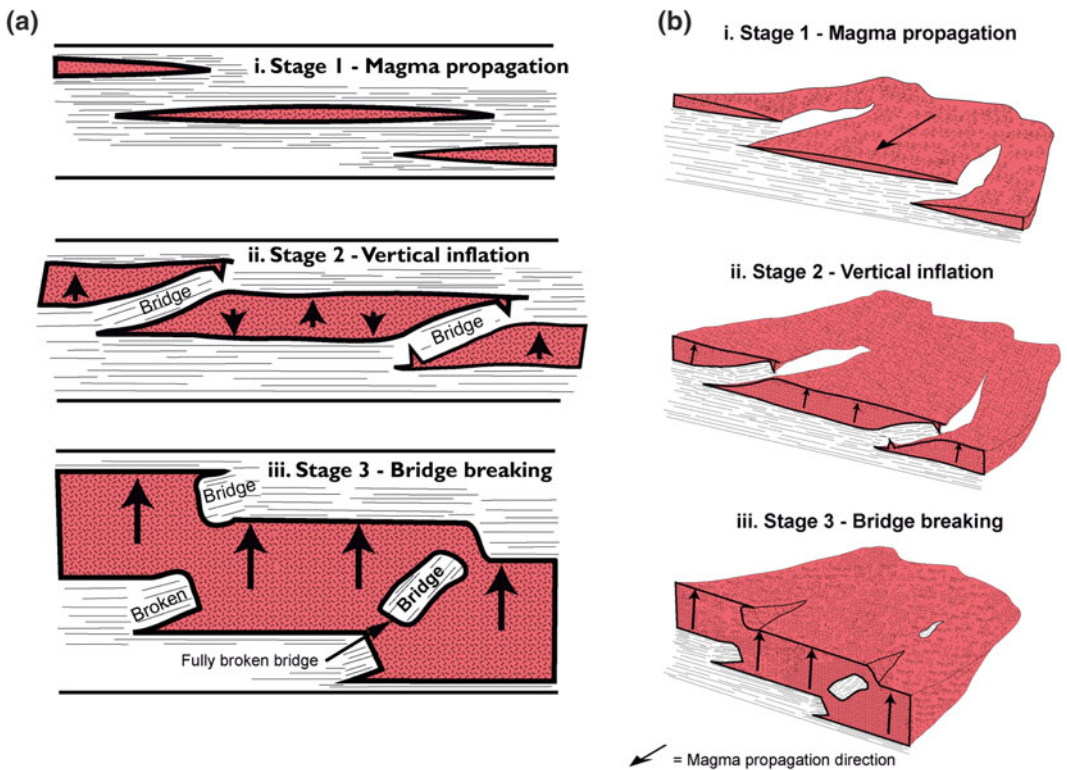


Fig. 3 Figure showing the development of bridge and broken bridge structures in 2D (a) and (b) 3D. Bridge structures are a common occurrence within the Trotternish

Sill Complex and provide a useful tool for assessing the magma flow axis within the sills forming the complex

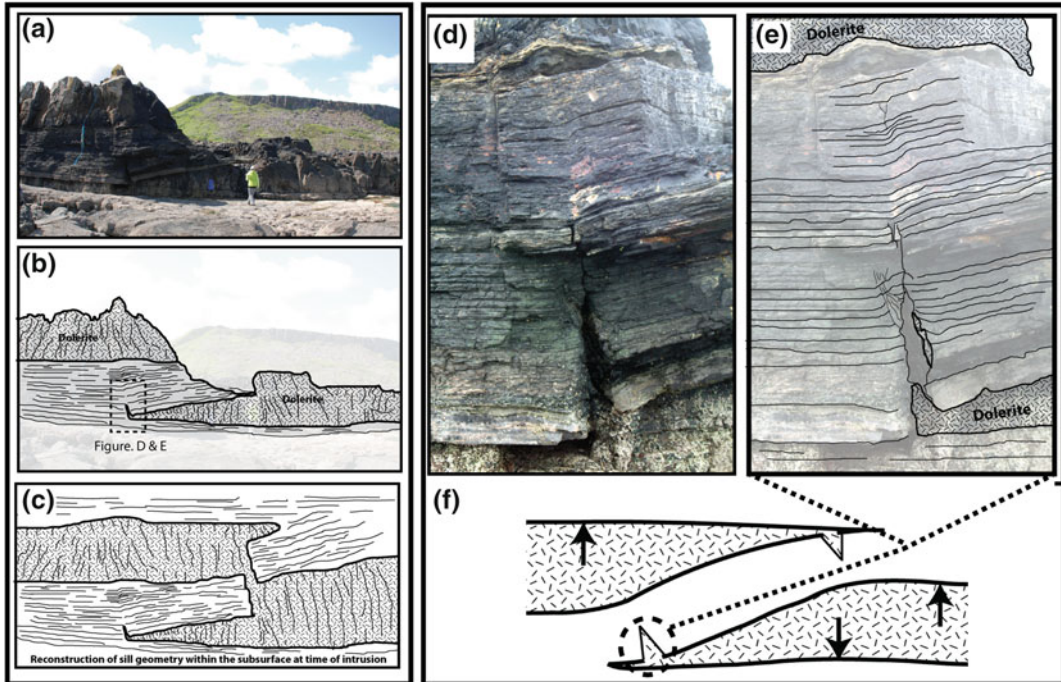


Fig. 4 **a** Bridge structure visible at low tide at the Rubha nam Brathairean (Brothers Point) foreshore. Note person for scale. **b** A inclined bridge of Lealt shale can be seen to occur between the upper (now eroded) sill and lower sill, a tensile cross-fracture can be seen to have formed at the tip of the lower sill, see **(d)**, **(e)** and **(f)**. **c** Reconstruction of the likely emplacement geometry within the subsurface prior to erosion. **d** and **e** Showing zoom in of the tensile cross-fracture which has formed as a result of the inflation

of the sill bodies during magma emplacement (see **f**), note that ahead of the actual tensile fracture, a zone of deformation can be seen within the host rock bridge. The magma, which has formed the lower dolerite sill, can also be seen to have intruded into the fracture, confirming that the formation and deformation of the bridge occurred during magma emplacement. **f** Figure showing zone in which tensile failures are developed across the bridge during sill inflation

result of inflation of the two sills is clearly visible, which has resulted in the development of a tensile fracture extending upwards from the lower sill tip. Although large portions of bridge have now been removed, the lowermost unit of the bridge can be seen to directly contact the lower sill.

The example on the foreshore of Rubha nam Brathairean provides an excellent demonstration of bridge formation as a result of sill intrusion, and the 3D exposure of these bridges on the Rubha nam Brathairean foreshore gives a clear indication of the magma flow axis of the sills in this area of SW–NE, as the axis of the bridges of Lealt shale exposed are orientated approximately perpendicular to the magma flow axis (Hutton 2009; Schofield et al. 2012a, b) (Figs. 4 and 5).

The Rubha nam Brathairean foreshore provides an important example of sill intrusion into

a potential source rock region. The sills exposed at Rab Nam Brathairean occur in the same stratigraphic interval (the Lealt Shale Formation.), where within the Upper Glen-1 well, sills were also intersected, implying that the formation has acted as an important regional horizon that has focused sill emplacement. The implication of this is that offshore, in regions such as the Jurassic of the North Atlantic, potentially regional mudstone/source rock horizons may be intruded by sills over a large areal extent within individual fault blocks.

Case Study 2 (intrusion into potential reservoir intervals) The Dun Dearg and Kilt Rock exposure begins approximately 400 m northwards along the coast from Rubha nam Brathairean, where the coastline is characterized by a series of

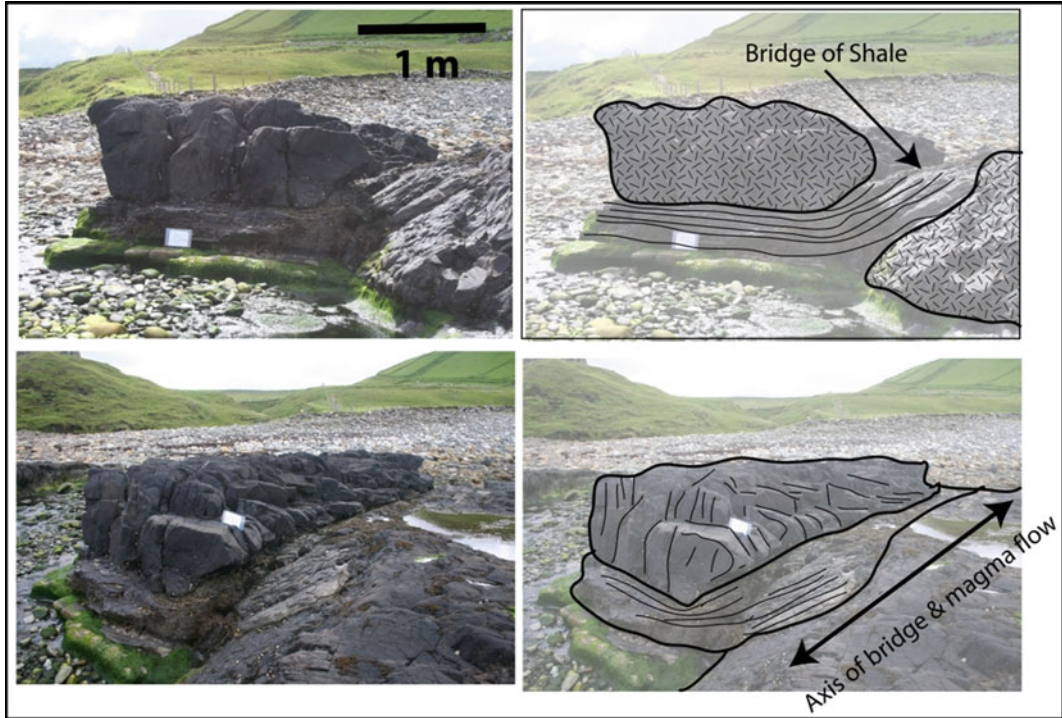


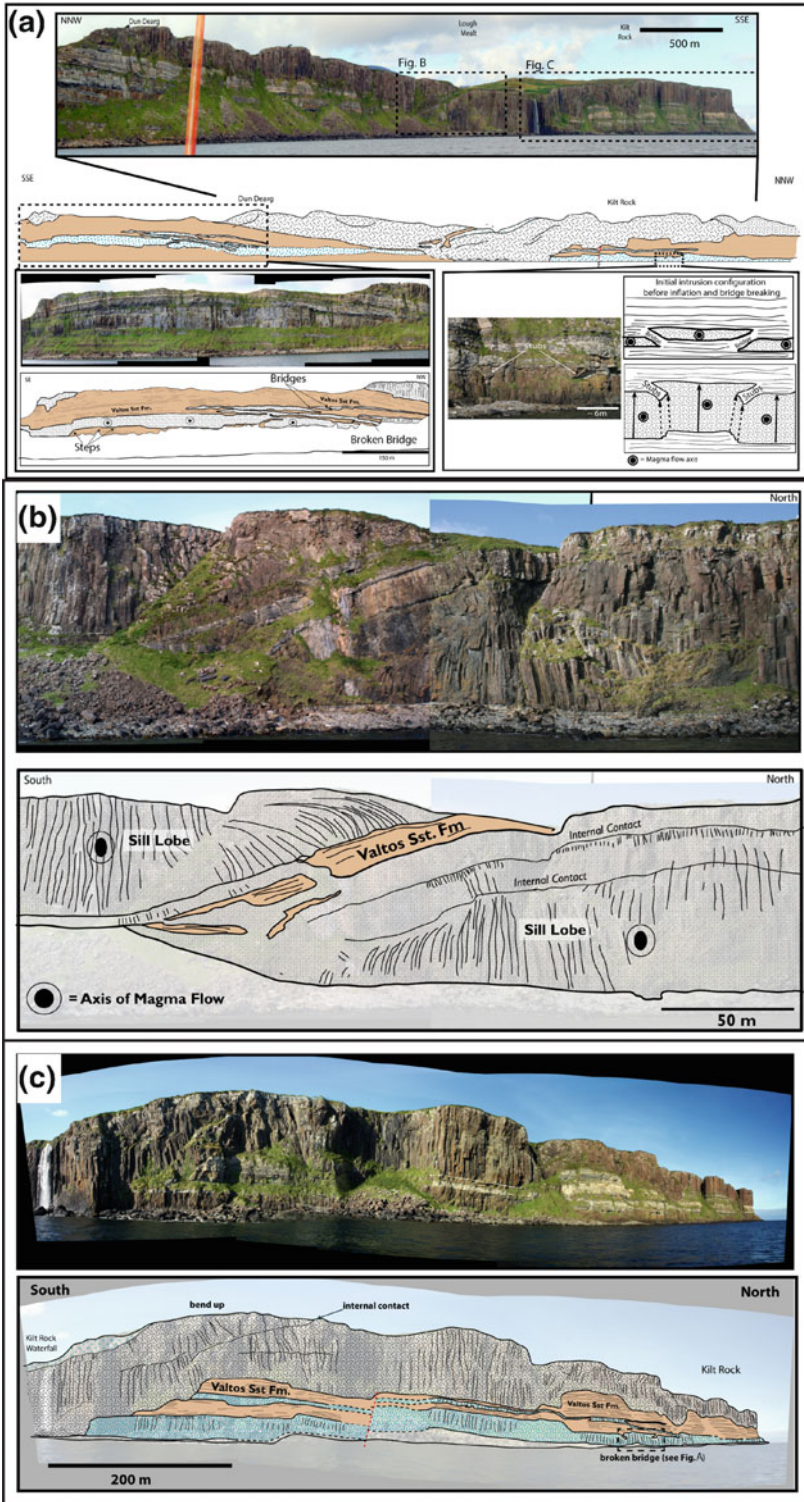
Fig. 5 Another bridge structure exposed on the Rubha nam Brathairean (Brothers Point) foreshore, with a bridge of shale showing the axis of the bridge (and therefore magma flow axis). The bridge separates two separate sill lobes

steep cliff faces composed of the Valtos Sandstone Formation (Fig. 6a). The Dun Dearg section is characterized by a series of bedding parallel dolerite intrusions, ranging from 10s of centimetres to 10s of metres in thickness. The section contains several structures related to magma intrusion, in the forms of steps, offset sill segments, un-broken and broken bridges, including isolated rafts of the Valtos Sandstone Formation (Fig. 6a). The prevalence of such features along strike within the cliff face suggests that the current orientation of the cliff face is orientated approximately perpendicular to the axis of magma flow within the intrusions, approximately West–East.

The section is characterised by multiple intrusions of sills; Gibson and Jones (1991) showed that the sills within the section are all crinaitic in composition (Dolerite with <5 % olivine). However, evidence for multiple intrusion phases is observed in the form of cross-cutting relationships

by separate dolerite sheets, and also in the form of internal contacts within the intrusion (Fig. 6b, c), which suggests a series of temporally restricted magma pulses. Local transgression or ‘stepping-up’ of the sills can be seen to occur, particularly at the headland of Kilt Rock (e.g. Fig. 6c). The thickness of the dolerite is fairly uniform at ~40–50 m in thickness, except in the structurally lowest area of the sill at Lough Mealt where the sill thickness is in the region of 80 m (Fig. 6b).

Several key structural elements related to magma flow can be identified when the sills are examined from offshore. It can be seen that the sill that forms the upper cliff is actually composed of two separate sill lobes (Fig. 6a, b). The most striking feature of this section is the occurrence of a large bridge structure inclined at approximately 35° between the sill lobes (Fig. 6b). This indicates that the axis of magma flow was approximately perpendicular to orientation of the current cliff



◀ **Fig. 6** a Figure showing Kilt Rock sills from offshore. Note the numerous occurrences of broken bridge structures within the cliff face. b A bridge of the Valtos Sandstone Formation can be seen to be sandwiched between two separate sill lobes which form the prominent cliffs of the section. c Figure showing the northern exposure of the Kilt Rock outcrop. At least two phases of

sill intrusion can be seen (note the cross-cutting relationship in the *bottom left* of the figure). Also note the compartmentalization and isolation of entire rafts of the Valtos Sandstone Formation between separate sill intrusions, see main text for details. Internal contacts within the intrusions appear to indicate separate pulses of magma that occurred during the inflation of the sills

section at Kilt Rock. This aspect appears to be additionally confirmed by the occurrence of a broken-bridge structures in the lower tier sill around sea-level (e.g. Fig. 6a), which were formed as result of the initial propagation and subsequent inflation of three separate offset but overlapping sill segments.

In terms of their impact on petroleum aspects, the sills at Kilt Rock and Dun Dearg offer a good opportunity to see the highly compartmentalizing effect that intrusions can have on a reservoir section (see Holford et al. 2012; Rateau et al. 2013). It is clear to see that entire sections of Valtos Sandstone Formation, which would potentially make a viable reservoir in the subsurface, is compartmentalized and isolated between separate tiers of sill intrusions. Within the subsurface, such a scenario may lead to impeded fluid flow and hydrocarbon migration in the subsurface, if the sills (or surrounding contact metamorphic zones) act as barriers or baffles (see discussion).

Case Study 3 (Seismic-scale sill structure 1) The area of Staffin Harbour consists of two main tiers of sills, intruded into the upper Great Estuarine Group. The uppermost tier is intruded into the lower portion of the Kilmaluag Formation with the lower tier forming a wave cut platform having intruded into the Duntulm Formation (Fig. 7a, b). The top contact of the lower sill is extensively exposed forming the harbour and foreshore area. Upon its top surfaces, flow indicators in the form of aligned vesicles and ropy flow structures can be found in abundance, such features can be successfully used to infer both the axis of magma flow (aligned vesicles; Rickwood 1990) and direction of flow (ropy flows; Liss et al. 2002) (Fig. 7c).

The wave cut platform exposes the top contact of the lower tier sill, where in places erosion has removed the overlying Kilmaluag Formation, the

top surface of the dolerite sill can be seen to possess an abundance of flow indicators, in the form of aligned vesicles and ropy flow structures (Fig. 7d, e). Ropy flow structures, which appear as small scale pahoehoe textures, form as a result of a free-surface of gas being created at the interface between magma and host rock during emplacement of magma (Liss et al. 2002). In places the ropy flow structures form chaotic structures, however where the top contact with the limestone country rock was uneven, pendants of limestone country rock protruded into the underlying magma as it flowed (Fig. 7e). This caused the ropy flows to drape and drag around the roof pendants, giving a direction of magma flow (Fig. 7e).

Another feature which can be seen at Staffin Harbour in the upper tier of dolerite is the presence of a convex top surface to the sills (Fig. 7a, b), which resemble morphologies of large scale magma fingers that have been documented from the field (Schofield et al. 2010), and in seismic reflection data (Thomson and Schofield 2008). These convex-up profiles are preserved inland, and can be traced for 800 m in a SSE orientation through changes in slope and on aerial photographs where they form tapering finger-like landforms. When the axes of these convex-up fingers is compared to the flow indicators in the other sills at Staffin Harbour, it indicates that they are orientated approximately along the direction of inferred magma emplacement, suggesting that the structures are indeed related to magma flow and therefore do represent magma fingers (sensu Schofield et al. 2010) (Fig. 7c). The magma fingers seen at Staffin Harbour have not been identified previously in the published volcanic literature on Skye, possibly because the features were interpreted to be the result of glaciation and erosion. However, the features do not appear to be related to later stage glacial processes, as the Devensian ice-flow across the Trotternish

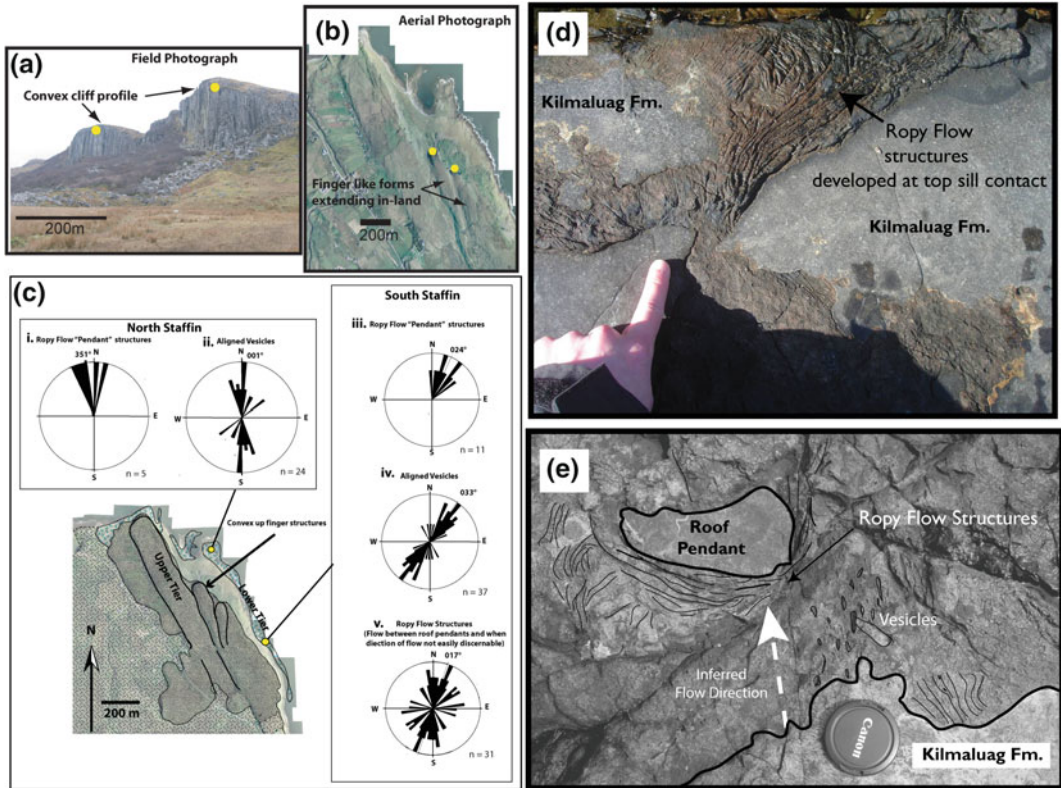


Fig. 7 Figure showing Staffin Harbour sill outcrops. **a** The upper tier of sills can be seen to display the presence of convex magma finger-like cliff profiles (see Schofield et al. 2010). **b** These finger-like structures can be seen to extend inland. **c** Flow indicators occurring within the sills show that the direction of flow of magma appeared to orientated approximate parallel to the

finger-like structures. **d** Ropy flow structures preserved on the top surface of the sills at Staffin Harbour. **e** Also visible at Staffin Harbour is a roof pendant of the Kilmaluag Fm which shows draping of ropy flow structures around it, indicating magma flow direction (see main text for details)

Peninsula is thought to be oblique to the axis of the fingers (Benn 1997).

Case Study 4 (Seismic-scale sill structure 2) The sills exposed at Niest Point, located on the western most extent of the Duirinish Peninsula, represent the most westerly onshore exposed example of the Minch Sill Complex. The locality also offers a good opportunity to study the immediate sub-basalt structure where the underlying sediments have been intruded by sills.

Exposed on the foreshore of Moonen Bay, 1 km southwards along the coast from Niest Point, are a series of intrusions which intruded into the Lealt Shale Formation (Fig. 8). The most striking aspect of the outcrop is the occurrence of

a large, seismic-scale bridge of Lealt Shale which is ~40 m in thickness, oriented at ~40° between two separate sills (the top most sill has been partially eroded away from the cliff edge). The bridge of Lealt Shale can be seen to be cut by a series of dyke segments. These appear to be primarily related to cross-connecting fractures that would have formed during the inflation of sills (and subsequent deformation of the bridge). The orientation of the bridge within the cliff face, which does offer enough exposure to see the bridge exposed in three dimensions, indicates that the magma flow axis within the sills was orientated approximately in an east–west orientation.

The sills at Niest Point and Moonen Bay are some of the thickest and most complex sills exposed

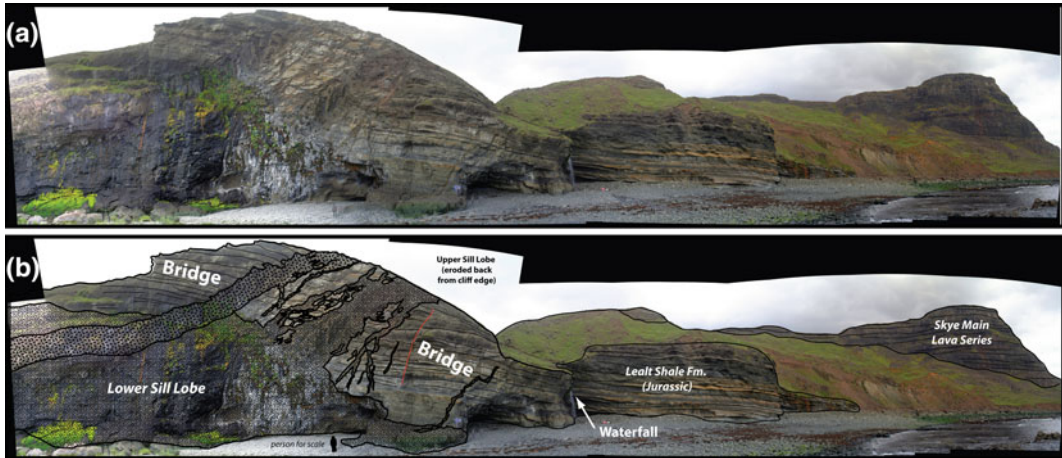


Fig. 8 **a** Outcrop at Moonen Bay, Duirinish Peninsula, West Skye, showing a large-scale bridge structure of the Lealt Shale Formation. **b** The bridge shows a complicated

array of cross-fractures as a result of bridge deformation during intrusion

onshore Skye, and the near seismic-scale bridge structure at Moonen Bay additionally represents the biggest visible at outcrop on the Isle of Skye.

6 Discussion

6.1 Emplacement of the Trotternish/Minch Sill Complex Compared with the North Atlantic Margin Sill Complexes

The close spatial distribution of the Trotternish/Minch Sill Complex in relation to the onshore Skye main lava field and associated dykes, suggests potentially that the sill complex is being fed laterally from feeders running under the main Skye lava field, with the sills having been emplaced away from what is now the Skye landmass into the Sea of Hebrides region. However, as noted by Kerr (1993), the sill complex shows a distinctly different geochemistry from that of the lava fields, suggesting that the source of magma (and ultimately plumbing system) was different than for that of the Trotternish/Minch Sill Complex. Additionally, the sill complex can be seen to have locally cut the lava field in areas, suggesting that the Trotternish/Minch Sill

Complex (or at least parts of it) post-dated the eruption of at least the basal sequences of the Skye Main Lava Sequence.

The points discussed above raise the question as to where the Trotternish/Minch Sill Complex was actually sourced from. Work on Palaeogene sills in adjacent basins to the Inner Hebridean margins along the Atlantic margin, e.g. the Faroe-Shetland Basin, have demonstrated that pre-existing basin structure imparts a large control sill emplacement (Schofield et al. 2015). More specifically, the bounding faults of half-grabens and hanging walls created during pre-intrusion rifting appeared to have acted as controlling sites for magma input into the sedimentary basins, with sills then transiting up-dip within the half-graben basins over 10s of kilometres laterally (Schofield et al. 2015) (see Fig. 9a).

The Inner-Hebridean basins are thought to be composed essentially of series of Jurassic half-graben structures (Roberts and Holdsworth 1999), created by Triassic and Jurassic rifting being accommodated on largely what was dip-slip movement on the Outer Minch Fault and Camasunary-Skerryvore Fault (see Fig. 1). Therefore given the relationship of magma input in relation to half-grabens seen in basins along the Atlantic margin, the disparity in timing and geochemistry between the lava fields and sills in

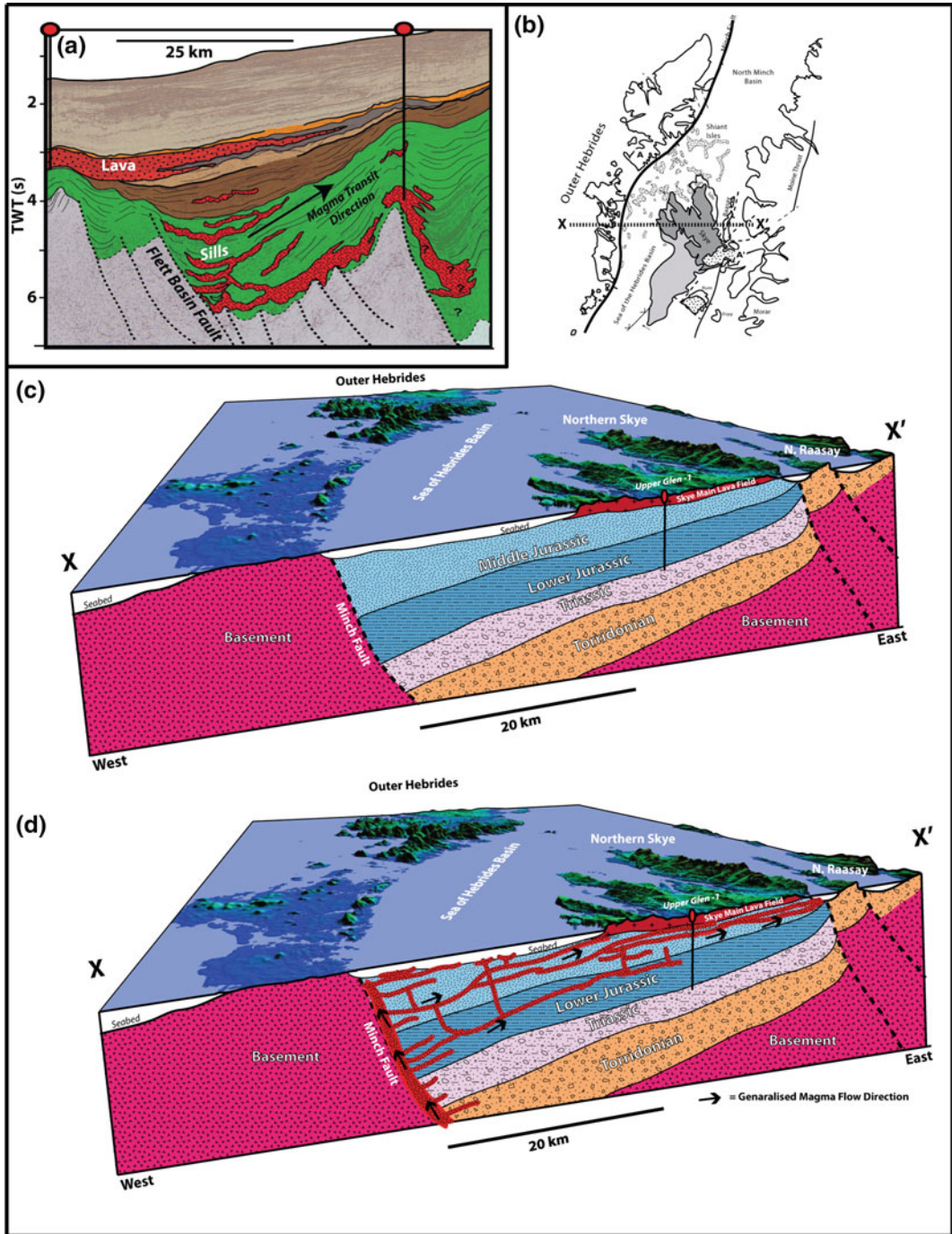


Fig. 9 a A geo-seismic line from the Faroe-Shetland Basin (from Schofield et al. 2015), showing the emplacement of sills into the half-graben hanging wall of the Flett Basin, with magma having transited up-dip. b Figure showing line of section in 3D schematic. c 3D schematic east to west cross-section (see b for orientation) showing Upper Glen-1 well, and the hypothesised half-graben structure of the Sea of Hebrides Basin.

d Potential similar scenario utilizing the relationship seen in a. We therefore hypothesise that the Trotternish/Minch Sill Complex was intruded into the half-graben away from the Minch fault. Such a scenario would explain the discrepancies in magma source and timing of the Trotternish/Minch Complex in respect to the lava field on Skye (see main text for details)

the Inner Hebrides, could suggest that the Trotternish/Minch Sill Complex may not have been fed away from what is now the Skye Landmass, but actually towards it. We suggest that magma was emplaced into the half-graben hanging wall of the Sea of Hebrides, away from the outer Minch fault and Isle of Lewis transiting in an essentially W–E direction towards Skye (Fig. 9), in a fashion similar to that seen within the Faroe-Shetland Basin (e.g. Fig. 9a).

Although it is currently difficult to prove this hypothesis offshore, based on the poor and sparse 2D seismic data that exists within the Sea of Hebrides, invoking this mechanism of magma would explain the inferred separate source of the sill complex from the main lava series, and also the occurrence of the significant sill bodies mapped on the seafloor within the Sea of Hebrides and Minch basin (Fig. 1).

In terms of onshore evidence for such propagation, it is worth noting that the sills exposed on the far west coast of Skye, i.e. those at Niest Point and Moonen Bay (Fig. 8), represent some of the thickest visible on Skye, and the axis of magma flow of the Moonen Bay bridge is oriented in an approximately West–East direction, which is what would be expected if magma was intruded into the basins away from the outer Minch Fault. Along the east coast of the Trotternish Peninsula, which sits at the inferred up dip extent of the Sea of Hebrides half-graben, the axis and directional magma flow indicators appear to show a dominant general West to East magma flow (Fig. 10), again consistent with magma being emplaced up-dip away from the Outer Minch Fault (Fig. 9).

6.2 How Does the Structure of the Trotternish/Minch Sill Complex Compare to Offshore Examples in Other Sedimentary Basins?

The sills on the Trotternish Peninsula and throughout Skye offer a good opportunity to explore seismic scale-to-sub-seismic scale relationships within sill intrusions in sedimentary

basins. Some of the bed parallel geometrical relationships of the sills on Skye also offer a chance to examine structures in more planar/concordant parts of the sill system, seen in the deeper areas of many sedimentary basins (e.g. Karoo Basin).

Sills within sedimentary basins are known to display lobe like morphology formed during the intrusion of magma, as illustrated in both seismic and field data (Schofield et al. 2010, 2012a). They occur essentially as a result of separate sills, with a common magma source, propagating through host rock together on the same or slightly offset horizons (Schofield et al. 2012a, b). The Flett Ridge Sill, imaged within the sub-surface of the Faroe-Shetland Basin, represents a good example of a sill intrusion that displays clear magma lobes (Schofield et al. 2012a; Fig. 11).

The two separate sills/magma lobes forming the Kilt Rock viewpoint represent a good onshore near seismic-scale example of the potential geometry of magma lobes in cross-section, which can be directly compared to those magma lobes imaged within the Faroe-Shetland Basin, offering the chance to understand the sub-seismic relationships which are not visible within the 3D seismic data (Fig. 11). In particular, although the presence of bridge structures between separate magma lobes has been inferred from seismic data through detailed analysis of sill structures (e.g. Flett Ridge Sill—Schofield et al. 2012b), the constraint of seismic imaging and limited vertical resolution means that bridges are difficult to image directly. From an offshore viewpoint at Kilt Rock, the two sills can be seen to be separated by a host rock bridge of the Valtos Sandstone Formation, in the same way that a bridge would be expected to occur in the subsurface between the magma lobes of the Flett Ridge Sill (e.g. Fig. 11).

Bridge structures are potentially an important element within prospective sedimentary basins which contain extensive intrusions located in stratigraphic levels between the source rock and reservoir rock intervals, as the bridge structures potentially offer a permeable fluid pathway for migrating hydrocarbon through potentially

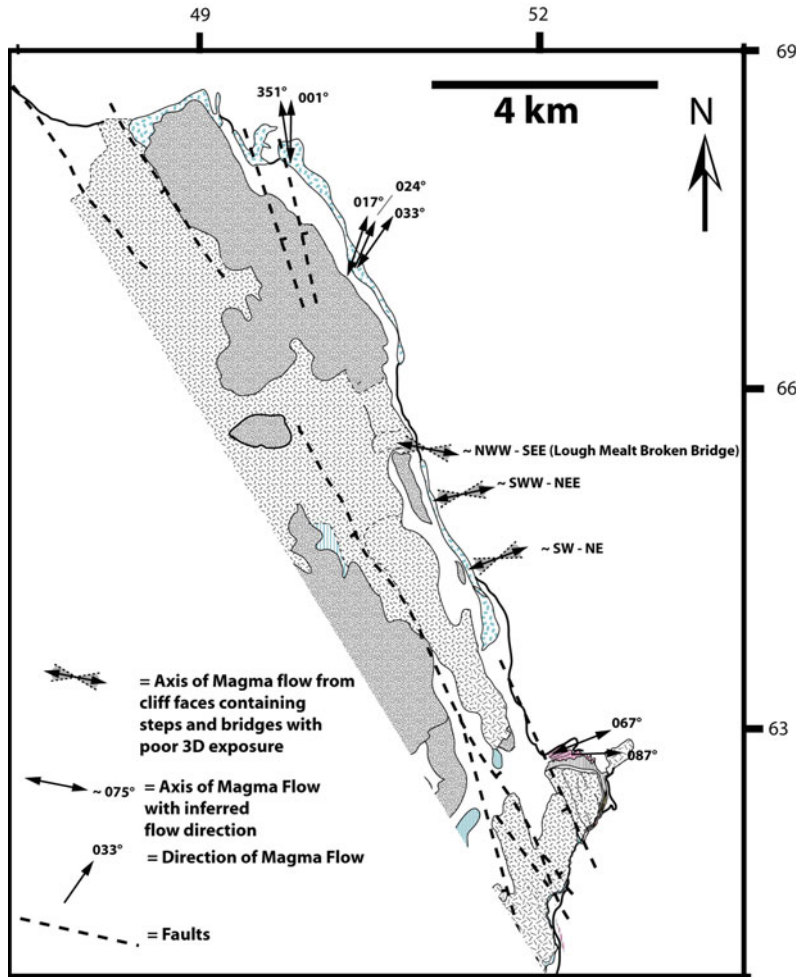


Fig. 10 Overview map of the axis of magma flow and magma flow directions within sills along approx. 8 km coastal profile, from Rubha nam Brathairean (Brothers Point) to Staffin Harbour showing that magma flow within

the sills appears to have been predominantly in a W-E and W-NE orientation, aside from at Staffin Harbour where the magma flow appears to have been orientated in a NW to N direction

sealing sills (or contact metamorphic zones), which may act to inhibit hydrocarbon migration (Schofield et al. 2012a).

6.3 Effect of Sill Intrusions on Jurassic Sequences and Source Rocks

The Jurassic sequences on the Isle of Skye, represent the most westerly exposed example of Jurassic strata on the UK mainland before

encountering the buried Jurassic of the North Atlantic and Rockall Trough. Therefore they provide some insight into the interaction of igneous intrusions with the Jurassic sedimentary sequences of the prospective basins along the Atlantic margin where the Jurassic strata are often unresolvable on 2D and 3D seismic reflection datasets, due to the extensive sub-surface sill complexes intruded into the Cretaceous strata.

The Jurassic sequences of the north Trotternish Peninsula, Isle of Skye, are heavily

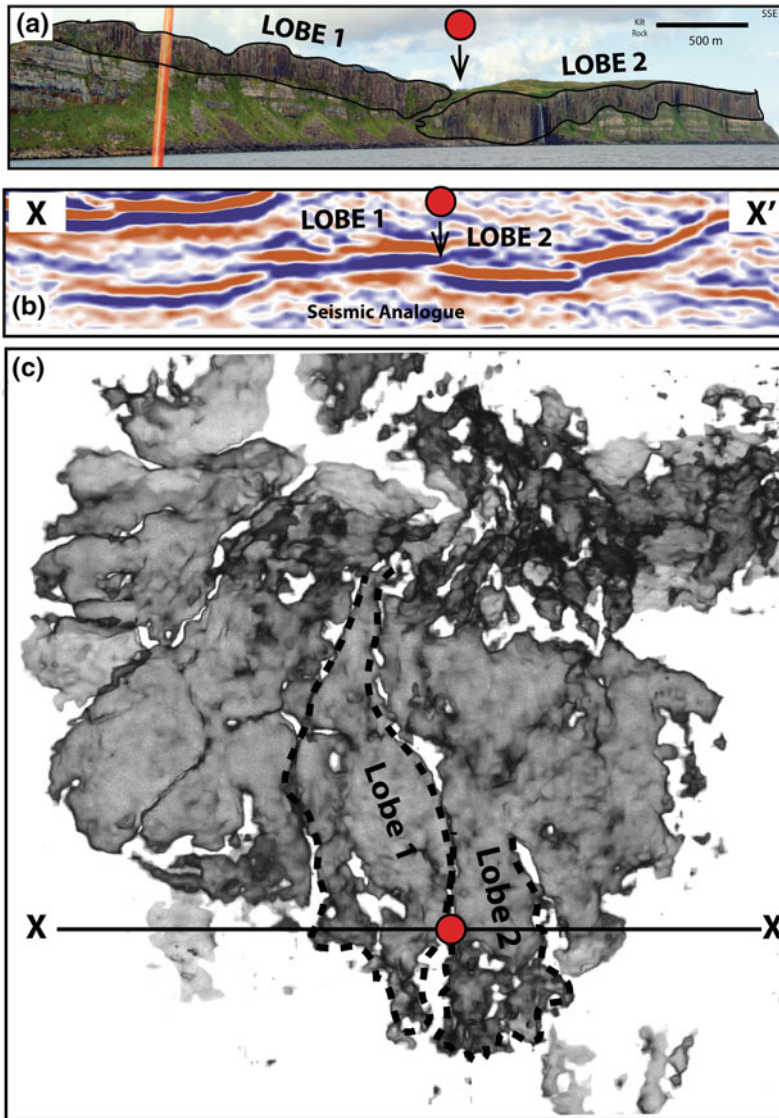


Fig. 11 **a** Figure showing the two separate sills lobes that form Kilt Rock, **b** Seismic line (X–X') through the Flett Ridge Sill (modified from Schofield et al. 2012a) showing the separate magma lobes in cross-section,

analogous to the outcrop at kilt rock in **a**. **c** Plan view of the Flett Ridge Sill showing separate magma lobes (modified from Schofield et al. 2012a) visible within the seismic data, seismic line X–X' marked

intruded by sills (Emeleus and Bell 2005; Schofield 2009), with entire sections of the Jurassic (incl. of reservoir and source rock intervals), being isolated and compartmentalized between different tiers of intrusions (Schofield 2009). If such a scenario occurs in similar Jurassic sequences within the offshore basins along the Atlantic margin, the potential for the

compartmentalization and creation of completely isolated volumetrically extensive 'pods' of source and reservoir rocks exists (Fig. 12).

On the Isle of Skye, the Trotternish/Minch Sill Complex preferentially exploit the Middle-Upper Jurassic Great Estuarine Group, above the main source rock regions (3–6 % TOC) in the Lower Jurassic. This also seems to be the case offshore

End-Member effects of Igneous Intrusion on Conventional Sandstone Plays

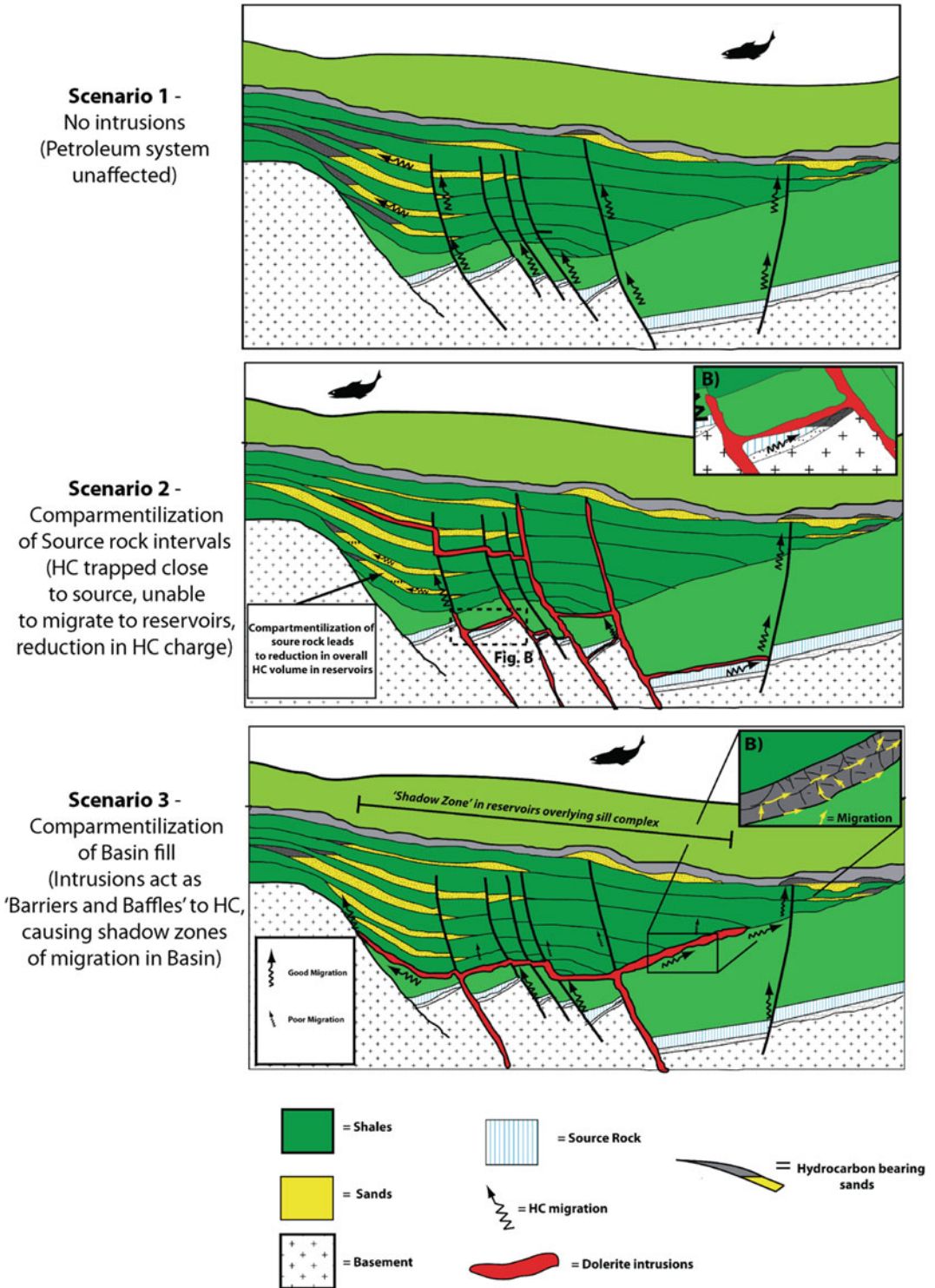


Fig. 12 Figure showing end-member models of potential effect of igneous compartmentalization on reservoir and source rock intervals within a prospective sedimentary basin (modified from Rateau et al. 2013)

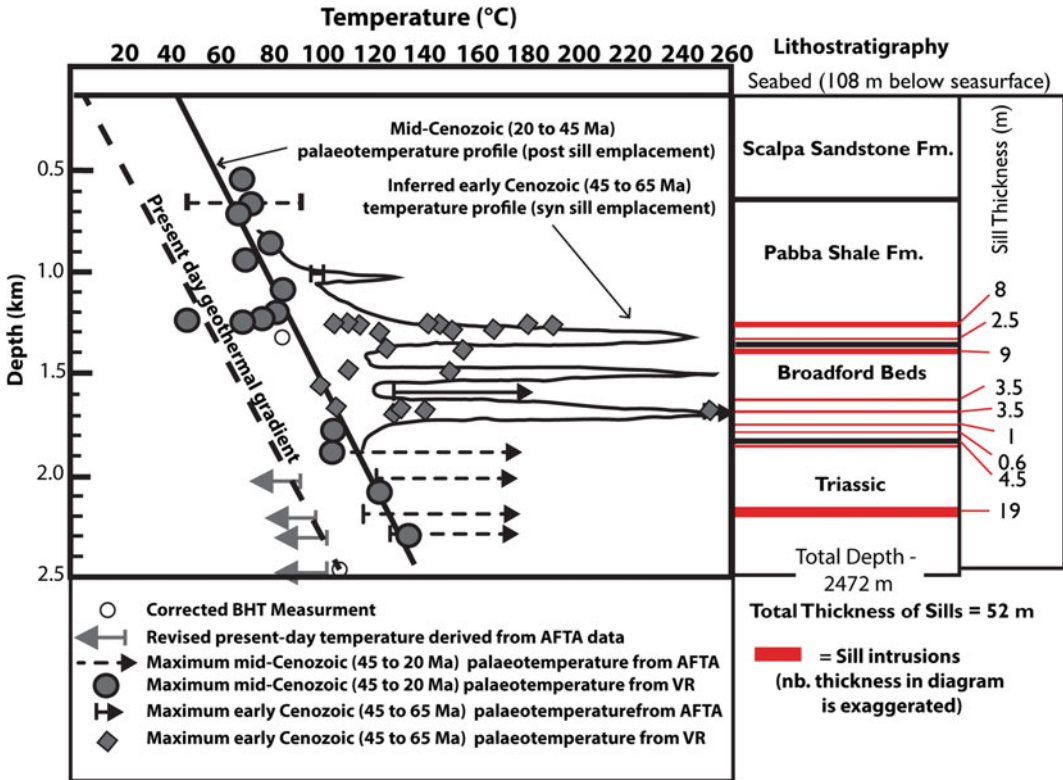


Fig. 13 Modified from Holford et al. (2010), showing palaeotemperature reconstruction through the offshore Sea of Hebrides well (134/5-1). The well intersected nine separate sill intrusions ranging in thickness from 0.6 to

19 m in thickness (totalling ~52 m in thickness). The sill caused surrounding sediments to be heated to between 100 and 260 °C

into the Sea of Hebrides Basin, located to the NW and west of the Trotternish Peninsula, where many of the intrusions crop out on, or are close to the gently dipping Jurassic seabed, suggesting that they also exploit the upper-middle Jurassic. However, to the southern Sea of Hebrides Basin, the Sea of Hebrides well (134/5-1) intersected 9 sill intrusions between 1 and 2 km below the sea bed, within the lower Jurassic Pabba shale and Broadford Beds (Fig. 13). This suggests that towards the southern Sea of Hebrides Basin, sill intrusion may occur into the potential source rock regions of Lower Jurassic age as well.

Apatite fission track analysis (AFTA) and vitrinite reflectance (VR) data from Well 134/5-1 clearly show that Lower Jurassic rocks have experienced palaeotemperature of up to 260 °C as result of contact heating associated with the igneous intrusions penetrated by the well

(Holford et al. 2010) (Fig. 13). The perturbation in palaeotemperature caused by the intrusions affected approximately 1 km of host rock vertically, even despite the total thickness of the intrusions penetrated by the well being only 52 m, and aside from one intrusion of 19 m in thickness, all the other eight intrusions penetrated by the well are <10 m in thickness.

6.4 Thermal Effects of the Skye Central Complex on Reservoir and Source Intervals

Although the main focus of this paper has been the Trotternish/Minch Sill Complex, Skye also contains one of the major onshore exposures of an igneous centre, forming the Cuillins and

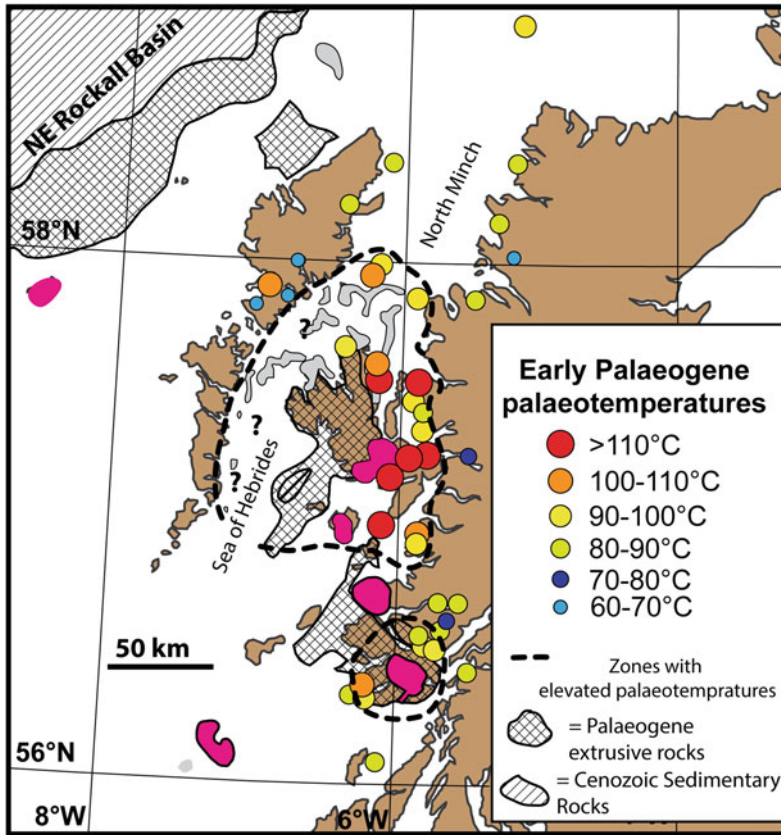


Fig. 14 Modified from Holford et al. 2010, showing map of early Palaeogene paleotemperature. The thermal influence of the Cuillin Centre is clear, with elevated Paleotemperature (90 °C) being apparent, even beyond

what would be expected from a normal contact aureole. Note the thermal effect of the Mull Igneous Centre, which appears to be less areally extensive compared to the Cuillin Centre

Redhills (see Fig. 1) (termed the Cuillin Centre in this study). Offshore, the basins along the Atlantic margin also contain a number of large igneous centres analogous to the Cuillin Centre on Skye (e.g. Rosemary Bank, NE Rockall Trough). These centres have the potential to also significantly influence the thermal history of the basins, and where these are coincident with sill complexes, such as in Skye, the combined thermal influence should be taken into account.

Although the direct contact metamorphic effect of the Cuillin Centre on Skye appears to be limited to a ring of hornfels that can be mapped at its contact (Emeleus and Bell 2005), the thermal impact of the complex is much further reaching. This influence is shown when examining AFTA data from around the complex and the region

(Fig. 14). It is apparent from the AFTA data that the thermal impact of the Cuillin Centre occurs at considerable distances away from the centre (potentially up to 80 km) (Fig. 14), and this effect may also have been enhanced by the emplacement of the sill complex. Initially, Lewis et al. (1992) showed resetting of AFTA ages in a radius of approximately 20 km away from the Cuillin Centre, suggesting that the rocks in these areas had undergone at least some degree of hydrothermal fluid flow. More detailed analysis (Holford et al. 2010) from around the Hebridean region, shows the degree to which heating occurred. In the zone between 5 and 10 km away from the Cuillin centre it can be seen that the rocks have consistently been subjected to temperature of >110 °C during the Palaeogene.

Interestingly, however, even within the North Minch Basin, and on the Scottish mainland at Applecross (some 35 km away), the rocks have seen paleotemperature in the region of 90–100 °C during the Palaeogene (Fig. 14). This suggests that within the Inner Hebridean regions and in at least some areas of the Hebrides, long distance hydrothermal fluid flow may have occurred through sedimentary aquifers which were present during the Palaeogene. The exact impact of this on the source and reservoir rocks is not fully constrained over this much larger area, but clearly the influence of sill complexes and igneous centres on the thermal history need to be taken into account within basin models in volcanic margins containing large igneous centres (e.g. Archer et al. 2005; NE Rockall).

Acknowledgments We would like to thank both Sergio Rocchi and Christoph Breitzkreuz for guidance on the paper and patience. As we believe, during the drilling of the Upper Glen-1 well, a rig worker was killed during a rig-site accident. This paper is dedicated to that individual. This paper is also dedicated to the memories of Ken Thomson and Bill Owens. Both who along with Donny Hutton, did initial work on the peninsula and Owens accompanied Schofield in first trip to Trotternish Peninsula. Chloe Parker is thanked for discussions. Funding from NERC studentship (NER/S/A/2005/13237) held at the University of Birmingham is gratefully acknowledged. DTM data from NEXTmap, via NERC earth observation data centre. Dougal Jerram is supported by the Research Council of Norway through its Centres of Excellence funding scheme, project number 223272 (CEED).

References

- Archer SG, Bergman SC, Iliffe J, Murphy CM, Thornton M (2005) Palaeogene igneous rocks reveal new insights into the geodynamic evolution and petroleum potential of the Rockall Trough, NE Atlantic margin. *Basin Res* 17(1):171–201
- Anderson FW, Dunham KC (1966) *Geology of Northern Skye*. Memoirs of the Geological Survey, Scotland, Sheet 80 and parts of 81, 90 and 91
- Benn DI (1997) Glacier fluctuations in western Scotland. *Quatern Int* 38:137–147
- Bryan SE, Ukstins Peate I, Peate DW, Self S, Jerram DA, Mawby MR, Marsh JS, Miller JA (2010) The largest volcanic eruptions on Earth. *Earthscience Rev.* 102(3):207–229
- Butterworth P, Holba A, Hertig S, Hughes W, Atkinson C (1999) Jurassic non-marine source rocks and oils of the Porcupine Basin and other North Atlantic margin basins. In: Geological Society, London, petroleum geology conference series, vol. 5. Geological Society of London, pp 471–486
- Cartwright J, Hansen DM (2006) Magma transport through the crust via interconnected sill complexes. *Geology* 34:929–932
- Emeleus CH, Bell BR (2005) *British regional geology: the Palaeogene Volcanic Districts of Scotland* 4th ed. British Geological Survey. 214 pp. doi:10.1017/S0016756806213050
- England RW, Butler RWH, Hutton DH (1993) The role of Palaeocene magmatism in the Tertiary evolution of basins on the NW seaboard, In: Parker JR (ed) *Petroleum geology of Northwest Europe: proceedings of the 4th conference*. The Geological Society, London, pp 97–105
- Font L, Davidson JP, Pearson DG, Nowell GM, Jerram DA, Ottley CJ (2008) Sr and Pb isotope micro-analysis of plagioclase crystals from Skye lavas: an insight into open-system processes in a flood basalt province. *J Petrol* 49(8):1449–1471
- Gibson SA, Jones AP (1991) Igneous stratigraphy and internal structure of the Little Minch Sill Complex, Trotternish Peninsula, northern Skye, Scotland. *Geol Mag* 128(1):51–66
- Hautot S, Single RT, Watson J, Harrop N, Jerram DA, Tarits P, Whaler K (2007) 3-D magnetotelluric inversion and model validation with gravity data for the investigation of flood basalts and associated volcanic rifted margins. *Geophys J Int* 170(3):1418–1430
- Holford SP, Green PF, Hillis RR, Underhill JR, Stoker MS, Duddy IR (2010) Multiple post-Caledonian exhumation episodes across NW Scotland revealed by apatite fission-track analysis. *J Geol Soc* 167(4):675–694
- Holford S, Schofield N, MacDonald J, Duddy I, Green P (2012) Seismic analysis of igneous systems in sedimentary basins and their impacts on hydrocarbon prospectivity: examples from the southern Australian margin
- Hutton DHW (2009) Insights into magmatism in volcanic margins: bridge structures and a new mechanism of basic sill emplacement—Theron Mountains, Antarctica. *Petrol Geosci* 15(3):269–278
- Jerram DA, Widdowson M (2005) The anatomy of Continental Flood Basalt Provinces: geological constraints on the processes and products of flood volcanism. *Lithos* 79:385–405
- Jerram DA, Single RT, Hobbs RW, Nelson CE (2009) Understanding the offshore flood basalt sequence using onshore volcanic facies analogues: an example from the Faroe-Shetland basin. *Geol Mag* 146:353–367
- Jerram DA, Svensen HH, Planke S, Polozov AG, Torsvika TH (2015) The onset of flood volcanism in the north-western part of the Siberian traps: explosive volcanism versus effusive lava flows. *Palaeogeogr Palaeoclimatol Palaeoecol*. Available online 30 April 2015. <http://dx.doi.org/10.1016/j.palaeo.2015.04.022> (in press)

- Kerr AC (1993) Current research in the British Tertiary Igneous Province. *J Geol Soc* 150(6):1193–1194. doi:10.1144/gsjgs.150.6.1193
- Lewis CL, Carter A, Hurford AJ (1992) Low-temperature effects of the Skye Tertiary intrusions on Mesozoic sediments in the Sea of Hebrides Basin. *Geol Soc Lond Spec Publ* 62(1):175–188
- Liss D, Hutton DH, Owens WH (2002) Ropy flow structures: a neglected indicator of magma-flow direction in sills and dikes. *Geology* 30(8):715–717
- Magee C, Jackson CL, Schofield N (2014) Diachronous sub-volcanic intrusion along deep-water margins: insights from the Irish Rockall Basin. *Basin Res* 26(1):85–105
- Mahoney JJ, Coffin MF (1997) Large igneous provinces: continental, oceanic, and planetary flood volcanism, vol 100. American Geophysical Union
- Morton N, Hudson JD (1995) Field guide to the Jurassic of the Isles of Raasay and Skye, Inner Hebrides, NW Scotland. *Field Geol Br Jurassic* 209:280
- Muirhead DK (2011) The evolution and preservation of organic matter exposed to heating. Doctoral dissertation, University of Aberdeen
- Nelson CE, Jerram DA, Hobbs RW (2009) Flood basalt facies from borehole data: implications for prospectivity and volcanology in volcanic rifted margins. *Petrol Geosci* 15:313–324
- Nelson CE, Jerram DA, Hobbs RW, Terrington R, Kessler H (2011) Reconstructing flood basalt lava flows in three dimensions using terrestrial laser scanning. *Geosphere* v. 7 no. 1 p. 87–96. doi:10.1130/GES00582.1
- Rateau R, Schofield N, Smith M (2013) The potential role of igneous intrusions on hydrocarbon migration, West of Shetland. *Petrol Geosci* 19(3):259–272
- Rickwood PC (1990) The anatomy of a dyke and the determination of propagation and magma flow directions. In: Parker AJ, Rickwood PC, Tucker DH (eds) *Mafic Dykes and emplacement mechanisms*. Rotterdam, Balkema, pp 81–100
- Roberts AM, Holdsworth RE (1999) Linking onshore and offshore structures: Mesozoic extension in the Scottish Highlands. *J Geol Soc* 156(6):1061–1064
- Röhl HJ (2005) Lower Toarcian (Upper Liassic) black shales of the Central European epicontinental basin: a sequence stratigraphic case study from the SW German Posidonia Shale
- Schofield N (2009) Linking sill morphology to emplacement mechanisms. Ph.D. thesis, University of Birmingham
- Schofield N, Stevenson C, Reston T (2010) Magma fingers and host rock fluidization in the emplacement of sills. *Geology* 38(1):63–66
- Schofield N, Heaton L, Holford S, Archer S, Jackson C, Jolley DW (2012a) Seismic imaging of ‘Broken-Bridges’: linking seismic to outcrop scale investigations of intrusive magma lobes. *J Geol Soc* 169:421–426
- Schofield N, Brown DJ, Magee C, Stevenson C (2012b) Sill morphology and comparison of brittle and non-brittle emplacement mechanisms. *J Geol Soc Lond* 169:127–141. doi:10.1144/0016-76492011-078
- Schofield N, Holford S, Millett J, Brown D, Jolley D, Passey S, Muirhead D, Grove C, Magee C, Murray J, Hole M, Jackson CA-L, Stevenson C (2015) Regional magma plumbing and emplacement mechanisms of the Faroe-Shetland Sill Complex: implications for magma transport and petroleum systems within sedimentary basins. *Basin Res* ISSN:1365-2117
- Single RT, Jerram DA (2004) The 3D facies architecture of flood basalt provinces and their internal heterogeneity: examples from the Palaeogene Skye Lava Field. *J Geol Soc* 161:911–926
- Stein AM, Blundell DJ (1990) Geological inheritance and crustal dynamics of the northwest Scottish Continental Shelf. *Tectonophysics* 173:455–467
- Thomson K (2005) Extrusive and intrusive magmatism in the North Rockall Trough. In: Dore AG, Vining BA (eds) *Petroleum geology: North-West Europe and global perspectives—proceedings of the 6th petroleum geology conference*, 1621–1630. q Petroleum Geology Conferences Ltd. Published by the Geological Society, London
- Thomson K, Hutton D (2004) Geometry and growth of sill complexes: insights using 3D seismic from the North Rockall Trough. *Bull Volc* 66(4):364–375
- Thomson K, Schofield N (2008) Lithological and structural controls on the emplacement and morphology of sills in sedimentary basins, structure and emplacement of high-level magmatic systems. *Geol Soc Lond Spec Publ* 302:31–44
- Thrasher J (1992) Thermal effect of the Tertiary Cuillins intrusive complex in the Jurassic of the Hebrides: an organic geochemical study. *Geol Soc Lond Spec Publ* 62(1):35–49
- Williamson IT, Bell BR (1994) The Palaeocene lava field of west-central Skye, Scotland: Stratigraphy, palaeogeography and structure. *Trans Roy Soc Edinburgh Earth Sci* 85:39–75
- Wright KA, Davies RJ, Jerram DA, Morris J, Fletcher R (2012) Application of seismic and sequence stratigraphic concepts to a lava-fed delta system in the Faroe-Shetland Basin, UK and Faroes. *Basin Res* 24(1):91–106

The Subvolcanic Units of the Late Paleozoic Halle Volcanic Complex, Germany: Geometry, Internal Textures and Emplacement Mode

Christoph Breitkreuz, Bodo-Carlo Ehling,
and Nicole Pastrik

Abstract

The Late Paleozoic Halle Volcanic Complex (HVC) formed in the Saale basin, a NE-SW-trending intermountain depositional system located in the Variscan orogen in Central Europe. Apart from minor lava flows and pyroclastic deposits, the HVC is dominated by a c. 300 km³ rhyolitic laccolith complex. The individual porphyritic rhyolite units display aspect ratios between 0.04 and 0.07. They initially emplaced at different levels of the Saale basin fill. As a consequence, the units are separated by tilted host sediments. Precursory to the emplacement of the rhyolitic laccoliths, a small-volume intermediate sill complex formed at the northern margin of the HVC. This chapter summarizes knowledge on the geometry, composition, internal textures, age, and host rock deformation of the HVC subvolcanic units.

1 Introduction

In central Europe, the aftermath of the Variscan orogeny during the Late Paleozoic was characterized by, among others, the formation of extended subvolcanic complexes (Fig. 1; Von Seckendorff 2012). Outcrops, intensive quarrying and drilling provide, in places, excellent 3d

exposure which has been utilized to improve our understanding for the evolution of large scale dyke, sill and laccolith complexes. Awdankiewicz (2004) reported on silica-rich laccoliths and basic sill complexes that formed in the Intra-Sudetic basin. Lorenz and Haneke (2004) discussed the sill and laccolith systems that developed during the Early Permian in the Saar-Nahe basin in south western Germany. Awdankiewicz et al. (2004) carried out a detailed textural analysis of a 30 km andesitic sill system exposed in the Flechtingen-Roßlau Block (FRB in Fig. 1) emplaced during the Carboniferous-Permian transition above folded Variscan basement and below a thick welded ignimbrite. Extensive dyke swarms developed co-genetically with the Altenberg-Teplice Volcanic Complex during the Late Carboniferous (Winter et al. 2008; Hoffmann et al. 2013, and references therein). A number of sills and dykes

C. Breitkreuz (✉)
TU Bergakademie Freiberg, Freiberg, Germany
e-mail: cbreit@geo.tu-freiberg.de

B.-C. Ehling
State Survey for Geology and Mining
of Sachsen-Anhalt, Halle, Germany

N. Pastrik
Geoforschungszentrum Potsdam, Potsdam, Germany

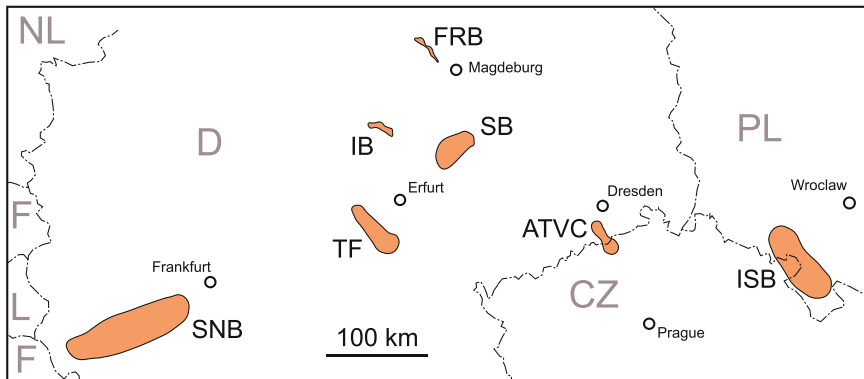


Fig. 1 Sketch map of central Europe depicting the location of Late Paleozoic basins and volcanic complexes which comprise a large portion of subvolcanic units; ATVC Altenberg-Teplice Volcanic Complex, FRB

Flechtingen-Roßlau Block, IB Ilfeld Basin, ISB Intra-Sudetic Basin, SB Saale Basin, including the HVC Halle Volcanic Complex, SNB Saar-Nahe Basin, TF Thuringian Forest

have been reported from the Thuringian Forest (Fig. 1; e.g. Obst et al. 1999).

Breitzkreuz and Mock (2004) employing examples from Late Paleozoic complexes in Germany (i.e., Saar-Nahe basin, Ilfeld basin, and the Halle Volcanic Complex, Fig. 1) proposed a genetic relation between laccolith formation and the activity of trans-tensional basin systems. They suggest that in these intra-montane basins the accumulation of thick sedimentary infill and the vertical orientation of the maximum principal stress (i.e., $\sigma_1 = \sigma_v = \rho g z$) favoured low ascent rates and devolatilisation of magma resulting in their emplacement as subvolcanic complexes. Also, sub-horizontal strength anisotropies in the host rock may arrest the ascent of rising magma (Hogan and Gilbert 1995).

This chapter integrates 20 years of joint research of the authors on the Halle Volcanic Complex (HVC). Our work has benefited from 200 years of research in the area and a long-standing debate about the effusive versus subvolcanic nature of the HVC rhyolitic and intermediate magmatic bodies (see references in Ehling and Breitzkreuz 2006; Breitzkreuz et al. 2009). In the present contribution, a geometric model for the Halle Intermediate Subvolcanic Complex (HISC), precursory to the HVC rhyolitic laccoliths, is presented; however, the HVC rhyolitic laccolith complex comprises the focus of this chapter. The HVC is dominated by a 300 km³ rhyolitic laccolith

complex the units of which were emplaced at different depths within a pile of then unconsolidated sediments¹ (Fig. 2). As such, Breitzkreuz and Mock (2004) defined the HVC rhyolites as a type of laccolith complex (“Halle Type”). As will be shown below, the intrusive nature of the main HVC rhyolites is indicated by the geometry of the units, its textural homogeneity and the deformation of the hosting sediments (Mock et al. 2003, 2005; Schmiedel et al. online).

2 The Tectonic and Stratigraphic Framework of the Halle Volcanic Complex (HVC)

The HVC formed in the north eastern part of the Late Paleozoic Saale Basin (Fig. 1). The NE-SW trending basin developed as an intra-montane system under dextral trans-tension in the Saxothuringian Block during the decay of the Variscan orogen (Ehling and Gebhardt 2012). Subsidence and sedimentation started in the Moscovian

¹ The HVC comprises subvolcanic bodies and a minor amount of lava and pyroclastic deposits. The rhyolitic subvolcanic units have non-plutonic textures. Therefore we maintain the term “rhyolite” for the laccolith bodies and we use the notion “Halle Volcanic Complex”, both terms have been established in regional literature over the last 200 years.

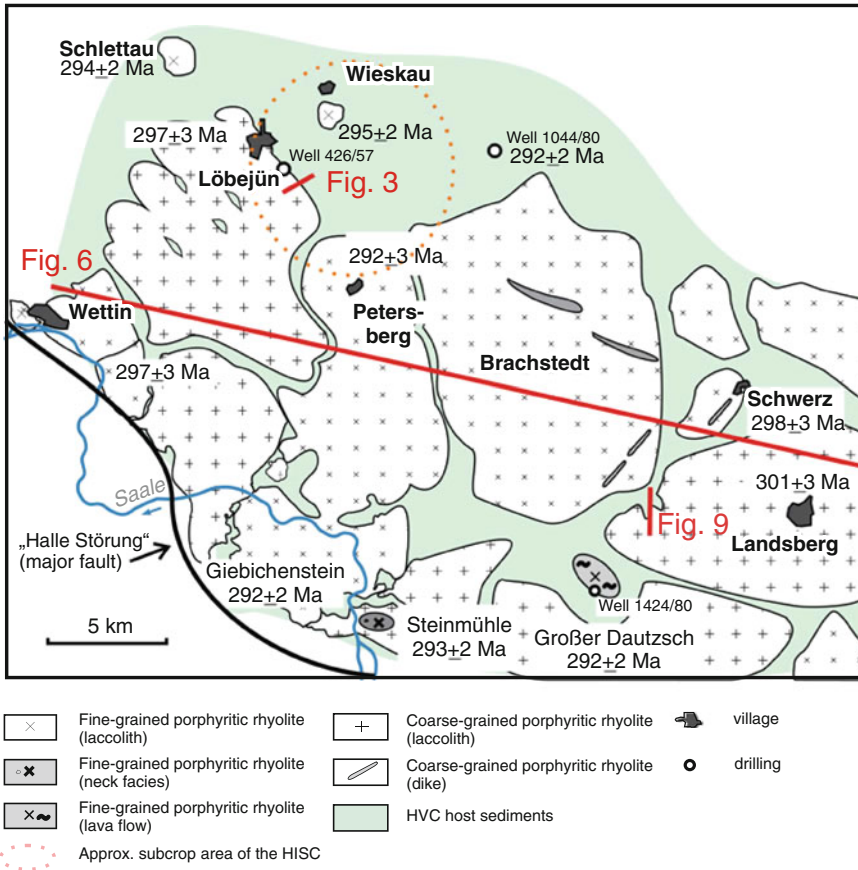


Fig. 2 Outcrop/subcrop map of the Halle Volcanic Complex (HVC) in the north eastern Saale Basin (Fig. 1), post-HVC cover not depicted; the age data have been taken from Breitzkreuz et al. (2009)

(Westfalian) and continued into the Permian. Part of the basin fill consists of alluvial to fluvial conglomeratic to sandy red beds, the Siebigerode Formation (lower Gzhelian), which is replaced in the basin centre by grey coal-bearing clastics of the Wettin Member (≤ 350 m thickness; Ehling and Breitzkreuz 2006; Breitzkreuz et al. 2009). In some drill cores, the Wettin Member contains silica-rich volcanic fragments and subvolcanic intrusions demonstrating initial volcanic activity. Thus, the Saale Basin was affected relatively late by magmatism in its evolution.

The Halle Formation (Gzhelian-Asselian) overlies, locally unconformably, the Wettin Member. The >700 m thick Halle Fm. comprises reddish to green alluvial, fluvial to lacustrine (volcani-) clastic deposits (Ehling and Gebhardt 2012). It starts with a characteristic fluvial

quartzite-chert sandstone-conglomerate complex ("Kieselschiefer-Quarzit-Konglomerat", KQK, Kampe et al. 1965) which contains up to 20 % of carbonate pebbles (stromatolith fragments, ooids, onkoids, and pedogenic nodules; Ehling and Gebhardt 2012). Field relations and radiometric dating (Breitzkreuz et al. 2009) indicate that the subvolcanic intrusions and volcanic eruptions of the HVC took place for some 9 Ma (292–301 Ma; Breitzkreuz et al. 2009) contemporaneously to the deposition of the Halle Formation.

Only about 20 % of the HVC is exposed in natural outcrops or quarries (Mock et al. 2005). The area is relatively flat with a total relief less than 140 m. It was levelled by Pleistocene glaciers and the HVC rocks are partly covered by Cenozoic sediments. The 3d geometry of the HVC is constrained by data from more than

6,000 wells; most of which are shallow wells for foundation ground investigation and raw material exploration. Nevertheless, several hundreds of wells (coal and uranium exploration, and scientific investigation) have perforated the HVC to a depth of a couple of hundred metres (one well reached 1,100 m depth; Breitzkreuz et al. 2009). A fraction of the recovered drill core is preserved in the core depository of the Sachsen-Anhalt Survey for Geology and Mining in Halle; documentation exists for every well.

3 The Magmatic Units of the HVC

Figure 2 depicts the outcrops and subcrops of the HVC. In the south west, the HVC is truncated along the “Halle Störung” (Knoth et al. 1998), a major fault which apparently confined the HVC already during its activity. This is suggested by drillings located some 10 km south west of the fault, such as well Querfurt 1/64 which does not cross HVC rhyolitic bodies (Hoth et al. 1993; Gebhardt and Lütznier 2012). Whether this fault acted as a feeding system for HVC laccoliths, as e.g. Grocott et al. (2009) documented for plutons in northern Chile, is not known.

The HVC is dominated by rhyolitic laccoliths (Mock et al. 2005). Apart from these, the following other volcanic and subvolcanic rock types are known:

- Lava complexes developed late in the evolution of the HVC; e.g., a c. 100 m thick porphyritic lava flow with a basal and top breccia has been documented by Geißler (2001) in drilling 1044/80 (Fig. 2) and it has been dated with SHRIMP U/Pb on zircon at 292 ± 2 Ma (Breitzkreuz et al. 2009); another, aphanitic lava is exposed in well 1424/80 (Fig. 2).
- Ignimbrites and other pyroclastic deposits such as fallout and flow deposits, some associated with vulcanian eruptions, are present within the Halle Fm. (Breitzkreuz et al. 2009).
- Within the city of Halle, a number of permanent and temporary outcrops exposed products of explosive volcanic centres such as the Steinhöfen Vent Complex with diatreme

breccias and pyroclastic dykes (Fig. 2, 293 ± 3 Ma; Ehling and Bachmann 2006; Breitzkreuz et al. 2009).

- The Halle Intermediate Sill Complex (HISC), scarcely outcropping, but intensively drilled, has been discovered at the northern margin of the HVC (Fig. 2; Kampe et al. 1965; Schulz 2010). Furthermore, a number of other drillings detected intermediate sills and dykes in the eastern HVC (Breitzkreuz et al. 2009).

The HISC rocks are of trachybasaltic to trachydacitic composition, and contain petrographic features that are interpreted to indicate magma mixing (Siegert 1967a; Romer et al. 2001). In contrast, the HVC rhyolites have a very homogenous, calc-alkaline, mildly peraluminous low-SiO₂ composition (71.2–72.2 wt% SiO₂, A/CNK = 1.04 – 1.21; Romer et al. 2001). Major and trace element whole rock composition, and Nd-, Pb-, Sr-isotope ratios in alkali feldspar phenocrysts indicate the source for HVC magma was an enriched mantle mixed with a large crustal component. The trace element and isotope systematics indicate that the HVC rocks were affected by hydrothermal alteration (Romer et al. 2001), presumably during the early Mesozoic (Brecht 1999; Jacobs and Breitzkreuz 2003).

4 The Halle Intermediate Subvolcanic Complex (HISC)

The HISC located in the north of the HVC (Fig. 2) has been interpreted as a lava complex by Kampe et al. (1965) and subdivided into four units which allegedly evolved over a long time during the deposition of the Wettin Member and Halle Formation (Siegert 1967a, b). Subcrop relations indicate that the HISC is a precursor of the HVC rhyolitic laccoliths (Fig. 3). Using data from 1,200 wells in a 58 km² area at the northern margin of the HVC (Fig. 2), we constrained the 3d geometry of the 3rd and 4th series of HISC (Schulz 2010²). The geological objects were

² Unpublished diploma thesis by Nicole Schulz, co-author of the present contribution (N. Pastrik)

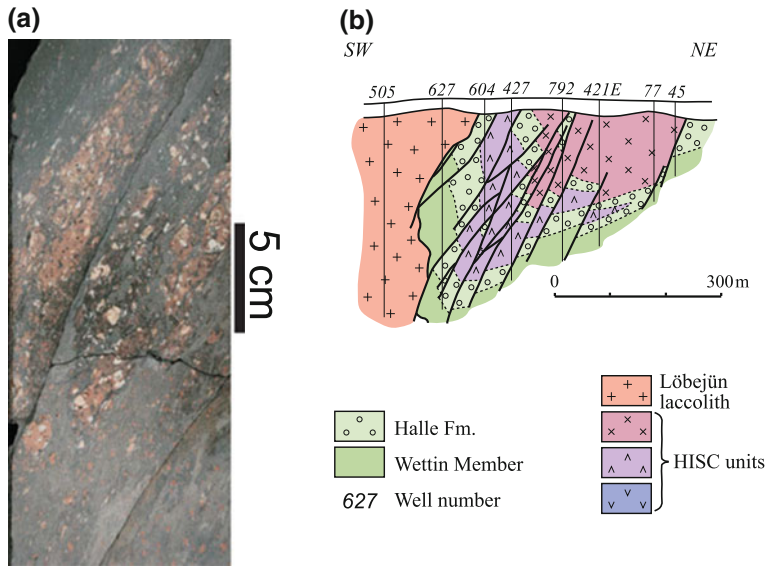


Fig. 3 The NE margin of the Løbejün laccolith unit: **a** In the contact zone of the intrusive-extrusive complex peperitisation and intense shearing took place; the *photo* shows aligned fragments of porphyritic rhyolite in highly

deformed host sediments (drill core 426/57, for location see Fig. 2); **b** SW-NE profile through the margin of the rhyolite and its deformed and overturned host sediments and HISC units (after Kampe et al. 1965; for location see Fig. 2)

modeled and interpreted by the 3d-software GOCAD which is based on Discrete Smooth Interpolation (DSI) and uses nodes and control points to define heterogeneous data. GOCAD incorporates other numeric properties, not only the geometry like other 3d-modeling software (Mallet 2002). The Delauney-triangulation (min-max-criterion) is used for minimizing the roughness of the interpolation surface by the optimization of the triangulated mesh.

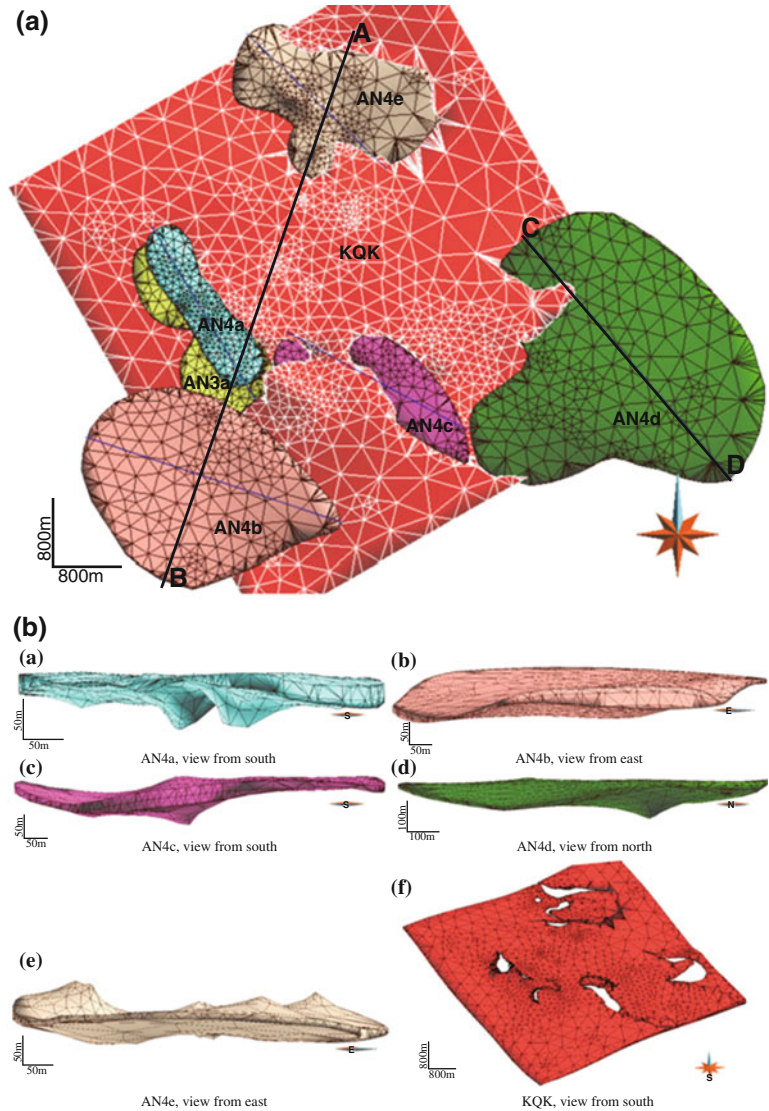
A number of HISC bodies cross cut the KQK at the base of the Halle Fm.; an observation that resulted in a reinterpretation of the HISC as a subvolcanic system of saucer-shaped sills (Fig. 4). Figures 4b, c illustrate that the HISC units, up to 290 m thick and up to 3.6 km long with aspect ratios between 0.08 and 0.14, were emplaced into the Wettin Member and the Halle Formation on both sides of a NW-SE trending horst structure marked by the KQK (Fig. 4c). Complex interactions between tectonic, volcanic activities and sedimentation affected magma rising, sill emplacement and subsequently displacements. Some units appear to be stacked one upon the other (e.g. HISC units AN 3a and 4a;

Fig. 4c), possibly fed by common conduits. The andesites are mainly fed by single-feeder systems (e.g. HISC unit AN 4c, Fig. 4b) but also multi-feeder dykes are identifiable (e.g. HISC unit AN 4a, Fig. 4b). The model reveals geometric relationships of the HISC with the KQK which suggests that the then unconsolidated conglomeratic horizon facilitated initial sill emplacement (Fig. 4a, c). Furthermore, from the modelled cross-sections (e.g. Fig. 4c) we infer that the KQK was displaced into today's horst structure before the HISC melts took place (Schulz 2010).

5 Geometry of the HVC Rhyolitic Laccoliths

The HVC is dominated by ca. 300 km³ of rhyolitic laccoliths (Mock et al. 2005). This is a minimum estimation, as it includes known units and does not consider parts of laccoliths removed by erosion. The larger rhyolitic HVC units are (i) the coarsely porphyritic laccoliths, such as Løbejün-, Giebichenstein-, Großer Dautzsch- and Landsberg units, and (ii) the finely porphyritic

Fig. 4 The Halle Intermediate Sill Complex (HISC) in the northern part of the HVC (see Fig. 2 for location); **a** birds eye's view of the 3d HISC model (GOCAD) showing the top plane of the KQK (red; see text) and subvolcanic units AN 3a and 4a–e, AN 3b covered by KQK; **b** lateral geometry of five HISC bodies and the KQK viewed from different directions; the white areas in the KQK plane mark locations where the HISC units pierced the KQK; **c** profiles A–B and C–D (see Fig. 4a for location) generated from the 3d model emphasizing the cross cutting relation of the HISC bodies with respect to the horst structured KQK (=base of the Halle Fm.), showing the nested units AN 3a and AN 4a, the conical feeding structure of AN 4d and the implications of the Löbejün fault for the sill emplacement on the western margin of KQK (from Schulz 2010), note the vertical exaggerations



units like Wettin, Petersberg, Brachstedt and Schwerz (Figs. 2 and 5; Breitzkreuz et al. 2009). The most intriguing aspect of the HVC are the domains of deformed host sediments (Siebigrode Formation, Wettin Member and Halle Formation) separating the laccolithic units (Figs. 2 and 6). Integration of field observations, drill hole data, and modelling of the magnetic field intensity (Fig. 7; Lange 2000) were used to constrain the distribution of the intervening sediments and the thickness of the HVC laccolith units (see also Schmiedel et al. online).

The Wettin laccolith unit has been eroded down to about 50 m (Mock et al. 1999; Exner and Schwab 2000). The Petersberg unit measures about 380 m (Mock et al. 2003), and the Brachstedt laccolith about 500 m. For the other units such as Löbejün and Landsberg only minimum thickness estimates (>600 m) can be given as the floor of these laccoliths has never been penetrated by drilling (Breitzkreuz et al. 2009). Schmiedel et al. (online) calculated aspect ratios between 0.04 and 0.07 for the HVC rhyolitic laccoliths.

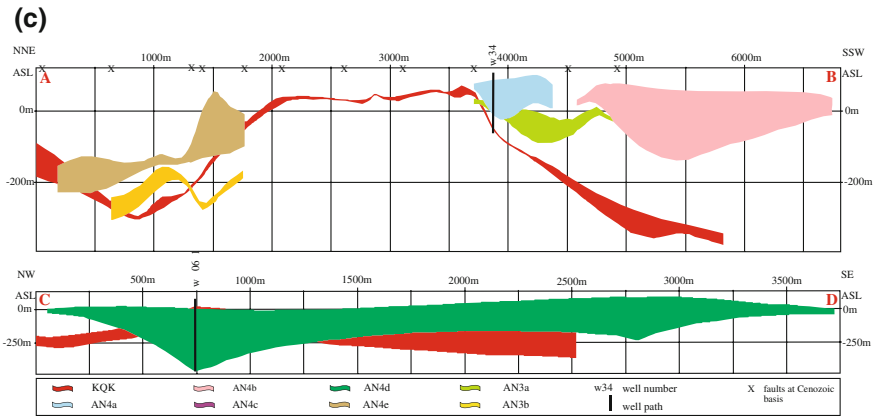
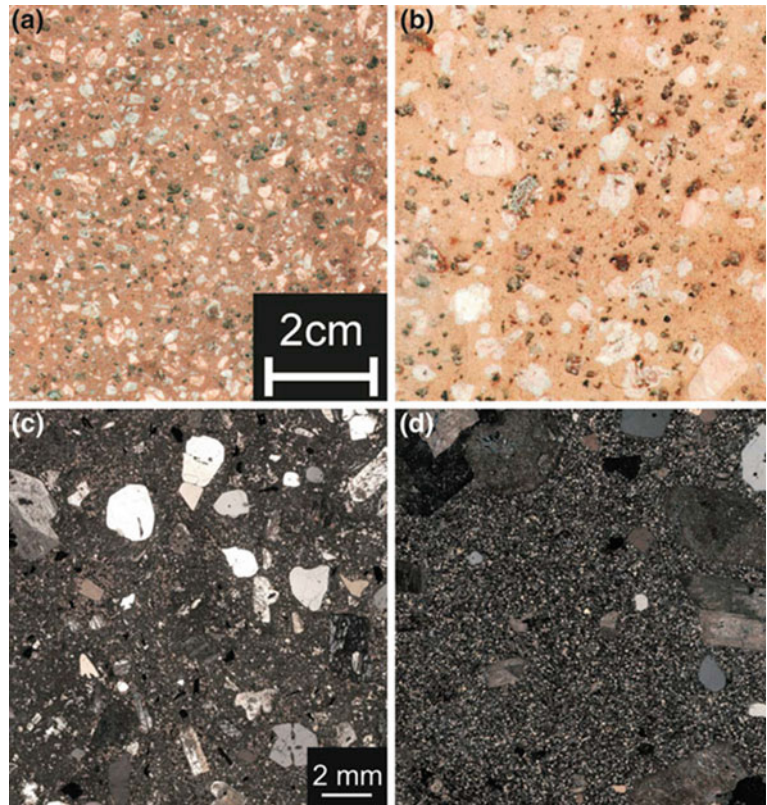


Fig. 4 (continued)

Fig. 5 Photographs of polished rock slabs and thin sections of HVC rhyolites; **a** finely porphyritic Petersberg unit; **b** coarsely porphyritic Löbejün unit; **c** Petersberg unit, x nicols; **d** Löbejün unit, x nicols



The Löbejün and the Landsberg units display features indicative of intrusive-extrusive complexes. Intrusive-extrusive complexes receive high volumes of viscous magma sufficient to lift up the overburden and pierce the sedimentary cover (Stark 1912; Lorenz and Haneke 2004).

Coal exploration drilling at the north eastern margin of the Löbejün complex revealed vertical to overturned contact zones of the coarsely porphyritic magmatic body with the host succession (Fig. 3; Kampe et al. 1965; Mock et al. 2005). Piercing is also inferred from the fact that

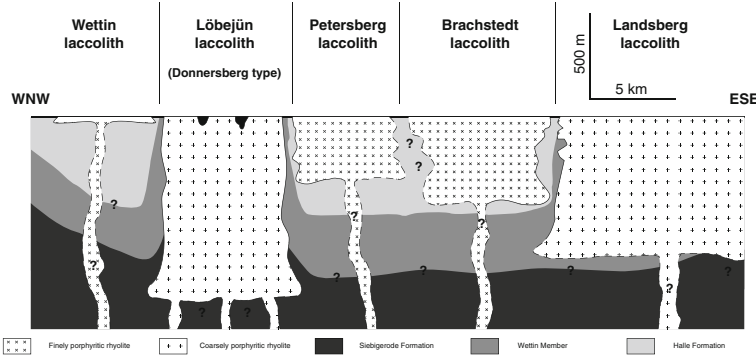


Fig. 6 Schematic WNW-ESE profile through the major HVC laccolith units; topography and post-emplacment tectonic displacement not depicted; for location see

Fig. 2; note strong vertical exaggeration (Schmiedel et al. online)

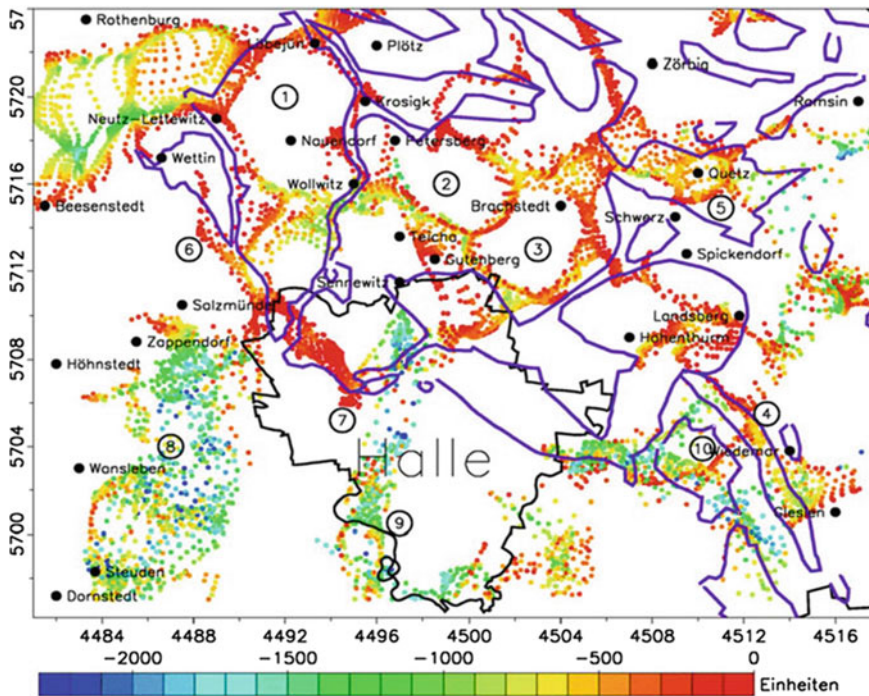


Fig. 7 Euler de-convolution of the pole-reduced magnetic field of the HVC area (from Lange 2000); the coloured dots display only a relative depth trend; the violet lines mark the geological HVC borders according

to Knoth et al. (1998); The model indicates the position of the host sediments separating HVC laccolith units (compare to Fig. 2)

different units of the overburden (Siebigerode Formation, Wettin Member, Halle Formation, and intercalated HISC units) are in direct contact with the magmatic body, in places displaying intensive shearing and peperites (Fig. 3). Finally,

four isolated pockets of Siebigerode Fm. have been detected by drilling in the top region of the Löbejün subvolcanic body (Figs. 2 and 6). These pockets are interpreted as remnants of the upper host sediments of the initial sill intrusion. Similar

pockets of host sediments have been mapped in the summit area of the Late Paleozoic Donnersberg intrusive-extrusive complex in the Saar-Nahe basin in western Germany (Fig. 1; Lorenz and Haneke 2004). Therefore we infer that the Löbejün intrusive-extrusive complex represents a Donnersberg-type laccolith (Breitkreuz and Mock 2004), where several rhyolitic units were initially emplaced at a common level in the Siebigerode Fm.

For the Landsberg unit, evidence of an extrusive late phase comes from the presence of monomict mass flow deposits exposed in the Halle Fm. in the lower part of drilling WISBAW 1424/80 (Fig. 2). These sedimentary breccias comprise exclusively clasts of Landsberg porphyritic rhyolite, and are interpreted as gravitational mass flow deposits originating from the upper extrusive part of the Landsberg laccolith.

6 Internal Textures of the HVC Laccoliths

The HVC rhyolitic laccoliths are highly porphyritic with phenocrysts of alkali feldspar, plagioclase, and quartz (and minor amounts of biotite) in a finely crystalline groundmass (65 to 90 %, Figs. 5 and 8; Mock et al. 2005). Except for some domains of black rhyolites in the Schwerz laccolith unit (Fig. 2) which contains magnetite in the groundmass (Krauß 2003), the

rhyolites are typically reddish to pink in color due to fine-grained hematite in the groundmass and in the alkali feldspar phenocrysts. The most noticeable difference between the coarse and fine-grained HVC units is the size of alkali feldspar that ranges from less than 10 to almost 40 mm (Figs. 5 and 8). Crystal size distribution analysis (CSD) suggests that the size of felsic phenocrysts in HVC rhyolites did not change significantly after emplacement (Mock et al. 2003, 2005). Instead, it must have been attained during magma ascent and temporal storage in magma chambers below the Saale basin at mid-crustal level (Breitkreuz and Mock 2004).

A major difference between subvolcanic rhyolites (sills and laccoliths) and subaerial lava is the dominance of carapace facies over core facies, the latter being characterized by brecciation, vesiculation, and the formation of spherulites and lithophysae (Manley and Fink 1987; Paulick and Breitkreuz 2005; Breitkreuz 2013). With the HVC subvolcanic rhyolites, the carapace facies is restricted to dm-wide marginal domains with spherulitic and perlitic groundmass and sheared phenocrysts (Mock et al. 2005; Schmiedel et al. online). Drilling Brachwitz 2/62 revealed larger brecciated domains at the south western margin of the Wettin laccolith unit (Fig. 8 in Mock et al. 2005). The rest of the HVC laccolith units display core facies with a homogenous finely crystalline groundmass (Fig. 5c, d).

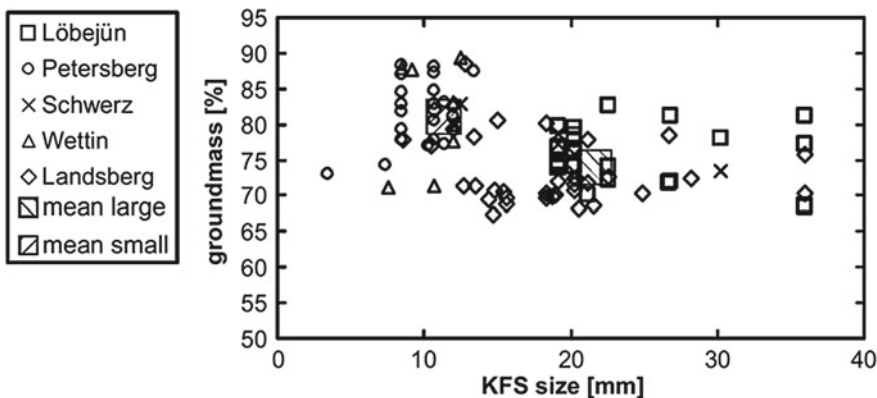


Fig. 8 Maximum particle size (MPS) of alkali feldspar phenocrysts versus area % of groundmass of HVC rhyolites (Mock et al. 2005)

Only the finely porphyritic units show flow foliation and scarce irregular-shaped vesicles (Mock et al. 2005). Mock et al. (1999) reported brecciation planes associated with the flow foliation from the Wettin laccolith unit. Flow foliation is marked by a variation in phenocryst concentration and size, the presence of brecciated lenses, and scarce vesicles aligned along flow planes. Distance between foliation planes is 20–40 cm. In the Wettin laccolith unit, the flow foliation resembles a bowl-shaped architecture, with the planes dipping towards the centre of the laccolith body with dip angles between 8°–80° (Mock et al. 2005). The bowl-shaped flow geometry is consistent with the assumption of advanced erosion removing the upper portions of the Wettin laccolith such that only the lower third remains. In contrast, the flow foliation architecture in the Petersberg laccolith unit resembles a complex cupola shape with dip angles of 18°–83° away from the centre of the magmatic body. This and the occurrence of carapace facies in the summit area of the Petersberg hill suggest that the today's erosional level exposes the upper third of that unit (Mock et al. 1999, 2005).

7 Emplacement of HVC Laccoliths: Textures and Models

Different models have been proposed for the horizontal and vertical growth of silica-rich subvolcanic systems. Inflation by periodic or continuous magma intrusions into the central part of the growing laccolith is the traditional model (“ballooning”; e.g., Schwab 1959; Corry 1988; Lorenz and Haneke 2004). Successive emplacement of magma sheets at the top of the growing subvolcanic body is the other, more current concept (Horsman et al. 2009). As will be discussed below, in the HVC laccolith complex we find indications for both models.

With some local exceptions, such as the Wettin (Mock et al. 1999) and the Schwerz laccolith complex (Krauß 2003), outcrops and drill cores of the HVC typically do not show prominent liquid-solid contacts within a given laccolith

unit. From this, a batch-wise or continuous laccolith growth can be inferred, where the following magma batch was emplaced before the previous batch solidified (Horsman et al. 2009).

In R-value versus matrix % plots, the spatial distribution patterns (SDP) can be differentiated for ordered versus clustered distribution of phenocrysts (Jerram et al. 1996). This plot also allows for a distinction between touching and non-touching phenocryst frameworks. Mock et al. (2003) explored the SDP for six samples from a 300 m well through the Petersberg laccolith, revealing a non-touching framework (see also Mock and Jerram 2005) and a clustering to ordered distribution of felsic phenocrysts. R-value versus sample depth (from drill cores) plots have been applied for the Petersberg-, Löbejün- and Landsberg laccolith units to estimate the thickness of emplacing sheets in the growing laccolith (Mock et al. 2005). The data suggest sheet thickness in the order of 100 and up to 200 m.

In some areas of HVC, well spacing density allows for a more detailed geometric modelling of the laccolith margins. “Fingering” of rhyolite melt (Hutton 2009) into the sedimentary host has been documented for the Wettin laccolith unit (Fig. 8 in Mock et al. 2005), and for the western margin of the Petersberg laccolith unit (Schmiedel et al. online). Drill core data, from a dense cluster of uranium exploration wells, allowed the spectacularly complex margin of the Landsberg laccolith unit to be constrained by GOCAD geometric modelling (Schmiedel et al. online). Based on these results, the Landsberg laccolith is interpreted to have formed from melt sheets 100–300 m thickness. At its north western margin, the melt batches tilted, engulfed, and deformed rafts, up to 1,400 m in diameter, of the host Wettin Member and Halle Formation, (Fig. 9). A few xenoliths of sedimentary and crystalline rocks up to several meters in diameter have also been described from other HVC laccoliths (Koch 1981; Mock et al. 2005).

Similar deformed sedimentary domains surrounded by subvolcanic sheets, however on much smaller scale, have been described from the margin of the Trachyte Mesa laccolith in the Henry Mountains, Utah (Morgan et al. 2008;

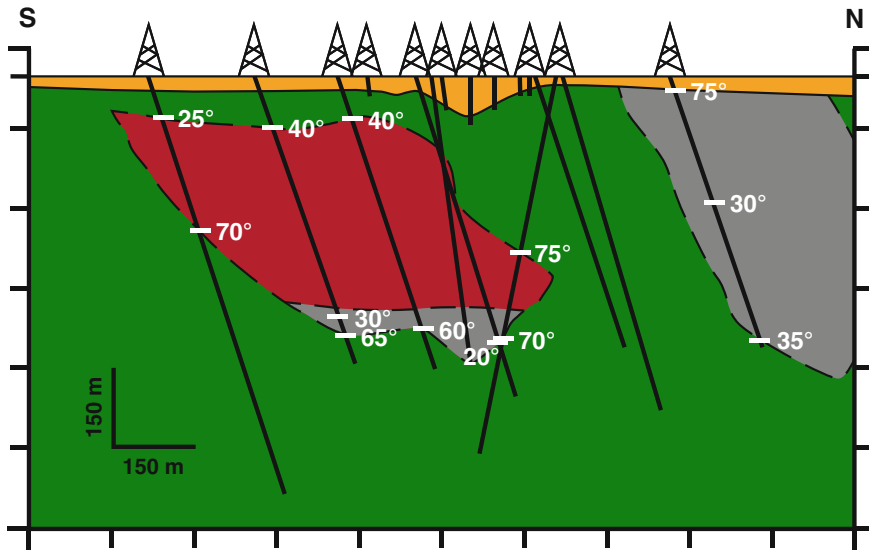


Fig. 9 GOCAD modelled cross section through the Landsberg margin (for location of profile see Fig. 2); green Landsberg laccolith, grey Wettin Member, red

Halle Formation, yellow Cenozoic cover, dip angles bedding relative to drill axis; (Schmiedel et al. under review)

Horsman et al. 2009). Textural and AMS analysis in the Trachyte Mesa, Maiden Creek and Black Mesa intrusions in the Henry Mountains of Utah (USA) revealed that a series of sub-horizontally stacked dacitic magma sheets were emplaced at 3–4 km depth into consolidated sediments resulting in horizontal and vertical growth of the subvolcanic bodies (Horsman et al. 2005, 2009; Morgan et al. 2008). Individual sheets measure between 1 and 20 m thick. We speculate that the greater thickness of HVC sheets is probably related to a higher viscosity of the porphyritic rhyolites and to a shallower depth of intrusion (<1,000 m).

Estimating an original thickness of about 1,000 m for the Löbejün and Landsberg laccolith units may have formed by emplacement of 5–6 successive batches of magma. Assuming a cooling time of about 300 years per batch— inferred from calculations carried out by Mock et al. (2005)—emplacement of the c. 65 km³ Löbejün and Landsberg units would have lasted less than 2,000 years. This corresponds to magma ascent rates of 0.01–0.1 km³ a⁻¹, which are typical values for magmatic bodies of this size (de Saint-Blanquat et al. 2011).

In summary, HVC evolution lasted about 9 Ma (Breitkreuz et al. 2009), punctuated by the short-lived formation (<2,000 years each) of coarsely and finely porphyritic laccoliths some of which grew up to 65 km³ (Löbejün and Landsberg units). Explosive and effusive volcanic eruptions occurred late in the HVC evolution. As emphasized by Romer et al. (2001), throughout the HVC evolution the rhyolitic rocks are of remarkably homogenous composition, implying the longstanding existence of a large mid-crustal magma chamber which had been tapped repeatedly during active phases of HVC construction (Breitkreuz and Mock 2004). In this *Halle-type* laccolith complex, highly porphyritic units emplaced initially at deeper levels of the Saale basin fill, compared to less porphyritic units such as Wettin, Petersberg- and Brachstedt. During ascent and emplacement, the highly porphyritic Löbejün and Landsberg melts presumably were characterized by density 17–20 kg/m³ higher than the finely and less porphyritic melts (Mock et al. 2005). High density together with high viscosity, the latter inferred from the high phenocryst content and thus higher supercooling, presumably led to a deeper level of initial

emplacement, and to a stronger vertical inflation of the Landsberg and Löbejün units (Mock and Bretkreuz 2006).

Acknowledgments This contribution is in parts based on a number of unpublished diploma theses, among these the excellent theses of Marion Geißler, Dietrich Lange and Alexander Mock, carried out under the supervision by two of us (C.B. and B.-C.E.). In this context, we highly acknowledge co-supervision of diploma thesis by Peggy Melzer and Hajo Götzte. We highly appreciate permission for access and sampling of wells of the WISMUT GmbH and the Bundesanstalt für Geologie und Rohstoffe (BGR) in Berlin-Spandau. Thoughtful reviews by John Hogan and Sergio Rocchi were very helpful to improve the text.

References

- Awdankiewicz M (2004) Sedimentation, volcanism and subvolcanic intrusions in a late Palaeozoic intramontane trough (The Intra-Sudetic Basin, SW Poland). *Geol Soc Lond Spec Publ* 234:5–11
- Awdankiewicz M, Bretkreuz C, Ehling B-C (2004) Emplacement textures in Late Palaeozoic andesite sills of the Flechtingen-Roßlau Block, north of Magdeburg (Germany). *Geol Soc Spec Publ* 234:5–12
- Brecht G (1999) Authigene Phyllosilikate in permokarbonen SiO₂-reichen Vulkaniten Ostdeutschlands. *Berl Geowiss Abhandl* A201:1–181
- Bretkreuz C (2013) Spherulites and lithophysae—200 years of investigation on high-temperature crystallization domains in silica-rich volcanic rocks. *Bull Volcanol* 75:1–16
- Bretkreuz C, Mock A (2004) Are laccolith complexes characteristic of transensional basin systems?—Examples from Permocarboniferous Central Europe. *Geol Soc Spec Publ* 234:13–32
- Bretkreuz C, Ehling B-C, Sergeev S (2009) Chronological evolution of an intrusive/extrusive system: the Late Paleozoic Halle Volcanic Complex in the north-eastern Saale Basin (Germany). *Zeitschr dt Gesell Geowiss* 160:173–190
- Corry CE (1988) Laccoliths; mechanics of emplacement and growth. *Spec Pap Geol Soc Am* 220:1–110
- de Saint Blanquat M, Horsman E, Habert G, Morgan S, Vanderhaeghe O, Law R, Tikoff B (2011) Multiscale magmatic cyclicality, duration of pluton construction, and the paradoxical relationship between tectonism and plutonism in continental arcs. *Tectonophysics* 500:20–33
- Ehling B-C, Bachmann G (2006) Geologie von Halle (Saale) (Exkursion A am 18. April 2006). *Jber Mitt oberrhein geol Ver N F* 88:121–144
- Ehling B-C, Bretkreuz C (2006) Das klassische Rotliegend bei Halle (Saale): Sedimentation und Vulkanismus im neuen Licht (Exkursion K am 21. April 2006). *Jber Mitt oberrhein geol Ver N F* 88:369–404
- Ehling B-C, Gebhardt U (2012) Rotliegend im Saale-Becken. *Schriftenr Deutsch Gesell Geowiss H* 61:504–516
- Exner M, Schwab M (2000) Der Wettin-Rhyolith - Beitrag zur Oberflächenverbreitung und Entstehung eines Halleschen Quarzporphyrs. *Hercynia* 33:173–190
- Gebhardt U, Lütznert H (2012) Innervariscische Rotliegendebcken und Norddeutsches Becken - Fragen ihrer stratigraphischen Verknüpfung. *Schriftenr Deutsch Ges Geowiss H* 61:715–730
- Geißler M (2001) Korrelation und Faziesanalyse der oberkarbonen Sedimente und Vulkanite im nördlichen Bereich des Halle Vulkanit-Komplexes unter besonderer Berücksichtigung der Bohrung Wis BAW 1044/81. Unpublished diploma thesis, TU Bergakademie Freiberg
- Grocott J, Arévalo C, Welkner D, Cruden A (2009) Fault-assisted vertical pluton growth: coastal Cordillera, north Chilean Andes. *J Geol Soc Lond* 166:295–301
- Hoffmann U, Bretkreuz C, Breiter K, Sergeev S, Stanek K, Tichomirowa M (2013) Carboniferous-Permian volcanic evolution in Central Europe—U/Pb-ages of volcanic rocks in Saxony (Germany) and northern Bohemia (Czech Republic). *Int J Earth Sci* 102:73–99
- Hogan JP, Gilbert MC (1995) The A-type Mount Scott Granite Sheet: importance of crustal magma traps. *J Geophys Res* 100:15779–15793
- Horsman E, Tikoff B, Morgan S (2005) Emplacement-related fabric and multiple sheets in the Maiden Creek Sill, Henry Mountains, Utah, USA. *J Struct Geol* 27:1426–1444
- Horsman E, Morgan S, de Saint Blanquat M, Habert G, Nugent A, Hunter RA, Tikoff B (2009) Emplacement and assembly of shallow intrusions from multiple magma pulses, Henry Mountains, Utah. *Earth Environ Sci Trans Royal Soc Edinb* 100:117–132
- Hoth K, Rusbült J, Zagora K, Beer H, Hartmann O (1993) Die tiefen Bohrungen im Zentralabschnitt der Mitteleuropäischen Senke - Dokumentation für den Zeitabschnitt 1962-1990. *Schriftenr Geowiss* 2:7–145
- Hutton DHW (2009) Insights into magmatism in volcanic margins: bridge structures and new mechanism of basic sill emplacement—Theron Mountains, Antarctica. *Geol Soc Lond Petrol Geosci* 15:269–278
- Jacobs J, Bretkreuz C (2003) Zircon and apatite fission-track thermochronology of Late Carboniferous volcanic rocks of the NE German Basin. *Int J Earth Sci* 92:165–172
- Jerram DA, Cheadle MJ, Hunter RH, Elliott MT (1996) The spatial distribution of grains and crystals in rocks. *Contrib Mineral Petrol* 125:60–74
- Kampe A, Luge J, Schwab M (1965) Die Lagerungsverhältnisse in der nördlichen Umrandung des Löbejüner Porphyrs bei Halle (Saale). *Geologie* 14:26–46
- Knoth W, Kriebel U, Radzinski K-H, Thomae M (1998) Die geologischen Verhältnisse von Halle und Umgebung. *Hall Jb Geowiss Beiheft* 4:7–34
- Koch RA (1981) Die Großxenolithe im großkristallinen Quarzporphyr des Galgenberges von Halle (Saale). *Hall Jb Geowiss* 6:105–106

- Krauß G (2003) Der Schwerzer Rhyolith-Komplex: Ein Beitrag zur Verbreitung und Struktur einer der ältesten Einheiten des Halleschen Vulkanitkomplexes. *Hercynia* 36:129–150
- Lange D (2000) Geophysikalisch-geologische Untersuchung und dreidimensionale Modellierung des Halleschen Porphyrykomplexes. Unpublished diploma thesis, Free University Berlin
- Lorenz V, Haneke J (2004) Relationship between diatremes, dykes, sills, laccoliths, intrusive-extrusive domes, lava flows, and tephra deposits with unconsolidated water-saturated sediments in the late Variscan intermontane Saar-Nahe Basin, SW Germany. *Geol Soc London Spec Publ* 234:75–124
- Mallet J-L (2002) Geomodeling. Applied geostatistic series. Oxford University Press, New York, 599S
- Manley CR, Fink JH (1987) Internal textures of rhyolite flows as revealed by research drilling. *Geology* 15:549–552
- Mock A, Breitzkreuz C (2006) Parameters controlling emplacement of shallow-level silicic intrusions—an exploratory study in a Late Paleozoic laccolith complex. *Visual Geosci* 11:47–48
- Mock A, Jerram DA (2005) Crystal size distributions (CSD) in three dimensions: Insights from the 3D reconstruction of a highly porphyritic rhyolite. *J Petrol* 46:1525–1541
- Mock A, Lange D, Exner M, Breitzkreuz C, Schwab M, Ehling B-C (1999) Räumliche Erfassung des Fließgefüges der kleinporphyrischen Lakkolithe im Halle-Vulkanit-Komplex. *Geol Mitt Sachsen-Anhalt* 5:169–175
- Mock A, Jerram DA, Breitzkreuz C (2003) Using quantitative textural analysis to reveal emplacement mechanisms of shallow level rhyolitic laccoliths. *J Petrol* 44:833–849
- Mock A, Ehling B-C, Breitzkreuz C (2005) Anatomy of a laccolith complex—Geometry and texture of porphyritic rhyolites in the Permocarboneous Halle Volcanic Complex (Germany). *Neues Jb Geol Paläontol Abh* 237:211–271
- Morgan SS, Stanik A, Horsman E, Tikoff B, de Saint-Blanquat M, Habert G (2008) Emplacement of multiple magma sheets and wallrock deformation: Trachyte Mesa intrusion, Henry Mountains, Utah. *J Struct Geol* 30:491–512
- Obst K, Katzung G, Hammer J (1999) Dating of the Late Autunian basic magmatism in the Thuringian Forest. *Neues Jb Geol Palaeont Monat* 1999:1–10
- Paulick H, Breitzkreuz C (2005) The Late Paleozoic felsic lava-dominated large igneous province in North East Germany: volcanic facies analysis based on drill cores. *Int J Earth Sci* 94:834–850
- Romer R, Förster H-J, Breitzkreuz C (2001) Intracontinental extensional magmatism with a subduction fingerprint: the late Carboniferous Halle Volcanic Complex (Germany). *Contrib Mineral Petrol* 141: 201–221
- Schmiedel T, Breitzkreuz C, Götz I, Ehling B-C (online) Geometry of laccolith margins: 2d and 3d models of the Late Paleozoic Halle Volcanic Complex (Germany). *Int J Earth Sci*
- Schulz N (2010) Dreidimensionale geologische Modellierung eines spätpaläozoischen intermediären subvulkanischen Komplexes nördlich von Halle (Saale). Unpublished diploma thesis, TU Bergakademie Freiberg, Germany
- Schwab M (1959) Zur Deutung des Quarzporphyrs vom Kahlbusch bei Dohna (Sachsen) als Quellkuppe. *Geol Rundsch* 48:43–54
- Siebert C (1967a) Zur Petrochemie der Vulkanite des Halleschen Permokarbonkomplexes. *Geologie* 16: 1122–1135
- Siebert C (1967b) Die zeitliche und räumliche Entwicklung des intermediären Vulkanismus im Halleschen Permokarbonkomplex. *Geologie* 16:889–900
- Stark M (1912) Beiträge zum geologisch-petrographischen Aufbau der Euganeen und zur Lakkolithenfrage. *Mineralog Petrogr Mitteil* 31:1–80
- Von Seckendorff V (2012) Der Magmatismus in und zwischen den spätvariszischen permokarbonen Sedimentbecken in Deutschland. *Schrift Deutsch Gesellschaft Geowiss* 61:743–860
- Winter C, Breitzkreuz C, Lapp M (2008) Textural analysis of a Late Palaeozoic coherent to pyroclastic rhyolitic dyke system near Burkersdorf (Erzgebirge, Saxony, Germany). *Geol Soc Lond Spec Publ* 302:197–219

Rise and Fall of a Multi-sheet Intrusive Complex, Elba Island, Italy

D.S. Westerman, S. Rocchi, A. Dini, F. Farina, and E. Roni

Abstract

Elba Island intrusive complex: multisheet laccoliths, sheeted pluton, mafic dyke swarm. Laccolith magma fed from dykes and emplaced in crustal discontinuities (traps). Pluton growth by downward stacking of three magma pulses. Laccoliths and plutons: different outcomes of similar processes in different conditions. Emplacement of excess magma in a short time led to massive gravity slide.

1 Introduction

Elba Island is the site of a prime example of a very young intrusive complex including multiple multisheet laccoliths, a sheeted pluton and an extensive dyke swarm, all emplaced at the same location in about 1.5 Ma. Elba Island is located at the northern end of the Tyrrhenian Sea, a region affected by

extensional processes leading to the opening of an ensialic back-arc basin behind the eastward progressing compressive front of the Apennine mobile belt (Malinverno and Ryan 1986).

The structural framework of Elba Island (Fig. 1) developed during the Apenninic compressional event before 20 Ma, which led to the stacking of five major tectonic complexes on east-verging thrusts. The three lowest complexes (I–III) have continental features consisting of metamorphic basement and shallow-water clastic and carbonate rocks, while the upper two complexes (IV–V) have oceanic characteristics: Complex IV consists of Jurassic oceanic lithosphere of the western Tethys Ocean (peridotite, gabbro, pillow basalt and ophiolite sedimentary breccia) and its late Jurassic—middle Cretaceous sedimentary cover (chert, limestone, and argillite interbedded with siliceous limestone); Complex V consists mostly of a late Cretaceous siliciclastic turbidite sequence (Pertusati et al. 1993). This stacking of tectonic complexes on top of the Apennine fold-and-thrust belt is characterized by a large number of physical discontinuities such

D.S. Westerman
Department of Earth and Environmental Science,
Norwich University, Northfield, VT, USA

S. Rocchi (✉) · E. Roni
Dipartimento di Scienze della Terra,
Università di Pisa, Pisa, Italy
e-mail: sergio.rocchi@unipi.it

A. Dini
Istituto di Geoscienze e Georisorse,
CNR (Consiglio Nazionale delle Ricerche),
Pisa, Italy

F. Farina
Departamento de Geologia,
Universidade Federal de Ouro Preto,
Ouro Preto, Minas Gerais, Brazil

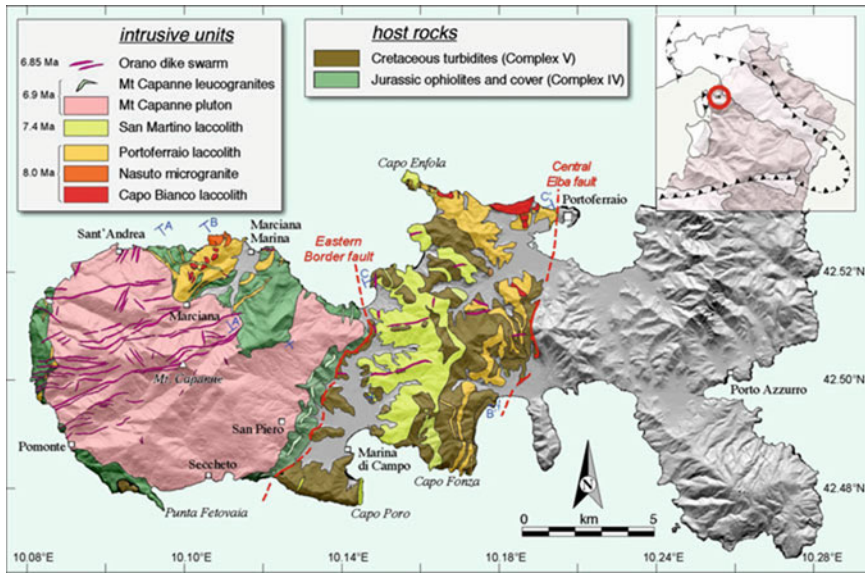


Fig. 1 Simplified geological map of western and central Elba Island. In the *inset*, the *hatched line* represents the present front of the Apennine-Maghrebide and Alpine chains

as thrust contacts between tectonic complexes and bedding planes within the turbidite sequence of Complex V.

After 20 Ma, compression continued, but the stalled subduction transformed to an eastward-migrating slab rollback and lithospheric delamination of the Adriatic plate (Serri et al. 1993). Asthenosphere rose against the base of the middle-upper crust, became partially molten by decompression, and generated uplift and extension of the crust, heat transfer, and ultimately anatectic melting of crustal materials. In turn, extensional tectonics produced low- and high-angle normal faults, adding physical discontinuities to the stacked Tuscan tectonic complexes.

In this framework, magmas were generated in the crust and in the mantle, leading to the variety of intrusive and extrusive products of the Tuscan Magmatic Province exposed across an area of about 30,000 km² of southern Tuscany and the northern Tyrrhenian Sea. This igneous activity migrated from west (14 Ma) to east (0.2 Ma) (Serri et al. 1993).

Igneous activity in western-central Elba Island (Tuscany) led to the emplacement of several magma bodies over a time span of about 1.5 Ma

during the Late Miocene, with the relative chronology of all units firmly established on the basis of consistent crosscutting relations. The igneous sequence can be subdivided into three main events: (1) the construction of three multilayer laccoliths, first by the emplacement of the layers of Capo Bianco aplite, followed in succession by the layers of the Portoferraio laccolith and finally, the San Martino laccolith (Rocchi et al. 2002); (2) intrusion and/or deformation of the deepest laccolith layers by the Monte Capanne pluton and its associated late leucocratic dykes and veins (Farina et al. 2010); (3) emplacement of the mafic Orano dyke swarm, cutting through the entire succession (Dini et al. 2008). Absolute ages, noted subsequently, are consistent with the relative chronology constrained by field relations.

Shortly after the intrusive sequence was assembled, the upper part of the igneous-sedimentary system was tectonically translated eastward along the low-angle Central Elba Fault (Fig. 1). Following this eastward translation, a “west side up” movement occurred along the high-angle Eastern Border Fault (Fig. 1) with a throw of 2–3 km so that the lower part of the sequence is presently exposed in western Elba at

the same level as the upper part in central Elba (Westerman et al. 2004). This process, coupled with nearly 100 % coastal exposure on the island, led to the serendipitous exposure of a 5-km-thick crustal section including nine intrusive layers of late Miocene age that built up three multilayer Christmas-tree laccoliths.

2 The Intrusive Sheets (Multilayer Laccoliths)

2.1 Christmas Tree Geometry of the Laccolith Complex

Magmatism in Elba was initiated with emplacement at c. 8.5 Ma of the Capo Bianco aplite, a bony white rock, so unique that it is also reported in ancient Greek myths (Dini et al. 2007). This unit is found in two layers, within tectonic Complexes IV and V (Fig. 1): the lower layer is preserved as caps on ridges with a minimum thickness of 50 m, while the upper horizon crops out along the north coast of central Elba with a minimum thickness of 120 m. Mineralogy includes microphenocrysts of sanidine, plagioclase and muscovite, with significant amounts of tourmaline occurring as dark blue orbicules (Dini et al. 2007). Intrusive contacts are very rare for the Capo Bianco aplite, seen only locally against flysch of Complex V. Elsewhere, the stratigraphic

and tectonic thrust surfaces along which Capo Bianco magma intruded also served as the loci for magma injection during the next episode of magmatism. This resulted in the remaining Capo Bianco aplite material being entirely encased in younger laccolith horizons. Calculated minimum volume for the Capo Bianco system is 0.63 km³, and can be thought of as the crust “breaking a sweat” of anatectic melt generated by muscovite dehydration melting, setting the stage for arrival of a much larger volume of magma derived by a higher degree (muscovite and biotite involved), and much greater amount, of melting in the source area (Dini et al. 2002).

This second episode of magmatism led to the emplacement, at c. 8 Ma, of the Portoferraio porphyry at the same magmatic center, ultimately occupying four major horizons with two thin sheets (75 m) and one thick sheet (700 m) in Complex IV, and another thick sheet (400 m) in the flysch sequence of Complex V (Figs. 2 and 4). These porphyries are characterized by sanidine phenocrysts typically averaging 1–2 cm (Fig. 3a). Quartz and biotite phenocrysts are ubiquitous, all set in a very fine-grained matrix predominantly made of quartz and K-feldspar.

The third and final episode of laccolith emplacement occurred following a delay in magmatic activity of approximately 0.6 Ma. It was marked by the arrival of the very distinctive

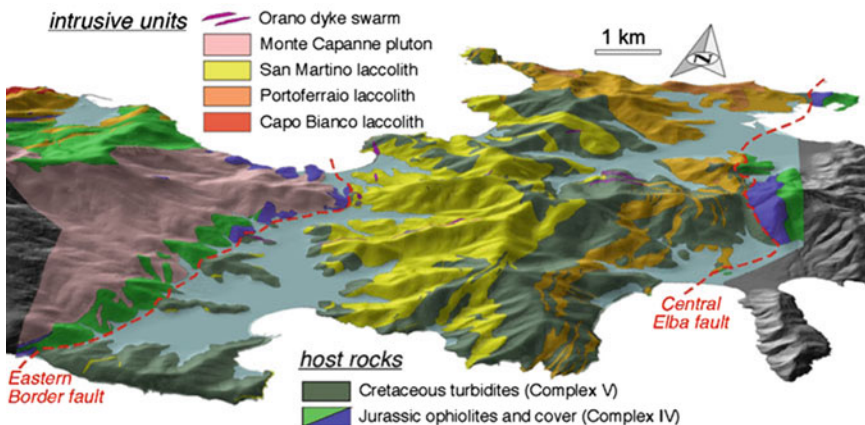


Fig. 2 Geological map of the western-central Elba laccolith layers draped over a digital elevation model. View from the south. Scale varies in perspective view

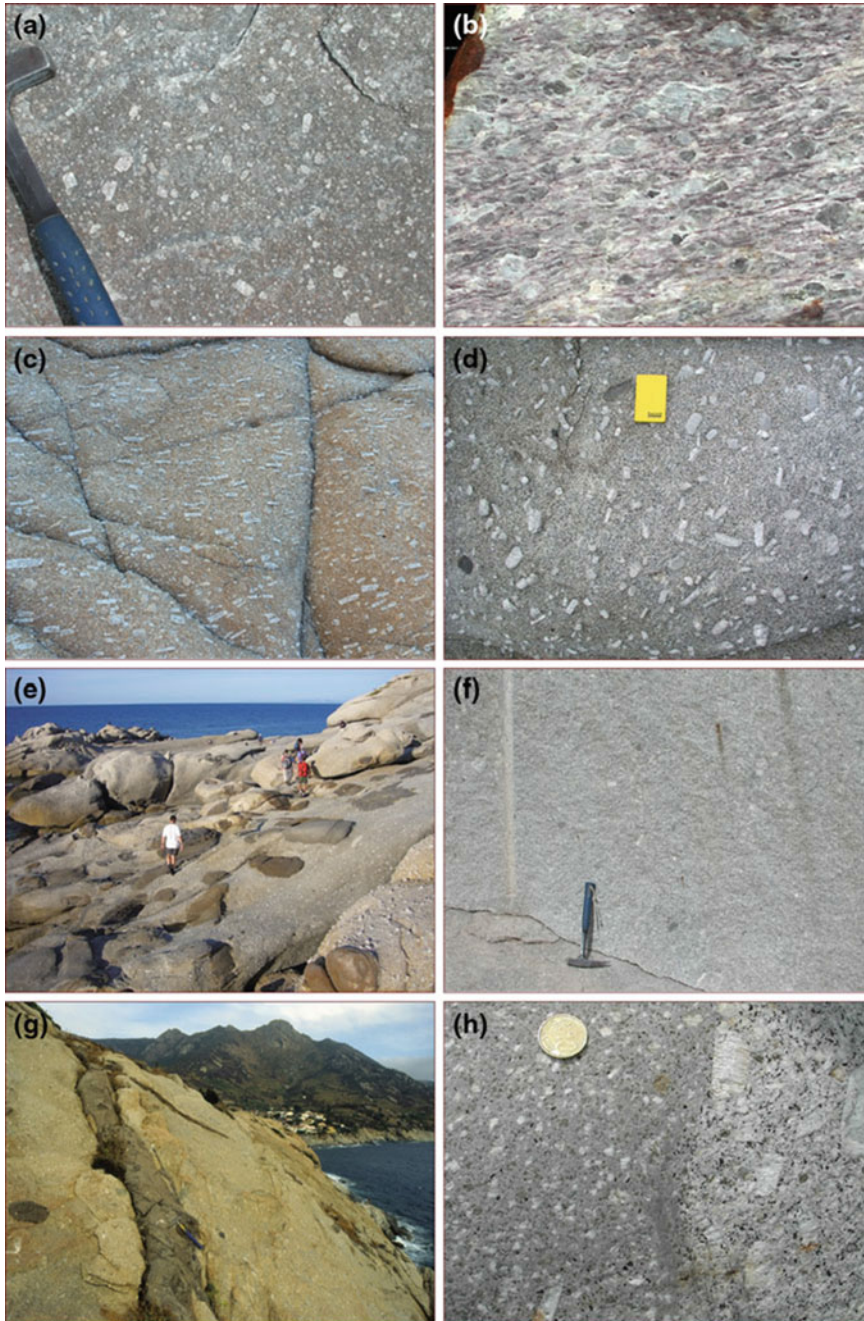


Fig. 3 **a** Portoferraio porphyry, with sanidine phenocrysts up to 2 cm long; hammer for scale. **b** Foliated Portoferraio porphyry, 1.5 km NW of Marciana; the foliation is N52W, 55N (parallel to the local contact with the Monte Capanne pluton) with stretching lineation 50, N5E, pointing out a genetic link between pluton emplacement and deformation; width of the field of view: 15 cm. **c** San Martino porphyry, eastern side of Marina di Campo Bay, showing abundant aligned sanidine megacrysts in relief (width of field of view: 1.6 m). **d** Megacryst-rich Sant'Andrea facies of the Monte Capanne pluton, Sant'Andrea shore; note the euhedral shapes of megacrysts (as opposed to those in the

San Piero facies) and the coarse-grained matrix (as opposed to the San Martino porphyry); notebook for scale is 20 cm-long. **e** Megacryst- and mafic microgranular enclave-rich Sant'Andrea facies, Sant'Andrea shore. **f** Megacryst-poor San Piero facies of the Monte Capanne pluton, abandoned quarry close to Seccheto; hammer for scale. **g** Typical Orano dyke within Monte Capanne granite, close to Chiessi; hammer for scale. **h** Orano dyke (*left*) in contact with Monte Capanne granite (*right*); note the dyke contains xenocrysts of quartz with ocellar texture and of K-feldspars with rounded shape; coin for scale

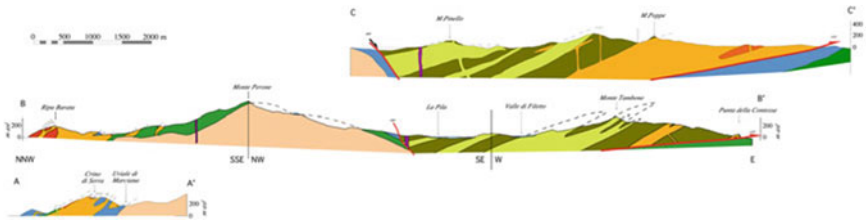


Fig. 4 Geological cross-sections of the western-central Elba laccolith units

San Martino porphyry characterized by prominent euhedral decimetric megacrysts of sanidine (Fig. 3c). These megacrysts are accompanied by remarkable amounts of quartz, plagioclase and biotite phenocrysts, all suspended in a very fine-grained isotropic groundmass of quartz and feldspars, with mafic microgranular enclaves generally present as well (Dini et al. 2002). With the exception of a principal feeder dyke located in western Elba (Fig. 1), the three main horizons of the San Martino laccolith are currently located in central Elba where they were translated by the tectonic-gravitational decapitation of the complex (Figs. 2 and 4). Two lower horizons (100–200 m thick) occur beneath the main 700-m thick sheet that has a reconstructed diameter of nearly 10 km (Fig. 5) (Rocchi et al. 2002); the emplacement sequence for these three sheets is unresolved.

2.2 Magma Flow in the Laccolith

One aspect of the study of laccoliths involves developing insight to processes of magmatic flow associated with the feeding and filling of such bodies. The San Martino laccolith system (Fig. 5) lends itself very well to this type of work owing to the ubiquitous presence of euhedral sanidine megacrysts, and platy biotite phenocrysts, which can reveal the occurrence of a fabric via attitude measurements or via AMS analysis (anisotropy of the magnetic susceptibility), respectively. A combined analysis of megacryst orientations and AMS fabric (Roni et al. 2014) demonstrated a strong correlation between orientations of megacrysts and magnetic fabric, strengthening the use of AMS as a magma strain indicator. It

further suggests that: (i) together the lack of post-emplacement tectonic deformation, as well as the fast cooling of the shallow igneous system, the quick emplacement, and the high magma viscosity, permit direct correlation between strain in the rock and magma flow, (ii) a central dyke with sub-vertical flow fed the main laccolith horizons, (iii) magma spreading laterally from the feeding system built the laccolith layers as single propagating and inflating pulses, in which the planar surfaces of particles became aligned perpendicular to the magma displacement direction (Fig. 6) in an inferred divergent flow field (Paterson et al. 1998), and (iv) the absence of internal discontinuities agrees with the hypothesis of continuous feeding of the magma injected as a single pulse or a series of pulses that quickly coalesced, confirming rapid emplacement of the body.

2.3 Laccolith Growth

Excellent exposure and significant 3-D relief has allowed detailed mapping leading to reconstruction of the geometries of nested multi-layered laccoliths on Elba, with each lithologically recognizable laccolith consisting of a set of individual sheets with measured thicknesses and diameters (Rocchi et al. 2002). The dimensional parameters of these intrusive layers fit a power-law distribution (Fig. 7) indicating that, after a likely first stage of horizontal expansion, the layers underwent a second stage of dominantly vertical inflation (Rocchi et al. 2002). It is worth noting that, once the layers of the Portoferraio and San Martino laccolithic layers are virtually merged as two single intrusive bodies and plotted again in the length versus thickness diagram, they

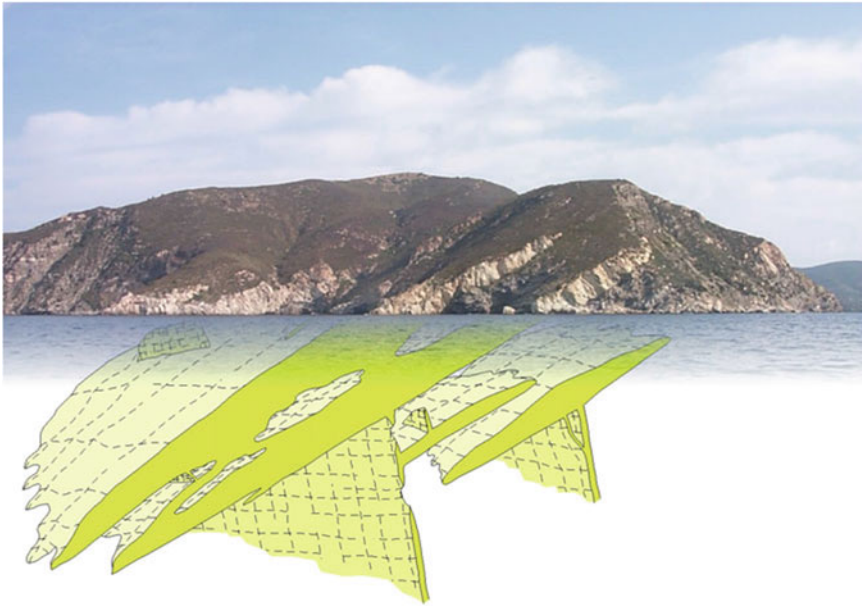


Fig. 5 Schematic representation of the San Martino multilayer laccolith, superimposed on a field photo of the laccolith layers cropping out on the south-facing cliffs east of Marina di Campo Bay (width of photo is ~ 1 km)

plot on the fit lines proposed for plutons (Cruden and McCaffrey 2002) (Fig. 7). This evidence shows that, if the laccolith sheets had coalesced, they would have ended up as two plutons having aspect ratios compatible with both (i) the power-law fit curves for plutons worldwide (McCaffrey and Petford 1997; Cruden and McCaffrey 2001) and (ii) the S-type fit curve proposed for all intrusive bodies (Cruden and McCaffrey 2002). Taken together, the laccoliths from Elba can be seen as sheet-like intrusions that did not coalesce to form single laccoliths or plutons.

2.4 Laccolith Emplacement

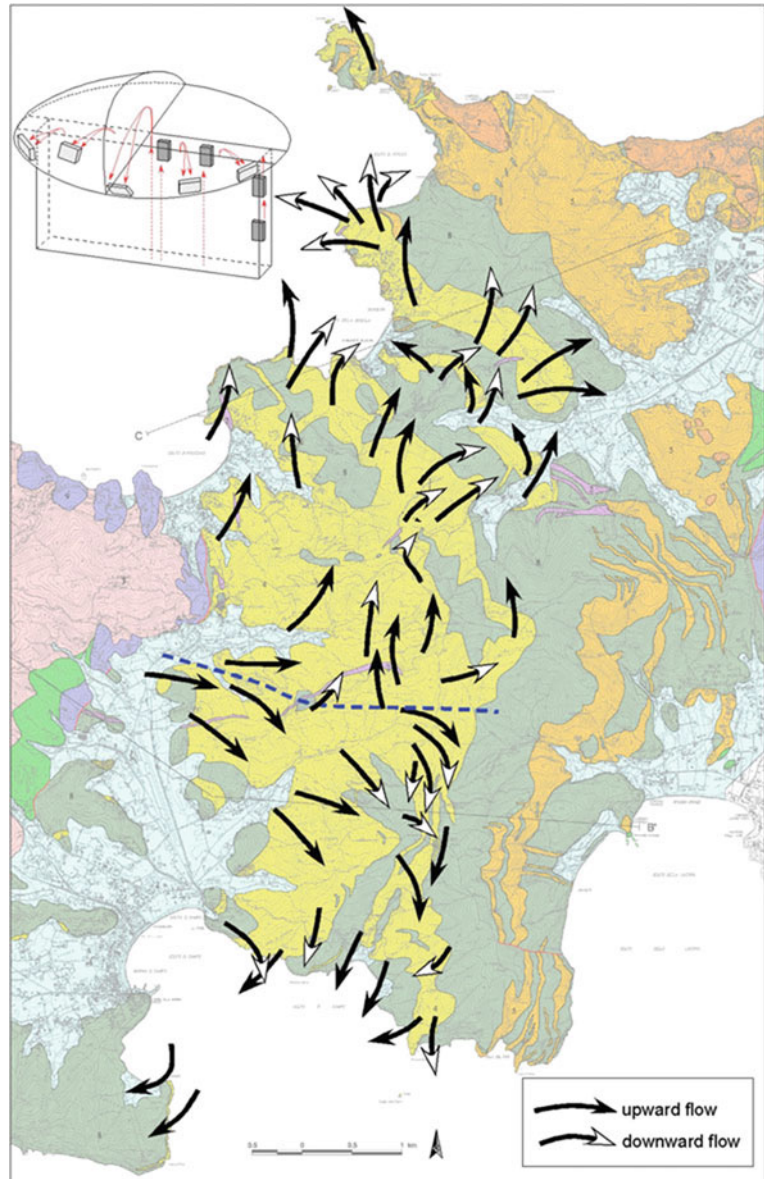
The observation that the laccolith failed to coalesce to form a composite pluton but emplaced as separate sheets in a Christmas tree geometry raises questions regarding the mechanisms governing the emplacement of shallow level granitic intrusions. Each magma batch created its own

room by lifting the rock overburden, indicating that the magma driving pressure was greater than the vertical stress (Hogan et al. 1998; Kerr and Pollard 1998). These conditions provide evidence that crustal magma traps arrested the vertical ascent of Elba magmas (Hogan and Gilbert 1995; Hogan et al. 1998). A significant control on the ascent of Elba magma by magma driving pressure is supported by the aspect ratios of all the Elba intrusions (i.e. their overall tabular shapes), coupled with the occurrence of vertical dykes below the subhorizontal sheets, indicating that magma ascent at Elba occurred through feeder dykes that likely remained connected to the magma reservoir (Brown and Solar 1998; Dehls et al. 1998; Hogan et al. 1998). The magma driving pressure is

$$P_d = P_h + P_0 - P_{vis} - S_h$$

(Reches and Fink 1988; Baer and Reches 1991; Hogan and Gilbert 1995; Hogan et al. 1998),

Fig. 6 Magmatic flow pattern in the San Martino laccolith based on poles of restored magmatic and magnetic foliations projected on the current map pattern. *Dashed blue line* trending E-W marks separation of N and S halves of the main laccolith layer, with the west end representing the approximate eastern terminus of the Marciana feeder dyke system. The *upper-left inset* depicts the relationships between magma flow (*red arrows*) and the orientation of the platy K-feldspar and biotite crystals (Roni et al. 2014)



where P_h is the hydrostatic pressure, P_0 is the magma chamber overpressure, P_{vis} is the viscous pressure drop, and S_h is the horizontal stress, i.e. perpendicular to the ascending dyke walls. In the case of the Elba magmas, the magma chamber overpressure can be considered negligible due to the low volatile contents, and the viscous pressure drop is of little influence when values of 0.5 MPa km^{-1} are adopted (Baer and Reches 1991; Hogan et al. 1998). The hydrostatic pressure,

defined as the difference between the lithostatic pressure at the top of the magma reservoir (i.e. at the source depth) and the pressure at the tip of the column of magma as it rises through the crust (Hogan and Gilbert 1995) can be calculated at any depth based on the knowledge of the depth of the magma source, the integrated density of the crust overlying the magma source, and the integrated density of the rising magma (Rocchi et al. 2010). The horizontal stress is the sum of the lithostatic

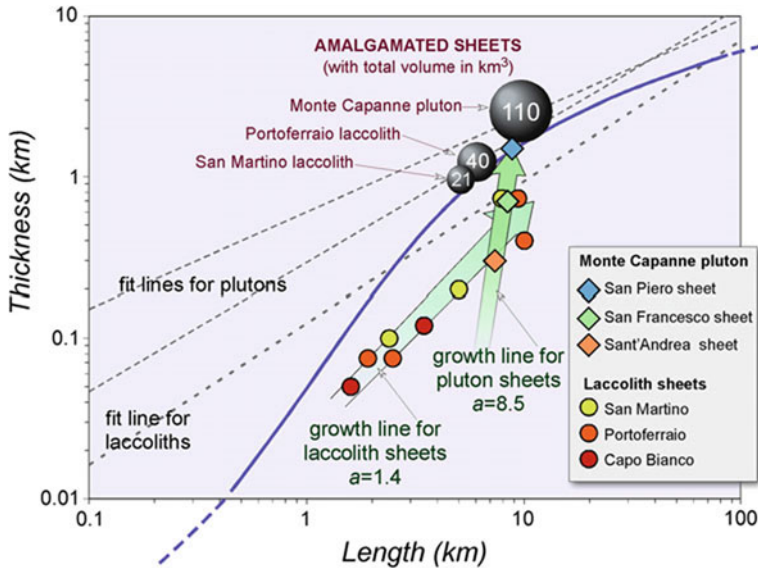


Fig. 7 Log-log plot of T versus L (T = thickness; L = diameter of sheets). The general power-law equation describing the relationships between L and T has the form $L = kT^a$ (where k is a constant and a is the slope of a regression line in a log-log plot). Dimensional data for laccoliths from (Rocchi et al. 2002) and for Monte Capanne pluton sheets from (Farina et al. 2010). *Fit lines* for plutons and laccoliths from McCaffrey and Petford (1997) and Cruden and McCaffrey (2001); *bold violet*

S-type fit line for all intrusive bodies from Cruden and McCaffrey (2002). The *grey balls* represent the L - T values for virtually amalgamated laccoliths and the naturally amalgamated pluton: laccolith values calculated from total thickness and average diameter; pluton value from all sheets naturally amalgamated as a result of the intrusion process. The *number* inside each *grey ball* indicates the intrusion volume (in km^3)

load and the tectonic stress, which is a function of the regional state of crustal stress. In late Miocene time, the upper crust at Elba was in a tensional stress regime, and all the intrusions were emplaced within the two uppermost Apennine tectonic units, i.e. in the brittle crust (Rocchi et al. 2010).

All the Elba magma batches project a positive driving pressure value at the surface, thus having the potential to erupt (Fig. 8), yet, to our knowledge, none of them did so. The only known volcanoclastic material in the late Miocene sediments in mainland Tuscany has an isotopic age (7.4 Ma) comparable to that of the San Martino laccolith, yet its mineral and chemical features correlate this material to the volcanic activity of Capraia Island (Rocchi et al. 2010). The two main laccolith units were emplaced at depths shallower than where the ascending magma driving pressure first exceeded the vertical stress. The Portoferraio laccolith layers were emplaced on a set of available

physical discontinuities in a depth zone only slightly shallower than that point, that is the magma switched from vertical to horizontal movement as soon as the magma left behind the densest host rock unit (the ophiolite sequence) and acquired the ability to lift the overburden (i.e. driving pressure exceeds vertical stress; Fig. 8a). Furthermore, a prominent physical discontinuity occurred at that depth, namely the thrust surface between tectonic complexes IV and V. The San Martino magma layers were emplaced in a zone some 1,000 m above the Portoferraio laccolith layers, in that the younger magma was able to ascend higher than the previous batch. It switched from vertical to horizontal propagation and had the ability to lift the overburden when it met a set of crustal magma traps (Fig. 8b), i.e. the physical discontinuities within the turbidite sequence (competence contrast between sandstone and shaly layers, plus internal thrusts).

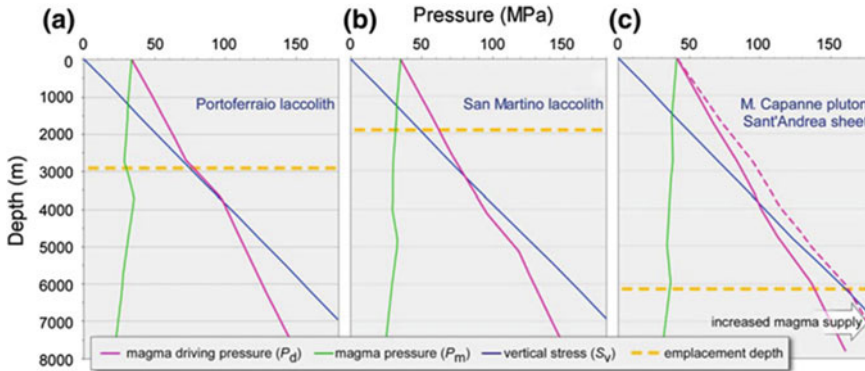


Fig. 8 Variations in magma driving pressure ($P_d = P_h + P_0 - P_{vis} - S_h$; see text), magma pressure ($P_m = P_h + P_0 - P_{vis} - S_v$) and vertical stress ($S_v = \rho gh$, where ρ = integrated crustal density, g = gravity acceleration, h = depth) as a function of depth for **a** Portoferraio laccolith magma, **b** San Martino laccolith magma, and **c** the Sant'Andrea sheet magma, the first magma batch of

the Monte Capanne pluton; magenta dashed line corresponds to increased magma driving pressure resulting from a 40 % horizontal stress reduction. Each curve is constructed according to Hogan and Gilbert (1995) and Hogan et al. (1998) using published crustal density profiles for Elba (Rocchi et al. 2010)

3 The Sheeted Intrusion (Pluton)

3.1 Internal Structure of the Monte Capanne Pluton

Western Elba is dominated by the Monte Capanne pluton with its nearly circular map pattern and impressive relief as it rises 1 km out of the sea. Formal study of the geology of Elba has gone on for more than two centuries, fueling controversy on both absolute and relative ages of the porphyries and the granite pluton (Dini et al. 2009). Despite the absence of mappable internal contacts, the Monte Capanne pluton is now recognized as consisting of three distinct facies (Fig. 3d, f) emplaced at approximately 6.9 Ma (Dini et al. 2002). Common characteristics of the three facies include a monzogranitic composition with variable proportions of plagioclase, K-feldspar (commonly as large megacrysts), quartz, and biotite, and the occurrence of mafic microgranular enclaves, displaying strongly variable size and composition (Dini et al. 2002; Farina et al. 2010). Detailed mapping, along with petrographic and geochemical analyses (Farina et al. 2010) indicate that these three facies represent three subhorizontal sheets sequentially emplaced

by underplating as discrete magma batches (Fig. 9). Radiometric dating has not yet substantiated the emplacement sequence, and arguments rely primarily on (i) the absence of feeding structures to the uppermost, highly distinctive Sant'Andrea facies, despite excellent field exposures (Farina et al. 2010), and (ii) emplacement of increasingly more mafic facies (from Sant'Andrea to San Piero facies) following the overall temporal trend of progressive increase of mantle contribution to the magmas as reported for all of western-central Elba magmatism (Dini et al. 2002). The total thickness of the pluton has been estimated at ~ 2.5 km using magnetic data (Dini et al. 2008). Rocks of the Sant'Andrea facies are preserved along the pluton margin and at high elevations, and are characterized by the highest SiO_2 content, highest biotite Mg#, highest K-feldspar megacryst content (area % is 3.37 ± 0.56 (1σ), corresponding to ~ 57 megacrysts/ m^2), and highest mafic microgranular enclave content. The facies exposed at the deepest levels is the San Piero facies, which has opposing characteristics (area % is 0.26 ± 0.21 (1σ); ~ 4 megacrysts/ m^2), while rocks of the San Francesco facies are intermediate both in character and in spatial distribution (Fig. 9). The process of stepwise emplacement of the pluton

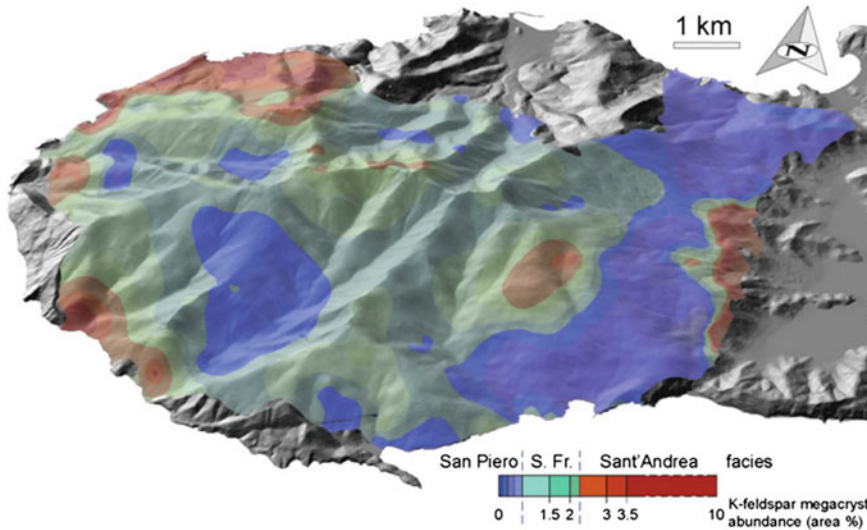


Fig. 9 Geological map area% of K-feldspar megacrysts, translated to intrusive facies of the Monte Capanne pluton, draped over a digital elevation model. Data for

map construction after Farina et al. (2010). View from the south. Scale varies in perspective view

deformed the surrounding host rocks while metamorphosing them, resulting in flattening of its thermal aureole with mylonitization of the deepest porphyry layers of the Portoferraio laccolith (Fig. 3b).

3.2 Sheet Growth and Pluton Build-Up

The reconstructed original dimensional parameters of the three intrusive sheets making up the Monte Capanne pluton (Farina et al. 2010) display a power-law correlation that, in analogy with the laccolith layers, can be interpreted as indicative of a similar vertical inflation stage in the sheet growth history (Fig. 7), such that both the multilayer laccoliths and the sheeted pluton formed in a “laccolithic” way.

When the dimensional parameters of the Monte Capanne pluton as a whole (i.e. the result of the amalgamation of three sheets in a single intrusive body) are plotted in the length-thickness diagram, they fit those predicted for plutons worldwide (McCaffrey and Petford 1997; Cruden and McCaffrey 2001, 2002). In summary, the magma batches forming the pluton did amalgamate in a

single, composite intrusive body, while the amalgamation was not possible for the laccolith sheets since they were emplaced on multiple surfaces separated by intercalating host rocks and “frozen” in their vertical inflation stage (Rocchi et al. 2010).

3.3 Magma Sheet Emplacement

The sequence of events that led to formation of an amalgamated pluton such as the Monte Capanne pluton, rather than a set of discrete sheets such as Portoferraio and San Martino laccoliths, has significant implications for our understanding of magma emplacement mechanisms in the upper crust (Rocchi et al. 2010).

The first magma batch of the Monte Capanne pluton (Sant’Andrea sheet) was emplaced deeper than the laccoliths, at about 6 km, but its petrochemical features do not differ enough from those of the San Martino magma to explain such a difference in emplacement level. Therefore, there is no straightforward explanation why the ~8 Ma and the ~7.4 Ma magma batches were emplaced at depths of less than 3 km as separated intrusive sheets with aphanitic groundmass,

whereas the three ~ 7 Ma magma batches did, in fact, coalesce at a deeper level to form a single, coarse-grained intrusive body. A plausible explanation is linked to the combined occurrence of (i) magma source deepening as a direct consequence of the addition of ~ 2.4 km of porphyry to the uppermost crust, and (ii) increase of the magma supply rate, as suggested by the abundant mafic microgranular enclaves of metric size in the Sant'Andrea magma batch (Westerman et al. 2003). The inferred increase in rate of supply and resulting dilational stress gave way to a transient reduction of the horizontal stress (Hogan and Gilbert 1995), possibly supplemented by ongoing slab roll-back. In this context, a stress reduction of about 40 % is enough to cause an increase in magma driving pressure (Fig. 8c, magenta dashed line) sufficient to overcome the vertical stress at a depth corresponding to the emplacement depth of the Sant'Andrea magma pulse (Rocchi et al. 2010). This batch of magma thus emplaced as a rather thin (250 m) sheet, very rich in K-feldspar megacrysts, large quartz phenocrysts and large mafic microgranular enclaves. The following San Francesco magma batch was emplaced below the Sant'Andrea sheet, with the cryptic nature of the contact between the two facies suggesting that the second one was emplaced at the base of a mushy tabular body (Saint-Blanquat et al. 2006; Farina et al. 2010). Such mushy bodies are natural traps for ascending batches of magma (Brown 2007) because they generate a rigidity anisotropy that triggers horizontal expansion of subsequent magma batches (Menand 2008) and growth of the intrusion by under-accretion. A similar history was repeated on the arrival of the third (San Piero) magma batch that was emplaced at the base of the San Francesco sheet.

The remarkable increase in matrix grain size from laccoliths to pluton is a consequence of the more extended crystallization history of the pluton's magma batches. This is, in turn, linked to the greater depth of the pluton's magma trap in two ways: (i) the higher temperature of the crust at the depth of pluton emplacement results in a slower crystallization, and (ii) the slightly higher

depth of emplacement, at such low pressures (<200 MPa), may result in significant increase in water solubility, depression of solidus temperature, and more extended crystallization temperature range, all leading to a coarser-grained matrix (Hogan et al. 2000). This extended crystallization can also help explain the cryptic nature of the contacts between facies of the pluton. Taken together, all three pulses of magma were assembled in a downward stack by exploiting traps of their own making, thus building a "successful" pluton. This is contrasted with the slightly older multisheet laccoliths located above (Fig. 7), which exploited pre-existing structural traps and, therefore, could be seen as "failed" plutons. Additionally, progressive warming of the crust during magma emplacement throughout growth of the entire igneous complex is also suggested by the increasing evidence of mafic magma intruding the crust, as seen from the growing amount of mafic enclaves through time, and the emplacement of the late mafic Orano magma (Dini et al. 2002).

3.4 Plutons Versus Laccoliths

The shape, emplacement and assembly history of the Monte Capanne intrusion raises questions as to which category of intrusive bodies it belongs. For its medium- to coarse-grained texture and emplacement depth, Monte Capanne has been classically regarded as a pluton. Nevertheless, it could also be regarded as a sheeted laccolith that was emplaced deeper than the normal depth limit of about 3 km, and slightly exceeded the ca. 2 km limiting thickness owing to the rapid removal of the roof by tectonic-gravitational collapse. However, more important than its classification is the understanding that at Elba Island, similar magma batches in similar settings resulted in intrusive bodies that significantly differ in their shape, texture and emplacement depth.

As a take-home lesson, in an upper crust characterized by abundant magma traps, the failed (laccolith) or successful (pluton) assembly of magma batches can thus be linked to different

outcomes of the same geological process operating under different transient conditions. The transition from a laccolithic to a plutonic intrusive shape having a higher thickness-to-diameter ratio can be governed by a combination of factors such as variations in rates of magma supply and horizontal extensional tectonic stress, as well as downward migration of both the source region and the magma traps as a result of the addition of magma layers at higher levels in the crust.

4 The Dyke Swarm

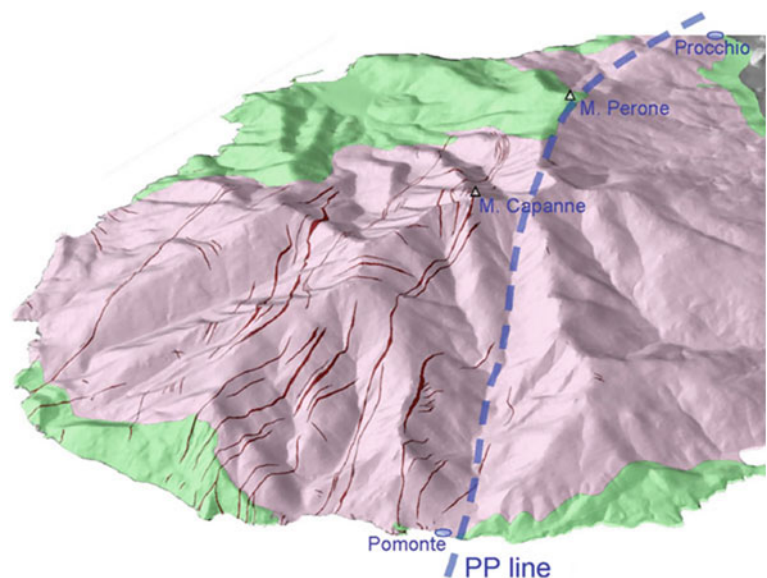
4.1 Geometry of the Orano Dykes

More than 200 individual dykes with cumulative length in excess of 90 km were emplaced 6.85 Ma mostly in the northwestern half of the still not completely solidified Monte Capanne pluton (Figs. 1 and 10) and, more limitedly, in its covering laccolith layers (Fig. 1) (Dini et al. 2008). These dark dykes (Fig. 3g), are porphyritic, with plagioclase, biotite, clinopyroxene and amphibole phenocrysts set in a very fine-grained matrix of plagioclase, K-feldspar and phlogopite. Some dykes, generally the thickest, are zoned with borders similar to unzoned dykes, and inner portions reaching monzogranitic compositions

owing to the incorporation of abundant quartz and K-feldspar xenocrysts (Fig. 3h) from the still mushy Monte Capanne magmatic system. The original melt derived from a specific mantle source with geochemical–isotopic characteristics intermediate between Capraia K-andesites and Tuscan lamproites (Dini et al. 2002).

Vertical expression of the dykes exceeds 4 km, ranging from sea level exposures in the Monte Capanne pluton, upward through the exposed thickness of the pluton, and finally through the entire exposed cover sequence tectonically translated to the east and now preserved in central Elba. The dykes were probably fed by a mafic magma reservoir located below the northwestern half of the Monte Capanne pluton, as suggested by magnetic data (Dini et al. 2008). The dykes reveal an organized structural pattern with a dominant system made of one set trending ENE, and a minor system consisting of two sets trending NNE and NW (Fig. 11). Analysis of the structural patterns in conjunction with established tectonic conditions at the time of emplacement of the dyke swarm suggests that they developed in a NE-SW dextral shear zone within which zones of differential strain created local zones of sinistral shear (Dini et al. 2008). It is interesting to note that an overall N-S extensional stress field apparently persisting at this

Fig. 10 Geological map of the Orano dyke swarm draped over a digital elevation model, view from the SW. The Pomonte-Prochchio (PP) line, bordering the SE margin of the outcrop area of Orano dykes, is also reported



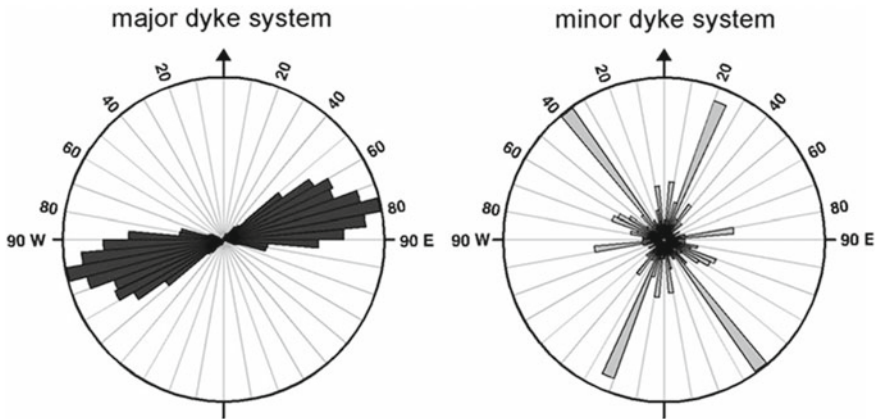


Fig. 11 Rose diagrams of the strike of dykes (see maps in Figs. 1 and 10) for zones dominated by the major and minor systems, respectively. Each 10 m section of the 90 km of dykes mapped in the swarm generated a strike value, producing the ~9,000 data points making up the

two rose diagrams (from Dini et al. 2008). The diagram on the right has a radius scaled 4x with respect to the one on the left to emphasize the strike distribution within the minor system

location from the time of emplacement of the San Martino laccolith system with its E-W feeder system, through emplacement of the Monte Capanne plutonic complex, and into emplacement of the Orano dyke swarm.

producing a trace of progressively younger magmatic centers (Dini et al. 2008).

4.2 Insight to the Regional Geology

Emplacement of the Orano dyke swarm closed a ~1.5 Ma long episode of magmatism located at a single center and fed by sources from both the crust and underlying mantle. This final stage in the development of the entire igneous complex, with the high degree of hybridization and xenocryst capture, documents that a late-plutonic dyke swarm can intrude before complete consolidation of its host. The Orano dyke swarm offers further evidence for a regionally significant implication that magmatic activity in the late Miocene occurred within a transfer zone in the northern Tyrrhenian region. However, as important as the sequence of igneous activity is, its cessation at an individual center also carries significance. Regional patterns of magmatism in the Tuscan Magmatic Province shows how that transfer zone structure, and perhaps others aligned parallel to it, served as a “fire line” along which magmatism migrated northeastward

5 Post-magmatic Evolution: The Structural Failure

5.1 Collapse of the Magmatic Edifice

The rocks comprising western Elba prior to the magmatism discussed above had been assembled as a stack of eastward-directed thrusts of bedded sedimentary rocks above an ocean lithosphere sequence. In approximately 1 Ma, this 2.7 km thick tectonostratigraphic section was inflated by the addition of a total of 2.4 km of intrusive layers (Rocchi et al. 2002) in a roughly circular region with a diameter of approximately 10 km located over a common magmatic center (Fig. 12). The primary crustal magma trap for the first half of that magmatism was at the well-defined top of the Complex IV ophiolite sequence and beneath the overlying Complex V flysch sequence. This structure was located at the middle of the newly thickened section that defined a domal structure with a new slope of about 25° (Westerman et al. 2004).

As pulses of Monte Capanne magma approached the base of Complex IV, adding an

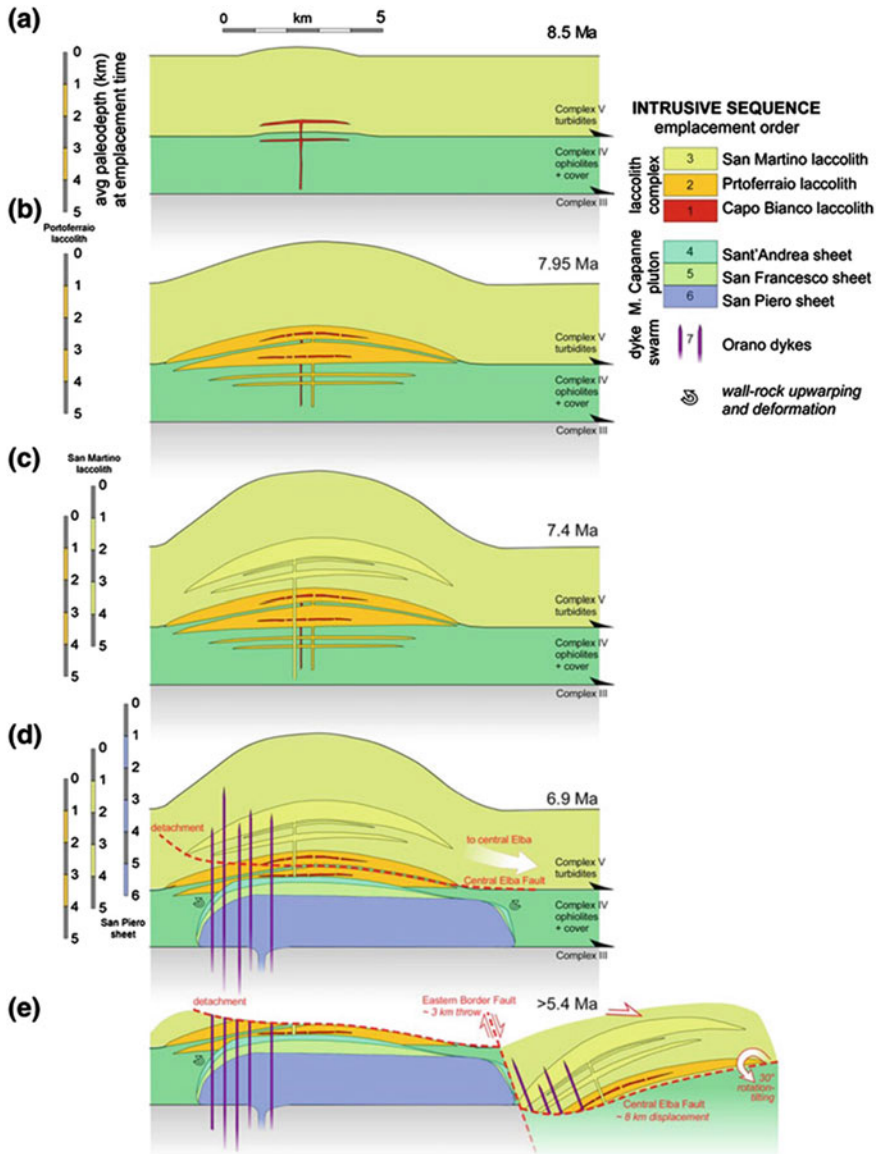


Fig. 12 Rise and fall of the western Elba laccolith-pluton-dyke complex: a schematic summary. **a** Emplacement of the Capo Bianco laccolith layers. **b** Emplacement of the Portoferraio laccolith layers. **c** Emplacement of the San Martino laccolith layers. **d** Emplacement of the Sant’Andrea, San Francesco and San Piero magma

batches (as sheets building the Monte Capanne pluton from the *top down*), closely followed by the emplacement of the Orano mafic dyke swarm in the northwestern part of the pluton. **e** Décollement of the upper part of the nested laccolith-pluton-dyke complex, with translation to central Elba and unroofing of the Monte Capanne pluton

additional estimated 2.5–3 km of new rock under the laccolith intrusions (Dini et al. 2008), the slopes would have steepened (Fig. 12). The system held in place throughout emplacement of the Monte Capanne pluton and long enough for

the Orano dyke swarm to be injected throughout the whole vertical section. Ultimately, however, the Complex IV/V boundary failed and triggered the catastrophic eastward tectonic-gravitational décollement on the Central Elba Fault that

transported the top “half” of the laccolith complex about 8 km to the east over a <1.5 Ma period, with a rate of displacement in excess of 5–6 mm/a (Fig. 12) (Westerman et al. 2004). This combination of (i) loading central Elba with several km of igneous rock, and (ii) the unweighting of western Elba by the removal of that rock, promoted the development of the Eastern Border Fault, with back-tilting of the central Elba stack west side down and uplift of the unroofed western Elba rocks. This ultimately achieved 3–4 km of normal movement on a steep, eastward-dipping surface.

5.2 A Lesson From Destruction

The story of the “fall of western Elba” (Westerman et al. 2004), illustrates how basic geological relationships can document geologic history on a grand scale. The onset of major movement on the Central Elba Fault is constrained by fragments of the Monte Capanne contact aureole (~6.9 Ma) in the footwall mélange located at least 8 km east of the pluton, along with the translation of the upper portion of the slightly younger Orano dyke swarm. Constraint on the termination of the major displacement is also provided with simple geologic relations, as cobbles of western Elba lithologies from just above the fault are found in conglomerates deposited close to the end of the Messinian (~5.3 Ma) about 50 km away on mainland Italy (Pandeli et al. 2010).

These relationships suggest that gravity-assisted fast sliding average (5–6 mm a⁻¹) of a 2.5 km-thick crustal slice decapitated western Elba (Westerman et al. 2004). This activity would undoubtedly have been associated with numerous seismic events over of an extended period, and awareness of such possibilities should be incorporated into hazard assessment of highly over-steepened magmatic centers. As a final implication of this entire body of work, there is simply no substitute for detailed mapping coupled with the tools from all branches of geology.

6 Conclusions

The western Elba igneous system serves as a prime example of a full range of emplacement styles at a long-lasting magmatic center, with successive generation of a nested set of multi-layer laccoliths, a downward-developing amalgamated pluton, an extensive throughgoing dyke swarm, with a final collapse of the whole complex triggered by the overwhelming thickness of magma added to the uppermost crust in a short time.

Pre-existing structures provided strong constraints on emplacement style, and resulted in very similar magmas producing both porphyritic (subvolcanic) as well as granitic (plutonic) textures. The Elba laccolith sheets failed to coalesce and form a larger pluton/laccolith with typical dimensions due to the availability of a large number of magma traps in the host crust that consists of a thrust stack of well-layered rocks. On the other hand, the three magma pulses of the Monte Capanne pluton were assembled in a downward stack, building a “successful” pluton as opposed to the “failed” plutons represented by the multi-sheet laccoliths. Also possible is the opposite view that regards the Monte Capanne pluton as a “failed” laccolith, as opposed to the “successful” multilayer laccoliths of Portoferraio and San Martino.

In the upper crust, laccoliths and plutons represent different outcomes of the same process in different settings. The “tipping point” allowing for transition from a laccolithic to a plutonic intrusive shape is controlled by factors such as variabilities of magma supply rate and horizontal tectonic stress, as well as downward migration of the source region and/or the magma traps as a result of the progressive addition of magma at higher crustal levels. On Elba the rate of magma addition to the crust dramatically increased corresponding to the emplacement of the Monte Capanne pluton (Fig. 13). Although magma emplaced in pulses separated by quiescence gaps, it can be noticed that during the laccolith events, the long-term rate of magma production, ascent and accumulation in the shallow crust was

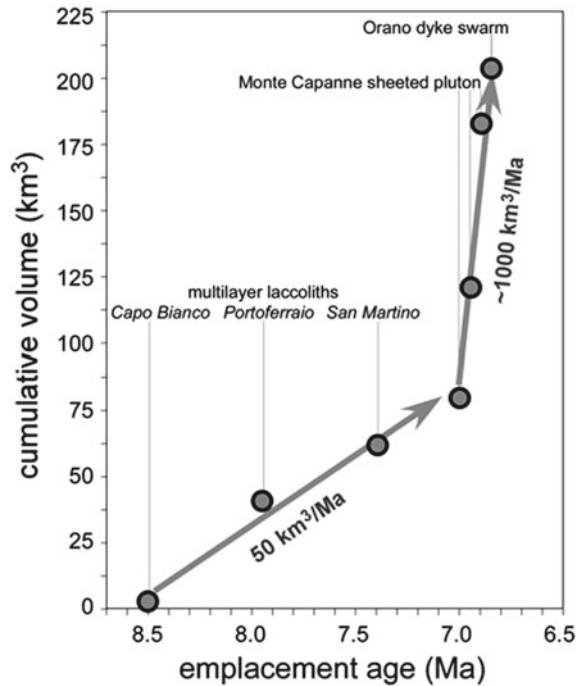


Fig. 13 Plot of the cumulative volume of the western-central Elba intrusions through time. The volumes of each of the three laccoliths have been determined layer by layer (Rocchi et al. 2002), but they are represented here as a *single dot* per laccolith since the emplacement sequence of the different layers within the same multilayer laccolith cannot be discerned. On the other hand, the Monte

Capanne pluton is represented by *three dots* based on the emplacement sequence and lags between pulse emplacement reported by Farina et al. (2010). The volume of the Orano swarm has been calculated by adding the estimated total volume of the mapped dykes to the volume inferred for the mafic reservoir located below the northwestern Monte Capanne pluton (Dini et al. 2008)

around $50 \text{ km}^3/\text{Ma}$, while around 7 Ma, the Monte Capanne and the mafic Orano episodes, magma was added at an accelerated rate ten to twenty times higher. Reasons for this boost can be linked to the increased production of mafic melt acting as an additional heat source promoting the shift of the crustal melt-producing reactions from muscovite-biotite breakdown to the more productive biotite-hornblende breakdown (Dini et al. 2002; Farina et al. 2014). Finally, the addition of excess magma at a unique igneous center in a short time span can trigger gravity slides displacing km-thick slices of crust by several kilometers at geologically fast rates.

References

- Baer G, Reches Z (1991) Mechanics of emplacement and tectonic implications of the Ramon dike systems, Israel. *J Geophys Res* 96:11895–11910
- Brown M (2007) Crustal melting and melt extraction, ascent and emplacement in orogens: mechanisms and consequences. *J Geol Soc London* 164:709–730
- Brown M, Solar GS (1998) Granite ascent and emplacement during contractional deformation in convergent orogens. *J Struct Geol* 20:1365–1393
- Cruden AR, McCaffrey KJW (2001) Growth of plutons by floor subsidence: implications for rates of emplacement, intrusion spacing and melt-extraction mechanisms. *Phys Chem Earth* 26:303–315

- Cruden A, McCaffrey K (2002) Different scaling laws for sills, laccoliths and plutons: mechanical thresholds on roof lifting and floor depression. In: Breikreuz C, Mock A, Petford N (eds) *Physical Geology of Subvolcanic Systems—Laccolith, Sills and Dykes (LASI)*, Freiberg, pp 15–17, 12–14 Oct 2002
- Dehls JF, Cruden AR, Vigneresse JL (1998) Fracture control of late Archean pluton emplacement in the northern Slave Province, Canada. *J Struct Geol* 20:1145–1154
- Dini A, Innocenti F, Rocchi S, Tonarini S, Westerman DS (2002) The magmatic evolution of the laccolith-pluton-dyke complex of Elba Island, Italy. *Geol Mag* 139:257–279
- Dini A, Corretti A, Innocenti F, Rocchi S, Westerman DS (2007) Sooty sweat stains or tourmaline spots? The Argonauts on the Island of Elba (Tuscany) and the spread of Greek trading in the Mediterranean Sea. In: Piccardi L, Masse WB (eds) *Myth and Geology*, vol 273. Geological Society, London, pp 227–243 (Special Publications)
- Dini A, Westerman DS, Innocenti F, Rocchi S (2008) Magma emplacement in a transfer zone: the Miocene mafic Orano dyke swarm of Elba Island (Tuscany). In: Thomson K, Petford N (eds) *Structure and Emplacement of High-Level Magmatic Systems*, vol 302. Geological Society, London, pp 131–148 (Special Publication)
- Dini A, Rocchi S, Westerman DS, Farina F (2009) The late Miocene intrusive complex of Elba Island: two centuries of studies from Savi to Innocenti. *Acta Vulcanologica* 20(21):11–32
- Farina F, Dini A, Innocenti F, Rocchi S, Westerman DS (2010) Rapid incremental assembly of the Monte Capanne pluton (Elba Island, Tuscany) by downward stacking of magma sheets. *Geol Soc Am Bull* 122:1463–1479
- Farina F, Dini A, Rocchi S, Stevens G (2014) Extreme mineral-scale Sr isotope heterogeneity in granites by disequilibrium melting of the crust
- Hogan JP, Gilbert MC (1995) The A-type Mount Scott Granite sheet: importance of crustal magma traps. *J Geophys Res* 100(B8):15779–15792
- Hogan JP, Price JD, Gilbert MC (1998) Magma traps and driving pressure: consequences for pluton shape and emplacement in an extensional regime. *J Struct Geol* 20:1155–1168
- Hogan JP, Gilbert MC, Price JD (2000) Crystallisation of fine- and coarse-grained A-type granite sheets of the Southern Oklahoma Aulacogen, USA. *Trans Royal Soc Edinburgh: Earth Sci* 91:139–150
- Kerr AD, Pollard DD (1998) Toward more realistic formulations for the analysis of laccoliths. *J Struct Geol* 20:1783–1793
- Malinverno A, Ryan WBF (1986) Extension in the Tyrrhenian Sea and shortening in the Apennines as result of arc migration driven by sinking of the lithosphere. *Tectonics* 5:227–245
- McCaffrey KJW, Petford N (1997) Are granitic intrusions scale invariant? *J Geol Soc, London* 154:1–4
- Menand T (2008) The mechanics and dynamics of sills in layered elastic rocks and their implications for the growth of laccoliths and other igneous complexes. *Earth Planet Sci Lett* 267:93–99
- Pandeli E, Bartolini C, Dini A, Antolini E (2010) New data on the paleogeography of Southern Tuscany (Italy) since Late Miocene time. *Int J Earth Sci* 99:1357–1381
- Paterson SR, Fowler TK Jr, Schmidt KL, Yoshinobu AS, Yuan ES, Miller RB (1998) Interpreting magmatic fabric patterns in plutons. *Lithos* 44:53–82
- Pertusati PC, Raggi G, Ricci CA, Duranti S, Palmeri R (1993) Evoluzione post-collisionale dell'Elba centro-orientale. *Mem Soc Geol It* 49:297–312
- Rechens Z, Fink J (1988) The Mechanism of intrusion of the Inyo Dike, Long Valley Caldera, California. *J Geophys Res* 93:4321–4334
- Rocchi S, Westerman DS, Dini A, Innocenti F, Tonarini S (2002) Two-stage laccolith growth at Elba Island (Italy). *Geology* 30:983–986
- Rocchi S, Westerman DS, Dini A, Farina F (2010) Intrusive sheets and sheeted intrusions at Elba Island (Italy). *Geosphere* 6:225–236
- Roni E, Westerman DS, Dini A, Stevenson C, Rocchi S (2014) Feeding and growth of a dyke-laccolith system (Elba Island, Italy) from AMS and mineral fabric data. *J Geol Soc* 171:413–424
- Saint-Blanquat Md, Habert G, Horsman E, Morgan SS, Tikoff B, Launeau P, Gleizes G (2006) Mechanisms and duration of non-tectonically assisted magma emplacement in the upper crust: the Black Mesa pluton, Henry Mountains, Utah. *Tectonophysics* 428:1–31
- Serri G, Innocenti F, Manetti P (1993) Geochemical and petrological evidence of the subduction of delaminated Adriatic continental lithosphere in the genesis of the Neogene-Quaternary magmatism of central Italy. *Tectonophysics* 223:117–147
- Westerman DS, Dini A, Innocenti F, Rocchi S (2003) When and where did hybridization occur? The case of the Monte Capanne pluton. *Atlantic Geol* 39:147–162
- Westerman DS, Dini A, Innocenti F, Rocchi S (2004) Rise and fall of a nested Christmas-tree laccolith complex, Elba Island, Italy. In: Breikreuz C, Petford N (eds) *Physical Geology of High-Level Magmatic Systems*, vol 234. Geological Society, London, pp 195–213 (Special Publication)

Progressive Construction of Laccolithic Intrusive Centers: Henry Mountains, Utah, U.S.A

Eric Horsman, Robert J. Broda, Nathan Z. Gwyn,
Elizabeth A. Maurer, Erik D. Thornton
and Mitchell T. Ward

Abstract

The intrusions of the Henry Mountains of southern Utah provide an exceptional setting for the study of igneous emplacement processes in the shallow crust. The five separate intrusive centers intruded the flat-lying stratigraphy of the Colorado Plateau at 2–4 km depth. The intrusions are Oligocene in age and postdate the minor Laramide orogenic activity that affected this part of the Colorado Plateau. These intrusions can therefore be interpreted as having formed through purely magmatic processes, with no tectonic involvement or modification. Each of the five separate intrusive centers in the Henry Mountains preserves a different stage in the evolution of an igneous system constructed in the shallow crust. Each intrusive center is comprised of numerous small intrusive bodies surrounding a large laccolithic body assembled from several magma pulses. Collectively, the five intrusive centers provide a series of snapshots of the progressive growth of an igneous system in the shallow crust. A compilation of data from these intrusive centers allows development of a generalized model for progressive construction of a magmatic system in the shallow crust. This model involves three main stages. First, an early network of dikes and sills is intruded. Second, a relatively voluminous laccolithic central igneous body begins to form. The central laccolith may initiate though inflation of a sill that grew to a radius sufficient to lift the overburden, as hypothesized in traditional growth models. However, field evidence suggests progressive laccolith growth in the Henry Mountains involved numerous rapidly emplaced magma pulses separated by periods

E. Horsman (✉) · R.J. Broda · N.Z. Gwyn
E.A. Maurer · E.D. Thornton · M.T. Ward
Department of Geological Sciences, East Carolina
University, Greenville, NC 27858, USA
e-mail: horsmane@ecu.edu

of no appreciable activity. In the final stage, satellite intrusions, many with a tongue-like geometry, are emplaced radially outward from the margin of the main laccolith, initiating in the lower hinge region where bending and fracturing of overburden is most intense. The step-wise assembly of these intrusive centers from multiple discrete pulses of magma calls into question the applicability of theoretical models of laccolith growth that presuppose the entire intrusion remains in a liquid state throughout the full emplacement history.

Keywords

Laccolith • Sill • Emplacement • Pluton • Magmatism

1 Introduction

In recent years, it has become generally accepted that many igneous intrusions in the shallow crust are assembled from a series of discrete, sequentially emplaced magma pulses, and did not exist as a single “big tank” system. While the pulsed assembly of intrusions is not a new topic (e.g. Hamilton and Myers 1967; Pitcher and Berger 1972; Hardee 1982; Wiebe 1988), recent field and theoretical work has appreciably improved our understanding of these processes by documenting the incremental assembly of intrusions over scales ranging from batholiths to individual sills (e.g. Cruden and McCaffrey 2001; Saint Blanquat et al. 2001, 2011; Glazner et al. 2004; de Silva and Gosnold 2007; Lipman 2007; Bartley et al. 2008; Vigneresse 2008; Rocchi et al. 2010). Other studies have used radiogenic isotope and chemical diffusion methods to study timescales of pulsed pluton assembly and thereby constrain magma fluxes (Coleman et al. 2004; Matzel et al. 2006; Miller et al. 2007; Walker et al. 2007; Turner and Costa 2007; Michel et al. 2008).

The utility of studying ancient igneous systems is immediately apparent when we compare results from these studies with those from geodetic studies of modern systems. Three characteristics are shared by many of the magma systems, both old and new: pulsed construction, tabular geometry, and lateral magma transport. As described above, pulsed construction of

ancient intrusions is apparent over a wide range of spatial scales. In modern systems, cyclic surficial displacement of up to a few centimeters per year is commonly observed near active volcanoes (Dzurisin 2003). This displacement occurs on timescales of months to years, even during periods of volcanic quiescence, and is commonly inferred to be the result of injection of magma bodies (e.g. Dvorak and Dzurisin 1997; Pritchard and Simons 2004a) or expansion and contraction of geothermal systems at depth (e.g. Wicks et al. 1998; Battaglia et al. 2006).

The tabular geometry of ancient intrusions is clear from 3-d reconstructions of many plutons of all sizes, irrespective of the tectonic context or composition of magmas involved (McCaffrey and Petford 1997; Petford et al. 2000; Cruden and McCaffrey 2001). Similarly, modern subsurface magma bodies commonly have shallowly dipping ($<20^\circ$), sheet-like geometries (Wicks et al. 2002; Dzurisin et al. 2006; Lundgren and Lu 2006) and lie at less than 10 km depth, with most between 3 and 6 km (e.g. Dzurisin 2003; Lu et al. 2005; Froger et al. 2006).

Finally, the importance of lateral transport of magma in the shallow crust is clear from the existence of sill complexes in many tectonic settings (e.g. Thomson and Hutton 2004; Hansen and Cartwright 2006) and the considerable distances sills can sometimes transport magma (e.g. Elliott et al. 1999). In modern systems, forward modeling of geodetic data from volcanoes suggest

dilating magma chambers that produce surface deflections may be offset many kilometers from vent regions. Offset distances are generally less than 10 km but range up to at least 13 km (Curtis 1968; Nishi et al. 1999; Nishimura et al. 2001; Lu et al. 2002; Wicks et al. 2002; Masterlark and Lu 2004; Pritchard and Simons 2004b).

The similarity between modern shallow igneous systems and their ancient counterparts suggests there is much to learn about modern systems from ancient systems and vice versa. We can observe the roots of modern volcanic systems only through indirect processes like geodesy and geophysics. While the roots of ancient systems are sometimes exposed, it is commonly difficult to study processes involved in their formation. In particular, syn-emplacement tectonic processes commonly modify or entirely overprint evidence of magmatic processes (Barbey 2009), making it difficult to study the construction of ancient intrusive systems (Paterson et al. 1998).

This paper describes examples of upper crustal igneous systems emplaced in a setting that allows for relatively straightforward interpretation of intrusive processes: the Henry Mountains of southern Utah. This region experienced effectively no syn- or post-emplacement tectonism. Additionally, the host rocks consist of initially flat-lying sedimentary rocks; all host rock deformation is due entirely to intrusive processes. This setting presents an opportunity to study pluton growth where all associated deformation and magma flow were driven solely by interaction between magma and host rock.

Perhaps the most compelling aspect of studying the Henry Mountains intrusions is the fact that igneous systems there preserve a range of total emplaced magma volume. Systems with small total igneous volumes can be interpreted as an early stage of development of a magmatic system in the shallow crust, while those with larger volumes represent more advanced stages of development. Thus the Henry Mountains provide an opportunity to piece together a progressive history of development and growth of an igneous system in the shallow crust.

2 The Henry Mountains

2.1 Regional Magmatism

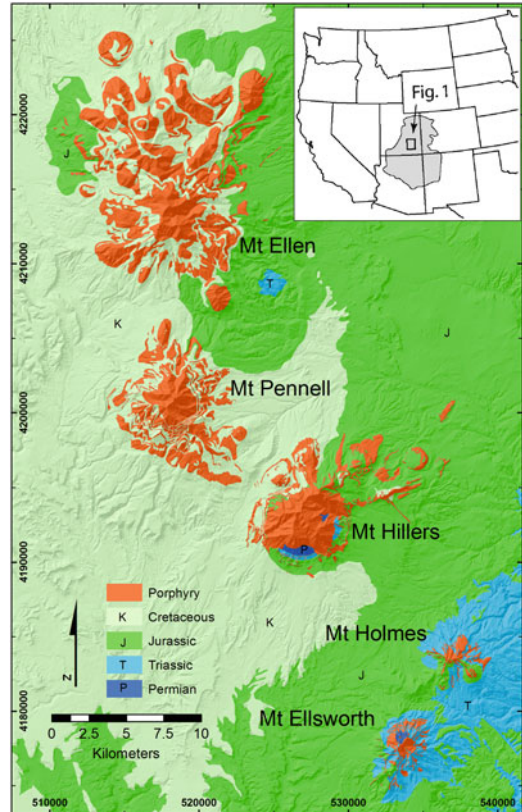
The intrusions of the Henry Mountains of southern Utah are part of a regional group of igneous complexes, all of late Eocene to Oligocene age (Nelson et al. 1992), that intruded into the shallow crust of the Colorado Plateau. Other igneous complexes of this group in the vicinity include the La Sal Mountains (Hunt and Waters 1958), the Abajo Mountains (Witkind 1964), and Navajo Mountain (Condie 1964). The main intrusions in all of these igneous complexes are generally regarded to have a laccolith geometry, with a largely concordant sub-horizontal base and a bell-shaped upper surface beneath uplifted and rotated host rock (Gilbert 1877).

Nelson and Davidson (1993) suggest all of these intrusive complexes are part of a widespread late Paleogene magmatic episode in the North American Cordillera. Although late Paleogene magmatism was voluminous around the margins of the Colorado Plateau (Armstrong and Ward 1991), magmatism on the plateau includes only a few hundred cubic kilometers of igneous rock, a considerable portion of which is now exposed in the laccolithic intrusive centers of the Henry, La Sal and Abajo Mountains.

2.2 Henry Mountains Geology

The intrusions exposed in the Henry Mountains (Fig. 1) were emplaced at $\sim 2\text{--}4$ km depth into the nearly flat-lying stratigraphy of the Colorado Plateau (Jackson and Pollard 1988). Magmatism lasted from approximately 32 to 23 Ma (Nelson et al. 1992) and postdates the relatively minor regional deformation on the Colorado Plateau during the Laramide orogeny. These temporal and spatial relationships, along with the exceptional exposure of both plutons and host rock, make the Henry Mountains ideal for examination of upper crustal magma emplacement without the complications of synmagmatic tectonic deformation.

Fig. 1 Simplified geological map of the Henry Mountains region. Modified from Hunt et al. (1953). Inset shows the location of the Henry Mountains region on the Colorado Plateau. UTM coordinates, zone 12, datum NAD83



The Henry Mountains are comprised of five intrusive centers (Fig. 1), each of which is an amalgam of smaller component intrusions (Hunt et al. 1953). Geophysical data and structural analysis of deformed host rock demonstrate that each intrusive center is a large laccolithic body with a sub-horizontal concordant base (Jackson and Pollard 1988). The first-order geometry of the intrusions in the Henry Mountains was, however, the subject of considerable debate for some time (e.g. see Jackson and Pollard 1988; Hunt et al. 1988). While this debate has been largely resolved, the differing interpretations are presented in some detail in the Discussion section below because the debate is quite instructive.

The majority of the igneous rock throughout the Henry Mountains is remarkably consistent in bulk composition. Approximately 95 % of the exposed igneous rock has a bulk andesite/trachyandesite composition, with 58–63 % SiO_2

and 5–7 % $\text{Na}_2\text{O} + \text{K}_2\text{O}$. The remaining $\sim 5\%$ of exposed igneous rock is principally rhyolite and syenite porphyry cross-cutting earlier andesitic porphyry on Mount Pennell (Hunt et al. 1953; Hunt 1988; Nelson and Davidson 1993; Ward 2014). Texturally, the dominant igneous rock is a plagioclase-hornblende porphyry. Phenocrysts generally constitute 20–35 % of the rock and consist of 15–25 % feldspar (An₂₀ to An₆₀), 5–15 % hornblende, and 1–2 % accessory minerals including clinopyroxene, titanite, apatite, oxides, quartz and calcite. The groundmass makes up 50 % or more of the rock and is composed of microlites of feldspar with a grain size of ~ 20 – $30\ \mu\text{m}$, as well as lesser amounts of amphibole and oxide grains of similar or smaller size. Xenoliths are present at many outcrops and usually comprise 1–2 % by volume. Most xenoliths are mafic (amphibolite, garnet amphibolite, tonalite) but rare sedimentary xenoliths exist, usually in close proximity to contacts with host rock.

The sedimentary section in the Henry Mountains region consists of approximately 4.5 km of Cambrian to Upper Cretaceous strata above Proterozoic-age crystalline basement (Hunt et al. 1953; Doelling 1975; Peterson et al. 1980). The lowermost known igneous intrusions of the Henry Mountains were emplaced into Permian sandstones of the Cutler Formation. The uppermost exposed igneous intrusions were emplaced into Cretaceous shale of the Blue Gate member of the Mancos Shale. The total stratigraphic thickness between the lowermost and uppermost intrusions is approximately 2700 m. At the time of emplacement, the lowermost intrusions (into Permian strata) were overlain by an estimated 3.5–4 km of sedimentary overburden (Jackson and Pollard 1988).

Host rock metamorphism in the Henry Mountains is minimal and very localized. Appreciable metamorphism (e.g. shale to slate) of sedimentary strata is found only immediately adjacent to the largest volumes of igneous rock, and is then confined to the nearest 100–200 m of strata. Adjacent to component intrusions with volumes smaller than $\sim 1 \text{ km}^3$, very little evidence of metamorphism can be found farther than a few tens of centimeters from igneous-sedimentary contacts. This lack of metamorphism implies very rapid emplacement and cooling of the magma, which is consistent with the shallow depth.

3 Snapshots of Intrusive Center Architecture

Each of the five Henry Mountains intrusive centers is cored by a broadly dome-shaped laccolithic body that has tilted and uplifted surrounding sedimentary host strata. A network of sills, dikes, and other relatively small-volume intrusions structurally overlie the main laccolithic dome. The five intrusive centers differ in the total volume of igneous rock emplaced and consequently the amount of host rock deformation. This variation in igneous volume and host rock deformation can be interpreted to represent a series of snapshots in the progressive development of an igneous system in the shallow crust. In this section, three of the

five Henry Mountains intrusive centers are described in some detail: an early-stage center (Mount Ellsworth), and intermediate-stage center (Mount Hillers), and an advanced-stage center (Mount Ellen). These descriptions focus primarily on the geometry of the intrusions and structural relationships with host rock.

3.1 Mount Ellsworth

At the Mount Ellsworth intrusive center (Figs. 2a and 3a), stratigraphy is uplifted a maximum of approximately 1800 m, and deflection from the regional bedding orientation extends over an area with a diameter of approximately 10 km (Fig. 4). The dome is slightly elliptical in plan view, with elongation in a NNE-SSW direction. Host rock strata are well preserved over much of the upper surface of the laccolithic dome. Strata dip shallowly ($<20^\circ$) atop the topographic dome and on the margins dip consistently outward, away from the center. Strata consistently dip more steeply on the northwest side of the intrusive center (maximum of $\sim 55^\circ$) than on the SE side (maximum $\sim 40^\circ$). The total igneous rock volume of the intrusive center is estimated at $\sim 18 \text{ km}^3$ based on deflection of stratigraphy from the regional orientation.

Igneous rock is exposed near the summit of Mount Ellsworth over an area of roughly 1.5 km^2 . This area is interpreted to be an exposure of the crest of the main laccolithic intrusion (Koch 1981; Jackson and Pollard 1988). On the north and west sides of the intrusive center a network of sills and subsidiary dikes is intruded into outward-dipping Permian and Triassic strata. On the south and east sides of the intrusive center, the proportional area of exposed igneous rock is less and consists largely of radial dikes, small sills, and a few irregularly shaped bodies, generally intruded into Upper Triassic and Lower Jurassic strata. Thus, the overall geometry of the igneous rock is an almost radially symmetric central laccolithic body underlying a network of sills and dikes intruded into overburden host rock strata.

The exposures on Mount Ellsworth provide clear evidence of overburden faulting during the relatively early stage of laccolith growth

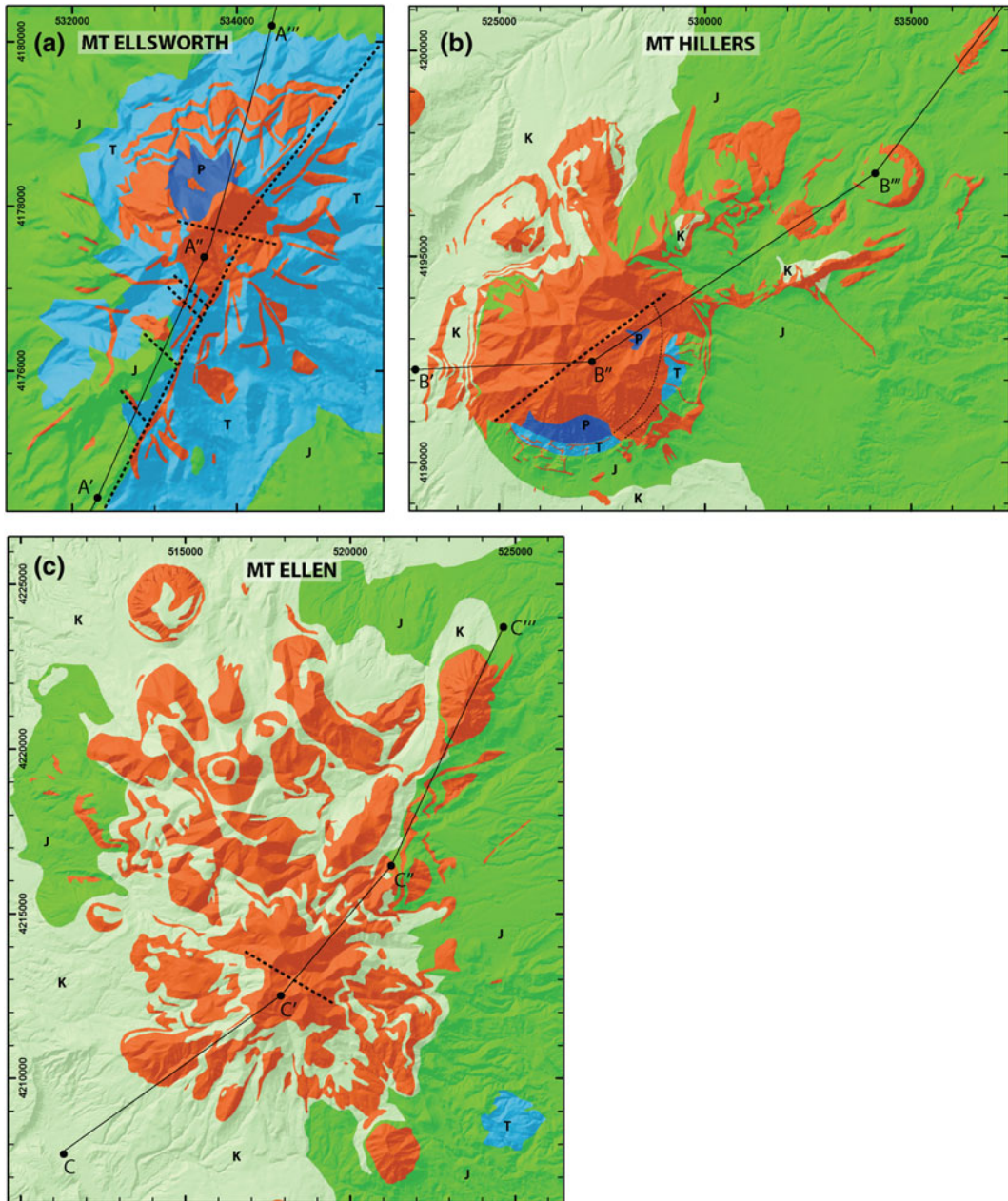


Fig. 2 Simplified bedrock geological maps of selected Henry Mountains intrusive centers. Rock unit colors correlate with those in Fig. 1. Endpoints and direction changes are indicated on each map for cross sections shown in Fig. 3. **a** Map of the Mount Ellsworth intrusive center. Modified from Koch (1981) and Jackson and

Pollard (1988). **b** Map of the Mount Hillers intrusive center. Modified from Larson et al. (1985), Broda (2014), and Thornton (2015). **c** Map of the Mount Ellen intrusive center. Modified from Dubiel et al. (1985), Morton (postdated early sills), and Maurer (2015). UTM coordinates, zone 12, datum NAD83

preserved there. One important result of the faulting is the moderately asymmetric geometry of the laccolith roof. At the same elevation near

the top of the intrusive center, older strata (Permian) are exposed in the northwestern portion of the laccolith roof than in the southeastern portion

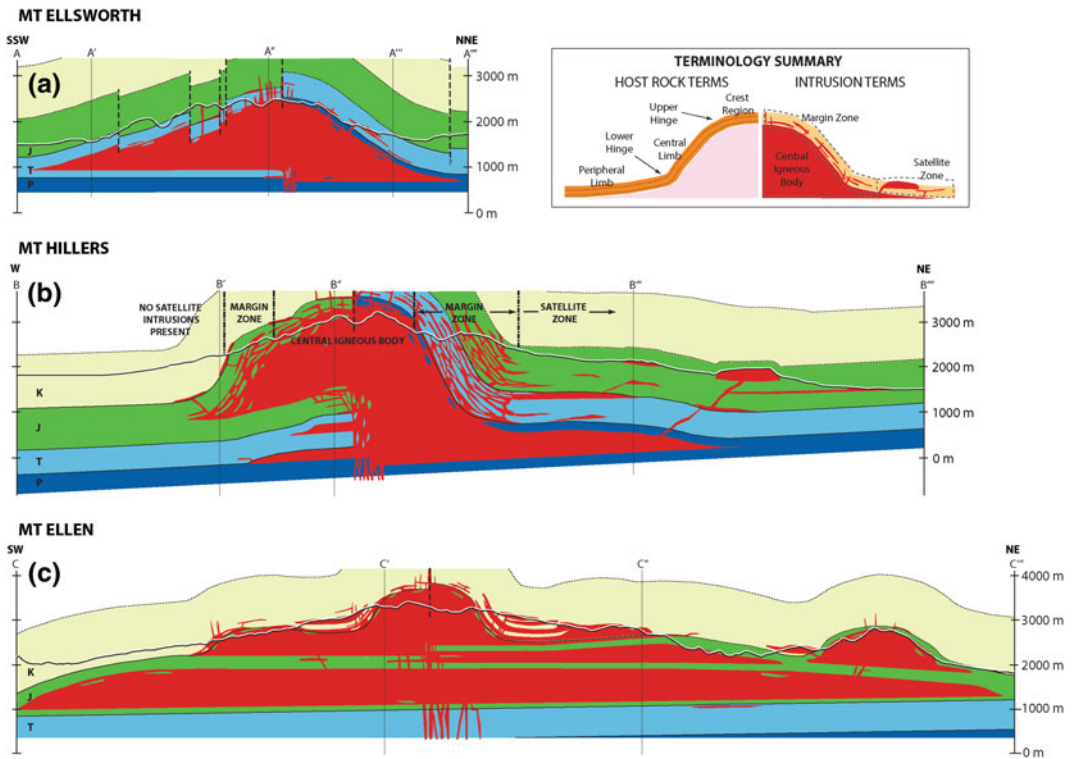


Fig. 3 Cross sections through selected Henry Mountains intrusive centers. Rock unit colors correlate with those in Fig. 2. *Thick black line* shows modern topography. Section line landmarks are indicated on both the cross sections here and maps in Fig. 2. The inset presents an outline of some basic terminology useful for description of host rock

deformation (*on the left*) and regions of a generic intrusive center (*on the right*). **a** Cross section through the Mount Ellsworth intrusive center, modified from Koch (1981). **b** Cross section through the Mount Hillers intrusive center, modified from Broda (2014). **c** Cross section through the Mount Ellen intrusive center, modified from Morton (1986)

(Triassic). These regions are separated by a fault zone (Koch 1981), and the largest component fault stretches for several kilometers in a NNE-SSW direction and has a maximum throw of over 500 m. One interpretation of these observations is that the base of the main laccolithic body is intruded at different stratigraphic levels in the northwestern and southeastern portions of the intrusive center (e.g. Fig. 3a).

In addition to the main NNE-SSW fault, several other faults offset the host rock stratigraphy of the roof with smaller amounts of throw. Vertical displacement on most faults, determined by offset of stratigraphy, increases toward the center of Mount Ellsworth. Many of the faults in strata of the laccolith roof are intruded by dikes. The greatest abundance of dikes is found near the

crest of the laccolith dome, where the maximum amount of extension is expected during inflation and growth (Pollard and Johnson 1973). Age relationships between faults and igneous bodies are complex, but generally suggest faulting postdated early sills and was contemporaneous with or older than most of the dikes (Koch 1981).

3.2 Mount Hillers

At the Mount Hillers intrusive center (Figs. 2b and 3b), stratigraphy is uplifted a maximum of approximately 2500 m, and deflection from the regional bedding orientation extends over an area with a diameter of approximately 12 km. The first-order map-view geometry of the dome is

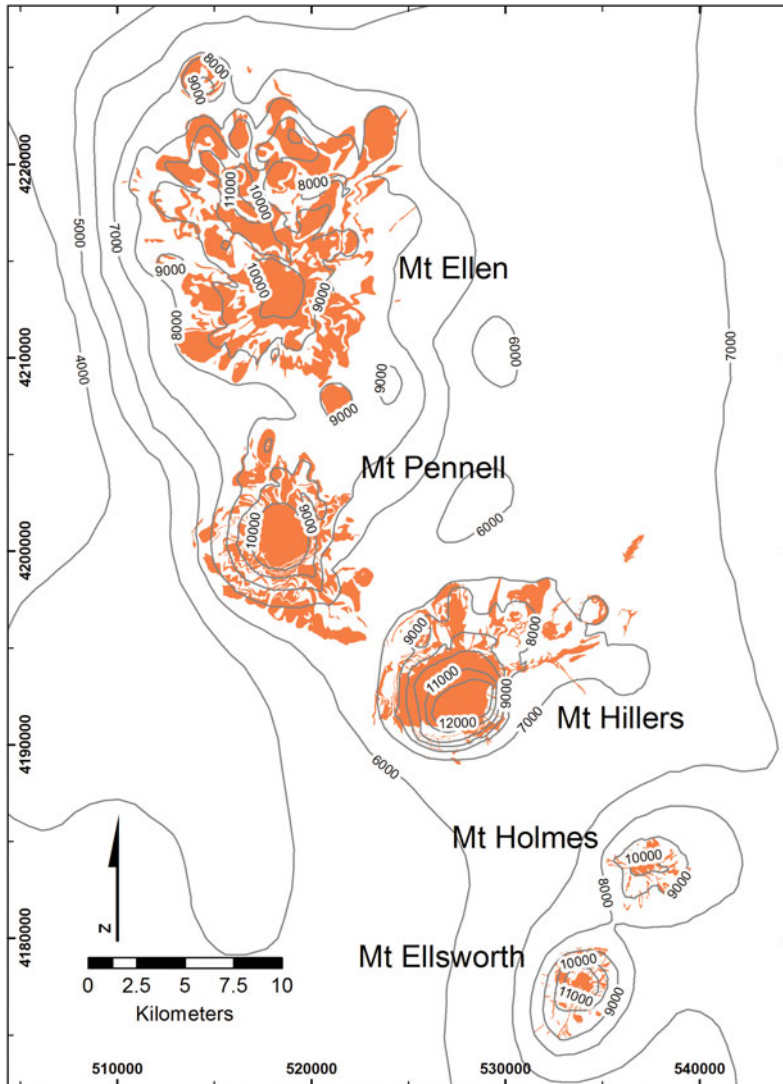


Fig. 4 Structure contour map for the Henry Mountains region. The patterns clearly show deflection of host rock from the regional shallow dip to the W due to intrusive centers. Contours are in 1000 foot intervals and are

drawn for the top of the Cretaceous Ferron sandstone member of the Blue Gate Shale. Contours simplified from Hunt et al. (1953). UTM coordinates, zone 12, datum NAD83

moderately asymmetric (Fig. 4), with elongation in a WSW-ENE direction. The maximum dip of host rock strata on the southeast side of the dome is generally steeper (maximum $\sim 90^\circ$ dip) than the northwest side (maximum $\sim 45^\circ$ dip). On the north and east sides of Mount Hillers, several smaller asymmetric domes are superimposed on the margins of the main dome. These smaller domes represent local deflection of stratigraphy

by intrusions radiating outward from the main laccolithic body. The total igneous volume of the Mount Hillers intrusive center is estimated at $\sim 35 \text{ km}^3$ (Broda 2014). Interpretation of U-Pb zircon geochronology data from 10 samples suggests assembly of the Mount Hillers intrusive center spanned no more than approximately 1 m.y., from $24.75 \pm 0.5 \text{ Ma}$ (Paquette et al. 2010).

Igneous rock is exposed over an area of $\sim 10 \text{ km}^2$ near the center of the Mount Hillers intrusive center. This igneous rock is interpreted to be part of the main laccolithic intrusion (Jackson and Pollard 1988; Broda 2014). The roof strata of the Mount Hillers laccolith are preserved locally at the crest of the dome, where they dip shallowly ($<20^\circ$). The geometry of the host rock strata implies the laccolith is asymmetric in cross section. On the SE side of the intrusive center, the upper contact of the main laccolithic body lies within the upper portion of Permian strata. On the NW side of the intrusive center, the upper contact of the main laccolithic body lies within Jurassic strata, approximately 1000 m higher in the stratigraphic section (Broda 2014). Assuming these strata record the stratigraphic level of the main laccolith, the intrusion must have a highly asymmetric base that is approximately 1000 m deeper in the crust on the southeast portion than the northwest portion of the intrusion. This geometry is different from the symmetrical interpretation favored by previous authors (cf. Gilbert 1877; Hunt et al. 1953; Jackson and Pollard 1988), but is based on considerably more detailed mapping.

Faulting of preserved host rock strata overlying the main laccolith dome is readily apparent in some locations. Most prominently, the distinct regions of the main Mount Hillers laccolith, with different strata preserved and bedding dips, are interpreted to be separated by a SW- to NE-striking subvertical tear fault (Broda 2014). Smaller faults, both radial and tangential, are apparent from local offset or repetition of stratigraphic units. The boundary zones between repeated or missing units are commonly filled with igneous rock, which presumably intruded along faults. The strata immediately overlying the crest of the laccolith dome are modestly metamorphosed (e.g. shale to slate, sandstone to quartzite), but individual sedimentary units are clearly recognizable.

The strata deflected from their regional orientation by the main structural dome of the Mount Hillers intrusive center are locally very well exposed. For example, on the south and east sides of the intrusive center, strata from Permian

to Cretaceous age dip consistently outward from the center of the dome and are intruded by a network of sills and dikes (Thornton 2015). The boundary is diffuse between this region of both sedimentary and igneous rock and the inner region of solely igneous rock, which is inferred to be the main laccolith body. Along a radial profile, the relative abundance of igneous rock increases toward the center of the structural dome, which corresponds to deeper levels in the outward-dipping stratigraphic section. However, an abrupt increase in the relative abundance of igneous rock occurs within Permian-age strata of the Cutler Formation. No host rock strata from deeper in the stratigraphic section are exposed, leading to the conclusion that this is the stratigraphic level of the main laccolith intrusion on the SE side of the tear fault that divides the intrusive center.

3.3 Mount Ellen

The Mount Ellen intrusive center (Figs. 2c and 3c) is the largest of the Henry Mountains in aerial extent and igneous rock volume. In general, the Mount Ellen intrusive center is more deeply eroded and somewhat less well exposed than the two centers already described. However, the basic geometries of component igneous bodies can be constrained, and exposure of both igneous and sedimentary rock is locally excellent. Stratigraphy is uplifted a maximum of approximately 2000 m over a region with a diameter of 15–20 km (Fig. 4). The dome is elongated in map view in a NW-SE direction, but numerous relatively small (usually $<3 \text{ km}$ across) bulges project radially outward from the main dome. The total igneous volume responsible for the doming is estimated at approximately 100 km^3 .

The oldest sedimentary rocks exposed within and deformed by the Mount Ellen intrusive center are sandstones of uppermost Triassic to lowermost Jurassic age, which are locally exposed near the outer perimeter of the structural dome. The deepest intrusions must therefore be within or below Triassic strata. Morton (1984, 1986) hypothesized that unexposed intrusions of

the Mount Ellen intrusive center emplaced relatively deep in the crust have generally sill-like shapes, while those emplaced into younger strata tend to have more convex roofs (e.g. Fig. 3c). Similar to the smaller intrusive centers, strata generally dip outward from the middle of the intrusive center, but local variation from this trend is common around relatively small component intrusive bodies. Exposures are generally insufficient to recognize faulting of sedimentary host rock like that observed at the Mount Ellsworth and Hillers intrusive centers. However, in the exposure area interpreted to be at the core of the main laccolithic dome (near location C' on Figs. 2c and 3c), the contact between igneous and sedimentary rock is locally discordant (Hunt et al. 1953) and a steeply dipping tear fault with a throw of 200 m or more is probably the simplest explanation. This geometric complexity suggests the central igneous intrusion is asymmetric in cross section and that emplacement was locally accommodated by faulting.

More generally, the geometry of the upper surface of igneous rock at the Mount Ellen intrusive center, as inferred from deflection of stratigraphy, is considerably more complicated than at any of the four smaller-volume intrusive centers of the Henry Mountains (Fig. 4). The NW- to SE-elongated central dome is surrounded in nearly all directions by numerous radiating tongue-shaped lobes, which in some cases extend outward several kilometers from the main dome. Deflection of stratigraphy suggests individual radiating intrusions have volumes ranging up to approximately 3 km³ (Copper Ridge laccolith—Maurer 2015). In some cases, these radiating intrusions are themselves assembled from multiple component magma pulses (Maurer 2015).

4 Discussion

The three Henry Mountains intrusive centers described here can be interpreted as snapshots in the progressive construction of an igneous system in the shallow crust through emplacement of multiple component pulses of magma. The total

igneous rock volume for each intrusive center (see Table 1) can therefore be used as a rough measure of the degree of development. The Mount Ellsworth intrusive center, with the smallest igneous rock volume of the three described in detail above, then represents a relatively early stage of development of a generalized igneous center. The Mount Hillers intrusive center represents an intermediate stage of development in which host rock has been uplifted and deformed considerably more, and additional lobes of magma began to intrude radially outward from the margin of the main laccolithic body. The Mount Ellen intrusive center records an advanced stage of development, with a relatively voluminous and geometrically complex central laccolithic body and radiating intrusions extending out in nearly all directions.

Previous authors working in the Henry Mountains also interpreted the intrusive centers to represent different stages along a progression of growth (Hunt et al. 1953; Jackson and Pollard 1988). However, earlier interpretations of first-order intrusion geometries differed from those favored here, in some cases considerably. Therefore, to provide context for the interpretations favored here, a brief review of previous authors' interpretations is presented here.

4.1 Earlier Interpretations of Intrusive Center Geometry and Development

The subsurface geometry of the intrusions in the Henry Mountains has been the subject of long-standing debate. The first-order laccolithic geometry of igneous intrusions in the Henry Mountains was initially proposed by Gilbert (1877), who coined the term “laccolite” based on his observations there. He hypothesized a two-stage laccolith emplacement process where an initial sill grew laterally until it reached a critical radius, where horizontal spreading ceased and the roof began to inflate, uplifting and rotating overlying host rock. The end result was an intrusion with a subhorizontal base and a dome-shaped roof (Fig. 5a).

Table 1 Characteristics of Henry Mountains intrusive centers

Intrusive center	Development stage	Approx. igneous volume (km ³)	Approx. diameter (km)	Max. vertical deflection (m)	Central limb, max. bedding dip	Satellite intrusions?
Mt Holmes	Early	18	9	~1200	~25°	No
Mt Ellsworth	Early	23	10	~1800	~55°	No
Mt Pennell	Intermediate	30	12	~2000	~80°	Yes, N and E sides
Mt Hillers	Intermediate	35	12	~2500	~90°	Yes, N and E sides
Mt Ellen	Advanced	100	20	~2000	~90°	Yes, all directions

In contrast to Gilbert's (1877) interpretation, the broad domal geometry of each intrusive center was hypothesized by Hunt et al. (1953) to be result of radial expansion of a highly discordant stock. In this emplacement model, a sub-vertical cylindrical stock intruded early in the history of each intrusive center and expanded radially, uplifting and bending the host strata into the domal pattern observed (Fig. 5b). The intrusive volume estimates provided in Hunt et al. (1953) rely on this concept of a central stock extending to considerable depth and are therefore inaccurate (Koch 1981).

One of the major observations used by Hunt et al. (1953) to prefer the stock model over Gilbert's (1877) original laccolith model is the locally discordant nature of the major contact between the main central igneous body and overlying host rock. To reach this conclusion, Hunt et al. (1953) relied on an idealized model of a laccolith that always remains concordant, with a smooth domed roof, despite acknowledging that some laccoliths are in fact asymmetric and discordant (see their Fig. 66). As described in detail above, the main laccolith bodies in the Henry Mountains are locally discordant, especially near the centermost region of the roof of each intrusive center, where radial and tangential faulting related to extension of the host rock is common. In each of the cases described here, different host rock units in the main laccolith roof

are juxtaposed across a fault zone. This geometry suggests the base the main laccolith body lies at different stratigraphic levels in different regions of the intrusive center (e.g. Fig. 3).

Another feature of each intrusive center original described by Hunt et al. (1953) is a so-called "shatter zone" generally located around the margin of the regions they mapped as stocks. This term should be abandoned, both because it unnecessarily implies a genesis process (fracturing) and because it misleadingly suggests the areas are chaotic. Careful mapping demonstrates that the region in question in each intrusive center is comprised of numerous igneous sheets and occasional intercalated sedimentary rock bodies, still in correct stratigraphic order (e.g. Ward 2014; Broda 2014). While igneous breccias and other evidence of fracturing during emplacement do exist, they are relatively rare and always localized. To avoid further confusion, we use descriptive terminology for intrusive center architecture rather than terms implying genetic processes for Henry Mountains intrusions.

The two models (laccolith vs. stock) for the first-order geometry of Henry Mountains intrusions were tested by Jackson and Pollard (1988, 1990). Detailed host rock mapping and structural analysis led to an interpretation more in agreement with the laccolith model of Gilbert (1877)—i.e. the five intrusive centers are largely concordant "floored" laccoliths and not stocks (Fig. 5c).

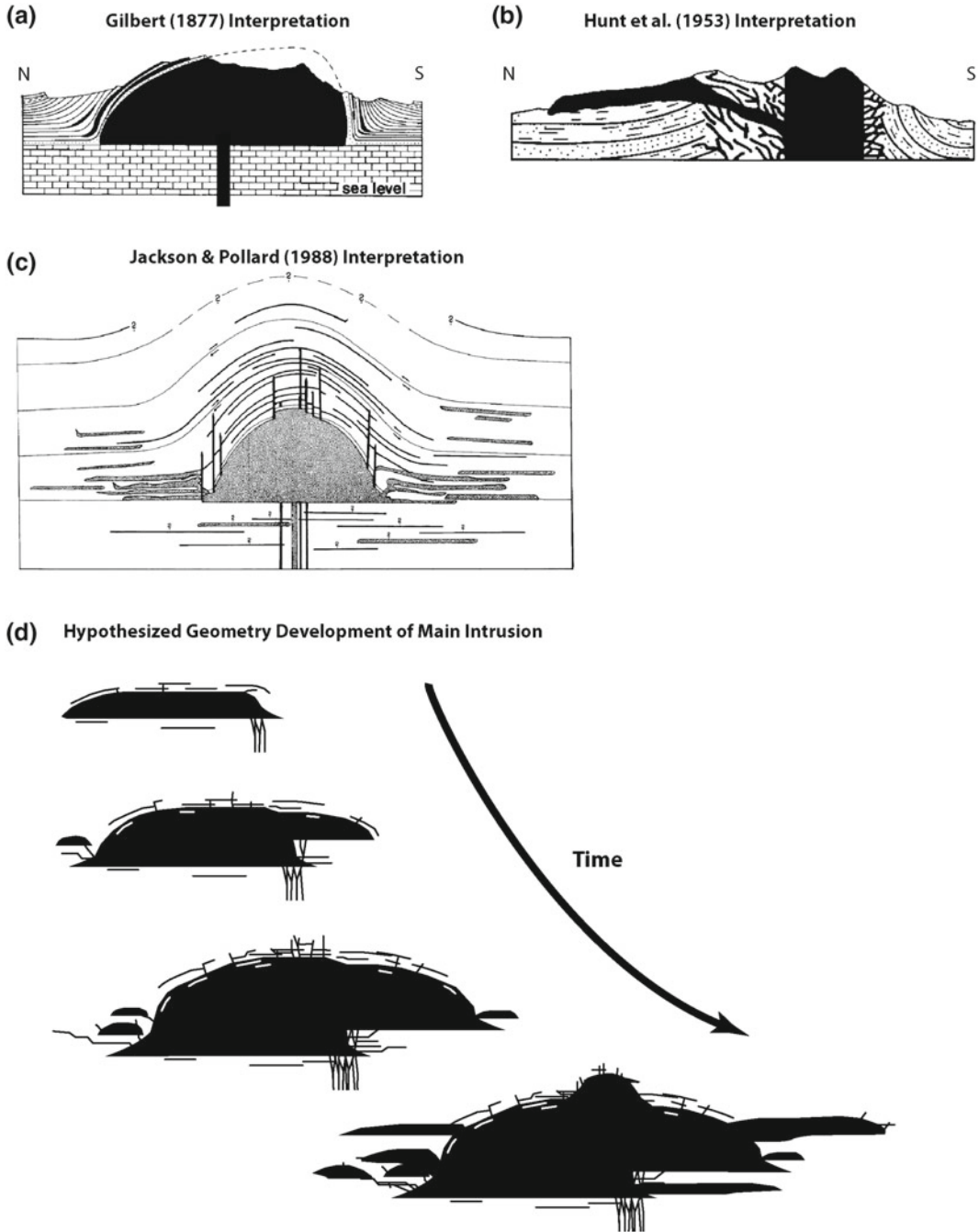


Fig. 5 Evolution of hypotheses about Henry Mountains intrusion center cross sectional geometry. **a** Idealized geometry of the Mount Hillers intrusive center, presumably along a general N to S profile. The main intrusion has classic laccolith shape with a planar concordant floor and a domed roof, and no satellite intrusions are shown. Modified from Gilbert (1877). **b** Schematic geometry of the Mount Hillers intrusive center along a general N to S profile. The main intrusion is a discordant stock surrounded by a “shatter zone,” and a prominent and

voluminous satellite intrusion extends laterally outward. Modified from Hunt et al. (1953). **c** Idealized geometry of a generic Henry Mountains intrusive center. The main intrusion has a classic laccolith shape, but it is surrounded by an extensive network of sills and dikes. Modified from Jackson and Pollard (1988). **d** Hypothesized evolution of cross sectional geometry of the main intrusive body and directly associated intrusions for a generic intrusive center in the shallow crust. Based on interpolation from geometries of Henry Mountains intrusive centers

One especially important observation from Jackson and Pollard (1988) was that radial expansion of a stock would result in buckling of strata in cross-sectional view, rather than the geometrically simpler bending pattern observed (see their Fig. 18). Jackson and Pollard (1988) also suggested, based on analysis of a limited suite of paleomagnetic data, that steeply dipping sills on the margins of the Mount Hillers intrusive center cooled while still sub-horizontal and were rotated by later underlying intrusions. Although earlier workers inferred that multiple injections of magma were responsible for assembly of each Henry Mountains intrusive center, this observation provided the first evidence of a protracted, pulsed emplacement history.

4.2 Generalized Architecture of an Intrusive Center

The general structure of a generic, fully developed Henry Mountains intrusive center can be divided into three regions (see inset on Fig. 3). However, as we describe below in the more detailed descriptions of these regions, not all of the intrusive centers reached a state of development in which all three regions are developed (Table 1). The most voluminous part of an intrusive center is the *central laccolithic body* (generally analogous to the area mapped as “stock” by Hunt et al. 1953), which has an overall domal, laccolithic geometry. Surrounding the central intrusion is a *margin zone* of host rock intruded by a complex network of sills, dikes, and other relatively small igneous bodies. Around the margin of the intrusive center is a *satellite zone*, including relatively small sills, laccoliths and other bodies generally intruded into shallowly dipping host rock. The satellite intrusions are fed from the central intrusion, but are not always physically connected to it at the surface. Mount Hillers includes well-developed and well-exposed examples of all three component zones (e.g. Fig. 3b). The other two large intrusive centers, Mounts Ellen and Pennell, also include examples of all three component zones.

The two smaller centers, Mounts Holmes and Ellsworth, are preserved at an earlier stage of development and do not include any significant satellite intrusions.

4.3 Central Laccolithic Body

The central laccolithic body in each intrusive center in the Henry Mountains generally has a bell-shaped upper surface in cross section. This geometry can be seen most clearly by studying deflection of host rock strata (see inset on Fig. 3). Along a radial profile from the outside of the dome toward the inside, the geometry of the host rock overlying a laccolithic intrusion typically includes a shallowly dipping *peripheral limb*, a more steeply dipping *central limb*, and a relatively shallow-dipping crest region atop the laccolith (Jackson and Pollard 1988, 1990). These three regions are typically separated by two hinges: a *lower hinge* between the peripheral and central limbs, and an *upper hinge* between the central limb and the *crest region*. In the host rock overlying the main laccolith body, curvature is higher and fracturing more intense in these hinge regions than in the adjacent limbs (Jackson and Pollard 1990). Minor faulting is observed throughout the deformed host rock, but faulting is especially well-developed in the crest region. There, faults juxtapose host rock of different stratigraphic level and are commonly intruded by dikes. Roof faulting appears to be an important process in laccolith dome growth, and faulting has long been recognized as an important mechanism for accommodation of magma emplacement (e.g. Grocott et al. 2009; Kloppeberg et al. 2010). As first noted by Gilbert (1877), roof faulting is required to accommodate the extension of strata above a growing laccolith (e.g. Pollard and Johnson 1973).

The lower surface of the central laccolithic body is never exposed in the Henry Mountains. However, constraints on the general geometry of this surface are available from two independent data sets. The lower surface of each central laccolithic body appears to be largely concordant

with sub-horizontal host rock strata based on interpretation of aeromagnetic data (e.g. Jackson and Pollard 1988). In more detail, however, careful mapping and structural analysis of preserved host rock strata (e.g. Broda 2014) suggest the base of each main laccolithic body is stepped. The inferred height of the floor step follows from the stratigraphic separation between sedimentary units juxtaposed in the laccolith roof. For the three intrusive centers described in detail here, this inferred floor step height ranges from ~ 200 m at Mount Ellen (on Fig. 3c, Jurassic and Cretaceous strata are juxtaposed in the roof) to ~ 500 m at Mount Ellsworth (on Fig. 3a, Permian and Triassic strata are juxtaposed) and ~ 1000 m at Mount Hillers (on Fig. 3b, Permian and Jurassic strata are juxtaposed).

Each central laccolithic body is comprised almost exclusively of igneous rock. The only exposed sedimentary material is generally metamorphosed xenoliths up to a few centimeters in size, and these are rare. The texture of the igneous rock sometimes changes dramatically over spatial distances of just a few meters (Broda 2014), with distinct differences in phenocryst abundance, mean phenocryst size, and ground-mass grain size. In some cases these changes are gradual but in most instances a clear contact exists. Cross-cutting relationships between distinct textures are usually complex, but in some cases consistent relative ages of two different textures can be inferred (e.g. Ward 2014). The variation in textures within each central laccolithic body suggests it was assembled from the emplacement of separate magma pulses (e.g. Pownall et al. 2012), with sufficient time in some cases between injections for earlier pulses to cool enough that magma mingling is minimal or non-existent.

4.4 Margin Zone

The margin zone of each intrusive center includes a complex, but not chaotic, intermingling of igneous rock and sedimentary host rock. Blocks of isolated sedimentary rock are almost always found in the correct stratigraphic order

when moving from the margin to the core of each intrusive center. Similar isolated blocks or “rafts” of sedimentary strata were identified in 3-d well data from laccoliths of the Halle Volcanic Complex in Germany by Schmiedel et al. (2015). The 3-d well data allowed these authors to recognize that many of the sedimentary rock rafts are prolate in geometry and up to 1400 m long and 500 m thick. No clear pattern of raft size or geometry is immediately apparent in the Henry Mountains.

The transition between the margin zone and the central laccolithic body is gradual. Toward the core of the intrusive center exposures of sedimentary host rock become progressively less abundant relative to igneous rock. The exceptional exposure of the host rock strata overlying the crest of the main laccolithic body at Mount Ellsworth suggests that sills and dikes of the margin zone are developed over essentially the entire bell-shaped upper surface of the laccolith dome. Similar exposures at the Mount Holmes intrusive center are consistent with this observation (unpublished mapping by Murdoch 1984; Jackson and Pollard 1988).

Taken together, these data suggest that the dip of sedimentary strata and sills in the margin zone varies both in space and time. At a given stage in the development (e.g. as observed at a single intrusive center in the Henry Mountains) the dip profile along a radial section is bell-shaped, with a shallow dip on the peripheral limb, a steeper dip on the central limb, and once again a shallow dip over the crest of the laccolith dome. Comparing dip profiles between different time steps (preserved at different intrusive centers), the dip of the central limb appears to increase along with the igneous volume of the central laccolithic body. The dip within the peripheral limb and crest region appears to remain relatively shallow throughout the growth of the dome.

Evidence of any appreciable amount of host rock metamorphism is absent throughout most of the margin zone. This situation changes considerably in close proximity to the central laccolithic body. Typically, within the 100–200 m of stratigraphic section immediately above the exposed outer margin of the main laccolithic

body, the degree of host rock metamorphism increases substantially. In this region shale has been metamorphosed to slate and sandstone to quartzite. An excellent example of this concentrated zone of metamorphism is preserved on the south side of Mount Hillers (Thornton 2015), where Permian-age strata form the roof of the main laccolithic body. There sedimentary host rock within the ~100–200 m of strata structurally overlying the intrusion has undergone considerable metamorphism. The transition to relatively unmetamorphosed sedimentary rock is narrow but gradual; farther from the main intrusion host rock shows little or no field evidence of metamorphism.

Large portions of the margin zone were generally included in the so-called “shatter zone” of Hunt et al. (1953). The outer edge of each shatter zone mapped by Hunt et al. (1953) was drawn at the base of an arbitrarily chosen sedimentary unit (e.g. the Triassic Chinle formation on Mount Hillers, Hunt et al. 1953). More detailed mapping (e.g. Gwyn 2011; Ward 2014; Broda 2014) reveals a clearer general architecture that in turn provides better constraints on the construction history.

4.5 Satellite Zone

The satellite zone lies outside the margin zone and, where present, typically includes a series of isolated, relatively small-volume intrusions (generally $<3 \text{ km}^3$) distributed outside the edge of the main laccolith dome. These intrusions lie within shallowly dipping ($<20^\circ$) host rock strata of the peripheral limb, usually within the 2–3 km immediately outside the lower hinge region. The Trachyte Mesa intrusion (Morgan et al. 2008; Wetmore et al. 2009) of the Mount Hillers intrusive center is a notable exception, being located ~10 km from the nearest exposures of intrusions in the main laccolithic body or margin zone.

The satellite zone is not developed at the two smallest volume Henry Mountains intrusive centers, Mounts Holmes and Ellsworth. These two main laccolithic domes are relatively smooth and do not show evidence either at the surface or at

depth of smaller, second-order intrusions around their margins (Fig. 4). Perhaps the emplacement of satellite intrusions proceeds only when the main laccolithic dome has grown enough that further bending and uplift of host rock to accommodate emplacement of new magma becomes mechanically unfavorable compared to injection around the heavily fractured lower hinge region. This general spatial and temporal pattern was observed by Henry et al. (1997) in the Solitario lacco-caldera of the Trans-Pecos region. There emplacement of satellite intrusions occurred during the final stage in the episodic magmatic history of the intrusive center and was localized in the vicinity of the ring fault bounding an earlier caldera.

The satellite zone does exist at the two intermediate-stage intrusive centers, Mounts Hillers and Pennell. There the first-order laccolithic domes each have superposed on them a few second-order tongue-shape bodies protruding radially outward (Fig. 4). Some of these bodies have inflated enough to dome overlying strata. In these cases strata along the distal margin dip away from the intrusive center and strata above the proximal margin commonly dip back toward the intrusive center (Hunt et al. 1953). In a few cases, these bodies have inflated enough to develop in to bysmaliths, which lift overlying host rock in a piston-like manner (e.g. Saint Blanquat et al. 2006). Many of the tongue-shaped bodies can be directly connected with the larger main laccolithic body, and are clearly fed laterally. A similar overall lobate geometry was inferred for the Trawenagh Bay Granite (Stevenson et al. 2007). Lobate growth has also been observed in analog models of laccolith emplacement (Currier and Marsh 2015).

The progressive growth of satellite intrusions on Mount Hillers was studied in detail by Horsman et al. (2010). Exceptional 3-d exposure of the satellite intrusions there allowed development of a general construction history through detailed analysis of bodies with different geometries. The intrusion shapes are interpreted as snapshots of the progressive development of an initially tabular igneous body in the shallow crust. In the earliest stage of development, intrusions initiate as sills with complex, lobate,

map-view geometries (Horsman et al. 2005). Many of these relatively small intrusions are constructed from multiple magma pulses intruded as component sills. The initial pulse closely controls the geometry of subsequently pulses due to introduction of strong mechanical anisotropy. Magma flow patterns are closely related to details of intrusion geometry and radial or fanning patterns are common. In the next stage of evolution, a laccolith shape develops as additional magma sheets are emplaced (Morgan et al. 2008; Wetmore et al. 2009). Sheet boundaries can be recognized near fast-cooling intrusion margins but become more cryptic in the slower cooling center of the body. Magma flow patterns commonly include a central conduit that feeds flow toward the laterally growing margins of the intrusion. In the final stage, as still more magma intrudes, the body becomes over-inflated and may develop into a bysmalith by lifting overlying host rock in a piston-like manner along a cylindrical fault (e.g. Saint Blanquat et al. 2006). Magma flow patterns become simpler and more consistent as intrusion geometry stabilizes, with a central conduit again feeding magma to intrusion margins. The work of Maurer (2015) largely supports this general model.

4.6 Stocks or Laccoliths?

The new detailed mapping of the Henry Mountains discussed here suggests the first-order geometry of the central laccolithic body in each of the five intrusive centers is neither a fully discordant stock, as proposed by Hunt et al. (1953), nor an idealized concordant and axisymmetric laccolith, as proposed by Pollard and Johnson (1973) and Jackson and Pollard (1988). Instead, each intrusive center is cored by a main laccolithic body with a slightly to moderately asymmetric cross sectional geometry. Clear evidence of the cross-sectional asymmetry of each intrusive center is given by the different stratigraphic units juxtaposed near the crest of the main laccolithic body. This crest region is where radial and tangential faulting would be

concentrated during doming of overburden (e.g. Jackson and Pollard 1990). These faults were apparently exploited as preferential magma migration pathways, leading to a concentration of dikes and other more discordant bodies near the crest of each intrusive center.

Localization of faulting and dike intrusion near the crest of each main laccolith likely occurred throughout a considerable portion of the assembly history. Consequently, breccias incorporating both sedimentary and igneous clasts, as well as other evidence of brittle fracture processes, are concentrated near the core of each intrusive center. These observations led Hunt et al. (1953) to interpret the presence of a “shatter zone” near the core of most of the intrusive centers, which they attributed to radial expansion of the hypothesized central stock. These regions, however, are better interpreted as areas of concentrated, repeated magma intrusion and local faulting during progressive growth of the first-order laccolith dome.

4.7 Progressive Growth of Intrusive Centers

The synthesis of observations presented here allows an interpretation of the geometric development of a generalized Henry Mountains intrusive center during its progressive growth. Two essential aspects of the assembly process in the Henry Mountains were recognized by previous workers. First, each intrusive center was assembled from numerous sequentially emplaced component intrusions, or magma pulses (Hunt et al. 1953; Hunt 1988). Second, early sub-horizontal sills were rotated upward by later, underlying intrusions to create the observed large and complex, but broadly laccolithic, shapes (Jackson and Pollard 1988).

The three intrusive centers described in detail here can be interpreted to represent snapshots of distinct stages in the progressive assembly of a laccolithic igneous system in the shallow crust. The Mount Ellsworth intrusive center represents a relatively early stage of development, after initial uplift and rotation of the overburden host strata has

started. The upper surface of the main laccolithic body has a bell-shaped geometry in cross section, but the amplitude of uplift is relatively small compared to the area over which strata are deflected. The juxtaposition of different sedimentary units at the same elevation at the crest of the laccolith dome suggests portions of the main intrusion have different thicknesses. This thickness variation is likely due to the base of the laccolith having intruded at different stratigraphic levels in the distinct portions of the body.

A well-developed margin zone exists at the Mount Ellsworth intrusive center, with a network of sills dipping away in all directions from the middle of the intrusive center. Dikes near the summit of Mount Ellsworth clearly cross cut earlier altered porphyry bodies, suggesting dike ascent in that region persisted until relatively late in the laccolith growth history. No dikes or satellite intrusions are exposed on the periphery of Mount Ellsworth and none in the subsurface are apparent from deflection of overlying host rock strata (Fig. 4). No evidence of intrusions of any geometry exists above the well-preserved outer hinge of the main laccolith dome, where most satellite intrusions on other intrusive centers seem to emerge from the central igneous body. This suggests that at this stage of laccolith dome development it is still more mechanically favorable to accommodate additional magma through further uplift of the main roof than through ascent in the fracture networks in the lower hinge region (e.g. Jackson and Pollard 1990).

The Mount Hillers intrusive center represents an intermediate stage of development. The central laccolithic body there is clearly comprised of multiple magma pulses with distinct, cross-cutting textures (Broda 2014). Each significant pulse was probably a few cubic kilometers in volume. The upper surface of the main laccolith is bell-shaped, but has a larger ratio of amplitude to width than the less mature Mount Ellsworth intrusive center. Sedimentary strata from different stratigraphic levels are juxtaposed at the crest of the main laccolith across a fault zone, again suggesting the presence of topography on the base of the intrusion. A well-developed margin zone surrounds the entire intrusive center. Satellite intrusions are

present around the NE half of the intrusive center, but are essentially absent on the SW side. The volume of these satellite intrusions can be as large as $\sim 1.5\text{--}2\text{ km}^3$, although many are considerably smaller.

The Mount Ellen intrusive center represents the most advanced stage of development present in the Henry Mountains. The overall geometry of the main laccolith dome is generally similar to the intermediate stage of development preserved at Mount Hillers, although at Mount Ellen the crest of the dome is elongated in a NW-SE direction, instead of being nearly axisymmetric. The satellite zone, however, is very different from the less developed intrusive centers, with many more intrusions and a much larger areal extent and total igneous rock volume. Satellite intrusions extend out in all directions from the central intrusive body at Mount Ellen (cf. Currier and Marsh 2015), whereas at Mount Hillers they are restricted in radial direction. The satellite zone at Mount Ellen is so much more advanced in development that it somewhat obscures the geometry of the central laccolithic body. Magma feeding the most distal satellite intrusions, if fed primarily from the central laccolithic body, must have travelled laterally several kilometers (e.g. Magee et al. 2012). In cross section, the Mount Ellen intrusive center is quite similar to the geometry of the Elba Island laccolith complex (e.g. Rocchi et al. 2010).

The duration of assembly of the Henry Mountains intrusive centers is not yet well constrained by geochronology. However, a limited dataset suggests the Mount Hillers intrusive center was assembled over approximately 1 m.y. (Paquette et al. 2010). The Christmas-tree-shaped laccolith complex on Elba Island, Italy was assembled in stages over a similar period of time (Rocchi et al. 2010). The laccolith-caldera system of the Solitario in the Trans-Pecos region was also assembled in stages over approximately 1 m.y. (Henry et al. 1997). The magma fluxes implied by the total volumes of these intrusions and the duration of assembly agree well with typical fluxes estimated for magma emplacement in continental crust in a wide variety of tectonic settings (Saint Blanquat et al. 2011).

5 Conclusions

The Henry Mountains of southern Utah provide an opportunity to study in detail the development of magmatic systems in the shallow crust driven solely by magmatic processes. The complications commonly associated with syn-tectonic magma emplacement are absent. The region can therefore serve as a relatively simple, end-member example of magma emplacement processes in the shallow upper crust.

Each of the five separate intrusive centers in the Henry Mountains preserves a different stage of the evolution of an igneous system constructed in the shallow crust. Each intrusive center is comprised of numerous small intrusive bodies surrounding a central laccolithic body assembled from several magma pulses. Collectively, the five intrusive centers provide a series of snapshots of the progressive growth of an igneous system in the shallow crust. A compilation of data from these intrusive centers allows development of a generalized model for progressive construction of a magmatic system in the shallow crust. This model involves three main stages. First, an early network of dikes and sills is intruded. Second, a relatively voluminous laccolithic central igneous body begins to form. The central laccolith may initiate though inflation of a sill that grew to a radius sufficient to lift the overburden, as hypothesized in traditional growth models. However, field evidence suggests progressive laccolith growth in the Henry Mountains involved numerous rapidly emplaced magma pulses separated by periods of no appreciable activity. In the final stage, satellite intrusions, many with a tongue-like geometry, are emplaced radially outward from the margin of the main laccolith, initiating in the lower hinge region where bending and fracturing of overburden is relatively intense. As additional magma is emplaced into an advanced-stage intrusive center, the satellite zone expands laterally and perhaps vertically while the geometry of the main laccolithic body remains essentially unchanged.

One important question raised by this work is whether or not theoretical models of laccolith

initiation and growth are applicable to these intrusive centers. In particular, the intrusive centers in the Henry Mountains and elsewhere appear to have been assembled from multiple discrete pulses of magma, many of which may not have been liquid at the same time. This observation calls into question the applicability of theoretical models of laccolith growth that presuppose the entire intrusion remains in a liquid state throughout the entire history (e.g. Pollard and Johnson 1973; Bungler and Cruden 2011). Interestingly, the geometric predictions of the models (e.g. bell-shaped upper laccolith surface) generally agree well with observations in the Henry Mountains, despite the apparent disconnect between the inferred step-wise assembly of the intrusions and the single-magma-body assumption of the models.

Acknowledgements The authors are very appreciative for the helpful reviews of this manuscript provided by Christoph Breitzkreuz and Christopher Henry. Funding for this work was provided by National Science Foundation grant EAR-1220318 and the U.S. Geological Survey EDMAP program to EH. Additional funding was provided by Geological Society of America Student Research Grants to EM and MW, and Sigma Xi Grants-in-Aid of Research to NG and ET. Many thanks for helpful conversations are due to Michel de Saint Blanquat, Sven Morgan, Scott Giorgis, Thierry Menand, and Paul Wetmore.

References

- Armstrong RL, Ward P (1991) Evolving geographic patterns of Cenozoic magmatism in the North American Cordillera: the temporal and spatial association of magmatism and metamorphic core complexes. *J Geophys Res Solid Earth* 96:13201–13224
- Barbey P (2009) Layering and schlieren in granitoids: a record of interactions between magma emplacement, crystallization and deformation in growing plutons. *Geol Belg* 12:109–133
- Bartley JM, Coleman DS, Glazner AF (2008) Incremental pluton emplacement by magmatic crack-seal. *Trans R Soc Edinb Earth Sci* 97:383–396
- Battaglia M, Troise C, Obrizzo F, Pingue F, De Natale G (2006) Evidence for fluid migration as the source of deformation at Campi Flegrei caldera (Italy). *Geophys Res Lett* 33(1)
- Broda RJ (2014) Geometry and progressive development of a shallow crustal intrusive complex, Mount Hillers,

- Henry Mountains, Utah. Unpublished M.S. thesis, East Carolina University, p 100
- Bunger AP, Cruden AR (2011) Modeling the growth of laccoliths and large mafic sills: role of magma body forces. *J Geophys Res: Solid Earth* 116(B2)
- Coleman DS, Gray W, Glazner AF (2004) Rethinking the emplacement and evolution of zoned plutons: geochronologic evidence for incremental assembly of the Tuolumne Intrusive Suite, California. *Geology* 32:433–436
- Condie KC (1964) Crystallization pO₂ of syenite porphyry from Navajo Mountain, southern Utah. *Geol Soc Am Bull* 75:359–362
- Cruden AR, McCaffrey KJW (2001) Growth of plutons by floor subsidence: implications for rates of emplacement, intrusion spacing and melt extraction mechanisms. *Phys Chem Earth* 26(4–5):303–315
- Currier RM, Marsh BD (2015) Mapping real time growth of experimental laccoliths: The effect of solidification on the mechanics of magmatic intrusion. *J Volcanol Geoth Res* 302:211–224
- Curtis GH (1968) The stratigraphy of the ejecta from the 1912 eruption of Mount Katmai and Novarupta, Alaska. *Geol Soc Am Mem* 116:153–210
- de Silva SL, Gosnold WD (2007) Episodic construction of batholiths: insights from the spatiotemporal development of an ignimbrite flare-up. *J Volcanol Geoth Res* 167:320–335
- Doelling HH (1975) Geology and mineral resources of Garfield County, Utah. *Utah Geol Min Surv Bull* 107:175
- Dubiel RF, Bromfield CS, Church SE, Kemp WM, Larson MJ, Peterson F, Gese DD (1985) Mineral resource potential map of the Mt. Ellen-Blue Hills Wilderness Study Area and Bull Mountain Study Area, Garfield and Wayne counties, Utah. USGS Miscellaneous Field Studies map, MF-1756A
- Dvorak JJ, Dzurisin D (1997) Volcano geodesy: the search for magma reservoirs and the formation of eruptive vents. *Rev Geophys* 35:343–384
- Dzurisin D (2003) A comprehensive approach to monitoring volcano deformation as a window on the eruption cycle. *Rev Geophys*. doi:[10.1029/2001RG000107](https://doi.org/10.1029/2001RG000107)
- Dzurisin D, Lisowski M, Wicks CW, Poland MP, Endo ET (2006) Geodetic observations and modeling of magmatic inflation at the Three Sisters volcanic center, central Oregon Cascade Range, USA. *J Volcanol Geoth Res* 150:35–54
- Elliott DH, Fleming TH, Kyle PR, Foland KA (1999) Long distance transport of magmas in the Jurassic Ferrar large igneous province, Antarctica. *Earth Planet Sci Lett* 167:89–104
- Froger J-L, Remy D, Bonvalot S, Legrand D (2006) Dynamic of long term multi-scale inflations at Lastarria-Cordon del Azufre volcanic complex, central Andes, revealed from ASAR-ENVISAT interferometric data. *Earth Planet Sci Lett*. doi:[10.1016/j.epsl.2006.12.012](https://doi.org/10.1016/j.epsl.2006.12.012)
- Gilbert GK (1877) Report on the geology of the Henry Mountains. U.S. Geographical and Geological Survey, Rocky Mountains Region, p 160
- Glazner AF, Bartley JM, Coleman DS, Gray W, Taylor ZT (2004) Are plutons assembled over millions of years by amalgamation from small magma chambers? *GSA Today* 14:4–11
- Grocott J, Arévalo C, Welkner D, Cruden A (2009) Fault-assisted vertical pluton growth: Coastal Cordillera, north Chilean Andes. *J Geol Soc* 166:295–301
- Gwyn N (2011) Progressive assembly of complex intrusions in the shallow crust, Henry Mountains, Utah. Unpublished M.S. thesis, East Carolina University, p 100
- Hamilton WB, Myers WB (1967) The nature of batholiths. U.S. Geological Survey Professional Paper 554-C, p 30
- Hansen DM, Cartwright J (2006) The three-dimensional geometry and growth of forced folds above saucer-shaped igneous sills. *J Struct Geol* 28:1520–1535
- Hardee HC (1982) Incipient magma chamber formation as a result of repetitive intrusions. *Bull Volcanol* 45 (1):41–49
- Henry CD, Kunk MJ, Muehlberger WR, McIntosh WC (1997) Igneous evolution of a complex laccolith-caldera, the Solitario, Trans-Pecos Texas: Implications for calderas and subjacent plutons. *Geol Soc Am Bull* 109(8):1036–1054
- Horsman E, Morgan S, Saint-Blanquat (de) M, Habert G, Hunter RS, Nugent R, Tikoff B (2010) Emplacement and assembly of shallow plutons through multiple magma pulses, Henry Mountains, Utah. In: Clemens JD (ed) 6th Hutton Symposium on the Origin of Granite and Related Rocks, Geological Society of America Special Paper 472, p 117–132
- Horsman E, Tikoff B, Morgan SS (2005) Emplacement-related fabric and multiple sheets in the Maiden Creek sill, Henry Mountains, Utah. *J Struct Geol* 26:1426–1444
- Hunt GL (1988) Petrology of the Mt Pennell central stock, Henry Mountains, Utah. *Brigham Young Univ Geol Stud* 35:81–100
- Hunt CB, Waters AC (1958) Structural and igneous geology of the La Sal Mountains, Utah. U.S. Geological Survey Professional Paper, n. 294i, p 85
- Hunt CB, Averitt P, Miller RL (1953) Geology and geography of the Henry mountains region, Utah. USGS Professional Paper 228, p 234
- Hunt CB, Jackson MD, Pollard DD (1988) The laccolith-stock controversy: new results from the southern Henry Mountains, Utah: discussion and reply. *Geol Soc Am Bull* 100:1657–1659
- Jackson MD, Pollard DD (1988) The laccolith-stock controversy: new results from the southern Henry Mountains, Utah. *Geol Soc Am Bull* 100:117–139
- Jackson MD, Pollard DD (1990) Flexure and faulting of sedimentary host rocks during growth of igneous domes, Henry Mountains, Utah. *J Struct Geol* 12:185–206

- Kloppenburg A, Grocott J, Hutchinson D (2010) Structural setting and synplutonic fault kinematics of a Cordilleran Cu-Au-Mo porphyry mineralization system, Bingham Mining District, Utah. *Econ Geol* 105:743–761
- Koch FG (1981) The structure of the Mount Ellsworth intrusion, Henry Mountains, Utah. Unpublished M.S. thesis, Stanford University, p 132
- Larson MJ, Bromfield CS, Dubiel RF, Patterson CG, Peterson F (1985) Geologic map of the Little Rockies Wilderness Study Area and the Mt Hillers and Mt Pennell Study Areas and vicinity, Garfield County, Utah. USGS Miscellaneous Field Studies map, MF-1776B
- Lipman PW (2007) Incremental assembly and prolonged consolidation of Cordilleran magma chambers: evidence from the Southern Rocky Mountain volcanic field. *Geosphere* 3(1):42–70
- Lu Z, Wicks CW Jr, Dzurisin D, Power JA, Moran SC, Thatcher WR (2002) Magmatic inflation at a dormant stratovolcano: 1996–1998 activity at Mount Peulik Volcano, Alaska, revealed by satellite radar interferometry. *J Geophys Res* 107. doi:10.1029/2001JB000471
- Lu Z, Masterlark T, Dzurisin D (2005) Interferometric synthetic aperture radar study of Okmok Volcano, Alaska, 1992–2003: magma supply dynamics and post-emplacement lava flow deformation. *J Geophys Res* 110:8–10
- Lundgren P, Lu Z (2006) Inflation model of Uzon caldera, Kamchatka, constrained by satellite radar interferometry observations. *Geophys Res Lett* 33. doi:10.1029/2005GL025181
- Magee C, Stevenson CT, O'Driscoll B, Petronis MS (2012) Local and regional controls on the lateral emplacement of the Ben Hiatt Dolerite intrusion, Ardnamurchan (NW Scotland). *J Struct Geol* 39:66–82
- Masterlark T, Lu Z (2004) Transient volcano deformation sources imaged with interferometric synthetic aperture radar: application to Seguam Island, Alaska. *J Geophys Res* 109:B01401. doi:10.1029/2003JB002568
- Matzel JEP, Bowring SA, Miller RB (2006) Time scales of pluton construction at differing crustal levels: examples from the Mount Stuart and Tenpeak intrusions, North Cascades, Washington. *Geol Soc Am Bull* 118(11/12):1412–1430
- Maurer E (2015) Geometry and construction history of the Copper Ridge laccolith, Mount Ellen, Henry Mountains, Utah. Unpublished M.S. thesis, East Carolina University, p 104
- McCaffrey KJW, Petford N (1997) Are granitic intrusions scale invariant? *Geol Soc (Lond) J* 154:1–4
- Michel J, Baumgartner L, Pultitz B, Schaltegger U, Ovtcharova M (2008) Incremental growth of the Patagonian Torres del Paine laccolith over 90 k.y. *Geology* 36:459–462
- Miller JS, Matzel JEP, Miller CF, Burgess S, Miller RB (2007) Zircon growth and recycling during the assembly of large, composite arc plutons. *J Volcanol Geoth Res* 167:282–299
- Morgan S, Stanik A, Horsman E, Tikoff B, Saint-Blanquat (de) M, Habert G (2008) Emplacement of multiple magma sheets and wall rock deformation: Trachyte Mesa intrusion, Henry Mountains, Utah. *J Struct Geol* 30(4):491–512
- Morton LB (1984) Geology of the Mount Ellen quadrangle, Henry Mountains, Garfield County, Utah. *Brigham Young Univ Geol Stud* 331:67–95
- Morton LB (1986) Provisional geologic and coal resources map for the Mt. Ellen quadrangle, Henry Mountains, Garfield County, Utah. Utah Geological and Mineral Survey Map 90, 15 p., 3 pl., scale 1:24,000
- Nelson ST, Davidson JP (1993) Interaction between Mantle-Derived Magmas and Mafic Crust, Henry Mountains, Utah. *J Geophys Res* 98:1837–1852
- Nelson ST, Davidson JP, Sullivan KR (1992) New age determinations of central Colorado Plateau laccoliths, Utah: recognizing disturbed K-Ar systematics and re-evaluating tectonomagmatic relationships. *Geol Soc Am Bull* 104:1547–1560
- Nishi K, Ono H, Mori H (1999) Global positioning system measurements of ground deformation caused by magma intrusion and lava discharge: the 1990–1995 eruption at Unzendake volcano, Kyushu, Japan. *J Volcanol Geoth Res* 89:23–34
- Nishimura T, Miyazaki S-I, Sagiya T, Tada T, Miura S, Tanaka K, Hirasawa T (2001) Spatio-temporal distribution of interplate coupling: east off northeastern Japan deduced from GPS observation. *Geophys J* 36:254–256
- Paquette JL, Saint-Blanquat (de) M, Delpech G, Horsman E, Morgan S (2010) LA-ICPMS U-Pb zircon dating of Mount Hillers laccolith and satellite intrusions: short-length emplacement and large Proterozoic inheritance. LASI 4 conference: Physical geology of subvolcanic systems: laccoliths, sills, and dykes
- Paterson SR, Fowler TK, Schmidt KL, Yoshinobu AS, Yuan ES, Miller RB (1998) Interpreting magmatic fabric patterns in plutons. *Lithos* 44:53–82
- Peterson F, Ryder RT, Law BE (1980) Stratigraphy, sedimentology, and regional relationships of the Cretaceous System in the Henry Mountains region, Utah. In Picard MD (ed) *Henry Mountains Symposium: Utah Geological Association Guidebook*, p 151–170
- Petford N, Cruden AR, McCaffrey KJW, Vigneresse JL (2000) Granite magma formation, transport and emplacement in the Earth's crust. *Nature* 408:669–673
- Pitcher WS, Berger AR (1972) The geology of Donegal: a study of granite emplacement and unroofing. Wiley
- Pollard DD, Johnson AM (1973) Mechanics of growth of some laccolith intrusions in the Henry Mountains, Utah, II: bending and failure of overburden layers and sill formation. *Tectonophysics* 18:311–354
- Pownall JM, Waters DJ, Searle MP, Shail RK, Robb LJ (2012) Shallow laccolithic emplacement of the Land's End and Tregonning granites, Cornwall, UK: evidence from aureole field relations and PT modeling of cordierite-anthophyllite hornfels. *Geosphere* 8:1467–1504

- Pritchard ME, Simons M (2004a) Surveying volcanic arcs with satellite radar interferometry; the Central Andes, Kamchatka, and beyond. *GSA Today* 14:4–11
- Pritchard ME, Simons M (2004b) An InSAR-based survey of volcanic deformation in the central Andes. *Geochem Geophys Geosyst* 5(2):Q02002. doi:10.1029/2003GC000610
- Rocchi S, Westerman DS, Dini A, Farina F (2010) Intrusive sheets and sheeted intrusions at Elba Island, Italy. *Geosphere* 6:225–236
- Saint-Blanquat (de) M, Habert G, Horsman E, Morgan S, Tikoff B, Launeau P, Gleizes G (2006) Mechanisms and rates of non tectonically-assisted emplacement in the upper-crust: the Black Mesa pluton, Henry Mountains, Utah. *Tectonophysics* 428:1–31
- Saint-Blanquat (de) M, Horsman E, Habert G, Morgan S, Vanderhaeghe O, Law R, Tikoff B (2011) Multiscale magmatic cyclicality, duration of pluton construction, and the paradoxical relationship between tectonism and plutonism in continental arcs. *Tectonophysics* 500:22–33
- Saint-Blanquat (de) M, Law RD, Bouchez JL, Morgan SS (2001) Internal structure and emplacement of the Papoose Flat pluton: an integrated structural, petrographic, and magnetic susceptibility study. *Geol Soc Am Bull* 113(8):976–995
- Schmiedel T, Breitreuz C, Götz I, Ehling BC (2015) Geometry of laccolith margins: 2D and 3D models of the Late Paleozoic Halle Volcanic Complex (Germany). *Int J Earth Sci* 104:323–333
- Stevenson CT, Owens WH, Hutton DH (2007) Flow lobes in granite: the determination of magma flow direction in the Trawenagh Bay Granite, northwestern Ireland, using anisotropy of magnetic susceptibility. *Geol Soc Am Bull* 119:1368–1386
- Thomson K, Hutton DHW (2004) Geometry and growth of sill complexes: insights using 3-d seismic from the North Rockall Trough. *Bull Volcanol* 66:364–375
- Thornton E (2015) Timing, internal flow characteristics, and emplacement mechanisms of the intrusive sheet network on the southern margin of Mount Hillers, Henry Mountains, southern Utah. Unpublished M.S. thesis, East Carolina University, p 104
- Turner S, Costa F (2007) Measuring timescales of magmatic evolution. *Elements* 3:267–272
- Vignerresse JL (2008) Granitic batholiths: from pervasive and continuous melting in the lower crust to discontinuous and spaced plutonism in the upper crust. *Trans R Soc Edinb Earth Sci* 97:311–324
- Walker BA, Miller CF, Claiborne LL, Wooden JL, Miller JS (2007) Geology and geochronology of the Spirit Mountain batholith, southern Nevada: implications for timescales and physical processes of batholith construction. *J Volcanol Geoth Res* 167:239–262
- Ward M (2014) Geometry and construction history of a complex intrusive center in the shallow crust, Mount Pennell, Henry Mountains, Utah. Unpublished M.S. thesis, East Carolina University, p 130
- Wetmore PH, Connor CB, Kruse SE, Callihan S, Pignotta G, Stremtan C, Burke A (2009) Geometry of the Trachyte Mesa intrusion, Henry Mountains, Utah: implications for the emplacement of small melt volumes into the upper crust. *Geochem Geophys Geosyst* 10(8)
- Wicks CW Jr, Dzurisin D, Ingebritsen SE, Thatcher WR, Lu Z, Iverson J (2002) Magmatic activity beneath the quiescent Three Sisters volcanic center, central Oregon Cascade Range, USA. *Geophys Res Lett* 29. doi:10.1029/2001GL014205
- Wicks C, Thatcher W, Dzurisin D (1998) Migration of fluids beneath Yellowstone caldera inferred from satellite radar interferometry. *Science* 282 (5388):458–462
- Wiebe RA (1988) Structural and magmatic evolution of a magma chamber: the Newark Island layered Intrusion, Nain, Labrador. *J Petrol* 29:383–411
- Witkind IJ (1964) Geology of the Abajo Mountains area, San Juan County, Utah. U.S. Geological Survey Professional Paper, p 125

Sub-volcanic Intrusions in the Karoo Basin, South Africa

Henrik H. Svensen, Stéphane Polteau, Grant Cawthorn,
and Sverre Planke

Abstract

The Karoo Basin in South Africa contains the world's best exposed sub-volcanic part of a Large Igneous Province. Dolerite sills and dikes crop out across the 630,000 km² large basin, from base to top of the stratigraphy. We present data from a compilation of 32 boreholes drilled since the 1960's, showing that the sill percentage in the stratigraphy for individual boreholes varies from 0 to 54 %. Borehole depth is the key factor determining the sill proportion in specific regions, as shorter boreholes give higher sill proportions. When focusing on eight boreholes that were drilled through almost complete stratigraphic sections, the cumulative sill content is between 250 and 720 meters (average 440 m), yielding a proportion of sills to total thickness of 32 %. Using this average number as a proxy for the average sill content in the basin, the resulting sill volume is on the order of 250,000 to 300,000 km³ when extrapolating to basin scale. The volume of dikes remains unknown, but all are quite thin and so have relatively small volume, estimated to less than 15 % of the sill volume. The sills may have been a thermal source for the generation of oil and gas, as well as leading to their volatilization and escape to the Early Jurassic atmosphere.

1 Introduction

Outcrops and boreholes in the Karoo Basin provide a unique opportunity to study the processes and consequences of shallow sub-volcanic intrusions related to a Large Igneous Province (LIP). The intrusions were emplaced in clastic sedimentary rocks and led to contact metamorphic aureole formation, changes in the maturity state of the host organic matter, devolatilization and fluid expulsion, and mineral reactions and

H.H. Svensen (✉) · S. Planke
Centre for Earth Evolution and Dynamics (CEED),
University of Oslo, Oslo, Norway
e-mail: hensven@fys.uio.no

S. Polteau · S. Planke
Volcanic Basin Petroleum Research (VBPR),
Oslo Innovation Center, Oslo, Norway

G. Cawthorn
School of Geosciences, University of Witwatersrand,
Johannesburg, South Africa

compaction. The emplacement of the sub-volcanic complex was a major event that affected rheology and fluid generation at the time of emplacement in the Early Jurassic and onwards (Chevallier and Woodford 1999; Jamtveit et al. 2004; Svensen et al. 2006, 2007; Aarnes et al. 2011). However, previous work on the sills has mainly focussed on outcrops, not boreholes. In this contribution, we present a new compilation of borehole data from the Karoo Basin. The aim is to improve the understanding of the distributions and thicknesses of the sub-volcanic part of the Karoo LIP.

2 The Karoo Basin and the Sub-volcanic Complex

The Upper Carboniferous to Triassic Karoo Supergroup in South Africa is divided in five groups (the Dwyka, Ecca, Beaufort, Stormberg and Drakensberg groups) with a postulated maximum cumulative thickness of 12 km and a preserved maximum thickness of 5.5 km (Tankard et al. 2009). The current area with outcropping Karoo sedimentary rocks in South Africa is about 630,000 km² (Fig. 1). The depositional environments range from marine and glacial (the Dwyka Group), marine to deltaic (the Ecca Group), to fluvial (the Beaufort Group) and finally eolian (the Stormberg Group) (Cattaneo et al. 1998). The Karoo Basin is overlain by 1.65 km of preserved volcanic rocks of the Drakensberg Group, consisting mainly of stacked basalt flows erupted in a continental and dry environment (e.g., Bristow and Saggerson 1983; Duncan et al. 1984; Duncan and Marsh 2006). The plumbing system of the Karoo continental flood basalts is a basin-scale intrusive complex consisting of sills and dykes of varying thickness (Figs. 1, 2, 3 and 4) (du Toit 1920; Walker and Poldervaart 1949; Marsh and Eales 1984; Chevallier and Woodford 1999). The sills were emplaced at about 182.6 Ma (Svensen et al. 2012). The composition of the sills is tholeiitic with minor volumes of more evolved andesitic

intrusions (Marsh and Eales 1984). Most of the thicker sills in the basin show internal compositional variations due to mild differentiation, a few of the thickest showing strong fractionation, such as the Mount Ayliff, Birds River, and New Amalfi complexes. The Mount Ayliff Complex near Kokstad, with its four lobes (Insizwa, Tabankulu, Tonti and Ingeli) is over 1,000 m thick, and represents an anomaly and has not been included in our compilation (Marsh et al. 2003).

Hundreds of breccia pipes and hydrothermal vent complexes are rooted in the contact aureoles of intrusions in the Karoo Basin and formed as a consequence of pressure build-up related to devolatilization reactions or boiling (Jamtveit et al. 2004; Svensen et al. 2007; Aarnes et al. 2012). The resulting release of carbon-rich gases is proposed as a major source of the ¹²C-enriched carbon required to explain the Toarcian negative carbon isotope excursion and global environmental change (e.g., Svensen et al. 2007; Mazzini et al. 2010). The status of this hypothesis, and new data from contact aureoles in the Karoo Basin, is presented in Sect 9.2.

3 Methods

Surface geology is given by the 1:1,000,000 bedrock lithostratigraphical map from the Council of Geoscience through onegeology.org. The regional profile presented in Fig. 1b is constructed using borehole and surface geology data. We have compiled data from 32 boreholes, including several that intersect the basement below the Karoo sequence (Table 1). 27 of the boreholes contain sills and 18 of those logs are presented in Fig. 5. The logs were obtained from the Council for Geoscience in Pretoria and from our own core studies. When compiling sill thicknesses, we assumed that none of the drilled dolerites represent inclined dykes and that the sill thicknesses in the boreholes represent the real thicknesses. Histograms and percentile calculations were done using the PAST software (Hammer et al. 2001).

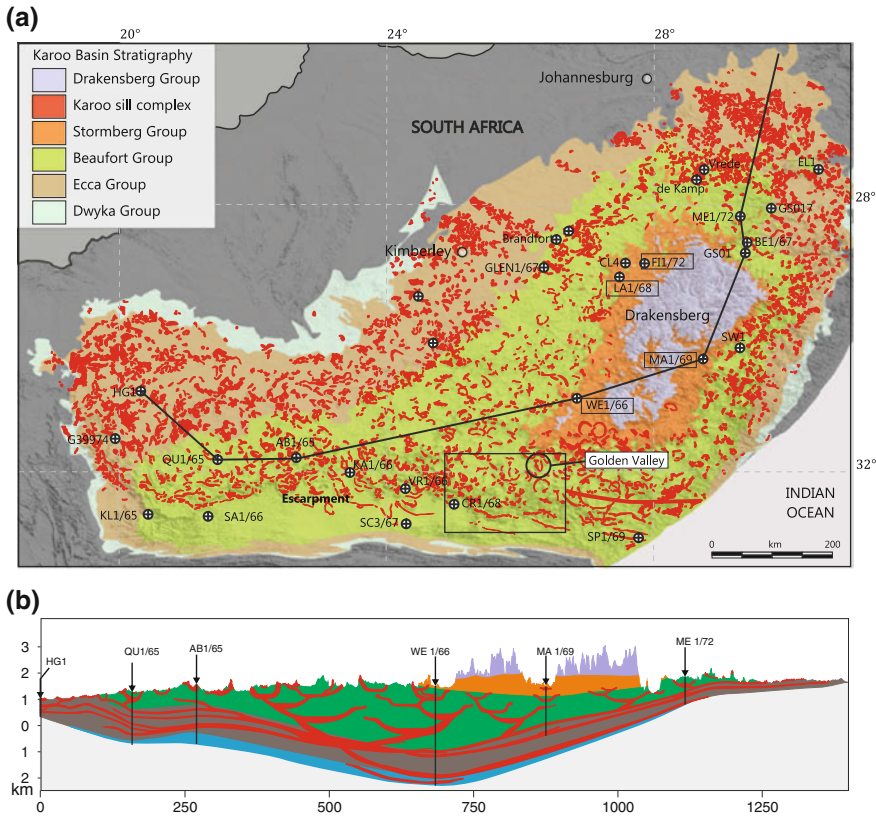


Fig. 1 **a** Geological map of the Karoo Basin showing the distribution of sill intrusions and the locations of the boreholes used in this study. The line across the basin is the trace of the profile presented below. See Fig. 2 for a close-up image of the rectangle in the southern Karoo

Basin. b Composite profile across the basin based on surface geology and borehole data. The schematic subsurface geology between the boreholes is constructed based on the typical sill geometries in the Ecca and Beaufort groups. Note the ~22 times vertical exaggeration

4 Results

The sill geometries in the Karoo Basin vary with the depth of emplacement. Sills in the Ecca Group are laterally extensive, whereas sills in the Beaufort Group commonly have saucer-like morphologies with climbing limbs that cut across the horizontal stratigraphy of the sedimentary rocks (Figs. 2, 3 and 4) (Polteau et al. 2008a). Sills are rare in the Stormberg Group although dykes are common. Contact aureoles around the sills are well developed and are characterized by bleached hornfels with organic carbon contents approaching zero (Svensen et al. 2007; Aarnes et al. 2011).

The parameters we have extracted from the Karoo Basin logs include sediment thickness to base Dwyka Group (or base Ecca Group if Dwyka is absent), total sill thickness, the number of sills, the percent of sills (defined as the total thickness of sills divided by total thickness of sills plus sedimentary rocks), the thickest sill, and the emplacement levels (Table 1). As seen in the compiled logs in Fig. 5, the sill thicknesses vary considerably between boreholes and within the various stratigraphic units. For the 197 sills in our database, the average thickness is 35 m with most less than 90 m thick (Table 1). The thickest sill in our database is 282 m (GS017), but note that this represents a minimum thickness as the collar of the borehole was located within the sill.



Fig. 2 Satellite image of the escarpment in the southern parts of the Karoo Basin. The escarpment is defined by *thick sill* intrusions emplaced in the Beaufort Group. Few sills are

present south of the escarpment. The locations of the 4,658 m deep CR1/68 borehole, the Golden Valley saucer (Fig. 3a), and the Nico Malan Pass (Fig. 3b) are also shown

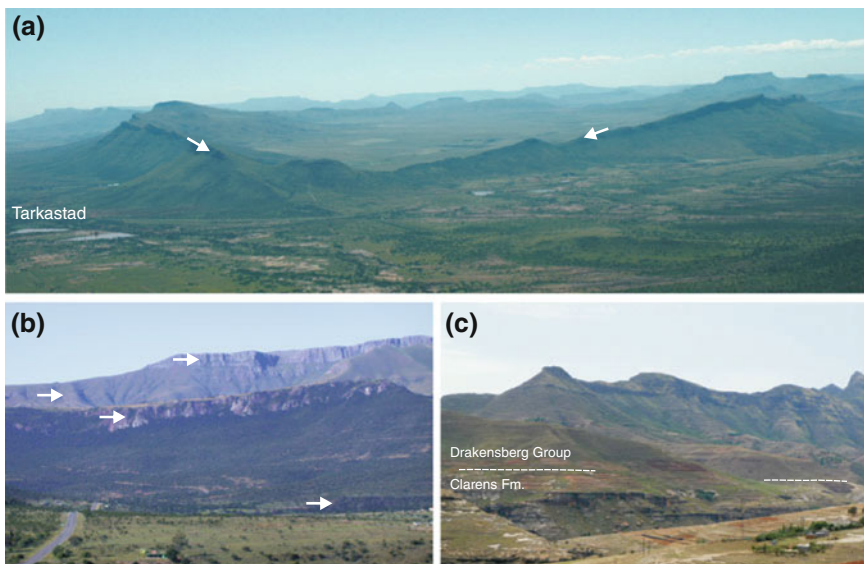


Fig. 3 **a** The Golden Valley sill complex with characteristic inclined sheets (*white arrows*). The saucer-shaped sill is about 100 m thick and the complex is up to 11 km wide. **b** The escarpment near the Nico Malan Pass seen towards the north. Four sills are present at various levels

in the landscape (*arrows*). **c** The Karoo Basin was flooded by basalt in the Early Jurassic covering the landscape with at least 1.65 km of basalt. Here is the contact between the Clarens Formation (Stormberg Group) and the Drakensberg Group lava exposed in northern Lesotho

We cannot exclude the possibility that some of the sills represent composite sills, although these are rarely seen in the field. The sill thicknesses in

the boreholes are highly variable with an average value of 21 %. SW1/67 contains the highest number of sills (33) and the Vrede borehole the

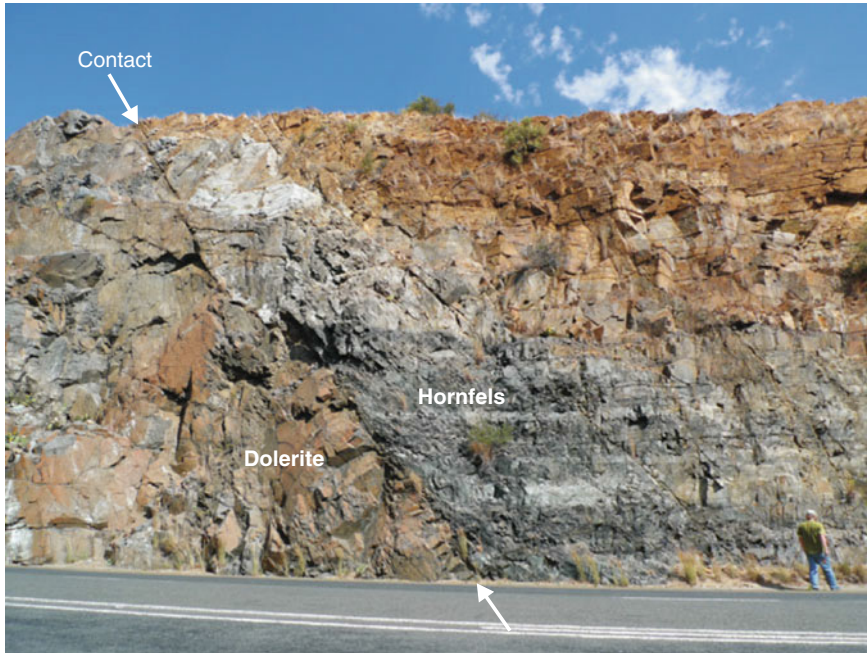


Fig. 4 Transgressive sills are common in the Beaufort Group sedimentary rocks and form an important feature of the saucer-shaped intrusions in the basin. Here we see the sill contact north-east of Beaufort West. Sandstone and

siltstone are transformed to hornfels in the contact aureole. Note the oxidized weathering profile in the upper part of the hornfels

highest content (54 %) when comparing with the sediment thickness. We stress that the sill content variation across the basin is heterogeneous and that is not possible to draw sensible contour maps as done by Winter and Venter (1970).

An important finding is that the percentage of sills varies with borehole depth and location relative to the escarpment (Fig. 6a). Also, the intuitive positive relationship between the number of sills and the total content of sills shows that sill thicknesses are evenly distributed among the boreholes (Fig. 6). Short boreholes (and those intersecting only the lowermost stratigraphy) contain a high percentage of sills but also few meters in total. Figure 7 shows the importance of the total stratigraphic succession intersected for understanding the sill content in the boreholes. When plotting the sill content in meters versus percent, the dataset falls mainly along two trends. By differentiating between short boreholes (<1,000 m) and long boreholes (>1,000 m), we show that short boreholes are skewed towards a higher percentage of sills.

A well-known aspect of the sill distribution in the Karoo Basin is the scarcity of sills located south of the Karoo escarpment (see Fig. 1). This can be seen in the logs in Figs. 5 and 8, where the sill content is plotted against the perpendicular distance from the escarpment.

The histograms in Fig. 9 show that the sill thicknesses vary according to emplacement level. The Beaufort Group has a higher abundance of both thin sills (<30 m) and thick sills (90–150 m) than the Ecca Group. The predominance of thin sills in our data set is demonstrated in Fig. 10, showing that most sills (60 %) are less than 30 m thick. In Fig. 11 we show how much sills with thicknesses within 20 m bins contribute to the cumulative sill thicknesses. For instance, even the thinnest sills (<20 m in thickness) in our database sum to 659 m. Sills in the 20–40 m range sum up to almost the same cumulative thickness as the sills in the 40–60, 60–80, and 80–100 m ranges. Note that the few sills thicker than 140 m result in 1:1 relationship between cumulative sill thickness and bin size in cases

Table 1 Overview of cores and sill thicknesses

Core	Farm	Lat	Long	TD/ BK	Sediments	Sills	Sills	Volume	Thickest
					m	m	#	%	m
QU1/65	Quagga's Fontein 357	-31,83	21,44	1935	1516	419	10	28	128
WE1/66	Weltevreden 117	-30,90	26,84	3732	2911	821	14	28	129
BE1/67	Bergville	-28,57	29,38	1045	772	273	16	35	64
HG1	Hans Gat 249	-30,80	20,29	672	503	169	6	34	44
LA1/68	Olney 280 (Ladybrand)	-29,09	27,48	1710	1444	266	11	18	127
GLEN1/67		-28,95	26,33	769	450	291	7	61	221
VREDE1/66		-32,26	24,25	3310	3256	54	4	2	42
MA1/69		-30,30	28,72	1892	1502	390	22	26	129
FI1/72	Ficksburg Township 75	-28,89	27,85	1873	1582	291	8	18	21
ME1/72	Meijers Geluk	-28,19	29,28	1037	779	258	6	33	70
AB1/65	Abrahams Kraal 206	-31,80	22,62	2298	1640	658	6	40	282
CR1/68	Drooge Rivier	-32,48	25,00	4658	4631	27	4	0,6	9
KL1/78	Klein Kareelaagte 168	-29,38	24,45	140	125	15	1	12	15
BE1/67	Bergville	-28,73	29,35	1045	772	273	16	35,4	64
GSO17	Hanover 2964	-28,06	29,75	442	403	39	2	9,7	36
	Brandfort	-28,53	26,52	723	607	117	10	19	47
CL4	Clockolan	-28,88	27,55	892	895	95	5	13	
SW1	Swartberg	-30,15	29,27	2805	2090	717	33	34	199
KA1	Kareebosch	-32,02	23,42	2516	2404	112	3	5	76
	Kliprivier			685	510	175	3	34	127
	Petrusville	-30,08	24,67	711	577	133	3	23	62
		28,77	30,32	1857	1608	248	8	15	97
SO1	Somkele	-28,35	32,10	2291	1730	561		32	
	de Kamp	-27,63	28,62	722	425	300	6	70	111
	Vrede	-27,48	28,73	650	298	352	3	118	168
EL1	Elandsnek	-27,47	30,45	576	396	189		45	
	Theunissen	-28,40	26,70	482	428	54	1	13	54
G39974	Kopoas Fontein	-31,49	19,89	1016	807	209	3	26	116
KL1/65	Klipdrift 156	-31,38	20,45	2034	1864	170		9	

where only one sill is present. In total, the sills in the database sum to a thickness of 6,647 m.

We use our database to constrain the volume of sills in the whole Karoo Basin. The approach we use is to extract the average thickness and standard deviation of the sill content in the 12 deep boreholes (>1,000 m). These boreholes are listed in Table 1, and the average is 426 ± 211 m. When scaling to the size of the Karoo Basin (630,000 km²), the resulting sill volume is $270,000 \pm 130,000$ km³. Note that (1) the 12

deep boreholes are the best representation of the sill content in the basin, (2) the lack of sills in the Ecca Group south of the Escarpment has not been taken into account, (3) we assume that the entire Karoo stratigraphy, including the Stormberg Group, was present across the present-day size of the basin, and (4) the sill volume is likely significantly underestimated considering the presence of Karoo LIP sills outside South Africa. The volume of dykes in the Karoo Basin remains unknown as there are no studies on dyke

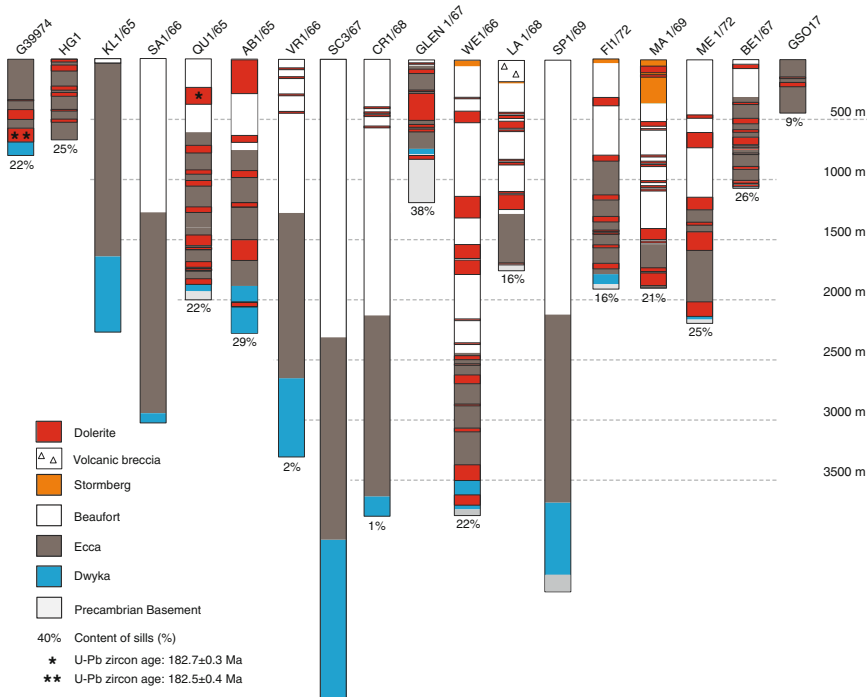


Fig. 5 Lithological logs from 18 of the 32 studied boreholes. The boreholes are sorted according to longitude. Note that only four boreholes contain complete Ecca and Beaufort Group stratigraphy (LA1/68, MA1/69, FI1/72, and WE1/66). The thickest sill is found in the AB1/65

borehole (at least 282 m). Sills are rare in the Dwyka Group and only one sill is emplaced exclusively in basement rocks (GLEN1/67). The boreholes without sills are all from areas near the southern escarpment

statistics. However, with a few exceptions, most outcropping dykes are thin (1–10 m). If we turn all sills in our database into 5 m wide dykes, the cumulative dike width becomes 985 m (197 × 5) or 15 % of the cumulative sill thickness.

182.3 ± 0.6 Ma. Both the U-Pb and Ar/Ar ages are shown in the compilation in Fig. 12. Monte Carlo simulations of the emplacement duration based on the new U-Pb ages suggests that 95 % of the sills were emplaced within 0.47 m.y. (Svensen et al. 2012).

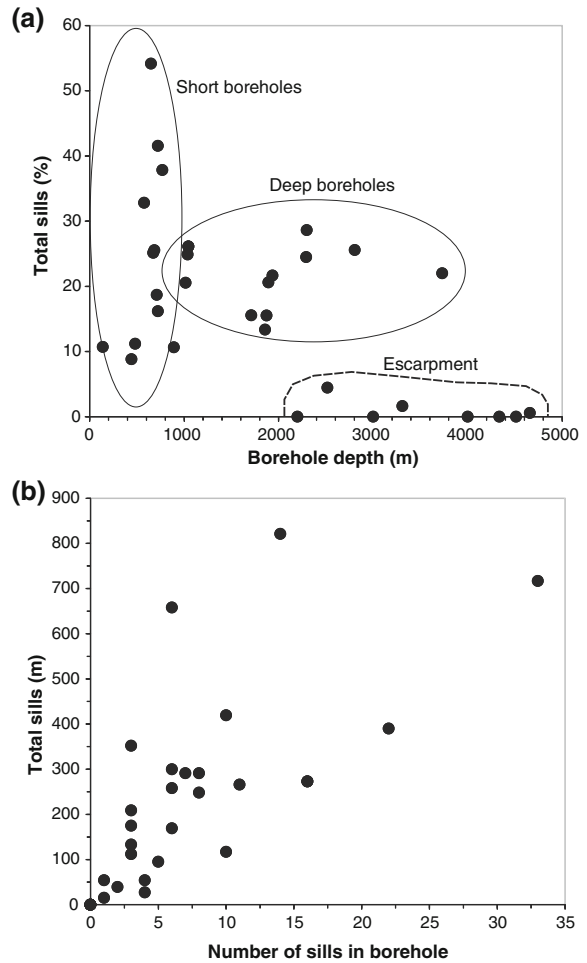
5 Discussion

5.1 Age and Geochemistry of the Karoo Dolerites

Based on an ⁴⁰Ar/³⁹Ar study of 15 sills in the eastern Karoo Basin, it was concluded that the Karoo sills were emplaced over a sustained period of some 3 m.y. (Jourdan et al. 2008). A recent study presented 15 U-Pb zircon ages of sills across the whole Karoo Basin which gave overlapping ages within small errors (Svensen et al. 2012), ranging from 183.0 ± 0.5 to

The ages of the lavas, in contrast, are poorly constrained. The geochronology of the basal flood basalt, the Mosheshe’s Ford unit, is characterized by variable and uncertain ages: 184.8 ± 2.6 Ma (K–Ar; Moulin et al. 2011), 186.5 ± 1.1 Ma (uncorrected ⁴⁰Ar/³⁹Ar plateau age; Duncan et al. 1997), and 181.0 ± 2.0 Ma (⁴⁰Ar/³⁹Ar plateau age from the lowermost flow in Lesotho; Jourdan et al. 2007). There have been many attempts to find zircons in both the basal lavas and other flows in South Africa and Lesotho, without success. Thus so far, the direct link between Karoo sills and lavas relies on the geochemical fingerprinting of sills, dykes and lavas (Marsh et al. 1997).

Fig. 6 Systematics of the 27 boreholes in the database containing sills. **a** The percentage of sills versus the depth to the base of the borehole or top of the basement. Most boreholes contain more than 10 % sills, except the boreholes drilled near the escarpment in the south. **b** The number of sills in each borehole varies from 1 to 33. Generally, boreholes with many sills (>10) have a high proportion of sills on the basis of total sill thickness



There is no systematic variation in sill geochemistry from base to top in the basin (Neumann et al. 2011 and Chap. 7 of this book). Figure 13 shows a compilation of sill analyses from two boreholes that were drilled through the Ecca and Beaufort groups (LA1/68 and QU1/65). The MgO content is fairly consistent, clustering between 5 and 8 wt. %. Previous studies based on fieldwork in various regions in the basin have given similar results. However, a high-resolution study from the Golden Valley sill complex suggested that variations between sills can be substantial in terms of trace element concentrations, both due to internal processes within each sill and due to sills sourced from reservoirs with slightly different chemistry (Galerie et al. 2008; Neumann et al. 2011).

5.2 Sill Distribution and Thicknesses

The escarpment in the southern Karoo is defined by more than 1,000 m elevation difference and by the presence of thick sills emplaced in the middle Beaufort Group (Fig. 2). There are few sills emplaced south of the escarpment, and they are thin and not present everywhere. The thick sills cropping out in the upper part of the escarpment (Fig. 3b) likely extended southwards towards the Cape Fold Belt, but are now eroded due to the northward migration of the escarpment. The reason for the general absence of sills south of the escarpment below the middle Beaufort Group is debated. The Cape Fold Belt is suggested to have reduced the ability of horizontal migration of magma deep in the basin

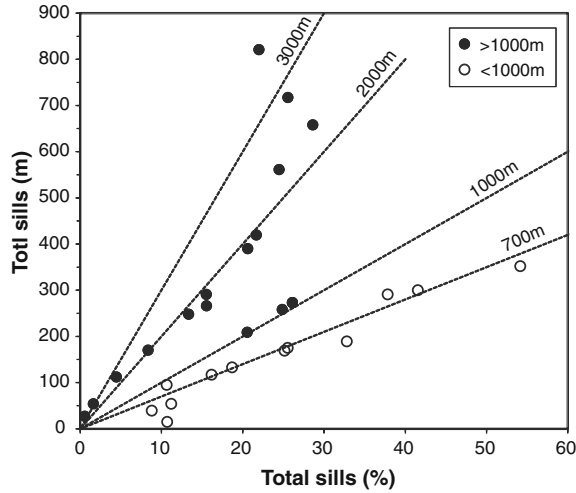


Fig. 7 The relationship between sill content in percent and total thickness (m). The two trends in the data can be explained when distinguishing between short (*open circles*) and long boreholes (*filled circles*). The *stippled lines* show the theoretical systematics of boreholes in which the total depth and the sill content is varied systematically

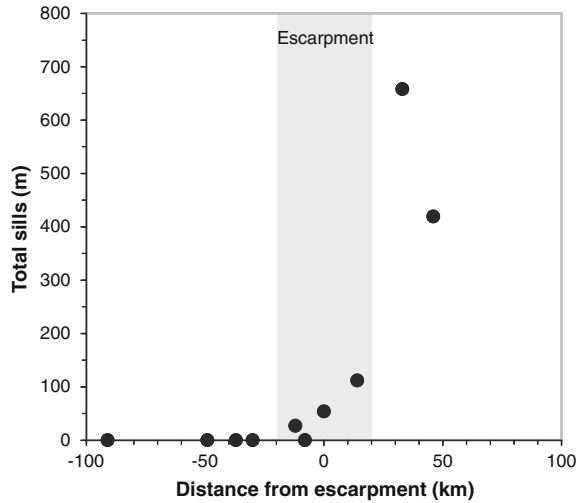


Fig. 8 The sill content in meters as a function of distance from the southern escarpment along a longitudinal band. Sill are absent in the south and start to appear near the escarpment. Note that the escarpment is a gradual feature in the terrain, usually confined to a ~40 km wide zone. This zone is shown as a *grey band*

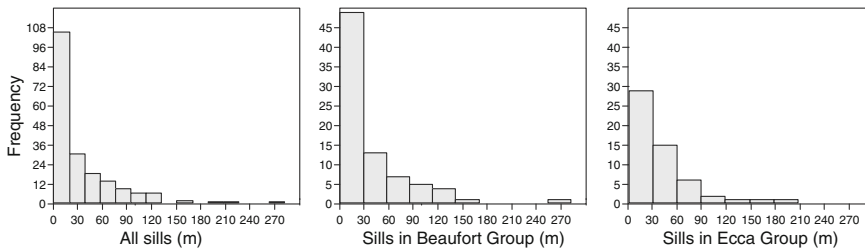


Fig. 9 Histograms of all sill thicknesses (**a**), sills in the Beaufort Group (**b**), and the Eccca Group (**c**). The major difference between **b** and **c** is the higher abundance of both thin sills (<30 m) and thick sills (90–150 m) in the Beaufort Group

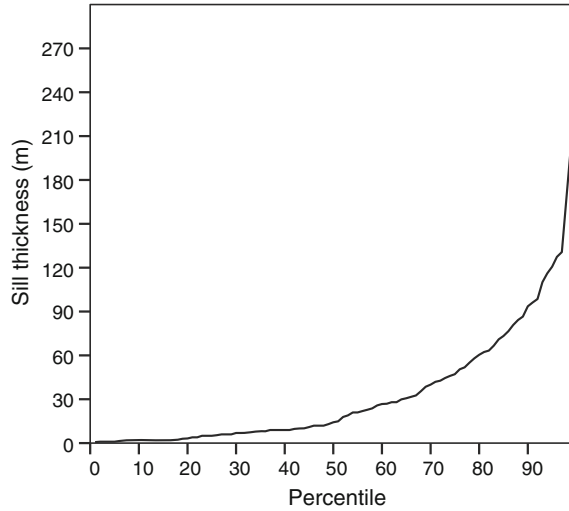


Fig. 10 Percentile plot showing the distribution of sill thicknesses scaled to 100 %. For instance, 60 % of the sills are thinner than 30 m

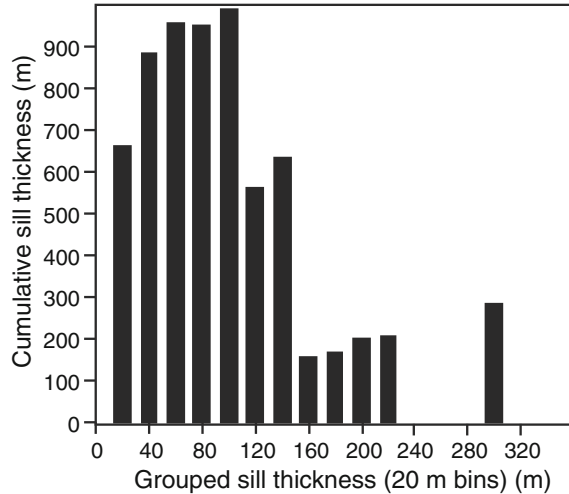


Fig. 11 Cumulative sill thicknesses summarized within 20 m sill thickness bins. Note the high cumulative sill thickness even for sills <20 m thick and the minor contribution from rare >140 m thick sills

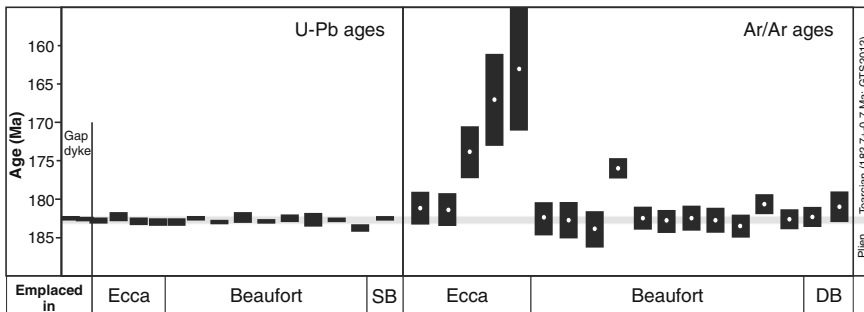


Fig. 12 Published sill ages from the Karoo Basin. The U-Pb zircon ages are compiled from Svensen et al. (2012) and the Ar/Ar sill ages from Jourdan et al. (2007, 2008). The extrapolated GTS2012 age of the Pliensbachian-

Toarcian boundary is also shown. Note that the age of the huge Gap dyke, the only dyke dated by zircons in the basin, is identical to the sill ages. SB: Stormberg Group. DB: Drakensberg Group

(Winter and Venter 1970). Our data support this view as the lower part of the Beaufort Group and the entire Ecca and Dwyka groups in this region are depleted of sills as well (Figs. 5 and 8).

There is an east-west trending zone to the east of Kimberley where the basement has been deformed upward with the result that the thickness of Karoo sedimentary rocks is anomalously thin. In one hole, GLEN1/67, there is a single sill that is 221 m thick (the second thickest of all recorded sills). These two facts result in this one hole yielding a sill content of 38 %, but note that the borehole is less than 1,000 m deep and thus not representative for the full stratigraphy in that area. If this one value were to be ignored then the greatest sill content would appear to be in the northeast of the Karoo Basin. However, in this region only the lowermost rocks (mainly the Ecca Formation) have survived erosion. The boreholes that ring Lesotho (shown in boxes in Fig. 1) show a higher sill content than the other deep boreholes and so do not support the conclusions by earlier workers (Winter and Venter 1970).

The 12 deep boreholes containing sills may hold the key to quantifying the basin-scale sill volume. These boreholes minimize the skewed data from short and un-representative boreholes, and the effect of erosion and removal of the upper parts of the sedimentary sequences. Our sill volume estimate is $270,000 \pm 130,000 \text{ km}^3$. Alternative methods include map view outcrop estimates and integrated cross sections. The latter method was used by Svensen et al. (2012), where the sill volume in a cross-section similar to the one in Fig. 1b was extrapolated to the entire basin giving a volume of $340,000 \text{ km}^3$.

5.3 The Emplacement of a Sill

The cross-section of the Karoo Basin (Fig. 1b) graphically presents two fundamental aspects: (1) individual sills in the Ecca Group may be laterally extensive (across 100s of kilometres), and (2) the sills in the Beaufort Group do not necessarily form extensive sheets that can be mapped for great distances, but form saucers. This

implies that the tradition of giving individual sills names, such as in the Tunguska Basin in Siberia, does not make sense for the Karoo as sills transgress, pinch out, merge with inclined dykes, and form an intricate network throughout the basin. This is demonstrated in a series of publications from the Golden Valley Sill Complex project, where a large number of geochemical profiles were made together with detailed geochemical fingerprinting of magma batches and detailed fieldwork (Galerie et al. 2008, 2010; Polteau et al. 2008a, b).

The boreholes we have studied have records of the different emplacement from the region in which they were drilled. This means that the question of how many of the 197 sill intersections we have recorded represent the same intrusions is impossible to answer. Extensive sills should in theory be overrepresented in the dataset if these were penetrated by several boreholes. Our data shows that the 60 % of the sills are thinner than about 30 m (Fig. 10), although thin sills should intuitively be the least laterally extensive. Figure 11 shows that the sills thinner than 40 m contribute as much to the cumulative thickness as those in the 40–140 m range (Fig. 11). The reason for the higher abundance of thin sills (<30 m) in the Beaufort Group compared to in the Ecca Group (Fig. 9) is unclear. A possible explanation is that sill thickness is partly controlled by host rock properties (sandstone versus shale) or the depth of emplacement. For instance, a detailed borehole study of saucer-shaped sills has shown that sill offshoots are common near the transgressive segments of thick sills (Chevallier and Woodford 1999). This is potentially an explanation for the many thin sills in the vicinity of thick sills in our borehole compilation (Fig. 5). Moreover, there is apparently a higher proportion of thick sills (90–150 m) in the Beaufort Group compared to in the Ecca Group (Fig. 9), possibly due to emplacement depth, inflation processes, or variations in the melt emplacement flux. Whether the sills were emplaced in time sequence from the base upward, downwards or randomly is unresolvable, but the flux was likely highly variable over the ~500 ky emplacement duration.

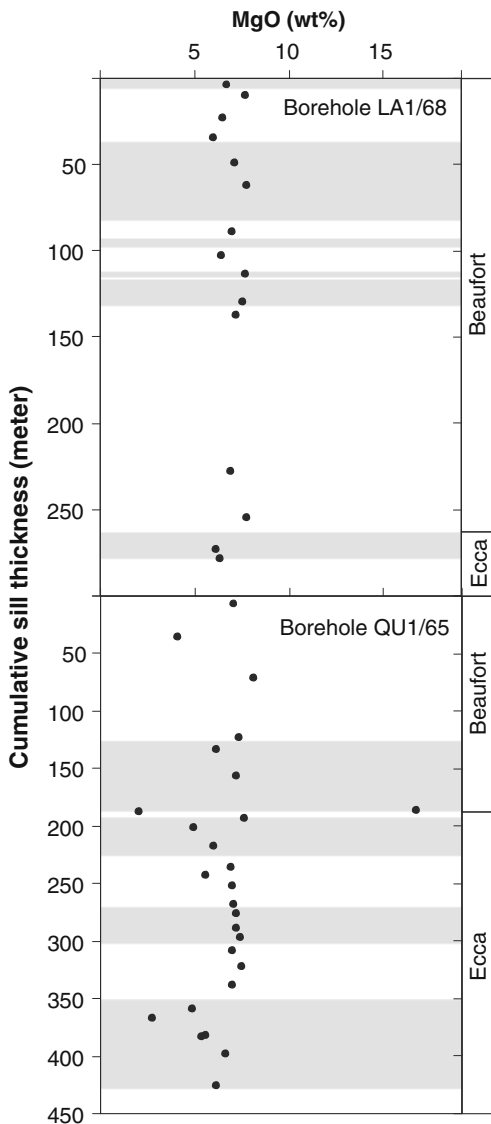


Fig. 13 Whole-rock wt. % MgO data from sills analysed from core material in the LA1/68 and QU1/65 boreholes. The plot shows the stacked sills from the two boreholes without including the sedimentary rocks. Individual sills are shown as alternating white and grey bands. The MgO content is rather consistent throughout the stratigraphy and does not show any specific trends. Note that some of the spread in the data can be due to internal differentiation, as sampling was not restricted to the chilled margins where the primary composition of the magma is likely recorded. Data from Neumann et al. (2011)

5.4 Consequences of Sill Emplacement

When South African companies explored the petroleum potential in the Karoo Basin during the 1960s and 1970s, many were concerned about the influence of sills on the petroleum systems. Rowsell and De Swart (1976) compiled borehole data demonstrating the temperature effect of sills on clay minerals and petroleum systems. For instance, the LA1/68 borehole contained dry gas in the lower half of the hole, whereas oil shows were common in the upper part. Both the thermal input from the sills and the weight of the overlying lava pile must have played a key role in the petroleum generation, as the sedimentary sequence in LA1/68 is only 1,444 m thick (Table 1). Even with a very high thermal gradient, this is insufficient for generating temperatures needed for oil and gas generation unless the effect of the lava pile was significant.

During the last decade, contact metamorphism of organic-rich shale in the Karoo Basin has been linked to methane degassing and the Toarcian climate perturbations (Svensen et al. 2007; Aarnes et al. 2011). These studies applied a combination of field investigations, borehole studies, and numerical modelling, and show that methane was generated in sufficient quantities within the Eccla Group contact aureoles to have had an environmental effect if vented to the atmosphere. These findings are moreover important for the outlook for shale gas in the Karoo Basin. New borehole information and gas geochemistry from the Eccla Group, with and without sills, are needed to resolve if sills in a particular region have been beneficial or destructive for the local petroleum systems.

6 Conclusions

The Karoo Basin contains the world's best exposed sub-volcanic part of a LIP. Both borehole data and exposed sills have great potential

for addressing detailed processes related to sill geochemistry and emplacement, and contact aureole processes. We conclude that:

- Sills form an integral part of the Karoo stratigraphy, and comprise up to 54 % of the local stratigraphy, but for the 27 boreholes with sills we have studied, the average sill content is 21 %.
- Thin sills (<30 m) are more abundant than thick sill and represent 60 % of a total of 197 individual sill intersections in our database. The Beaufort Group contains more sills in the 90–150 m range than the Ecca Group, possibly reflecting a combination of emplacement processes and host rock lithology.
- Borehole data are crucial for understanding the sill distribution in a sedimentary basin. However, short boreholes may give artificially higher sill percentages than deep boreholes.
- Boreholes from around the Karoo escarpment suggest a tectonic explanation for the absence of sills in the Dwyka and Ecca groups south of the escarpment.
- The Karoo sills represent the best geochronologically constrained subvolcanic part of a LIP. A recent study of 15 dated sills suggested a very rapid emplacement around 182.6 Ma. The lavas are only dated by the $^{40}\text{Ar}/^{39}\text{Ar}$ and K–Ar methods with a considerable age scatter around 183 Ma, and a revision is critically needed.

Acknowledgments We gratefully acknowledge support from the Norwegian Research Council (a grant to H. Svensen and a Centre of Excellence grant to CEED, project number 223272). We also would like to thank the Council of Geoscience and the National Core Library in Pretoria for providing borehole material and logs (handled by David Motloi).

References

- Aarnes I, Svensen H, Polteau S, Planke S (2011) Contact metamorphic devolatilization of shales in the Karoo Basin, South Africa, and the effects of multiple sill intrusions. *Chem Geol* 281:181–194
- Aarnes I, Podladchikov Y, Svensen H (2012) Devolatilization-induced pressure build-up: implications for reaction front movement and breccia pipe formation. *Geofluids*. doi:10.1111/j.1468-8123.2012.00368.x
- Bristow JW, Saggerson EP (1983) A review of Karoo volcanicity in southern Africa. *Bull Volcanol* 46:135–159
- Catuneanu O, Hancox PJ, Rubidge BS (1998) Reciprocal flexural behaviour and contrasting stratigraphies: a new basin development model for the Karoo retroarc foreland system, South Africa. *Basin Res* 10:417–439
- Chevallier L, Woodford A (1999) Morpho-tectonics and mechanism of emplacement of the dolerite rings and sills of the western Karoo, South Africa. *S Afr J Geol* 102:43–54
- du Toit AI (1920) The Karoo dolerites of South Africa: a study in hypabyssal injection. *Trans Geol Soc S Afr* 23:1–42
- Duncan AR, Erlank AJ, Marsh JS (1984) Regional geochemistry of the Karoo igneous province. In: Erlank AJ (ed) *Petrogenesis of the Volcanic Rocks of the Karoo Province*. Geological Society of South Africa Special Publication, Johannesburg, pp 355–388
- Duncan RA, Hooper PR, Rehacek J, Marsh JS, Duncan AR (1997) The timing and duration of the Karoo igneous event, southern Gondwana. *J Geophys Res* 102:18127–18138
- Duncan RA, Marsh JS (2006) The Karoo Igneous Province. In: Johnson MR, Anhaeusser CR, Thomas RJ (eds) *The Geology of South Africa*. Geological Society of South Africa/Council for Geoscience, Johannesburg/Pretoria, pp 501–519
- Galerne CY, Neumann ER, Planke S (2008) Emplacement mechanisms of sill complexes: information from the geochemical architecture of the Golden Valley Sill Complex, South Africa. *J Volcanol Geoth Res* 177:425–440
- Galerne CY, Neumann ER, Aarnes I, Planke S (2010) Magmatic Differentiation processes in saucer-shaped sills: evidence from the Golden Valley Sill in the Karoo Basin, South Africa. *Geosphere* 6(2):1–26
- Hammer Ø, Harper DAT, Ryan PD (2001) PAST: Paleontological statistics software package for education and data analysis. *Palaeontol Electron* 4(1)
- Jamtveit B, Svensen H, Podladchikov Y, Planke S (2004) Hydrothermal vent complexes associated with sill intrusions in sedimentary basins, Physical geology of high-level magmatic systems. Geological Society Special Publication, London, pp. 233–241
- Jourdan F, Féraud G, Bertrand H, Watkeys MK, Renne PR (2007) Distinct brief major events in the Karoo large igneous province clarified by new $^{40}\text{Ar}/^{39}\text{Ar}$ ages on the Lesotho basalts. *Lithos* 98(2007):195–209
- Jourdan F, Féraud G, Bertrand H, Watkeys MK, Renne PR (2008) The $^{40}\text{Ar}/^{39}\text{Ar}$ ages of the sill complex of the Karoo large igneous province: Implications for the Pliensbachian-Toarcian climate change. *Geochem. Geophys. Geosyst.* 9:Q06009
- Marsh JS, Eales HV (1984) The chemistry and Petrogenesis of igneous rocks of the Karoo central area, Southern Africa. In: Erlank AJ (ed) *Petrogenesis of the volcanic rocks of the Karoo Province*. Special Publication of the Geological Society of South Africa, Johannesburg, vol 13, pp 27–67
- Marsh JS, Allen P, Fenner N (2003) The geochemical structure of the Insizwa lobe of the Mount Ayliff Complex with implications for the emplacement and

- evolution of the complex and its Ni-sulphide potential. *S Afr J Geol* 106:409–428
- Marsh JS, Hooper PR, Rehacek J, Duncan RA (1997) Stratigraphy and age of the Karoo basalts of Lesotho and implications for correlations within the Karoo igneous province. In: Mahoney JJ, Coffin MF (eds) Large igneous provinces: continental, oceanic, and planetary flood volcanism. Geophysical Monograph, American Geophysical Union, vol 100, pp 247–272
- Mazzini A, Svensen H, Leanza HA, Corfu F, Planke S (2010) Early Jurassic shale chemostratigraphy and U-Pb ages from the Neuquén Basin (Argentina): implications for the Toarcian Oceanic Anoxic Event. *Earth Planet Sci Lett* 297(3–4):633–645
- Moulin M, Fluteau F, Courtillot V, Marsh J, Delpéch G, Quidelleur X, Gerard M, Jay AE (2011) An attempt to constrain the age, duration, and eruptive history of the Karoo flood basalt: Naude's Nek section (South Africa). *J Geophys Res Solid Earth* 116. doi: [10.1029/2011JB008210](https://doi.org/10.1029/2011JB008210)
- Neumann E-R, Svensen H, Galerne CY, Planke S (2011) Multistage evolution of dolerites in the Karoo large igneous province, Central South Africa. *J Petrol* 52:959–984
- Polteau S, Mazzini A, Galland O, Planke S, Malthe-Sørenssen A (2008a) Saucer-shaped intrusions: occurrences, emplacement and implications. *Earth Planet Sci Lett* 266(1–2):195–204
- Polteau S, Ferré E, Planke S, Neumann E-R, Chevallier L (2008b) How are saucer-shaped sills emplaced? Constraints from the Golden Valley Sill, South Africa. *J Geophys Res* 01(2008):113. doi:[10.1029/2008JB005620](https://doi.org/10.1029/2008JB005620)
- Rowell and De Swart (1976) Diagenesis in Cape and Karoo sediments, South Africa and its bearing on their hydrocarbon potential. *Trans Geol Soc S Afr* 79:81–145
- Svensen H, Jamtveit B, Planke S, Chevallier L (2006) Structure and evolution of hydrothermal vent complexes in the Karoo Basin. *S Afr J Geol Soc London* 163:671–682
- Svensen H, Planke S, Chevallier L, Malthe-Sørenssen A, Corfu B, Jamtveit B (2007) Hydrothermal venting of greenhouse gases triggering early Jurassic global warming. *Earth Planet Sci Lett* 256:554–566
- Svensen H, Corfu F, Polteau S, Hammer Ø, Planke S (2012) Rapid magma emplacement in the Karoo large igneous province. *Earth Planet Sci Lett* 325–326:1–9
- Tankard A, Welsink H, Aukes P, Newton R, Stettler E (2009) Tectonic evolution of the Cape and Karoo basins of South Africa. *Mar Pet Geol* 26:1379–1412
- Winter H de la R, Venter JJ (1970) Lithostratigraphic correlation of recent deep boreholes in the Karoo-Cape sequence. In: Proceedings of the second Gondwana symposium, South Africa. Council for Scientific and Industrial Research, Pretoria, pp 395–408
- Walker F, Poldervaart A (1949) Karoo dolerites of the Union of South Africa. *Geol Soc Amer Bull* 60:591–706

Dykes, Sills, Laccoliths, and Inclined Sheets in Iceland

Agust Gudmundsson, Federico A. Pasquarè,
and Alessandro Tibaldi

Abstract

Dykes and inclined sheets are extremely common in the volcanic systems of Iceland, both the fossil ones as well as the active systems. Until recently, comparatively few sills and laccoliths were known, but recent studies show that many laccoliths occur in the lava pile and that sills are also very common. Many, perhaps most, shallow magma chambers in Iceland (including laccoliths) develop from sills, so that understanding the conditions for sill formation is of great volcanotectonic importance. Some of the laccoliths described here are felsic, others are mafic, and reach a maximum thickness of several hundred metres. They were emplaced at shallow depths (several hundred metres below the surface) and presumably acted as short-lived shallow magma chambers. Most sills in Iceland are mafic. The largest sills reach at least 120 m in thickness and presumably many kilometres in diameter. Inclined sheets and vertical dykes supply magma to essentially all eruptions in Iceland. Sheet swarms are confined to central volcanoes (stratovolcanoes, calderas), whereas regional dykes occur outside central volcanoes. Most inclined sheet are injected from shallow magma chambers. Individual swarms of inclined sheets are circular to slightly elliptical in plan view (with a maximum diameter of about 18 km), contain up to tens of thousands of sheets, generating a crustal dilation of as much as 80 % (measured in a profile roughly perpendicular to the average sheet attitude), the sheets being

A. Gudmundsson (✉)

Department of Earth Sciences, Royal Holloway
University of London, Queen's Building,
Egham, UK
e-mail: a.gudmundsson@es.rhul.ac.uk

F.A. Pasquarè

Department of Theoretical and Applied Sciences,
Insubria University, Varese, Italy

A. Tibaldi

Department of Earth and Environment Sciences,
University of Milan-Bicocca, Milan, Italy

Adv in Volcanology (2018) 363–376

DOI 10.1007/11157_2014_1

© Springer International Publishing Switzerland 2014

Published Online: 08 December 2014

mostly <1 m thick and dipping 30°–60° towards the shallow magma source chamber. By contrast, the regional dyke swarms are highly elongated (elliptical) in plan view (with common maximum lengths of 50 km and widths of 5–10 km), contain hundreds of dykes at the level of exposure, mostly subvertical and 2–6 m thick. Recent studies suggest that many regional dykes were emplaced through inclined or vertical magma flow. We conclude that, while much progress has been made, we still do not have reliable models for forecasting the likely paths of sheet-like intrusions during volcanic unrest periods with magma-chamber rupture.

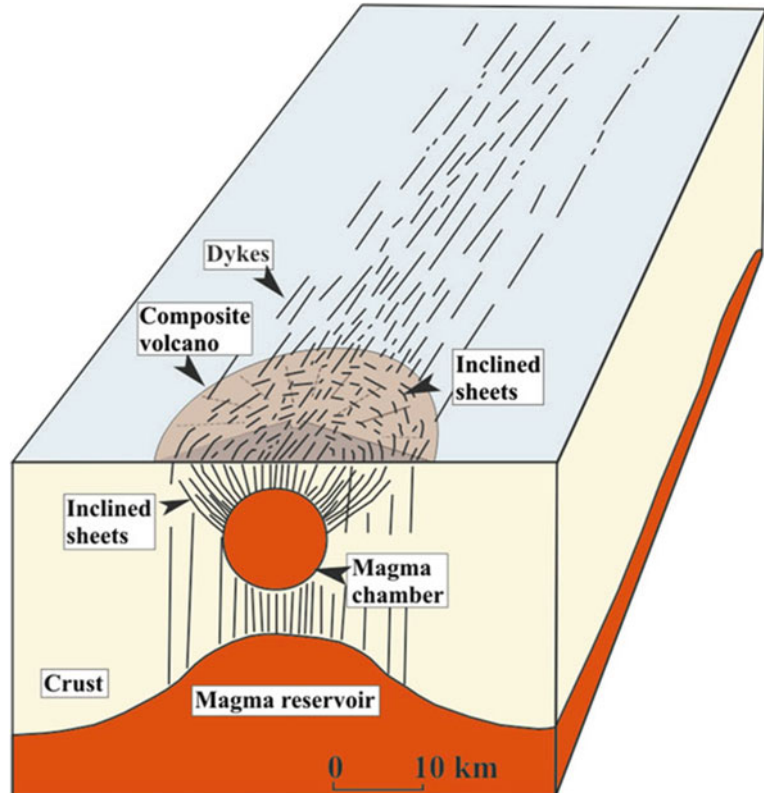
1 Introduction

There are numerous dykes in Iceland; tens of thousands have been studied for more than a century and their characteristics are well known. Inclined sheets were discovered later, primarily through the work of Walker (1974, 1975), and are now known to be very common in central volcanoes (stratovolcanoes and calderas). Few laccoliths and sills, however, were known in Iceland until comparatively recently, whereby

studies have shown these intrusions to be much more common than they were thought to be.

Dykes occur mainly in elongated swarms outside the central volcanoes, whereas the inclined sheets are mostly confined to the central volcanoes (Fig. 1). The dykes are mostly controlled by the regional stress field associated with the divergent and propagating plate boundaries, whereas the inclined sheets are primarily controlled by the local stress field associated with the shallow crustal magma chambers that supply magma to the

Fig. 1 Schematic overview of the internal structure of volcanic systems in Iceland. Associated with the central volcano (here a composite volcano) is a shallow magma chamber which, in turn, is supplied with magma from a deep-seated magma reservoir. It is likely the many, perhaps most, of the regional dykes are fed by deep-seated reservoirs, whereas most or all the inclined sheets are supplied with magma from shallow magma chambers



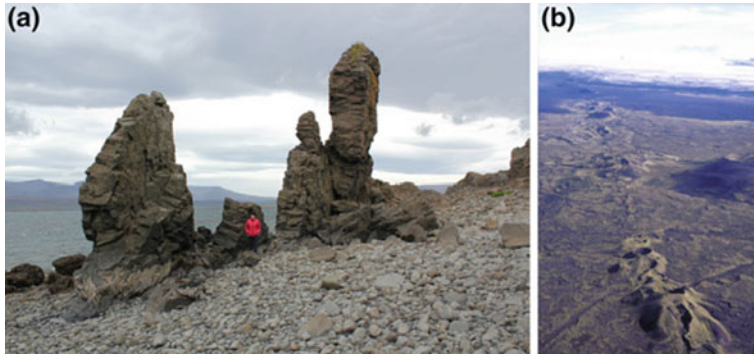


Fig. 2 Regional dykes. **a** A dyke on the coast in Southwest Iceland, view northeast, the dyke strike is N30°E, the dip 82°W, and the thickness 3 m. **b** View northeast, part of the 27-km-long (but segmented)

volcanic fissure/crater row formed during the AD 1783 Laki eruption in southern Iceland. The feeder dyke must have been at least 27 km long

sheets and to the eruptions of the central volcanoes. Sills and laccoliths occur both inside and outside central volcanoes. Sills and laccoliths are potential shallow magma chambers, and many function as such. Many, and presumably most, shallow magma chambers (including laccoliths) initiate from sills (Gudmundsson 2012a). Traditionally, the dyke and sheet swarms are, depending on age, referred to as Tertiary, Pleistocene, and Holocene swarms. The oldest rocks in Iceland are about 15 Ma, so that Tertiary swarms in Iceland were formed in Miocene and Pliocene.

The main aim of this paper is to discuss and describe briefly all these four types of intrusions, their structure and mechanism of emplacement. Dykes in Iceland have been treated very extensively in the literature (e.g., Walker 1960, 1974; Gudmundsson 1995; Paquet et al. 2007; Galindo and Gudmundsson 2012) and so have inclined sheets, although to a lesser degree (Walker 1975; Gudmundsson 1995; Klausen 2004, 2006; Siler and Karson 2009; Tibaldi et al. 2011). By contrast, laccoliths and sills in Iceland have received comparatively little attention (Pasquarè and Tibaldi 2007; Gudmundsson and Lotveit 2012).

2 Dykes

The regional dykes occur in elongated swarms, commonly around 50 km long and 5–10 km wide, outside the central volcanoes (Fig. 1). The

regional dykes are mostly close to vertical (Fig. 2a) and have generally similar strike (are subparallel) within each swarm. In the southern half of Iceland, the dyke trend is mostly north-east, whereas in the northern half of the country, the dyke trend is mostly north-northeast—similar to the general trends of the active volcanic systems (Fig. 3; Gudmundsson et al. 2014). The change in tectonic orientation from north to south across Iceland reflects the change in the trend of the ocean ridges north and south of the island; the Reykjanes Ridge, to the south, strikes northeast whereas the Kolbeinsey Ridge, to the north, strikes north-northeast (Fig. 3).

The dykes vary in thickness from a few centimetres to about 60 m. The thick dykes are mostly formed in multiple magma injections; the individual injections can often be recognised as ‘columnar rows’ (Gudmundsson 1995). The most common (mode) thickness of dykes in a given swarm is normally 1–2 m. The Tertiary (Miocene-Pliocene) and Pleistocene swarms, however, have different mean thicknesses; the Tertiary swarms have a mean dyke thickness of 4–6 m whereas the Pleistocene swarms have mean thickness of 1–2 m. Thus, generally, the mean thickness of regional dykes in Iceland is 2–6 m. Some Tertiary dykes have been traced along their lengths or strike dimensions to distances exceeding 20 km, but the total lengths are unknown since one or both lateral ends are normally uncertain.

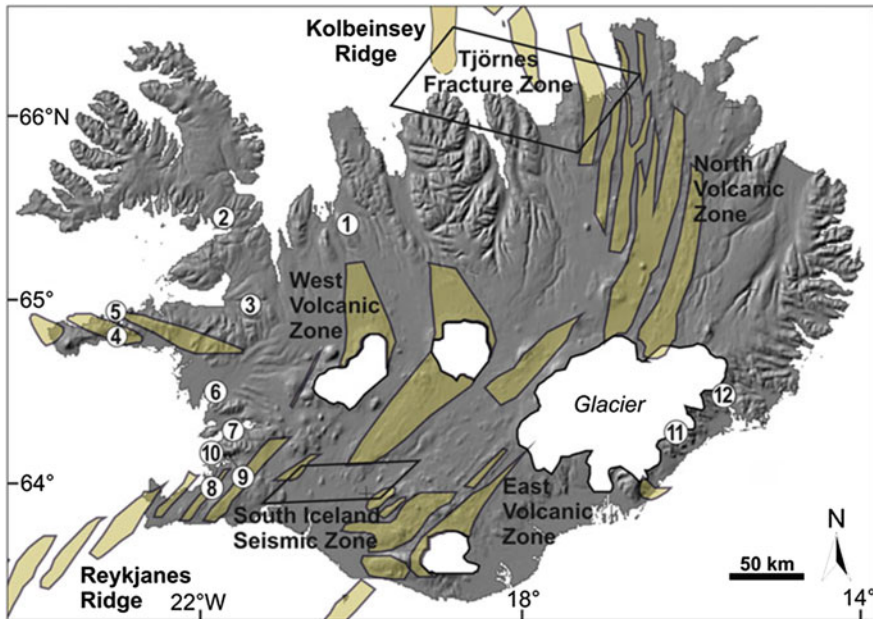


Fig. 3 Volcanic zones and systems as well as the associated transform zones (the Tjörnes Fracture Zone and the South Iceland Seismic Zone) in Iceland. The strike of volcanic systems in the northern part of the country reflects that of the Kolbeinsey Ridge, whereas that in the southern part of the country reflects that of the

Reykjanes Ridge. Numbers are locations of the centrally-inclined sheet swarms described in the present paper and of the gabbro plutons: 1 Vatnsdalur, 2 Kroksfjörður, 3 Reykjadalur, 4 Midhyma-Lysuskard, 5 Kolgrafarmúli, 6 Thverfell, 7 Stardalur, 8 Kjalarnes, 9 Hvalfjörður, 10 Hafnarfjall, 11 Thverartindur, 12 Geitafell

Volcanic fissures are the surface expressions of feeder dykes (Fig. 2b). The longest (segmented) Holocene volcanic fissure in Iceland is about 65 km long, and there are several that reach tens of kilometres (Gudmundsson 1995). The associated feeder dykes must reach at least the same lengths. Comparatively few feeder dykes have been reported as being directly connected to their eruptive materials—this applies not only to Iceland but worldwide (Galindo and Gudmundsson 2012). One reason for the rarity of reported connections of this kind is lack of systematic research. For example, when the exposures are exceptionally good in active volcanoes, such as in Miyakejima in Japan, careful studies reveal many feeder dykes connected to their eruptive materials (Geshi et al. 2010).

The propagation direction of dykes have received considerable attention (Gudmundsson et al. 2014). There is considerable evidence that many dykes propagate essentially laterally from shallow magma chambers or conduits in many

large volcanic edifices such as Etna and Stromboli (Acocella and Neri 2003; Acocella and Tibaldi 2005). In fact, simple analytical models (Gudmundsson 2011a, b) suggest that lateral dyke propagation may, under certain conditions, be favoured (over vertical propagation) out to distances of many kilometres from the centre of the source conduit or a magma chamber. But such dykes are normally thin, of rather evolved composition, and form a part of the general sheet swarm of the volcano. In Iceland swarms of inclined sheets are up to 18 km in diameter. And even if many dykes may propagate to a degree laterally within the sheet swarm, all the feeders must reach the surface and thus propagate at least partly vertically. In fact, fractures in solids normally propagate in various directions (Pook 2002; Sun and Jin 2012), and the same must apply to dykes and other rock fractures. Detailed studies of sheet swarms also show that many sheets can be traced to the fossil magma chambers (plutons), so that there is generally no doubt

about their source and the direction of propagation (e.g., Gudmundsson 2002; Klausen 2004; Burchardt and Gudmundsson 2009).

While the sources and propagation directions of local dykes and inclined sheets are thus well known, the same does not apply to the thick and long and subvertical regional dykes. For these, two basic ideas have been discussed: (1) the dykes are primarily injected vertically from reservoirs in the lower crust or at the crust-mantle boundary; (2) the dykes are primarily injected laterally from shallow magma chambers at the depth of a few kilometres (e.g., Sigurdsson and Sparks 1978; Paquet et al. 2007). The lateral propagation is here supposed to apply to dykes that, in Iceland, reach tens of kilometres in length, and in other areas (such as Canada) hundreds of kilometres (e.g., Ernst et al. 2001).

As for Iceland, the common differences in chemistry and volume between typical eruptive materials associated with feeder dykes inside and outside central volcanoes (the erupted materials outside the volcanoes tend to be much more primitive in composition and of larger volumes) is often taken as an indication that the regional feeder dykes do not form through lateral propagation from shallow magma chambers (which normally hold rather evolved magmas) but rather in primarily vertical flow from deep-seated reservoirs (Gudmundsson 1990; Hartley and Thordarson 2012, 2013). Recently, there have been many magnetic anisotropy studies in Iceland focusing on the direction of magma flow in regional dykes. All kinematic indicators for dykes are subject to somewhat different interpretations, and it should also be noted that the direction of magma flow does not necessarily reflect the main direction of fracture propagation. This latter is well known from volcanic-fissure formation. Thus, close to the surface the magma flow is necessarily primarily vertical. This follows because the flow must reach the commonly flat surface and form volcanic fissures, crater cones, and other structures. At the same time the volcanic-fissure propagation is necessarily primarily lateral at the surface. Thus, commonly, a laterally propagating volcanic fissure channels vertically flowing magma to the surface. However, these

recent magnetic anisotropy results indicate primarily inclined, at 30°–60° (Eriksson et al. 2011), or vertical magma flow (Kissel et al. 2010). So far as these results go, they tend to support inclined or vertical magma flow rather than lateral for the regional dykes of Iceland.

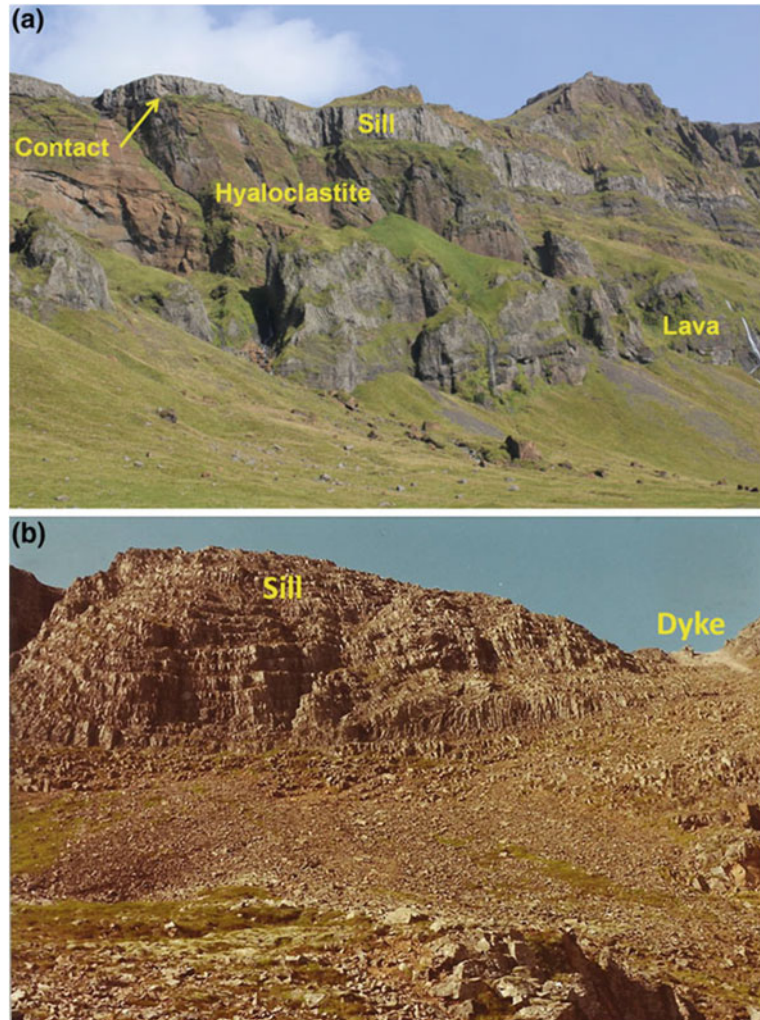
3 Sills

Until recently, sills were rarely reported from Iceland. Studies by the present authors in the past decade, however, show that sills are common in Iceland. They occur in the Tertiary and Pleistocene lava piles, as well as in the active volcanic zones (Fig. 4). Sills are particularly common in Pleistocene rocks, partly because of the common abrupt changes in mechanical properties between layers—changes that encourage dyke deflection into sills (Gudmundsson 2011a, b; Gudmundsson and Lotveit 2012). Abrupt changes of this type occur, for example, where lava flows or earlier sills alternate with basaltic breccias, hyaloclastites.

Since the active volcanic systems and central volcanoes contain numerous lava flows and hyaloclastite layers, sill formation is very common in many active volcanoes. Examples include many sills in the Eyjafjallajökull Volcano in South Iceland (Fig. 4a). The emplacement of similar sills is thought to have taken place prior to the 2010 eruptions in Eyjafjallajökull (Sigmundsson et al. 2010; Gudmundsson et al. 2012; Tarasewicz et al. 2012). In some of these interpretations, there were many sill injections in Eyjafjallajökull in the decade before the 2010 eruptions, and some of the sills, it is suggested, reached lateral dimensions (diameters) of as much as 17 km (Sigmundsson et al. 2010).

Sill emplacement and propagation direction are reasonably well understood in general terms. The sills tend to form when dykes or inclined sheets become deflected along discontinuities such as contacts between dissimilar rock layers (Gudmundsson 1990, 2011a, b; Kavanagh et al. 2006). The details of sill formation and propagation are, however, poorly understood. In particular, the conditions that allow dykes to become deflected into sills are still a matter of intense

Fig. 4 Sills. **a** Basaltic sills, lava flows, hyaloclastite layers, and contacts in the southern slopes of the Eyjafjallajökull Volcano. **b** View north, part of a 120-m-thick basaltic sill in East Iceland. The sill was formed through multiple injections



research. Also, some dykes become doubly deflected along contacts to form sills, while other dykes are singly deflected; the reasons for these propagation differences are not well understood. Also, sills show many different geometric shapes (Gudmundsson and Lotveit 2012) whose origin are still being studied and analysed.

Observed sills in Iceland range in thickness from centimetres to at least 120 m (Fig. 4b). Little systematic work has been made to trace the sills laterally. Some extend for several kilometres (Gudmundsson and Lotveit 2012), but the ends are often eroded so that the true dimensions are poorly known. Common aspect ratios (lateral dimension/thickness) of sills in the Faeroe Islands

are between about 167 and 500 (Hansen et al. 2011), which agrees well with predictions based on simple analytical fracture-mechanics models (Gudmundsson and Lotveit 2012). Based on these ratios, which are likely to be similar for Iceland, many of the thicker sills in Iceland could be many kilometres in diameter.

Sills are important in their own right as one of the three main types of sheet-like intrusions. But they are also widely regarded as the primary structures from which shallow magma chambers in central volcanoes develop (Gudmundsson 1990, 2012a). Some chambers develop from single sill injections, whereas others form gradually through many injections. Many magma chambers

maintain their sill-like geometry during the lifetimes of the associated central volcano. Sill-like chambers may generate stress fields that encourage the formation of collapse calderas. Other magma chambers change their shapes as they expand and evolve from the initial sill. Such magma chambers include laccoliths.

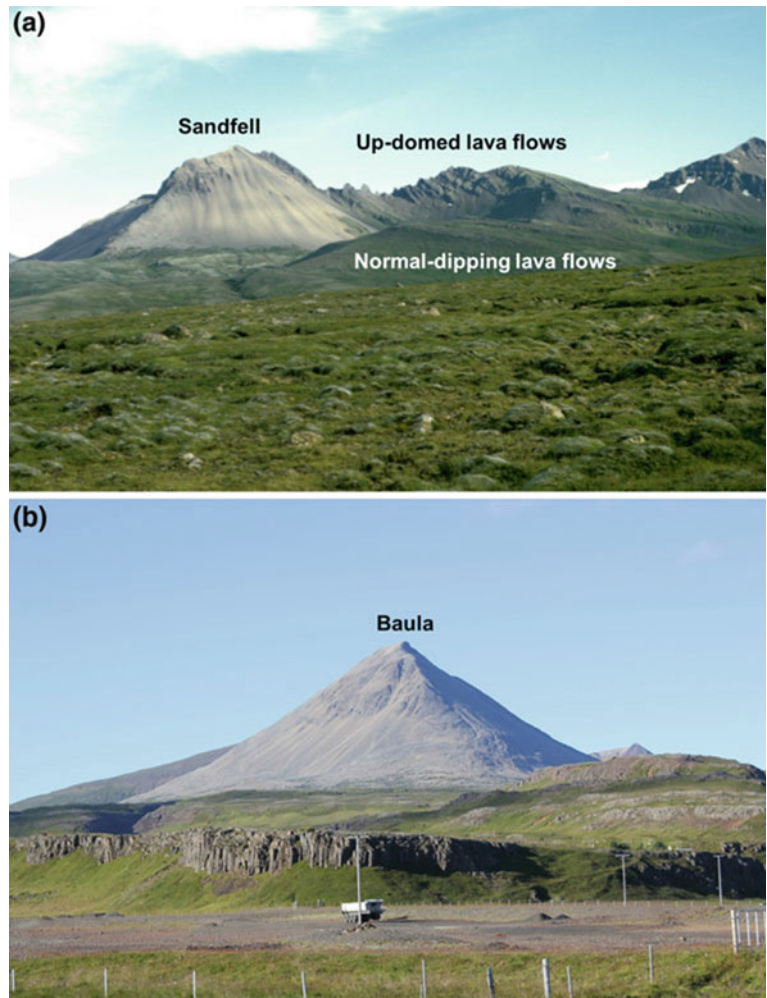
4 Laccoliths

There are many laccoliths in Iceland, most of which are composed of acid (felsic) rocks. The best known laccolith is Sandfell in East Iceland. This laccolith is exceptionally well preserved, with part of the roof—a basaltic lava pile—still

maintained (Fig. 5a). Sandfell peaks at 743 m a.s.l. and at the time of emplacement the roof of the laccolith was within about 500 m of the surface of the volcanic system within which it formed (Hawkes and Hawkes 1933). It is likely to have acted as a shallow magma chamber for a while, as most shallow intrusions in Iceland apparently do.

Another felsic laccolith is Baula in West Iceland (Fig. 5b). Baula peaks at about 934 m a.s.l. and has an estimated age of 3.5 Ma (Johannesson 1974). The lava pile next to the laccolith shows evidence of upbending, but the roof is not nearly as well preserved as in the Sandfell laccolith. Baula and Sandfell are both several hundred metres thick and composed of felsic rocks.

Fig. 5 Felsic laccoliths in the Tertiary lava pile. **a** The laccolith Sandfell in East Iceland. **b** The laccolith Baula in West Iceland



There are also some mafic (basaltic) laccoliths in Iceland. Perhaps the best studied is the mafic laccolith at Stardalur in Southwest Iceland. This laccolith was generated through multiple sheet intrusion, reaches a total thickness of about 200 m, and is located in the middle of a swarm of inclined sheets associated with the 1.8 Ma Stardalur Volcano (Pasquarè and Tibaldi 2007). This laccolith is thus generated in a somewhat similar way as thick, multiple sills (Fig. 4b).

The basic conceptual model of laccolith formation was proposed long ago, and analysed mechanically by Pollard and Johnson (1973). Subsequently, many similar analyses have been made (e.g., McCaffrey and Petford 1997; Rocchi et al. 2002; Bungler and Cruden 2011; Michaut 2011). The basic model, however, remains the same; bending of an elastic crustal plate, the overburden, as a result of magmatic overpressure. The general idea is that laccoliths, like many other plutons (and magma chambers), develop from sills, namely once the sills start to deflect their overburden. While this general model is still used as a basis for understanding laccolith formation, it is clear that elastic bending alone cannot account for the shape of many laccoliths, including those

in Iceland (Fig. 5). The bending and uplift is simply too great for elastic deformation to be plausible. Fracturing and plastic deformation are likely to have played a major role in the formation of the laccoliths in Iceland.

5 Inclined Sheets

Most inclined sheets in Iceland are arranged into centrally-dipping swarms departing from a focus area (e.g. Pasquarè and Tibaldi 2007; Tibaldi et al. 2008). The central-dipping sheet geometry and symmetrical arrangement suggest the location and depth of the source magma chamber (e.g. Tibaldi et al. 2011), although uncertainties remain regarding the possibility of reconstructing the exact shape and size of the shallow magma chamber (Figs. 1 and 6).

Outcrops of centrally-inclined sheet swarms below eroded volcanoes are usually limited in lateral/vertical extent, with different geometries of inclined sheets being found, as well as different models proposed to explain them. These models comprise: (i) Concave-downward (trumpet-shaped) sheets with increasing dip closer to the

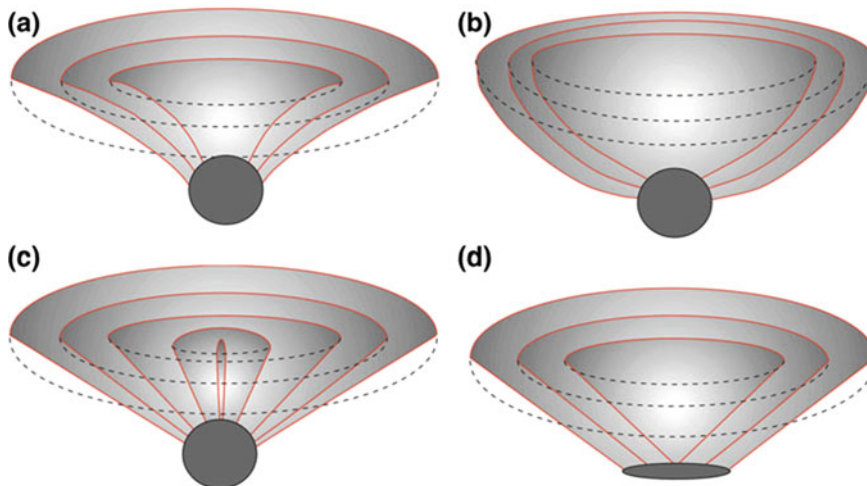


Fig. 6 Possible geometries of centrally-inclined sheet swarms resulting from internal excess magma pressure: **a** radial planar sheets from a spherical magma chamber (after Chadwick and Dieterich 1995; Gudmundsson 1998); **b** concave-upward (bowl-shaped) sheets from a spherical magma chamber (after Chadwick and Dieterich

1995; Gudmundsson 1998); **c** concave-downward (trumpet-shaped) sheets from a sill-shaped magma chamber (after Phillips 1974; Chadwick and Dieterich 1995); **d** planar parallel sheets from a laccolith-like chamber (after Bistacchi et al. 2012)

magmatic source (Fig. 6a) (Phillips 1974); sheets are missing in the central part. (ii) Concave-upward (bowl-shaped) sheets with decreasing sheet dip with depth from a pressurised magma chamber (Fig. 6b) (Phillips 1974); sheets are missing in the central part. (iii) Radial planar sheets from a spherical magma chamber (Fig. 6c) (Chadwick and Dieterich 1995; Gudmundsson 1998). (iv) Planar parallel to sub-parallel sheets originated from a lobate (sill-like) magma chamber (Fig. 6d) (Gudmundsson 1998; Tibaldi et al. 2011; Bistacchi et al. 2012). Here we will review the inclined sheet data collected all over Iceland (Fig. 3) by various authors in order to highlight the common features and possible factors controlling their emplacement.

5.1 West Iceland

In northwest Iceland, inclined sheet swarms are present in three locations in the Vatnsdalur area (Fig. 3) (Siler and Karson 2009). These swarms consist of mafic sheets generally <1.0 m thick that dip radially inward, with dips between 20° and 60°. The largest sheet swarm is 16 km in diameter. Sheets have a planar geometry and 3D reconstructions at the best site (Vididalsfjall) indicate here two cone sheets swarms focusing at 1.0 and 5.0 km bsl respectively. “Hot slickenlines” created during intrusion exclusively plunge down-dip in the planes of the sheets, indicating they were fed from below. These centrally-inclined sheets are associated with major gabbroid intrusions and to eroded volcanoes.

To the southwest, in the area of Kroksfjörður, there is a complex of centrally-inclined sheets associated with a depression (Hald et al. 1971) (Fig. 3). These sheets intrude basal lava flows, breccia and a series of basaltic plugs. Above the centre of the complex, which is about 10 km in diameter, cone sheets are almost lacking. The individual sheets have thickness usually <3 m with most common thickness of 0.5–1.0 m. The sheet complex shows a weak tendency to decrease in dip away from the centre. In the area, a gabbro body crops out over an area of about 1 km² but it is not cut by the inclined sheets.

Further to the south, in the Tertiary Reykjadalur Volcano, there is a swarm of centrally-inclined sheets with a total diameter of about 18 km (Gautneb and Gudmundsson 1992) (Fig. 3). The sheets have an average dip of 45° and thickness of 1.0 m. Locally, the sheets make up nearly 90 % of the rock, but in 1–1.5-km-long profiles they are 5.8–7.9 %. One-third of the sheets are porphyritic, containing as much as 50 % of plagioclase phenocrysts. The local magmatic stress field associated with the shallow magma chamber controlled the geometry and, partly, thickness of the sheets to a distance of 9 km from the centre of the volcano.

In westernmost Iceland, in the Snaefellsnes Peninsula that is essentially made up of Tertiary-Quaternary basalts, there are three major intrusions, each one surrounded by a centrally-inclined sheet swarm (Fig. 3). Along the southern side there are the Midhyrna gabbroid and Lysuskard granophiric intrusions (Upton and Wright 1961), whereas on the northern coast there is the Kolgrafarmúli gabbro. All of them intrude the Tertiary basaltic lava flows. The Midhyrna and Lysuskard intrusions are surrounded and intruded by two centrally dipping sheet swarms (Fig. 7) (Tibaldi et al. 2013); these sheets show no gradual variation in dip with distance from the focus area, are rectilinear in section view, and intrude with the same geometry the main intrusive bodies as well as the layered Tertiary lavas. The diameter of both sheet swarms is about 12 km, the average sheet thickness is 0.63 m, and the average dip is 28° (Tibaldi et al. 2013), lower than for other sheet swarms in Iceland whose average dip is 34°. The Kolgrafarmúli gabbro is located near a centrally-inclined sheet swarm (Fig. 3) that corresponds to the Setberg volcanic centre (Sigurdsson 1966). These sheets are inclined 25°–40° towards a focus at about 3 km depth underneath a caldera, filled with silicic breccia and the gabbro intrusion. Based on the Sigurdsson’s (1966) map, the sheets cut also the gabbro body. The diameter of the sheet swarm is 11 km.

To the south, the mountain Esja has three centrally-inclined sheet swarms that were emplaced mostly within almost isotropic hyaloclastite deposits (Pasquare and Tibaldi 2007;

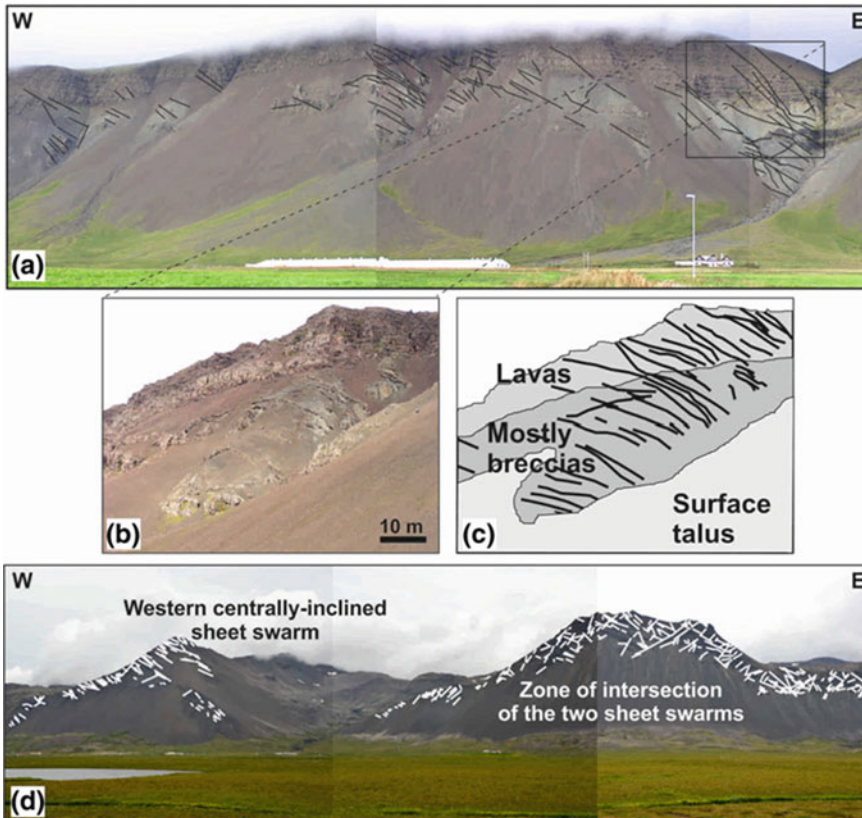


Fig. 7 Examples of centrally-inclined sheet swarms at two different locations in Western Iceland. **a** At Thverfell, SW Iceland, sheets are dipping toward the centrally-located focus area. **b** Detailed image of the sheets intruding the earlier, effusive sequence. **c** Interpretation

of the previous image, showing lavas and breccias intruded by inclined sheets. **d** At the Snæfellsnes Peninsula, two different swarms converge toward two different focus areas. The eastward-dipping swarm and the area where the two swarms cross-cut are clearly visible

Tibaldi et al. 2008) (Fig. 3). These sheet swarms were emplaced during a transcurrent fault phase, in plan view have an E-W elongation and alignment parallel to the strike-slip faults, and show a slight but systematic gradual dip decrease outwards. All of them are associated with dioritic laccoliths (Tibaldi and Pasquarè 2008). At the Thverfell swarm, 8 km in diameter, the average sheet thickness is 1.1 m and the dip is 32° . At Stardalur swarm, 12 km in diameter, sheets are associated with a caldera, have average thickness of 1.7 m and dip of 35° . At Kjalarnes the sheet swarm diameter is 5 km.

At the extinct Hvalfjörður Volcano, of Tertiary age, in southwest Iceland (Fig. 3) sheet

strike is spread over the whole circle, with a slight peak in the northeastern sector, parallel with the trend of the rift zone in southwest Iceland within which the swarm formed (Gudmundsson 1995). The dip of the sheets ranges 5° – 90° . The dip-frequency distribution has two peaks at 70° – 90° and at 10° – 40° . The sheets range in thickness from several centimeters to 14 m, the most common thickness being <0.5 m.

In southwest Iceland, the 4–6 Ma old Hafnarfjall Volcano was studied by Gautneb et al. (1989) who documented a centrally-inclined sheet swarm that deviates from a circular distribution more than other swarms in Iceland: in particular, the sheets are preferentially NE-striking, that is,

parallel to the NE-trending West Volcanic Zone and partly controlled by the associated regional stress field.

5.2 East Iceland

The exposed interior of the Thverartindur igneous centre (Fig. 3; Klausen 2004) is characterised by a dense circular swarm of centrally inclined sheets. The study of the orientation and thickness of 745 mafic sheets suggest a bowl- and slightly fan-shaped swarm geometry, located above a 4-km-thick, $\sim 140\text{-km}^3$ -large, slightly flattened magma source. The sharp decrease in sheet density along the inner and outer margins of the swarm suggest that most sheets were injected from a narrower source area than the swarm's estimated 2–3 km width at the surface. The sheet swarm is marked by a significant ($17^\circ/\text{km}$) outward decrease away from the source, as noted also at several other eroded central volcanoes in Iceland, such as Reykjadalur (Gautneb and Gudmundsson 1992) and Stardalur (Pasquare and Tibaldi 2007). The 0.1 m/km decrease in the average sheet thickness through the swarm reflects the upward narrowing of sheets, while the relatively low number of $<0.5\text{-m}$ -thick sheets in the uppermost part of the swarm is interpreted to reflect the subsurface arrest of more than a third of all sheets injected from the source.

The 5–6 Ma old Geitafell Volcano in South-east Iceland (Fig. 3) is located in an area marked by the deepest glacial erosion in Iceland (2 km). Glacial valleys cut the centre of the volcano and expose sections that reach down to the roofs of several gabbro plutons, which in turn are surrounded by dense swarms of inclined sheets and remnants of a high-temperature geothermal system (Fridleifsson 1983, 1984). Inclined sheets, exposed along several deep canyons in the vicinity of the gabbros, comprise about 10,000, mainly basaltic, sheet intrusions. Burchardt and Gudmundsson (2009) suggest that the Geitafell sheet swarm is most likely bowl-shaped (i.e., concave upward), and field studies support that most of the sheets are related to the gabbros in

the area, presumably the uppermost part of the shallow magma chamber of the Geitafell Volcano. A second swarm of younger and steeper-dipping inclined sheets may represent a later and deeper magma source located a few hundred meters to the east that may indicate an independent pulse of activity.

6 Discussion

Field studies of dykes, sills, laccoliths and inclined sheets improve our understanding of their mechanics of emplacement and general transport of magma in the crust. In particular, since almost all eruptions are fed by dykes or inclined sheets, understanding how they propagate to the surface or, alternatively, become arrested in some crustal layers at depth is of fundamental importance for interpreting volcanic unrest periods and hazards in active volcanoes and, in particular, the geophysical and geochemical data obtained through volcano monitoring.

As indicated above, the details of the mechanics of propagation and path formation for sheet-like intrusions are still poorly understood and subject to intensive research. For the Icelandic intrusions, it is reasonably clear that most of the inclined sheets (including the associated local dykes) can be traced to shallow magma chambers, located at 1–5 km depth below the surface of the volcano at the time of sheet formation. From these shallow magma chambers, the sheets propagate in all directions—but those that are located above the magma chambers must to a large degree propagate upwards and dip-parallel, particularly the feeders for eruptions. For the regional dykes, the results are not so clear; some data may suggest primarily lateral flow of magma from shallow magma chambers, whereas other data indicate primarily inclined or vertical flow of magma from deep-seated reservoirs.

The details of the propagation path itself, whether generated through lateral flow, vertical flow, or a mixture of both, is of fundamental importance for hazard assessment. When a magma chamber ruptures and injects a sheet-like intrusion

during an unrest period, the propagation path and final geometry of that intrusion depends on various factors. These include the elastic energy available to produce the fracture (the surface energy) and propagate the intrusion, the local stresses in the host rock, and the rheological properties of the magma (e.g., Gudmundsson 2012b; Tait and Taisne 2013; Gonnermann and Manga 2013). When the host rock is modelled as a homogeneous, isotropic elastic half space, as is common in some deformation studies, the primary constraint on the rate of intrusion propagation is the viscosity of the magma (Spence and Turcotte 1985; Lister and Kerr 1991).

Volcanic zones and, in particular, central volcanoes (stratovolcanoes, calderas) are characterised by layers that commonly have widely different properties (Fig. 4; Apuani et al. 2005; Geshi et al. 2010). They are thus analogous to composite materials whose mechanical properties commonly vary abruptly between layers. A primary control on fracture propagation and arrest in composite materials is the variation in their mechanical properties, particularly abrupt changes in Young's modulus between layers as well as the properties of the layer contacts or interfaces in relation to those of the adjacent layers (He and Hutchinson 1989; Pook 2002; Sun and Jin 2012). In fact, composite materials are made strong—that is, resistant to fracture propagation—through alternating layers and contacts of widely different mechanical properties.

Most arrested dykes become arrested at contacts between layers (Gudmundsson 2002). Similarly, most deflected dykes become deflected (commonly into sills) at contacts (Gudmundsson 2011a). It is thus clear that layering in volcanoes has great effects on sheet-intrusion propagation paths. This is well known from field studies (Geshi et al. 2010), and is also implied in the interpretation of geodetic and seismic studies during unrest periods in volcanoes. For example, there appear to have been several episodes of dyke injections in the Eyjafjallajökull Volcano in the 1990s and again in 2009 before the dyke-fed eruptions of 2010 occurred (Jakobsdottir 2008; Sigmundsson et al. 2010). The earlier dykes apparently became

arrested, presumably at contacts between mechanically dissimilar rocks (Fig. 4a), and some dykes are thought to have been deflected into sills (Sigmundsson et al. 2010; Gudmundsson et al. 2012; Tarasewicz et al. 2012).

While Eyjafjallajökull was very well monitored prior to the 2010 eruptions, the details of the paths of the dykes and sills and inclined sheets that eventually resulted in the eruptions are poorly known and understood. Mechanical layering is a major factor that largely controls the sheet-intrusion paths, including their attitudes (and thus whether they propagate as dykes, inclined sheets, or sills) and arrest (and thus whether they become feeders to eruptions). Another factor is the elastic energy available to drive the sheet-fracture propagation (Gudmundsson 2012b). While both these aspects of sheet-intrusion propagation and magma movement have received considerable attention in recent years, the mechanical complexity of many volcanic zones and central volcanoes means that much research is needed before reasonably accurate models will be available for forecasting the likely sheet-intrusion propagation paths during unrest periods.

Acknowledgments This is a contribution to the International Lithosphere Program Task Force II “Volcanoes and society: environment, health and hazards”. Sergio Rocchi and Valerio Acocella are acknowledged for their helpful reviews of an earlier version of the manuscript.

References

- Acocella V, Neri M (2003) What makes flank eruptions? The 2001 Etna eruption and its possible triggering mechanism. *Bull Volcanol* 65:517–529
- Acocella V, Tibaldi A (2005) Dike propagation driven by volcano collapse: a general model tested at Stromboli, Italy. *Geophys Res Lett* 32:L08308. doi:10.1029/2004GL022248
- Apuani T, Corazzato C, Cancelli A, Tibaldi A (2005) Physical and mechanical properties of rock masses at Stromboli: a dataset for volcano instability evaluation. *B Eng Geol Environ* 64:419–431
- Bistacchi A, Tibaldi A, Pasquarè FA, Rust D (2012) The association of cone–sheets and radial dykes: data from the Isle of Skye (UK), numerical modelling, and

- implications for shallow magma chambers. *Earth Planet Sci Lett* 339–340:46–56
- Bunger AP, Cruden AR (2011) Modeling the growth of laccoliths and large mafic sills: role of magma body forces. *J Geophys Res* 116:B02203
- Burchardt S, Gudmundsson A (2009) The infrastructure of Geitafell Volcano, Southeast Iceland, in studies in volcanology: the legacy of George Walker. In: Thordarson T et al (eds) Special Publication of IAVCEI, vol 2. Geological Society, London, pp 349–370
- Chadwick WW Jr, Dieterich JH (1995) Mechanical modelling of circumferential and radial dike intrusion on Galapagos volcanoes. *J Volcanol Geoth Res* 66:37–52
- Ernst RE, Grosfils EB, Mege D (2001) Giant dike swarms: earth, venus and mars. *Ann Rev Earth Planet Sci* 29:489–534
- Eriksson PI, Riishuus MS, Sigmundsson F, Elming SA (2011) Magma flow directions inferred from field evidence and magnetic fabric studies of the Streitisvarf composite dike in East Iceland. *J Volcanol Geoth Res* 206:30–45
- Fridleifsson GO (1983) Mineralogical evolution of a hydrothermal system. *GRC Trans* 7:147–152
- Fridleifsson GO (1984) Mineralogical evolution of a hydrothermal system II. Heat sources–fluid interactions. *GRC Trans* 8:1–5
- Galindo I, Gudmundsson A (2012) Basaltic feeder dykes in rift zones: geometry, emplacement, and effusion rates. *Nat Hazard Earth Sys* 12:3683–3700
- Gautneb H, Gudmundsson A (1992) Effect of local and regional stress fields on sheet emplacement in West Iceland. *J Volcanol Geoth Res* 51:339–356
- Gautneb H, Gudmundsson A, Oskarsson N (1989) Structure, petrochemistry, and evolution of a sheet swarm in an Icelandic central volcano. *Geol Mag* 126:659–673
- Geshi N, Kusumoto S, Gudmundsson A (2010) Geometric difference between non-feeder and feeder dikes. *Geology* 38:195–198
- Gonnermann HM, Manga M (2013) Dynamics of magma ascent in the volcanic conduit. In: Fagents SA, Gregg TKP, Lopes RMC (eds) Modeling volcanic processes. Cambridge University Press, Cambridge, pp 55–84
- Gudmundsson A (1990) Emplacement of dykes, sills and crustal magma chambers at divergent plate boundaries. *Tectonophysics* 176:257–275
- Gudmundsson A (1995) Infrastructure and mechanics of volcanic systems in Iceland. *J Volcanol Geoth Res* 64:1–22
- Gudmundsson A (1998) Magma chambers modeled as cavities explain the formation of rift zone central volcanoes and their eruption and intrusion statistics. *J Geophys Res* 103(B4):7401–7412
- Gudmundsson A (2002) Emplacement and arrest of sheets and dikes in central volcanoes. *J Volcanol Geoth Res* 116:279–298
- Gudmundsson A (2011a) Deflection of dykes into sills at discontinuities and magma-chamber formation. *Tectonophysics* 500:50–64
- Gudmundsson A (2011b) Rock fractures in geological processes. Cambridge University Press, Cambridge
- Gudmundsson A (2012a) Magma chambers: formation, local stresses, excess pressures, and compartments. *J Volcanol Geoth Res* 237:19–41
- Gudmundsson A (2012b) Strengths and strain energies of volcanic edifices: implications for eruptions, collapse calderas, and landslides. *Nat Hazard Earth Sys* 12:2241–2258
- Gudmundsson A, Lotveit IF (2012) Sills as fractured hydrocarbon reservoirs: examples and models. In: Spence GH, Redfern J, Aguilera R, Bevan TG, Cosgrove JW, Couples GD, Daniel J-M (eds) Advances in the study of fractured reservoirs. Geological Society of London Special Publication, London, p 374 (doi.org/10.1144/SP374.5)
- Gudmundsson A, Lecoer N, Mohajeri N, Thordarson T (2014) Dike emplacement at Bardarbunga, Iceland, induces unusual stress changes, caldera deformation, and earthquakes. *Bull Volcanol* 76. doi:10.007/s00445-014-0869-8
- Gudmundsson MT, Thordarson T, Höskuldsson A, Larsen G, Björnsson H, Prata FJ, Oddsson B, Magnússon E, Högnadóttir T, Petersen GN, Hayward CL, Stevenson JA, Jonsdóttir I (2012) Ash generation and distribution from the April–May 2010 eruption of Eyjafjallajökull, Iceland. *Sci Rep* 2:572. doi:10.1038/srep00572
- Hald N, Noe-Nygaard A, Pedersen A (1971) The Krokksfjörður central volcano in North-West Iceland. *Acta Naturalia Islandica* 10:29 p
- Hansen J, Jerram DA, McCaffrey K, Passey SR (2011) Early Cenozoic saucer-shaped sills of the Faroe Islands: an example of intrusive styles in basaltic lava piles. *J Geol Soc London* 168:159–178
- Hartley ME, Thordarson T (2012) Formation of Oskjuvatn caldera at Askja, North Iceland: mechanism of caldera collapse and implications for the lateral flow hypothesis. *J Volcanol Geoth Res* 227–228:85–101
- Hartley ME, Thordarson T (2013) The 1874–1876 volcano-tectonic episode at Askja: lateral flow revisited. *Geochem Geophys Geosy*. doi:10.1002/ggge.20151
- Hawkes L, Hawkes HK (1933) The sandfell laccolith and ‘dome of elevation’. *Q J Geol Soc London* 89:379–400
- He MY, Hutchison JW (1989) Crack deflection at an interface between dissimilar elastic materials. *Int J Solid Struct* 25:1053–1067
- Jakobsdóttir S (2008) Seismicity in Iceland: 1994–2007. *Jökull* 58:75–100
- Johannesson H (1974) Structure and petrochemistry of the Reykjadalur central volcano and surrounding areas, Midwest Iceland. PhD thesis, University of Durham, 273 p
- Kavanagh JL, Menand T, Sparks RSJ (2006) An experimental investigation of sill formation and propagation in layered elastic media. *Earth Planet Sci Lett* 245:799–813
- Kissel C, Laj C, Sigurdsson H, Guillou H (2010) Emplacement of magma in Eastern Iceland dikes: insights from magnetic fabric and rock magnetic analyses. *J Volcanol Geoth Res* 191:79–92

- Klausen MB (2004) Geometry and mode of emplacement of the Thverartindur cone sheet swarm, SE Iceland. *J Volcanol Geoth Res* 138:185–204
- Klausen MB (2006) Geometry and mode of emplacement of dike swarms around the Birudalstindur igneous centre, SE Iceland. *J Volcanol Geoth Res* 151(4):340–356
- Lister JR, Kerr RC (1991) Fluid-mechanical models of crack propagation and their application to magma transport in dykes. *J Geophys Res* 96:10049–10077
- McCaffrey KJW, Petford N (1997) Are granitic intrusion scale invariant? *J Geol Soc London* 154:1–4
- Michaut C (2011) Dynamics of magmatic intrusions in the upper crust: theory and applications to laccoliths on earth and the moon. *J Geophys Res Solid Earth* 116:B05205
- Paquet F, Dauteuil O, Hallot E, Moreau F (2007) Tectonics and magma dynamics coupling in a dyke swarm of Iceland. *J Struct Geol* 29:1477–1493
- Pasquarè F, Tibaldi A (2007) Structure of a sheet-laccolith system revealing the interplay between tectonic and magma stresses at Stardalur volcano, Iceland. *J Volcanol Geoth Res* 161(1–2):131–150
- Phillips WJ (1974) The dynamic emplacement of cone sheets. *Tectonophysics* 24:69–84
- Pollard DD, Johnson AM (1973) Mechanics of growth of some laccolithic intrusions in Henry Mountains, Utah: 2. Bending and failure of overburden layers and sill formation. *Tectonophysics* 18:311–354
- Pook LP (2002) Crack paths. WIT Press, Ashurst
- Rocchi S, Westerman DS, Dini A, Innocenti F, Tonarini S (2002) Two-stage laccolith growth at Elba Island (Italy). *Geology* 30:983–986
- Sigmundsson F, Hreinsdóttir S, Hooper A, Árnadóttir T, Pedersen R, Roberts MJ, Óskarsson N, Auriac A, Decriem J, Einarsson P, Geirsson H, Hensch M, Ófeigsson BG, Sturkell E, Sveinbjörnsson H, Feigl KL (2010) Intrusion triggering of the 2010 Eyjafjallajökull explosive eruption. *Nature* 468:426–430
- Sigurdsson H (1966) Geology of the setberg area, snaefellsnes, Western Iceland. *Societas Scientiarum Islandica, Greinar* 4(2):53–122
- Sigurdsson H, Sparks RSJ (1978) Lateral magma flow within rifted Icelandic crust. *Nature* 274:126–130
- Siler DL, Karson JA (2009) Three-dimensional structure of inclined sheet swarms: implications for crustal thickening and subsidence in the volcanic rift zones of Iceland. *J Volcanol Geoth Res* 18(8):333–346
- Spence DA, Turcotte DL (1985) Magma-driven propagation of cracks. *J Geophys Res* 90:575–580
- Sun CT, Jin ZH (2012) Fracture mechanics. Elsevier, Amsterdam 432 p
- Tait S, Taisne B (2013) The dynamics of dike propagation. In: Fagents SA, Gregg TKP, Lopes RMC (eds) Modeling volcanic processes. Cambridge University Press, Cambridge, pp 32–54
- Tarasewicz J, White RS, Woods AW, Brandsdóttir B, Gudmundsson MT (2012) Magma mobilization by downward-propagating decompression of the Eyjafjallajökull volcanic plumbing system. *Geophys Res Lett* 39. doi:10.1029/2012GL053518
- Tibaldi A, Pasquarè F (2008) A new mode of inner volcano growth: the “flower intrusive structure”. *Earth Planet Sci Lett* 271:202–208
- Tibaldi A, Vezzoli L, Pasquarè FA, Rust D (2008) Strike-slip fault tectonics and the emplacement of sheet-laccolith systems: the Thverfell case study (SW Iceland). *J Struct Geol* 30:274–290
- Tibaldi A, Pasquarè FA, Rust D (2011) New insights into the cone sheet structure of the Cuillin Complex, Isle of Skye, Scotland. *J Geol Soc* 168:689–704
- Tibaldi A, Bonali F, Pasquarè FA, Rust D, Cavallo A, D’Urso A (2013) Structure of regional dykes and local cone sheets in the Midhyrna-Lysuskard area, Snaefellsnes Peninsula (NW Iceland). *Bull Volcanol* 75:764. doi:10.1007/s00445-013-0764-8
- Upton BGJ, Wright JB (1961) Intrusions of gabbro and granophire in the Snaefellsness, Western Iceland. *Geol Mag* 98(6):488–492
- Walker GPL (1960) Zeolite zones and dike distribution in relation to the structure of the basalts of Eastern Iceland. *J Geol* 68:515–528
- Walker GPL (1974) The structure of Eastern Iceland. In: Kristjánsson L (ed) Geodynamics of Iceland and the North Atlantic area. Reidel, Dordrecht, pp 177–188
- Walker GPL (1975) Intrusive sheet swarms and the identity of crustal layer 3 in Iceland. *J Geol Soc London* 131:143–161

Laccolithic Emplacement of the Northern Arran Granite, Scotland, Based on Magnetic Fabric Data

C.T.E. Stevenson and C. Grove

Abstract

The Northern Arran Granite is regarded as an example of an upper-crustal granite diapir due to its sub circular outcrop and deformed aureole. However diapiric emplacement to shallow levels in the crust is physically difficult and unambiguous evidence for shouldering aside of country rocks by a diapir as opposed to shouldering due to in situ expansion of a laccolith or ballooning pluton is difficult to find. The key is in finding evidence for vertical ascent of a diapiric body where a diapir should preserve vertical stretching either around the periphery or in central portions. A laccolith on the other hand is unlikely to have consistently vertical or steep lineations but contain mainly gently plunging lineations or evidence of multiple horizontal pulses or lobes. Therefore evidence for diapiric ascent and emplacement should be dominated by vertical kinematic indicators. These structures may however be too subtle if preserved within the granite, and those in the aureole may become overprinted by late stage insitu expansion. To test whether the internal structure of the Northern Arran Granite is consistent with diapiric or laccolithic emplacement we have measured the anisotropy of magnetic susceptibility from oriented block samples from the Northern Arran Granite to determine if there are subtle or weak fabrics that will support either diapirism with vertically oriented stretching, or laccolithic emplacement where lateral emplacement is dominant and vertical motion only restricted to vertical thickening of an initially thin sheet. Our results reveal concordant dome shaped planar fabrics with mainly gently plunging or horizontal lineation, i.e. an absence of vertical stretching or flow, and

C.T.E. Stevenson (✉) · C. Grove
School of Geography Earth and Environmental
Sciences, University of Birmingham,
Birmingham B15 2TT, UK
e-mail: c.t.stevenson@bham.ac.uk

C. Grove
Department of Earth Sciences, Durham University,
South Road, Durham DH1 3LE, UK

Advs in Volcanology (2018) 377–401
DOI 10.1007/11157_2014_3
© Springer International Publishing Switzerland 2014
Published Online: 08 December 2014

possible evidence of partial lobes in the north western margins and Inner Granite. We interpret these fabrics and the deformation of the aureole in terms of dome-shaped expansion consistent with the latter model. In more detail the lineation pattern indicates convergence toward a south or south eastern point, consistent with the deepest part of the pluton (from previously published gravity modelling). Our model suggests that there may be some link to a major crustal structure (the Highland Boundary Fault) providing insight into the ascent route of the magma and possible influence of the Highland Boundary fault zone. This model also suggests that the magmatism on Arran including the central complex and sill complexes in the south of the island may have been supplied by a long lived, deeply penetrating feeder zone controlled by this major tectonic structure.

1 Introduction

The ascent and emplacement of granite as a diapiric body is a classic emplacement mechanism based on analogue models carried out by Grout (1945) using oil and corn syrup and developed by Ramberg (1967) with centrifuge experiments. However in the 1990s the ‘dykes versus diapirs’ debate (e.g. Castro 1987; Rubin 1993, 1995; Petford et al. 1993, 1994, 2000; Petford 1996a, b; Weinberg 1996; Clemens 1998; Vigneresse and Clemens 2000; Petford and Clemens 2000) casts some doubt on the diapir mechanism based largely on structural observations and numerical modelling. The principal argument for diapiric emplacement hinges on the difficulty in accounting for the amount of horizontal shortening perpendicular to the pluton margins recorded in the deformation aureole of some plutons (e.g. Paterson and Vernon 1995; Miller and Paterson 1999), i.e. the diapir model as a solution to the space problem, requires that the country rocks had flowed vertically in response to the ascent and emplacement of the diapir. The arguments against diapirs include a lack of evidence in deeply eroded terranes of the passage of diapirs (e.g. Clemens 1998; Petford and Clemens 2000), detailed examination of the kinematics of magma flow inside granite bodies that preclude upward flow but support ballooning (e.g. Holder 1980; Sanderson and Meneilly 1981; Hutton 1988; Ramsay 1989; Brun et al.

1990; Molyneux and Hutton 2000; Siegesmund and Becker 2000; Hutton and Siegesmund 2001), physical modelling of the crust which demonstrated the difficulty in ascending large batches of magma as a diapir (e.g. Petford et al. 1993) and numerical modelling which demonstrated that creation of dykes is a more efficient ascent mechanism (e.g. Rubin 1993, 1995).

The evidence for shouldering aside of country rocks due to diapiric ascent or inflation of a laccolith or ballooning pluton is ambiguous as both have been argued to produce similar features including annular or rim synforms and either radial or vertical stretching depending on the position relative to the pluton (e.g. Bateman 1985; Galadí-Enríquez et al. 2003; Paterson and Fowler 1993; Vernon and Paterson 1993). The principal parts of the diapir model are summarised in Fig. 1. In some cases the uplift of strata from beneath the pluton have been used as evidence of diapiric ascent, for example He et al. (2009) argued that strata exposed around the Fangshan pluton, Southern China, should be much deeper. The Northern Arran Granite is another example of this (England 1988, 1990, 1992) (Fig. 2).

The principal tenet of the diapir model is vertical movement of the entire body as opposed to situ expansion with or without doming from an initially laterally emplaced tabular or sill-like body as in a laccolithic/ballooning style emplacement (cf. Fig. 1). Therefore the current study aims to test the diapir emplacement model

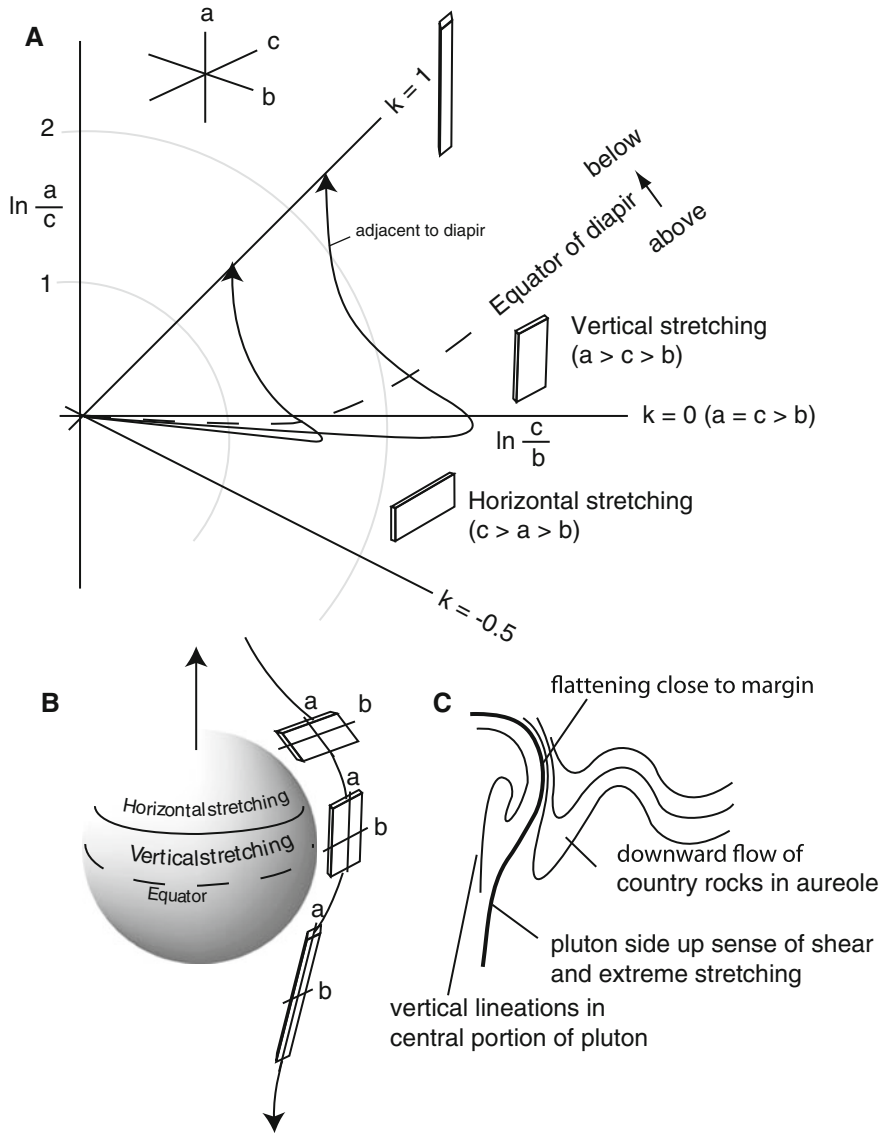


Fig. 1 **A** Model for the evolution of strain in the aureole of a rising diapir after Cruden (1988). This diagram illustrates how vertical stretching should be observed above the equator of the diapir. The principal axes a , b and c are Cartesian where b and c are horizontal and a is vertical. These are also relative to the diapir where b is radial and c is tangential; a becomes deflected as the

diapir passes. **B** Illustrates diagrammatically the evolution of strain using the system described in part A, emphasising the relative disposition of vertical stretching, i.e. when a becomes the longest axis. **C** typical model for the fabrics in and around a rising diapiric body drawn as a semi-cross section (cf. Cruden 1988)

by examining deformation of the granite itself by attempting to identify evidence for vertical ascent. Anisotropy of magnetic susceptibility (AMS) measurements have proven to be a sensitive fabric analysis tool especially when applied

to granitic rocks (e.g. Bouchez 1997; Borradaile and Henry 1997; Borradaile and Jackson 2004) and would be able to detect any subtle evidence of vertical movement (such as vertical stretching) as long as it has not been completely obliterated

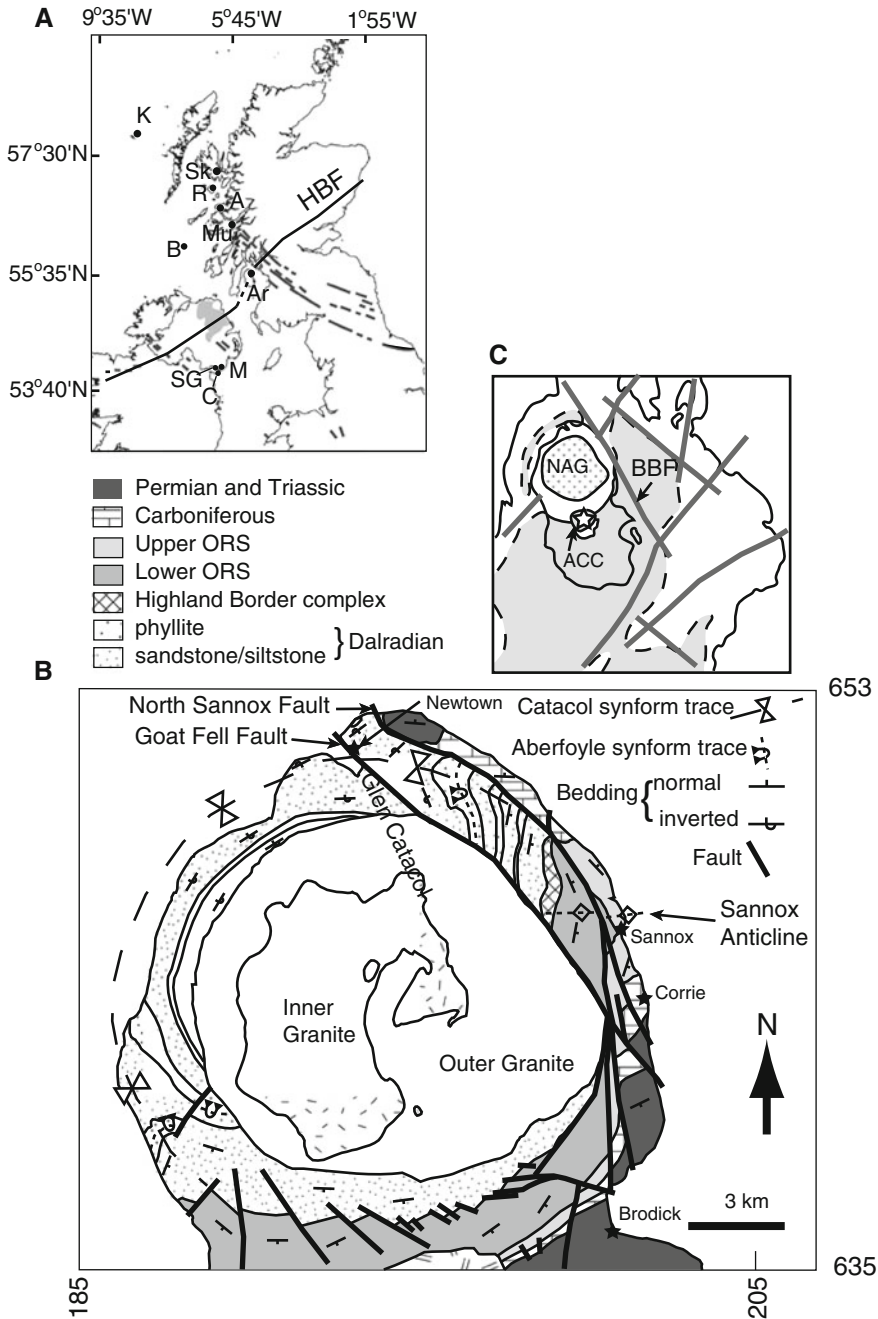


Fig. 2 A Location of the main igneous centres in the British and Irish Palaeogene Province: *S&C* Slieve Gullion and Carlingford, *M* Mournes, *Ar* Arran granite, *Mu* Mull, *A* Ardnamurchan, *R* Rhum, *Sk* Skye, *K* St. Kilda (adapted from Bell and Emeleus 2004; Cooper and Johnson 2004). **B** Simplified geological map of the north of Arran. Location indicated by British National Grid

numbers from square NR. Redrawn from Woodcock and Underhill (1987); Hull et al. (1987). *ORS* Old Red Sandstone. **C** Distribution of off shore faults around the Isle of Arran. Grey area indicates extent of outcrop of New Red Sandstone (NRS) enclosed by a dashed line when off shore and a solid line onshore. *BBF* Brodick Bay Fault. Redrawn from Woodcock and Underhill (1987)

or totally overprinted by late stage expansion or tectonic deformation.

Our magnetic fabric results indicate that there is expansion, consistent with the deformation in the aureole during in situ expansion. There are however no consistently vertical or steeply plunging linear fabrics but a tendency toward gently plunging concentric stretching which supports lateral emplacement followed by domed expansion in situ. In central and north western portions, foliations are usually gently dipping and any linear components are also gently plunging. The fabric pattern allows us to reconstruct the unroofed portion of granite, which takes the form of a dome up to 5 km thick at its culmination (i.e. ca. 3.5–4 km unroofed granite). We argue that in the case of an expanded diapir, that if radial stretching was extreme to the point of obliterating or overprinting vertical linear fabrics, then it should be recorded pervasively and fabrics in the Inner Granite should be continuous with fabrics in the Outer granite. What is preserved however only shows occasional steeply plunging lineations and a variable fabric. We conclude that this fabric is more likely to be modified fabrics of an expanded incrementally assembled tabular pluton, similar to a laccolith (*sensu* Cruden 1988), rather than a diapir. We suggest that the host rock deformation may be explained by shouldering during doming and not necessarily by diapiric uplift. We then examine the implications for the evolution of the Highland Boundary Fault zone in light of our emplacement model and links to other igneous centres on Arran.

2 Geological Background

The oldest rocks that crop out around the Northern Arran Granite are meta-sediments of the mid-Neoproterozoic to early Ordovician Dalradian Supergroup (Fig. 2B). The Dalradian Supergroup comprises mainly clastic meta-sediments with some volcanic units that were deposited from around 730 Ma, during the break-up Rhodinia, onto the continental slope of what would become Laurentia (Stephenson et al. 2013) and underpins much of the geology of NW

Scotland and Ireland. The Dalradian rocks on Arran consist of greenschist facies interbedded meta-pelites and meta-psammites with beds between 0.5 and 1 m thick (England 1988) and have been correlated to the Southern Highlands Group (Harris et al. 1978; Halliday et al. 1989; Tanner 2008). The Dalradian rocks crop out to the north, west and south of the Northern Arran Granite today.

The Dalradian strata were deformed during Caledonian polyphase deformation (480–500 Ma), resulting in the NE–SW trending downward facing Aberfoyle anticline (Shackleton 1957; England 1988). The Dalradian meta-sediments are faulted against the younger rocks by the Highland Boundary Fault (HBF) which has an uncertain trace in northern Arran (Woodcock and Underhill 1987; England 1988; Tanner 2008) (Fig. 2A).

The HBF is a major terrane boundary that separates the Grampian Terrane to the north–west, which is dominated by Dalradian meta-sediments and Caledonian aged plutons, from the Mildand Valley Terrane to the south–east, which is dominated by late-Silurian to early-Carboniferous sediments and volcanics (Tanner 2008). The HBF is currently manifest at the surface as a mid-Devonian steep reverse fault, although it may have begun as a transcurrent fault as early as 420 Ma (see Tanner 2008 for detailed discussion).

The Ordovician age Highland Border Complex (HBC) lies just beneath the younger Devonian rocks and marks the end of the Caledonian sequence on Arran (Fig. 2B). This complex was obducted onto the Grampian Terrane and consists (on Arran) of black shale and spilite (England 1988), it crops out along the accepted trace of the HBF in the north of the island, and is cut by the granite. The Devonian sediments of the ‘old red sandstone’ are faulted against the Dalradian rocks in the north of the island and overlie Dalradian sediments to the south of the northern Arran Granite.

The post-Devonian rocks were deposited in a rift basin, with evidence of syn-sedimentary faulting and consist of Carboniferous limestones conformably overlain by Permian fluvial mudstones, siltstones and sandstones which crop out to the east of the granite. The rocks within the

Midland Valley Terrane are commonly faulted, the system of NNW–SSE trending faults east of the granite including the Goat Fell Fault and the North Sannox Fault (probably also including the off shore Brodic Bay Fault) is called the Laggan Fault Zone (Woodcock and Underhill 1987) (Fig. 2B, C). This system downthrows to the east and was active during deposition Palaeozoic sediments and were reactivated in the Palaeogene during the emplacement of the granite (McLean and Deegan 1978; Woodcock and Underhill 1987; England 1988).

3 The British and Irish Palaeogene Igneous Province

The British and Irish Palaeogene Igneous Province (BIPIP) here refers to all the onshore igneous material that was extruded and emplaced mainly in north–west Britain and Ireland during the early to mid-Palaeogene (ca. 55 Ma) (Fig. 3). Some studies refer to the North Atlantic Igneous Province which includes all the igneous activity in north–west Britain and Ireland, Faroe Islands, Iceland and East Greenland, including all off-shore occurrences (e.g. Jolley and Bell 2002; Jolley and Widdowson 2005; Meyer et al. 2007). Other studies are more restricted to the intrusions and volcanics of north–west Scotland and refer to the British Palaeogene Igneous Province (BPIP) (e.g. Brown et al. 2009). Older work refers to Tertiary (now Cenozoic) instead of Palaeogene (e.g. Emeleus et al. 1992).

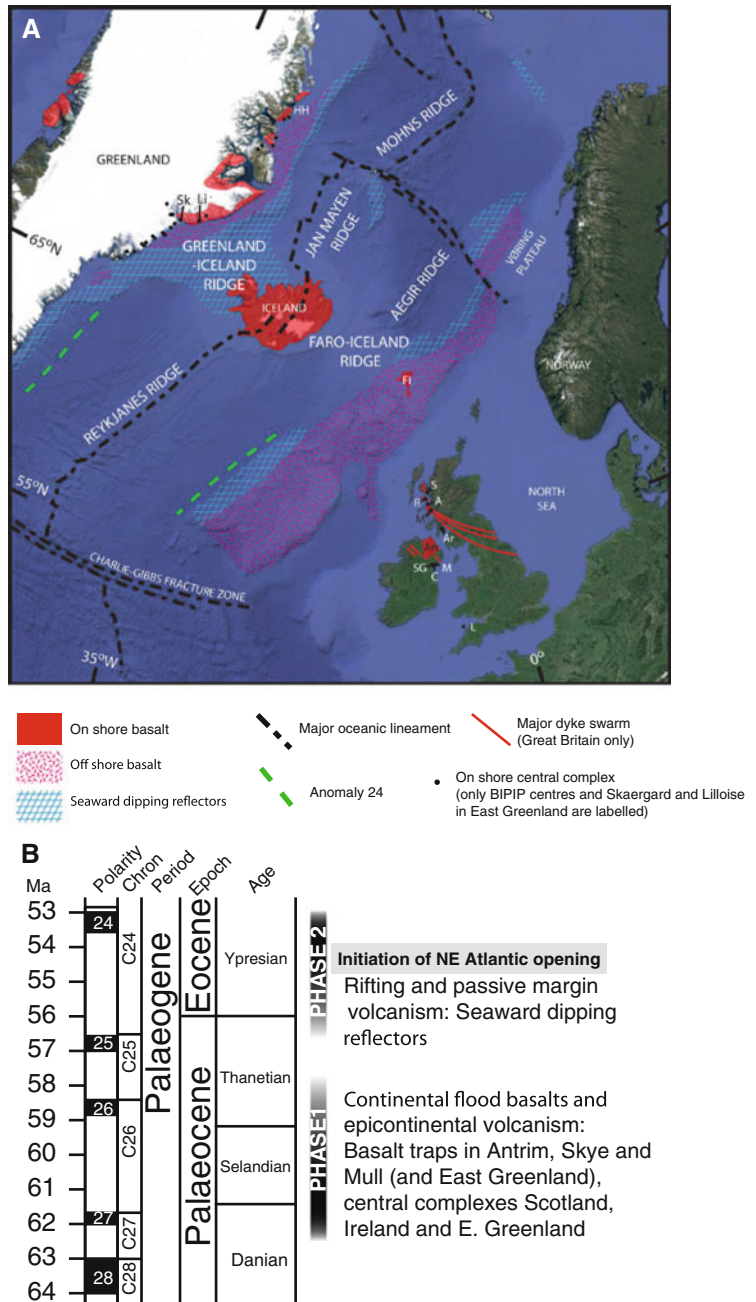
The BIPIP is a classic region for volcanologists and produced several of the key models for upper-crustal igneous emplacement that guide our current understanding of volcanology. The BIPIP is famous for exposing geological features that document extrusive activity as well as deeply eroded volcanic edifices and the subsurface volcanic plumbing. There are a number of extremely useful general reviews of the BIPIP (and NAIP) (Thompson 1982; Emeleus et al. 1992; Saunders et al. 1997; Trewin 2002) and guides (e.g. Emeleus and Bell 2005) available for

more detailed information and in-depth discussion on these features. In this contribution we will highlight some of the most important features which are found in NW Scotland, Inner Hebrides and Northern Ireland (Figs. 2A and 3) and include basalt traps in Antrim, Mull, Skye, Rum, Muck and Eigg; dolerite sill complexes in Skye and Antrim, central complexes found on Mull, Skye, Ardnamurchan, Rum, Arran, Slieve Gullion and Carlingford; and anorogenic granite plutons including the Mourne Granite Centres, Western Red Hills of Skye, Northern Arran Granite, the Ailsa Craig and the Lundy granite.

3.1 Plume Related Origins

The magmatism that generated the BIPIP intrusions and volcanics is now widely accepted to be linked with impingement of the proto-Icelandic plume into the base of the Laurasian crust in the early Palaeocene and subsequent break-up of this continent into Laurentia (N. America and Greenland) and Eurasia (Europe and Asia) around 56 Ma (Doré et al. 1999; Jolley and Bell 2002; Trewin 2002; Meyer et al. 2007; Saunders et al. 2007). The initial effects of the plume event were marked by a rapid and short-lived uplift of Mesozoic basins in this region at the Cretaceous–Palaeogene boundary 65 Ma followed roughly 2–3 Myr later by more uplift and the earliest onset of volcanism (Phase 1 of Saunders et al. 1997; see also Trewin 2002). Phase 1 continued for roughly 4 Myr and included the main phase of continental flood basal eruption resulting in basal-t traps in Antrim, Skye and Mull (as well as East Greenland). During this time most of the on-shore BIPIP activity took place (Saunders et al. 1997). The second major phase of activity began around 56 Ma and heralded the opening of the North Atlantic at 55–54 Ma. This phase included passive margin volcanism and has resulted in a series of seaward-dipping reflectors in the North Atlantic and off-shore East Greenland (Saunders et al. 1997). The timing of phases 1 and 2 magmatism in the NAIP is summarised in Fig. 3.

Fig. 3 **A** Map showing the main features of the NAIP (see text for explanation) (taken from Saunders et al. 1997; Trewin 2002; Emeleus and Bell 2005). **B** Summary chart of the main phases of activity that formed the NAIP with special reference to the BIPIP (from dates reported in Saunders et al. 1997; Emeleus and Bell 2005). In this chart the date in millions of years before present (Ma), polarity (magnetic polarity), chron (magnetostratigraphic), period, epoch and age are all taken from the current USGS chronostratigraphic chart



3.2 Magma Genesis and Evolution

The magma that formed the BIPIP was generated by fractional crystallisation of melt derived from depressurized upper mantle (Saunders et al. 1997;

Ellam and Stuart 2000). This was triggered by the thermal uplift caused by the proto-Icelandic plume. The 1st phase of magmatism was varied but dominated by basalts. These were of transitional alkali and tholeiitic varieties reflecting the

respectively lower and higher structural level at which their parent melts were generated (Saunders et al. 1997).

The great variety of magma types in the BIPIP (and the initial phase of the NAIP) is most likely due to contamination of basaltic magma from the continental crust through which it ascended. Many studies have focused on identifying sources for magma contamination focusing on two isotopically distinct lower crustal sources; viz. granulite and amphibolite, based mainly on the lower $^{87}\text{Sr}/^{86}\text{Sr}$ of the granulite gneiss (Saunders et al. 1997). Various other mid and upper crustal sources have also been included in similar contamination studies of BIPIP magmas (e.g. Thompson et al. 1986; Wallace et al. 1994; Troll et al. 2005; Meyer et al. 2009; Meade et al. 2009).

3.3 Central Complexes

Central complexes, or centres, mostly formed during phase 1 of the NAIP magmatism. These features are the most relevant aspect of the BIPIP to this volume as they preserve a range of exposure levels of large and explosive volcanic edifices, from surface calderas (e.g. Central Arran) to deeply eroded sill, dykes and magma chambers (e.g. Ardnamurchan) and are where some of the classic models for ring-dyke and cone-sheet systems were developed (Bailey 1924; Richey 1928, 1932; Richey and Thomas 1932; Anderson 1937). A central complex in the BIPIP usually consists of a sub circular outcrop of igneous rock greater than c. 5 km diameter with steeply dipping external boundaries. Central complexes are often highly heterogeneous including crescent shaped or annularly distributed internal variations. The internal structure of these is often taken to be subvertical or steeply outward dipping following the ring-dyke model of Richey (1928). It is in the component parts of central complexes where early workers developed some of the key models that guide our current understanding of volcanology. The specific emplacement models that were developed to their current understanding in the BIPIP are cauldron subsidence (Bailey 1924),

ring-dyke (Richey 1928) and cone-sheet (Anderson 1937).

Ring-dykes: A ring-dyke is an annular or crescent shaped intrusion with steep boundaries outwardly dipping about a central point. The model involves the downward movement of a central block, such that they represent essentially magma filled reverse faults. The intrusive material in a ring-dyke emanated from an underlying magma chamber into which the central block foundered. Ring-dykes are linked to caldera volcanoes, where they then provide vent structures, and cauldron subsidence (described next).

Cauldron subsidence: This is essentially the subterranean version of a caldera volcano where, instead of erupting, the ring-dyke stops propagating upwards and propagates toward the centre to form a roof. The relationship with a subjacent magma chamber is the same as a caldera volcano.

Cone-sheet: These form confocally dipping sheets. They could be regarded as the opposite of ring-dykes to the extent where a ring-dyke is formed when buoyancy permits a large block to founder, cone-sheets are formed due to excess magma pressure in a magma chamber, greater than buoyancy, that forces up the roof. Cone-sheets are the resultant magma-filled fractures.

The elegant way that these models link together to explain the dynamics of upper-crustal magma emplacement often requires, however, a superficial treatment of the space problem (assuming assimilation is volumetrically insignificant, the volume of country rocks now occupied by intrusive igneous material must be accounted for). It is worth considering this issue and putting the current study in the context of recent work on the emplacement of key centres in the BIPIP.

3.4 Recent Work on the Emplacement of Some Centres

The plate tectonics paradigm and 20th century advances in geophysical techniques have come along since the early work in the BIPIP generated

these classic models. Walker (1975) attempted to draw together geophysical evidence of positive gravity anomalies often observed beneath central complexes and the association of mafic and felsic magmas in a unified generic model that could explain most features of typical BIIP centres. This model was the first to attempt to explain the BIIP on a crustal scale and involved a diapir that ascended to a high level in the crust. This diapir caused doming at the surface resulting in a caldera edifice including ring dykes and surrounded by cone-sheets. The diapir was followed by denser mafic magma that was emplaced at the base of the main granitic body and caused isostatic equilibrium of this buoyant body. As isostatic equilibrium was reached, subsidence occurred resulting in the formation of cauldron subsidence.

A number of recent studies have offered some alternative emplacement models for each of these key examples using novel data on the internal fabrics and structure of the intrusions using anisotropy of magnetic susceptibility analyses (e.g. O'Driscoll et al. 2006; Stevenson et al. 2007a, 2008; Petronis et al. 2009; Stevenson and Bennett 2011; Magee et al. 2012a, b). O'Driscoll et al. (2006) showed that the Ardnamurchan Great Eucrite is more likely a lopolith with an inverted cone shaped geometry than a traditional ring-dyke. Stevenson et al. (2007b) and Stevenson and Bennett (2011) revealed internal fabrics in the Mourne Granite centres (Eastern and Western respectively) that supported a laccolithic as opposed to cauldron subsidence emplacement, principally from the dome shaped foliation disposition and lateral lineation direction. Other evidence in this study included deformation of the host rocks and previously published geophysical data. Stevenson et al. (2008) studied the Slieve Gullion Ring Complex, focusing on the granitic ring-dyke part. This study concluded that the traditional ring-syke model was not unambiguously supported and presented an alternative interpretation that included laterally emplaced sheets cut by ring-faults. In addition to Stevenson et al. (2008), Emeleus et al. (2012) have highlighted and reiterated Richey's (1928) observations regarding Slieve Gullion, presenting a

strong argument in favour of a traditional ring-dyke model emphasising the relationships between fault rocks and tuffsites. Magee et al. (2012a) used AMS data to test the classic cone sheet emplacement model for the archetypal Ardnamurchan cone-sheet swarm. The data revealed dominantly lateral magma flow directed around the Ardnamurchan centre rather than emanating from beneath it. This observation coupled with some simple mechanical modelling produced a model that described magma exploiting concentric fractures and not necessarily creating them. The implication was that the cone-sheet magma may have emanated from the nearby Mull igneous centre and therefore intrusions from nearby centres can overlap. This conclusion was supported by Magee et al. (2012b) who, in a related study, found the Ben Hiant dolerite intrusion on Ardnamurchan was emplaced in a northwestward direction toward the Ardnamurchan centre and from Mull and not the other way round.

4 The Northern Arran Granite

The Northern Arran Granite is roughly sub-circular in outcrop with a maximum diameter of 13 km (Fig. 2B). The granite consists of two distinct units: an inner fine-grained granite which intruded an outer coarse-grained granite (Bell and Williamson 2002; Emeleus and Bell 2005). In general the granite is mineralogically homogeneous. Any variations are subtle and it can be described as a medium to coarse-grained weakly porphyritic biotite syenogranite. The Northern Arran Granite was intruded into the country rocks described above at between 60.5 and 58.5 Ma from Rb-Sr and $^{40}\text{Ar}/^{39}\text{Ar}$ dating respectively (Dickin and Bowes 1991; Dickin 1994; Mussett et al. 1988) at around 4–5 km depth (Woodcock and Underhill 1987).

The country rocks surrounding the granites are thermally affected within 500 m of the granite with a maximum temperature of 550 °C in contact with the granite, no muscovite is present in the metamorphic aureole (England 1988). In the west the granite is in contact with Dalradian

rocks where the contact is characterised by a region of sheared contact metamorphosed rock. The eastern contact is marked by the Goat Fell Fault which is downthrown to the east, the fault brecciates the granite on a microscopic scale (England 1988).

The Northern Arran Granite was produced by contamination of basic differentiates by crust resembling exposed Dalradian units (Dickin 1994) associated with a mantle plume (Meighan et al. 1992). Both granites contain drusy cavities which are interpreted to occur in sheets (England 1988) but cannot be traced over distance due to poor outcrop quality. The cavities are frequently lined with quartz, alkali feldspar and mica together with several rare minerals (Emeleus and Bell 2005). The most recent and comprehensive petrological assessment was carried out by England (1988) who identified three petrographical zones within the coarse-grained granite and six drusy layer bound sheets within the fine-grained granite.

4.1 Previous Work on the Emplacement of the Northern Arran Granite

The Palaeogene aged Northern Arran Granite (Fig. 2) has been interpreted as an upper crustal diapiric intrusion by England (1988). This pluton has a roughly circular outcrop with an approximately 11 km diameter and is situated close to where the Highland Boundary Fault should cross the island (Anderson 1947; Stone and Kimbell 1995; Pharaoh et al. 1996; Emeleus and Bell 2005; Tanner 2008; Woodcock and Strachan 2012). The Northern Arran Granite comprises two units; a relatively fine grained Inner Granite and a relatively coarser grained Outer Granite. It was emplaced into Dalradian interbedded sandstone and phyllite, and Devonian Old Red Sandstone at 60.3 ± 1.6 Ma (Dickin et al. 1981).

The diapiric emplacement model for the Northern Arran Granite is based mainly on the deformation of the aureole in particular the formation of a rim synform, the Catacol Synform,

which refolds a downward facing Caledonian fold, the Aberfoyle Synform (England 1988, 1990, 1992). The key part of this model is that the formation of the Catacol Synform to its current geometry involved the uplift of one limb of the Aberfoyle Synform by 2–3 km and thus required the ascent of the granite body over a distance greater than its radius precluding an expansion (ballooning) model. England (1992) explained that the dominant flattening strain was due to late stage radial expansion of the granite that overprinted the early vertical stretching. The lack of steep lineation, England (1992) argued, was consistent with the predicted pattern of deformation around a rising diapir recorded above the equator according to Cruden (1988).

Gouly et al. (2001) presented a gravity model for the Northern Arran Granite that yielded a horizontal floor 0.3–1.2 km deep, much shallower than expected from a roughly spherical diapir. The shape of the pluton according to Gouly et al. (2001) was a laccolith although Gouly et al. (2001) concluded that there may have been significant lateral or radial expansion—‘mushrooming’—to achieve this shape and ultimately did not dispute the diapir model.

However, aside from the physical difficulties in ascending a mass of molten magma to a high level in the crust (e.g. Petford et al. 2000), the evidence for upward motion of the diapir either from inside the granite or in the aureole, including vertical stretching in the aureole or near the margins in the granite or in any central portion of the granite (Schmelling et al. 1988; Cruden 1988, 1990) (Fig. 1) are lacking. This problem is compounded by the possibility that a diapir may expand in situ as further diapiric pulses enter the pluton from beneath or if the diapir flattens or mushrooms at a late stage. The key of this model therefore is, given the roughly equatorial (or just above the equator) position of the current exposure level (based on England 1988), vertical stretching should be present in central portions even if it has been modified or obliterated at the margins. We would also expect evidence of ‘pluton up’ sense of shear.

5 Anisotropy of Magnetic Susceptibility Analyses

Anisotropy of magnetic susceptibility (AMS) is a measure of the variation of the magnetic susceptibility with orientation of a sample. In rocks the AMS signal is usually controlled by the orientation and distribution of magnetite grains and sometimes biotite, pyroxene or other Fe bearing minerals (Tarling and Hrouda 1993). Because magnetite is often aligned with, forms inclusions within or forms around the main rock forming silicate phases, AMS data usually provides information about the preferred orientation of silicate minerals and has often been used as a fabric analysis technique (e.g. O'Driscoll et al. 2008). AMS is particularly useful when visible fabrics are too weak or subtle to be recorded otherwise.

Thirty-eight oriented samples were collected from mainly the northern and eastern portions (most accessible and best exposed) of the Northern Arran Granite. From these samples an average of 10 sub specimens were taken (each 10 cm³), according to the methods outlined by Owens (1994). The AMS of each sub-specimen was measured at the University of Birmingham using an Agico KLY-3S Kappabridge. Data from each sub-specimen were subject to statistical analysis according to Jelinek (1981). Both the statistical analysis and reorientation of data from the specimen frame to the geographical frame were carried out using a modified version of Anisoft (supplied by M. Chadima, personal communication 2013). Data calculated for each station using Jelinek (1981) statistics which assumes that the data represents a single multi-normal population.

The AMS signal may be viewed as a second order ellipsoid in which three orthogonal principal susceptibilities are defined. The AMS signal thus has 6 linked quantities; the orientation of each principal susceptibility axis and their magnitude. In this case we use volumetric susceptibility, K , which is equal to the applied field divided by the resultant magnetisation. The kappabridge that we used measures the difference

in the field detected by a pickup coil caused by the presence of a sample. As the sample is rotated inside this coil, the change in field is detected and produces a sine curve. This is repeated in three orthogonal reference positions and a final control reading taken along a single axis (bulk susceptibility of K_{bulk}) is used to calculate the complete tensor.

In this contribution we will use conventional parameters to report AMS data. The components of the AMS tensor are as follows: Maximum susceptibility axis is K_1 , intermediate susceptibility axis is K_2 , minimum susceptibility axis is K_3 , mean susceptibility (taken as the susceptibility representative of a particular station) is equal to $(K_1 + K_2 + K_3)/3$. There are then a series of linked parameters that describe the shape and anisotropy of the tensor. These are the lineation strength, L , which is equal to K_1/K_2 , the foliation strength, F , which is equal to K_2/K_3 . The total anisotropy, P' (a more sophisticated version of $P = K_1/K_3$ which includes K_2) is defined by (after Jelinek 1981):

$$\ln P' = \sqrt{2((\eta_1 - \eta_m)^2 + (\eta_2 - \eta_m)^2 + (\eta_3 - \eta_m)^2)^{1/2}}$$

In the case of L , F and P' , the values start at a minimum of 1 and may be roughly converted to percentage as 1.01 = 1 %, 1.05 = 5 %, 1.10 = 10 % and so on. The shape parameter, T , is calculated as follows:

$$T = (2\eta_2 - \eta_1 - \eta_3)/(\eta_1 - \eta_3)$$

where $T = -1$ is prolate, $T = 1$ is oblate and $T = 0$ is triaxial. It is standard practice to plot T against P' , however we note here that this style of plot is of limited use at very low anisotropies as the uncertainty of the shape at very low anisotropies is not accounted for in the T value because as P' tends to 1.0 the errors of T tend to infinity (Tarling and Hrouda 1993).

In addition to the definition of these parameters, the AMS data is also plotted stereographically on lower hemisphere equal area plots. The orientation of the three principal susceptibilities are plotted along with 95 % confidence limits.

To test the effect of outlying data we have stripped anomalous data from each station (original data is also reported) and assessed the effect on the overall fabric orientation. No obvious examples of sub-populations which seem to represent more than one fabric orientation within a station are seen. The rules applied to the data rejection are: (1) all 3 axes must be $>40^\circ$ outside 95 % confidence ellipses; (2) when only 2 axes are anomalous (and not obviously due to inverse fabric) then the mean shape parameter was considered such that a dominantly linear AMS signal K_1 axes significantly outside confidence ellipses are more likely to be anomalous. It is impossible for only one axis to be anomalous. Where samples had weak signals then data selection was avoided. This exercise never significantly altered fabric orientations (generally $<10^\circ$ or within original confidence ellipse).

6 AMS Results

The AMS data for the Arran Granite is summarised in Table 1 and plotted graphically in Fig. 4. K_{mean} is between 1.98×10^{-4} and 3.47×10^{-2} similar other Palaeogene granitoids in Britain and Ireland (Table 2) and consistent with a magnetite concentration of 0.001–0.1 wt% (Tarling and Hrouda 1993). P' ranges between 1.049 and 1.007. T values are scattered but tend marginally toward oblateness.

6.1 Magnetic Fabrics

The AMS tensor may be simplified to derive structural data in the form of a plane (normal to K_3) and a lineation (parallel to K_1) where the shape and confidence ellipses permit. This data is plotted on Fig. 5 which allows an overview of the fabric pattern. Figure 4 highlights that there is no obvious relationship between P' and T, but a positive trend (tendency to oblateness with higher P') is discernible. This allows us to plot a summary of the fabric in Fig. 6. Overall the AMS data describe a concentric and dome-like foliation in

the east and south east, with a dominantly sub-horizontal and north–south trending lineation (Figs. 5 and 6). In this region the foliation is slightly stronger (Figs. 5 and 6).

To the northwest, the fabric is weaker and more irregular but in general can be described by a dominantly sub horizontal foliation and lineation except close to the granite boundary where the foliation tends to be steep and concentric. In addition there is a zone along Glen Catacol (Fig. 6) where fabrics seem discordant to any overall trend. Here they are steep and trend north–south.

7 Insights into the Structure of the Northern Arran Granite and Surrounding Deformation Aureole

7.1 Geometry of Granite Contacts

The boundary of the Outer Granite is mainly steeply dipping or near vertical. The Inner Granite however seems generally to have gently dipping contacts across the central portions of its outcrop. England (1988) suggested that the Inner Granite was emplaced due to foundering of a large block of Outer Granite in a cauldron subsidence style model. In this model a vertical fracture near the north west of the Outer Granite somehow ceased to propagate upward and instead propagated laterally to the south east causing a large block of Outer Granite to founder into a magma chamber of Inner Granite magma.

8 3D Geometry of the Pluton

The overall pattern is of a dome shaped foliation with a generally subhorizontal lineation. No consistent vertical lineation pattern is found and lineations near the margins are usually gently plunging. This appears to be more consistent with a laccolithic model. The unusual fabric pattern found in Glen Catacol may represent some kind of late magmatic shear zone where partially

Table 1 AMS data

Sample	1,000 km grid system		K_{mean} ($E^\circ - 3$)	L	F	T	P'	Pole to foliation (K_3)			Foliation plane			Lineation (K_1)	
	Easting	Northing						Azimuth	Plunge	Dip	Dip azimuth	Plunge	Azimuth		
AG 1	191650	645532	3.25	1.00	1.30	0.97	1.04	120	82	8	300	294	8		
AG 2	191760	645873	3.50	1.01	1.01	0.34	1.02	340	1	89	160	70	33		
AG 3a	191877	646066	3.95	1.01	1.03	0.54	1.04	114	77	13	294	167	2		
AG 3b	191879	646070	1.68	1.01	1.02	0.38	1.02	123	63	27	303	344	21		
AG 4	191984	646304	3.80	1.01	1.02	0.36	1.03	94	71	19	274	186	1		
AG 5	192142	647971	4.32	1.01	1.00	-0.49	1.01	331	54	36	151	62	1		
AG 6	192100	648138	4.75	1.01	1.02	0.26	1.02	157	11	79	337	20	75		
AG 7	192021	648302	4.47	1.02	1.02	0.09	1.03	182	42	48	2	357	48		
AG 10	195186	646483	1.06	1.00	1.00	0.03	1.01	25	55	35	205	256	24		
AG 11	195213	646648	1.16	1.01	1.01	0.35	1.02	101	20	70	281	196	11		
AG 14	195142	647546	1.87	1.01	1.03	0.34	1.04	262	2	88	82	162	76		
AG 16	195055	647965	2.26	1.01	1.01	-0.01	1.02	65	43	47	245	182	26		
AG 17	195007	648211	2.63	1.01	1.00	-0.23	1.01	320	56	34	140	129	33		
AG 18	194860	648271	2.95	1.02	1.01	-0.57	1.02	37	10	80	217	278	70		
AG 20	194782	648841	5.04	1.01	1.01	0.05	1.02	101	27	63	281	7	9		
AG 21	194777	648949	3.35	1.02	1.01	-0.02	1.03	34	20	70	214	129	12		
AG 23	193219	646021	0.35	1.00	1.00	-0.20	1.01	274	3	88	94	5	6		
AG 24	193116	646192	0.46	1.03	1.01	-0.49	1.04	297	22	68	117	161	61		
AG 26	192825	646624	3.01	1.00	1.01	0.83	1.02	87	77	13	267	352	1		
AG 34	189745	645804	2.66	1.01	1.00	-0.43	1.01	335	20	70	155	241	9		
AB 1	200152	644446	19.80	1.02	1.01	-0.33	1.04	256	24	66	76	151	31		
AB 2	200182	644135	5.02	1.01	1.01	0.18	1.02	251	23	67	71	153	17		
AB 3	200002	643502	4.20	1.01	1.02	0.37	1.02	244	35	55	64	124	48		
AB 5	200101	643219	2.71	1.01	1.02	0.37	1.02	254	59	31	74	108	26		
AB 14	199153	642002	2.52	1.01	1.11	-0.14	1.03	283	23	67	103	16	7		
AB 15	199150	641750	0.72	1.00	1.00	0.07	1.01	265	16	74	85	53	71		

(continued)

Table 1 (continued)

Sample	1,000 km grid system			Pole to foliation (K_3)			Foliation plane			Lineation (K_1)			
	Easting	Northing	$K_{mean} (E^c - 3)$	L	F	T	P'	Azimuth	Plunge	Dip	Dip azimuth	Plunge	Azimuth
AB 17	199262	641492	4.61	1.00	1.03	0.89	1.03	298	36	54	118	199	13
AB 19	200388	641352	3.75	1.00	1.01	0.53	1.02	287	31	59	107	18	31
AB 21	200844	641725	3.12	1.01	1.03	0.60	1.04	285	36	55	105	127	36
AB 23	197750	644400	9.00	1.01	1.01	0.40	1.02	272	53	37	92	139	27
AB 26	199100	645855	3.14	1.01	1.01	-0.07	1.01	250	5	85	70	3	78
AB 27	198003	641919	3.16	1.01	1.00	-0.78	1.02	279	21	69	99	183	171
AB 28	198059	641760	4.50	1.01	1.00	-0.82	1.01	45	34	56	225	169	5
AB 29	198001	641615	3.40	1.01	1.00	-0.29	1.01	31	56	34	211	191	33
AB 32	198226	639032	4.08	1.00	1.04	0.84	1.05	283	38	52	103	116	52
AB 33	198240	638856	2.42	1.00	1.01	0.53	1.02	287	37	53	107	156	41
AB 39	198009	646710	1.35	1.01	1.03	0.67	1.04	248	66	24	68	123	14
AB 42	198395	643638	2.91	1.01	1.01	-0.43	1.02	288	30	60	108	188	18

Fig. 4 AMS parameters for the Northern Arran Granite plotted to show the variation of data and test any potential relationships. **A** P' versus $\text{Log } K_{\text{mean}}$ shows essentially no trend but shows the dominant susceptibility value of 3×10^{-3} . **B** T versus P' shows a very weak positive trend meaning that at higher anisotropies the anisotropy tends toward oblateness

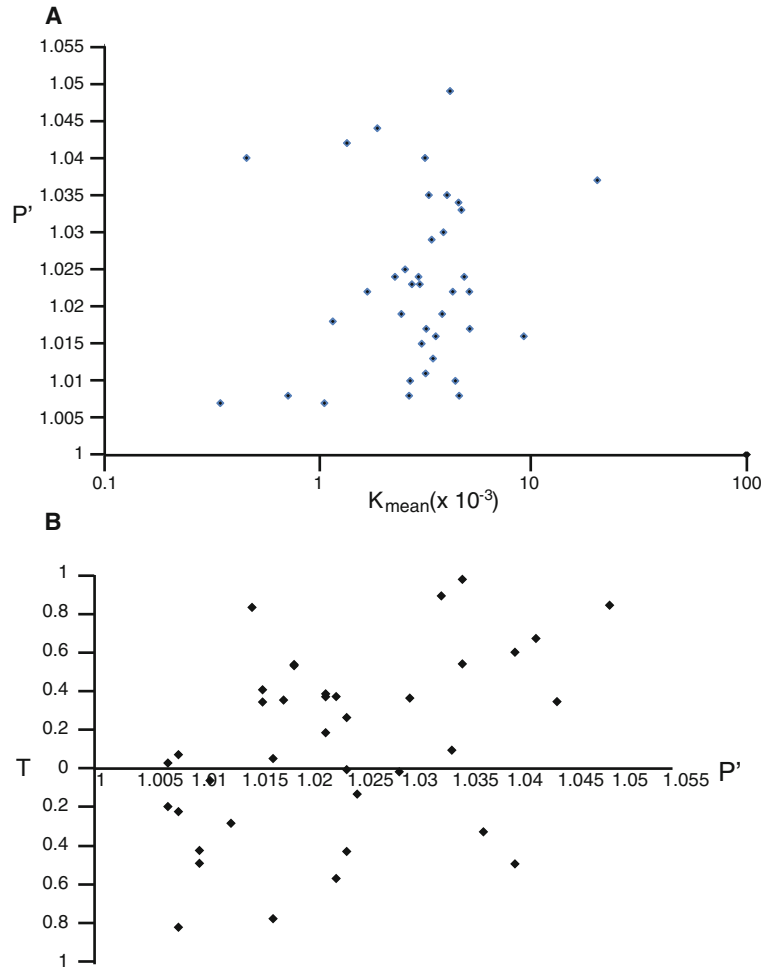


Table 2 Susceptibility values from Palaeogene granitoids from the UK and Ireland

Intrusion	Susceptibility	Reference
Eastern Mourne Granite, NE Ireland	4.7×10^{-5} – 1×10^{-2}	Stevenson et al. (2007b)
Western Mourne Granite, NE Ireland	1.7×10^{-4} – 5.2×10^{-2}	Stevenson and Bennett (2011)
Slieve Gullion porphyritic microgranite, NE Ireland	ca. 1×10^{-2}	Stevenson et al. (2008)
Western Red Hills Granite, Skye	Usually $>5 \times 10^{-3}$ (within the range 10^{-4} – 10^{-2})	Geoffroy et al. (1997)
Western Granite, Rum	2.9×10^{-2}	Petronis et al. (2009)

crystallised magma was able to concentrate shear close to the internal Inner–Outer Granite boundary. It is also possible that this kind of feature

could identify the boundary between internal granite lobes (sensu Stevenson et al. 2007a; Magee et al. 2012b).

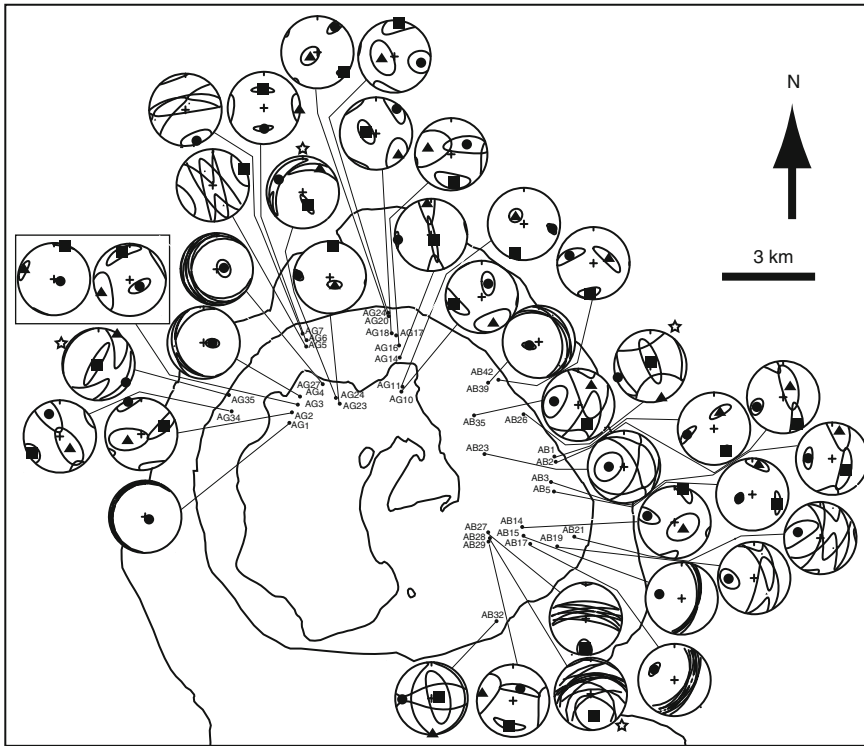


Fig. 5 AMS data plotted stereographically showing the orientation of the principal susceptibility axes for each station. The data for each station has been processed using Jelinek (1981) statistics where the mean orientation is taken using a normalised susceptibility. Confidence ellipses around each axis are 95 % limits. Where no

confidence ellipse is visible the ellipse is smaller than the symbol. Axis symbols: $K_1 = \text{square}$, $K_2 = \text{triangle}$, $K_3 = \text{circle}$. Data where fabrics are weak or the Jelinek statistics do not provide a robust signal are indicated with a *star*

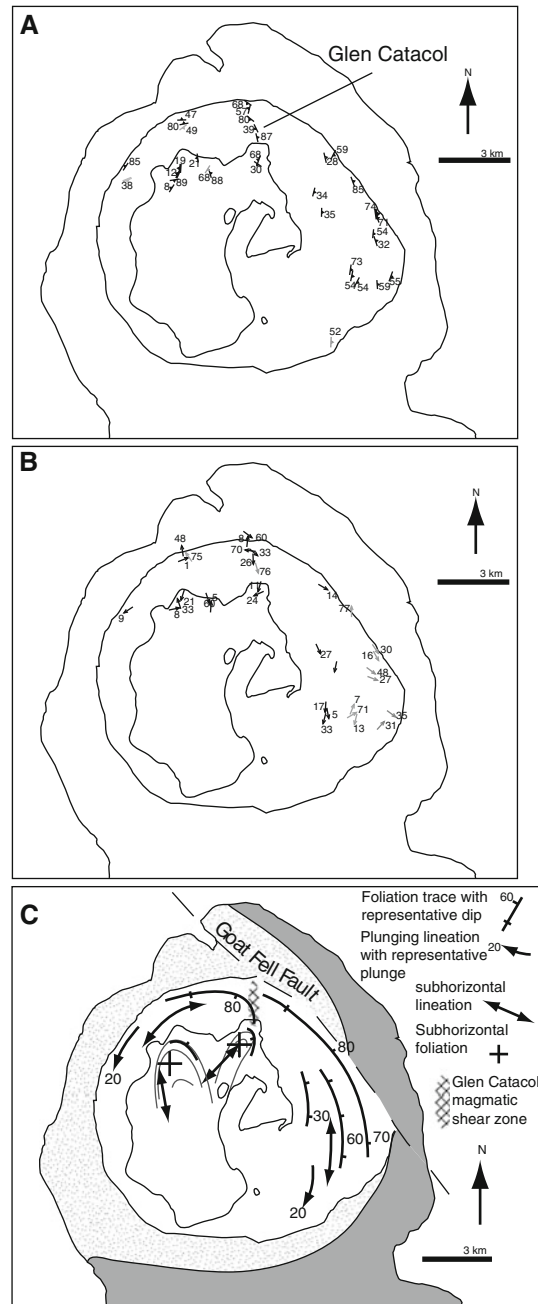
Gouly et al. (2001) gravity modelling suggested that the floor of the pluton lay at 0.3–1.2 km depth. In detail this model indicated a shallower floor in the northwest and the deepest granite in the south east. Although Gouly et al. (2001) concluded that this could be part of England's (1988) diapir model, this depth estimate is at least half the suggested depth in England's (1988) diapir model.

The geometry of the AMS fabrics provides information that enables us to reconstruct the unroofed part of the granite and combine this with the Gouly et al. (2001) gravity model. In the southeast and east, AMS fabrics are concentric and define a partial dome. If we assume the concentric pattern reflects a concordant fabric, we can project the granite contact parallel to the dome shape. This results in a roof that at its

apex would today be projected to roughly 4 km above sea level.

In contrast, the western portions of the pluton contain variable fabrics. Some of these lie within the Inner Granite where the consistent pattern is of gently dipping foliations that parallel mapped contacts (Fig. 6A). Lineations in the Inner Granite are also gently plunging and trend north–south, diverging to the north (Fig. 6B). The Outer Granite fabrics in the north western region do not seem to be concordant with the Inner Granite contacts and we suspect these may preserve parts of or partial lobes or fingers (e.g. Pollard et al. 1975; Stevenson et al. 2007a; Schofield et al. 2010). The Inner Granite seems to form a series of at least two sheets or tongue-like lobes that may coalesce northward and dip south (Fig. 6C).

Fig. 6 Summary of the fabric determined by AMS data. **A** Foliation data plotted using a *strike and dip bar* with a tick indicating dip and dip value stated. Foliations from dominantly linear stations should be viewed with caution and are drawn as *grey symbols*. **B** lineation data plotted using an *arrow* to indicate plunge azimuth and plunge value stated. Lineations from dominantly planar stations should be viewed with caution and are drawn as *grey symbols*. **C** Summary of the AMS fabric data



8.1 Re-examination of Host Rock Deformation

Previous studies have noted the dichotomy of deformation into folding and faulting around the Northern Arran Granite in the Dalradian and post

Caledonian sediments respectively. Folding is dominated by the Catacol Synform affecting only the Dalradian sediments. Doming, in addition, affects post Caledonian sediments, but faulting is the dominant mode of deformation in these younger sediments. This evidence is described in

detail by England (1988, 1992) and Woodcock and Underhill (1987) respectively.

8.1.1 Evidence for Doming of Pre-existing Folds

Sediments above the post Caledonian unconformity display outward dips but are not arranged in a simple dome. Examination of dips along the north eastern shore (from Corrie to Lochranza) indicates a northeast plunging fold that is tighter than the curvature of the granite contact. Woodcock and Underhill (1987) performed an analysis of this fold, the North Sannox anticline, and concluded that it was a conical fold plunging outward consistent with granite related doming. There may be some discordance due to the Goat Fell fault system (Woodcock and Underhill 1987), but we suggest that this conical fold is due to doming, reactivation and modification of a more cylindrical pre-existing east–west trending anticline. We also propose that the variable dip, although mainly outward, in the Devonian sediments directly south of the pluton may also be explained by doming of already folded sediments.

8.1.2 Catacol Synform as the Outer Limit of Laccolithic Doming

The geometry of the Catacol synform was analysed by England (1988, 1992) based on the only onshore exposure of its southeast dipping limb near Newtown (Fig. 2B). We note here however that the strike of this outer limb of this rim synform is not demonstrably deflected around the pluton as would be expected from an expanding diapir model. The strike of the outer limb may be traced in a roughly straight line from the northeast to the southwest with an apparent jog that can be explained by down throw to the northeast across the Goat Fell fault (Fig. 7A, B). Therefore the Catacol synform may simply delineate the extent of upward doming much like examples in the Henry Mountains, Utah, N. America (Johnson and Pollard 1973; Jackson and Pollard 1990;

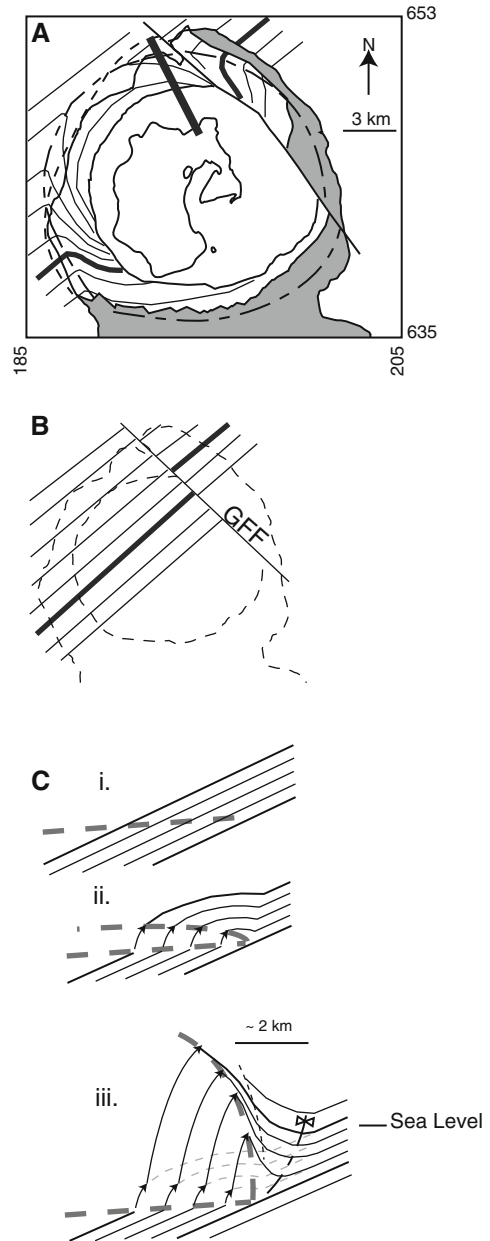


Fig. 7 A Sketch map showing the *strike* of the Dalradian strata highlighting the trace of the Catacol Synform and the Caledonian unconformity. **B** Shows the *strike* of the Dalradian strata without the Catacol synform or the granite. Note the offset across the Goat Fell Fault (GFF). **C** Evolution of the Catacol synform due to doming associated with a laccolith emplacement model for the granite

Horsman et al. 2005), i.e. around a laccolith. In Fig. 7C we outline the development of a concentric rim synform due solely to shouldering from a domed laccolith. Our schematic model uses an approximate scale based on England's (1992) sections. This model allows the Dalradian structure (the Aberfoyle synform) to be reconstructed to pre-granite geometry without a requirement to uplift a large area from beneath 3 km. We have assumed that flexural slip is dominant during the early stages of emplacement of the initial thin sheet, then similar folding takes over where hotter host rocks close to the pluton (in the hornfels zone) and closer to the tip zone of the initial sill flow or deform more. Although our model seems to predict a slightly deeper granite floor than the Goultly et al.'s (2001) gravity model, it demonstrates how a roughly equivalent fold may be generated without a diapir. The evolution and location of the trace of this synform relative to the granite margin depends on dynamic rheology of the aureole.

8.1.3 Reactivation of Pre-existing Transtensional Faults

Woodcock and Underhill (1987) carried out a detailed analysis of brittle deformation around the Northern Arran Granite. These authors noted that the main faulting along the eastern side of the pluton (i.e. the Goat Fell Fault and North Sannox Fault systems) may have initiated before granite emplacement. Here we suggest that, coupled with perpendicular folding (e.g. the Sannox anticline, Fig. 2B) this faulting may represent transtensional faulting caused due to Variscan or early Cenozoic reactivation along the Highland Boundary Fault zone. These faults may have facilitated granite emplacement in a similar way to a bysmalith or 'trap door laccolith' (e.g. Corry 1988; Stevenson et al. 2007b).

The fabric pattern from Glen Catatol (Fig. 6C), if this was fault related, could be a splay off the Goat Fell Fault as it reactivated. This would be

supported if fault related fluid movement was seen to affect the granite in this zone. However this was not examined in this study.

9 Discussion

Our model presents an alternative to the diapir model that fits previously published evidence and is supported by new data. A key tenet of our model is that the Northern Arran Granite must have been emplaced at shallow depths as the adjacent Arran Central Complex (also Palaeogene) contains volcanic lithologies (King 1954). Although the age of emplacement of the latter has not been radiometrically dated, there is evidence that it is younger than the Northern Arran Granite as it cuts southward dipping Devonian strata (domed due to emplacement of the Northern Arran Granite) in the southern aureole of the Northern Arran Granite. Given that the total thickness of the Northern Arran Granite is 4–5 km, and that in the Central Complex there is evidence of Mesozoic cover and probably c. 1 km of denudation, there is a requirement to erode 3–4 km between the emplacement of the Northern Arran Granite and the Arran Central Complex. This may be facilitated by doming associated with the Northern Arran Granite, which was identified by Woodcock and Underhill (1987) as far-field deformation (up to 15 km radius) due to the emplacement of the Northern Arran Granite.

We have suggested that the Northern Arran Granite was emplaced south to north based partly on the south dipping floor (assuming that it was emplaced up dip) but mainly from the north–south trending lineation and the northward divergence in the Inner Granite. This presents the possibility of linking the Northern Arran Granite to the location of a regional gravity high (Emeleus and Bell 2005, p 96). Although a gravity high is more likely to be caused by a mafic complex at depth, the association of felsic and mafic magma in the British and Irish Palaeogene is well

documented (McQuillin and Tuson 1963; Bott and Tuscon 1973; Emeleus and Bell 2005; Gamble 1979) and presents a similar situation to the Mourne Granites and a subjacent laterally offset gravity high (Stevenson and Bennett 2011).

The reason for a northward emplacement may have been due to a thinner post Caledonian overburden north of the Highland Boundary fault zone. This may have allowed the proto-Northern Arran Granite sill to propagate northward dipping gently south, and partly exploiting a pre-existing fold, begin to dome and then form a cupola in the post Caledonian unconformity.

It has been suggested that the Highland Boundary Fault may have provided an ascent route for the Northern Arran Granite magma (e.g. Woodcock and Underhill 1987). However it is also recognised that the HBF is not distinct on Arran, whereas it forms a clear terrane boundary on mainland Scotland (Young and Caldwell 2012). On Arran, the deflection of the basal Devonian unconformity and the Highland Border Complex are the nearest equivalent outcrop expression of this boundary. The HBF's location to the south west onshore Northern Ireland is also ambiguous and is only identified from a geophysical anomaly in a line from Fair Head to Clew Bay, viz. the Fair Head-Clew Bay line. This roughly correlates with the trace of the HBF in Scotland (Max and Riddihough 1975), and stratigraphic correlations made in the West of Ireland (Chew 2003). Most terrane maps show the HBF to be offset left laterally between Northern Ireland and Scotland bending around the Mull of Kintyre (e.g. Woodcock and Strachan 2012, p 33). We suggest here that the HBF may have a significant jog or overstep beneath Arran that provides a focus for magma ascent. The centre of this feature would lie close to the centre of the Island and coincident with the location of the Arran Central Complex and a significant gravity high. This inference presents the possibility of a long lived major crustal structure that could have provided a deeply penetrating ascent route for all the igneous rocks on Arran. Following this the location of the upper crustal magma chamber that fed this activity may have also been controlled by this structure and thus

would have been located beneath the Central Complex and be responsible for the positive gravity anomaly. Sinistral reactivation of the HBF at least pre intrusion of the Northern Arran Granite would explain some weak east-west trending folding and NNW-SSE trending extensional faulting.

9.1 An Emplacement Model for the Northern Arran Granite and the Evolution of the Highland Boundary Fault Zone off Shore Scotland

The pre-Palaeogene structure of the area around Arran was dominated by north-south trending faults, such as the Brodick Bay Fault, that controlled Carboniferous basins in this area (Fig. 1B). It is noteworthy that this activity formed the famous Hutton Unconformity at Catacol Point. The north-south trending faults were probably activated during reactivation of the NE-SW trending HBF during the Variscan Orogeny and acted as a transfer zone between left lateral overstep in the HBF zone that exists in this region. Few obvious NE-SW trending faults exist at the present surface, but it is likely that the HBF zone existed at depth.

During Palaeogene north Atlantic rifting, the HBF was reactivated in a left lateral transtensional sense so the north-south faults offshore Ayrshire and Kintyre acted once again as a transtensional transfer zone (Fig. 8A). This transfer zone likely concentrated magmatism and provided a crustal weak zone facilitating deeply penetrating ascent routes. It is unlikely therefore that magma crossed back and forth across this zone (*sensu* Meade et al. 2009) but probably accessed crustal elements from both sides during its ascent. This ascent site is possibly marked by the major positive gravity anomaly situated beneath the Central Complex.

During Palaeogene rifting, east-west extension focused in a left lateral transtensional transfer zone also generated east-west trending folds exemplified by the North Sannox fold (Woodcock and Underhill 1998). This folding modified the

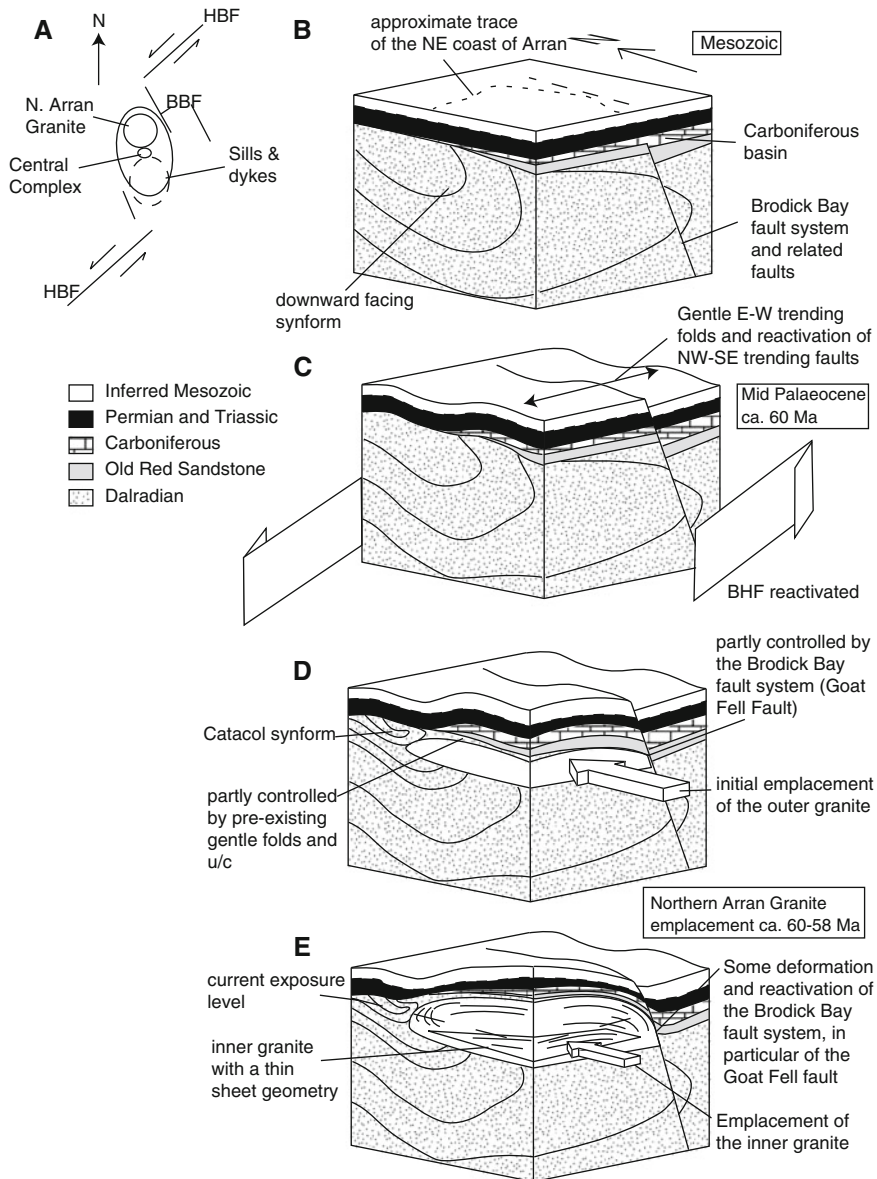


Fig. 8 Final model for the emplacement of the Northern Arran Granite. **A** Schematic representation of the key tectonic elements surrounding Arran highlighting the potential left lateral step in the HBF. **B** Initial stratigraphy pre-Palaeogene. **C** Pre-granite sinistral transension

associated with reactivation of the HBF and focused on the step in the HBF. **D** Initial emplacement of the outer granite from the south as a relatively thin or tabular sheet. **E** Final emplacement stage showing the doming and internal fabric pattern as revealed by AMS data

preexisting downward facing Caledonian folds and created a gently dipping ‘flat’ in the base Permian unconformity next to the HBF (Fig. 8B, C). The timing of this extension relative to the timing of emplacement suggests that extension

began during phase 1 of the NAIP activity (Fig. 3). This extension was at least incipient and may have been focused or concentrated close to pre-existing tectonic structures such as the HBF (cf. Stevenson and Bennett 2011).

The base Permian unconformity NW of the HBF and west of the Brodick Bay fault then acted as a lateral weakness that controlled the emplacement location of the North Arran Granite aided by the flat zone created by the transtensional folding (Fig. 8D). The Inner Granite was emplaced as a gently dipping sheet facilitated partly by further reactivation of the Brodick Bay fault system (Fig. 8D, E).

Thus the Northern Arran Granite was emplaced south to north as an initially thin gently south dipping sheet. As the initial sill thickened vertically, to the east this was accommodated by reactivation of extant north–south trending faults, e.g. the Goat Fell Fault, and by folding and shouldering to the north, west and south—the Catacol Synform.

10 Conclusion

AMS data reveals a subtle internal fabric within the Northern Arran Granite providing information about its emplacement. This fabric describes a gently south dipping laccolith. Steep concordant AMS foliations in the east are consistent with a forceful emplacement and gently dipping foliations in the inner granite suggest that this was emplaced as a gently dipping sheet. Close to the north and north western margins, the foliation pattern can fit with the northward termination of tongue like lobes. The linear component is weak and gently plunging, inconsistent with the diapir model, which warranted a re-examination of the deformed aureole. We demonstrate that the Catacol Synform can be explained by doming and shouldering from a laccolith and does not require several kilometres of uplift. The laccolith was probably emplaced into gentle east-west trending folds created during Palaeogene sinistral reactivation of the HBF zone. The northward emplacement of the granite may have emanated from a deeply penetrating feeder located approximately beneath where the Central Complex is currently situated and there is thus the possibility of a single deeply penetrating crustal ascent route for all the magmatism on Arran, potentially controlled by a left lateral overstep on the HBF zone.

Acknowledgments This work was completed as part of C. Grove's MSci research at the University of Birmingham. We are grateful to M. Binks for field assistance and the Lochranza Distillery for bringing out their first 10 year malt during our field season on Arran.

References

- Anderson EM (1937) The Dynamics of the formation of cone-sheets, ring-dykes and caldron-subsidences. In: Proceedings of the Royal Society of Edinburgh, 56:128–157
- Anderson JGC (1947) The geology of the Highland Border: Stonehaven to Arran. *Trans Royal Soc Edinb: Earth Sci* 61:479–515
- Bailey EB (1924) Tertiary and post-tertiary geology of mull, loch aline, and oban: a description of parts of sheets 43, 44, 51, and 52 of the geological map. HM Stationery Office
- Bateman R (1985) Aureole deformation by flattening around a diapir during in situ ballooning: the Cannibal Creek granite. *J Geol* 293–310
- Bell B, Williamson I (2002) Tertiary igneous activity. *Geol Scotland* 371–407
- Borradaile G, Jackson M (2004) Anisotropy of magnetic susceptibility (AMS): magnetic petrofabrics of deformed rocks. In: Martin-Hernandez F, Luneburg CM, Aubourg C, Jackson M (eds) *Magnetic fabric: methods and applications*, geological society, London. Special Publications, London, pp 299–360
- Borradaile GJ, Henry B (1997) Tectonic applications of magnetic susceptibility and its anisotropy. *Earth Sci Rev* 42:49–93
- Bott MHP, Tuson J (1973) Deep structure beneath the Tertiary volcanic regions of Skye, Mull and Ardnamurchan, north-west Scotland. *Nat Phys Sci* 242:114–116
- Bouchez JL (1997) Granite is never isotropic: an introduction to AMS studies of granitic rocks. In: Bouchez JL, Hutton DHW, Stephens WE (eds) *Granite: from segregation of melt to emplacement fabrics*. Kluwer Academic Publishers, Dordrecht, pp 95–112
- Brown DJ, Holohan EP, Bell BR (2009) Sedimentary and volcano-tectonic processes in the British Paleocene Igneous Province: a review. *Geol Mag* 146(03):326–352
- Brun JP, Gapais D, Cogne JP, Ledru P, Vignerresse JL (1990) The Flamanville granite (northwest France): an unequivocal example of a syntectonically expanding pluton. *Geol J* 25(3–4):271–286
- Castro A (1987) On granitoid emplacement and related structures. *Rev Geol Rundschau* 76(1):101–124
- Chew D (2003) Structural and stratigraphic relationships across the continuation of the Highland Boundary Fault in western Ireland. *Geol Mag* 140(01):73–85
- Clemens JD (1998) Observations on the origins and ascent mechanisms of granitic magmas. *J Geol Soc* 155(5):843–851

- Corry CE (1988) Laccoliths: mechanics of emplacement and growth. *Geol Soc Am*
- Cruden AR (1988) Deformation around a rising diapir modeled by creeping flow past a sphere. *Tectonics* 7 (5):1091–1101
- Cruden AR (1990) Flow and fabric development during the diapiric rise of magma. *J Geol* 681–698
- Dickin A, Moorbath S, Welke H (1981) Isotope, trace element and major element geochemistry of Tertiary igneous rocks, Isle of Arran, Scotland. *Trans Royal Soc Edinb: Earth Sci* 72(03):159–170
- Dickin AP (1994) Nd isotope chemistry of Tertiary igneous rocks from Arran, Scotland: implications for magma evolution and crustal structure. *Geol Mag-London* 131:329
- Dickin AP, Bowes DR (1991) Isotopic evidence for the extent of early proterozoic basement in Scotland and northwest Ireland. *Geol Mag* 128(4):385–388
- Doré A, Lundin E, Jensen L, Birkeland Ø, Eliassen P, Fichler C (1999) Principal tectonic events in the evolution of the northwest European Atlantic margin. In: Geological society, London, petroleum geology conference series. Geological Society of London, pp 41–61
- Ellam RM, Stuart FM (2000) The sub-lithospheric source of north atlantic basalts: evidence for, and significance of, a common end-member. *J Petrol* 41(7):919–932
- Emeleus CH, Bell BR (2005) The Palaeogene volcanic districts of Scotland. British Geological Survey
- Emeleus CH, Gyopari M, Britain G (1992) British Tertiary volcanic province. Chapman & Hall, London
- Emeleus CH, Troll VR, Chew DM, Meade FC (2012) Lateral versus vertical emplacement in shallow-level intrusions? The Slieve Gullion Ring-complex revisited. *J Geol Soc* 169(2):157–171
- England RW (1988) The ascent and emplacement of granitic magma: the northern Arran granite. Department of geological sciences, Durham University, Durham, p 212
- England RW (1990) The identification of granitic diapirs. *J Geol Soc* 147(6):931–933
- England RW (1992) The genesis, ascent, and emplacement of the Northern Arran Granite, Scotland: implications for granitic diapirism. *Geol Soc Am Bull* 104 (5):606–614
- Galadi-Enriquez E, Galindo-Zaldívar J, Simancas F, Expósito I (2003) Diapiric emplacement in the upper crust of a granitic body: the La Bazana granite (SW Spain). *Tectonophysics* 361(1–2):83–96
- Gamble JA (1979) Some relationships between coexisting granitic and basaltic magmas and the genesis of hybrid rocks in the Tertiary central complex of slieve-gullion, northeast Ireland. *J Volcanol Geoth Res* 5(3–4):297–316
- Goffroy L, Olivier P, Rochette P (1997) Structure of a hypovolcanic acid complex inferred from magnetic susceptibility anisotropy measurements: the Western Red Hills granites (Skye, Scotland, Thulean Igneous Province). *Bull volcanol* 59(2):147–159
- Gouly NR, Dobson AJ, Jones GD, Al-Kindi SA, Holland JG (2001) Gravity evidence for diapiric ascent of the Northern Arran Granite. *J Geol Soc* 158(5):869–876
- Grout FF (1945) Scale models of structures related to batholiths. *Am J Sci* 243:260–284
- Halliday AN, Graham CM, Aftalion M, Dymoke P (1989) Short paper: the depositional age of the Dalradian Supergroup: U-Pb and Sm-Nd isotopic studies of the Tayvallich Volcanics, Scotland. *J Geol Soc* 146(1):3–6
- Harris A, Baldwin C, Bradbury H, Johnson H, Smith R (1978) Ensialic basin sedimentation: the Dalradian Supergroup. *Crustal Evol Northwest Br Adjacent Reg* 10:115–138
- He B, Xu Y-G, Paterson S (2009) Magmatic diapirism of the Fangshan pluton, southwest of Beijing, China. *J Struct Geol* 31(6):615–626
- Holder MT (1980) An emplacement mechanism for post-tectonic granites and its implications for their geochemical features. In: Origin of granite batholiths. Springer, Berlin, pp 116–128
- Horsman E, Tikoff B, Morgan S (2005) Emplacement-related fabric and multiple sheets in the Maiden Creek sill, Henry Mountains, Utah, USA. *J Struct Geol* 27 (8):1426–1444
- Hutton DHW (1988) Granite emplacement mechanisms and tectonic controls: inferences from deformation studies. *Trans Royal Soc Edinb: Earth Sci* 79(2–3):245–255
- Hutton DHW, Siegesmund S (2001) The Ardara Granite: reinflating the balloon hypothesis. *Zeitschrift der Deutschen Geologischen Gesellschaft* 152(2–4):309–323
- Jackson MD, Pollard DD (1990) Flexure and faulting of sedimentary host rocks during growth of igneous domes, Henry Mountains, Utah. *J Struct Geol* 12 (2):185–206
- Jelinek V (1981) Characterization of the magnetic fabric of rocks. *Tectonophysics* 79(3–4):T63–T67
- Johnson AM, Pollard DD (1973) Mechanics of growth of some laccolithic intrusions in the Henry mountains, Utah, I: field observations, Gilbert's model, physical properties and flow of the magma. *Tectonophysics* 18 (3):261–309
- Jolley DW, Bell BR (2002) The evolution of the North Atlantic Igneous Province and the opening of the NE Atlantic rift. *Geol Soc London Spec Publ* 197(1):1–13
- Jolley DW, Widdowson M (2005) Did Paleogene North Atlantic rift-related eruptions drive early Eocene climate cooling? *Lithos* 79(3–4):355–366
- King BC (1954) The Ard Bheinn area of the central igneous complex of Arran. *Q J Geol Soc* 110(1–4):323–355
- Magee C, Stevenson C, O'Driscoll B, Schofield N, McDermott K (2012a) An alternative emplacement model for the classic Ardnamurchan cone sheet swarm, NW Scotland, involving lateral magma supply via regional dykes. *J Struct Geol* 43:73–91
- Magee C, Stevenson CTE, O'Driscoll B, Petronis MS (2012b) Local and regional controls on the lateral emplacement of the Ben Hiant Dolerite intrusion, Ardnamurchan (NW Scotland). *J Struct Geol* 39:66–82

- Max MD, Riddihough RP (1975) Continuation of the Highland Boundary fault in Ireland. *Geology* 3 (4):206–210
- McLean A, Deegan C (1978) A synthesis of the solid geology of the firth of clyde region. HM Stationery Office
- McQuillin R, Tuson J (1963) Gravity measurements over the Rhum Tertiary Plutonic complex. *Nature* 199 (4900):1276–1277
- Meade FC, Chew DM, Troll VR, Ellam RM, Page LM (2009) Magma Ascent along a major terrane boundary: crustal contamination and Magma mixing at the Drumadoon Intrusive complex, Isle of Arran, Scotland. *J Petrol* 50(12):2345–2374
- Meighan IG, Fallick AE, McCormick AG (1992) Anorogenic granite magma genesis: new isotopic data for the southern sector of the British Tertiary Igneous Province. *Trans Royal Soc Edinb Earth Sci* 83:227–233
- Meyer R, Nicoll GR, Hertogen J, Troll VR, Ellam RM, Emeleus CH (2009) Trace element and isotope constraints on crustal anatexis by upwelling mantle melts in the North Atlantic Igneous Province: an example from the Isle of Rum, NW Scotland. *Geol Mag* 146(03):382–399
- Meyer R, van Wijk J, Gernigon L (2007) The north Atlantic igneous province: a review of models for its formation. *Geo Soc Am Spec Pap* 430:525–552
- Miller RB, Paterson SR (1999) In defense of magmatic diapirs. *J Struct Geol* 21(8–9):1161–1173
- Molyneux SJ, Hutton DHW (2000) Evidence for significant granite space creation by the ballooning mechanism: the example of the Ardara pluton, Ireland. *Geol Soc Am Bull* 112(10):1543–1558
- Mussett AE, Dagley P, Skelhorn RR (1988) Time and duration of activity in the British Tertiary Igneous Province. *Geol Soc London Spec Publ* 39(1):337–348
- O'Driscoll B, Stevenson CT, Troll VR (2008) Mineral lamination development in layered gabbros of the British Palaeogene Igneous Province: a combined anisotropy of magnetic susceptibility, quantitative textural and mineral chemistry study. *J Petrol* 49 (6):1187–1221
- O'Driscoll B, Troll V, Reavy R, Turner P (2006) The Great Euclite intrusion of Ardnamurchan, Scotland: reevaluating the ring-dike concept. *Geology* 34 (3):189–192
- Owens WH (1994) Laboratory drilling of field-orientated block samples. *J Struct Geol* 16(12):1719–1721
- Paterson SR, Fowler TK (1993) Reexamining pluton emplacement processes. *J Struct Geol* 15(2):191–206
- Paterson SR, Vernon RH (1995) Bursting the bubble of ballooning plutons—a return to nested diapirs emplaced by multiple processes. *Geol Soc Am Bull* 107 (11):1356–1380
- Petford N (1996a) Dykes or diapirs? *Earth Environ Sci Trans Royal Soc Edinb* 87(1–2):105–114
- Petford N (1996b) Dykes or diapirs? *Trans Royal Soc Edinb: Earth Sci* 87(1–2):105–114
- Petford N, Clemens JD (2000) Granites are not diapiric! *Geol Today* 16(5):180–184
- Petford N, Cruden AR, McCaffrey KJW, Vigneresse JL (2000) Granite magma formation, transport and emplacement in the Earth's crust. *Nature* 408 (6813):669–673
- Petford N, Kerr RC, Lister JR (1993) Dike transport of granitoid magmas. *Geology* 21(9):845–848
- Petford N, Lister JR, Kerr RC (1994) The ascent of felsic magmas in dykes. *Lithos* 32(1–2):161–168
- Petronis MS, O'Driscoll B, Troll VR, Emeleus CH, Geissman JW (2009) Palaeomagnetic and anisotropy of magnetic susceptibility data bearing on the emplacement of the Western Granite, Isle of Rum, NW Scotland. *Geol Mag* 146(3):419–436
- Pharaoh TC, Morris J, Long CB, Ryan PD (1996) Tectonic map of Britain Ireland and adjacent areas. British Geological Survey, Nottingham
- Pollard DD, Muller OH, Dockstader DR (1975) The form and growth of fingered sheet intrusions. *Geol Soc Am Bull* 86(3):351–363
- Ramberg H (1967) Gravity, deformation and the earth's crust. Academic Press, London
- Ramsay JG (1989) Emplacement kinematics of a granite diapir: the Chindamora batholith, Zimbabwe. *J Struct Geol* 11(1):191–209
- Richey JE (1928) Structural relations of the Mourne Granites (Northern Ireland). *Q J Geol Soc London* 83:653
- Richey JE (1932) Tertiary ring structures in Britian. *Trans Geol Soc Glasgow* 88:776
- Richey JE, Thomas HH (1932) The tertiary ring complex of slieve gullion, Ireland. *Q J Geol Soc London* 88:776–849
- Rubin AM (1993) Dikes verses diapirs in viscoelastic rock. *Earth Planet Sci Lett* 117(3–4):653–670
- Rubin AM (1995) Getting granite dikes out of the source region. *J Geophy Res: Solid Earth* 100(B4):5911–5929
- Sanderson DJ, Meneilly AW (1981) Analysis of three-dimensional strain modified uniform distributions: andalusite fabrics from a granite aureole. *J Struct Geol* 3(2):109–116
- Saunders A, Fitton J, Kerr A, Norry M, Kent R (1997) The north Atlantic igneous province. Large Igneous Provinces: Continental, Oceanic Planetary Flood Volcanism, pp 45–93
- Schmeling H, Cruden AR, Marquart G (1988) Finite deformation in and around a fluid sphere moving through a viscous medium: implications for diapiric ascent. *Tectonophysics* 149(1):17–34
- Schofield N, Stevenson C, Reston T (2010) Magma fingers and host rock fluidization in the emplacement of sills. *Geology* 38(1):63–66
- Shackleton RM (1957) Downward-facing structures of the Highland Border. *Q J Geol Soc* 113(1–4):361–392
- Siegesmund S, Becker JK (2000) Emplacement of the Ardara pluton (Ireland): new constraints from magnetic fabrics, rock fabrics and age dating. *Int J Earth Sci* 89(2):307–327

- Stephenson D, Mendum JR, Fettes DJ, Leslie AG (2013) The Dalradian rocks of Scotland: an introduction. *Proc Geol Assoc* 124(1):3–82
- Stevenson C, Bennett N (2011) The emplacement of the Palaeogene Mourne Granite Centres, Northern Ireland: new results from the Western Mourne Centre. *J Geol Soc* 168(4):831–836
- Stevenson CT, O’Driscoll B, Holohan EP, Couchman R, Reavy RJ, Andrews GD (2008) The structure, fabrics and AMS of the Slieve Gullion ring-complex, Northern Ireland: testing the ring-dyke emplacement model. *Geol Soc London Spec Publi* 302(1):159–184
- Stevenson CTE, Owens WH, Hutton DHW (2007a) Flow lobes in granite: the determination of magma flow direction in the Trawenagh Bay Granite, northwestern Ireland, using anisotropy of magnetic susceptibility. *Geol Soc Am Bull* 119(11–12):1368–1386
- Stevenson CTE, Owens WH, Hutton DHW, Hood DN, Meighan IG (2007b) Laccolithic, as opposed to cauldron subsidence, emplacement of the Eastern Mourne pluton, N. Ireland: evidence from anisotropy of magnetic susceptibility. *J Geol Soc* 164(1):99–110
- Stone P, Kimbell G (1995) Caledonian terrane relationships in Britain: an introduction. *Geol Mag* 132(05):461–464
- Tanner G (2008) Tectonic significance of the highland boundary fault, Scotland. *J Geol Soc* 165(5):915–921
- Tarling D, Hrouda F (1993) *Magnetic anisotropy of rocks*. Springer, Berlin
- Thompson R (1982) Magmatism of the British Tertiary volcanic province. *Scottish J Geol* 18(1):49–107
- Thompson R, Morrison M, Dickin A, Gibson I, Harmon R (1986) Two contrasting styles of interaction between basic magmas and continental crust in the British Tertiary Volcanic Province. *J Geophys Res: Solid Earth* (1978–2012) 91(B6):5985–5997
- Trewin NH (2002) *The geology of Scotland*. Geological Society, London
- Troll VR, Chadwick JP, Ellam RM, Mc Donnell S, Emeleus CH, Meighan IG (2005) Sr and Nd isotope evidence for successive crustal contamination of Slieve Gullion ring-dyke magmas, Co. Armagh, Ireland. *Geol Mag* 142(06):659–668
- Vernon RH, Paterson SR (1993) The ardara pluton, Ireland—deflating all expanded intrusion. *Lithos* 31(1–2):17–32
- Vignerresse JL, Clemens JD (2000) Granitic magma ascent and emplacement: neither diapirism nor neutral buoyancy. *Geol Soc London Spec Publ* 174(1):1–19
- Walker GP (1975) A new concept of the evolution of the British Tertiary intrusive centres. *J Geol Soc* 131(2):121–141
- Wallace J, Ellam R, Meighan I, Lyle P, Rogers N (1994) Sr isotope data for the Tertiary lavas of Northern Ireland: evidence for open system petrogenesis. *J Geol Soc* 151(5):869–877
- Weinberg RF (1996) Ascent mechanism of felsic magmas: news and views. *Earth and Environ Sci Trans Royal Soc Edinb* 87(1–2):95–103
- Woodcock NH, Strachan R (2012) *Geological history of Britain and Ireland*. Wiley, New York
- Woodcock NH, Underhill JR (1987) Emplacement-related fault patterns around the Northern Granite, Arran, Scotland. *Geol Soc Am Bull* 98(5):515–527
- Young GM, Caldwell WGE (2012) The northeast Arran trough, the corrie conundrum and the highland boundary fault in the firth of clyde, SW Scotland. *Geol Mag* 149(4):578–589

Erratum to: Sub-volcanic Intrusions in the Karoo Basin, South Africa

Henrik H. Svensen, Stéphane Polteau, Grant Cawthorn,
and Sverre Planke

Erratum to: *Advances in Volcanology* DOI: [10.1007/11157_2014_7](https://doi.org/10.1007/11157_2014_7)

The chapter was inadvertently published without updating Table 1. The erratum chapter has been updated with the change.

The updated original online version for this chapter can be found at [10.1007/11157_2014_7](https://doi.org/10.1007/11157_2014_7)

H.H. Svensen (✉) · S. Planke
Centre for Earth Evolution and Dynamics (CEED), University of Oslo, Oslo, Norway
e-mail: hensven@fys.uio.no

S. Polteau · S. Planke
Volcanic Basin Petroleum Research (VBPR), Oslo Innovation Center, Oslo, Norway

G. Cawthorn
School of Geosciences, University of Witwatersrand, Johannesburg, South Africa



Erratum to: Physical Geology of Shallow Magmatic Systems

Christoph Breitkreuz and Sergio Rocchi

Erratum to:
**C. Breitkreuz and S. Rocchi (eds.), *Physical Geology
of Shallow Magmatic Systems*,**
<https://doi.org/10.1007/978-3-319-14084-1>

The original version of the book was inadvertently published with incorrect chapter DOIs and Copyright Year information for all chapters. They have been updated with original DOIs and Copyright Year as per online first chapters. Further, the series subtitle has been included in the series page.

The updated online version of the book can be found at
<https://doi.org/10.1007/978-3-319-14084-1>

Advances in Volcanology (2018) E3
https://doi.org/10.1007/11157_2018_2005
© Springer International Publishing AG, part of Springer Nature 2018

Index

A

- Absaroka volcanic field, 18
- Altenberg-Teplice Volcanic Complex, 295
- Analogue experiments, 8
- Analogue modelling, 148
 - air, 151
 - caldera, 188, 192
 - caldera collapse, 190
 - collapse, 190
 - compaction, 162
 - compressive, 200
 - cryptodome related, 195
 - dyke related, 194
 - effect of regional tectonics, 190
 - effect of topography, 190
 - explosive eruption, 18, 198
 - extensional, 200
 - gelatine, 151
 - granular model host rock, 160
 - ground deformation, 193
 - host rock, 149
 - magma-fault interaction, 197, 200
 - magma, 149
 - mechanical properties, 157, 159, 160
 - model host, 162
 - model host rock, 154
 - model magma, 154, 157
 - model material, 149
 - non-granular model host rock, 159
 - resurgence, 192
 - saucer-shaped sill related, 195
 - scaling, 162
 - strikeslip, 200
 - surface deformation, 194, 195
 - cryptodome related, 7
 - tumescence, 192
 - types, 157, 159, 160
 - water, 151
- Anisotropy of Magnetic Susceptibility (AMS), 4, 20, 21, 28, 30, 31, 305, 367
- Antecrysts, 76
- Apatite fission track analysis, 291
- Ardnamurchan intrusive complex, 176
- Ariake, 29
- Arrhenius law, 149

Aureole thickness, 265

B

- Back flow, 5
- Balloning, 3
- Bandai, 11
- Banded aplite, 19
- Barú, 5
- Batholiths, 2, 4, 10, 23, 77
- Baula (laccolith), 369
- Bezymianny, 9, 11
- Biotite, 20
- Black Mountains, 18
- Blackstones igneous centre, 278
- Block-and-ash-flows, 7
- Bookshelf, 29
- Bookshelf textures, 23
- Bore hole data, 350
- Boulder Batholith, 198
- Bowl-shaped flow geometry, 304
- Breccia dykes, 27
- Breccia pipe, 251, 269, 350
- Breccias, 49
- Brecciation planes, 304
- Bridge, 3, 6, 284
 - broken, 5, 6, 7
- Bridge structures, 279
- Brittle, 5
- Buckingham Π -theorem, 164
- Building materials, 7
- Bulbous terminations, 11
- Bulldozer, 10
- Buoyancy, 168
- Buoyant forces, 150
- Bysmalith, 2, 4, 10, 11, 19, 341

C

- Caldera, 2, 44, 148, 185, 363
 - piecemeal, 193
 - trapdoor, 187
- Caldera collapse, 46, 187
- Caldera-forming ignimbrites, 77
- Canary Islands, 176

Cape Fold Belt, 356
 Carapace facies, 303
 Carbon isotope, 250, 350
 Casagrande shear box, 161
 Cataclastic lineations, 30
 Cataclastic shear zones, 22
 Centrifuge, 183
 Chilled margin, 2, 7, 14, 23, 25, 30
 Cinder cone, 148
 Clastic dykes, 26
 Climate change, 7, 249
 Coaxial flow, 15
 Coefficient of friction, 29
 Colorado Plateau, 327
 Columnar joints, 27
 Composite dyke, 7, 19, 169
 Compressional settings, 5
 Computed tomography, 19
 Cone sheet, 4, 5, 48, 148
 Contact breccias, 26
 Contact metamorphic aureole, 20
 Continental Flood Basalt Provinces (CFBPs), 43
 Continental flood basalts, 274, 350
 Convergent flow, 15
 Cooling columns, 26, 27
 Cooling times, 65
 Core facies, 303
 Country rock, 54
 Cryptodomes, 7, 182
 Crystal graveyards, 73
 Crystal mush, 46, 63, 74, 77
 Crystal population, 54, 55, 57
 Crystal recycling, 54, 55
 Crystal settling, 25
 Crystal Size Distribution (CSD), 54, 303
 Crystal stretching, 30
 Cupola-shaped flow geometry, 304

D

Debris avalanche, 4, 5, 22, 28
 Debris flow, 4, 6, 26, 29
 Diapirs, 41
 Diatomite, 161, 198
 Diatremes, 27
 Dimensional analysis, 163
 Dimensionless scaling, 163
 Distribution coefficients, 70
 Divergent flow, 15
 Dolerite, 258
 Drag folds, 14
 Drakensberg flood basalts, 257
 Drakensberg Group, 350
 Drakensberg Group lavas, 267
 Driving pressure, 5, 12
 3D seismic, 288
 3D seismic reflection, 273
 Dyke, 5, 167, 363
 coeval propagation, 174

 cooling during propagation, 176
 composition, 367
 dyke swarm, 3, 5, 6, 41
 en echelon, 2, 5, 6, 41
 feeder, 2, 4
 intravolcanic, 2
 nucleation, 168
 radial, 331
 thickness-to-length ratio, 167
 vertical vs. lateral injection, 367
 Dyke propagation, 168, 170
 Dyke swarm, 41, 295, 363
 Iceland, 365

E

Einstein-Roscoe law, 149
 Elasticity-Dominated materials, 161
 Elastic plate models, 23
 Elasto-plastic materials, 161
 Elba, 182
 Elba Island, 19, 343
 El Reventador Volcano, 198
 Emplacement
 emplacement depth, 331
 level, 6, 13
 Emplacement time, 20, 21
 En-echelon, 7, 12
 Erosional thrust sheets, 17
 Etna, 366
 Extensional settings, 6
 Eyjafjallajökull Volcano, 367, 374

F

Fabric, 21, 28
 Faeroe Islands, 368
 Fall-back breccia, 27
 Faeroe-Shetland Basin, 285
 Feather, 12
 Feeder dyke, 28, 29
 Ferrar large igneous province, 5
 Fiamme, 26, 27
 Finger (magma), 10, 11, 27, 304
 Fissure, 41, 148
 Fissure type eruptions, 44
 Flank collapses, 9
 Flattening, 11
 Flechtingen-Roßlau Block, 295
 Flett Ridge Sill, 287
 Flood basalts, 42, 52, 249
 Floor, 10
 Floor depression, 22, 24
 Floor subsidence, 2
 Flowage differentiation, 19
 Flow banding, 19
 Flow direction, 19, 30
 Flow folds, 14
 Flow foliation, 23, 304

Flow lineations, 14
 Flow lines, 28, 31
 Fluid flow, 268, 283
 Fluidization, 6, 11, 21, 27, 30
 Flux, 75
 Folds, 14
 Foliation, 21
 Forced fold, 180
 Fractional crystallization, 74, 77
 Fracture toughness, 12, 23, 161
 Fragmentation processes, 5
 Franklin Sills, 20
 Funnel sheets, 4

G

Galápagos Islands, 176
 Gas, 269
 Gelatine, 197
 birefringence, 161
 Geodetic measurement, 194
 Geo-logical, 29, 31
 Geothermal heat, 7
 Geothermal systems
 expansion-contraction, 328
 Glencoe caldera, 190
 Golden syrup, 153, 198
 Golden Valley Sill Complex, 352, 356, 359
 Granite sheets, 64
 Granitic mushes, 73
 Granophyres, 26
 Gravitational forces, 3
 Gravity settling, 2
 Grooves, 14, 18
 Ground deformation, 52
 Growth
 emplacement, 7
 horizontal, 3
 incremental, 3, 6
 radial, 3
 two-stage, 3
 vertical, 3
 Guagua Pichincha Volcano, 198

H

Halle Intermediate Subvolcanic Complex, 296
 Halle-type laccolith complex, 296, 305
 Halle Volcanic Complex, 295
 Hazard assessment, 21, 374
 Heart Mountain gravity slide, 18
 Henry Mountains, 8, 17, 182, 305, 327
 earlier models, 336
 geometry data, 337
 Henry Mtns, 4
 Horizontal flow, 5, 28
 Horizontal length, 2
 Host rock, 11
 deflection, 334

 deformation, 333
 faulting, 335, 336
 metamorphism, 331, 341
 Host-rock strength, 190
 Host sediments, 300, 302
 Hot slickenlines, 14
 Hubbert-type shear box, 161
 Hummocks, 24
 Hydraulic fracturing, 167
 Hydrocarbon, 7
 Hydrocarbon migration, 283, 287
 Hydrothermal alteration, 28
 Hydrothermal vent, 2, 4, 151, 200, 350
 Hydrothermal vent complexes, 27, 198, 251

I

Iceland, 176
 Igneous breccia, 26
 Ignimbrite powder, 153, 161
 Ignimbritic dykes, 26
 Ilfeld basin, 296
 Imbricated fabric, 28
 Imbrication (tiling), 19
 Inclined sheets
 concave-downward, 370
 concave-upward, 370
 Iceland, 363, 370
 radial planar, 370
 Incremental emplacement, 62
 Inherited grains, 76
 Inner Hebrides, 273
 Intra-Sudetic basin, 295
 Intrusion
 asymmetric, 335
 emplacement depth, 16, 23
 incremental growth, 328
 lateral propagation, 374
 length-thickness, 10, 11
 sheet-like geometry, 328
 vertical inflation, 8, 306
 volume, 335
 Intrusion growth, 23
 Intrusive/extrusive complexes, 7, 301
 Iron Axis magmatic province, 11
 Isle of Skye, 274

J

Jigsaw texture, 25
 Joints, 12

K

Karoo basin (sill complex), 178, 249, 287, 349
 paleoclimate perturbation, 360
 radiometric ages of sills, 358
 Katmai caldera, 193
 Kimberlite pipes, 151, 200

L

Laboratory experiments, 148
 Laccolith, 4, 8, 10, 19, 303
 aeromagnetic measurements, 340
 central body, 339
 central igneous body, 327
 central limb, 339
 central piston, 2
 Christmas-tree, 2, 4, 5, 10
 crest, 335, 337, 339, 342
 dioritic, 372
 Donnersberg-type, 2, 303
 emplacement, 1, 11, 13, 184
 emplacement depth, 329
 emplacement time, 334, 343
 evolution, 338, 343
 gravitational spreading, 184
 growth, 1, 11, 13, 14, 16
 Halle-type, 2
 height to width ratio, 183
 hinge, 339
 hinge region, 328
 Iceland, 369
 magma viscosity, 149, 184
 multifeeder, 2
 multilayer, 2
 paleomagnetic measurements, 339
 peripheral limb, 339
 regional tectonic control, 184
 roof faulting, 339
 satellite bodies, 2
 satellite intrusion, 328
 satellite zone, 339, 341
 sedimentary rock raft, 340
 stepped base, 340
 volume, 331
 Laccolith complex
 evolution, 338, 343
 Lahar, 3, 6
 Laminar flow, 26
 Landslide, 1, 4, 7
 submarine, 2
 trigger, 28
 La Reunion, 174
 Large Igneous Provinces (LIPs), 5, 43, 249, 349
 Large-volume eruptions, 74, 76
 Large-volume ignimbrites, 74
 Large volume plutons, 74, 76
 La Sal Mountains, 329
 Lateral and vertical growth, 10
 Lateral flow, 5, 42
 Lateral propagation, 30
 Lateral volcanic blasts, 195
 Lava, 2
 Lava flow, 148
 Lava plateaus, 2
 Lava shields, 44
 Layered intrusions, 10
 Layered mafic intrusions, 4, 22, 23

Layering, 25
 Lineation, 21, 30
 Lithophysae, 25, 303
 Lithostatic pressure, 13
 Lobe, 10, 11, 21, 27
 Long pluton lifetimes, 62
 Long valley caldera, 190, 193
 Lopolith, 2, 4, 64

M

Maar-diatremes, 151, 200
 Mafic Microgranular Enclaves (MME), 15, 17
 Mafic sills, 26, 64
 Magma
 cooling, 305
 density, 305
 overpressure, 169
 vesiculation, 18
 Magma ascent rate, 7, 296
 Magma chamber, 4, 41, 48, 153
 mid-crustal, 305
 Magma chamber stresses, 42
 Magma composition, 11
 Magma driving pressure, 5
 Magma emplacement
 ballooning, 6, 304
 incremental, 304
 Magma finger, 283
 Magma flow, 2–5, 15, 21, 28, 30
 Magma flow directions, 15, 52
 Magma fluxes, 74
 Magma intrusion-emplacement, 3
 Magma pathway, 52
 Magma plumbing networks, 57
 Magma plumbing system, 54
 Magma pressure, 6
 Magma productivity, 24
 Magma reservoir, 167
 Magma supply, 21, 23, 24
 Magmatic “folds”, 19
 Magmatic flow, 3, 12, 19
 Magmatic foliation, 19, 23
 Magmatic layering, 25
 Magmatic lineation, 19
 Magmatic lobes
 radial, 336
 Magmatic stress field, 371
 Magma viscosities, 169
 Magnetic carrier, 21
 Magnetic fabric, 20
 Magnetic field intensity, 300
 Magnetic foliation, 20
 Magnetic lineation, 30
 Magnetic lineation is parallel, 20
 Magnetite, 20
 Magnetotelluric data, 274
 Marginal faults, 12
 Markagunt gravity slide, 18, 23

Mars, 2
 Marysvale volcanic field, 18
 Mass extinctions, 250
 Matrix, 2
 Mauna Loa, 18
 Miarolitic cavities, 26
 Mid-ocean ridges, 44
 Minch Sill Complex, 278, 284
 Mineral deposits, 7
 Mineral lineation, 19, 29
 Mineral Mountains, 18
 Mingling, 6
 Mining-induced collapse, 190
 Mixed plumbing system, 57
 Miyakejima caldera, 187, 193
 Model material
 mechanical properties, 151
 Mohr-Coulomb criterion, 158, 161
 Mombacho, 5
 Monte Carlo simulations, 355
 Mount Ayliff Complex, 350
 Mount Belknap caldera, 19
 Mount Ellen, 332, 335
 Mount Ellsworth, 331
 Mount Hillers, 332
 Mount Pennell, 330
 Mount St. Helens, 1, 2, 7, 183, 193, 195
 Mt. Etna, 174
 Mt. Holmes, 330, 340
 Mt. Shasta, 11, 25
 Mud Volcanoes, 151
 Mull, 174
 Multi-layered sills, 11
 Multiple dykes, 7
 Multiple pulses, 23
 Multi-stage model, 12
 Mush columns, 46

N

Natural hazards, 1
 Navajo Mountain, 329
 Nested sill complex, 51, 57
 Neutral buoyancy, 5, 180
 Nevado de Colima, 10
 Newtonian fluid, 149
 Non-brittle, 5
 Non-coaxial, 19
 Non-coaxialflow, 15, 25
 Non-Newtonian, 151
 North Atlantic Igneous Province (NAIP), 275
 North Atlantic volcanic margins, 178
 Northwest Atlantic margin, 274

O

Oblate shapes, 17
 Oceanic anoxia, 249
 Offsets, 7

Oil shows, 257
 Olney pipe, 257
 Ore deposits, 7
 Outer Hebrides, 276
 Overburden, 6, 10
 Overplating, 6
 Oxygen isotope, 260

P

Pahoehoe, 30
 Palisades sill, 20
 Parinacota, 5
 Partial melting, 74, 77
 Patagonia, 19
 Pegmatites, 26
 Peperite, 6, 27
 Peripheral flexure, 13
 Perlite, 303
 Pervasive fractures, 73
 Petroleum system, 268, 273, 278
 Phenocryst frameworks, 304
 Phenocrysts, 2
 Phreatic eruptions, 269
 Phreatomagmatic dykes, 26, 27
 Pipes, 27
 Piston-like, 4
 Piton de la fournaise, 169
 Plinian eruptions, 29
 Plumbing system, 39, 41
 Pluton, 10, 22, 23, 63, 64
 Plutonic-volcanic connection, 77
 Poisson's ratio, 161
 Polygenetic Volcanoes, 44, 57
 Porphyries, 29
 Porphyritic rhyolite, 301
 Porphyry copper, 7
 Protolobes, 7
 Pseudotachylyte, 18, 19
 Pulse, 10
 Punched laccolith, 13, 14, 19
 Pyroclastic dykes, 5, 26

R

Radial growth, 6
 Ramp-and-flat, 5
 Rayleigh number, 165
 Reynolds number, 164, 190
 Rhyolite domes, 48
 Riedel shears, 18
 Rift, 44
 Rifted margins, 274
 Rifted settings, 44
 Ring dyke, 48, 148
 Ring faults, 192
 Rockall Trough, 288
 Rock Eval, 255
 Roof, 10

- Roof lifting, 2, 24
 Ropes, 15
 Ropy flow structures, 283
 Ropy structure, 30
 RTV silicone, 153, 198
- S**
- Saar-Nahe basin, 295
 Sand/silicone models, 197
 Sandfell (laccolith), 369
 Satellite intrusions, 4
 Saucer, 4, 49
 Saucer-shaped sheets, 10
 Scaling laws, 163
 Scour marks, 14
 Sector collapse, 2, 9
 Sedimentary basins, 7
 Sedimentary raft, 11, 283
 Sediment raft, 304
 Seismic bursts, 176
 Seismicity
 dyke-induced, 169
 Sense of flow, 15, 28
 Shallow-level intrusions, 1, 2
 Shallow magma chambers, 373
 Shallow plutons, 74
 Shape (intrusion)
 bell-jar, 9, 14
 Shape
 bell-jar, 6
 tabular, 6
 Shape-Preferred Orientation (SPO), 15
 Sheeted intrusion, 153, 304
 Sheet-like bodies, 23
 Sheet-like pulses, 20
 Sheets
 (sub-)horizontal, 6, 8
 Shiveluch, 9
 Showa-Shinzan, 11
 Showa-Shinzan uplift, 183
 Sieved ignimbrite, 198
 Silica flour, 153, 161, 198
 Silicone oil, 151
 Silicone polymer, 149
 Silicone putty, 162, 198
 Sill, 1–4, 5, 6, 10, 16, 42, 148, 178
 aspect ratio, 368
 composition, 356
 contact aureole, 353
 convex top surface, 283
 cooling during emplacement, 182
 cumulative volume, 349
 depth of emplacement, 351
 formation, 363
 gas show, 268, 360
 geometry, 351, 363
 geometrybore hole data, 353
 hydrocarbon reservoirs, 180
 hydrocarbon trap, 179
 Iceland, 367
 intravolcanic, 2
 lateral extent, 359, 367
 mafic, 6, 8, 20, 23
 magmatic differentiation, 350
 oil show, 360
 ring dyke, 3, 4, 190
 saucer-shaped, 2, 7, 8, 180
 (sub-)horizontal, 10
 top contact, 283
 Sill complexes, 44
 Sill lobes, 281
 Slaufudalur pluton, 190
 Slide, 4
 Slumps, 49
 Socompa, 5
 Solid-state deformation, 3, 29
 Solid-state fabric, 30
 Solid-stateflow, 21, 22
 Solitario lacco-caldera, 341, 343
 Soufriere Hills, 9
 Spatial distribution patterns, 304
 Spherulites, 25, 303
 Spherulitic nodules, 26
 SPO, 20, 28, 31
 Stacked intrusions, 8
 Stardalur (mafic laccolith), 370
 Steps, bridges, 5, 7
 Stocks, 182
 Strain rates, 23
 Stratovolcano, 1, 44, 363
 Streitishorn dyke, 170
 Stress field
 far field component, 197
 Stretched crystals, 23
 Stretching lineations, 29
 Striations, 18
 Strike-slip settings, 5
 Stromboli, 366
 Structures, 1
 Subhorizontal sheets, 7
 Sub-volcanic plumbing systems, 40, 57
 Surface displacement
 geodetic measurement, 328
 recent, 328
- T**
- Tabular intrusion, 23
 Tejada caldera, 193
 Tenerife, 174
 Tensile fracture, 280
 Thermal fluidization, 27
 Thermal gradients, 3
 Thermal lifetimes, 62, 64
 Thermal modelling, 263
 Thermogenic gas hypothesis, 250
 Thickness, 2, 10, 11, 16, 17, 19

Thuringian Forest, 296
Thverartindur igneous centre, 373
Timescales, 20, 24, 46, 63
Titanite, 73, 74
Tongues, 11
Toreva blocks, 5
Torres del Paine, 185
Total Organic Carbon (TOC), 255, 278, 289
Trachyte Mesa, 341
Transtensional basin systems, 296
Trawenagh Bay Granite, 341
Triggered fluidization, 27
Tromen Volcano, 198
Trotternish/Minch Sill Complex, 274
Tsunami, 3, 29
Tushar Mountain, 18
Two-stage growth, 6, 22

U

Underplating, 6, 12
Unerrupted magma, 63
Unzen, 11
Upwards flow, 42
Usu Volcano, 183

V

Valles caldera, 193
Vegetable oil, 153, 198
Venus, 2
Vertical and horizontal growth, 6
Vertical flow, 28
Vertical growth, 11
Vertical inflation, 11, 30

Vertical stacking, 20, 23, 24
Vesicles, 17, 283, 304
Visco-elastic, 151
Viscometer, 149, 153
Viscosity, 305
Vitrinite, 255
Vitrinite reflectance, 26, 291
Volcanic destabilization, 27
Volcanic field collapse, 18
Volcanic fissure, 365
Volcanic plumbing systems, 148
Volcanic-plutonic connection, 63–65
Volcanic rifted margins, 52
Volcanic vents, 5
Volcano monitoring, 373

W

Wall rock, 14
Wave, 14, 23
Waveforms, 30
Wrinkles, 14

X

Xenolith, 15, 17

Y

Young's modulus, 161

Z

Zircon growth, 75, 76